

AD-A231 631

(12)

DTIC FILE COPY
Final Report of Research

to

Office of Naval Research

"The Effect of Propellant Optical Properties on Composite Solid Propellant Combustion"

Principal Investigator: M. Q. Brewster

Department of Mechanical and Industrial Engineering
University of Illinois, Urbana

Contract No. N00014-87-0547
Period (original): July 1987 - June 1990
(with extension): July 1987 - December 1990

January 1991



Summary of Research Results

The results of this research program are summarized below in five categories. Only a brief synopsis of the results and their significance are given here. Details are provided in attached technical reports (indicated by TR) and publications (indicated by P). These technical reports and publications are numbered according to the Index of Technical Reports and Index of Publications which follow.

1. Propellant Optical Properties (TR-1)

The optical properties of Ammonium Perchlorate (AP)-Aluminum (Al)-composite solid propellants are discussed. A model is developed to calculate propellant radiative properties (such as absorptivity) from fundamental constituent parameters, such as particle size, concentration, etc. This capability is of importance in laser ignition and all types of radiation-augmented combustion of solid propellants, including oscillatory laser flux-driven combustion instability studies.

2. Combustion of Aluminum Droplets with Water

- droplet burning rate (TR-7, TR-8)
- radiative emission (TR-8, P-2, P-5)

The combustion characteristics of aluminum droplets with water as an oxidizer are important for many applications including solid propellants and underwater explosives. The results of a relatively simple diffusion-limited droplet combustion model indicated that radiative transfer effects are important. The difference between the radiative environment of an aluminized rocket motor chamber and that of a laboratory (where most droplet burning rate studies are conducted) is significant; whereas, the difference in convective environment is probably not. Radiant emission from a vigorously burning aluminum droplet is dominated by emission from an optically thin (but very hot) detached flame envelope which surrounds the droplet. The chief emitter in the detached flame is sub-micron, molten aluminum oxide particles.

3. Aluminum Oxide Optical Properties (TR-2, TR-4, P-3)

The optical properties (size and complex refractive index) of sub-micron, molten aluminum oxide particles are important in determining the radiative energy balance (and therefore combustion rate) of burning aluminum droplets as well as the radiative feedback to burning aluminized propellents. In-situ light scattering and extinction measurements were used to determine the optical constants and size of Al_2O_3 in propellant flames.

4. Influence of Metals on Steady State Propellant Combustion (TR-3, TR-9, P-1, P-6, P-7, P-8)

The steady state combustion characteristics of metalized (particularly aluminized) propellants have long been thought to be little influenced by the behavior of the metal near the propellant surface. However, new

evidence has been obtained of the influence that metal combustion plays in the overall combustion behavior of the propellant through both conductive and radiative heat feedback from the burning metal to the propellant. Quench bomb tests, thermocouple temperature measurements, fiber optic radiation measurements and rapid de-pressurization were used to investigate the influence of burning metals (aluminum, magnesium and boron) on propellant combustion. The nature of the metal-propellant interaction was found to be very dependent on the type of metal; however, in most cases radiative feedback, which is usually ignored in propellant combustion studies, was found to be a significant factor.

5. Oscillatory Radiant Heat Flux Technique for Measuring Solid Propellant Combustion Instability (TR-5, TR-6, TR-10, TR-11, TR-12)

The oscillatory radiant heat flux method represents a promising alternative to the T-burner method for characterizing combustion instability of solid propellants. It is much quicker and less expensive and appears to be one of the primary techniques used by the Soviets, if not the primary technique. However, it has not been widely used in the United States. Initial progress has been made in this study in developing a combustion model so that radiant heat flux-coupled data can be converted to pressure-coupled data. A collaborative effort has been established with researchers at the Naval Weapons Center (China Lake) which has been very fruitful. Support is being sought from ONR to continue this aspect of the study.

Summary of Student Support

Student	Date of Graduation	Degree	ONR Support
B. E. Hardt	January 1989	M. S.	Full
D. L. Parry	May 1989	Ph.D.	Partial
T. Prevish	May 1990	M. S.	Full
M. R. Jones	August 1990	M. S.	Full
A. Ishihara	January 1991	Ph.D.	Partial
K.C. Tang	May 1991	Ph.D.	Partial
S. F. Son	1993 (expected)	Ph.D.	Full

Statement "A" per telecon Dr. Richard Miller Office of the Chief of Naval Research Code 1132P Arlington, Va.

22217-5000

VHG

2/7/91

COPY ASPECTED

Attachment to:

FROM: CDR ARD

TO: DR. RICHARD MILLER

DATE: 2/7/91

RE: Statement "A" per telecon Dr. Richard Miller

22217-5000

VHG

2/7/91

By *treat as one report per*

Dr. Richard Miller

22217-5000

VHG

2/7/91

A-1

Distribution of Final Report

Scientific Officer (1 copy)

Dr. Dick Miller
Program Manager, Propulsion and Energetics
Code 1132P
Office of Naval Research
800 North Quincy Street
Arlington, Virginia 22217-5000

Administrative Contracting Officer (1 copy)

John Chiappe
Office of Naval Research Resident Representative
Room 286
536 South Clark Street
Chicago, Illinois 60605-1588

Director Naval Research Laboratory (6 copies)

Director of Naval Research Laboratory
Attn: Code 2627
Washington, D. C. 20375

Defense Technical Information Center (12 copies)

Defence Technical Information Center
Building 5
Cameron Station
Alexandria, Virginia 22314

Index of Technical Reports

1. Brewster, M. Q. and B. E. Hardt, "Selective Radiation Absorption in Aluminized Composite Propellant Combustion," 24th JANNAF Combustion Meeting, October 1987, Monterey, CA, CPIA Publication 476, Vol. 1, pp. 157-163.
2. Parry, D. L. and M. Q. Brewster, "Optical Constants and Size of Propellant Combustion Aluminum Oxide (Al_2O_3) Smoke," AIAA/ASME/SAE/ASEE 24th Joint Propulsion Conference, July 1988, Boston, MA, paper AIAA 88-3350.
3. Hardt, B. E. and M. Q. Brewster, "Investigation of Al and Mg/Al Alloy Behavior in Composite Solid Propellant Combustion," 25th JANNAF Combustion Meeting, October 1988, Huntsville, AL, CPIA Publication 498, Vol. 1, pp. 199-206.
4. Parry, D. L. and M. Q. Brewster, "Propellant Al_2O_3 Particle Size and Optical Constants from In-Situ, Inverse Light Scattering and Extinction Measurements," 25th JANNAF Combustion Meeting, October 1988, Huntsville, AL, CPIA Publication 498, Vol. 3, pp. 283-292.
5. Prevish, T. and M. Q. Brewster, "Combustion Response of a Homogeneous Solid Propellant to an Oscillatory Radiant Heat Flux," Western States Section - The Combustion Institute, March 1989, Pullman WA, paper 89-30.
6. Prevish, T. and M. Q. Brewster, "Combustion Response of Solid Propellants to Oscillatory Radiant Heat Flux," 26th JANNAF Combustion Meeting, October 1989, Pasadena, CA, CPIA Publication 529, Vol. 2, pp. 127-142.
7. Brewster, M. Q. and K. C. Tang, "Combustion of Aluminum and Water," Progress Report 1989, Department of Mechanical and Industrial Engineering, University of Illinois, Urbana, IL.

8. Jones, M. R., M. Q. Brewster, and K. C. Tang, "An Investigation of the Combustion of Aluminum in Water," 26th JANNAF Combustion Meeting, October 1989, Pasadena, CA, CPIA Publication 529, Vol. 2, pp. 213-222.
9. Ishihara, A., M. Q. Brewster, T. A. Sheridan, and H. Krier, "The Influence of Radiative Heat Feedback on Burning Rate of Metalized Propellants," 27th JANNAF Combustion Meeting, November 1990, Cheyenne, WY, CPIA Publications.
10. Finlinson, J . C., D. Hanson-Parr, S. F. Son, and M. Q. Brewster, "Measurement of Propellant Combustion Response to Sinusoidal Radiant Heat Flux," 27th JANNAF Combustion Meeting, November 1990, Cheyenne, WY, CPIA Publications.
11. Finlinson, J . C., D. Hanson-Parr, S. F. Scn, and M. Q. Brewster, "Measurement of Propellant Combustion Response to Sinusoidal Radiant Heat Flux," 29th Aerospace Sciences Meeting, January 1991, Reno, NV, paper AIAA-91-0204.
12. Son, S. F., R. F. Burr, M. Q. Brewster, J. C. Finlinson, and D. Hanson-Parr, "Nonsteady Burning of Solid Propellants with an External Radiant Heat Flux: A Comparison of Models with Experiment," AIAA/ASME/SAE/ASEE 27th Joint Propulsion Conference, June 1991, Sacramento, CA.

Index of Publications

1. Brewster, M. Q. and D. L. Parry, "Radiative Heat Feedback in Aluminized Solid Propellant Combustion," *J. Thermophysics and Heat Transfer*, Vol. 2, No. 2, April. 1988, pp. 123-130.
2. Brewster, M. Q. and D. M. Taylor, "Radiative Properties of Burning Aluminum Droplets," *Combustion and Flame*, Vol. 72, 1988, pp. 287-299.
3. Parry, D. L. and M. Q. Brewster, "Optical Constants of Al_2C_3 Smoke in Propellant Flames," *J. Thermophysics and Heat Transfer*, Vol. 5, No. 1, Jan. 1991.
4. Brewster, M. Q., "Heat Transfer in Heterogeneous Propellant Combustion Systems," to appear in *Annual Review of Heat Transfer, Volume IV*.
5. Jones, M. R. and M. Q. Brewster, "Radiant Emission from the Aluminum-Water Reaction," to appear in *Journal of Quantitative Spectroscopy and Radiative Transfer*.
6. Brewster, M. Q. and B. E. Hardt, "Influence of Metal Agglomeration and Heat Feedback on Composite Propellant Burning Rate," to appear in *Journal of Propulsion and Power*.
7. Ishihara, A., M. Q. Brewster, T. A. Sheridan, and H. Krier, "The Influence of Radiative Heat Feedback on Burning Rate in Metalized Propellant," to appear in *Combustion and Flame*.
8. Tang, K. C. and M. Q. Brewster, "Analysis of Radiative Heat Transfer in an Aluminum Distributed Combustion Region," submitted to *Journal of Heat Transfer*.

SELECTIVE RADIATION ABSORPTION IN
ALUMINIZED COMPOSITE PROPELLANT COMBUSTION

M. Q. Brewster and B. E. Hardt
University of Illinois
Urbana, Illinois

ABSTRACT

This paper describes the optical properties of aluminized AP composite propellants, including Fe_2O_3 . The correlation between spectral absorptivity and propellant composition is investigated. The possibility of selective aluminum heating due to absorption of radiation by aluminum is discussed. And a possible link between optical properties and catalytic behavior of transition metal oxides in aluminized AP composite propellants is suggested.

INTRODUCTION

The effect of thermal radiation on the combustion of non-metallized solid propellants has been studied by many investigators¹⁻⁵. It has been shown that radiative heat flux is equivalent to an increase in initial temperature and that burn rate is a strong (nearly linear) function of radiative flux. In most of these studies which report experimental results, incident radiation has been absorbed by black opacifying agents (in the case of double base propellants) or by oxidizer crystals (in the case of composite propellants). Little attention has been given to the absorption of radiation by aluminum or catalyst particles which are usually present in solid propellants⁶. Yet, in the absence of special opacifiers, it is these two constituents which dominate the absorption of radiation from aluminized propellant flames. This paper describes the optical properties of aluminized AP composite propellants and considers the possible effects of radiative heat feedback on combustion behavior.

OPTICAL PROPERTIES OF COMPOSITE PROPELLANTS

To understand how aluminized composite propellants absorb radiation it is necessary to examine the optical properties of the individual constituents. In this paper the infrared and optical properties of AP, aluminum and ferric oxide will be considered. First the single scattering properties of the constituents will be discussed.

SINGLE SCATTERING PROPERTIES

Ammonium Perchlorate. Based on Fresnel reflectance measurements, FTIR transmission measurements and a dispersion equation curve fit, the optical constants (complex refractive index) of propellant grade AP have been determined⁷. Ammonium perchlorate is non-absorbing in the visible and near infrared (0.4 to 2.7 μm) and becomes absorbing in the infrared region (2.7 to 3.8 and 4.3 to 11.8 μm). Therefore AP is predominantly transparent to high temperature radiation ($>3000\text{K}$), such as arc-image radiation or emission from burning aluminum droplets, and opaque to low temperature radiation ($<1000\text{K}$).

Since AP is present as crystalline particles in the propellant its single scattering properties must also be considered. Although not perfect spheres, propellant AP crystals may be modeled as spheres since there is no systematic deviation from sphericity which would warrant a non-spherical treatment. The general treatment for single scattering by homogeneous spheres is the Mie theory, which must be used when particle size is the order of the wavelength. However, as is the case for most propellant AP, when the particles are much larger than wavelength the simpler results of geometric optics may be used for the single scattering properties. Also, the particles of a given mode size (e.g. 24 μm , 180 μm , etc.) may be treated as monodisperse for the purpose of determining single scattering properties.

Aluminum. The optical constants of aluminum have been studied extensively and are very well characterized⁸. Aluminum is a good reflector throughout the visible and infrared region, with reflectivity increasing from 90 percent in the visible and near infrared to 98 percent in the infrared region. Although aluminum readily forms an oxide skin when exposed to the atmosphere, the thickness of the skin is small enough (tens of angstroms) that the reflectivity is diminished only a few percent by the dielectric oxide. Upon heating in an oxidizing environment, the thickness of the oxide skin will increase. However a significant decrease in reflectivity will not occur until

This work was performed under grant N00014-87-K-0547 with the Office of Naval Research.
Approved for public release; distribution is unlimited.

the oxide melts. Like AP, propellant aluminum particles may also be treated as monodisperse spheres for determining the single scattering properties and the particles are usually large enough that the geometric optics relations hold.

Ferric Oxide. Ferric oxide (Fe_2O_3) is a transition metal oxide which behaves optically like a semi-conductor. For photon energies above the fundamental energy gap ($0.6 \text{ } \mu\text{m}$ wavelength at 300K) ferric oxide absorbs radiation. In the near infrared and infrared regions (0.6 to $14 \text{ } \mu\text{m}$) it does not absorb. Several studies have reported on the optical properties of ferric oxide at 300K⁹⁻¹¹.

At temperatures above 300K property data are scarce. However it is likely that the absorption edge would shift to longer wavelengths and absorption in the band gap would increase as temperature increased. These trends would agree with reported visual observations of ferric oxide turning from red to black upon heating to nearly 1400K, and back to red again upon cooling¹². This temperature dependence could be very important in solid propellants, since the spectral absorptivity could change markedly as the propellant surface temperature increased. Absorption during ignition, for example, could be very different from that during steady state combustion. Unfortunately, the temperature dependence of the optical constants has not been well documented and can only be estimated at this time.

Ferric oxide and other catalyst particles used in solid propellants are typically non-spherical and sub-micron in size to achieve high specific surface area. They are usually the smallest particulate constituent in the propellant. This means that even for very small mass fractions (less than one percent) catalyst particles, if present, will usually dominate the optical properties of the propellant. This statement holds true for ferric oxide at 300K through the visible and near infrared regions. An exception occurs in the infrared for ferric oxide because the imaginary refractive index becomes very small and Rayleigh scattering occurs. Since Rayleigh scattering is characterized by very small scattering cross-sections, the optical properties of another constituent (either aluminum or AP, depending on wavelength) will become more dominant in the infrared.

From just this much discussion it can be seen that the single scattering properties of composite propellant constituents are very complex functions of composition, particle size and wavelength. To maintain a tractable solution, the assumption of homogeneous, spherical, monodisperse particles is made for each of the constituents and Mie theory used to calculate the single scattering properties. Optical constants ($n-i_k$) are taken from the references noted above.

MULTIPLE SCATTERING PROPERTIES

To determine the effective absorptivity of a composite propellant, the single scattering properties described above must be combined with a solution of the radiative transfer equation to yield the fraction of incident radiation which would be absorbed by the propellant, including the effect of multiple scattering. A solution of the transfer equation applied specifically to composite solid propellants has been described elsewhere⁶ using the two-flux model. Since the two-flux model is well known and details are contained in Ref. 6 only results will be presented in this paper.

Propellant Formulation. The formulation to be considered for illustrating the effect of optical properties is a bimodal AP composite propellant with the following composition: 49 percent (by mass) large AP, 21 percent small AP ($24 \text{ } \mu\text{m}$), 16 percent aluminum ($25 \text{ } \mu\text{m}$), 0, 0.5, and 1.5 percent ferric oxide ($0.1 \text{ } \mu\text{m}$) and the rest transparent binder. The large AP is assumed to be much larger than the other constituents such that it is more appropriate to consider the optical properties of the "pocket propellant" between the large AP particles separately. The composition of the pocket propellant then becomes 41 percent AP, 31 percent aluminum and between 0 and 3 percent ferric oxide.

Spectral Absorptivity. The spectral absorptivity of the pocket propellant is calculated as described above using the Mie single scattering properties for the various propellant constituents in the two-flux transfer equation solution. The results for $0.1 \text{ } \mu\text{m}$ ferric oxide particles are given in Fig. 1.

For the case of no catalyst particles, it can be seen in Fig. 1 that aluminum and AP dominate the spectral absorptivity of the propellant. In the visible region (0.4 to $0.7 \text{ } \mu\text{m}$) aluminum dominates the absorptivity because the AP is transparent. The magnitude of the absorptivity in this region is fairly constant at about 0.45 which corresponds to the gray appearance characteristic of aluminized propellants containing no catalysts or opacifiers. In comparison with the single scatter absorptivity for aluminum of 0.1 in the visible, the effective value of 0.45 is substantially higher due to the influence of multiple scattering. Beyond the visible region the absorptivity decreases to a minimum of 0.22, corresponding to a single scatter absorptivity of 0.02 at $2.0 \text{ } \mu\text{m}$. From 2.7 to 3.8 and 4.3 to $10 \text{ } \mu\text{m}$ the absorptivity has a value of 0.82 which is due to absorption by AP.

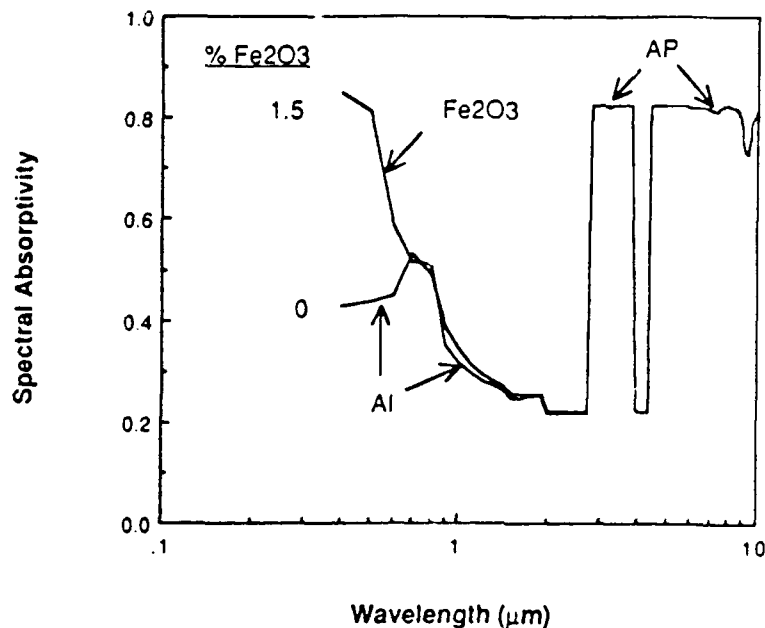


Fig. 1 Spectral Absorptivity of Al/AP/Fe₂O₃ Propellant at 300K

As the percentage of 0.1 μm ferric oxide is increased from 0 to 1.5 it can be seen in Fig. 1 that over most of the spectrum absorptivity is unchanged. However in the visible region the absorptivity increases, especially at 0.4 to 0.5 μm , due to the influence of the red catalyst. The absorptivity decreases with increasing wavelength from 0.4 to 0.7 μm , accounting for the reddish color of propellants containing this catalyst.

Total Absorptivity and Emissivity. It is also interesting to examine how the total absorptivity and emissivity of the propellant are influenced by the propellant composition. The total absorptivity is calculated for incident radiation with the spectral distribution of a blackbody at 400K. This is an estimate of the spectral distribution (and not necessarily the magnitude) of the radiation which would be emitted back to the propellant surface by burning aluminum droplets¹³⁻¹⁴. The total emissivity is calculated based on 1000K, which is an estimate of the surface temperature. Two curves each for total emissivity and absorptivity as a function of ferric oxide percentage are plotted in Fig. 2. The curve labelled 0.6 is for the room temperature ferric oxide optical constants which display a cutoff wavelength (transition from absorption to non-absorbing) at 0.6 μm . The curve labelled 1.6 assumes a shift of the absorption edge to 1.6 μm and is intended to illustrate the shift in optical properties which might be expected as a result of heating ferric oxide to temperatures near 1000K.

For the set of curves in Fig. 2 for 300K ferric oxide (cutoff wavelength = 0.6) it is seen that the total emissivity is greater than the total absorptivity. This can be understood by considering the spectral distributions of 4000K and 1000K blackbody radiation and the spectral absorptivity of Fig. 1. The Planck function is weighted heavily in the visible and near infrared for 4000K radiation, and primarily in the infrared for 1000K radiation. The total emissivity is influenced strongly by the AP contribution at infrared wavelengths while the total absorptivity is influenced mostly by the aluminum and ferric oxide contributions at visible and near infrared wavelengths. The total emissivity is rather insensitive to the percentage of ferric oxide while the total absorptivity increases as ferric oxide percentage increases. As the cutoff wavelength is increased from 0.6 to 1.6 the sensitivity of total absorption to percentage ferric oxide increases dramatically.

It is important to consider some of the major sources of uncertainty in the foregoing analysis. One major characteristic of AP propellant combustion which has been ignored here is the liquid layer which has been observed on the surface of deflagrating AP crystals at moderate pressures, 3 to 7 MPa (500 to 1000 psi). The optical properties of this liquid layer may be quite different from those of solid AP. Yet, as far as emission by the propellant is concerned the optical properties of the hot liquid layer would be more important than those of the colder underlying AP. If the hot liquid layer was non-absorbing in the infrared as well as the visible region, then the addition of catalyst particles would tend to increase the total emissivity of the propellant, in contrast to the results just considered. In addition there is the uncertainty in the high temperature optical properties of ferric oxide, which has already been noted.

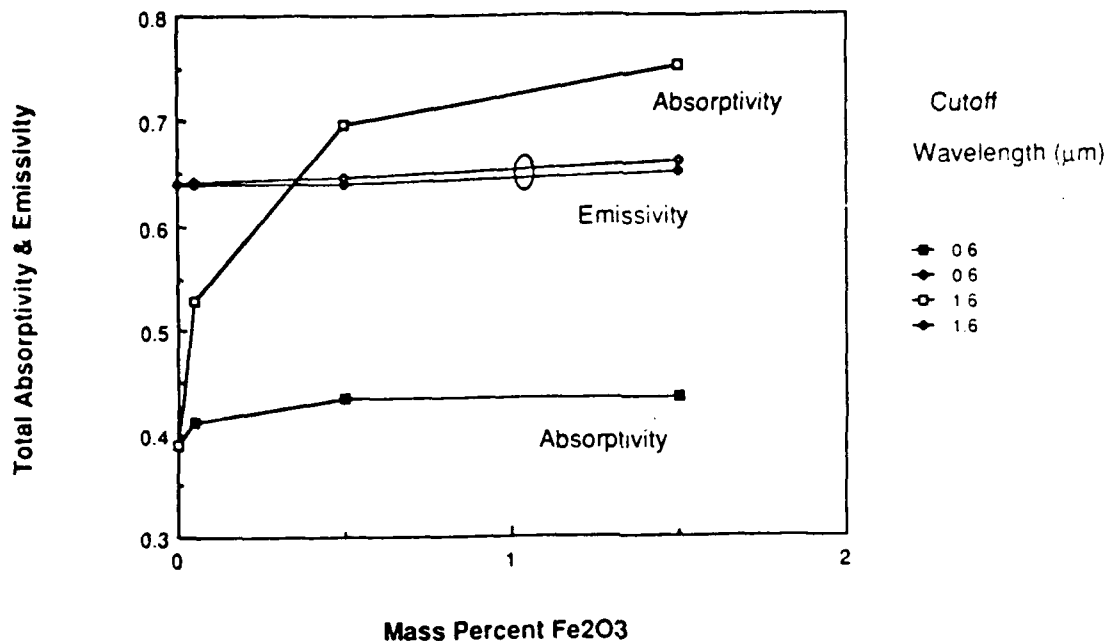


Fig. 2 Total Absorptivity and Emissivity of Al/AP/Fe₂O₃

SELECTIVE HEATING OF ALUMINUM BY ABSORPTION OF RADIATION

One of the possible effects which arises as a result of the spectrally selective nature of composite propellants, is the selective, in-depth heating of aluminum by absorption of radiation. Radiative heat feedback in aluminized propellants is generated by burning aluminum droplets near the surface of the propellant. The spectral distribution of this radiation is probably similar to that of a 4000K blackbody while the actual flux level is comparable to a 3000K blackbody (450 W/cm²). This level of flux represents approximately 20 percent of the total energy flux required to heat the solid propellant. Moreover, it is concentrated in the visible and near infrared spectral region where it will be selectively absorbed by aluminum. Since the AP and binder surrounding the aluminum are relatively poor thermal conductors, it is conceivable that the aluminum could be selectively heated, below the surface of the propellant, particularly in the absence of any catalyst or opacifier particles.

In an earlier paper, Brewster and Patel⁶, investigated theoretically the phenomenon of selective radiative heating of aluminum by solving the coupled aluminum and AB/binder energy equations as well as the radiative transfer equation. It was concluded in that work that it was possible for aluminum to reach temperatures several hundred degrees (K) above the surrounding temperature and that the aluminum temperature wave extended as much as ten times deeper into the propellant than the surrounding matrix temperature wave. However those conclusions were based on a thermal conductivity for the AP/binder matrix which was probably an order of magnitude too small (4×10^{-4} W/cmK) and aluminum optical properties which overestimated the aluminum absorptivity substantially. Consequently, the problem has been reconsidered here, using what are felt to be more accurate thermophysical and optical properties. The AP/binder matrix thermal conductivity has been increased to 4×10^{-3} W/cmK, and the reflectivity of aluminum has been increased to correspond to the actual aluminum properties rather than the properties of the oxide skin.

The governing equations and their solution have been presented elsewhere⁶ and only the pertinent results for the selective aluminum heating problem will be given here. Input parameters include the propellant optical properties and characteristics of the incident radiation which have been described above. The burn rate is assumed to be 0.93 cm/s, the surface temperature is assumed to be 1000K, and the percentage of ferric oxide is zero. For these conditions the aluminum and matrix temperatures are plotted as a function of distance below the propellant surface in Fig. 3. It can be seen that there is no increase in aluminum temperature over the matrix due to selective absorption. In fact, the aluminum temperature remains slightly below the matrix temperature, indicating that selective radiative heating of aluminum below the propellant surface is probably not a significant concern.

In Fig. 4 the temperature of an aluminum particle as it arrives at the surface is plotted as a function of aluminum diameter for an assumed matrix surface temperature of 1000K. For very fine aluminum (<5 μm) heat conduction from the matrix is very efficient and the aluminum temperature

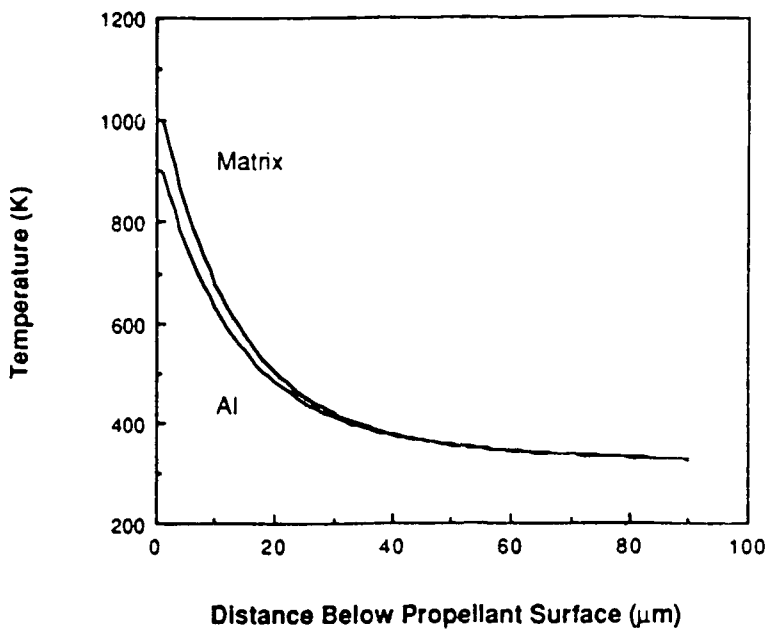


Fig. 3 Aluminum and Matrix Temperature Profile in Al/AP Propellant

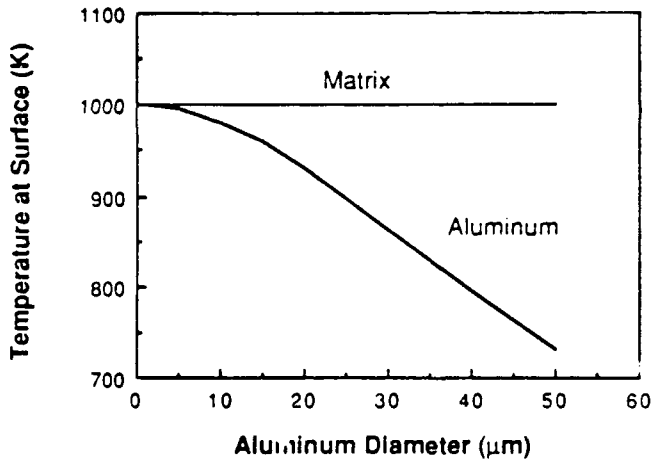


Fig. 4 Aluminum Temperature upon Arrival at Propellant Surface

keeps up with the matrix. As the aluminum size increases heat conduction from the matrix becomes less efficient and the aluminum temperature tends to lag further behind that of the matrix. It should be noted that for aluminum sizes of the order of the thermal wave thickness or greater ($>20\mu\text{m}$) trace dimensional conduction effects, which are not included here, would become important. The significant result of this analysis, however, is that selective radiative heating of aluminum above the matrix temperature does not appear to be a concern, for any size of aluminum.

RADIANT VS. MOLECULAR HEAT FLUX

It is of interest to compare the magnitudes of the molecular (conductive) heat flux at the surface of the propellant from Fig. 3 with the absorbed radiative flux. The molecular heat flux at the surface, from Fourier's law, using a thermal conductivity of $4 \times 10^{-3} \text{ W/cmK}$, is 1880 W/cm^2 . The incident radiant flux is 460 W/cm^2 . The total absorptivity from Fig. 2 is 0.39, giving an absorbed radiant flux of 180 W/cm^2 . Radiation therefore represents 9 percent of the total energy flux required to heat the uncatalyzed solid propellant. By adding small quantities of ferric oxide this percentage could probably be doubled. This reasoning suggests the possibility that propellant optical properties may be playing a role in the observed catalytic behavior of transition metal oxides, such as Fe_2O_3 , Cu_2O , Cr_2O_3 , and copper chromite.

SPECTRALLY SELECTIVE OPTICAL PROPERTIES OF CATALYSTS

It has been observed that certain compounds, notably the transition metal oxides Fe_2O_3 , Cu_2O , Cr_2O_3 and copper chromite are particularly effective in catalyzing AP monopropellant and composite propellant deflagration^{12,15-18}. It has also been observed that small concentrations of these compounds inhibit combustion by increasing the low pressure deflagration limit, while higher concentrations enhance combustion by decreasing the low pressure limit¹⁵⁻¹⁸. It has been suggested that this behavior may be due to a balance between radiative heat loss from the surface and radiative feedback from the flame¹⁶⁻¹⁷. At small catalyst concentrations the surface emissivity would be higher than if no catalyst were present, which would increase the surface radiative loss. At high catalyst concentrations the surface emissivity would be saturated and the emissivity of the flame would begin to increase as the concentration of catalyst particles in the flame increased. Thus radiative heat loss from the surface could partially explain the influence of certain catalyst particles on AP deflagration.

It is interesting to speculate on a possible correlation between optical properties and the effectiveness of various catalysts. Most of the transition metal oxides which are effective catalysts also behave optically as semi-conductors. That is, they absorb and emit photons in the shorter wavelength visible region (photon energies above the fundamental band gap) and they do not absorb at longer infrared wavelengths. This behavior tends to make these materials more favorable for reducing surface radiation loss from deflagrating AP. The presence of these particles in the propellant and in the flame would selectively enhance emission of visible and near infrared photons by the hot flame while minimizing the increase of longer wavelength infrared emission by the surface of the propellant.

There is some evidence in support of this mechanism which comes from a study of thermal-radiative feedback using both copper chromite (spectrally selective) and carbon black (non-spectrally selective) particle additives in pressed AP pellets¹⁷. When carbon alone was added to AP the low pressure limit was found to increase with carbon percentage until the carbon content was high enough (20 percent) to begin to increase the flame temperature thermochemically. Only then did the low pressure limit begin to decrease. This could be because the high surface emission loss due to the carbon particles could not be offset by radiative feedback until the carbon content became so high that the flame thermochemistry began to be altered. When a mixture of carbon black and copper chromite was tried very different behavior was observed. With a fixed copper chromite fraction of 1 percent the carbon fraction was varied from 0.1 to 2 percent. From 0.1 to 1 percent carbon the low pressure limit decreased from 6.8 MPa (1000 psi) to 0.34 MPa (50 psi). From 1 to 2 percent carbon the low pressure limit increased from 0.34 MPa (50 psi) to 0.68 MPa (100 psi). These levels of carbon are two low for the observed variation of the low pressure limit to be attributable to changes in flame thermochemistry. Since copper chromite content was fixed it is also unlikely that catalytic effects were playing a role in the observed behavior.

In light of the difference in optical properties between carbon black and copper chromite it is possible to offer an explanation to the observations just described in terms of the balance between radiative loss from the propellant surface and radiative feedback from the flame. As carbon content increased from 0.1 to 1 percent, copper chromite (a selective emitter and absorber) dominated the surface emissivity of the pellets, and maintained a relatively constant surface emissivity. The flame emissivity and radiative feedback increased, due to the increasing carbon content in the gas phase. As a result low pressure limit decreased. As carbon content increased from 1 to 2 percent, the carbon (a non-selective absorber and emitter) began to dominate the surface emissivity and emission loss from the surface increased. As a result the low pressure limit began to increase.

SUMMARY

There is a significant radiant flux ($300-500 \text{ W/cm}^2$) generated by aluminum combustion near the surface of aluminized composite propellants. This radiant energy occurs primarily in the visible and near infrared spectral regions, where AP is non-absorbing, and the optical properties of the propellant are dominated by other constituents such as aluminum and catalyst particles.

The possibility of selective absorption of this radiant energy by aluminum, leading to subsurface heating, melting and agglomeration of aluminum, has been investigated. It appears that the process of heat transfer to the surrounding matrix is efficient enough that the aluminum and matrix will stay nearly in thermal equilibrium with each other.

The possibility of selective absorption of the radiant flux by catalyst particles has also been investigated. A possible link between optical behavior and effectiveness as a burn rate catalyst has been suggested. It has been observed that many compounds which are effective catalysts of AP monopropellant and AP/aluminum composite propellant combustion are also spectrally selective absorbers with a sharp absorption edge in the visible or near infrared region. It also appears that the temperature dependence of the optical properties of the catalyst may be very important in

this regard. Since a satisfactory theory of catalytic behavior is still lacking it would seem appropriate to continue the investigation of a possible link between propellant optical properties and combustion behavior, particularly in aluminized propellants.

REFERENCES

1. Caveny, L.H., Ohlemiller, T.J. and Summerfield, M., "Influence of Thermal Radiation on Solid Propellant Burning Rate," AIAA J., Vol. 13, No. 2, Feb. 1975, pp. 202-205.
2. Ibiricu, M.M. and Williams, F.A., "Influence of Externally Applied Thermal Radiation on the Burning Rates of Homogeneous Solid Propellants," Combustion and Flame, Vol. 24, 1975, pp. 185-198.
3. Penner, S. and Olfe, O., "The Influence of Radiant Energy Transfer on Propellant Burning Rates," Astronautica Acta, Vol. 11, No. 1, 1965, pp. 65-78.
4. Horton, M.O. and Youngberg, L.Z., "Effect of Radiant Energy on the Burning Rate of a Composite Solid Propellant," AIAA J., Vol. 8, No. 10, Oct. 1970, pp. 1738-1741.
5. Coates R.L. and Kwak, S., "Effect of External Radiation on the Burning Rates of Solid Propellants," J. Spacecraft and Rockets, Oct. 1972, pp. 742-745.
6. Brewster, M.Q. and Patel, R.S., "Selective Radiative Preheating of Aluminum in Composite Solid Propellant Combustion," J. Heat Transfer, Vol. 109, Feb. 1987, pp. 179-184.
7. Patel, R.S. and Brewster, M.Q., "Optical Constants of Propellant-Grade Ammonium Perchlorate," AIAA J., Vol. 24, No. 11, Nov. 1986, pp. 1878-1880.
8. Palik, E.D., Handbook of Optical Constants of Solids, Academic Press, Orlando, 1985, pp. 395-403.
9. Winterbottom, A.B., "Optical Studies of the Oxidation of Iron at Temperatures in the Range 20-265 C," J. Iron and Steel Institute, May 1950, pp. 9-22.
10. Mori, K., Ropke, U., Knappe, B., Lehmann, J., Perthel, R., and Schroder, H., "Optical Properties of Sputtered Fe_2O_3 Films," This Film Solids, Vol. 60, 1979, pp. 49-53.
11. Shafey, H.M., "Studies on Radiative Heat Transfer in Dispersed Media with Application to Painted Layers," Doctoral Thesis, Mechanical Engineering Department, Kyoto University, 1981, pp. 21-22.
12. Boggs, T.L., Zurn, D.E., and Cordes, H.F., "The Combustion of Ammonium Perchlorate and Various Inorganic Additives," AIAA paper 75-233, presented at AIAA 13th Aerospace Sciences Meeting, Pasadena, CA, Jan. 1975.
13. Brewster, M.Q. and Taylor, D.M., "Radiative Properties of Burning Aluminum Droplets," presented as paper WSS/CI 87-13 at Western States Section of Combustion Institute Meeting, Provo, UT, Apr. 1987; to appear in Combustion and Flame.
14. Brewster, M.Q. and Parry, D.L., "Radiative Heat Feedback in Aluminized Solid Propellant Combustion," presented as paper WSS/CI 87-15 at Western States Section of Combustion Institute Meeting, Provo, UT, Apr. 1987; submitted to J. Thermophysics and Heat Transfer.
15. Shadman-Yazdi, F. and Petersen, E.E., "The Effect of Catalysts on the Deflagration Limits of Ammonium Perchlorate," Combustion Science and Technology, Vol. 5, 1972, pp. 61-67.
16. Kishore, K. and Gayathri, V., "Chemistry of Ignition and Combustion of Ammonium Perchlorate Based Propellants," Prog. in Astronautics and Aeronautics Series, Vol. 90, eds., K.K. Kuo and M. Summerfield, AIAA, New York, 1984, p. 99.
17. Brewster, M.Q., "Particle Radiative Feedback in Ammonium Perchlorate Deflagration," AIAA J., Vol. 24, No. 7, July 1986, pp. 1141-1147.
18. Levy, J.B. and Friedman, R., "Further Studies of Pure Ammonium Perchlorate Deflagration," Eighth Symposium (International) on Combustion, Williams and Wilkins Co., Baltimore, 1962, pp. 663-672.

AIAA'88

AIAA 88-3350

Optical Constants and Size
of Propellant Combustion

Aluminum Oxide (Al_2O_3) Smoke

D. L. Parry and M. Q. Brewster

University of Illinois at Urbana-Champaign
Urbana, IL

AIAA/ASME/SAE/ASEE 24th JOINT PROPULSION CONFERENCE

JULY 11-13, 1988/Boston, Massachusetts

OPTICAL CONSTANTS AND SIZE OF PROPELLANT COMBUSTION
ALUMINUM OXIDE (Al_2O_3) SMOKE

David L. Parry* and M. Quinn Brewster**
Department of Mechanical and Industrial Engineering
University of Illinois at Urbana-Champaign
Urbana, Illinois

Abstract

The optical constants (n and k) at two wavelengths ($\lambda_1 = 0.6328 \mu\text{m}$ and $\lambda_2 = 1.064 \mu\text{m}$) and the optical mean particle size, d_{32} , of aluminum oxide (Al_2O_3) particles in ammonium perchlorate (AP) composite solid propellant flames were determined. An inverse light scattering technique was developed that used *in situ* absolute scattering and extinction experimental data. Measured values of optical depth and bi-directional transmittance and reflectance were used to obtain optical properties (i.e. optical constants and size) for molten Al_2O_3 . Al_2O_3 smoke formed by detached "vapor-phase" aluminum oxidation dominated the optical characteristics. Therefore, the assumption of a mono-modal polydisperse size distribution was adequate for predicting optical properties. Solutions to the inverse scattering problem were found for d_{32} values between $0.86 \mu\text{m}$ and $1.08 \mu\text{m}$, n_{λ_1} values between 1.60 and 1.72 , n_{λ_2} values between 1.59 and 1.71 , and k values between 2×10^{-3} and 10^{-2} . For this particle size range the width of the size distribution was not a critical parameter ($d_{\text{mp}}/d_{32} < 0.3$ is recommended). Recommended Al_2O_3 optical properties (i.e. those values that best matched the experimental data) are: $d_{32} = 0.97 \pm 0.11 \mu\text{m}$, $n_{\lambda_1} = 1.65 \pm 0.03$, $n_{\lambda_2} = 1.64 \pm 0.03$, and $k = 6 \times 10^{-3} \pm 4 \times 10^{-3}$. A new correlation for n of molten Al_2O_3 was recommended that scales the quantity ($n - 1$) according to the density ratio of the liquid to the solid phase. The values obtained for k were consistent with values reported by other researchers based on extinction and emission measurements. A value of 0.94 ± 0.02 was obtained for the single scatter albedo ω_0 at an effective temperature of 3300 K . The scattering asymmetry factor $\langle p \rangle$ was 0.65 ± 0.02 , indicating that scattering was predominantly in the forward direction.

Nomenclature

d	particle diameter
f	function (e.g. $f(x)$)
f_v	particle volume fraction
I	radiant intensity or integral (i.e. I_{net})
k	absorption index
L	slab (flame or reference cell) thickness
n	refractive index
\bar{n}	complex refractive index ($\bar{n} = n - ik$)
N	particle size number distribution ($N(r)$) or particle number density (N_s)
$p(\theta)$	scattering phase function
$\langle p \rangle$	asymmetry factor
Q_e	particle extinction efficiency
r	particle radius
t	optical depth
T	temperature
x	particle size parameter, $\pi d/\lambda$

Greek

α	parameter in gamma size distribution
β	parameter in gamma size distribution
Γ	Gamma function
λ	wavelength
u	cosine of slab polar angle
θ	single scatter polar angle or slab polar angle
ρ	density
ρ''	bi-directional reflectance
τ''	bi-directional transmittance
τ	direct transmission
ω_0	single scatter albedo
Ω	solid angle

Scripts

b	backward
e	extinction
f	forward
l	liquid
m	melting point
mp	most probable
ref	reference
s	solid or scatter
32	volume/surface optical mean averaged over particle size

Introduction

Radiative heat transfer becomes significant in the analysis of composite solid propellant combustion when a metal, such as aluminum, is included in the propellant composition. Areas in aluminized solid propellant rocket motors where radiative heat transfer is particularly important are the insulator, nozzle, and burning propellant surfaces^{1,2}. Prediction of the plume radiosity is important in the determination of radiant heating of external equipment on rocket motors. Liquid aluminum oxide (Al_2O_3) smoke particles dominate the thermal radiative behavior in aluminized propellant flames and plumes^{1,3}. Therefore, obtaining reliable values for the optical properties of Al_2O_3 is an integral part of predicting the radiative heat transfer in aluminized solid propellant motors. Optical properties of Al_2O_3 particles consist of the optical constants (n and k) and the particle size distribution. This work is aimed at obtaining reliable values of the optical properties of Al_2O_3 smoke particles from the combustion of aluminized solid propellants.

All experimental data will be taken in situ from actual burning propellant flames. Therefore, the Al_2O_3 optical constants obtained will be effective values that include the effects of temperature variation through the flame, impurities, deviation from stoichiometry, polycrystalline structure, and porosity.

Literature Search

There is still a great deal of uncertainty about the optical properties of Al_2O_3 . Pearce¹ and Edwards and Bobco³ modeled isothermal radiative heat transfer within a solid propellant rocket motor but acknowledged limitations due to uncertainties in the optical properties of Al_2O_3 .

Optical Constants

The optical constants of Al_2O_3 have been measured by a variety of techniques⁴⁻¹⁶.

Reported refractive index, n , values for Al_2O_3 vary depending on wavelength, temperature, and phase^{5,8,11-13,16}. These data are plotted in Fig. 1. Malitson¹¹ measured the refractive index of a synthetic sapphire prism (i.e. solid Al_2O_3 (n_s)) at room temperature (300 K) over the 0.2 to 6 μm wavelength region and found the value of n_s to vary between 1.8 and 1.6 with a normal dispersion relation ($dn/d\lambda < 0$). Plass¹² predicted the refractive index at elevated temperatures (1470 to 2300 K) assuming a linear variation with temperature and a constant temperature coefficient ($dn/dT = 2.9 \times 10^{-5}$ per K). This temperature coefficient was based on the refractive index reported by Gryvnak and Burch¹⁰ at 1973 K compared to Malitson's data at 300 K. Plass¹⁷ also stated that Mie calculations are very sensitive to the refractive index when the absorption index is small.

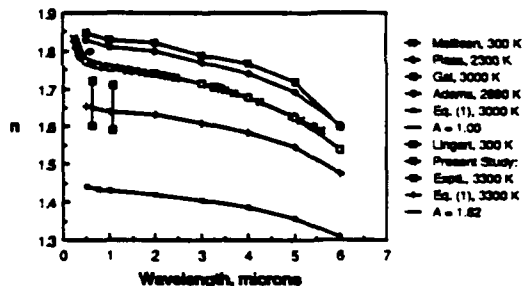


Figure 1 Aluminum Oxide Smoke Refractive Index

Most researchers^{4,5,8,9,18} use Plass's values or some other extrapolated value of n_s even for the refractive index of liquid Al_2O_3 n_l ⁵. No data could be found for actual measured values of n_l . In the absence of data for n_l Reed¹³ suggested estimating n_l (at wavelengths between 0.5 and 6.0 μm) by scaling the quantity ($n-1$) according to the density ratio of the liquid to the solid. Following this recommendation and using the data of solid Al_2O_3 at 2300 K¹² as a reference state, Eq. (1) is given for determining n_l .

$$\frac{n_l - 1}{n_s - 1} = A \times \frac{\rho_l}{\rho_s} \quad (1)$$

$$\alpha_1 = 3.01 \times \left(1 - \frac{T-T_m}{2684}\right), T_m = 2320 \text{ K} \quad (2)$$

where:

$$\begin{aligned} \lambda, \mu\text{m} &= 0.5 \quad 1 \quad 2 \quad 3 \quad 4 \quad 5 \quad 6 \\ n_s &= 1.83 \quad 1.81 \quad 1.80 \quad 1.77 \quad 1.74 \quad 1.69 \quad 1.60 \\ \rho_s &= 3.93 \text{ g/cm}^3 \text{ at } 2300 \text{ K}^{20} \\ A &= \text{empirical constant} \end{aligned}$$

The values of n_s determined by Eq. (1) are plotted in Fig. 1 for $A = 1$.

Figure 2 illustrates that most of the data for k (at wavelengths between 1 to 5 μm) appearing in the literature are in the range of 10^{-3} to 10^{-2} for liquid Al_2O_3 and 10^{-6} to 10^{-3} for solid Al_2O_3 ^{4-6,8-10,13}. The absorption index, k , for solid synthetic sapphire at elevated temperatures (up to 2290 K) have been reported by Gryvnak and Burch¹⁰ and more recently by Myers et al.¹⁵. These data for k and other data just below the melting point of Al_2O_3 (2320 K) are orders of magnitude higher than the corresponding room temperature values for sapphire.

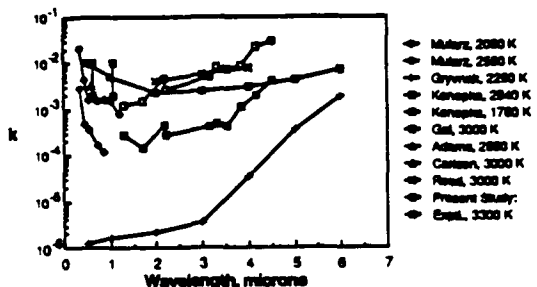


Figure 2 Aluminum Oxide Smoke Absorption Index

Experiments have been performed by Carlson⁶, Adams⁸, and Mularz and Yuen⁹ to measure k by heating micron-sized Al_2O_3 particles in gas flames. Data from these studies are also plotted in Fig. 2 and the value of k can be seen to be several orders of magnitude larger than Gryvnak's data for pure sapphire. This might be expected for the liquid state ($T > 2320 \text{ K}$) but even the data for $T < 2320 \text{ K}$, measured by this technique, show this tendency⁹. One possible explanation for the difference is impurities in the particle samples used. Konopka et al.⁴ have presented data that suggest the value of k in the solid state

varies significantly depending on the level and type of impurities, while the value of k in the liquid state is primarily determined by the Al_2O_3 itself. There is some experimental evidence that shows that stoichiometry can significantly influence the k value for even liquid Al_2O_3 ²¹⁻²³.

Lee and Kingery¹⁴ studied the transmission of both single crystal (sapphire) and sintered ceramic Al_2O_3 samples. They suggest that polycrystalline structure and porosity also play a potentially significant role in determining k .

Reed¹³ recommended a relation for estimating k for liquid Al_2O_3 between 1.7 and 4.5 μm , based on extinction and emission measurements.

$$k_1 = 3.7 \times 10^{-4} \times T^{1.5} \times \lambda(\mu\text{m}) \times 10^{-13461.5/T} \quad (3)$$

Reed's predictions for k are in reasonable agreement with other data plotted in Fig. 2. However, Eq. (3) does not predict the upswing in k at short wavelengths due to electronic transitions.

Al_2O_3 Particle Size Distribution

Al_2O_3 particle size distribution in the nozzle and plume of aluminized rocket motors has been studied extensively over the years²⁴⁻³¹. A critical review of the work up to 1980 has been given by HermSEN³¹. Little experimental work has been done to determine particle sizes inside the motor. It is generally recognized that the particle size distribution is bi-modal due to two competing mechanisms of aluminum oxidation²⁴. One is detached "vapor-phase" oxidation that produces smoke (0.1 - 2 μm) and the other is surface oxidation/condensation that produces large residual caps (10 - 100 μm).

Experimental determination of the size distribution has been discussed in detail by Kraeutle²⁵. By breaking the distribution up into sub-fractions, analyzing the sub-fractions using appropriate microscopy (i.e. optical or electron), and recombining the sub-fractions, Kraeutle demonstrated that the size distribution was bi-

modal with the transition between lobes occurring between 2 and 20 μm . This study pointed out that although microscopic analysis could be done accurately, it was very tedious.

Recently efforts have been reported³² at the Naval Postgraduate School to measure particle size inside a small motor by using purged windows on the motor. A diffraction-scattering technique similar to the Malvern system³³ was used. This work represents an important step in trying to look inside the motor. However, the diffraction-scattering technique is limited to larger particle sizes ($\pi d/\lambda \geq 5$). Therefore, only a portion of the size distribution can be characterized.

Scope of Work

An in situ light scattering technique was developed without the major limitations that exist for most light scattering techniques, namely single scattering and a minimum detectable particle size. This technique was developed to determine a consistent and compatible set of data for both optical constants and particle size distribution for molten Al_2O_3 particles produced in an aluminized composite propellant flame.

The technique made use of two wavelength extinction and scattering measurements of composite aluminized propellant flames in a window combustion bomb. Absolute (not relative) scattered intensity was measured. Extinction measurements, coupled with the absolute scattering measurements essentially allowed direct determination of the albedo. Multiple scattering was included so that single scattering was not a restriction. There was not a particle size limitation because diffraction dominated scattering was not assumed.

Experimental Apparatus

Light scattering and extinction measurements were made using a window combustion bomb and the experimental apparatus shown schematically in Fig. 3.

The window combustion bomb was equipped with a nitrogen gas purge to exhaust the combustion products, keep the windows clean, and control the pressure in the combustion chamber. The propel-

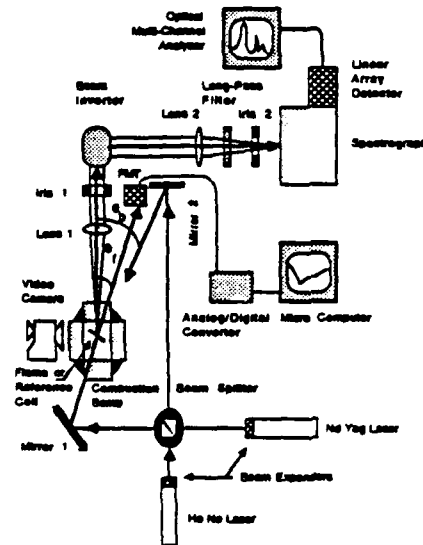


Figure 3 Optical Apparatus Schematic Diagram

lant strand and reference cell were mounted on the same pedestal inside the combustion bomb. This helped in taking reference measurements for obtaining absolute scattered intensity. A video camera was used to estimate the linear propellant burn rate and record the combustion process to allow rejection of uneven strand burns.

Both a He-Ne laser ($\lambda_1 = 0.6328 \mu\text{m}$) and a Nd-Yag laser ($\lambda_2 = 1.064 \mu\text{m}$) were used to obtain data at visible and near infrared wavelengths, respectively. A beam splitter cube was used to separate each laser beam into two paths. One path was used for bi-directional transmittance (forward scattering) measurement and the other for bi-directional reflectance (backward scattering) measurement. Only one beam (i.e forward or backward) was allowed to be incident on the flame zone at a time. Azimuthal angle dependence of the scattered light was eliminated by aligning the incident laser beam perpendicular to the flame zone. Light scattered in the forward direction was measured at approximately 11 degrees from the normal to the flame ($\theta_f = 11$ degrees) and light scattered in the backward direction at approximately 17 degrees from the normal ($\theta_b = 17$ degrees).

The optical system was set up and aligned to direct the scattered laser light to the entrance slit of the spectrograph. The vertical spectrograph entrance slit was imaged as a horizontal slit at the center of the flame zone by lenses 1 and 2 and the beam inverter. An optical multi-channel analyzer with a diode array detector was used to measure the scattered light. A long-pass filter ($\lambda_{cutoff} = 0.630 \mu\text{m}$) was used to prevent higher order wavelengths (e.g. $\lambda/2$, $\lambda/3$, etc.) from reaching the diode array detector.

A photomultiplier tube (PMT) and silicon diode detector (SDD) were used to detect the directly transmitted He-Ne laser and Nd-Yag laser light, respectively. The directly transmitted beam passed through a narrow band pass filter, corresponding to the respective laser wavelength, to prevent a significant amount of flame emission from reaching the PMT or SDD. The output signals of the PMT and SDD were recorded by a computer using an analog/digital converter. The computer was also used to signal the ignition of the propellant and activate the optical multi-channel analyzer.

Experimental Procedure

Samples of composite propellant were cut into $1 \times 6 \times 15 \text{ mm}$ strands. The propellant contained ammonium perchlorate (AP), a polymer binder (HTPB), and aluminum (20 percent by mass). A single strand was mounted in the bomb and the nitrogen gas purge was regulated to maintain a pressure of 1.72 MPa (250 psi) in the combustion zone. An electrical potential applied across a nichrome wire was used to ignite the propellant. A linear burn rate of approximately 0.5 cm/sec was determined.

Output voltages from the PMT and SDD were recorded and corresponded to the direct, unscattered transmission τ through the flame or reference cell.

The optical multi-channel analyzer recorded the intensity of the scattered light in the spectral region of interest (ROI) as a net integral (I_{net}). The spectral ROI included the wavelengths from 628 to 639 nm and from 1059 to 1069 nm for the He-Ne and Nd-Yag data measurements, respectively.

A glass slide reference cell (slab thickness, $L = 1 \text{ mm}$) filled with an aqueous suspension of polystyrene latex spheres (two percent by mass) was used to obtain reference scattering ($I_{net,ref}$) and extinction (τ_{ref}) values. Latex spheres with a diameter of $107 \pm 3 \text{ nm}$ and $220 \pm 6 \text{ nm}$ were used for the He-Ne and Nd-Yag reference measurements, respectively. The latex spheres had a reported index of refraction value of 1.59 at a wavelength of 589 nm and an insignificant absorption index.

Data Reduction

The data used in the reduction process represented the analysis of a region from 4 to 7 mm above the propellant surface. The optical depth, t_L , of the flame and reference for both wavelengths was obtained from the direct transmittance, τ , using

$$\tau = \exp(-t_L) \quad (4)$$

Flame bi-directional transmittance, τ'' , and reflectance, ρ'' , values at both wavelengths were determined from the following equations.

$$\text{Forward: } \tau''/\tau''_{ref} = I_{net}/I_{net,ref} \quad (5)$$

$$\text{Backward: } \rho''/\rho''_{ref} = I_{net}/I_{net,ref} \quad (6)$$

The one-dimensional, planar scattering geometry for this absolute scattering technique is shown in Fig. 4.

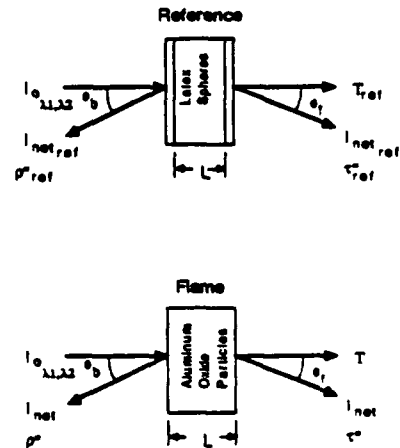


Figure 4 One-Dimensional, Planar Scattering Geometry for the Absolute Scattering Technique

The reference values, τ^{ref} and ρ^{ref} , were obtained by solving the radiative transfer equation for the reference cell. The effects of multiple reflection inside and between the glass slides as well as refraction and total internal reflection were included in the determination of τ^{ref} and in the transfer equation solution for τ^{ref} and ρ^{ref} . The resulting bi-directional transmittance and reflectance reference values were: $\tau^{\text{ref},1} = 0.40$, $\rho^{\text{ref},1} = 0.43$, $\tau^{\text{ref},2} = 0.42$, and $\rho^{\text{ref},2} = 0.43$.

Particle Size Distribution

A mono-modal gamma function size distribution was assumed to represent the Al_2O_3 particle sizes.

$$N(r) = \frac{N_s \theta^{a+1}}{\Gamma(a+1)} r^a \exp(-\theta r) \quad (7)$$

where $N(r)$ is the number density of the specified particle radius r . A mono-modal representation is adequate if one mode dominates the optical properties. In the present investigation the Al_2O_3 smoke particles dominated the optical scattering and extinction properties near the surface of the burning propellant. A mono-modal gamma distribution can be characterized by two parameters: The optical mean size, d_{32} ,

$$d_{32} = \frac{2(3+a)}{a} = 2 \frac{\int_0^\infty r^3 N(r) dr}{\int_0^\infty r^2 N(r) dr} \quad (8)$$

and the most probable size, d_{mp} , (i.e. where $dN/dr = 0$)

$$d_{mp} = \frac{2a}{\theta} \quad (9)$$

For a monodisperse analysis (e.g. reference calculations) $d_{32} = d_{mp}$.

MIE Scattering Parameters

The averaged extinction and scattering efficiency is given by

$$\bar{Q}_{e,s} = \frac{\int_0^\infty Q_{e,s} r^2 N(r) dr}{\int_0^\infty r^2 N(r) dr} \quad (10)$$

The single scattering albedo $\bar{\omega}_0$ is given by

$$\bar{\omega}_0 = \frac{\bar{Q}_s}{\bar{Q}_e} \quad (11)$$

Rather than presenting the full angular distribution of the phase function, $p(\theta)$, it is convenient to present a factor that represents the distribution. The asymmetry factor $\langle p \rangle^{34}$ describes the relative forward-to-backward scattering ratio. The asymmetry factor is given by

$$\langle p \rangle = \frac{1}{4\pi} \int_0^\pi p \cos\theta d\Omega \quad (12)$$

or

$$\langle p \rangle = \frac{1}{2} \int_{-1}^1 p \cos\theta d(\cos\theta) \quad (13)$$

The value of $\langle p \rangle$ ranges from -1 for maximum backward scattering to 1 for maximum forward scattering.

A mono-modal gamma distribution, as discussed in the previous section, was assumed to represent the number densities of Al_2O_3 particles of different sizes. The MIE scattering theory was applied to each interval of particle diameters. The averaged phase function, $\bar{p}(\theta)$, and asymmetry factor, $\langle \bar{p} \rangle$, were then calculated for an ensemble of particles by integrating over particle size.

The MIE scattering parameters can be expressed functionally by Eqs. (14) through (17).

$$\bar{Q}_{e,s} = \bar{Q}_{e,s} (n, k, x_{32}, \frac{x_{mp}}{x_{32}}) \quad (14)$$

$$\bar{\omega}_0 = \bar{\omega}_0 (n, k, x_{32}, \frac{x_{mp}}{x_{32}}) \quad (15)$$

$$\bar{p}(\theta) = \bar{p}(\theta, n, k, x_{32}, \frac{x_{mp}}{x_{32}}) \quad (16)$$

$$\langle p \rangle = \langle p \rangle (n, k, x_{32}, \frac{x_{mp}}{x_{32}}) \quad (17)$$

where

$$x_{32,mp} = \frac{\pi d_{32,mp}}{\lambda} \quad (18)$$

The Radiative Transfer Equation

The radiative transfer equation for a non-emitting, one-dimensional, plane-parallel slab is

$$u \frac{dI}{dt} = -I + (\bar{w}_0/2) \int_{-1}^1 I \bar{p}(u) du \quad (19)$$

where I is spectral intensity, u is the cosine of the slab polar angle θ [where: $(0 < \theta_f < \pi/2)$ and $(\pi/2 < \theta_b < \pi)$], and t is the optical depth. The radiative transfer equation (Eq. (19)) is solved by the discrete ordinate method³⁵. The solution of Eq. (19) can be expressed functionally as

$$\tau'', \rho'' = \frac{\pi I}{I_0} = f(\theta_f, b, t_L, \bar{w}_0, \bar{p}(\theta)) \quad (20)$$

where I_0 is the normal incident spectral flux. The albedo, \bar{w}_0 , and phase function, $\bar{p}(\theta)$, are obtained from MIE scattering theory using the assumed Al_2O_3 particle size distribution.

Flame Inverse Scattering Solution

An inverse solution technique using the MIE scattering theory and the radiative transfer equation is used to determine the effective optical constants (n and k) and the parameters describing the size distribution of the Al_2O_3 particles (i.e. d_{32} and d_{mp}/d_{32}). For a mono-modal polydispersion of particles at two wavelengths, bi-directional transmittance and reflectance can be expressed functionally for a given θ_f and θ_b by the following equations.

$$\tau''_{\lambda 1} = \tau''_{\lambda 1} (t_{L_{\lambda 1}}, n_{\lambda 1}, k_{\lambda 1}, d_{32}, \frac{d_{mp}}{d_{32}}) \quad (21)$$

$$\rho''_{\lambda 1} = \rho''_{\lambda 1} (t_{L_{\lambda 1}}, n_{\lambda 1}, k_{\lambda 1}, d_{32}, \frac{d_{mp}}{d_{32}}) \quad (22)$$

$$\tau''_{\lambda 2} = \tau''_{\lambda 2} (t_{L_{\lambda 2}}, n_{\lambda 2}, k_{\lambda 2}, d_{32}, \frac{d_{mp}}{d_{32}}) \quad (23)$$

$$\rho''_{\lambda 2} = \rho''_{\lambda 2} (t_{L_{\lambda 2}}, n_{\lambda 2}, k_{\lambda 2}, d_{32}, \frac{d_{mp}}{d_{32}}) \quad (24)$$

The intermediate determination of the MIE scattering parameters (w_0 , Eq. (15); and $\bar{p}(\theta)$, Eq. (16)) are incorporated into Eqs. (21) through (24). A relation for the optical depth t_L at each wavelength is given in Eqs. (25) and (26).

$$t_{L_{\lambda 1}} = \frac{1.5 f_v Q_{e_{\lambda 1}} (n_{\lambda 1}, k_{\lambda 1}, d_{32}, \frac{d_{mp}}{d_{32}})}{d_{32}} \quad (25)$$

$$t_{L_{\lambda 2}} = \frac{1.5 f_v Q_{e_{\lambda 2}} (n_{\lambda 2}, k_{\lambda 2}, d_{32}, \frac{d_{mp}}{d_{32}})}{d_{32}} \quad (26)$$

Since f_v is unknown the ratio of Eqs. (25) and (26) is taken

$$\frac{t_{\lambda 1}}{t_{\lambda 2}} = \frac{Q_{e_{\lambda 1}} (n_{\lambda 1}, k_{\lambda 1}, d_{32}, \frac{d_{mp}}{d_{32}})}{Q_{e_{\lambda 2}} (n_{\lambda 2}, k_{\lambda 2}, d_{32}, \frac{d_{mp}}{d_{32}})} \quad (27)$$

A linear relationship for the dependence of n on λ for $0.6328 \leq \lambda \leq 1.064 \mu\text{m}$ is assumed. The resulting dispersion relation is

$$n_{\lambda 1} = n_{\lambda 2} - 0.025 (\lambda 1 - \lambda 2) \quad (28)$$

This gives six equations [Eqs. (21) through (24), (27), and (28)] and six unknowns ($n_{\lambda 1}$, $n_{\lambda 2}$, $k_{\lambda 1}$, $k_{\lambda 2}$, d_{mp} , d_{mp}/d_{32}).

Results

The experimental optical depth and bi-directional transmittance and reflectance values were:

$$t_{L\lambda_1} = 1.28 \pm 0.11 \quad t_{L\lambda_2} = 1.21 \pm 0.23$$

$$\tau''_{\lambda_1} = 1.37 \pm 0.07 \quad \tau''_{\lambda_2} = 1.05 \pm 0.06$$

$$\sigma''_{\lambda_1} = 0.13 \pm 0.03 \quad \sigma''_{\lambda_2} = 0.13 \pm 0.07$$

Solutions to the six equations [Eqs. (21) through (24), (27) and (28)] were obtained numerically by a direct search method. The range of values searched for were: d_{32} , 0.1 to 2 μm ; n , 1.40 to 1.85; and k , 1×10^{-5} to 2×10^{-2} . Calculated values of τ'' and σ'' were matched to their corresponding experimental values. Calculated values of \bar{Q}_e were matched to experimental values of t_L according to Eq. (27). Assumed values of n at each wavelength were checked for adherence to Eq. (28). A solution was obtained when all these conditions were met simultaneously for the same assumed particle size distribution (d_{32} and d_{mp}/d_{32}) at both wavelengths.

A list of solutions that satisfies the six equations within the experimental uncertainty is given in Table 1.

Table 1 shows that there was a range of possible d_{32} sizes from 0.86 to 1.08 μm . For each size there was a range of possible values for n and for each n there was range of possible values for k . It should be noted that within the experimental uncertainty it was not possible to distinguish between values of k at the two wavelengths, thus k_{λ_1} and k_{λ_2} were treated as a single value k . Also, it was found that for realistic values of x_{mp}/x_{32} ($0.05 \leq x_{mp}/x_{32} < 0.3$) the results were insensitive to the value of x_{mp}/x_{32} (i.e. d_{mp}/d_{32}).

Although the results of this study indicate a range of multiple possible solutions for n , k , and d_{32} (due to experimental uncertainty), values that best match the average experimental values are:

Table 1. Aluminum Oxide Smoke Optical Properties

d_{32}	$n_{\lambda_2}^*$	$k \times 10^3$
0.86	1.63	2
0.88	1.61	2-8
	1.63	2-4
	1.65	2
0.90	1.59	6-10
	1.61	2-10
	1.63	2-6
	1.65	2
0.92	1.59	8-10
	1.61	4-10
	1.63	2-10
	1.65	2-6
	1.67	2
0.94	1.59	4
	1.61	10
	1.63	6-10
	1.65	2-10
	1.67	4-6
0.98	1.61	8-10
	1.63	2-10
	1.65	4-10
	1.67	4-8
1.00	1.59	6-10
	1.61	4-10
	1.63	4-10
	1.65	2-10
	1.67	4-10
	1.69	4-10
	1.71	6
1.02	1.61	10
	1.63	6-10
	1.65	2-10
	1.67	2-10
	1.69	2-10
1.04	1.63	8-10
	1.65	4-10
	1.67	4-10
	1.69	4-10
1.06	1.63	8-10
	1.65	4-10
	1.67	4-10
1.08	1.63	8-10
	1.65	6-10

$$* n_{\lambda_1} = n_{\lambda_2} + 0.01$$

$$d_{32} = 0.97 \pm 0.11 \mu\text{m} \quad (29)$$

$$n_{\lambda_1} = 1.65 \pm 0.03 \quad (30)$$

$$n_{\lambda_2} = 1.64 \pm 0.03 \quad (31)$$

$$k_{\lambda_1, \lambda_2} = 6 \times 10^{-3} \pm 4 \times 10^{-3} \quad (32)$$

The values for d_{32} given above correspond to the smoke component of Al_2O_3 . The fact that a mono-modal size distribution gives self-consistent results indicates that the large residual oxide cap mode probably does not influence the optical properties of Al_2O_3 inside the motor environment.

The values of n in Eqs. (30) through (31) are somewhat below the solid phase values that are usually assumed. However, a decrease in n upon melting is to be expected due to the expansion that takes place. Following Reed's recommendation for estimating n_1 and matching the values of n_1 from Eqs. (30) and (31) to Eq. (1), a value of 1.62 is obtained for the empirical coefficient A . The values of n_1 from Eqs. (30) and (31) and the results of Eq. (1) with $A = 1.62$ are plotted in Fig. 1.

The values for k in Eq. (32) are consistent with Reed's recommendation Eq. (3), depending on the assumed value for the effective temperature. An effective temperature of 3300 K is obtained, if Eq. (3) is extrapolated below $\lambda = 1.7 \mu\text{m}$ to $\lambda = 1.06 \mu\text{m}$ and matched with a value of $k = 6 \times 10^{-3}$. Therefore, Eqs. (30) through (32) are values of n and k at an effective temperature of 3300 K. This effective temperature seems reasonable for these experiments since the equilibrium adiabatic flame temperature is about 3600 K. The values of k from Eq. (32) are also plotted in Fig. 2.

Even for the moderate optical depth values measured (1.21 to 1.28) the experimental bi-directional transmittance values were an order of magnitude larger than the reflectance values. A value of 0.94 ± 0.02 was obtained for the single scatter albedo, $\bar{\omega}_0$, and the scattering asymmetry factor, $\langle \bar{p} \rangle$, was 0.65 ± 0.02 . These values all indicated that scattering was predominantly in the forward direction.

Conclusions

A new optical technique was developed to determine the optical constants (n and k) and mean optical size (d_{32}) for molten Al_2O_3 smoke particles produced by aluminized solid propellant combustion. This technique used *in situ* absolute scattering and extinction measurements at two wavelengths. A new correlation for n (Eq. (1) with $A = 1.62$) was recommended that accounts for the density change upon melting and variation with temperature. The values obtained for k were in good agreement with Reed's recommendation (Eq. (3)). A value of $0.97 \pm 0.11 \text{ mm}$ was recommended

for d_{32} . A value of 0.94 ± 0.02 was obtained for the single scatter albedo, $\bar{\omega}_0$, at an effective temperature of 3300 K. Scattering was predominantly in the forward direction with a scattering asymmetry factor, $\langle \bar{p} \rangle$, of 0.65 ± 0.02 .

Acknowledgments

Support for this work from Hercules/AFAL (Contract F04611-86-C-0016), the National Science Foundation (Grant CBT 83-51243), and the Office of Naval Research (Contract N00014-87-K-0547) is gratefully acknowledged.

References

1. Pearce, B. E., "Radiative Heat Transfer within a Solid-Propellant Rocket Motor," Journal of Spacecraft and Rockets, Vol. 15, No. 6, AIAA, New York, 1979.
2. Brewster, M. Q., "Particle Radiative Feedback in Ammonium Perchlorate Deflagration," AIAA Journal, Vol. 24, No. 7, July 1986, pp. 1141-1147.
3. Edwards, R. H., and Bobco, R. P., "Radiant Heat Transfer from Isothermal Dispersions with Isotropic Scattering," ASME J. of Heat Transfer, Vol. 89, 1967, pp. 300-308.
4. Konopka, W. L., Reed, R. A., and Calia, V. S., "Measurements of Infrared Optical Properties of Al_2O_3 Rocket Particles," Progress in Aeronautics and Astronautics, Vol. 91, 1984, pp. 180-197.
5. Gal, G., and Kirch, H., "Particulate Optical Properties in Rocket Plumes," AFRPL-TR-73-99, Nov. 1973, pp. 28-29.
6. Carlson, D. J., "Emittance of Condensed Oxides in Solid Propellant Combustion Products," Tenth (International) Symposium on Combustion, The Combustion Institute, 1965, pp. 1413-1424.
7. Bauer, E., and Carlson, D. J., "MIE Scattering Calculations for Micron Size Alumina and Magnesia Spheres," J. Quant. Spectrosc. Radiat. Transfer, Vol. 4, 1964, pp. 363-374.
8. Adams, J. M., "A Determination of the Emissive Properties of a Cloud of Molten Alumina Particles," J. Quant. Spectrosc. Radiat. Transfer, Vol. 7, 1967, pp. 273-277.
9. Mularz, E. J., and Yuen, M. C., "An Experimental Investigation of Radiative Properties of Aluminum Oxide Particles," J. Quant. Spectrosc. Radiat. Transfer, Vol. 12, 1972, pp. 1553-1568.
10. Gryvnak, D. A., and Burch, D. E., "Optical and Infrared Properties of Al_2O_3 at Elevated Temperatures," J. Opt. Soc. Am., Vol. 55, No. 6, 1965, pp. 625-629.

11. Malitson, L. H., "Refraction and Dispersion of Synthetic Sapphire," J. Opt. Soc. Am., Vol. 52, No. 12, 1962, pp. 1377-1379.
12. Plass, G. N., "Temperature Dependence of the MIE Scattering and Absorption Cross Sections for Aluminum Oxide," Applied Optics, Vol. 4, No. 12, 1965, pp. 1616-1619.
13. Reed, B., "Optical Properties for Liquid Al_2O_3 ," Private Communication, Arnold AFB, 29 Feb 1988.
14. Lee, D. W., and Kingery, W. D., "Radiation Energy Transfer and Thermal Conductivity of Ceramic Oxides," J. Am. Ceramic Soc., Vol. 43, No. 11, 1960, pp. 595-607.
15. Myers, V. H., Oro, A., and DeWitt, D. P., "A Method for Measuring Optical Properties of Semi-Transparent Materials at High Temperatures," AIAA J., Vol. 24, No. 2, 1986, pp. 321-326.
16. Lingart, et al., "Teplofizika Vysokikh Temperature," Vol. 20, No. 5, 1982, pp. 872-880.
17. Plass, G. N., "MIE Scattering and Absorption Cross Sections for Absorbing Particles," Applied Optics, Vol. 5, No. 2, 1966, pp. 279-285.
18. Bartky, C. D., and Bauer, E., "Predicting the Emittance of a Homogeneous Plume Containing Alumina Particles," J. of Spacecraft, Vol. 3, No. 10, 1966, pp. 1523-1527.
19. Kirshenbaum, A. D., and Cahill, J. A., "The Density of Liquid Aluminum Oxide," J. Inorg. Nucl. Chem., Vol. 14, 1960, pp. 283-287.
20. Raznjevic, K., Handbook of Thermodynamic Tables and Charts, New York, 1976, p. 4.
21. Nelson, L. S., and Richardson, N. L., "Effects of Oxygen and Argon Atmospheres on Pendant Drops of Aluminum Oxide Melted with Carbon Dioxide Laser Radiation," High Temp. Sci., Vol. 5, 1973, pp. 138-154.
22. Krautle, K. J., and Bradley, H. H. Jr., "Combustion of Aluminized Propellants: The Influence of Pressure and Propellant Composition on Formation of Aluminum Combustion Residue," 14th JANNAF Combustion Mtg., CPIA Publication, pp. 209-219.
23. Hauffe, Karl, Reaktionen in und an festen Stoffen, Springer-Verlag, Berlin, 1966, p. 219.
24. Price, E. W., "Combustion of Metallized Propellants," Fundamentals of Solid Propellant Combustion, Progress in Astro. and Aero., Vol. 90, eds. K. K. Kuo and M. Summerfield, AIAA, 1984, ch. 9, pp. 479-513.
25. Krautle, K. J., "Particle Size Analysis In Solid Propellant Combustion Research," Prog. in Aeronautics and Astronautics, AIAA, 1978, pp. 76-108.
26. Drew, C. M., et al., "Study of Quenched Aluminum Particle Combustion," AIAA Heterogeneous Combustion Conference, Preprint 63-487, Dec. 11-13, 1963.
27. Brown, B., and McArty, K. P., "Particle Size of Condensed Oxides from Combustion of Metalized Solid Propellants," Formation, Combustion, Explosion and Detonation of Solids, pp. 814-923.
28. Switzenbank, J., et al., "A Laser Diagnostic Technique For the Measurement of Droplet and Particle Size Distribution," AIAA 14th Aerospace Sciences meeting, Paper 76-69, Jan. 1978, pp. 421-439.
29. Chigier, N. A., and Stewart, G., "Guest Editorial: Particle Sizing and Spray Analysis," Opt. Engr., 23, 554, 1984.
30. Hofeldt, D. L., et al., "Instantaneous Two-Dimensional Multiple Particle Sizing Diagnostic," 24th JANNAF Combustion Meeting, Stanford University.
31. HermSEN, R. W., "Aluminum Oxide Particle Size for Solid Rocket Motor Performance Prediction," J. Spacecraft and Rockets, Vol. 18, No. 6, 1981, pp. 483-490.
32. Orguc, S., Pruitt, T. E., Edwards, T. D., Youngborg, E. D., Powers, J. P., and Netzer, D. W., "Measurement of Particulate Size in Solid Propellant Rocket Motors," Proceedings of 1987 JANNAF Combustion Meeting, Monterey, CA, CPIA Publications.
33. Switzenbank, J., et al., "A Laser Diagnostic Technique for the Measurement of Droplet and Particle Size Distribution," Prog. In Astro. and Aero., Vol. 53, 1978, pp. 421-439.
34. Hansen, J. E., and Travis, L. D., "Light Scattering in Planetary Atmospheres," Space Sci. Rev., Vol. 16, 1974, pp. 527-610.
35. Brewster, M. Q., and Tien, C. L., "Radiative Transfer in Packed/Fluidized Beds: Dependent versus Independent Scattering," J. of Heat Transfer, Vol. 14, No. 4, 1982, pp. 573-579.

PROPELLANT Al_2O_3 PARTICLE SIZE AND OPTICAL CONSTANTS
FROM IN SITU, INVERSE LIGHT SCATTERING AND EXTINCTION MEASUREMENTS

David L. Parry and M. Quinn Brewster
Department of Mechanical and Industrial Engineering
University of Illinois at Urbana-Champaign
Urbana, Illinois

ABSTRACT

The optical constants (n and k) at two wavelengths ($\lambda_1 = 0.6328 \mu\text{m}$ and $\lambda_2 = 1.064 \mu\text{m}$) and the optical mean particle size, d_{32} , of aluminum oxide (Al_2O_3) particles in ammonium perchlorate (AP) composite solid propellant flames were determined. An inverse light scattering technique was developed that used in situ absolute scattering and extinction experimental data. Measured values of optical depth and bi-directional transmittance and reflectance were used to obtain optical properties (i.e. optical constants and size) of liquid Al_2O_3 . Al_2O_3 smoke, formed by detached "vapor-phase" aluminum oxidation, dominated the optical characteristics near the surface of the burning propellant. Therefore, the assumption of a mono-modal polydisperse size distribution was adequate for predicting optical properties. Solutions to the inverse scattering problem were found for d_{32} values between $0.86 \mu\text{m}$ and $1.08 \mu\text{m}$, n_{λ_1} values between 1.60 and 1.72, n_{λ_2} values between 1.59 and 1.71, and k values between 2×10^{-3} and 10^{-2} . For this particle size range the width of the size distribution was not a critical parameter ($d_{mp}/d_{32} < 0.3$ is recommended). Recommended Al_2O_3 optical properties (i.e. those values that best matched the experimental data) are: $d_{32}=0.97 \pm 0.11 \mu\text{m}$, $n_{\lambda_1}=1.65 \pm 0.03$, $n_{\lambda_2}=1.64 \pm 0.03$, and $k=6 \times 10^{-3} \pm 4 \times 10^{-3}$. The recommended values for the refractive index of liquid Al_2O_3 correlated with the Lorentz-Lorenz equation for temperatures just above the melting point of Al_2O_3 ($T_m = 2320 \text{ K}$). The values obtained for k were significantly higher than values, reported by other researchers, obtained from the analysis of samples taken from rocket plumes at comparable temperatures and wavelengths. A value of 0.94 ± 0.02 was obtained for the albedo, $\bar{\omega}_0$. The scattering asymmetry factor $\langle p \rangle$ was 0.65 ± 0.02 , indicating that scattering was predominantly in the forward direction.

NOMENCLATURE

GENERAL

d	particle diameter
f	function (e.g. $f(x)$)
f_v	particle volume fraction
I	radiant intensity or integral (i.e. I_{net})
L	slab (flame or reference cell) thickness
n	refractive index
π	complex refractive index ($\pi = n - ik$)
$N(r)$	particle size number distribution
N_d	particle number density
$p(\theta)$	scattering phase function
$\langle p \rangle$	asymmetry factor
Q_e	particle extinction efficiency
Q_s	particle scatter efficiency
r	particle radius
t	optical depth
T	temperature, K
x	particle size parameter, $\pi d/\lambda$

SUPERSCRIPTS

-	averaged over particle size
-	complex number
-	incoming

SUBSCRIPTS

b	backward
e	extinction
f	forward
l	liquid
m	melting point
mp	most probable
ref	reference
s	solid or scatter
32	volume/surface optical mean

GREEK

α	parameter in gamma size distribution
β	parameter in gamma size distribution
Γ	Gamma function
λ	wavelength
μ	cosine of slab polar angle
θ	single scatter polar angle or slab polar angle
ρ	density
ρ^*	bi-directional reflectance
τ^*	bi-directional transmittance
T	direct transmission
ω_0	albedo
Ω	solid angle

Approved for public release; distribution is unlimited.

UNCLASSIFIED

INTRODUCTION

Radiative heat transfer becomes significant in the analysis of composite solid propellant combustion when a metal, such as aluminum, is included in the propellant composition. Areas in aluminized solid propellant rocket motors where radiative heat transfer is particularly important are the insulator, nozzle, and burning propellant [1,2]. Prediction of the plume radiosity is important in the determination of radiant heating of external equipment on rocket motors. Liquid aluminum oxide (Al_2O_3) smoke particles dominate the thermal radiative behavior in aluminized propellant flames and plumes [1,3]. Therefore, obtaining reliable values for the optical properties of Al_2O_3 is an integral part of predicting the radiative heat transfer in aluminized solid propellant motors. Optical properties of Al_2O_3 particles consist of the optical constants (n and k) and the particle size distribution. The refractive index, n , and the absorption index, k , define the complex refractive index, \bar{n} , where $\bar{n} = n - ik$. This work is aimed at obtaining reliable values of the optical properties of Al_2O_3 smoke particles produced from the combustion of aluminized composite solid propellants.

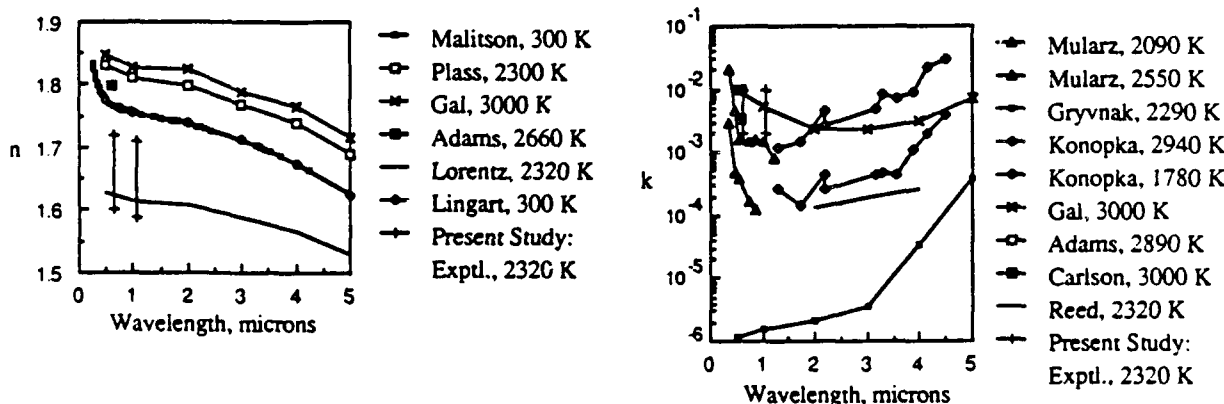
All experimental data have been taken in situ from actual burning propellant flames. Therefore, the Al_2O_3 optical constants obtained are effective values that include the effects of temperature variation through the flame, impurities, deviation from stoichiometry, polycrystalline structure, and porosity.

LITERATURE SEARCH

There is still a great deal of uncertainty about the optical properties of Al_2O_3 . Pearce [1] and Edwards and Bobco [3] modeled isothermal radiative heat transfer within a solid propellant rocket motor but acknowledged limitations due to uncertainties in the optical properties of Al_2O_3 .

OPTICAL CONSTANTS

The optical constants of Al_2O_3 have been measured by a variety of techniques [4-16]. Reported refractive index, n , values for Al_2O_3 vary depending on wavelength, temperature, and phase [5, 8, 11-13, 16]. These data are plotted in Fig. 1.



Figures 1 and 2. Aluminum Oxide Refractive Index, n , and Absorption Index, k .

Malitson [11] measured the refractive index of a synthetic sapphire prism (i.e. solid Al_2O_3 , n_s) at room temperature ($T=300$ K) over the 0.2 to 6 μm wavelength region and found the value of n_s to vary between 1.8 and 1.6 with a normal dispersion relation ($dn/d\lambda < 0$). Plass [12] predicted the refractive index at elevated temperatures (1470 to 2300 K) assuming a linear variation with temperature and a constant temperature coefficient ($dn/dT = 2.9 \times 10^{-5}$ per K). This temperature coefficient was based on the refractive index reported by Gryvnak and Burch [10] at 970 K compared to Malitson's data at 300 K. Plass [17] also stated that Mie scattering calculations are very sensitive to the refractive index when the absorption index is small.

Most researchers [4,5,8,9,18] use Plass' values or some other extrapolated value of n_s even for the refractive index of liquid Al_2O_3 (n_l) [5]. No data could be found for actual measured values of n_l . In the absence of data for n_l , the Lorentz-Lorenz equation [19] was used for determining n_l as a function of wavelength and temperature. Using the data of solid Al_2O_3 at 2300 K [12,20] as a reference state, Eq. (1) is given for determining n_l .

UNCLASSIFIED

$$\frac{n_1^2 - 1}{(n_1^2 + 2)\rho_1} = \frac{n_s^2 - 1}{(n_s^2 + 2)\rho_s} \quad (1)$$

where:

$$\rho_1 = 5.632 - 1.127 \times 10^{-3}T \text{ g/cm}^3 \quad (2)$$

$$\rho_s = 3.73 \text{ g/cm}^3 \text{ at } 2300 \text{ K}$$

$$\lambda, \mu\text{m} = \begin{matrix} 0.5 & 1 & 2 & 3 & 4 & 5 & 6 \end{matrix}$$

$$n_s = \begin{matrix} 1.83 & 1.81 & 1.80 & 1.77 & 1.74 & 1.69 & 1.60 \end{matrix}$$

The values of n_1 determined by Eq. (1) for a temperature of 2320 K are plotted in Fig. 1.

Figure 2 illustrates that most of the data for the absorption index, k , appearing in the literature for wavelengths from 1 to 5 μm are in the range of 10^{-3} to 10^{-2} for liquid Al_2O_3 and 10^{-6} to 10^{-3} for solid Al_2O_3 [4-6, 8-10, 13]. The absorption index, k , for solid synthetic sapphire at elevated temperatures (up to 2290 K) have been reported by Gryvnak and Burch [10] and more recently by Myers et al. [15]. These data for k and other data just below the melting point of Al_2O_3 ($T_m = 2320 \text{ K}$) are orders of magnitude higher than the corresponding room temperature values for sapphire.

Experiments have been performed by Carlson [6], Adams [8], and Mularz and Yuen [9] to measure k by heating micron-sized Al_2O_3 particles in gas flames. Data from these studies are also plotted in Fig. 2 and the value of k can be seen to be several orders of magnitude larger than Gryvnak's data for pure sapphire. This might be expected for the liquid state but even the data for the solid state, measured by this technique, show this tendency [9]. One possible explanation for the difference is impurities in the particle samples used. Konopka et al. [4] have presented data that suggest that the value of k in the solid state varies significantly depending on the level and type of impurities. There is some experimental evidence that shows that stoichiometry can significantly influence the k value for liquid Al_2O_3 [21-23].

Lee and Kingery [14] studied the transmission of both single crystal (sapphire) and sintered ceramic Al_2O_3 samples. They suggest that polycrystalline structure and porosity also play a potentially significant role in determining k . Reed [13] developed a relation for estimating k for liquid Al_2O_3 between 1.7 and 4.5 μm , based on extinction and emission measurements. These measurements analyzed particles that were collected from a rocket plume and heated in a shock tube.

$$k_l = 3.7 \times 10^{-4} \times T(\text{K})^{1.5} \times \lambda(\mu\text{m}) \times 10^{-13461.5/T(\text{K})} \quad (3)$$

Reed's predictions for k are in reasonable agreement with data, by other researchers, plotted in Fig. 2. However, Eq. (3) does not predict the upswing in k at short wavelengths due to interband electronic transitions.

Al_2O_3 PARTICLE SIZE DISTRIBUTION

Al_2O_3 particle size distribution in the nozzle and plume of aluminized rocket motors has been studied extensively over the years [24-31]. A critical review of the work up to 1980 has been given by Hermans [31]. It is generally recognized that the particle size distribution is bi-modal due to two competing aluminum oxidation mechanisms [24]. One mechanism is detached "vapor-phase" oxidation that produces smoke (0.1 - 2 μm) and the other is surface oxidation/condensation that produces large residual caps (10 - 100 μm). Kraeutle [25] used the appropriate microscopy (i.e. optical or electron) to demonstrated that the size distribution was bi-modal with the transition between lobes occurring between 2 and 20 μm .

Recently efforts have been reported to measure particle size inside a small motor [32] using a diffraction-scattering technique [33]. This work represents an important step in trying to look inside the motor. However, only a portion of the size distribution can be characterized because the technique is limited to larger particle size parameters ($x \geq 5$).

TECHNIQUE

An in situ light scattering technique was developed without the major limitations that exist for most light scattering techniques. Multiple scattering was included so that single scattering was not a restriction. There was not a particle size limitation because diffraction dominated scattering was not assumed in the data reduction process. This technique was developed to determine a consistent and compatible set of data for both optical constants and particle size distribution for liquid Al_2O_3 particles produced near the surface of a burning propellant. The technique made use of extinction and scattering measurements, at two wavelengths, of propellant flames in a window combustion bomb. Absolute (not relative) scattered intensity was measured. Extinction measurements, coupled with the absolute scattering measurements essentially allowed direct determination of the albedo, $\bar{\omega}_0$.

UNCLASSIFIED

EXPERIMENTAL APPARATUS

Light scattering and extinction measurements were made using a window combustion bomb and the experimental apparatus shown schematically in Fig 3.

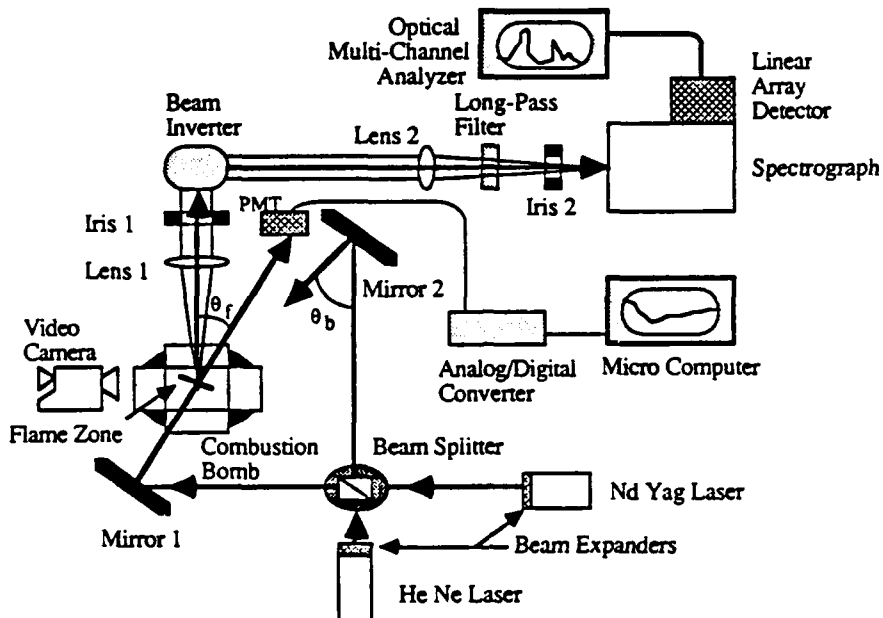


Figure 3. Optical Apparatus Schematic Diagram

The window combustion bomb was equipped with a nitrogen gas purge to exhaust the combustion products, keep the windows clean, and control the pressure in the combustion chamber. The propellant strand and reference cell were mounted on the same pedestal inside the combustion bomb. This helped in taking the necessary reference measurements for obtaining the absolute intensity of the scattered light. A video camera was used to estimate the linear propellant burn rate and record the combustion process to allow rejection of abnormal propellant burns.

Both a 5 mW He-Ne laser ($\lambda_1=0.6328 \mu\text{m}$) and a 50 mW Nd-Yag laser ($\lambda_2=1.064 \mu\text{m}$) were used to obtain data at visible and near infrared wavelengths, respectively. A beam splitter cube was used to separate each laser beam into two paths. One path was used for bi-directional transmittance (forward scattering) measurements and the other for bi-directional reflectance (backward scattering) measurements. Only one path and one laser beam were allowed to be incident on the flame zone (i.e reference cell or propellant flame) at a time. Azimuthal angle dependence of the scattered light was eliminated by aligning the incident laser beam perpendicular to the flame zone. Light scattered in the forward direction was measured at approximately 11 degrees from the normal to the flame ($\theta_f = 11$ degrees) and light scattered in the backward direction at approximately 17 degrees from the normal ($\theta_b = 17$ degrees).

The optical system was set up and aligned to direct the scattered laser light to the entrance slit of the spectrograph. The vertical spectrograph entrance slit was imaged as a horizontal slit at the center of the flame zone by lenses 1 and 2 and the beam inverter. An optical multi-channel analyzer with a diode array detector was used to measure the intensity of the scattered light. A long-pass filter ($\lambda_{\text{cutoff}} = 0.630 \mu\text{m}$) was used to prevent higher order wavelengths (e.g. $\lambda/2, \lambda/3$, etc.) from reaching the diode array detector.

A photomultiplier tube (PMT) and a silicon diode detector (SDD) were used to detect the directly transmitted He-Ne laser and Nd-Yag laser light, respectively. The directly transmitted beam passed through a narrow band pass filter, corresponding to the respective laser wavelength, to prevent a significant amount of flame emission from reaching the PMT or SDD. The output signals of the PMT and SDD were processed by a micro computer through an analog/digital converter. The computer was also used to signal the ignition of the propellant and activate the optical multi-channel analyzer.

UNCLASSIFIED

EXPERIMENTAL PROCEDURE

Samples of composite propellant were cut into $1 \times 6 \times 15$ mm strands. The propellant contained ammonium perchlorate (AP), polymer binder (HTPB), and aluminum (20 percent by mass). A single strand was mounted in the bomb and the nitrogen gas purge was regulated to maintain a pressure of 1.72 MPa (250 psi) in the combustion zone. The video camera was turned on and a 1000 power neutral density filter was placed in front of it. An electrical potential applied across a nichrome wire was used to ignite the propellant. Output voltages from the PMT and SDD were recorded and corresponded to the direct, unscattered transmission, T, through the flame or reference cell.

The optical multi-channel analyzer expressed the intensity of the scattered light in the spectral region of interest (ROI) as a net integral (I_{net}). The spectral ROI included the wavelengths from 628 to 639 nm and from 1059 to 1069 nm for the He-Ne and Nd-Yag data measurements, respectively. The data collected represented a spatial region from 4 to 7 mm above the burning propellant surface.

A glass slide reference cell (slab thickness, L = 1mm) filled with an aqueous suspension of polystyrene latex spheres (two percent by mass) was used to obtain reference scattering ($I_{net,ref}$) and extinction (T_{ref}) values. Latex spheres with a diameter of 107 ± 3 nm and 220 ± 6 nm were used for the He-Ne and Nd-Yag reference measurements, respectively. The latex spheres had a reported index of refraction value of 1.59 at a wavelength of 589 nm and an insignificant absorption index.

DATA REDUCTION

The optical depth, t_L , of the flame or reference for both wavelengths was obtained from the direct transmittance, T, using the following equation.

$$T = \exp(-t_L) \quad (4)$$

Flame bi-directional transmittance, τ'' , and reflectance, ρ'' , values at both wavelengths were determined from the following equations.

$$\text{Forward: } \frac{\tau''}{\tau''_{ref}} = \frac{I_{net}}{I_{net,ref}} \quad (5)$$

$$\text{Backward: } \frac{\rho''}{\rho''_{ref}} = \frac{I_{net}}{I_{net,ref}} \quad (6)$$

The one-dimensional, planar scattering geometry for this absolute scattering technique is shown in Fig. 4.

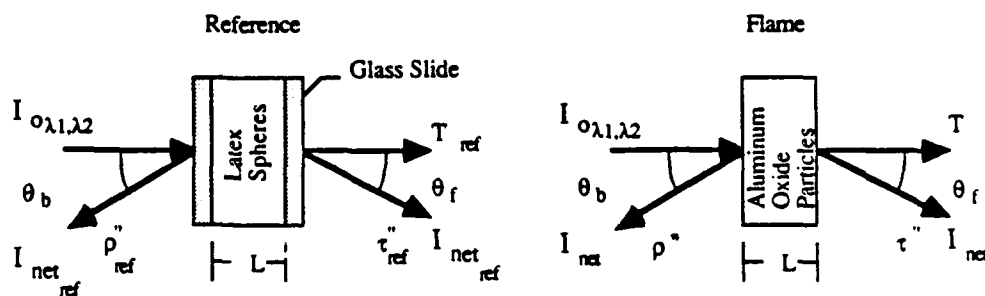


Figure 4. One-Dimensional, Planar Scattering Geometry for the Absolute Scattering Technique

The reference values, τ''_{ref} and ρ''_{ref} , were obtained by solving the radiative transfer equation for the reference cell. The aqueous solution used for the reference measurements was contained between glass slides. Therefore, the effects of multiple reflection inside and between the glass slides as well as refraction and total internal reflection were included in the determination of T_{ref} and in the transfer equation solution for τ''_{ref} and ρ''_{ref} . The resulting optical depth, bi-directional transmittance and reflectance reference values were:

$$t_{ref,\lambda_1} = 1.78 \quad \tau''_{ref,\lambda_1} = 0.40 \quad \rho''_{ref,\lambda_1} = 0.43$$

UNCLASSIFIED

$$n_{ref\lambda_2} = 1.89$$

$$\tau''_{ref\lambda_2} = 0.42$$

$$\rho''_{ref\lambda_2} = 0.43$$

PARTICLE SIZE DISTRIBUTION

A mono-modal gamma function size distribution was assumed to represent the Al₂O₃ particle sizes,

$$N(r) = \frac{N_d \beta^{\alpha+1}}{\Gamma(\alpha+1)} r^\alpha \exp(-\beta r) \quad (7)$$

where N(r) is the number density of specified particle radius r. A mono-modal representation is adequate if one mode dominates the optical properties. In the present investigation the Al₂O₃ smoke particles dominated the optical scattering and extinction properties near the surface of the burning propellant. A mono-modal gamma distribution can be characterized by two parameters, the optical mean size, d₃₂,

$$d_{32} = \frac{2(3+\alpha)}{\beta} = 2 \frac{\int_0^\infty r^3 N(r) dr}{\int_0^\infty r^2 N(r) dr} \quad (8)$$

and most probable size, d_{mp} (size where dN/dr = 0)

$$d_{mp} = \frac{2\alpha}{\beta} \quad (9)$$

For a monodisperse analysis (e.g. reference calculations) d₃₂ = d_{mp}.

MIE SCATTERING PARAMETERS

The averaged extinction and scattering efficiencies are given by

$$Q_{e,s} = \frac{\int_0^\infty Q_{e,s} r^2 N(r) dr}{\int_0^\infty r^2 N(r) dr} \quad (10)$$

The albedo $\bar{\omega}_0$ is given by

$$\bar{\omega}_0 = \frac{Q_s}{Q_e} \quad (11)$$

Rather than presenting the full angular distribution of the phase function, p(θ), it is convenient to present some moment of the distribution. The asymmetry factor $\langle p \rangle$ [34] describes the relative forward-to-backward scattering ratio. The asymmetry factor is given by

$$\langle p \rangle = \frac{1}{4\pi} \int p \cos\theta d\Omega \quad (12)$$

or

$$\langle p \rangle = \frac{1}{2} \int_0^1 p \cos\theta d(\cos\theta) \quad (13)$$

The value of $\langle p \rangle$ ranges from -1 for maximum backward scattering to 1 for maximum forward scattering.

A mono-modal gamma distribution, as discussed in the previous section, was assumed to represent the number densities of Al₂O₃ particles of different sizes. The Mie scattering theory was applied to each interval of particle diameters. The overall

UNCLASSIFIED

extinction efficiency, Q_e , scattering efficiency, Q_s , albedo, $\bar{\omega}_o$, phase function, $\bar{p}(\theta)$, and asymmetry factor, $\langle \bar{p} \rangle$, were then calculated for an ensemble of particles. These overall Mie scattering parameters were the weighted average of the parameter according to the number density of particle size.

The overall Mie scattering parameters can be expressed functionally by Eqs. (14) and (17).

$$Q_{e,s} = Q_{e,s}(n, k, x_{32}, \frac{x_{mp}}{x_{32}}) \quad (14)$$

$$\bar{\omega}_o = \bar{\omega}_o(n, k, x_{32}, \frac{x_{mp}}{x_{32}}) \quad (15)$$

$$\bar{p}(\theta) = \bar{p}(\theta, n, k, x_{32}, \frac{x_{mp}}{x_{32}}) \quad (16)$$

$$\langle \bar{p} \rangle = \langle \bar{p} \rangle(n, k, x_{32}, \frac{x_{mp}}{x_{32}}) \quad (17)$$

where

$$x_{32,mp} = \frac{\pi d_{32,mp}}{\lambda} \quad (18)$$

THE RADIATIVE TRANSFER EQUATION

The radiative transfer equation for a non-emitting, one-dimensional, plane-parallel slab is

$$\mu \frac{dI}{dt} = -I + (\bar{\omega}_o/2) \int_{-1}^1 I \bar{p}(\mu, \mu') d\mu' \quad (19)$$

where I is spectral intensity, μ is the cosine of the slab polar angle, θ , where $(0 < \theta_f < \pi/2)$ and $(\pi/2 < \theta_b < p)$, and t is the optical depth. The radiative transfer equation, Eq. (19), was solved by the discrete ordinate method [35]. The solution of Eq. (19) can be expressed functionally by Eq. (20).

$$\tau'' \rho'' = \frac{\pi I}{I_0} = \frac{\pi I}{I_0} (\theta_{f,b}, t_L, \bar{\omega}_o, \bar{p}(\theta)) \quad (20)$$

where I_0 is the normal incident spectral flux.

FLAME INVERSE SCATTERING SOLUTION

An inverse solution technique using the Mie scattering theory and the radiative transfer equation was used to determine the effective optical constants (n and k) and the parameters describing the size distribution of the Al_2O_3 particles (d_{32} and d_{mp}/d_{32}). For a mono-modal polydispersion of particles at two wavelengths, bi-directional transmittance and reflectance can be expressed functionally for a given θ_f and θ_b by the following equations.

$$\tau'' \lambda_1 = \tau'' \lambda_1(n \lambda_1, k \lambda_1, d_{32}, \frac{d_{mp}}{d_{32}}) \quad (21)$$

$$\rho'' \lambda_1 = \rho'' \lambda_1(n \lambda_1, k \lambda_1, d_{32}, \frac{d_{mp}}{d_{32}}) \quad (22)$$

$$\tau'' \lambda_2 = \tau'' \lambda_2(n \lambda_2, k \lambda_2, d_{32}, \frac{d_{mp}}{d_{32}}) \quad (23)$$

$$\rho'' \lambda_2 = \rho'' \lambda_2(n \lambda_2, k \lambda_2, d_{32}, \frac{d_{mp}}{d_{32}}) \quad (24)$$

The intermediate determination of the Mie scattering parameters are incorporated into Eqs. (21) through (24). A relation for the optical depth, t_L , at each wavelength is given in Eqs. (25) and (26). Note that d_{mp}/d_{32} is equal to x_{mp}/x_{32} .

$$t_{L\lambda_1} = \frac{1.5 f_v L Q_{e\lambda_1}(n \lambda_1, k \lambda_1, d_{32}, \frac{d_{mp}}{d_{32}})}{d_{32}} \quad (25)$$

$$t_{L\lambda_2} = \frac{1.5 f_v L Q_{e\lambda_2}(n \lambda_2, k \lambda_2, d_{32}, \frac{d_{mp}}{d_{32}})}{d_{32}} \quad (26)$$

UNCLASSIFIED

Since f_v is unknown the ratio of Eqs. (25) and (26) is taken

$$\frac{q_{\lambda_1}}{q_{\lambda_2}} = \frac{Q_{\lambda_1}(n_{\lambda_1}, k_{\lambda_1}, d_{32}, \frac{d_{mp}}{d_{32}})}{Q_{\lambda_2}(n_{\lambda_2}, k_{\lambda_2}, d_{32}, \frac{d_{mp}}{d_{32}})} \quad (27)$$

A linear relationship for the dependence of n on λ for $0.6328 \leq \lambda \leq 1.064 \mu\text{m}$ is assumed. The resulting dispersion equation is

$$n_{\lambda_1} - n_{\lambda_2} = -0.025 (\lambda_1 - \lambda_2) \quad (28)$$

This gives six equations [Eqs. (21) through (24), (27), and (28)] and six unknowns (n_{λ_1} , n_{λ_2} , k_{λ_1} , k_{λ_2} , d_{mp} , and $\frac{d_{mp}}{d_{32}}$).

RESULTS

The linear burn rate was estimated to be 0.5 cm/sec (0.2 in/sec). The experimental optical depth and bi-directional transmittance and reflectance values were:

$$\begin{aligned} t_{\lambda_1} &= 1.28 \pm 0.11 & t_{\lambda_2} &= 1.21 \pm 0.23 \\ \tau''_{\lambda_1} &= 1.37 \pm 0.07 & \tau''_{\lambda_2} &= 1.05 \pm 0.06 \\ \rho''_{\lambda_1} &= 0.13 \pm 0.03 & \rho''_{\lambda_2} &= 0.13 \pm 0.07 \end{aligned}$$

Solutions to the six equations were obtained numerically by a direct search method. The ranges considered for each variable were:

$$\begin{aligned} n &: 1.40 \text{ to } 1.85 \\ k &: 1 \times 10^{-5} \text{ to } 2 \times 10^{-2} \\ d_{32} &: 0.1 \text{ to } 2 \mu\text{m} \end{aligned}$$

$$\frac{d_{mp}}{d_{32}} = \frac{x_{mp}}{x_{32}} : .05 \text{ to } 1.0$$

There was a range of possible d_{32} sizes from 0.96 to $1.08 \mu\text{m}$ that satisfied the six equations within the experimental uncertainty. For each size there was a range of possible values for n and for each n there was a range of possible values for k . It should be noted that within the experimental uncertainty it was not possible to distinguish between values of k at the two wavelengths, thus k_{λ_1} and k_{λ_2} are treated as a single value k . This uncertainty was partially due to the fact that, for size parameters between 1.0 and 10 , scattering techniques are primarily dependent on n and d_{32} and secondarily dependent on k [36]. Note that for this size parameter range, emission measurements are primarily dependent on k and secondarily dependent on n [37]. Also, it was found that for realistic particle size distribution widths (i.e. $0.05 \leq d_{mp}/d_{32} \leq 0.3$) the results were insensitive to the value of d_{mp}/d_{32} . A value of 0.15 was used for d_{mp}/d_{32} in this study.

Although the results of this study indicate a range of multiple possible solutions for n , k , and d_{32} , values that best match the average experimental values are:

$$d_{32} = 0.97 \pm 0.11 \mu\text{m} \quad (29)$$

$$n_{\lambda_1} = 1.65 \pm 0.03 \quad (30)$$

$$n_{\lambda_2} = 1.64 \pm 0.03 \quad (31)$$

$$k_{\lambda_1, \lambda_2} = 6 \times 10^{-3} \pm 4 \times 10^{-3} \quad (32)$$

The values for d_{32} given above correspond to the smoke component of Al_2O_3 . The resulting size parameters for the two wavelengths are $x_{32\lambda_1} = 4.82$ and $x_{32\lambda_2} = 2.86$. The fact that a mono-modal size distribution gives self-consistent results, at both wavelengths, indicates that the large residual oxide cap mode probably does not influence the optical properties of Al_2O_3 inside the motor environment.

The values of n in Eqs. (30) through (31) are less than the solid phase values that are usually assumed. However, a decrease in n upon melting is to be expected due to the expansion that takes place. Using the Lorentz-Lorenz equation for estimating n_l and matching the values of n_l from Eqs. (30) and (31) to Eq. (1), an effective temperature near the melting point of

UNCLASSIFIED

Al_2O_3 is obtained ($T_m=2320$ K). The values of n_l from Eqs. (30) and (31) are plotted in Fig. 1 along with the Lorentz-Lorenz equation, Eq. (1), for $T= 2320$ K.

The values for k in Eq. (32) are an order of magnitude larger than Reed's recommendation Eq. (3), for an effective temperature of 2320 K. This increase in k is possibly due to electronic transitions at short wavelengths. The values of k from Eq. (32) are plotted in Fig. 2. Figure 2. also shows that other researchers report an order of magnitude upswing in k at short wavelengths. Stoichiometric effects, as mentioned earlier, could also have a significant influence on the value of k . An effective temperature close to the melting temperature of Al_2O_3 was predicted by a one-dimensional model of the distributed combustion of aluminum and production of Al_2O_3 near the surface of a burning aluminized composite solid propellant [38].

Even for the moderate optical depth values measured (1.21 to 1.28) the experimental bi-directional transmittance values were an order of magnitude larger than the reflectance values. A value of 0.94 ± 0.02 was obtained for the single scatter albedo, $\bar{\omega}_0$. The scattering asymmetry factor $\langle \bar{p} \rangle$ was 0.65 ± 0.02 . All these results indicated that scattering was predominantly in the forward direction.

CONCLUSIONS

A new optical technique was developed to determine the optical constants (n and k) and mean optical size, d_{32} , for liquid Al_2O_3 smoke particles produced by aluminized solid propellant combustion. This technique used *in situ* absolute scattering and extinction measurements, near the surface of the burning propellant, at two wavelengths. The Lorentz-Lorenz equation was consistent with the experimental data and can be used to predict the value of n for liquid Al_2O_3 at a given wavelength and temperature. The experimentally determined values of k for liquid Al_2O_3 near the burning propellant surface are an order of magnitude larger than comparable values (i.e. same wavelength and temperature) obtained from analyses of Al_2O_3 collected from rocket plumes. A value of $0.97 \pm 0.11 \mu\text{m}$ is recommended for d_{32} . Scattering is predominantly in the forward direction with a value of 0.94 ± 0.02 for the albedo and 0.65 ± 0.02 for the scattering asymmetry factor.

ACKNOWLEDGMENTS

Support for this work from Hercules/AFAL (Contract F04611-86-C-0016), the National Science Foundation (Grant CBT 83-51243), and the Office of Naval Research (Contract N00014-87-K-0547) is gratefully acknowledged.

REFERENCES

1. Pearce, B. E., "Radiative Heat Transfer within a Solid-Propellant Rocket Motor," *Journal of Spacecraft and Rockets*, Vol. 15, No. 6, AIAA, New York, 1979.
2. Brewster, M. Q., "Particle Radiative Feedback in Ammonium Perchlorate Deflagration," *AIAA Journal*, Vol. 24, No. 7, July 1986, pp. 1141-1147.
3. Edwards, R. H., and Bobco, R. P., "Radiant Heat Transfer from Isothermal Dispersions with Isotropic Scattering," *ASME J. of Heat Transfer*, Vol. 89, 1967, pp. 300-308.
4. Konopka, W. L., Reed, R. A., and Calia, V. S., "Measurements of Infrared Optical Properties of Al_2O_3 Rocket Particles," *Prog. In Astro. and Aero*, Vol. 91, 1984, pp. 180-197.
5. Gai, G., and Kirch, H., "Particulate Optical Properties in Rocket Plumes," AFRPL-TR-73-99, 1973, pp. 28-29.
6. Carlson, D. J., "Emittance of Condensed Oxides in Solid Propellant Combustion Products," Tenth (International) Symposium on Combustion, The Combustion Institute, 1965, pp. 1413-1424.
7. Bauer, E., and Carlson, D. J., "MIE Scattering Calculations for Micron Size Alumina and Magnesia Spheres," *J. Quant. Spectrosc. Radiat. Transfer*, Vol. 4, 1964, pp. 363-374.
8. Adams, J. M., "A Determination of the Emissive Properties of a Cloud of Molten Alumina Particles," *J. Quant. Spectrosc. Radiat. Transfer*, Vol. 7, 1967, pp. 273-277.
9. Mularz, E. J., and Yuen, M. C., "An Experimental Investigation of Radiative Properties of Aluminum Oxide Particles," *J. Quant. Spectrosc. Radiat. Transfer*, Vol. 12, 1972, pp. 1553-1568.
10. Gryvnak, D. A., and Burch, D. E., "Optical and Infrared Properties of Al_2O_3 at Elevated Temperatures," *J. Opt. Soc. Am.*, Vol. 55, No. 6, 1965, pp. 625-629.

UNCLASSIFIED

11. Malitson, I. H., "Refraction and Dispersion of Synthetic Sapphire," J. Opt. Soc. Am., Vol. 52, No. 12, 1962, pp. 1377-1379.
12. Plass, G. N., "Temperature Dependence of the Mie Scattering and Absorption Cross Sections for Aluminum Oxide," Applied Optics, Vol. 4, No. 12, 1965, pp. 1616-1619.
13. Reed, B., "Optical Properties for Liquid Al₂O₃," Private Communication, Arnold AFB, 29 Feb 1988.
14. Lee, D. W., and Kingery, W. D., "Radiation Energy Transfer and Thermal Conductivity of Ceramic Oxides," L. Am. Ceramic Soc., Vol. 43, No. 11, 1960, pp. 595-607.
15. Myers, V. H., Oro, A., and DeWitt, D. P., "A Method for Measuring Optical Properties of Semi-Transparent Materials at High Temperatures," AIAA J., Vol. 24, No. 2, 1986, pp. 321-326.
16. Lingart, et al., "Teplofizika Vysokikh Temperature," Vol. 20, No. 5, 1982, pp. 872-880.
17. Plass, G. N., "Mie Scattering and Absorption Cross Sections for Absorbing Particles," Applied Optics, Vol. 5, No. 2, 1966, pp. 279-285.
18. Bartky, C. D., and Bauer, E., "Predicting the Emittance of a Homogeneous Plume Containing Alumina Particles," L. of Spacecraft, Vol. 3, No. 10, 1966, pp. 1523-1527.
19. Slater, J. C., and Frank, N. H., Electromagnetism, Dover Publications, Inc., New York, 1969, pp. 109-114.
20. Kirshenbaum, A. D., and Cahill, J. A., "The Density of Liquid Aluminum Oxide," J. Inorg. Nucl. Chem., Vol. 14, 1960, pp. 283-287.
21. Nelson, L. S., and Richardson, N. L., "Effects of Oxygen and Argon Atmospheres on Pendant Drops of Aluminum Oxide Melted with Carbon Dioxide Laser Radiation," High Temp. Sci., Vol. 5, 1973, pp. 138-154.
22. Kraeutle, K. J., and Bradley, H. H. Jr., "Combustion of Aluminized Propellants: The Influence of Pressure and Propellant Composition on Formation of Aluminum Combustion Residue," 14th JANNAF Combustion Mtg., CPIA Publication, pp. 209-219.
23. Hauffe, Karl, Reaktionen in und an festen Stoffen, Springer-Verlag, Berlin, 1966, p. 219.
24. Price, E. W., "Combustion of Metallized Propellants," Fundamentals of Solid Propellant Combustion, Prog. in Astro. and Aero., Vol. 90, eds. K. K. Kuo and M. Summerfield, AIAA, 1984, ch. 9, pp. 479-513.
25. Kraeutle, K. J., "Particle Size Analysis In Solid Propellant Combustion Research," Prog. in Astro. and Aero., AIAA, 1978, pp. 76-108.
26. Drew, C. M., et al., "Study of Quenched Aluminum Particle Combustion," AIAA Heterogeneous Combustion Conference, Preprint 63-487, Dec. 11-13, 1963.
27. Brown, B., and McArty, K. P., "Particle Size of Condensed Oxides from Combustion of Metalized Solid Propellants," Formation, Combustion, Explosion and Detonation of Solids, pp. 814-923.
28. Switzenbank, J., et al., "A Laser Diagnostic Technique For the Measurement of Droplet and Particle Size Distribution," AIAA 14th Aerospace Sciences meeting, Paper 76-69, Jan. 1978, pp. 421-439.
29. Chigier, N. A., and Stewart, G., "Guest Editorial: Particle Sizing and Spray Analysis," Opt. Engr., 23, 554, 1984.
30. Hofeldt, D. L., et al., "Instantaneous Two-Dimensional Multiple Particle Sizing Diagnostic," 24th JANNAF Combustion Meeting, Stanford University.
31. Hermans, R. W., "Aluminum Oxide Particle Size for Solid Rocket Motor Performance Prediction," J. Spacecraft and Rockets, Vol. 18, No. 6, 1981, pp. 483-490.
32. Orguc, S., et al., "Measurement of Particulate Size in Solid Propellant Rocket Motors," Proceedings of 1987 JANNAF Combustion Meeting, Monterey, CA, CPIA Publications.
33. Switzenbank, J., et al., "A Laser Diagnostic Technique for the Measurement of Droplet and Particle Size Distribution," Prog. In Astro. and Aero., Vol. 53, 1978, pp. 421-439.
34. Hansen, J. E., and Travis, L. D., "Light Scattering in Planetary Atmospheres," Space Sci. Rev., Vol. 15, 1974, pp. 527-610.
35. Brewster, M. Q., and Tien, C. L., "Radiative Transfer in Packed/Fluidized Beds: Dependent versus Independent Scattering," J. of Heat Transfer, Vol. 14, No. 4, 1982, pp. 573-579.
36. Parker, T. E., Rosen, D. I., and Rawlins, W. T., "Infrared Optical Property Measurement Techniques: Definition and Preliminary Design," AFRPL-TR-86-034, 1986, pp. 35-45.
37. Ibid, pp. 46-53
38. Brewster, M. Q., and Parry, D. L., "Radiative Heat Feedback in Aluminized Solid Propellant Combustion," L. Thermophysics, Vol. 2, No. 2, 1988, pp. 123-130.

UNCLASSIFIED

INVESTIGATION OF AI AND Mg/AI ALLOY BEHAVIOR
IN COMPOSITE SOLID PROPELLANT COMBUSTION

Brian E. Hardt and M. Quinn Brewster
Department of Mechanical and Industrial Engineering
University of Illinois at Urbana-Champaign
Urbana, Illinois

ABSTRACT

The behavior of Al and Mg/Al in metalized solid composite propellants is addressed. Quench collection and burning rate measurements have been used to determine the correlation of burning rate with metal behavior in a series of HTPB composite propellants. It has been found that the temperature aluminum may reach before leaving the surface of an ammonium perchlorate composite solid propellant is close to the melting point of its oxide (2300 K). A simple energy balance at the surface coupled with a realistic surface temperature of aluminum has shown that the burning metal contributes a significant heat feedback. The heat feedback by burning aluminum in aluminized solid composite propellants may be a significant fraction of the total heat feedback. An explanation of the tendency of conventional composite burning rates models to over predict the burning rate in metalized formulations having wide oxidizer distributions has also been given based on the findings of this investigation.

INTRODUCTION

Metal combustion kinetics and agglomeration behavior may be playing a greater role in determining the burning rate in AP composite propellants than has been acknowledged. Evidence of this first appeared years ago when burning rate models were extended to aluminized composite solid propellants. When theoretical burning rates^{1,2,3} were compared to experimental burning rates,⁴ large discrepancies occurred in formulations with wide oxidizer distributions (Fig. 1). While holding the coarse oxidizer size constant and decreasing the fine oxidizer size in a propellant, burning rate models predicted increasing burning rates. However, the experimental burning rate data remained relatively constant. This discrepancy is surprising in light of the fact that in non-metalized propellants the agreement was generally within $\pm 10\%$. This suggests the possibility that metal combustion may influence the burning rate. In connection with this possibility, Sambamurthi et al.⁵ have recently shown that there is a correlation between oxidizer size distribution and aluminum agglomeration size, with wide oxidizer size distributions producing larger agglomerates. It is not unreasonable to expect that the aluminum behavior at the surface may affect the surface energy balance, and therefore, the burning rate. This may be the explanation for observed discrepancies between theoretical and experimental burning rate data for formulations with wide oxidizer size distributions. Independent evidence of burning rate dependence on metal content has been shown for pressed AP/metal pellets by Pai Verneker et al.⁶. It was found that for pressed AP/Al pellets a plot of burning rate versus percent metal revealed a maximum burning rate occurring at an intermediate metal content. The situation in AP pellets, however, is admittedly quite different than that in composite propellants.

In this study, the effect of the metal behavior on the burning rate of composite propellant is examined by using a surface energy balance. The steady state energy balance of the propellant surface, shown in Fig. 2, is

$$\rho_p r \sum_i (f_{mi} (C_{pi} (T_{si} - T_0) + L_i)) = (1 - f_{mAL}) \rho_p q_s' + q_{metal} \quad (1)$$

where

$$\rho_p q_s' = \rho_p r Q_s + \lambda_g \frac{dT}{dx} \Big|_{s+} = \lambda_s \frac{dT}{dx} \Big|_{s-} \quad (2)$$

The left side of equation (1) represents the energy required to raise the propellant from the initial temperature to the surface temperature and the energy of decomposition and phase change. The first term on the right side of equation (1) is representative of the heat feedback produced by the gas phase reactions (AP and binder flames), and surface heat release as shown in equation (2). The second term is the heat feedback from the burning metal, including both radiative and conductive modes.

This energy balance is basically the same as those analyzed in references [1,2,3]. The tendency has been to ignore the metal heat feedback and take the surface temperature of aluminum to be the same as the binder surface temperature. It has been suggested, however, that aluminum must be heated to temperatures well above its melting point (933 K)^{7,8} and perhaps near its oxide melting temperature (2320 K) before igniting and departing from the surface. This produces a large heat sink effect which tends to decrease the burning rate by robbing energy from the primary oxidizer-binder flame. On the other hand, a compensating heat feedback, radiative and possibly conductive, is produced by the combustion of the metal. The magnitude of this enhancement is dependent on the agglomeration characteristics of the propellant. Smaller agglomerates release energy closer to the surface, thus increasing the conductive feedback. The radiative heat feedback, which is less dependent on agglomeration characteristics, but might also increase slightly with smaller agglomerates. The magnitude of the radiative heat feedback has been measured⁹ and predicted theoretically¹⁰ to be of the order of 200 - 400 W/cm².

This work was performed under grant N00014-87-K-0547 with the Office of Naval Research.

Approved for public release; distribution is unlimited.

UNCLASSIFIED

This evidence suggests that most burning rate models for aluminized propellants tend to underestimate both the surface temperature of the aluminum and the heat feedback provided by the burning metal. The energy balance reveals that underestimation of the aluminum surface temperature may be offset by neglecting the metal contribution to the total heat feedback. Thus, in most situations the agreement between predicted and experimental burning rates can be expected. However, in certain situations, like wide oxidizer size distributions and large agglomerates, these errors may not offset, leading to considerable discrepancies between theoretical and experimental burning rates.

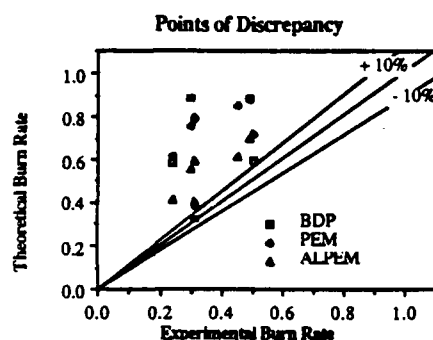


Fig. 1 Theoretical vs. Experimental Burning Rate

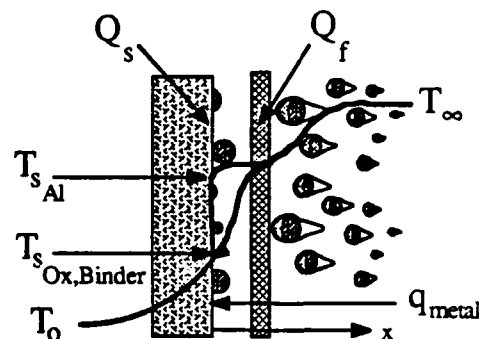


Fig. 2 Surface Energy Balance

The purpose of this study was to look for a correlation between agglomeration and burning rate, and see if this correlation coupled with the surface energy balance could explain the large discrepancies discussed above. The approach taken was to formulate a series of propellants such that the rate controlling flames would be similar between non-metalized and metalized formulations, gather experimental data, and then estimate the magnitude of the metal participation using the surface energy balance equation (1).

PROCEDURE

PROPELLANT PRODUCTION

The reported results are based on a series of hand-mixed propellants. For each formulation the AP, metal, and HTPB R-45 were carefully weighed, mixed, and placed in an oven at 60°C. The above samples were left in the oven in excess of one half-hour to achieve a temperature of 60°C. This was done to reduce the viscosity of the mixture and allowed easier removal of air pockets. In attempt to achieve a homogeneity, the mixture was then removed from the oven, mixed thoroughly and returned to the oven. After allowing the mixture to return to 60°C, the curative was mixed into the sample. The mixture was then placed in a vacuum oven at 60°C and 29 inches of Hg vacuum. To remove trapped air pockets, the mixture was kept under vacuum for thirty minutes before being removed and gently tamped. The propellant was then returned to the heated vacuum chamber. This cycle was executed until no visible surface changes were noticed. The absence of surface change indicated that a pressure difference would no longer aid in the removal of air from the propellant. To minimize the volume of any trapped air, the mixture was cured at atmospheric pressure. The propellant was left to cured at 60°C for 4 days.

PROPELLANT FORMULATIONS

Several propellants were formulated varying only the metal content and type of metal. The AP/binder ratio was kept constant to test the hypothesis that the primary AP/binder flame alone controls the burning rate. The AP to binder mass ratio was kept constant at 4.385 to 1. The ratio of coarse to fine AP was kept constant at 7 to 3. The AP was provided by Kerr-McGee. The coarse AP was 400 µm Rotary Round and the fine AP was 90 µm. Both AP sizes were coated with tricalcium phosphate (TCP). Hydroxyl terminated polybutadiene R-45 was used as the resin and isophorone diisocyanate, IPDI, was used as the curative to produce the HTPB binder. The mass percent metal content was varied from 0 to 30 in increments of 10. Two types of metals were used; Alcoa 123 Aluminum and A.D. Mackey Mg-Al alloy. The alloy was 10% Mg and 90% Al. The alloy was sieved to match the size of the aluminum. Both the aluminum and the alloy size distributions were found using a Coulter Counter. The median diameter of the Alcoa 123 Aluminium was 13 µm, and of the alloy was 19 µm. The distributions were similar. The actual formulations are given in Table I.

Table I. Propellant Formulations

Propellant*	% metal	% coarse AP	% fine AP	% R-45	% IPDI
H-400-90-0	0	57.00	24.43	17.33	1.244
H-400-90-10-Al	10	51.30	21.99	15.59	1.120
H-400-90-20-Al	20	45.60	19.54	13.86	0.9954
H-400-90-30-Al	30	39.90	17.10	12.13	0.8710
H-400-90-10-Mg	10	51.30	21.99	15.59	1.120
H-400-90-20-Mg	20	45.60	19.54	13.86	0.9954
H-400-90-30-Mg	30	39.90	17.10	12.13	0.8710

* Mg denotes the Mg-Al alloy

UNCLASSIFIED

DATA COLLECTION AND ANALYSIS

The 10 x 10 x 3 mm samples were mounted to a stainless steel plate and suspended inside a quartz tube. The propellant was attached to the plate by using three pins protruding from the plate. The experimental setup is shown in Fig. 3. To eliminate foreign particle contamination of the quench bath, a Nd-YAG pulsed laser was used as the ignition source. The quartz tube was used to direct the flow of products downward into the bath. The bath consisted of ammonium acetate dissolved in ethanol. The ammonium acetate was used to buffer the HCl present in the products. Particulate contaminants above 2 μm were removed from the quench bath fluid by filtering. Immediately following the collection of particulates, the bath was buffered with excess ammonium acetate-ethanol and transferred into sample containers. These samples were analyzed for size distribution by Anderson Physics Laboratory. The distributions were determined by use of a Coulter Counter. The analysis was completed within four hours of the collection. As a check, a sample was analyzed both initially and then again 3 days later. No significant changes in the distribution were noted.

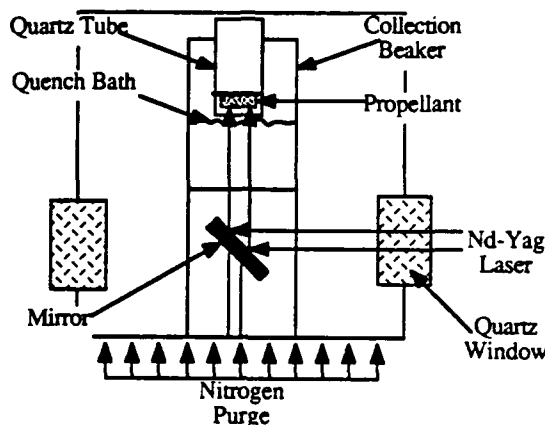


Fig. 3 Experimental Setup

BURNING RATE MEASUREMENTS

Burning rate data were measured using a standard strand burner in conjunction with a video cassette recorder. The strands were 6 x 2 x 15 mm. The strands were kept thin to insure void free propellant. It should be noted that with this small width, radiative and convective losses could result in a lower measured burning rate than the actual burning rate. However, the same physical trends should be seen. The strands were coated with a thin film of petroleum jelly to insulate the strands from convective losses of the sides and inhibit the ignition of the propellants sides. To verify that the burning rate measurements were reliable, burning rate data were logarithmically plotted against pressure as a check for realistic values for the pressure exponent.

RESULTS

PARTICLE SIZE ANALYSIS

The size distribution of the metal leaving the propellant surface was found to be bi-modal. The first peak occurred at diameters slightly larger than that of the ingredient metal, ~ 20 μm , and the second at a much larger value, 100 - 200 μm . The large agglomerates of the second peak dominated the volume/mass weighted distributions. Therefore, volume weighted data rarely revealed a bi-modal distribution but only a single peak at the size of the larger agglomerates. This can be seen in Fig. 4 and 5 and in Table II. The remainder of this discussion will be based on a number weighted basis and should not be confused with volume weighted data. The Mg/Al alloy tended to produce a greater number of small, unagglomerated particles. For 10% metal content, both Al and Mg-Al, the unagglomerated particles out numbered the agglomerated particles. As the metal content was increased to 20%, the number of unagglomerated particles was reduced close to the number of agglomerated particles, and at 30% metal content the number of unagglomerated were insignificant compared to the large agglomerates (Fig. 4). The distribution of the large agglomerated particles broadened with increasing pressure. Note that this broadening effect can not be seen in the standard deviations because they were calculated over the entire range and not for each peak (i.e. a bi-modal distribution would give a large standard deviation even if the peaks were sharp).

UNCLASSIFIED

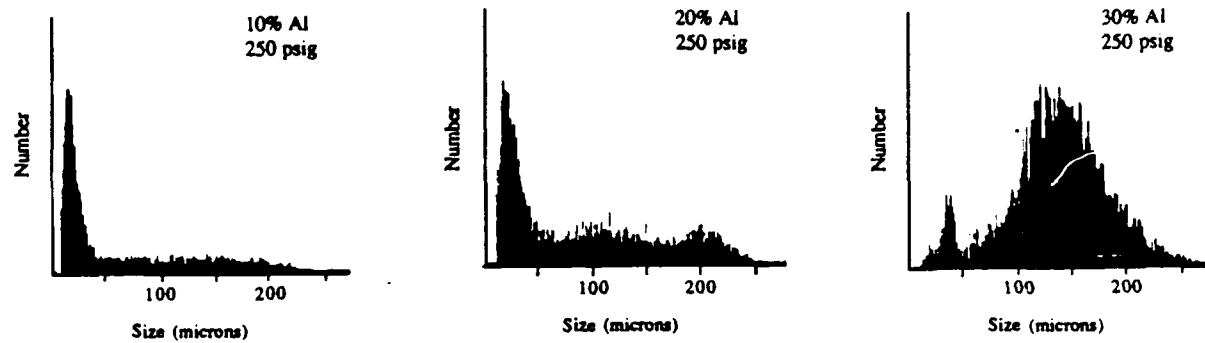


Fig. 4 Particle Size Distribution on a Number Basis

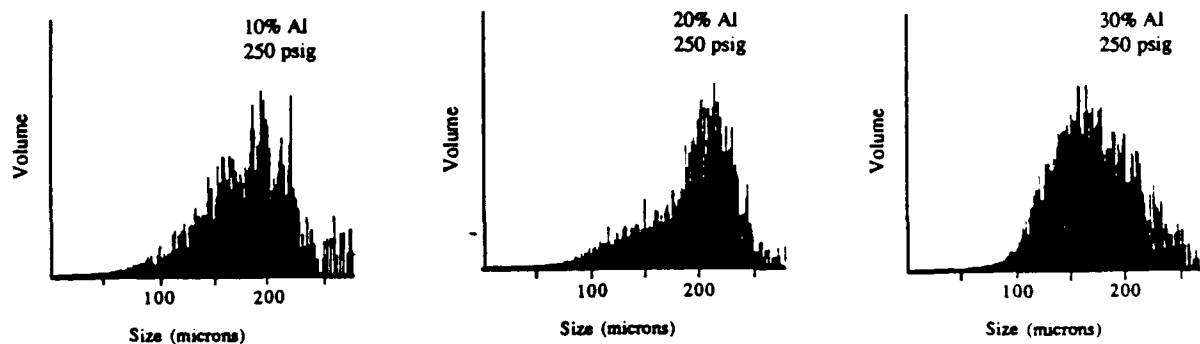


Fig. 5 Particle Size Distribution on a Volume Basis

Table. II Average Collected Particle Size

Propellant	P(psig)	Volume Weighted		Vol. Wt. Unweighted		Unweighted r (cm/s)
		Median (μm)	σ (μm)	Median (μm)	σ (μm)	
H-400-90-0	250	-	-	-	-	0.3322
	500	-	-	-	-	0.4688
	750	-	-	-	-	0.6008
H-400-90-10-AL	250	181.5	42.13	29.30	63.04	0.3648
	500	-	-	-	-	0.4800
	750	103.3	66.77	14.20	12.78	0.6033
H-400-90-20-AL	250	196.5	41.06	72.93	72.93	0.3644
	500	-	-	-	-	0.4225
	750	201.1	29.96	183.7	49.65	0.5205
H-400-90-30-AL	250	168.6	37.24	137.0	46.71	0.3304
	500	-	-	-	-	0.4054
	750	185.8	41.15	138.2	54.27	0.4643
H-400-90-10-MG	250	186.9	42.43	18.54	48.71	0.4037
	750	204.6	32.13	151.8	76.96	0.6186
H-400-90-20-MG	250	155.1	37.73	16.35	38.11	0.4113
	750	205.3	32.77	175.9	55.13	0.6316
H-400-90-30-MG	250	191.0	41.29	121.5	62.19	0.3949
	750	179.1	38.44	125.3	52.94	0.5948

BURNING RATE

Burning rate data for all propellants were taken at 250 and 750 psig, and also at 500 psig for the aluminized propellants. The burning rate versus pressure plots revealed that the Mg/Al alloy and pure aluminum affected the pressure exponent quite differently. These plots are shown in Fig. 6a and 6b. The addition of any amount of metal (either Al or Mg-Al) seems to decrease the pressure exponent. This is thought to be due to the influence of the extra radiative feedback, which is relatively insensitive to pressure. As expected, the value of the pressure exponent decreases with increasing aluminum concentration. However, the exponent for the Mg/Al propellants remains relatively constant for increasing metal concentrations. The magnesium alloy, which would tend to ignite at lower temperatures and burn more quickly than aluminum, would be expected to provide a strong conductive heat feedback as well as a significant radiative component. Aluminum would tend to release most of its energy farther away from the surface, resulting in a significant radiative but little conductive heat feedback compared with

UNCLASSIFIED

Mg-Al alloy. Therefore, the aluminized propellants, compared to alloy propellants, would tend to get a larger percent of the total heat feedback from radiation. Since radiation is much less pressure dependant than conduction, it is reasonable that the pressure exponent for the Mg/Al propellants would not decrease as much after the initial addition of metal as aluminized propellants.

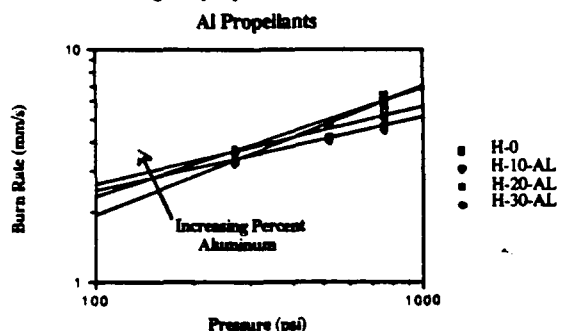


Fig. 6a Burning rate vs Pressure for Al Propellants

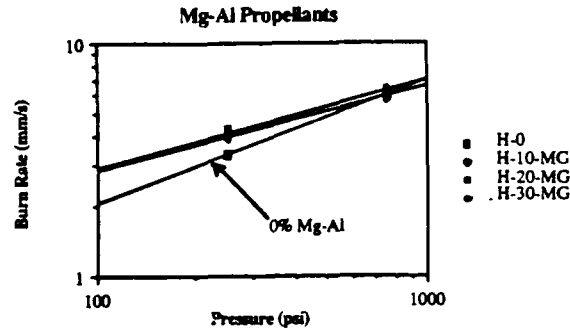


Fig. 6b Burning rate vs Pressure for Mg-Al Propellants

A plot of burning rate versus percentage metal is shown in Fig. 7. At low metal concentration, all propellants revealed that the enhanced heat feedback from the addition of the metal was greater than the heat sink, resulting in a positive slope of the burning rate versus percent metal curve. Due to magnesium's lower ignition temperature and stronger conductive feedback, the burning rates of the alloy propellants are higher and the slopes remain positive to a higher concentration of metal than in the case of pure aluminum. At high metal concentrations the metal heat sink effect is large enough to produce a decrease in burning rate with increasing metal concentration in all the propellants tested.

Note that the burning rate for the aluminized propellant at 750 psig drops sharply between 10 and 30 percent metal. The particle size data showed that this large drop in burning rate was accompanied by a large increase (100%) in agglomerate size (from 103 μm to 201 μm).

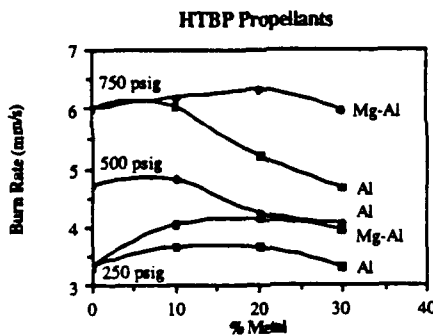


Fig. 7 Burning rate vs % Metal

ENERGY BALANCE

By coupling the experimental burning rate data with the surface energy balance equation (1), the magnitudes of the aluminum surface temperature and the metal heat feedback were estimated. The surface energy balance was initially solved for the gas phase (AP and binder flame) heat feedback q_s^* . For a nonmetallized propellant, equation (1) becomes

$$q_s^* = r \sum_i (f_{mi} (C_{pi} (T_{Si} - T_0) + L_i)) \quad (3)$$

The value of q_s^* for each pressure was calculated using the nonmetallized data. The AP and HTPB were assumed to follow the general pyrolysis law

$$f_{mi} \rho_p r = A_i \exp \left(\frac{-E_i}{R T_{Si}} \right) \quad (4)$$

The values of the parameters used in equation (4) are shown in Table IV.

UNCLASSIFIED

Table. IV Parameter Values

A_{AP}	$= 4.0 \times 10^5$ [g/(cm ² s)]	E_{AP}	$= 23.0$ [kcal/mole]
A_{HTPB}	$= 299$ [g/(cm ² s)]	E_{HTPB}	$= 16.9$ [kcal/mole]
L_{Al}	$= 95.5$ [cal/g]	C_{PAI}	$= 1.0$ [J/(g K)]
L_{AP}	$= 10.0$ [cal/g]	C_{PAP}	$= 1.3$ [J/(g K)]
L_{HTBP}	$= 433.$ [cal/g]	C_{PHTPB}	$= 1.3$ [J/(g K)]

Using the experimental burning rates, the surface temperatures of the AP and HTPB were calculated for each combination of propellant and pressure. These surface temperatures, experimental burning rate data, and an estimated surface temperature for metals were used in the energy equation to calculate the heat feedback from the burning metal, q_{metal} . When an aluminum surface temperature of 2300 K was used, the calculated values of q_{metal} for aluminized propellants ranged from 200 - 400 W/cm² (Table V). This value of q_{metal} represent 25 - 50% of the total heat feedback for this slow burning aluminized propellant. The percentage of the total heat feedback represented by q_{metal} for faster burning propellants would in general be expected smaller. Similar values for this radiative heat feedback have been experimentally⁹ and theoretically¹⁰ estimated for aluminized propellants. As expected, the corresponding values of q_{metal} for the alloy propellants were higher than for the aluminized propellants. Also, the increase in q_{metal} with increasing metal content, was greater for the alloy propellants. This was probably due to the Mg-Al having a greater conductive feedback than the pure aluminum propellants. Unrealistic values for the aluminum surface temperature, T_{sAl}^C , were found when zero metal heat feedback was assumed (Table V) for the aluminized propellants.

Table. V Calculated Heat Sinks/Feedbacks for Aluminized Propellants [W/cm²]

Pressure (psig)	% Metal	q_{metal}^{Al}	q_{metal}^{Al-Mg}	T_{sAl}^C [K]
		($T_{sAl} = 2300$ K, $T_{sMg} = 1000$ K)	($q_{metal} = 0$)	
750	0	-	-	-
	10	217.4	241.9	317.6
	20	266.1	493.4	714.5
	30	361.0	641.5	853.3
500	0	-	-	-
	10	185.8	-	217.4
	20	253.3	-	572.0
	30	397.1	-	534.4
250	0	-	-	-
	10	185.9	251.3	-101.9
	20	324.5	405.4	139.9
	30	388.6	515.2	336.0

Al Values of aluminum propellants based on $T_{sAl} = 2300$ K & $T_{sMg} = 1000$ K

Al-Mg Values for the alloy propellants based on $T_{sAl} = 2300$ K & $T_{sMg} = 1000$ K

c Values of T_{sAl}^C based on $q_{metal} = 0$

SUMMARY AND RECOMMENDATIONS

The goal of this study was to investigate the relationship between metal behavoir and burning rate in metalized solid composite propellants. Formulations were tailored to isolate the sole effect of metal behavoir from other burning rate determining variables. For this reason, the AP to binder ratio was kept constant at 4.385 to 1. This would insure that the AP-binder flames would be similar between nonmetalized and metalized propellants. Thus, the change in magnitude of the AP-binder heat feedback would be proportional to the change in the mass fraction of the sum of the AP and binder. The ratio of coarse to fine AP was also kept constant at 7 to 3. Once these propellants were produced, burning rate measurements taken and particle size distributions were determined.

The size distribution of the metal leaving the propellant surface was found to be bi-modal. The smaller peak occurred at diameters slightly larger than the ingredient metal. The large agglomerates (100 - 200 μ m) dominated the volume-mass weighted distributions. As the metal content was increased, the number of unagglomerated particles decreased. At 30% metal, the number of unagglomerated particles were practically unnoticeable. When the aluminum content was increased from 10 to 20%, a large increase in agglomeration size (100%) was accompanied by a sharp drop in burning rate for 750 psig.

Plots of burning rate versus pressure, revealed that the addition of metal, Al or Mg-Al, leads to a reduction of the pressure exponent. This is thought to be a result of the influence of raditive feedback, which is relatively independent of pressure. A plot of burning rate versus metal content, confirmed that the burning metal was providing an enhanced heat feedback to the propellant surface. This study has shown that for realistic surface temperatures of aluminum the enhanced heat feedback produced by the burning metal may be 25 - 50% of the total heat feedback for slow burning propellants.

In metalized composite solid propellants, the addition of metal produces both an additional heat sink and an enhanced heat feedback to the propellants surface. The extent of this heat feedback is dependant on the combustion kinetics and agglomeration characteristics of the metal. Radiation probably dominates this enhanced feedback for slow burning metals like aluminum. In past modeling efforts values assumed for the surface temperature of aluminum and for the magnitude of the metal heat feedback have probably been too small. These two effects will often compensate and the magnitude of the burning rate will not be affected

UNCLASSIFIED

significantly. However, in some cases (i.e. wide oxidizer size distributions) these effects may not offset and considerable errors may occur. Therefore, it is recommended that for future modeling efforts, the burning metal heat feedback should be included and the surface temperature be estimated at values near its oxide melting temperature of 2300 K.

ACKNOWLEDGMENTS

Support for this work from the Office of Naval Research (Contract N00014-87-k-0547) and the National Science Foundation (Grant CBT 83-51243) is gratefully acknowledged. The authors wish to thank colleagues, especially C. Freidhof & Anderson Physics Laboratory, A. Ishihara and T. Sheridan, for helpful discussions and irreplaceable assistance.

NOMENCLATURE

i	=	constituent (AP, metal, or binder)
ρ_p	=	density of the propellant [g/cm ³]
r	=	burning rate [cm/s]
f _{mi}	=	mass fraction of "i"
C _{pi}	=	specific heat of "i" [J/(g K)]
T _{Si}	=	surface temperature of "i" [K]
T ₀	=	initial temperature of the propellant [K]
L _i	=	heat of fusion (AP,metal) or decomposition of "i" [cal/(g K)]
q _{metal}	=	heat feedback from metal (conductive and radiative) [W/cm ²]
Q _s	=	AP chemical heat release at the surface generation [J/g]
$\lambda_{g,s}$	=	thermal conductivity of gas and solid phases [W/(cm K)]
s+	=	gaseous side of the surface
s-	=	propellant side of the surface
E _i	=	the activation energy of "i"
R	=	ideal gas constant
q̄ _i	=	energy required raise the temperature of "i" from T ₀ to T _{Si}
q _{net}	=	net energy produced by the addition of aluminum
T _{SAL}	=	calculated surface temperature of aluminum if no metal feedback is assumed

REFERENCES

1. Beckstead, M. W., "A Model for Solid Propellant Combustion," Proceedings of the Fourteenth JANNAF Combustion Meeting, CPIA Publication 292, Vol. 1, Dec. 1977, pp. 281-306.
2. Glick, R. L., and Condon, J. A., "Statistical Combustion Modeling - The Effect of Additives," Proceedings of the Fourteenth JANNAF Combustion Meeting, CPIA Publication 261, Vol. 1, Dec. 1977, pp. 341-378.
3. Renie, J. P., "Combustion Modeling of Composite Solid Propellants," Ph.D. Thesis, Purdue University, Dec. 1982.
4. Miller, R. R., et al., "Control of Solids Distribution in HTPB Propellants," AFRPL-TR-78-14, Hercules Inc., Allegheny Ballistics Laboratory, Cumberland, MD, April 1978.
5. Sambamurthi, J. K., Price, E. W., and Sigman, R. K., "Aluminum Agglomeration in Solid-Propellant Combustion," Georgia Institute of Technology, Atlanta, *AIAA Journal*, Vol. 22, August 1984, pp. 1132-1138.
6. Pai Verneker et al., "Role of Alloys in the Thermal Decomposition and Combustion of Ammonium Perchlorate," *Combustion and Flame*, Vol. 67, 1987, pp. 163-173.
7. Price, E. W., "Combustion of Metalized Propellants," Progress in Astronautics Series (K. K. Kuo, and M. Summerfield) AIAA, Vol. 90, 1988, pp. 479-513.
8. Sambamurthi, J. K., "Behavior of Aluminum on the Burning Surface of a Solid Propellant," Ph.D. Thesis, Georgia Institute of Technology, Atlanta, March, 1983.
9. Brewster, M. Q., and Taylor, D. M., "Radiative Properties of Burning Aluminum Droplets," *Combustion and Flame*, Vol. 72, 1988, pp. 287-299.
10. Brewster, M. Q., and Parry, D.L., "Radiative Heat Feedback in Aluminized Composite Solid Propellant Combustion.", *AIAA Journal of Thermophysics and Heat Transfer*, Vol. 2, No. 2, April, 1988, pp. 123-130.

UNCLASSIFIED

Combustion Response of a Homogeneous Solid Propellant to an
Oscillatory Radiant Heat Flux

by

T. D. Prevish*
and
M. Q. Brewster**

University of Illinois
Department of Mechanical and Industrial Engineering
Urbana, Illinois

Western States Section/The Combustion Institute
March 20-21, 1989
Pullman, Washington

* Graduate Research Assistant

** Associate Professor of Mechanical Engineering

***Supported by Office of Naval Research (N00014-87-K-0547)

NOMENCLATURE*

A_1 = preexponential constant in solid phase mass burning rate equation.
 B_1 = preexponential constant in gas phase mass burning rate equation.
 C_p = constant pressure specific heat of gas phase.
 C_s = specific heat of solid.
 E_f = gas-phase reaction activation energy.
 E_s = solid-phase reaction activation energy.
 K_a = extinction coefficient in Beer's Law.
 k_g = thermal conductivity of gas phase.
 k_s = thermal conductivity of solid phase.
 m = mass burning rate.
 n_p = steady state value of the pressure-coupled response function.
 n_q = steady state value of the heat flux-coupled response function.
 P = pressure.
 Q_f = Heat release from the gas-phase reactions (>0 exothermic).
 q_r = total external radiant heat flux.
 Q_s = Combination of latent heat and heat released in solid surface reactions (>0 exothermic).
 R_p = pressure-coupled response function.
 R_q = heat flux-coupled response function.
 R = universal gas constant.
 T_i = temperature deep within the solid.
 T_f = adiabatic flame temperature.
 T_s = temperature at solid surface.
 β = opacity constant = $k_g k_s / m \cdot C_s$.
 γ = ratio of gas phase specific heats.
 λ = eigenvalue in solid phase temperature solution.
 λ_i = imaginary part of eigenvalue.
 λ_r = real part of eigenvalue.
 v_1 = pressure exponent in gas phase mass burning rate equation.
 ρ = density.
 σ_p = temperature coefficient
 ϕ = temperature gradient
 ω = frequency in hertz.
 Ω = dimensionless frequency.

* a - denotes steady state values and a ' denotes perturbed values.

ABSTRACT

A theoretical burning rate model has been developed to predict the combustion response function for non-aluminized, homogeneous solid propellants subject to low amplitude (linear), oscillatory, external radiant heat flux or pressure perturbations. The solid is treated as homogeneous with in-depth radiation absorption. The gas phase is treated as quasi-steady. The high activation energy, asymptotic analysis of laminar flame theory is used to describe the gas phase conductive heat feedback. The heat flux response function is shown to be very sensitive to both the mean level of the radiant flux and the absorption coefficient of the propellant, with high radiant fluxes and large absorption coefficients giving the largest responses. For surface absorption the heat flux and pressure response functions demonstrate nearly the same frequency dependence but for in-depth absorption the two response functions have quite different frequency dependence.

INTRODUCTION

One of the key parameters in the analysis of unstable, time-dependent combustion in solid rocket motors is the pressure-coupled response function, R_p . This parameter has long been measured using T-burners and L*-burners. However, these devices are limited by physical restrictions and many questions associated with the interpretation of data. Because the oscillatory frequency of a test depends on the dimensions of the apparatus, many burners must be built to gain a knowledge of R_p over a range of frequencies. One alternative to these methods for studying the combustion response of solid propellants is to measure the burning rate response to an imposed external radiant heat flux, R_q . If a theory could be developed to relate R_q and R_p the costs associated with a solid rocket motor development program could be significantly reduced.

Instead of building a number of different test fixtures and running many different tests, one test with an oscillating external radiant heat flux impinging upon a small strand of propellant could conceivably cover a wide range of frequencies. In addition, the interpretation of data might be less controversial. The time and money saved in this manner make the heat flux-driven experiment an approach well worth pursuing.

PREVIOUS WORK

Many investigators have considered the effects of an external radiant heat flux on the burning rate of solid propellants. Several investigators (Hertzberg, Horton and Youngberg¹; Coates and Kwak²; Caveny, Ohlemiller and Summerfield³; and Ibiricu and Williams⁴) have studied the effect of a constant radiant heat flux q_r on the steady mass burning rate m . The principal conclusion of these studies is that at low to moderate flux levels (<100 cal/cm²sec) radiant energy absorbed in-depth, below the location of the rate-controlling chemical reactions, is equivalent to an increase of $\Delta T = \frac{q_r}{mC_s}$ in the initial temperature of the propellant, T_i (the so-called equivalence principle). This conclusion has both positive and negative consequences, as pointed out by Ibiricu and Williams and Caveny, Ohlemiller and Summerfield. On the positive side, it means that in-depth, radiation absorption effects can be relatively easily incorporated into the theoretical analysis of both steady and unsteady combustion (assuming the absorption takes place beneath the rate-controlling reaction layers). This result, of course, has favorable implications in terms of the objectives of the current study. On the negative side, the equivalence principle means that no new information about the chemical or physical reaction mechanisms can be obtained from radiant heat flux experiments that could not be obtained from burning rate temperature sensitivity data.

Many investigators (Mihlfeith^{5,6}, Mikheev⁷, Zarko^{8,9}, Ohlemiller¹⁰, Strand¹¹) have also studied the effect of time-varying radiant heat fluxes on the combustion response of solid propellants, including step input and oscillatory radiant fluxes. One of the first studies to examine the possibility of utilizing R_q measurements to obtain R_p was conducted by Mihlfeith, Baer and Ryan⁵. They used a piezoelectric, micro-force transducer to measure the combustion recoil induced by an oscillatory incident radiant flux. From a momentum balance they were able to obtain the instantaneous mass burning rate m' and thus R_q . They also developed a combustion model which made it possible to relate R_p and R_q . The combustion model of Mihlfeith used a small amplitude (linear perturbation) analysis of the unsteady solid phase. Their assumptions were very similar to those of the earlier Denison and Baum¹² analysis of unsteady combustion, including:

- (1) A one-dimensional homogeneous solid,
- (2) Quasi-steady gas phase (flame description approach),
- (3) Quasi-steady, simple surface pyrolysis, and
- (4) In-depth absorption with no sub-surface chemical heat release.

To describe the gas phase, a large activation energy flame model from Culick¹³ was used. The assumption of large activation energy has been shown to be equivalent to a flame sheet approximation. Culick's model was a derivative of the von Elbe laminar premixed flame theory which had been used by Denison and Baum, modified to account for the presence of the solid. (Using asymptotic analysis, Williams later argued that the original von Elbe description was actually the appropriate model in the limit of large gas flame activation energy.)¹⁴

Soon after Mihlfeith's work appeared, Mikheev, et.al.⁷ reported on a similar combustion recoil technique which made use of a capacitance transducer.

Corresponding theoretical analysis of Zarko⁸ made use of the Zel'dovich-Novozhilov approach rather than the gas phase flame description approach referred to in assumption (2) above. As discussed by Kuo, Gore and Summerfield¹⁵ in their recent review article, although the Zel'dovich approach simplifies the analysis by avoiding the details of the spatial distribution of heat release in the gas phase (e.g. flame sheet versus distributed heat release, etc.), it also requires more extensive steady-state burning rate data. Namely, the pressure and temperature sensitivity of the steady state burning rate $m(T_i, P)$ and the steady-state surface temperature as a function of pressure and burning rate $T_s(P, m)$ are required.

More recently, Strand and co-workers¹¹ have reported on a microwave doppler technique for measuring the instantaneous burning rate m' . Although the microwave technique is currently limited to non-metallized propellants (since the microwaves must be transmitted through the propellant for reflection at the burning surface and metal particles strongly scatter almost any wavelength of electromagnetic radiation, including microwaves), the superior frequency response of this technique still makes it an attractive option. In addition to this novel and promising experimental technique, the theoretical analysis of Strand also takes a new approach by considering non-linear, finite amplitude perturbations, in conjunction with the Zel'dovich approach.

OBJECTIVES

The primary objective in this particular study was to obtain a transfer function, $F = \frac{R_p}{R_q}$, that would bridge the gap between the desired pressure-coupled response function, R_p , and the more conveniently attainable heat flux-coupled response function, R_q . To do this, a theoretical burning rate model

was developed for the system. First a steady-state model was established and then a linear (small amplitude perturbation) transient model was developed. From the combined steady-state and transient models the theoretical response function was extracted.

STEADY-STATE COMBUSTION MODEL

The first step in the overall model is to describe the steady state characteristics of a burning propellant under the influence of an incident external radiant energy flux. This process is illustrated schematically in Figure 1. The frame of reference is fixed at the surface of the propellant and moves with the steady-state regression rate of the propellant.

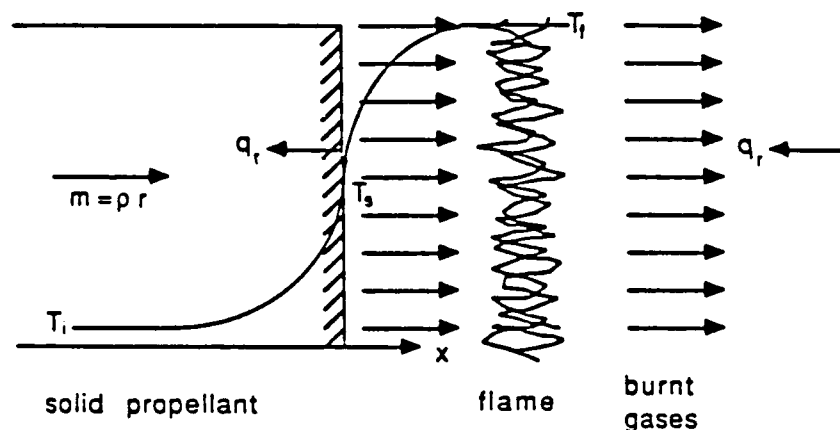


Figure 1. Schematic illustration of the burning surface

An energy balance is then written for condensed phase, the surface and the gas phase regions, respectively.

$$\bar{m} C_s (\bar{T}_s - T_i) = k_s \bar{\phi}_{s-} + \bar{q}_r \quad \text{where} \quad \phi = \frac{\partial T}{\partial x} \quad (1a)$$

$$k_s \bar{\phi}_{s-} = \bar{m} \bar{Q}_s + k_g \bar{\phi}_{s+} \quad (1b)$$

$$k_g \bar{\phi}_{s+} + \bar{m} C_p (\bar{T}_f - \bar{T}_s) = \bar{m} \bar{Q}_f \quad (1c)$$

The sum of these equations represents the overall steady-state energy balance.

$$\bar{m} \{C_s (\bar{T}_s - \bar{T}_i) + C_p (\bar{T}_f - \bar{T}_s)\} = \bar{q}_r + \bar{m} (\bar{Q}_f + \bar{Q}_s) \quad (2)$$

The radiation term \bar{q}_r represents the fraction of the external radiant flux incident at the surface which is absorbed by the propellant. The surface heat release term \bar{Q}_s (>0 , net exothermic) is assumed to include both latent energy for phase change and chemical energy for thermal decomposition. As pointed out by Ibiricu and Williams, the thermodynamic relation

$$\bar{Q}_s = (C_p - C_s) \bar{T}_s + \text{const} \quad (3)$$

insures that the final flame temperature \bar{T}_f is independent of the surface temperature \bar{T}_s . Eqn. (3) represents one equation with three unknowns, \bar{m} , \bar{T}_f , and \bar{T}_s . Two more equations are needed for closure of the steady-state problem. These two equations are provided by the gas phase flame description model and the surface pyrolysis relation.

For the gas flame description, the high activation energy (flame sheet) model of Williams is used.

$$\bar{m} = \left[\frac{2k_s B_1 R^2 C_p}{E_f^2 \bar{Q}_f^2} \right] \bar{p}^{v_1} \bar{T}_f^2 \exp \left[\frac{-E_s}{R \bar{T}_s} \right] \quad (4)$$

This relation gives the mass burning rate as a function of the final flame temperature and other gas phase thermochemical, thermophysical and kinetic properties. Use of this relation assumes that the gas phase reactions represent the rate limiting step which controls the overall mass burning rate of the propellant (as opposed to condensed phase reactions). The conditions for verifying this assumption are discussed by Ibiricu and Williams.

The solid region is assumed to be a non-metallized, homogeneous propellant with any condensed-phase reactions occurring within a sufficiently narrow depth to be considered surface reactions (i.e. simple surface pyrolysis).

$$\bar{m} = A_1 \exp \left[\frac{-E_s}{R \bar{T}_s} \right] \quad (5)$$

It should be noted that in place of Eqn. (5), Ibiricu and Williams use a similar result derived on the basis of a high activation energy, asymptotic analysis of the reactive-diffusive zone in the condensed phase (Eqn. (8) of Ibiricu and Williams). That relation includes a term for the fraction of external radiation which is absorbed below (i.e. on the cold side of) the condensed phase reactive-diffusive zone (Q_1). However, their asymptotic analysis also assumes the limit of large absorption coefficient (in order to push all of the in-depth absorption on the hot side of the reactive zone, Q_2 , into a surface layer thin relative to the dimension of the reactive-diffusive zone, thereby simplifying the equations). By doing so, it would seem that to be consistent, the Q_1 contribution of Ibiricu and Williams should be counted as part of Q_2 . That is, under the stated assumptions, no amount of radiant energy would be absorbed beneath the condensed phase reactive-diffusive zone, and the Q_1/m term of Eqn. (8) in Ibiricu and Williams should be set to zero, resulting in an expression equivalent

to the surface pyrolysis law, Eqn. (5). Based on this reasoning, it was decided in the initial phase of this study to simply use the surface pyrolysis relation, Eqn. (5), to determine the surface temperature.

TRANSIENT COMBUSTION MODEL

After establishing the steady-state description, the next step in the overall model is to describe the transient combustion response of the propellant to the action of either a low amplitude, oscillatory external radiant heat flux

$$q_r = \bar{q}_r + q_r' \exp(i\omega t), \quad q_r' \ll \bar{q}_r \quad (6)$$

or a low amplitude, oscillatory pressure perturbation

$$p = \bar{p} + p' \exp(i\omega t), \quad p' \ll \bar{p} \quad (7)$$

Under the influence of either of these time-dependent disturbances the propellant burns in an oscillatory fashion with instantaneous burning rate m .

$$m = \bar{m} + m' \exp(i\omega t), \quad m' \ll \bar{m} \quad (8)$$

The surface location therefore moves back and forth with respect to the mean surface location. The frame of reference is taken to be fixed at the surface of the propellant. Thus the origin moves with the instantaneous regression rate of the propellant. This approach has been shown to be analytically equivalent to an inertial reference frame which moves at the mean burning rate¹³.

The gas phase processes and the surface pyrolysis are assumed to be quasi-steady (i.e. no time lag with respect to the imposed oscillating

disturbance). Unsteadiness is accounted for only in the solid phase region which has the slowest time constant in the system (about 0.01 sec associated with thermal diffusion). This limits the analysis to frequencies below about 1000 hz as discussed by Kuo, Gore, and Summerfield. Since unsteadiness must only be accounted for in the solid phase, the unsteady equations can be obtained by simply perturbing (i.e. differentiating with respect to time) the surface and gas phase equations, Eqns. (1b, 1c, 3, 4, and 5).

$$k_s \dot{\phi}_s^- = k_g \dot{\phi}_s^+ + m' \bar{Q}_s + \bar{m} Q_s' \quad (9)$$

$$k_s \dot{\phi}_s^+ = \bar{m} [Q_f' - C_p(T_f' - T_s')] + m' [\bar{Q}_f - C_p(\bar{T}_f - \bar{T}_s)] \quad (10)$$

$$Q_s' = (C_s - C_p)T_s' \quad (11)$$

$$\frac{m'}{\bar{m}} = \nu_1 \frac{p'}{\bar{p}} + \left(2 + \frac{E_f}{2R\bar{T}_f} \right) \frac{T_f'}{\bar{T}_f} - \frac{Q_f'}{\bar{Q}_f} \quad (12)$$

$$\frac{T_s'}{\bar{T}_s} = \frac{m'}{\bar{m}} \frac{R\bar{T}_s}{E_s} \quad (13)$$

Compression heating of the gas is accounted for in the term Q_f' by assuming isentropic compression.

$$Q_f' = C_p \bar{T}_f \frac{\gamma-1}{\gamma} \frac{p'}{\bar{p}} \quad (14)$$

To complete the model, a transient analysis of the unsteady solid phase must be carried out to obtain a relation for the instantaneous temperature gradient on the solid side of the surface, ϕ'_s , for use in place of Eqn. (1a).

Unsteady Solid Phase Analysis

The unsteady energy equation in the solid phase, with in-depth absorption is

$$\rho C_s \frac{\partial T}{\partial t} + m C_s \frac{\partial T}{\partial x} = k_s \frac{\partial^2 T}{\partial x^2} + \dot{q}_r \quad (15)$$

For simplicity, the density, thermal conductivity, and heat capacity of the solid are considered constant. To include the effect of in-depth absorption, the solution of the radiative transfer equation is used

$$\dot{q}_r = q_r K_a \exp(K_a x) \quad (16)$$

where it has been assumed that scattering is negligible, the absorption coefficient K_a is spatially constant and independent of wavelength, thermal emission by the condensed phase is negligible, and the incident flux is collimated. Applying a linear perturbation to Eqn. (16)

$$T(x,t) = \bar{T}(x) + T'(x) \exp(i\omega t) \quad (17)$$

yields the steady state and perturbed forms of the solid phase energy equation.

$$\frac{\partial^2 \bar{T}}{\partial x^2} - \frac{\bar{m} C_s}{k_s} \frac{\partial \bar{T}}{\partial x} = - \frac{\bar{q}_r K_a}{k_s} \exp(K_a x) \quad (18)$$

$$\frac{\partial^2 T'}{\partial x^2} - \frac{\bar{m}C_s}{k_s} \frac{\partial T'}{\partial x} - \frac{\rho C_s}{k_s} (i\omega) T' = -\frac{q_r' K_a}{k_s} \exp(K_a x) + \frac{m' C_s}{k_s} \frac{dT}{dx} \quad (19)$$

The solution to Eqn. (18) with the boundary conditions $T(0)=T_s$ and $T(-\infty)=T_i$ gives the steady state temperature distribution in the solid.

$$\bar{T} = T_i + \left[(\bar{T}_s - T_i) + \frac{\bar{q}_r}{(k_s K_a - \bar{m} C_s)} \right] \exp\left(\frac{\bar{m} C_s}{k_s} x\right) - \frac{\bar{q}_r}{(k_s K_a - \bar{m} C_s)} \exp(K_a x) \quad (20)$$

Likewise, the solution to Eqn. (19) with $T'(0)=T_s'$ and $T'(-\infty)=0$ gives the perturbed temperature distribution.

$$T' = (T_s' - K_1 - K_2) \exp\left(\frac{\lambda \bar{m} C_s}{k_s} x\right) + K_1 \exp(K_a x) + K_2 \exp\left(\frac{\bar{m} C_s}{k_s} x\right) \quad (21)$$

where

$$K_1 = \frac{- \left[\frac{q_r'}{k_s} K_a + \frac{\bar{q}_r K_a}{(k_s K_a - \bar{m} C_s)} \left(\frac{m' C_s}{k_s} \right) \right]}{\left[K_a^2 - \frac{K_a \bar{m} C_s}{k_s} + \left(\frac{\bar{m} C_s}{k_s} \right)^2 \lambda (1-\lambda) \right]} \quad (22)$$

$$K_2 = \frac{\left[(\bar{T}_s - T_i) + \frac{\bar{q}_r}{(k_s K_a - \bar{m} C_s)} \right] \frac{m'}{\bar{m}}}{\lambda (1-\lambda)} \quad (23)$$

The root of the characteristic equation λ is

$$\lambda = \frac{1}{2} + \sqrt{\frac{1}{4} + i\Omega} \quad (24)$$

where the non-dimensional frequency is defined as

$$\Omega = \frac{\rho k_s \omega}{\bar{m}^2 C_s} \quad (25)$$

Separating λ into real and imaginary parts gives

$$\lambda_r = \frac{1}{2} \left[1 + \frac{1}{\sqrt{2}} (\sqrt{1+16\Omega^2} + 1)^{1/2} \right] \quad (26)$$

$$\lambda_i = \frac{1}{2\sqrt{2}} [\sqrt{1+16\Omega^2} - 1]^{1/2} \quad (27)$$

The instantaneous conductive heat flux on the solid side at the surface is obtained from Eqn. (21) as

$$k_s \phi'_s = \bar{m} C_s \lambda T_s' + \frac{m' C_s}{\lambda} (\bar{T}_s - T_i) - \frac{m'}{\bar{m}} \bar{q}_r \frac{(1-\lambda)}{\lambda(1-\lambda-\beta)} + q_r' \frac{\beta}{1-\lambda-\beta} \quad (28)$$

where

$$\beta = \frac{k_s K_a}{\bar{m} C_s}$$

represents the ratio of the characteristic length scale for thermal diffusion in the solid to that for absorption (mean free photon path). By combining Eqns. (9-14

and 28), T_s' and T_f' can be eliminated giving an equation for m' as a function of q_r' and P' .

$$\frac{m'}{\bar{m}} = R_q \frac{q_r'}{\bar{q}_r} + R_p \frac{P'}{\bar{P}} \quad (29)$$

where

$$R_q = \frac{\frac{m'}{\bar{m}}}{\frac{q_r'}{\bar{q}_r}} \Big|_P = \frac{\frac{-\beta \bar{q}_r}{(1-\lambda-\beta)}}{\left[R \bar{T}_s^2 + \lambda \bar{m} C_s \frac{E_s}{\bar{E}_s} + \frac{\bar{m} C_s}{\lambda} (\bar{T}_s - T_i) - \frac{(1-\lambda)\bar{q}_r}{\lambda(1-\lambda-\beta)} - \bar{m} (\bar{Q}_s + G_2) \right]} \quad (30)$$

$$R_p = \frac{\frac{m'}{\bar{m}}}{\frac{P'}{\bar{P}}} \Big|_{q_r} = \frac{\bar{m} C_p \left[G_1 \left(v_1 \cdot \left(\frac{\gamma-1}{\gamma} \right) \frac{C_p \bar{T}_f}{\bar{Q}_f} \right) + \bar{T}_f \left(\frac{\gamma-1}{\gamma} \right) \right]}{R \bar{T}_s^2 + \lambda \bar{m} C_s \frac{E_s}{\bar{E}_s} + \frac{\bar{m} C_s}{\lambda} (\bar{T}_s - T_i) - \frac{(1-\lambda)\bar{q}_r}{\lambda(1-\lambda-\beta)} - \bar{m} (\bar{Q}_s + G_2)} \quad (31)$$

$$G_2 = \bar{Q}_f \cdot C_p \left(\bar{T}_f \cdot \bar{T}_s + G_1 \cdot \frac{C_s}{C_p} \cdot \frac{R \bar{T}_s^2}{\bar{E}_s} \right) \quad (32a)$$

and

$$G_1 = \frac{\bar{T}_f}{2 + \frac{E_f}{2R\bar{T}_f}} \quad (32b)$$

The magnitude of the transfer function is found by taking the ratio of the magnitudes of the response functions

$$|F| = \frac{|R_p|}{|R_q|} \quad (33)$$

In this way the pressure-coupled response function for a propellant can be calculated by multiplying the transfer function by the heat flux-coupled response function measured in the laboratory.

The response functions can also be represented in a more standard form (after Culick) by normalizing with the steady state, or zero frequency, values.

$$\frac{R_p}{n_p} = \frac{AB + C}{\lambda + \frac{A}{\lambda} - (1 + A) + AB + \left[\frac{\beta\lambda + (1-\lambda)^2}{\beta\lambda + (1-\lambda)\lambda} \right] C} \quad (34)$$

$$n_p = R_p|_{\Omega \rightarrow 0} = \frac{\frac{\gamma-1}{\gamma} + \frac{C_p \bar{T}_f \frac{\gamma-1}{\gamma}}{2 + \frac{E_f}{2R\bar{T}_f}}}{\frac{C_p \bar{T}_f}{C_s \bar{T}_s} \left[\frac{1}{2 + \frac{E_f}{2R\bar{T}_f}} \right] + \frac{\bar{q}_r}{\bar{m} C_s \bar{T}_s}} \quad (35)$$

$$\frac{R_q}{n_q} = \frac{(AB + C) \frac{\beta}{(\beta+\lambda-1)}}{\lambda + \frac{A}{\lambda} - (1+A) + AB + \left[\frac{\beta\lambda + (1-\lambda)^2}{\beta\lambda + (1-\lambda)\lambda} \right] C} \quad (36)$$

$$n_q = R_q|_{\Omega \rightarrow 0} = \frac{\frac{\bar{q}_r}{m C_s \bar{T}_s}}{\frac{E_s}{R \bar{T}_s} \left\{ \frac{C_p \bar{T}_f}{C_s \bar{T}_s} \left[\frac{1}{2 + \frac{E_f}{2R \bar{T}_f}} \right] + \frac{\bar{q}_r}{m C_s \bar{T}_s} \right\}} \quad (37)$$

$$A = \frac{E_s}{R \bar{T}_s} \left(1 - \frac{T_i}{\bar{T}_s} \right) \quad (38)$$

$$B = \frac{C_f \bar{T}_f}{C_s \bar{T}_s} \left[\frac{1}{2 + \frac{E_f}{2R \bar{T}_f}} \right] \left[\frac{1}{1 - \frac{T_i}{\bar{T}_s}} \right] \quad (39)$$

$$C = \frac{\bar{q}_r}{m C_s \bar{T}_s} \cdot \frac{E_s}{R \bar{T}_s} \quad (40)$$

STEADY-STATE SOLUTION

Before a transient response function can be calculated, a steady-state solution must either be assumed (arbitrarily) or calculated. To be consistent, it would seem that the steady-state solution should be calculated using the steady-state model from which the transient model was derived. In the following

parametric study, assumed propellant property values are used to calculate a steady-state solution for \bar{m} , \bar{T}_f and \bar{T}_s . That steady-state solution is then used with the same propellant parameters in the transient model to calculate the response functions. In this manner, the steady-state and transient solutions are calculated in a self-consistent manner. Table 1 shows the values used for the propellant properties and other physical constants.

Table 1. Propellant Properties and Constants

Solid	Gas
$k_s = 0.0009 \text{ cal/cm-s-K}$	$k_g = 0.0005 \text{ cal/cm-s-K}$
$C_s = 0.33 \text{ cal/g-K}$	$C_p = 0.33 \text{ cal/g-K}$
$\rho = 1.60 \text{ g/cm}^3$	$\gamma = 1.25$
$E_s = 16,000 \text{ cal/gmole}$	$Q_f = 450 \text{ cal/g (exothermic)}$
$Q_s = 100 \text{ cal/g (exothermic)}$	$P = 20 \text{ atm}$
$T_i = 300 \text{ K}$	$v_1 = 0.5$
$A_1 = 3586 \text{ g/cm}^2\text{-s}$	$R = 1.986 \text{ cal/gmole-K}$

The parametric study was subdivided into two major cases. The first set of data was generated using a gas phase reaction activation energy, E_f , of 20,000 cal/gmole and the second for an activation energy of 40,000 cal/gmole. The gas phase pre-exponential constant, B_1 , was adjusted to obtain a reasonable mass burning rate of around 1 g/cm²sec. This gave values for B_1 of 17,000 for $E_f = 20,000 \text{ cal/gmole}$ and 10^7 for $E_f = 40,000 \text{ cal/gmole}$. For each case, the steady state values of mass burning rate, flame temperature, and surface temperature were solved using Eqns. (2,4, and 5). Figures 2 and 3 give the steady-state solutions as a function of \bar{q}_r for $K_a = 10^4 \text{ cm}^{-1}$.

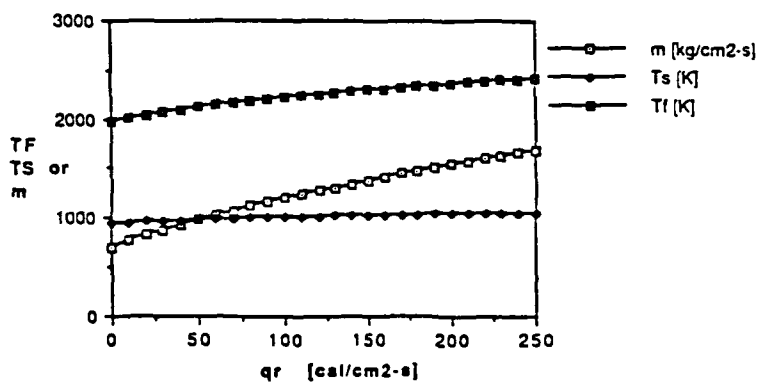


Figure 2. Steady-state solutions for $E_f = 20,000$ cal/gmole

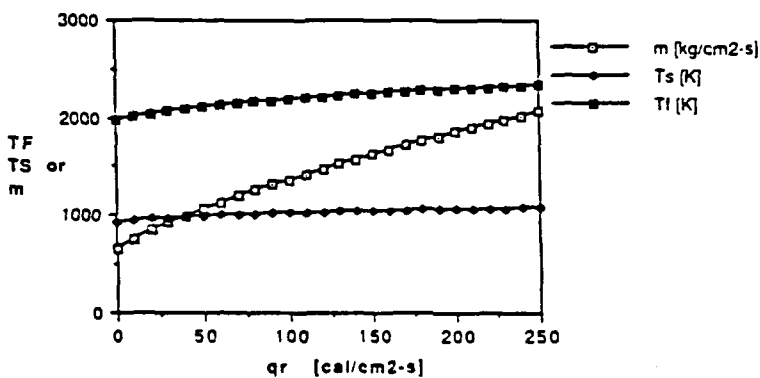


Figure 3. Steady-state solutions for $E_f = 40,000$ cal/gmole

Table 2 gives the values of the steady state solutions which are plotted in Fig. 2 and 3.

Table 2. Steady-State Solutions

		\bar{q}_r [cal/cm ² -s]					
		0	1	10	100	250	500
$E_f = 20,000$ cal/gmole	\bar{m} [g/cm ² -s]	.6987	.7541	.7648	1.194	1.693	2.336
	\bar{T}_s [K]	943	944	953	1006	1052	1098
$E_f = 40,000$ cal/gmole	\bar{T}_f [K]	1967	1971	2006	2221	2414	2616
	\bar{m} [g/cm ² -s]	.6548	.6656	.7553	1.364	2.063	
	\bar{T}_s [K]	936	938	952	1023	1080	
	\bar{T}_f [K]	1967	1971	2007	2189	2334	

As can be seen from the steady-state solution, increasing external flux increases both the final flame and surface temperatures. The increase in final flame temperature can be obtained from the overall energy balance Eqn. (2) as

$$\Delta \bar{T}_f = \frac{\bar{q}_r}{\bar{m}C_p} \quad (41)$$

The increase in surface temperature can also be expressed explicitly, assuming the temperature coefficient

$$\sigma_p = \frac{\partial \ln \bar{m}}{\partial T_i} \quad (\text{at constant } p \text{ and } \bar{q}_r = 0) \quad (42)$$

is constant, as demonstrated by Caveny, Ohlemiller and Summerfield.

$$\Delta \bar{T}_s = \left(\frac{R \bar{T}_s^2 \sigma_p}{E_s} \right) \left(\frac{\bar{q}_r}{\bar{m}C_s} \right), \quad (\sigma_p = \text{constant}) \quad (43)$$

For the steady-state model discussed here the temperature coefficient can be shown to be

$$\sigma_p = \frac{1}{\bar{T}_f} \left(2 + \frac{E_f}{2R\bar{T}_f} \right) \frac{C_s}{C_p} \quad (44)$$

The steady-state solution also demonstrates that the mass burning rate increases as external radiant flux increases. The magnitude of the increase of \bar{m} with \bar{q}_r can be estimated for the two limiting cases of weak ($\bar{q}_r \ll 100$

cal/cm²sec) and strong ($\bar{q}_r >> 100$ cal/cm²sec) external radiant fluxes from Eqn. (37). In the limit of a weak external flux

$$\frac{C_p \bar{T}_f}{C_s \bar{T}_s} \left[\frac{1}{2 + \frac{E_f}{2R\bar{T}_f}} \right] \gg \frac{\bar{q}_r}{\bar{m} C_s \bar{T}_s} \quad (45)$$

the burning rate can be shown to increase linearly with \bar{q}_r , assuming \bar{T}_s and \bar{T}_f are constant.

$$\bar{m} \propto \left(\frac{1}{C_s \bar{T}_s AB} \right) \bar{q}_r \quad (46)$$

The proportionality constant $\left(\frac{1}{C_s \bar{T}_s AB} \right)$ has a value of about 0.001 g/cal for the parameters assumed in the present model. Mihlfeith measured a value of about 0.004 in the composite propellants he studied and Caveny measured a value of about 0.01 in the double base propellants of that work.

In the limit of strong external flux

$$\frac{C_p \bar{T}_f}{C_s \bar{T}_s} \left[\frac{1}{2 + \frac{E_f}{2R\bar{T}_f}} \right] \ll \frac{\bar{q}_r}{\bar{m} C_s \bar{T}_s} \quad (47)$$

the burning rate can be shown to increase as \bar{q}_r to the $\frac{R\bar{T}_s}{E_s}$ power, assuming \bar{T}_s is constant.

$$\bar{m} \propto \bar{q}_r (\bar{R}\bar{T}_s/E_s) \quad (48)$$

Typically, the value of $\frac{\bar{R}\bar{T}_s}{E_s}$ is sufficiently small such that the slope of \bar{m} versus \bar{q}_r decreases as \bar{q}_r increases from the weak limit ($\bar{q}_r < 100$) toward the strong limit ($\bar{q}_r > 100$), as shown in Figs. 2 and 3.

TRANSIENT RESULTS

A parametric study was carried out to explore the sensitivity of the response functions R_q and R_p to different propellant and environmental parameters. In particular, the sensitivities of R_q to the radiant heat flux level \bar{q}_r and the propellant absorption coefficient K_a were investigated.

Figure 4 shows the sensitivity of the magnitude of R_q to \bar{q}_r for $E_f = 20,000$ cal/mole and $K_a = 10^4 \text{ cm}^{-1}$ as a function of non-dimensional frequency. Virtually no response is expected for an external flux of 1 cal/cm²-s, but as the flux is increased, the response function does likewise. A definite peak in the response is also noted, similar to what is typically observed in pressure-coupled response functions. The greater the heat flux is, the lower the frequency is at which this peak occurs.

The depth of the solid required to absorb the external flux also affects the response function, as indicated in Figure 5 for $\bar{q}_r = 100$ cal/cm²-s. For a propellant of relatively low opacity, no peak in the response is predicted. The higher the absorption coefficient, K_a , however, the greater the magnitude of R_q , up to a maximum of about 0.6 for an essentially opaque propellant. Typical propellants without any particle additives (carbon, catalysts or aluminum) have absorption coefficients in the visible and near infrared which are on the order of 10 cm^{-1} . Clearly this value is too low for the heat flux response technique to be

useful. Although the absorption coefficient can be increased by two to three orders of magnitude by adding only a few percent of sub-micron carbon particles [Brewster and Hardt]¹⁶, the best results with this technique will probably be achieved using an infrared source, such as a 10.6 μm CO₂ laser, which produces radiation at wavelengths where the bulk propellant ingredients (e.g. AP, etc.) have a higher absorption coefficient [Patel and Brewster]¹⁷.

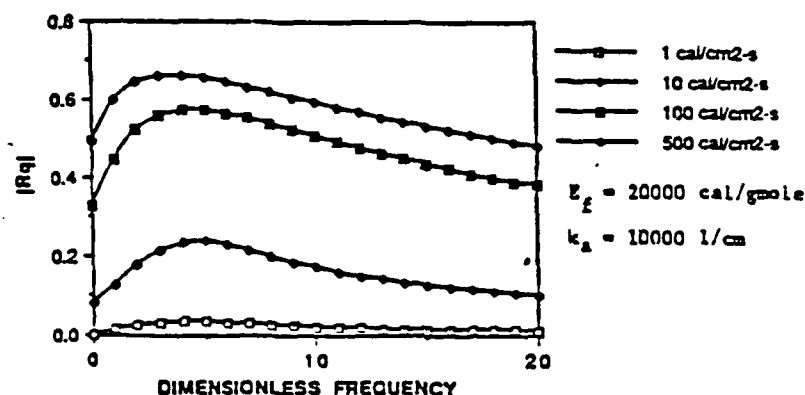


Figure 4. Effect of external flux on heat flux-coupled response function
(E_f = 20,000 cal/mole)

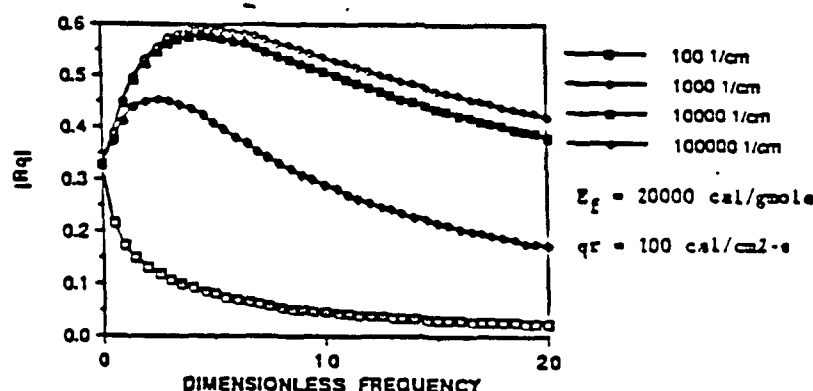


Figure 5. Effect of opacity on heat flux-coupled response function
(E_f = 20,000 cal/mole)

Another interesting effect to note is the behavior of the phase angle between the imposed heat flux and mass burning rate, shown in Figs. 6 and 7. For sufficiently opaque propellants, m' leads q_r' at low frequencies and lags at

higher frequencies. The crossover frequency usually occurs at or near the same frequency as the peak of the response function. For a weakly absorbing propellant no phase lead is predicted to occur. These predictions are in agreement with the measurements of Mihlfeith as well as the theory of Zarko and Kiskin which is based on the Zel'dovich-Novozhilov approach. An explanation of this behavior is given by Zarko and Kiskin based on the excess energy stored in the solid during irradiation compared with the case of no radiation. This effect is similar to the preheat effect discussed by Kuo, Gore and Summerfield in their review article for the pressure-driven case, except that in-depth radiation allows the possibility for complete phase lag even at low frequencies for weakly absorbing propellants.

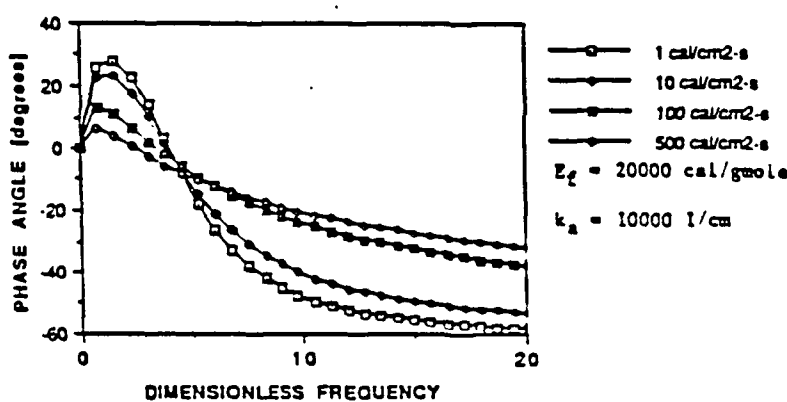


Figure 6. Effect of external flux on phase angle for R_q ($E_f = 20,000$ cal/mole)

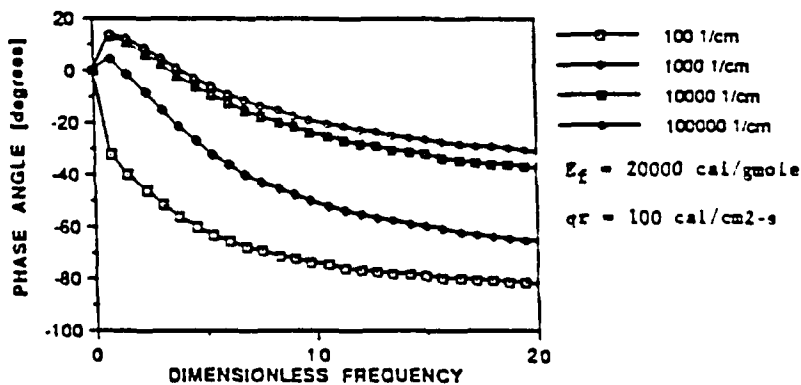


Figure 7. Effect of opacity on phase angle for R_q ($E_f = 20,000$ cal/mole)

Figure 8 shows the magnitude of R_p as a function of dimensionless frequency with $\bar{q}_r = 0$ to simulate non-metallized propellant combustion. The usual resonant behavior is observed, though the magnitude of the response is somewhat higher than that exhibited for R_q in Fig. 4 for the levels of external flux which were assumed. The phase angle also follows a pattern similar to that for R_q , as seen in Figure 9, crossing from a lead to a lag at the same frequency characteristic of the peak response. Since the external radiant flux is set equal to zero, the pressure-coupled response function does not vary with absorption coefficient.

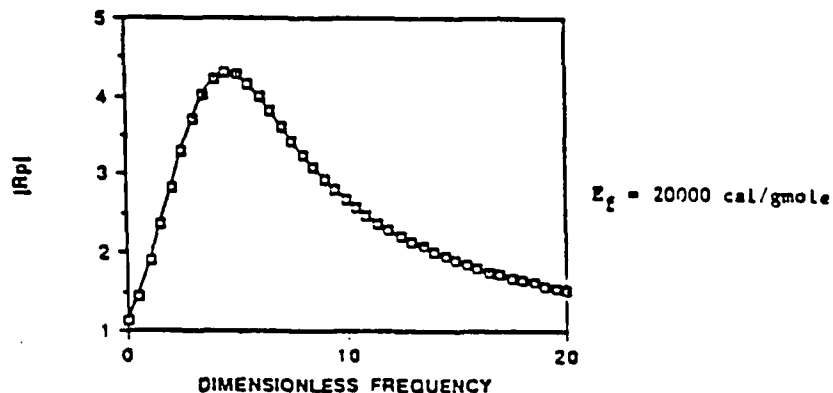


Figure 8. Magnitude of pressure-coupled response function
($E_f = 20,000 \text{ cal/mole}$)

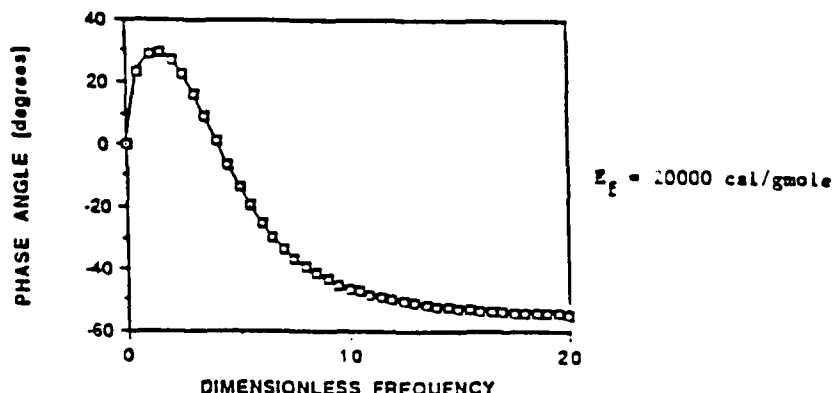


Figure 9. Phase angle for pressure-coupled response function
($E_f = 20,000 \text{ cal/mole}$)

The transfer function is presented in Figures 10 and 11. In Fig. 10 the transfer function is given for $K_a = 10^4 \text{ cm}^{-1}$ for various values of external flux. It can be seen that as q_r increases the magnitude of the transfer function decreases. This change is solely due to the change in the magnitude of R_q as indicated in Fig. 4. The effect of absorption coefficient is shown in Figure 11. For higher opacities (surface absorption) the transfer function is nearly independent of frequency. But for in-depth absorption, the transfer function becomes strongly dependent on frequency. This behavior can be explained by referring to Eqns. (30 and 31). For large absorptions coefficient (large β), the radiative term in the denominator of Eqns. (30 and 31) falls out. Likewise, the numerator of Eqn. (30) becomes independent of frequency. Since the denominators are nearly the same (at least to the degree the steady-state solutions are the same) the ratio of Eqns. (30) and (31), i.e. the transfer function, is also nearly independent of frequency. However, for small absorption (small β) the radiative term remains in the denominator of Eqn. (30) and R_q ($\bar{q}_r > 0$) has a different frequency dependence than R_p ($\bar{q}_r = 0$). In other words, since Eqns.(30) and (31) represent the same propellant burning under two different conditions--the first being a propellant in a laboratory subject to an external heat flux and the second being a propellant in a rocket motor subject to no appreciable external heat flux (ignoring metal combustion)--the denominators do not cancel when their ratio is taken. Additionally, an applied heat flux is going to change the steady state mass pyrolysis and surface and flame temperatures. This means the transfer function may have some frequency dependence even for high extinction coefficients, though the variation will be less than in the case of more translucent compositions.

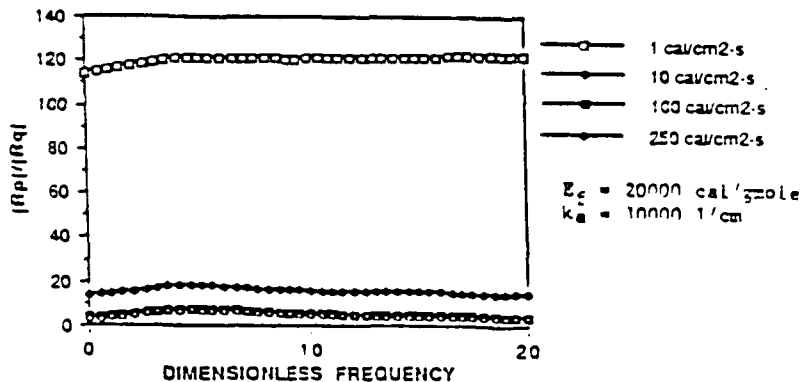


Figure 10. Effect of external flux on transfer function ($E_f = 20,000$ cal/mole)

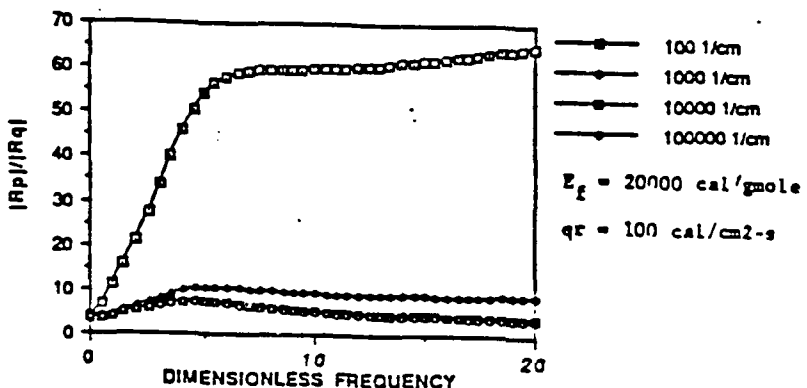


Figure 11. Effect of opacity on transfer function ($E_f = 20,000$ cal/mole)

The preceding calculations were also carried out for a gas phase reaction activation energy of 40,000 cal/gmole. The majority of results closely parallel those for the first case, though the effects are sometimes more dramatic. Several variations also arise. Figure 12 shows the magnitude of R_q for various external fluxes. Like the case for $E_f = 20,000$, little response is predicted for $\bar{q}_r = 1$ cal/cm²-s. However at 10 cal/cm²-s, the propellant exhibits a strong resonance response many times higher than normal. This instability appears to be an intrinsic instability of the same variety as that studied by Denison and Baum for the pressure-driven case. For still higher heat fluxes the peak response drops significantly, though the off-resonant response continues to increase with \bar{q}_r . This behavior is in significant contrast to the behavior for $E_f =$

20,000, apparently because the system was far from an intrinsic stability boundary for the earlier case.

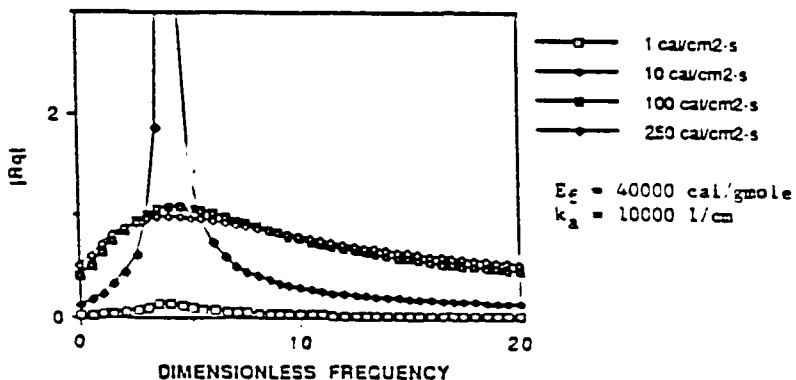


Figure 12. Effect of external flux on R_q ($E_f = 40,000$ cal/mole)

Figure 13 shows the dependence of R_q on K_a for $E_f = 40,000$ and $\bar{q}_r = 100$ cal/cm²-s. Since the value of $\bar{q}_r = 100$ places the system far from a stability boundary, the behavior is similar to that seen for the earlier case. However, as Figure 13 illustrates, the magnitudes of R_q are about a factor of two larger for the higher activation energy case.

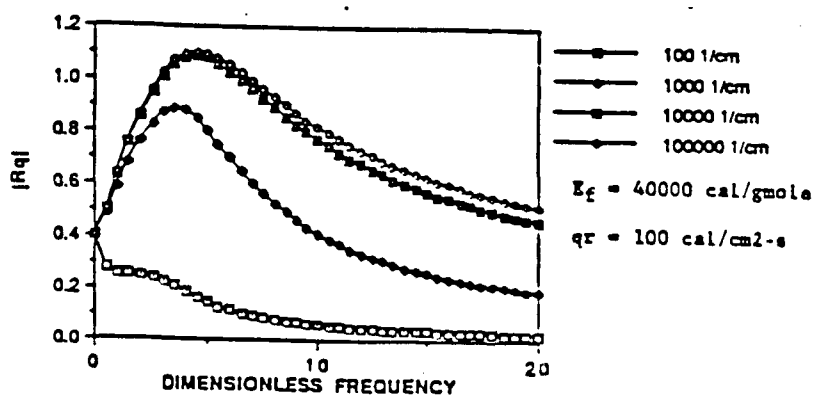


Figure 13. Effect of opacity on R_q ($E_f = 40,000$ cal/mole)

The phase angles for the heat flux-coupled response function are plotted in Figures 14 and 15. The trends are similar to those of the earlier case for $E_f =$

20,000. The apparent discontinuities in the plots are not real effects but arise from difficulty in choosing the correct sign for the argument of the arctangent function. A very strong dependence of phase angle with frequency is seen for the case of $\bar{q}_r = 10 \text{ cal/cm}^2\text{-s}$ in Fig. 14 near the resonance point due to the nearness of the system to a stability boundary, as previously discussed.

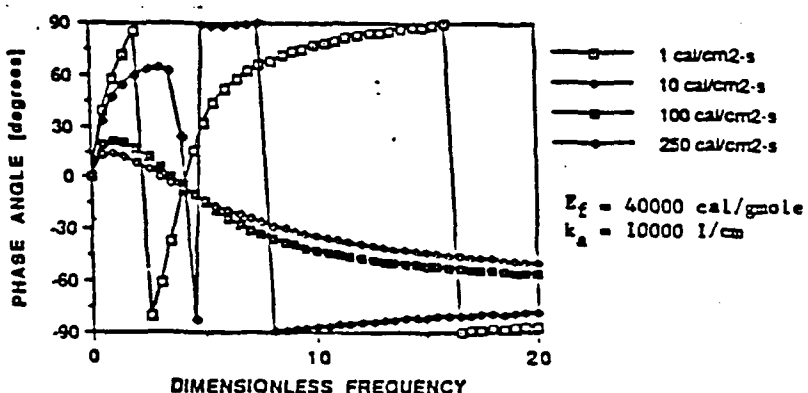


Figure 14. Effect of external flux on phase angle for R_q ($E_f = 40,000 \text{ cal/mole}$)

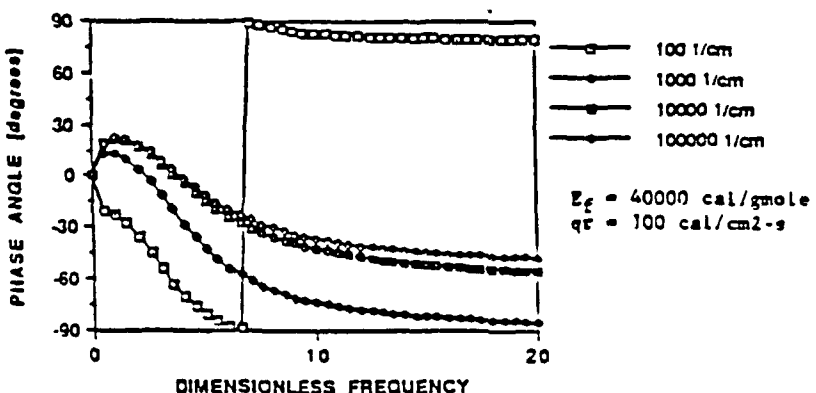


Figure 15. Effect of opacity on phase angle for R_q ($E_f = 40,000 \text{ cal/mole}$)

The magnitude of the corresponding pressure-coupled response function is plotted in Figure 16. The peak response is again much larger than that for the

heat flux-coupled response function for the assumed values of \bar{q}_r . The phase angle variation with frequency for R_p is illustrated in Figure 17.

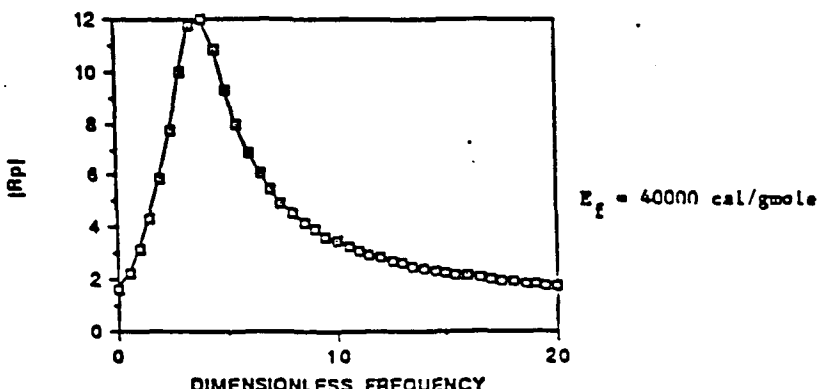


Figure 16. Magnitude of R_p ($E_f = 40,000 \text{ cal/mole}$)

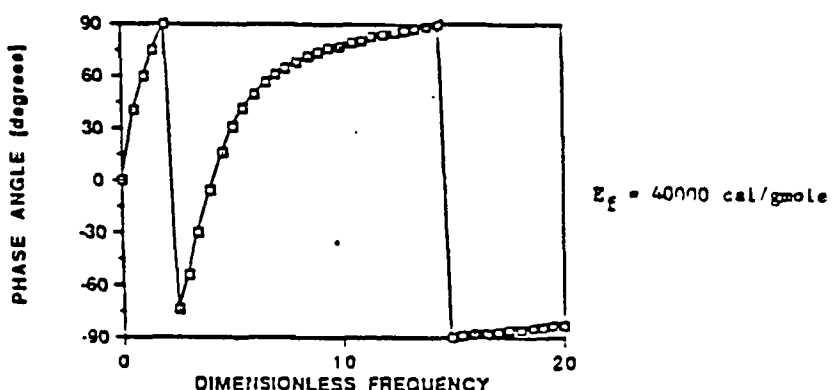


Figure 17. Phase angle for R_p ($E_f = 40,000 \text{ cal/mole}$)

The characteristics of the transfer function are similar to, but not quite the same as, those for the lower activation energy case. The magnitude of the transfer function still decreases markedly with increasing external flux, as plotted in Figure 18, with some interesting structure near the resonant frequency. For lower external fluxes, there is a dip in the transfer function. At higher values of \bar{q}_r , a small rise occurs near this point. As before, the sensitivity of the transfer function to frequency increases as absorption coefficient decreases, as shown in Figure 19.

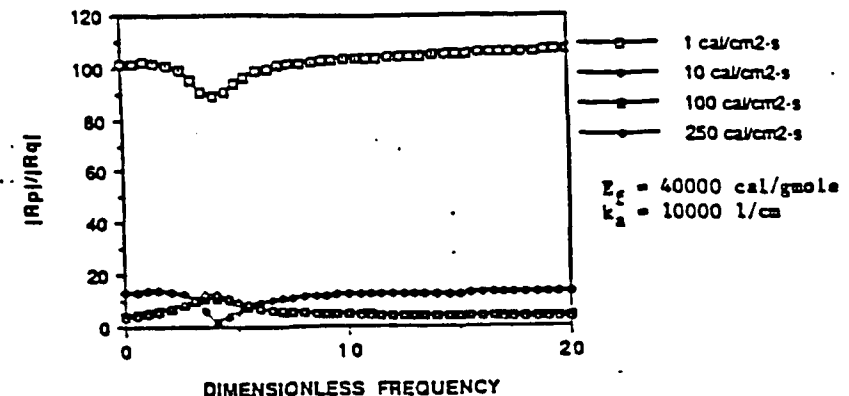


Figure 18. Effect of external flux on transfer function ($E_f = 40,000$ cal/mole)

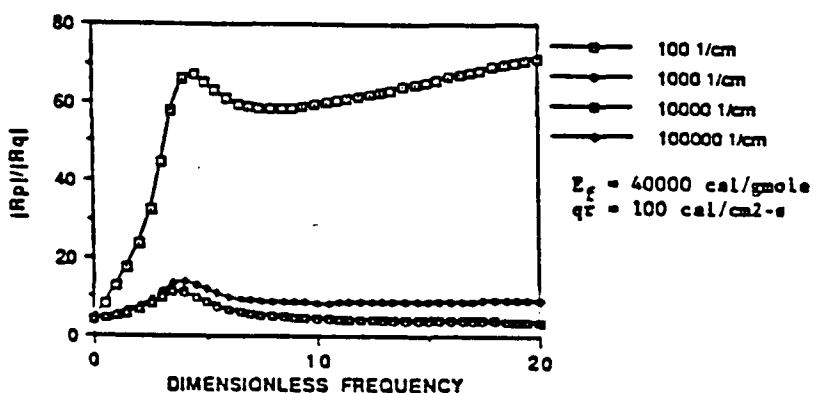


Figure 19. Effect of opacity on transfer function ($E_f = 40,000$ cal/mole)

CONCLUSIONS

The possibility of using an easily measured heat flux-coupled response function to predict pressure-coupled combustion response in solid propellants offers numerous advantages over L*-burners and T-burners in terms of reduced costs and more accurate results. A key requirement for the success of this approach is an accurate, descriptive combustion model to relate the two response functions. This paper has described a model based on the assumption of gas phase rate controlling processes. A distinguishing feature of this work is that the effect of radiant heat flux perturbations on the gas phase conductive heat feedback is accounted for. Also, the steady state solution is

included as part of the overall solution rather than simply assumed. The heat flux response function was found to be very sensitive to both the mean level of the radiant flux and the absorption coefficient of the propellant. It was seen that the most favorable results (larger response magnitudes) would be obtained with large fluxes and large absorption coefficients.

Future work will involve comparison with experiments to test the validity of the assumptions and to fit model parameters. This will require extensive burning rate data for pressure and temperature sensitivity. Perhaps a useful modification to this work would be to re-examine the Ibiricu and Williams condensed phase reactive-diffuse analysis, relaxing the large absorption coefficient assumption, and obtain an appropriate relation to replace Eqn. (5) for the case of finite absorption coefficient. Another possible modification is to eliminate the gas phase flame description (i.e. remove the large activation energy, gas phase rate controlling assumptions) and use the Zel'dovich-Novozhilov approach, although this would introduce the additional need for extensive temperature profile data using microthermocouples. Eventually, non-homogenous, metallized propellants will be considered. With the inclusion of metals it will probably be necessary to have direct measurements of the radiant heat flux incident at the propellant surface due to substantial thermal emission from the condensed phase burning droplets and oxide smoke product as well as extinction of external radiation by these same condensed species. A technique for doing this using optical fibers is being investigated.

REFERENCES

1. Horton, M. D., and Youngberg, L. Z., "Effect of Radiant Energy on the Burning Rate of a Composite Solid Propellant," *AIAA J.*, Vol. 8, No. 10, Oct. 1970, pp. 1738-1741.

2. Coates, R. L., and S. Kwak, "Effect of External Radiation on the Burning Rates of Solid Propellants," *J. Spacecraft*, Oct. 1972, pp. 742-744.
3. Caveny, L. H., T. J. Ohlemiller, and M. Summerfield, "Influence of Thermal Radiation on Solid Propellant Burning Rate," *AIAA J.*, Vol. 13, No. 2, Feb. 1975, pp. 202-205.
4. Ibiricu, M. M., and F. A. Williams, "Influence of Externally Applied Thermal Radiation on the Burning Rates of Homogeneous Solid Propellants," *Combustion and Flame*, Vol. 24, 1975, pp. 185-198.
5. Mihlfeith, C. M., A. D. Baer, and N. W. Ryan, "Propellant Combustion Instability as Measured by Combustion Recoil," *AIAA Journal*, Vol. 10, No. 10, Oct. 1972, pp. 1280-1285.
6. Mihlfeith, C. M., "Some Experiments on the Effect of Thermal Radiation on Composite Rocket Propellants," Ph.D. Thesis, University of Utah, Salt Lake City, Utah, 1971.
7. Mikheev, V. F., V. E. Zarko, S. M. Borin, K. P. Kutsenogii, and V. N. Simonenko, "Measurement of Burning Rates in Transient Combustion Processes Under the Influence of External Radiation," *AIAA Prog. Astro. and Aero.*, Vol. 63, Ed., T. Boggs and B. Zinn, 1978, pp. 173-187.
8. Zarko, V. E., and A. B. Kiskin, "Numerical Modeling of Nonsteady Powder Combustion Under the Action of a Light Flux," *Comb., Expl. and Shock Wave*, Vol. 16, No. 6, Nov.-Dec. 1980, pp. 650-654.
9. Zarko, V. E., V. N. Simonko, and K. P. Kutsenogii, "Effects of Light Intensity on the Nonstationary Combustion Rate in a Transient Process," *Comb., Expl. and Shock Wave*, Vol. 11, No. 4, July-Aug. 1975, pp. 459-464.
10. Ohlemiller, T. J., L. H. Caveny, L. DeLuca, and M. Summerfield, "Dynamic Effects on Ignitability Limits of Solid Propellants Subjected to Radiative Heating," Fourteenth Symposium (International) on Combustion, pp. 1297-1307.
11. Strand, L. D., K. Schwartz, and S. P. Burns, "Propellant Combustion Response to Oscillatory Radiant Heat-Flux," 24th JANNAF Combustion Meeting, CFIA publ. 476, Vol. I, Oct. 1987.
12. Denison, M. R., and E. Baum, "A Simplified Model of Unstable Burning on Solid Propellants," *ARS Journal*, Vol. 31, 1967, pp. 1112-1122.
13. Culick, F. E.C., "A Review of Calculations of the Admittance Function for a Burning Surface," *Combustion of Solid Propellants and Low Frequency Combustion Instability*, NOTS TP 4244, 1967, Naval Weapons Center, China Lake, CA, Appendix A.

14. Williams, F. A., "Quasi-Steady Gas-Phase Flame Theory on Unsteady Burning of a Homogeneous Solid Propellant," *AIAA Journal*, Vol. 11, No. 9, Sept. 1973, pp. 1328-1330.
15. Kuo, K. K., and M. Summerfield, *Fundamentals of Solid-Propellant Combustion*, *AIAA Prog. Aero. and Astro.*, Vol. 90, Ed. K. Kuo and M. Summerfield, NY, 1984.
16. Brewster, M. Q. and Hardt, B. E., "Selective Radiation Absorption in Aluminized Composite Propellant Combustion," 24th JANNAF Combustion Mtg., CPIA publ. 476, Vol. I, Oct. 1987, pp. 157-164.
17. Patel, R. S. and Brewster, M. Q., "Optical Constants of Propellant-Grade Ammonium Perchlorate," *AIAA J.*, Vol. 24, No. 11, Nov. 1986, pp. 1878-1880.
18. Culick, F. E. C., "A Review of Calculations for Unsteady Burning of a Solid Propellant," *AIAA Journal*, Vol. 6, No. 12, Dec. 1968, pp. 2241-2255.
19. Culick, F. E. C., "Calculation of the Admittance Function for a Burning Surface," *Astronautica Acta*, Vol. 13, 1967, pp. 221-237.
20. Culick, F. E. C., "An Elementary Calculation of the Combustion of Solid Propellants," *Astronautica Acta*, Vol. 14, 1969, pp. 171-181.
21. Summerfield, M., et al., "Theory of Dynamic Extinguishment of Solid Propellants with Special Reference to Nonsteady Feedback Law," *Journal of Spacecraft*, Vol. 8, No. 3, March 1971, pp. 251-258.
22. Krier, H., et al., "Nonsteady Burning Phenomenon of Solid Propellants: Theory and Experiments," *AIAA Journal*, Vol. 6, No. 2, Feb. 1968, pp. 278-285.
23. Renie, J. P., "Combustion Modeling of Composite Solid Propellants," Ph.D. Thesis, Purdue University, W. Lafayette, IN, 1982.
24. DeLuca, L., et al., "Unstable Burning of Thin Solid Propellant Flames," AIAA/SAE/ASME 16th Joint Propulsion Conference, Hartford, CN, June 30-July 2, 1980.
25. Hertzberg, M., "The Free-Laminar and Laser-Induced Combustion of Ammonium Perchlorate," *Comb. Sci. Tech.*, Vol. 1, 1970, pp. 449-460.

COMBUSTION RESPONSE OF SOLID ROCKET PROPELLANTS
TO OSCILLATORY RADIANT HEAT FLUX

T.D. Prevish and M.Q. Brewster*
Department of Mechanical and Industrial Engineering
University of Illinois at Urbana-Champaign
Urbana, Illinois

ABSTRACT

A theoretical burning rate model has been developed to predict the pressure-coupled response function of a propellant by relating it to an experimental heat flux-coupled response function, obtained for the same propellant by measuring its response to an external radiant flux. The model was developed for propellants subjected to low amplitude (linear), oscillatory, pressure or radiant heat flux perturbations. This radiant flux has been separated into two parts, to include both the imposed external flux and a natural feedback flux from the flame (for instance, in metallized combustion). The gas phase is treated as quasi-steady. William's high activation energy, asymptotic analysis for a premixed, homogeneous flame is used to describe gas phase conductive heat feedback. The condensed phase chemical reaction is assumed to occur within a quasi-steady reactive-diffusive zone. For a high activation energy, this zone is compressed into a very thin region at the surface. An appropriate expression for the propellant regression rate in this zone was derived by Ibiricu and Williams, and is incorporated into this model. The solid phase is treated as unsteady with in-depth absorption. In order to be consistent, the steady-state solution is retained for use in the unsteady model. Results were compared to experimental data for A-13 composite propellant. Though the homogeneous model can be used to reasonably match either the pressure-coupled response or heat flux-coupled response of a composite propellant, it does not appear capable of successfully relating the two functions. Some suggestions for future work are discussed, including the importance of in-depth absorption of radiant flux on the combustion of AP-based composite propellants.

INTRODUCTION

One of the key parameters in the analysis of unstable, time-dependent combustion in solid rocket motors is the pressure-coupled response function, R_p . This parameter has long been measured using T-burners and L*-burners. However, these devices are limited by physical restrictions and many questions associated with the interpretation of data. Because the oscillatory frequency of a test depends on the dimensions of the apparatus, many burners must be built to gain a knowledge of R_p over a range of frequencies. One alternative to these methods for studying the combustion response of solid propellants is to measure the burning rate response to an imposed external radiant heat flux, R_q . If a theory could be developed to relate R_q and R_p the costs associated with a solid rocket motor development program could be significantly reduced. Instead of building a number of different devices and running many different tests, one test with an oscillating external radiant heat flux impinging upon a small strand of propellant could conceivably cover a wide range of frequencies. In addition, the interpretation of data might be less controversial. The time and money saved in this manner make the heat flux-driven experiment an approach well worth pursuing.

PREVIOUS WORK

Many investigators have considered the effects of an external radiant heat flux on the burning rate of solid propellants. Several investigators (Hertzberg, Horton and Youngberg¹; Coates and Kwak²; Caveny, Ohlemiller and Summerfield³; Ibiricu and Williams⁴; and Yin⁵) have studied the effect of a constant radiant heat flux q_r on the steady mass burning rate m . The principal conclusion of these studies is that at low to moderate flux levels (<100 cal/cm²sec) radiant energy absorbed in-depth, below the location of the rate-controlling chemical reactions, is equivalent to an increase of $\Delta T = \frac{q_r}{mC_s}$ in the initial temperature of the propellant, T_i (the so-called equivalence principle). This conclusion has both positive and negative consequences, as pointed out by Ibiricu and Williams and Caveny, Ohlemiller and Summerfield. On the positive side, it means that in-depth, radiation absorption effects can be relatively easily incorporated into the theoretical analysis of both steady and unsteady combustion (assuming the absorption takes place beneath the rate-controlling reaction layers). This result, of course, has favorable implications in terms of the objectives of the current study. On the negative side, the equivalence principle means that no new information about the chemical or physical reaction mechanisms can be obtained from radiant heat flux experiments that could not be obtained from burning rate temperature sensitivity data.

Many investigators (Mihlfeith^{6,7}; Mikheev⁸; Zarko^{9,10}; Ohlemiller¹¹; Strand^{12,13}; and De Luca^{14,15}) have also studied the effect of time-varying radiant heat fluxes on the combustion response of solid propellants, including step input and oscillatory radiant fluxes. One of the first studies to examine the possibility of utilizing R_q measurements to obtain R_p was conducted by Mihlfeith, Baer and Ryan⁶. They used a piezoelectric, micro-force transducer to measure the combustion recoil induced by an oscillatory incident radiant flux. From a momentum balance they were able to obtain the instantaneous mass burning rate m' and thus R_q . They also developed a combustion model which made it possible to relate R_p and R_q . The combustion model of

*This work was performed under Contract N00014-87-K-0574 with the office of Naval Research and the Naval Weapons Center

Mihlfeith used a small amplitude (linear perturbation) analysis of the unsteady solid phase. Their assumptions were very similar to those of the earlier Denison and Baum¹⁶ analysis of unsteady combustion, including:

- (1) A one-dimensional homogeneous solid,
- (2) Quasi-steady gas phase (flame description approach),
- (3) Quasi-steady, simple surface pyrolysis, and
- (4) In-depth absorption with no sub-surface chemical heat release.

To describe the gas phase, a large activation energy flame model from Culick¹⁷ was used. The assumption of large activation energy has been shown to be equivalent to a flame sheet approximation. Culick's model was a derivative of the von Elbe laminar premixed flame theory which had been used by Denison and Baum, modified to account for the presence of the solid. (Using asymptotic analysis, Williams later argued that the original von Elbe description was actually the appropriate model in the limit of large gas flame activation energy.)¹⁸

De Luca^{14,15} also analyzed the effects of external heat flux using an approach similar to Mihlfeith's. However, his derivations offered two separate models for the gas phase conductive heat feedback, depending on whether a premixed or a diffusion flame was assumed. He argued that the pre-mixed flame description used by Mihlfeith was more appropriate for double-based propellants, and for AP-based composite propellants, a diffusion flame description would be a better approximation. He also drew attention to an anomaly between the value of energy released from the surface reactions Mihlfeith used and the value required to satisfy an energy balance across the propellant, suggesting the results calculated by Mihlfeith using the sharp flame front model were inaccurate. The idea of using a diffusion flame model to account for the energy feedback to the surface from the gas phase could make significant differences compared to the flame sheet approximation; the diffusion flame may provide a more physically realistic transient analysis of AP-composite propellants. However, the details of De Luca's approach available to the authors were sketchy, at best, so a comparison of the two flame models was not done in this study.

Soon after Mihlfeith's work appeared, Mikheev, et al.⁷ reported on a similar combustion recoil technique which made use of a capacitance transducer. Corresponding theoretical analysis of Zarko⁸ made use of the Zel'dovich-Novozhilov approach rather than the gas phase flame description approach referred to in assumption (2) above. As discussed by Kuo, Gore and Summerfield¹⁹ in their recent review article, although the Zel'dovich approach simplifies the analysis by avoiding the details of the spatial distribution of heat release in the gas phase (e.g. flame sheet versus distributed heat release, etc.), it also requires more extensive steady-state burning rate data. Namely, the pressure and temperature sensitivity of the steady-state burning rate $m(T_i, P)$ and the steady-state surface temperature as a function of pressure and burning rate $T_s(P, m)$ are required.

More recently, Strand and co-workers¹² have reported on a microwave doppler technique for measuring the instantaneous burning rate m' . Although the microwave technique is currently limited to non-metallized propellants (since the microwaves must be transmitted through the propellant for reflection at the burning surface and metal particles strongly scatter almost any wavelength of electromagnetic radiation, including microwaves), the superior frequency response of this technique still makes it an attractive option. In addition to this novel and promising experimental technique, the theoretical analysis of Strand also takes a new approach by considering non-linear, finite amplitude perturbations, in conjunction with the Zel'dovich approach.

OBJECTIVES

The primary objective in this particular study was to obtain a transfer function, $F = \frac{R_p}{R_q}$ that would bridge the gap between the desired pressure-coupled response function, R_p , and the more conveniently attainable heat flux-coupled response function, R_q . To do this, a theoretical burning rate model was developed for the system. First a steady-state model was established and then a linear (small amplitude perturbation) transient model was developed. From the combined steady-state and transient models the theoretical response function was extracted.

STEADY-STATE COMBUSTION MODEL

The first step in the overall model is to describe the steady-state characteristics of a burning propellant under the influence of an incident external radiant energy flux. This process is illustrated schematically in Figure 1. The frame of reference is fixed at the surface of the propellant and moves with the steady-state regression rate of the propellant. An energy balance is then written for condensed phase, the surface phase, and the gas phase regions, respectively.

$$\bar{m} C_s (\bar{T}_s - T_i) = k_s \bar{\phi}_{s-} + \bar{q}_{r1} + \bar{q}_{r2} \quad \text{where } \phi = \frac{\partial T}{\partial x} \quad (1a)$$

$$k_s \bar{\phi}_{s-} = \bar{m} \bar{Q}_s + k_g \bar{\phi}_{s+} \quad (1b)$$

$$k_g \bar{\phi}_{s+} + \bar{m} C_p (\bar{T}_f - \bar{T}_s) = \bar{m} \bar{Q}_f \quad (1c)$$

The sum of these equations represents the overall steady-state energy balance.

$$\bar{m} (C_s (\bar{T}_s - T_i) + C_p (\bar{T}_f - \bar{T}_s)) = \bar{q}_{r1} + \bar{q}_{r2} + \bar{m} (\bar{Q}_f + \bar{Q}_s) \quad (2)$$

The radiation terms, \bar{q}_r , represent the fraction of external radiant flux incident at the surface which is absorbed by the propellant. The fraction \bar{q}_{r1} corresponds to the radiant feedback resulting from thermal emission by the propellant flame (e.g., in aluminized propellants), while \bar{q}_{r2} corresponds to the average value of an oscillating heat flux from an external source, such as a laser. The surface heat release term $\bar{Q}_s (>0, \text{ net exothermic})$ is assumed to include both latent energy for phase change and chemical energy for thermal decomposition. As noted by Ibiricu and Williams, the thermodynamic relation

$$\bar{Q}_s = (C_s - C_p) \bar{T}_s + \text{const} \quad (3)$$

insures that the final flame temperature \bar{T}_f is independent of the surface temperature \bar{T}_s . Equations (2) and (3) represent two equations with five unknowns, \bar{m} , \bar{T}_f , \bar{T}_s , \bar{Q}_s , and \bar{Q}_r . Three more equations are needed for closure of the steady-state problem. One of these equations describes the heat released by the flame in relation to pressure

$$\bar{Q}_f = (\text{const}) P \gamma_p \quad (4)$$

Equation (4) is nothing more than an empirically fit equation to account for the change in flame temperature at different pressures. For some propellants, this may be significant, though for AP-based composites, γ_p is generally much less than 1.

The two remaining equations are provided by the gas phase flame description model and the surface regression rate of the propellant. For the gas phase description, the high activation energy (flame sheet) model of Williams for homogeneous, premixed flames is used.

$$\bar{m} = \left[\frac{2k_B R^2 C_p}{E_f^2 \bar{Q}_f^2} \right]^{1/2} \bar{P}^{\gamma_p} \bar{T}_f^2 \exp \left[\frac{-E_f}{2R\bar{T}_f} \right] \quad (5)$$

This relation gives the mass burning rate as a function of the final flame temperature and other gas phase thermochemical, thermophysical, and kinetic properties. Use of this relation assumes that the gas phase reactions represent the rate limiting step which controls the overall mass burning rate of the propellant (as opposed to condensed phase reactions). The conditions for verifying this assumption are discussed by Ibiricu and Williams.

The propellant regression rate in the condensed phase reactive-diffusive zone is modeled using an equation for high surface reaction activation energy developed by Ibiricu and Williams. Since Eqn. (2) is independent of \bar{T}_s , it should be noted that the following expression is used only to determine the surface temperature.

$$\bar{m} = \frac{(\rho_s A_l k_s R)^{1/2} \bar{T}_s \exp(-\frac{E_s}{2R\bar{T}_s})}{(E_s [C_s(\bar{T}_s - T_i) + \frac{1}{\bar{m}} (\bar{q}_{r1} f_1 + \bar{q}_{r2} f_2)])^{1/2}} \quad (6)$$

$$\text{where } f_{1,2} = \exp(-\beta_{1,2} \frac{R\bar{T}_s}{E_s}) \quad (7)$$

$$\beta_{1,2} = \frac{K_{1,2} k_s}{\bar{m} C_s} \quad (8)$$

This equation has been modified, as suggested by Ibiricu and Williams, by defining scaling factors f_1 and f_2 to include the correct qualitative behavior of radiant flux passing through the thin reactive-diffusive zone. As stated earlier, this flux has been separated into two parts. Because the wavelengths of these different types of fluxes will probably be different, the absorptivity of the propellant will also be different for each flux. To account for the amount of each radiant flux passing through the reactive-diffusive zone, a separate scaling factor is defined based upon the effective absorptivity of each. For example, an induced flux, \bar{q}_{r2} , from a CO₂ laser has a wavelength of 10.6 μm, which is conducive to absorption by AP, so β_2 , which represents the ratio of the characteristic length scale for thermal diffusion in the solid to that for absorption (mean free photon path), would be very large. This in turn leads to a value of f_2 approaching 0, and the amount of \bar{q}_{r2} absorbed below the surface is small. Conversely, radiation from metallized propellants would be concentrated in the visible and near infrared spectrum, and would penetrate deeper before being absorbed in an AP-based propellant. The low value of β_1 would result in a value of f_1 approaching 1, and a great portion of \bar{q}_{r1} would contribute to subsurface heating.

TRANSIENT COMBUSTION MODEL

After establishing the steady-state description, the next step in the overall model is to describe the transient combustion response of the propellant to the action of either a low amplitude, oscillatory external radiant heat flux

$$q_r = \bar{q}_r + q_r' \exp(i\omega t), \quad q_r' \ll \bar{q}_r \quad (9)$$

or a low amplitude, oscillatory pressure perturbation

$$p = \bar{p} + p' \exp(i\omega t), \quad p' \ll \bar{p} \quad (10)$$

Under the influence of either of these time-dependent disturbances the propellant burns in an oscillatory fashion with instantaneous burning rate m .

$$m = \bar{m} + m' \exp(i\omega t), \quad m' \ll \bar{m} \quad (11)$$

The surface location therefore moves back and forth with respect to the mean surface location. The frame of reference is taken to be fixed at the surface of the propellant. Thus the origin moves with the instantaneous regression rate of the propellant. This approach has been shown to be analytically equivalent to an inertial reference frame which moves at the mean burning rate¹⁷

UNSTEADY GAS PHASE ANALYSIS

The gas phase processes and the surface pyrolysis are assumed to be quasi-steady (i.e. no time lag with respect to the imposed oscillating disturbance). Unsteadiness is accounted for only in the solid phase region, which has the slowest time constant in the system (about 0.01 sec associated with thermal diffusion). This limits the analysis to frequencies below about 1000 Hz as discussed by Kuo, Gore, and Summerfield. Since unsteadiness must only be accounted for in the solid phase, the unsteady equations can be obtained by simply perturbing (i.e. differentiating with respect to time) the surface and gas phase equations, Eqns. (1b, 1c, 3, 4, 5, and 6), yielding

$$k_g \dot{\phi}_s^+ = k_g \phi_s^+ + m' \bar{Q}_s + \bar{m} Q_s' \quad (12)$$

$$k_g \dot{\phi}_s^+ = \bar{m} [Q_f' - C_p(T_f' - T_s')] + m' [\bar{Q}_f - C_p(\bar{T}_f - \bar{T}_s)] \quad (13)$$

$$Q_s' = (C_s - C_p) T_s' \quad (14)$$

$$Q_f' = \bar{Q}_f \gamma_p \frac{P'}{\bar{P}} \quad (15)$$

$$\frac{\dot{m}'}{\bar{m}} = v_1 \frac{\dot{p}}{\bar{p}} + \left(2 + \frac{E_f}{2R\bar{T}_f} \right) \frac{\dot{T}_f'}{\bar{T}_f} - \frac{\dot{Q}_r'}{\bar{Q}_r} \quad (16)$$

$$\frac{\dot{T}_s'}{\bar{T}_s} = \left(\frac{2}{P_2} - \frac{\bar{q}_{r1} f_1 + \bar{q}_{r2} f_2}{P_1 P_2 \bar{m}} \right) \frac{\dot{m}'}{\bar{m}} + \frac{f_1}{P_1 P_2 \bar{m}} q_{r1} + \frac{f_2}{P_1 P_2 \bar{m}} q_{r2} \quad (17)$$

where

$$P_2 = 2 + \frac{E_s}{R\bar{T}_s} \cdot \frac{C_s \bar{T}_s}{P_1} \quad (18)$$

$$P_1 = C_s (\bar{T}_s - T_i) \cdot \frac{1}{\bar{m}} (\bar{q}_{r1} f_1 + \bar{q}_{r2} f_2) \quad (19)$$

To complete the model, a transient analysis of the unsteady solid phase must be carried out to obtain a relation for the instantaneous temperature gradient on the solid side of the surface, ϕ_s' , for use in place of Eqn. (1a).

UNSTEADY SOLID PHASE ANALYSIS

The unsteady energy equation in the solid phase, with in-depth absorption is

$$\rho C_s \frac{\partial T}{\partial t} + m C_s \frac{\partial T}{\partial x} = k_s \frac{\partial^2 T}{\partial x^2} + q_{r1} + q_{r2} \quad (20)$$

For simplicity, the density, thermal conductivity, and heat capacity of the solid are considered constant. To include the effects of in-depth absorption, the solution of the radiative transfer equation is used

$$q_{r1} = q_{r1} K_{a1} \exp(K_{a1}x) \quad (21a)$$

$$q_{r2} = q_{r2} K_{a2} \exp(K_{a2}x) \quad (21b)$$

where it has been assumed that scattering is negligible, the absorption coefficients K_{a1} and K_{a2} are spatially constant, thermal emission by the condensed phase is negligible, and the incident flux is collimated. Applying a linear perturbation to Eqns. (21a) and (21b), and noting

$$T(x,t) = \bar{T}(x) + T'(x) \exp(i\omega t) \quad (22)$$

yields the steady-state form of the solid phase energy equation

$$\frac{d^2 \bar{T}}{dx^2} \cdot \frac{\bar{m} C_s d\bar{T}}{k_s dx} = - \frac{\bar{q}_{r1} K_{a1}}{k_s} \exp(K_{a1}x) - \frac{\bar{q}_{r2} K_{a2}}{k_s} \exp(K_{a2}x) \quad (23)$$

with boundary conditions $\bar{T}(0) = \bar{T}_v$ and $\bar{T}(-\infty) = \bar{T}_i$, and the time-dependent energy equation

$$\begin{aligned} \frac{d^2 T'}{dx^2} \cdot \frac{\bar{m} C_s dT'}{k_s dx} - \frac{\rho C_s}{k_s} (i\omega) T' &= - \frac{q_{r1} K_{a1}}{k_s} \exp(K_{a1}x) - \frac{q_{r2} K_{a2}}{k_s} \exp(K_{a2}x) \\ &\quad + \frac{i\omega C_s}{k_s} \frac{dT}{dx} \end{aligned} \quad (24)$$

with boundary conditions $T(0)=T_s$ and $T(-\infty)=0$.

The solutions to Eqn. (23) and (24) give unwieldy expressions for the steady-state and transient temperature distributions in the solid, which will not be presented here. When these solutions are combined with Eqns (12-17), T_s and T_f can be eliminated. If q_{r1}' is assumed to be zero, the resulting expression relates the fluctuations in the mass burning rate to those in the induced heat flux and the pressure.

$$\frac{\dot{m}'}{\bar{m}} = R_q \frac{q_{r2}'}{\bar{q}_{r2}} + R_p \frac{\dot{p}'}{\bar{p}} \quad (25)$$

where

$$R_q = \frac{\dot{m}/\bar{m}}{q_{r2}/\bar{q}_{r2}} \Big|_{P,q_{r1}} = \frac{n_q (AB + C(\bar{q}_{r1} + \bar{q}_{r2})) \left[\frac{\beta_2}{\beta_2 + \lambda - 1} + C_s \bar{T}_s (1-\lambda) \frac{f_1}{P_1 P_2} \right]}{\lambda + \frac{A}{\lambda} - (1+A) + AB + C \left[\bar{q}_{r1} \frac{(\lambda-1)^2 + \lambda\beta_1}{\lambda(\beta_1 + \lambda - 1)} \right] + \bar{q}_{r2} \left[\frac{(\lambda-1)^2 + \lambda\beta_2}{\lambda(\beta_2 + \lambda - 1)} \right]} \quad (26)$$

$$\text{where } n_q = \frac{\bar{q}_{r2}/(\bar{m} C_p \bar{T}_f)}{\left(\frac{1}{2 + \frac{E_f}{2R\bar{T}_f}} \right) + \frac{\bar{q}_{r1} + \bar{q}_{r2}}{\bar{m} C_p \bar{T}_f}} \quad (27)$$

$$R_p = \frac{\dot{m}/\bar{m}}{p/\bar{p}} \Big|_{q_{r1}=0} = \frac{n_p (AB + C(\bar{q}_{r1}))}{\lambda + \frac{A}{\lambda} - (1+A) + AB + C \left[\bar{q}_{r1} \frac{(\lambda-1)^2 + \lambda\beta_1}{\lambda(\beta_1 + \lambda - 1)} \right]} \quad (28)$$

$$\text{where } n_p = \frac{\frac{\bar{Q}_f}{C_p \bar{T}_f} \gamma_p + \frac{\nu_1 - \gamma_p}{(2 + \frac{E_f}{2R\bar{T}_f})}}{\frac{1}{2 + \frac{E_f}{2R\bar{T}_f}} + \frac{\bar{q}_{r1}}{\bar{m} C_p \bar{T}_f}} \quad (29)$$

$$A = \frac{P_2(1 - T_f/\bar{T}_s)}{(2 - \frac{\bar{q}_{r1} f_1 + \bar{q}_{r2} f_2}{P_1 \bar{m}})} \quad (30)$$

$$B = \frac{C_p \bar{T}_f}{C_s \bar{T}_s (1 - T_f/\bar{T}_s)} \frac{1}{(2 + \frac{E_f}{2R\bar{T}_f})} \quad (31)$$

$$C = \frac{P_2}{\bar{m} C_s \bar{T}_s (2 - \bar{q}_{r1} f_1 + \bar{q}_{r2} f_2)} \quad (32)$$

$$\lambda = \frac{1}{2} + \sqrt{\frac{1}{4} + i \Omega} \quad (33)$$

and the non-dimensional frequency is defined as

$$\Omega = \frac{\rho k_s \omega}{\bar{m}^2 C_s} \quad (34)$$

Note that the heat flux-coupled response function, Eqn (26), is defined at constant pressure, since the external radiant flux \bar{q}_{r2} would be the only driving oscillation during a laboratory test. Conversely, the pressure-coupled response function is defined at zero induced radiant flux, so the \bar{q}_{r2} terms disappear in Eqn. (28). In either case, a natural radiant flux may be present, so \bar{q}_{r1} appears in both definitions. The transfer function is found by taking the ratio of the real part of the pressure-coupled response function to the magnitude of the heat flux-coupled response function

$$F = \frac{\text{Re}\{R_p\}}{|R_q|} \quad (35)$$

In this way the in-phase component or real part of the pressure-coupled response function for a propellant can be calculated by multiplying the transfer function by the experimentally measured heat flux-coupled response function.

APPLICABILITY OF HOMOGENEOUS MODEL TO COMPOSITE PROPELLANTS

The model above was developed assuming a homogeneous solid and single flame above the propellant surface with 1-dimensional heat transfer. All theories predicated upon these assumptions can be algebraically manipulated (after Culick) to yield an expression similar in form to Eqn (28), where the constant A is a function of the solid phase properties and the constant B is dependent on the gas phase properties. As can be seen from Eqn (28) the value of A has the primary influence on the frequency response of the propellant (since it determines the relative contribution of λ) whereas the value of B tends to determine the magnitude of the response. For a given A and B, the variation of response frequency will be tied to the square of the burning rate (see definition of Ω , Eqn (34)). While this type of model is generally amenable to results for double-base propellants²⁰, it has met with little success when applied to composite propellants. This failure stems from the inherent heterogeneity of composite propellants, due to the juxtaposition of fuel and oxidizer as well as to the variation in oxidizer particle size within the propellant. Considering the widespread use of bi-modal and tri-modal composite propellants, the assumption of a homogeneous solid phase applied to a composite propellant would appear to invite serious limitations. Another important shortcoming of the homogeneous model is its inability to account for the multiple flames associated with composite propellants. The physical basis of these flames and the effects of oxidizer size and pressure are well characterized by BDP²¹ and later models by Beckstead²², Cohen and Strand²³, King²⁴, and Glick and Condon²⁵ for steady burning. For a comparative review of recent versions of these models, the reader is referred to Cohen²⁶. Briefly, all of the aforementioned composite models consider two types of flames: a monopropellant premixed flame over the oxidizer, and a diffusion flame effected by the oxidizer and binder. The relative importance of these flames is dependent primarily upon the chamber pressure and oxidizer size distribution. Clearly, the classic homogeneous models understate the complexities involved in composite propellant flame zones.

Unfortunately, while the steady-state burning of many composite propellants has been successfully modeled, the prediction of transient results has been far from adequate. For excellent reviews on several important attempts at this, see Cohen²⁷ and Boggs and Beckstead²⁸. Given the success of the BDP-type of models for steady burning, it was a logical step to apply the same principles to unsteady modeling. Hamann²⁹ perturbed the already complex BDP model and developed an expression for the pressure-coupled response function similar in form to Eqn (28), but with terms far more complicated than those derived for the homogeneous model. Condon, Osborn, and Glick²⁸ reported results for Hamann's model, which were not encouraging; the frequency response still shifted only in accordance with the square of burning rate, though T-burner and other tests on composite propellants have suggested otherwise.

Another approach which emphasized the heterogeneity of the solid propellant to a greater degree than the BDP-type models focused around the so-called "layer-frequency" (or "preferred-frequency") concept. Variations on this method have been

examined by Williams and Lengelle³¹, Cohen and Bowyer³², and Cohen³³. One of the earliest attempts, from Williams and Lengelle, assumed a "sideways sandwich" model, in which the properties of the propellant were varied sinusoidally with depth. The spatial periodicity as the propellant burned through these layers could be used to predict the effects of oxidizer size and the presence of binder. The resulting expression for the response function consisted of two terms--one the conventional homogeneous response and the other a "heterogeneous response". Although derived from an "artificial" frequency dependence, the predicted frequency response had the advantage of not being solely dependent on the square of burning rate. However, this model also had several practical shortcomings, as discussed by Cohen²⁷: it introduced a quasi-nonlinearity into the problem and required a great deal of information about the specifics of the propellant heterogeneity, including raw T-burner data. The mathematics necessary for the evaluation of the theory also promised to be tedious.

Cohen and Bowyer³² took a similar approach in their sideways sandwich model. Although they concentrated on the solid-phase heterogeneity, they also used an expression for the gas phase heat release to approximate the effects of the BDP model. The most significant departure from Williams and Lengelle, however, was to hold the layered geometry of the propellant fixed with respect to the burning surface. In this way, they eliminated the artificial periodicity induced by the motion of the alternating layers, and examined the interaction between the thermal lag and the layers. Their results indicated essentially no difference between the homogeneous and heterogeneous models for the solid, a conclusion which affords a major potential simplification of the problem.

Cohen³³ also postulated an equation which related the peak response frequency linearly to burn rate and inversely to particle size. A second postulate varied the peak magnitude with surface-to-volume ratio, a measure of the propellant's thermal response. While the first postulate has been supported by the trends observed in T-burners, the second has not been so successful in predicting response magnitude. Cohen believes this suggests the thermal wave response mechanism has a significant role, and cannot be ignored.

Yet another approach to predicting the transient behavior of composite propellants involves fitting the aforementioned A and B parameters of homogeneous theory to match heterogeneous results. This method is also artificial, but not in the same manner as the "preferred frequency" concept. Whereas a physical basis is clearly present for the assumption of stacked layers of differing properties, it is much more difficult to predict the proper values for A and B. For a homogeneous propellant, the thermochemical properties used to define these two parameters are relatively simple to determine. However, the extension of Eqn (28) to heterogeneous propellants is certainly not as simple as choosing average or oxidizer-weighted properties of a composite propellant and determining an equivalent A and B to use in homogeneous theory. The reason is, as summarized above, the physical mechanisms governing the combustion of composite propellants are vastly different than those used to develop the homogeneous theory. Thus, the values for A and B based on the physical constants of AP or a weight-averaged equivalent cannot yield predictions fundamentally different from those of a homogeneous propellant with those properties. Although the assumption of a homogeneous solid phase is probably a good one, as shown by Cohen and Bowyer, it has two important shortcomings which must be noted here. First, there is emerging evidence for the existence of multiple peaks in response functions which are believed to be due to the existence of different particle sizes in the propellant. Thus far, the model has been unable to include this mechanism. Second, the assumption of a homogeneous surface discards recognition of a potential instability caused by the possibly different temperatures of fuel and oxidizer. Whether this model can be expanded to intrinsically account for these effects is questionable at this time.

The goal of the analysis presented in this paper was not to develop a mechanistically complete model capable of predicting steady and transient effects for any propellant simply given the oxidizer distribution and fuel and binder properties. Rather, it was to develop a transfer function relating the experimentally observed heat flux coupled response function, R_Q , especially as affected by in-depth absorption, to the design-oriented pressure-coupled response function, R_P . Given the inadequate results of transient heterogeneous models thus far, it was presumed their application would not yield the desired results. And the development of a new model based on the same principles would only introduce numerous mathematical complications and would probably offer no greater success. Instead, the possibility of applying the homogeneous model to composite propellants was explored. The first step was to generate a steady-state model accordant with experimental results of selected AP-composite propellants. It was discovered that the effects of varying E_s and E_f on the steady-state solution could be countered by choosing appropriate values for the preexponential factors, B_1 and A_1 in Eqns (5) and (6). Thus, it was possible to match measured steady-state results of a particular propellant over a wide range of activation energies. This suggested the use of these terms, not as values limited to AP or binder-AP averaged properties, but as "effective" activation energies attempting to represent trends in composite propellants. While not based upon a particularly firm physical foundation, this approach could intrinsically account for the effects of particle size and multiple flames. After obtaining a high degree of success in modeling both the steady-state pressure-sensitivity and temperature-sensitivity of the selected composite propellants (see next section), the decision was made to use these effective activation energies to try to match experimental heat-flux coupled response functions, then extend the model to predict pressure-coupled response functions. It should be noted that this approach is essentially nothing more than the previously discussed method of fitting the appropriate A and B parameters. Recall, by definition (Eqns (30) and (31)) the flame activation energy is tied to the magnitude of the response function, through B, and the surface reaction activation energy is related to the peak frequency of the response function, through A.

STEADY-STATE SOLUTION

Before a transient response function can be calculated, a steady-state solution must either be assumed (arbitrarily) or calculated. To be consistent, it would seem that the steady-state solution should be calculated using the steady-state model from which the transient model was derived. In the following parametric study, propellant property values are used in Eqns. (2-6) to calculate a steady-state solution for \bar{m} , \bar{T}_f , \bar{T}_s , \bar{Q}_f , and \bar{Q}_s . This steady-state solution is then used with the same propellant parameters in the transient model to calculate the response functions.

To use this model for a particular propellant, experimental pressure sensitivity and temperature sensitivity should be available, or at least estimated with a reasonable degree of accuracy. The first step is to examine the temperature sensitivity of a given propellant. For the homogeneous theory of this paper, the temperature coefficient can be shown to be

$$\sigma_p = \frac{1}{\bar{T}_f} \left(2 + \frac{E_f}{2R\bar{T}_f} \right) \frac{C_s}{C_p} \quad (36)$$

This constraint narrows the range of effective flame activation energies which can be used in this model. Using the E_f predicted from Eqn. (36), the value of v_1 is adjusted until the steady-state model is matched with experimental pressure sensitivity data by As mentioned previously, the values of the preexponential factors, A_1 and B_1 , are calculated to give the appropriate steady burning rate for any E_f and v_1 . Since the gas phase reactions have been assumed to be the rate limiting step, Eqn. (5) is used to determine the overall mass burning rate of the propellant. Equation (6) is used solely to calculate the surface temperature. Subsequently, the steady-state burn rate and flame temperature are independent of E_s . This is an important feature, as discussed in the next section, on the transient results.

The propellant A-13 was chosen to assess the capability of this homogeneous model to predict the combustion response of composite propellants. Table 1 lists the composition and properties of this monomodal propellant. The value of .30 for the temperature coefficient was estimated for pressures in the vicinity of 20 atm. For this study, the value of K_{a2} represents the absorption in AP of an incident flux with a wavelength of 10.6 μm (i.e., from a CO₂ laser). To obtain a numerical value for this, the imaginary part of the refractive index for AP was estimated to be 0.17³⁴. Then, K_{a2} was calculated from

$$K_{a2} = \frac{4\pi k}{\lambda_w} \quad (37)$$

where k = imaginary part of the refractive index

λ_w = wavelength of radiant flux

This gives an absorption coefficient of about 2000 cm^{-1} . This value of K_{a2} may seem rather high, indicating that AP is opaque at 10.6 μm and in-depth absorption effects are negligible. However, as will be seen in the parametric calculations (Figure 5), for this value of absorption coefficient the effects of in-depth absorption may still be significant.

Using the process outlined above, the pressure and temperature sensitivity were matched to experimental results, Figures 2 and 3. As anticipated, a congruent model is easily obtained which estimates steady-state parameters for use in the transient calculations.

Finally, the effects of external radiant flux on the steady-state solutions is shown in Figure 4. The flame temperature, surface temperature, and mass burning rate all increase monotonically with increasing heat flux. These effects are expected, in light of the so-called "equivalence principle" already discussed in the section entitled Previous Work. For the development of equations predicting \bar{m} , \bar{T}_s , and \bar{T}_f as a function of external radiant flux, the reader is referred to the works cited in that section.

TRANSIENT RESULTS

Before attempting to apply the transient solution to experimental data for A-13, a parametric study was done to explore the sensitivity of the heat flux-coupled response function to different properties, specifically, E_s and K_{a2} . A steady-state solution was found for a fixed E_f and q_{f2} , and incorporated into the transient model to calculate \dot{R}_0 . Earlier it was stated that E_s had no impact on the steady-state solution, except in the calculation of \bar{T}_s . This variation in the surface temperature was found to contribute negligibly to the transient results compared to the corresponding variation in surface activation energy. Likewise K_{a2} ,

which also appears in the steady-state solution only through Eqn. (6), was found to alter \bar{T}_s only slightly at moderate radiant fluxes. Consequently, the effects of these parameters on the transient solution can be accurately conveyed without losing the close correlation of the steady-state results.

The effect of K_{d2} on the heat flux-coupled response function is plotted in Figure 5, where the constants in Table 1 were used to generate the different curves for $|R_{q1}|$. Propellants with higher opacities tend to exhibit more substantial response peaks than those with low absorption coefficients. However, the peak frequency appears to be only a very weak function of the absorptivity. The difference in the heat flux-coupled response function when the absorption coefficient is increased from 2000 cm^{-1} to 5000 cm^{-1} is an indication that the propellant is not so opaque that in-depth absorption effects are negligible. This conclusion is puzzling in light of Strand's results¹³ showing that the addition of 0.25% carbon to A-13 did not change $|R_{q1}|$ significantly. One potential explanation for this is that carbon may only alter the opacity of the binder, not the AP, so a change in response would not be expected. Also of interest is the effect K_{d2} has on the transfer function defined in Eqn. (35), shown in Figure 6. The transfer function exhibits less frequency dependence as the propellant opacity increases, which could lead to a nearly linear relationship between $|R_p|$ and $|R_{q1}|$ for opaque propellants. This is clear from Eqns. (26) and (28), where an opacity (represented by β) an order of magnitude or so greater than 1 results in the disappearance of the frequency dependence of the radiant flux terms. Likewise, the numerator of Eqn. (26) becomes independent of frequency, and when the ratio of these two equations is taken, the corresponding frequency dependence of the transfer function is greatly diminished. However, this dependence would not completely disappear even for a perfectly opaque propellant, since the steady-state solution used to calculate R_q will not be that used for R_p (due to the different conditions under which the propellant would be burned in either test). Thus the relative weight carried by the λ terms in Eqns. (26) and (28) will assure at least a small transfer function frequency dependence.

Figure 7 shows the variation in the heat flux-coupled response function for different effective surface activation energies. For this propellant, increasing the surface activation energy tends to produce higher peak frequencies. The magnitude increases initially, but then decreases at higher values of E_s . These characteristics of the model promise to facilitate matching the experimental heat flux-coupled response.

To test the feasibility of this technique, $|R_{q1}|$ data measured by Strand¹³ were used to find an appropriate effective condensed phase activation energy for A-13. The response peaks at about 625 Hz at a magnitude of approximately 1.9. Both of these features are modeled well with homogeneous theory using an E_s of 85000 cal/mole, as shown in Figure 8. The crucial step, however, is multiplying the matched heat flux-coupled response by the transfer function to obtain the pressure-coupled response for A-13. This predicted R_p is shown in Figure 9, as well as comparable R_p experimental data.³⁶ The experimental data appears to predict a peak response at a frequency of approximately 350 Hz. Unfortunately, the model predicts a negative response in that frequency range, an indication that the effective activation energies have been exaggerated beyond physically significant limits. High values of E_s , in particular, were determined to cause poor pressure-coupled response. This is illustrated in Figure 10, where a more "standard" value of solid-phase activation energy is used. For this case, the model yields a positive real part of R_p , a substantial improvement towards matching the measured data. This is very encouraging, since maintaining the high value of E_f also guarantees valid steady-state results. However, the heat flux-coupled response function corresponding to this case, Figure 11, is underpredicted in both magnitude and peak frequency.

Finally, for the sake of comparison, results were calculated using more generally accepted activation energies, $E_s=32000$ cal/mole and $E_f=30000$ cal/mole. The pressure sensitivity, Figure 12, still matches very well, but the reduced flame activation energy predicts a low temperature coefficient, as shown in Figure 13. For the transient results, the model predicts a very low $|R_{q1}|$, with an almost imperceptible peak in Figure 14. The pressure-coupled response, shown in Figure 15, observes the correct trends, but not with the correct magnitude.

CONCLUSIONS

The possibility of using an easily measured heat flux-coupled response function to predict pressure-coupled combustion response in solid propellants offers numerous advantages over T-burners and L*-burners in terms of reduced costs and more accurate results. A key requirement for the success of this approach is an accurate, descriptive combustion model to relate the two response functions. A model has been developed in this paper based on the assumptions of homogeneous solid and gas phases. Additionally, it was assumed that the gas phase kinetics defined the rate controlling mechanism for propellant combustion. To be consistent, the steady-state solution was included as part of the overall solution rather than simply assumed. When the transient analysis was applied to a heterogeneous propellant, the model underpredicted the response functions when "standard" activation energies were used. If a high effective flame activation energy was assumed, results for the pressure-coupled response function could be matched, but the corresponding heat flux-coupled response could not be accurately predicted. Conversely, adding the assumption of a high solid-phase activation energy enabled $|R_{q1}|$ to be suitably matched, but negative values were subsequently calculated for the real part of the pressure-coupled response function. As more experimental measurements are obtained for the heat flux-coupled response function and more predictions for the pressure-coupled response function are compared to experimental measurements, the limitations of this model will be determined. However, the initial results portend serious deficiencies associated with the application of this approach to heterogeneous propellants.

One aspect of this study worth further attention is the importance of in-depth absorption of the radiant flux. Although AP is known to be conducive to absorption for wavelengths near $10.6\text{ }\mu\text{m}$, the absorption coefficient estimated in this study implied a significant amount of heat flux absorbed below the reactive-diffusive zone. One study¹³ observed little difference between the measured heat flux-coupled response of A-13 and that of A-13 with a small amount of carbon added as an opacifier, when driven by a CO_2 laser. However, since the carbon would be contained in the binder, the conclusion that in-depth absorption is not important for a $10.6\mu\text{m}$ wavelength presumes the AP is not the controlling factor for this effect. The fraction of radiant energy absorbed below the reactive-diffusive zone and the consequences on the combustion response of the propellant must be further investigated. Additional future work will explore the incorporation of oxidizer size directly into the model. This might require embodying the heterogeneity of the entire solid phase, though it might be equally valid to maintain the assumption of a homogenous solid phase, and incorporate the oxidizer and fuel particle sizes in the reactive-diffusive zone only. The treatment of the gas phase flame description should also be modified to better represent the conductive heat feedback from AP composite flames. De Luca's diffusion flame analysis may be more appropriate than the flame sheet description. An approximation of the BDP-type competing flames, analogous to that assumed by Cohen and Bowyer, might also yield improved results. Perhaps a better modification would be to eliminate the need for a gas phase description altogether by using the Zel'dovich-Novozhilov approach, although this would introduce the need for extensive temperature profile data using microthermocouples. Eventually, metallized propellants will be considered. With the inclusion of metals it will probably be necessary to have direct measurements of the radiant heat flux incident at the propellant surface, due to substantial thermal emission from the condensed phase burning droplets and oxide smoke products as well as extinction of external radiation by these same condensed species. A technique for doing this using optical fibers is currently being investigated.

Table 1. Formulation and properties of A-13.

Composition:

76.0%	90 μ Ammonium Perchlorate
20.4%	PBAN
3.6%	Epon Resin 828

Properties and constants:

Solid	Gas
$k_s = 0.0006 \text{ cal/cm}\cdot\text{s}\cdot\text{K}$	$k_g = 0.0006 \text{ cal/cm}\cdot\text{s}\cdot\text{K}$
$C_s = 0.33 \text{ cal/g}\cdot\text{K}$	$C_p = 0.39 \text{ cal/g}\cdot\text{K}$
$\rho = 1.58 \text{ g/cm}^3$	$\gamma_p = 0.0$
$K_{a2} = 2000 \text{ cm}^{-1}$	$R = 1.986 \text{ cal/mole}\cdot\text{K}$
$\sigma_p = .30\%/\text{K}$	$v_f = 0.432$
$E_s = 85,000 \text{ cal/mole}$	$E_f = 61,000 \text{ cal/mole}$
$A_1 = 7.535E24$	$B_1 = 2.320E09$

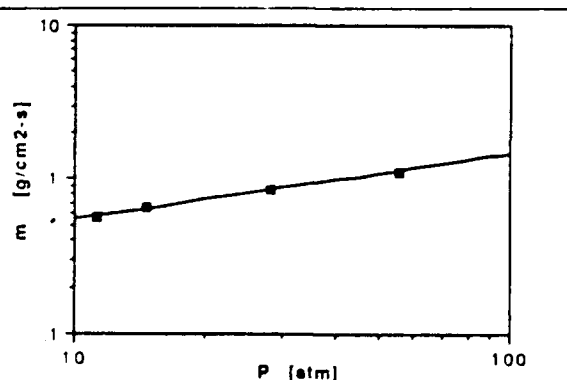


Figure 2. Pressure Sensitivity of A-13.
■ Experimental [ref 35] — Theory

$$E_f = 61 \text{ kcal/mole}; T_i = 300 \text{ K}; \bar{q}_{r2} = 0$$

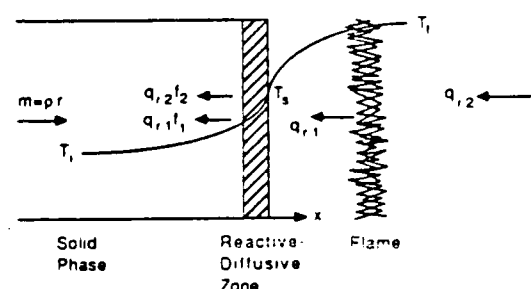


Figure 1. Schematic of propellant surface.

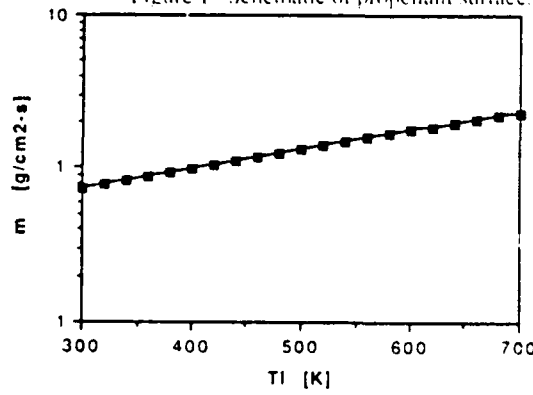


Figure 3. Temperature sensitivity of A-13.
■ "Experimental" ($\sigma_p = 30\%/\text{K}$) — Theory

$$E_f = 61 \text{ kcal/mole}; \bar{P} = 20.4 \text{ atm}; \bar{q}_{r2} = 0$$

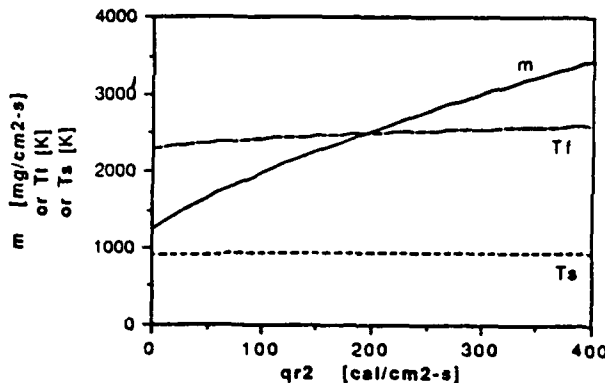


Figure 4. Effect of radiant flux on steady-state solution.

$$\bar{q}_{r2}=20 \text{ cal/cm}^2\text{-s}; \bar{P}=20.4 \text{ atm}; E_f=61 \text{ kcal/mole}; E_s=85 \text{ kcal/mole}$$

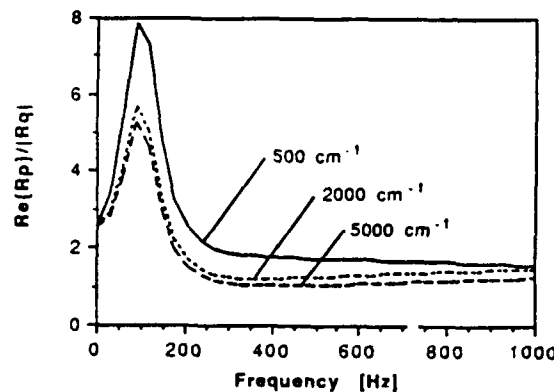


Figure 6. Effect of absorption depth on transfer function.

$$\bar{q}_{r2}=20 \text{ cal/cm}^2\text{-s}; \bar{P}=20.4 \text{ atm}; E_f=61 \text{ kcal/mole}; E_s=25 \text{ kcal/mole}$$

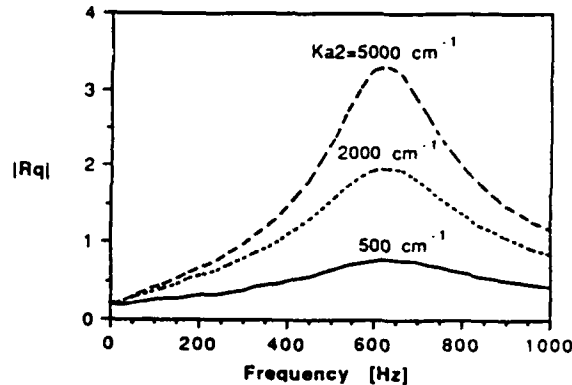


Figure 5. Effect of K_{a2} on magnitude of R_q .

$$\bar{q}_{r2}=20 \text{ cal/cm}^2\text{-s}; \bar{P}=20.4 \text{ atm}; E_f=61 \text{ kcal/mole}; E_s=85 \text{ kcal/mole}$$

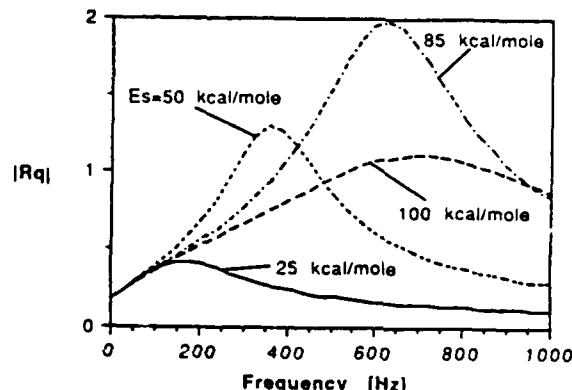


Figure 7. Effect of E_s on magnitude of R_q

$$\bar{q}_{r2}=20 \text{ cal/cm}^2\text{-s}; K_{a2}=2000 \text{ cm}^{-1}; E_f=61 \text{ kcal/mole}; \bar{P}=20.4 \text{ atm}$$

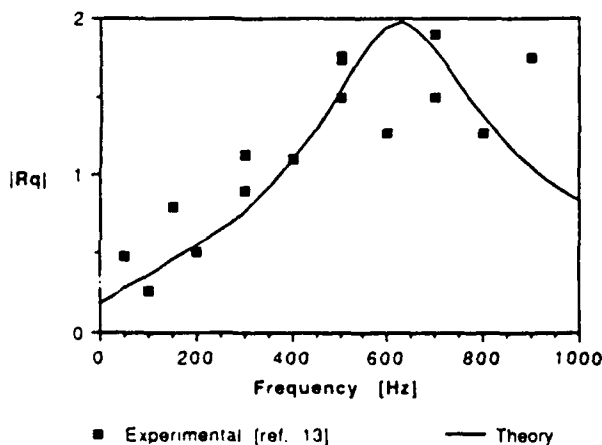


Figure 8. Magnitude of heat flux-coupled response

$$\text{function for A-13. } \bar{q}_{r2}=20 \text{ cal/cm}^2\text{-s}; K_{a2}=2000 \text{ cm}^{-1}; E_f=61 \text{ kcal/mole}; E_s=85 \text{ kcal/mole}; \bar{P}=20.4 \text{ atm}$$

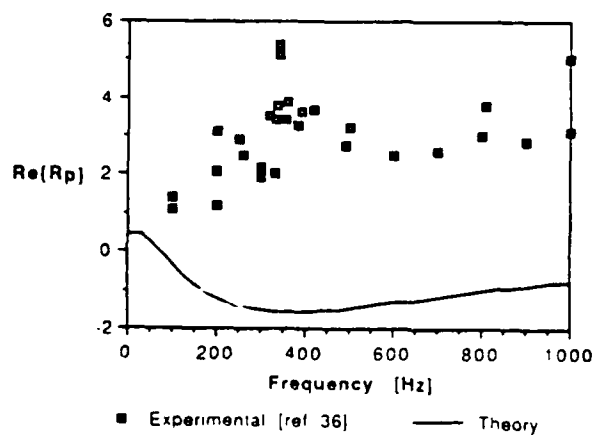


Figure 9. Real part of pressure-coupled response

$$\text{function for A-13. } E_f=61 \text{ kcal/mole}; E_s=85 \text{ kcal/mole}; \bar{P}=20.4 \text{ atm}$$

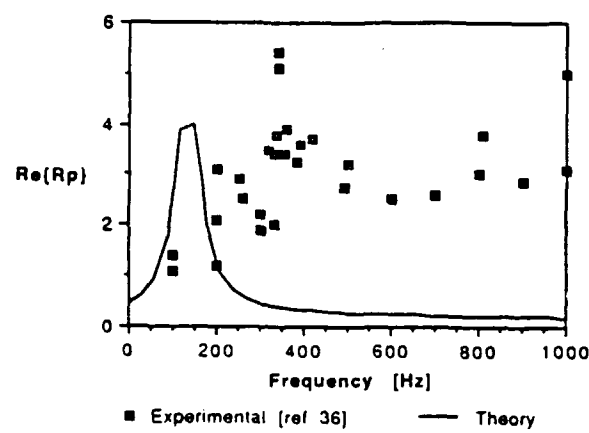


Figure 10. Pressure-coupled response function.

$E_f=61 \text{ kcal/mole}$; $E_s=32 \text{ kcal/mole}$; $\bar{P}=20.4 \text{ atm}$

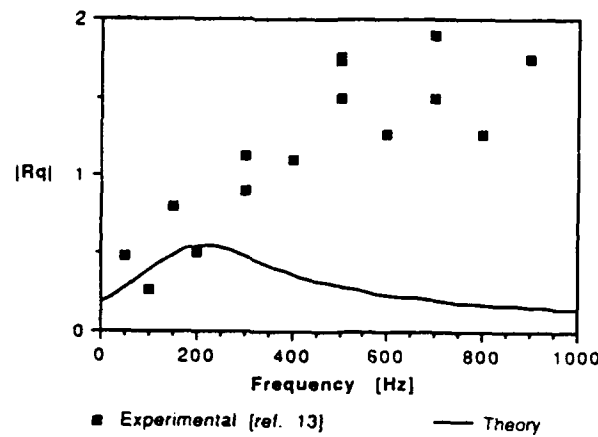


Figure 11. Heat flux-coupled response function.

$\bar{q}_{r2}=20 \text{ cal/cm}^2\cdot\text{s}$; $K_{a2}=2(XX) \text{ cm}^{-1}$;
 $\bar{P}=20.4 \text{ atm}$; $E_f=61 \text{ kcal/mole}$;
 $E_s=32 \text{ kcal/mole}$;

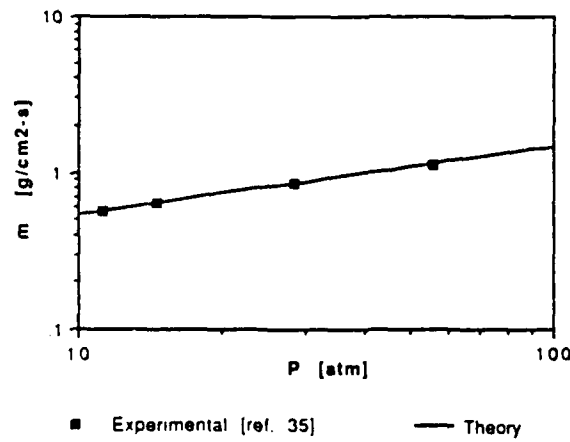


Figure 12. Pressure sensitivity with $E_f=30 \text{ kcal/mole}$;
 $T_1=3(X) \text{ K}$; $\bar{q}_{r2}=0$

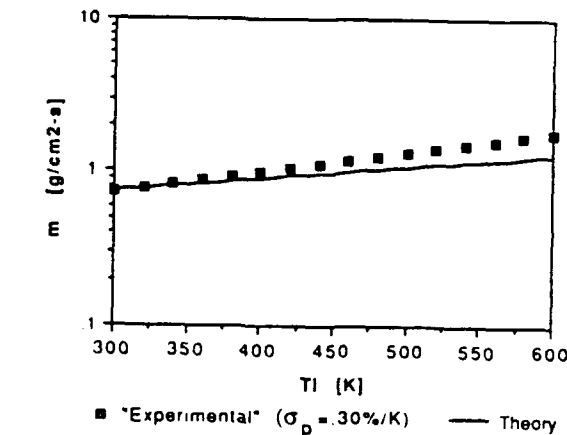


Figure 13. Temperature sensitivity with
 $E_f=61 \text{ kcal/mole}$; $\bar{P}=20.4 \text{ atm}$; $\bar{q}_{r2}=0$

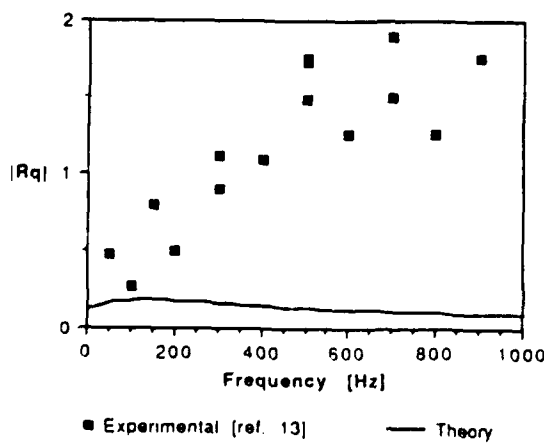


Figure 14. Heat flux-coupled response function.

$\bar{q}_{r2}=20 \text{ cal/cm}^2\cdot\text{s}$; $K_{a2}=2(XX) \text{ cm}^{-1}$;
 $\bar{P}=20.4 \text{ atm}$;
 $E_f=30 \text{ kcal/mole}$; $E_s=32 \text{ kcal/mole}$

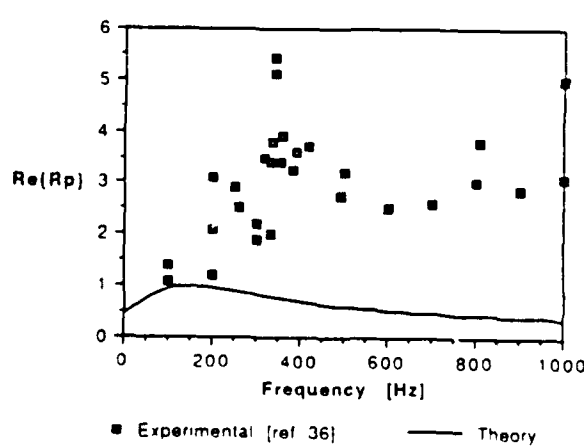


Figure 15. Pressure-coupled response function.

$\bar{P}=20.4 \text{ atm}$; $E_f=30 \text{ kcal/mole}$
 $E_s=32 \text{ kcal/mole}$

NOMENCLATURE*

A_1 = preexponential constant in solid phase mass burning rate equation.
 B_1 = preexponential constant in gas phase mass burning rate equation.
 C_p = constant pressure specific heat of gas phase.
 C_s = specific heat of solid.
 E_f = gas-phase reaction activation energy.
 E_s = solid-phase reaction activation energy.
 K_a = absorption coefficient in Beer's Law.
 k_g = thermal conductivity of gas phase.
 k_s = thermal conductivity of solid phase.
 m = mass burning rate.
 n_p = steady state value of the pressure-coupled response function.
 n_q = steady state value of the heat flux-coupled response function.
 P = pressure.
 Q_f = Heat release from the gas-phase reactions (>0 exothermic).
 q_{r1} = natural feedback external radiant heat flux (e.g., metallized propellants).
 q_{r2} = induced external radiant heat flux (e.g., laser)
 Q_s = Combined latent heat and heat released in surface reactions (>0 exothermic).
 R_p = pressure-coupled response function.
 R_q = heat flux-coupled response function.
 R = universal gas constant.
 T_d = temperature deep within the solid.
 T_f = adiabatic flame temperature.
 T_s = temperature at solid surface.
 β = opacity constant = $K_d k_s / m \cdot c_s$.
 γ_p = flame heat release pressure sensitivity
 λ = characteristic value in solid phase temperature solution.
 ν_1 = pressure exponent in gas phase mass burning rate equation.
 ρ = density.
 σ_p = temperature coefficient
 ϕ = temperature gradient
 ω = frequency in radians/second
 Ω = dimensionless frequency.

*a - denotes steady state values and a' denotes perturbed values.

REFERENCES

1. Horton, M. D., and Youngberg, L. Z., "Effect of Radiant Energy on the Burning Rate of a Composite Solid Propellant," *AIAA Journal*, Vol. 8, No. 10, Oct. 1970, pp. 1738-1741.
2. Coates, R. L., and Kwak, S., "Effect of External Radiation on the Burning Rates of Solid Propellants," *J. Spacecraft*, Oct. 1972, pp. 742-744.
3. Caveny, L. H., Ohlemiller, T. J. and Summerfield, M., "Influence of Thermal Radiation on Solid Propellant Burning Rate," *AIAA Journal*, Vol. 13, No. 2, Feb. 1975, pp. 202-205.
4. Ibiricu, M. M., and Williams, F. A., "Influence of Externally Applied Thermal Radiation on the Burning Rates of Homogeneous Solid Propellants," *Combustion and Flame*, Vol. 24, 1975, pp. 185-198.
5. Yin, J., et al., "Effect of External Radiation on the Burning Rates of Composite Solid Propellants," AIAA 89-2533, 25th Joint Propulsion Conference, July 1989.
6. Mihlfeith, C. M., Baer, A. D. and Ryan, N. W., "Propellant Combustion Instability as Measured by Combustion Recoil," *AIAA Journal*, Vol. 10, No. 10, Oct. 1972, pp. 1280-1285.
7. Mihlfeith, C. M., "Some Experiments on the Effect of Thermal Radiation on Composite Rocket Propellants," Ph.D. Thesis, University of Utah, Salt Lake City, Utah, 1971.

8. Mikheev, V. F., Zarko, V. E., Borin, S. M., Kutsenogii, K. P., and Simonenko, V.N., "Measurement of Burning Rates in Transient Combustion Processes Under the Influence of External Radiation," *AIAA Prog. Astro. and Aero.*, Vol. 63, Ed., T. Boggs and B. Zinn, 1978, pp. 173-187.
9. Zarko, V. E., and Kiskin, A. B., "Numerical Modeling of Nonsteady Powder Combustion Under the Action of a Light Flux," *Comb., Expl. and Shock Wave*, Vol. 16, No. 6, Nov.-Dec. 1980, pp. 650-654.
10. Zarko, V. E., Simonenko, V. N., and Kutsenogii, K. P., "Effects of Light Intensity on the Nonstationary Combustion Rate in a Transient Process," *Comb., Expl. and Shock Wave*, Vol. 11, No. 4, July-Aug. 1975, pp. 459-464.
11. Ohlemiller, T. J., Caveny, L. H., DeLuca, L., and Summerfield, M., "Dynamic Effects on Ignitability Limits of Solid Propellants Subjected to Radiative Heating," Fourteenth Symposium (International) on Combustion, pp. 1297-1307.
12. Strand, L. D., Schwartz, K., and Burns, S. P. "Propellant Combustion Response to Oscillatory Radiant Heat-Flux," 24th JANNAF Combustion Meeting, CPIA publ. 476, Vol. I, Oct. 1987.
13. Strand, L. D., Weil, M., and Cohen, N.S., "Solid Propellant Combustion Response to Oscillatory Radiant Heat Flux," AIAA 89-2667, 25th Joint Propulsion Conference, July 1989.
14. De Luca, L., "Frequency Response Function of Burning Solid Propellants," *Meccanica: Journal of the Italian Association of Theoretical and Applied Mechanics*, Dec. 1980, pp. 195-205.
15. De Luca, L., "Ignition and Other Unsteady Combustion Phenomena Induced by Radiation," Ph.D. Thesis. Princeton University, 1977.
16. Denison, M. R., and Baum, E., "A Simplified Model of Unstable Burning on Solid Propellants," *ARS Journal*, Vol. 31, 1967, pp. 1112-1122.
17. Culick, F. E. C., "A Review of Calculations of the Admittance Function for a Burning Surface," *Combustion of Solid Propellants and Low Frequency Combustion Instability*, NOTS TP 4244, Naval Weapons Center, China Lake, CA, Appendix A, 1967.
18. Williams, F. A., "Quasi-Steady Gas-Phase Flame Theory on Unsteady Burning of a Homogeneous Solid Propellant," *AIAA Journal*, Vol. 11, No. 9, Sept. 1973, pp. 1328-1330.
19. Kuo, K. K., and Summerfield, M., *Fundamentals of Solid-Propellant Combustion*, AIAA Prog. Aero. and Astro., Vol. 90, Ed. K. Kuo and M. Summerfield, NY, 1984.
20. Cohen, N. S., "Workshop Report: Analytical Models of Combustion Response Functions," 22nd JANNAF Combustion Meeting, CPIA Publ. 432, Vol. I, Oct. 1985, pp. 97-102.
21. Beckstead, M. W., Derr, R. L., and Price, C. F., "A Model of Solid Propellant Combustion Based on Multiple Flames," *AIAA Journal*, Vol. 8, Dec. 1970, pp. 2200-2207.
22. Beckstead, M. W., "A Model for Solid Propellant Combustion," 14th JANNAF Combustion Meeting, Aug. 1977, pp.281-306.
23. Cohen, N. S., and Strand, L. D., "An Improved Model for the Combustion of AP - Composite Propellants," *AIAA Journal*, Vol. 20, No. 12, Dec. 1982, pp. 1739-1746.
24. King, M. K., "Composite Propellant Combustion Modeling," 16th Joint Propulsion Conference, AIAA 80-1124, June 1980.
25. Glick, R. L., and Condon, J. A., "Statistical Combustion Modeling--the Effect of Additives," 14th JANNAF Combustion Meeting, CPIA Publ. 292, Aug. 1977.
26. Cohen, N. S., "Review of Composite Propellant Burn Rate Modeling," *AIAA Journal*, Vol. 18, No. 3, Mar. 1980, pp. 277-293.
27. Cohen, N. S., "Response Function Theories that Account for Size Distribution Effects--A Review," *AIAA Journal*, Vol. 19, No. 7, July 1981, pp. 907-912.
28. Boggs, T. L., and Beckstead, M. W., "Failure of Existing Theories to Correlate Experimental Nonacoustic Combustion Instability Data," *AIAA Journal*, Vol. 8, No. 4, Apr. 1970, pp. 626-631.

29. Harnann, R. J., "Three Solid Propellant Combustion Models, A Comparison and Some Application of Unsteady Cases," Memo. M-215, Delft University of Technology, Delft, Netherlands, Apr. 1974.
30. Condon, J. A., Osborn, J. R., and Glick, R. L., "Statistical Analysis of Polydisperse, Heterogeneous Propellant Combustion: Nonsteady-State," 13th JANNAF Combustion Meeting, CPIA Publ. 281, Vol II, 1976, pp. 209-223.
31. Williams, F.A., and Lengelle, G., "Simplified Model for Effect of Solid Heterogeneity on Oscillatory Combustion," *Astronautica Acta*, Vol. 14, Jan. 1968, pp. 97-118.
32. Cohen, N. S., and Bowyer, J. M., "Combustion Response Modeling for Composite Solid Propellants," AFRPL-TR-78-39, Jet Propulsion Laboratory, Pasadena, CA, 1978.
33. Cohen, N. S., et al., "Design of a Smokeless Solid Rocket Motor Emphasizing Combustion Stability," 12th JANNAF Combustion Meeting, CPIA Publ. 273, Vol. II, 1975, pp. 204-220.
34. Patel, R. S. and Brewster, M. Q., "Optical Constants of Propellant-Grade Ammonium Perchlorate," *AIAA Journal*, Vol. 24, No. 11, Nov. 1986, pp. 1878-1880.
35. "Experimental Studies on the Oscillatory Combustion of Solid Propellants," NWC TP 4393, Mar. 1969.
36. Strand, L. D., Magiawala, K. R., and McNamara, R. P., "Microwave Measurement of the Solid-Propellant Pressure-Coupled Response Function," *J. of Spacecraft and Rockets*, Vol. 17, No. 6, Nov.-Dec. 1980, pp. 483-488.
37. Brewster, M. Q. and Hardt, B. E., "Selective Radiation Absorption in Aluminized Composite Propellant Combustion," 24th JANNAF Combustion Mtg., CPIA publ. 476, Vol. I, Oct. 1987, pp. 157-164.
38. Culick, F. E. C., "A Review of Calculations for Unsteady Burning of a Solid Propellant," *AIAA Journal*, Vol. 6, No. 12, Dec. 1968, pp. 2241-2255.
39. Culick, F. E. C., "Calculation of the Admittance Function for a Burning Surface," *Astronautica Acta*, Vol. 13, 1967, pp. 221-237.
40. Culick, F. E. C., "An Elementary Calculation of the Combustion of Solid Propellants," *Astronautica Acta*, Vol. 14, 1969, pp. 171-181.
41. Summerfield, M., et al., "Theory of Dynamic Extinguishment of Solid Propellants with Special Reference to Nonsteady Feedback Law," *Journal of Spacecraft*, Vol. 8, No. 3, March 1971, pp. 251-258.
42. Krier, H., et al., "Nonsteady Burning Phenomenon of Solid Propellants: Theory and Experiments," *AIAA Journal*, Vol. 6, No. 2, Feb. 1968, pp. 278-285.
43. Renie, J. P., "Combustion Modeling of Composite Solid Propellants," Ph.D. Thesis, Purdue University, W. Lafayette, IN, 1982.
44. DeLuca, L., et al., "Unstable Burning of Thin Solid Propellant Flames," AIAA/SAE/ASME 16th Joint Propulsion Conference, Hartford, CN, June 30-July 2, 1980.
45. Hertzberg, M., "The Free-Laminar and Laser-Induced Combustion of Ammonium Perchlorate," *Comb. Sci. Tech.*, Vol. 1, 1970, pp. 449-460.

AN INVESTIGATION OF THE COMBUSTION OF ALUMINUM IN WATER

M.R. Jones, K.C. Tang, and M.Q. Brewster*
Department of Mechanical and Industrial Engineering
University of Illinois at Urbana - Champaign
Urbana, Illinois

ABSTRACT

A simplified diffusion limited vapor phase burning model was applied to the combustion of aluminum in water. Results of the diffusion flame model indicate the radiative environment has a strong effect on burning rate. Experimentally determined spectral intensities clearly indicate the presence of gaseous Al and AlO. These measurements also show a continuous spectrum, but the source of the continuum remains unclear. Based on the assumption that the continuum is emitted by condensed, sub-micron Al₂O₃ particles the radiative heat transfer contributes 10 to 15 percent of the energy needed to maintain vapor phase combustion of aluminum in a liquid water environment. The data also show that the effective blackbody temperature of aluminum burning in water at atmospheric pressure is between 3600 and 3850 K, and that the mean optical size, d₃₂, for Al₂O₃ is approximately 0.5 μ m.

INTRODUCTION

The burning of a metal droplet can take place on the surface of the droplet (surface oxidation process) or in a diffusion limited detached envelope flame around the droplet (vapor-phase burning). Glassman⁽¹⁾ postulates that the vapor phase burning occurs when the boiling or dissociation point of the metal oxide is higher than that of the metal. According to this criterion, Al, Mg, Li, Na, K, Ca, and Be can burn in the vapor phase, and B, Si, Ti, and Zr burn on the surface⁽²⁾. However, some experiments⁽²⁾ reveal that many metals can not burn in the vapor phase even if these metals satisfy Glassman's criterion. This phenomenon is due to the fact that the formation of a protective oxide layer and/or the radiation losses from the high temperature flame can inhibit the vapor phase burning⁽³⁾. The relative volatility of the metal and its oxide and the size of the particle also play an important role on the combustion mechanism of the particle^(3,4). Therefore, the criterion suggested by Glassman may be considered as a necessary but not sufficient condition for the occurrence of vapor phase burning. Although the metal and oxide boiling points change with pressure, for most metals the vapor pressure curves do not cross and therefore a metal which burns in the vapor phase will generally do so at all pressures⁽¹⁾.

Another general observation about vapor phase combustion of metals with non-volatile oxides is that the flame temperature is limited by the boiling or dissociation point of the metal oxide. The reason is⁽¹⁾ that the heat release from the chemical reaction is not enough to supply the heat required to vaporize or dissociate the oxide for most metals. It should be noted that the flame temperature can be less than the dissociation point of the metal oxide (in which case all the oxide recombines) depending on the heat loss from flame zone. However, within the context of a set of classical assumptions (including neglect of radiative heat transfer), it can be shown that it is not necessary to determine the flame temperature in order to obtain the droplet burning rate in a diffusion limited detached envelope flame⁽⁵⁾.

Although the burning mechanisms of metals have been extensively studied, the results can not be used to predict the combustion behavior in many practical applications such as explosives and rocket motors directly⁽³⁾. This difficulty is due to the differences in burning environments between laboratory studies and rocket motors or explosives. As a result, empirical correlations based on experiments are generally relied on for predictions. Hernisen provided an empirical equation to calculate the burning rate of aluminum with an empirical factor (R_k) introduced to account for the difference in burning rates between laboratory and motor conditions⁽⁶⁾. The difference in burning rates is believed to be due to the large difference in the radiation environments and the direct effect of velocity lags. Currently, this empirical factor, R_k , is determined by comparing the predicted value of burning rate with data obtained from motor firings. In order to extend this predictive capability to account for different convective and radiative environments, it is necessary to analyze the difference in burning rates between laboratory and other conditions theoretically.

This report presents the results of a simplified, initial investigation of the vapor phase burning of aluminum in water and the results of an experiment conducted to determine the significance of radiative heat transfer in this combustion process. A vapor phase diffusion limited model of burning of a single droplet in a quiescent atmosphere modified to include convective effects (without considering radiation heat losses) is used to calculate the burning rate of a fuel particle in an oxidizing atmosphere. The numerical results are compared with the burning rates which are calculated from Hernisen's model. This comparison shows it is necessary to consider the radiation heat losses from the condensed products in the flame at high temperature in order to examine the difference in burning rates between single particle laboratory conditions and multiple droplet conditions encountered in rocket motors and explosives. Measurements of the spectral, radiant intensity emitted by an aluminum wire burning under water were also performed to quantify the radiative heat loss. These results also indicate the radiative effect is important and should be included in a model that correlates laboratory measurements of burning rates to the burning rates obtained in rocket motors and explosives.

BURNING CHARACTERISTICS OF ALUMINUM

Aluminum is considered⁽³⁾ to be a non-volatile metal at most pressures. In addition, a thin protective oxide layer normally forms on the surface of aluminum which inhibits the vapor phase combustion. Further, aluminum oxide is insoluble in aluminum; therefore, upon heating aluminum will expand and produce stresses in the oxide layer. Whether the oxide layer is still protective upon heating depends on the magnitude of the stresses. Hence, whether or not the aluminum will burn in the vapor

* This work was performed under N00014-87-K-0547 with the Office of Naval Research

phase depends on the physicochemical properties of aluminum and aluminum oxide.

The fact that the dissociation point of aluminum oxide is higher than the boiling point of aluminum indicates that the burning of aluminum can be in the vapor phase⁽⁷⁾. When an aluminum particle is heated such that the temperature of the particle is higher than the melting point of the aluminum oxide, the molten aluminum oxide retracts and the molten aluminum evaporates and diffuses outward. This outward diffusing aluminum vapor reacts with inward diffusing oxidizer in a flame zone which is detached from the droplet surface and which is often modelled as a sheet. Although the reaction occurring in this zone is often referred to as vapor phase combustion, the actual mechanism is probably still heterogeneous, involving sub-micron molten Al₂O₃ particles. The chemistry of the reaction in the detached flame zone is usually considered to be stoichiometric reaction between Al and whatever oxidizing species are present (O₂, H₂O, CO₂, etc.)⁽³⁾. The main product in this region is sub-micron condensed Al₂O₃^(8,9). A fraction of the Al₂O₃ dissociates but most of it condenses because the energy release from chemical reaction is not enough to dissociate all of the Al₂O₃. The kinetics of product dissociation and recombination may be important but are not well known. The condensed aluminum oxide particles have the tendency to concentrate in the flame envelope due to the fact that there is little or no net convection of gas out of the flame⁽⁸⁾. It should be noted that the droplet temperature can become lower than the melting point of the oxide if the burning occurs under adverse combustion conditions such as low concentration of oxidizer, low pressure, and/or low temperature⁽⁸⁾. In this case, the vapor phase model is unacceptable because the evaporation of metal is eventually blocked by the accumulation of oxide on the surface of the solid.

The oxide particle-laden flame zone surrounding the aluminum droplets is highly luminous. Intensity measurements show that⁽¹⁰⁾ the effective blackbody emission temperature of the burning droplet is well above the temperature of the local ambient gas and often higher than the adiabatic flame temperature. This high intensity of radiation is due to continuous emission from condensed Al₂O₃ in the flame zone and emission from the Al droplet. The optical depth of the Al₂O₃ flame envelope surrounding the aluminum droplet has been estimated to be of the order of 0.01⁽¹⁰⁾. Since the flame temperature is very high, the radiation heat losses can be significant but a physically realistic model of radiant transport has not been incorporated into any of the metal droplet burning models and the influence of radiant transport is still ambiguous. Initial studies of the radiant transport in burning Al droplets have concluded that scattering and absorption by the flame envelope are negligible while emission by the flame envelope is significant⁽¹⁰⁾.

Some oxide is observed on the surface of the burning aluminum particle but the mechanism of its formation is not clear. Some of this oxide may be a residual of the original protective oxide skin but experiments show that additional oxide can form or collect continuously on the burning aluminum droplet⁽⁸⁾. The continuous accumulation of oxide on the surface of the burning aluminum droplet may be due to the heterogeneous recombination of dissociated vapor products on the surface or the accumulation of condensed sub-micron Al₂O₃ smoke particles which are thermophoretically driven to the relatively cold droplet surface. The question of which mechanism dominates is important to the surface energy balance due to the substantial source of heat associated with the heterogeneous recombination mechanism. The phenomenon of surface oxide accumulation can also play an important role in the droplet fragmentation characteristics in some combustion environments.

Because diffusion is generally believed to be the limiting mechanism in aluminum droplet vapor phase combustion, a d²-law is often used to model the burning rate. The exponent of the "d²-law" is generally between 1.5 and 2.0 based on experimental data which indicates that there is a significant pressure dependence in burning rate (about p^{0.3}). The pressure dependence may be due to radiant transfer effects (through the oxide product dissociation temperature), heterogeneous product recombination kinetics, or physicochemical properties of the combustion system.

ANALYSIS OF DIFFUSION LIMITED VAPOR PHASE BURNING

In diffusion limited vapor phase burning, fuel vapor, which evaporates from the liquid surface, diffuses outward and reacts with inward diffusing oxidizer vapor. A flame sheet is developed at a stand-off distance from the fuel droplet surface. At the flame stand-off point, the fuel vapor flux and oxidizer vapor flux are in stoichiometric proportion if the reaction kinetics are assumed to be infinitely fast. In general, the shape of the flame is non-spherical as shown in Figure 1. Non spherical flames are generally caused by relative motion between the surrounding gases and droplet, convection effects, and buoyant effects. When the droplet is very small, the diffusion flame surrounding the droplet becomes nearly spherical due to the small relative velocity between the gases and the droplet.

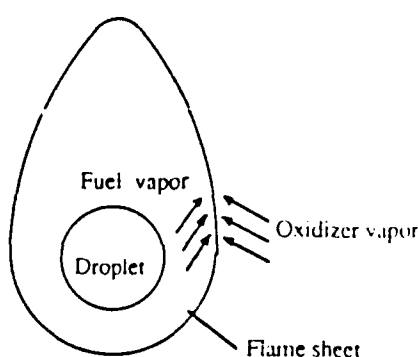


Figure 1. Vapor phase burning processes

Although the combustion of a fuel droplet will be influenced by the shape of the flame sheet, salient features other than the flame shape are found to be predicted with good accuracy by analyses which postulate that the flame sheet is spherically symmetric⁽¹¹⁾. Most experimenters have found that there is good agreement between predicted and measured burning rates, but poorer agreement in flame temperature and position⁽¹¹⁾.

The reaction rate is assumed to be so fast that the flame is infinitely thin and the combustion system is solely controlled by the transport properties of the fuel and the oxidizer. The oxidizer and fuel are assumed to be completely consumed at the flame front. That is, there is assumed to be no oxidizer present inside the flame sheet and no fuel present outside the flame sheet. The typical parameter variation in a vapor phase diffusion flame is plotted in Figure 2.

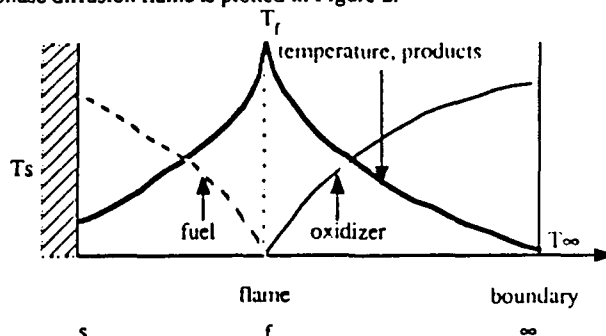


Figure 2. Parameter variation in single droplet burning

The analysis of diffusion limited evaporation and combustion of a spherical volatile fuel particle in a quiescent ambient oxidizing environment can be found in most combustion texts^(5,11,12,13). The following assumptions are usually invoked:

- (1) single spherically symmetrical droplet evaporation (i.e. the problem can be described by one-dimensional spherical coordinates system),
- (2) quasi-steady evaporation (i.e. the size of the droplet is fixed),
- (3) uniform droplet temperature (i.e. droplet has sufficiently high conductivity),
- (4) no free or forced convection around the fuel droplet,
- (5) Lewis number $Le=1$ (i.e. $\alpha=D$),
- (6) the mass diffusivities of oxidizer, fuel, and mixture are all equal (i.e. $D_O=D_f=D$),
- (7) local thermodynamic equilibrium at the droplet surface,
- (8) uniform pressure field,
- (9) constant mass fraction of oxidizers in the quiescent oxidizing atmosphere (i.e. infinite oxidizing atmosphere),
- (10) dissipation energies and body-force work are negligible,
- (11) constant properties,
- (12) radiation heat transfer is negligible.

The governing equations of the combustion of a fuel droplet under the assumptions listed above can be written as
Overall mass conservation equation :

$$\frac{d}{dr}(\rho u r^2) = 0 \quad (1)$$

Energy equation :

$$\rho C_p u \frac{dT}{dr} = \kappa \frac{1}{r^2} \frac{d}{dr} \left(r^2 \frac{dT}{dr} \right) - H \omega_f \quad (2)$$

Fuel species conservation equation :

$$\rho u \frac{dY_f}{dr} + \frac{1}{r^2} \frac{d}{dr} \left[r^2 \rho Y_f \left(-\frac{D}{Y_f} \frac{dY_f}{dr} \right) \right] = \dot{\omega}_f \quad (3)$$

Oxidizer species conservation equation :

$$\rho u \frac{dY_o}{dr} + \frac{1}{r^2} \frac{d}{dr} \left[r^2 \rho Y_o \left(-\frac{D}{Y_o} \frac{dY_o}{dr} \right) \right] = \dot{\omega}_o \quad (4)$$

Solving these equations for the mass burning rate gives

$$\dot{m}_{\text{evap}} = 4\pi r_s^2 \rho u_s = 4\pi \rho D r_s \ln(1 + B) \quad (5)$$

where the value of B can be either B_{FO} or B_{OT} , which are defined as

$$B_{FO} = \frac{i Y_{O,\infty} + Y_{f,s}}{1 - Y_{f,s}} \quad (6)$$

$$B_{OT} = \frac{C_p(T_\infty - T_s) + i Y_{O,\infty} H_f}{\Delta h_v} \quad (7)$$

and the stoichiometric fuel-oxidizer ratio is given by

$$i = \frac{\omega_f}{\omega_o} \quad (8)$$

Since local thermodynamic equilibrium was assumed at the droplet surface, the mass fraction of the fuel vapor at the droplet surface is given by

$$Y_{f,s} = \frac{P_{f,s} M_w f}{P M_w x,s} \quad (9)$$

When the velocity of the ambient gases relative to the velocity of the droplet is not zero, the convective heat transfer effect must be considered. The general mass transfer equation for any arbitrary fuel surface geometry and flow conditions can be described as (12)

$$\dot{m}_{\text{evap}} = A_s \frac{\bar{h}}{C_p} \ln(B + 1) \quad (10)$$

In the case of a spherical fuel droplet burning, equation (10) can be rewritten as (12)

$$\dot{m}_{\text{evap}} = \pi d_s \rho \alpha \overline{N u}_{d_s} \ln(B + 1) \quad (11)$$

where

$$\overline{N u}_{d_s} = 2.0 + 0.6 \overline{R e}_{d_s}^{1/2} \overline{P r}^{1/3} \quad (12)$$

$$\overline{R e}_{d_s} = \frac{\overline{u}_g \cdot \overline{u}_p d_s}{\nu_g} \quad (13)$$

$$\overline{P r} = \frac{\nu_g}{\alpha_g} \quad (14)$$

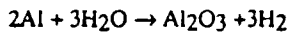
The effect of the convective flow is represented by the $\overline{N u}_{d_s}$ term which reduces to the value of 2 in the limit of no flow.

CALCULATION OF BURNING RATES FROM THE DIFFUSION FLAME MODEL

The following algorithm was used to calculate burning rates from the diffusion flame model.

- (1) guess the temperature of the fuel droplet T_s ,
- (2) calculate fuel vapor pressure for a given T_s ,
- (3) calculate $Y_{f,s}$ from Eq. (9),
- (4) calculate B_{FO} from Eq. (6),
- (5) calculate B_{OT} from Eq. (7),
- (6) if $B_{FO} \neq B_{OT}$, repeat (1)-(5),
if $B_{FO} = B_{OT}$, calculate the mass evaporation rate of the fuel from equation (11).

A reaction mechanism must be postulated before using the model, but the reaction mechanism of aluminum burning in water is not yet well understood. Some experimental studies indicate that Al, AlO, Al₂O, and Al₂O₂ are present in the gas phase as intermediates in the combustion processes (14). However, in this initial study, a simple, single-step reaction without dissociation has been assumed.



(15)

The droplet burning rate is characterized by calculating the change in droplet diameter as a function of time. The history of the droplet diameter obtained from the diffusion flame model is compared with that from Hermansen's model. Hermansen's burning rate model can be described as(6)

$$\frac{d/d_0}{dt} = (1 - k/t/d_0^{1.8})^{1/1.8} \quad (16)$$

where

$$k = 8.3144 \times 10^{-5} R_k A_k^{0.9} P(\text{psi})^{0.27} (\text{cm}^{1.8}/\text{sec}) \quad (17)$$

$$A_k = 100 \sum x_i / x_{go}; \quad i = \text{H}_2\text{O}, \text{CO}_2, \text{OH}, \text{O}, \text{O}_2 \quad (18)$$

The numerical results for the history of the droplet diameter of are presented in Figures 3-5. In these figures, the symbol "D(E)" stands for the droplet diameter history which was calculated from the diffusion limited vapor phase burning model (E stands for evaporation) and the symbol "D(H)" represents the droplet diameter history which was calculated from Hermansen's model. These figures show the effect of relative velocity on Al droplet diameter history for $Y_{O\infty} = 1.0, 0.5, .15$. The effect of R_k in Hermansen's model is also illustrated in each of these figures. The results from the diffusion flame model show that the effect of velocity lag is insignificant, but the results from Hermansen's model show that the value of R_k has a significant effect on the burning rate.

The empirical constant R_k in Hermansen's burning model is used to account for the change in burning rate due to the differences between laboratory and rocket motor environments. A R_k value of 1 is used to calculate the burning rate of the Al droplet in a non-convective, low temperature blackbody environment. A R_k value of 2.7 has been recommended for use in a rocket motor with a convective environment of unspecified magnitude (relative velocity probably on the order of 1 to 4 m/s) and a radiative environment of unspecified effective temperature(6). Since the results of the diffusion flame model show the effect of velocity lag is insignificant, the majority of the influence of the R_k factor in Hermansen's model can be attributed to the difference in radiative environments. Therefore, the thermal radiation effect should be included in the analysis, while the convective effect can be neglected.

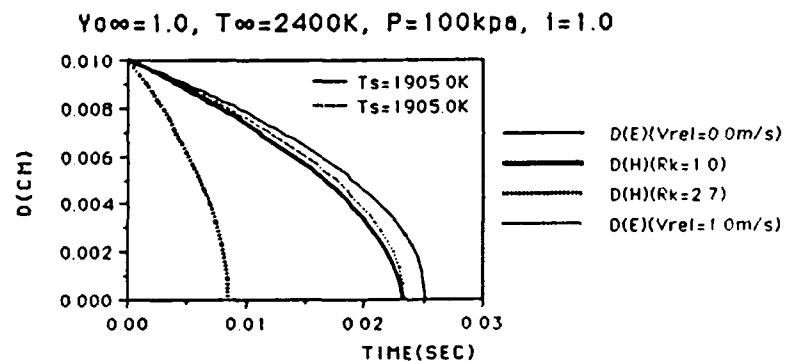


Figure 3. Droplet diameter history (effect of relative velocity at $Y_{O\infty} = 1.0$)

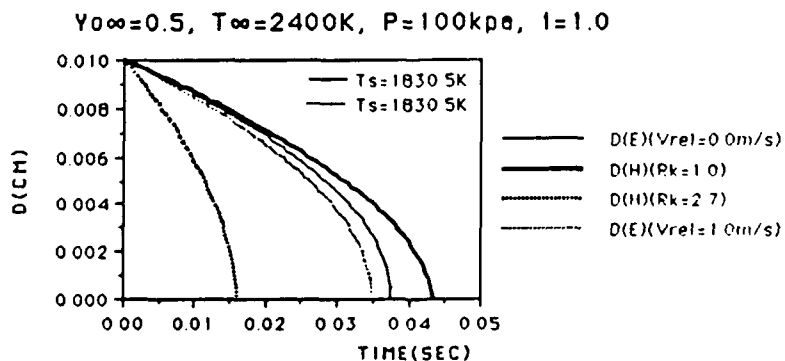


Figure 4. Droplet diameter history (effect of relative velocity at $Y_{O\infty} = 0.5$)

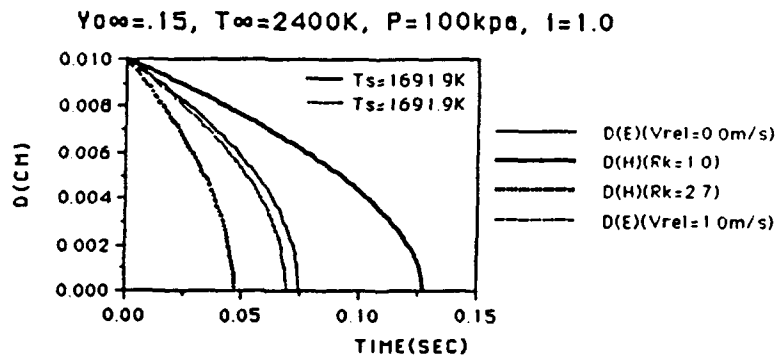


Figure 5. Droplet diameter history (effect of relative velocity at $Y_{\infty} = 0.15$)

INTENSITY MEASUREMENTS

A simple experiment was developed in order to begin to understand the nature and significance of radiative heat transfer in the combustion of aluminum in water. A 100 μm aluminum wire was ignited electrically in a water filled combustion chamber at atmospheric pressure. The emission from the burning wire was measured with a Spex Minimate 1681C spectrometer that was controlled by a Tracor Northern TN-6500 optical multi-channel analyzer. The spectral intensity was calculated from

$$I_{\lambda} = q_{\lambda, \text{ref}} \frac{S}{S_{\text{ref}} \Delta \Omega} \quad (19)$$

The source of the reference signal, S_{ref} , was a FEL coiled-coil tungsten filament quartz halogen spectral irradiance standard lamp. The solid angle, $\Delta \Omega$, was calculated from the following equation

$$\Delta \Omega = \frac{LD_{\text{wire}}}{s^2} \quad (20)$$

where L is the length of the wire that burned, D_{wire} is the diameter of the wire (100 μm) and s is the path length from the wire to the spectrometer slit. It should be noted that since the entire length of the wire used in calculating the solid angle was not burning at the same instant, the solid angle is overestimated and the calculated intensities are a lower limit. The spectral intensities are shown in Figure 6.

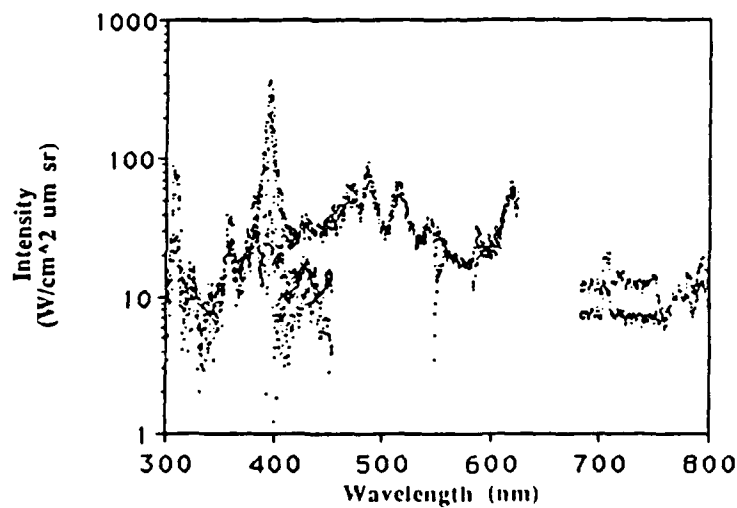


Figure 6. Measured spectral intensity

The lines near 300 and 400 nm are due to emission by aluminum which has strong lines at 308.2, 309.2, 394.4, and 396.1 nm(15). The lines centered around 490 nm are due to emission from AlO which has several strong lines in the spectral region from 465 to 510 nm(15). Since iron was an impurity in the wire, the line near 615 nm is probably due to emission by FeO which emits strongly at 618.1 and 621.9 nm(15).

Figure 7 shows the continuum emitted by the burning aluminum wire. This plot was obtained by removing the line contributions from the data shown in Figure 6. It should be noted that what appears to be line structure in this Figure 7 is data scatter, not line emission. While the lines appearing in the measured spectrum are easily identified, the source of the continuum remains unclear. A large number of free electrons and ions are produced in a combustion process, so a continuous spectrum could be emitted as these species recombine. The spectrum could also be band emission due to electronic and vibrational transitions. Brockman reports that AlO emits a band spectrum from 440 to 540 nm⁽¹⁶⁾. Assuming the continuum is due to emission by condensed, sub-micron Al₂O₃ particles, the measured spectral intensity can be correlated to Planck's function by multiplying by the spectral emissivity and a geometric constant, C, which includes the effect of multiple scattering and particle concentration.

$$I_{\lambda e} = \frac{C \epsilon_{\lambda} (37413/\pi)}{\lambda^5 (\exp(14388/\lambda T) - 1)} \text{ (W/cm}^2 \mu\text{m sr}) \quad (21)$$

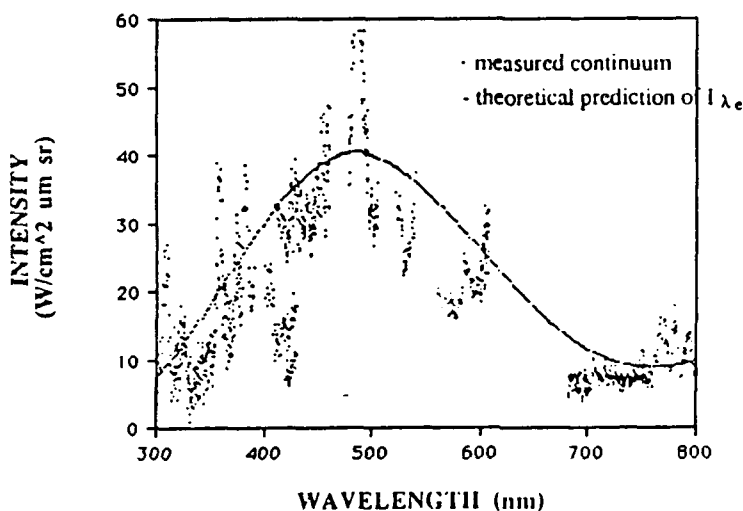


Figure 7. Continuum emission

The following equations which were derived from classical dispersion theory were used to calculate the real and imaginary parts of the refractive index for aluminum oxide over the spectral region of interest. A two oscillator model and the dispersion parameters shown in Table 1 were used in the calculations. The dispersion parameters are valid at 3000 K⁽¹⁷⁾.

$$n = \sqrt{\frac{\epsilon_r' + \sqrt{\epsilon_r'^2 + \epsilon_r''^2}}{2}} \quad (22)$$

$$k = \sqrt{\frac{-\epsilon_r' + \sqrt{\epsilon_r'^2 + \epsilon_r''^2}}{2}} \quad (23)$$

where

$$\epsilon_r' = n^2 - k^2 = 1 + \sum_j \frac{n_{pj}^2(\eta_{oj}^2 - \eta_j^2)}{(\eta_{oj}^2 - \eta_j^2)^2 + \gamma_j^2 \eta_j^2} \quad (24)$$

$$\epsilon_r'' = 2nk = \sum_j \frac{n_{pj}^2(\eta_{oj}^2 - \eta_j^2)}{(\eta_{oj}^2 - \eta_j^2)^2 + \gamma_j^2 \eta_j^2} \quad (25)$$

Table 1. Dispersion parameters for Al₂O₃ at 3000 K⁽¹⁷⁾

η_{p1}^2	8.934×10^{-1}
η_{p2}^2	8.839×10^{-3}
γ_1^2	1.995×10^{-1}
γ_2^2	1.088×10^{-4}

Mie theory was then used to calculate the spectral emissivity of aluminum oxide. In addition to the refractive index, a value for the mean optical size, d_{32} , of Al_2O_3 was needed to use Mie theory. Several values of d_{32} were assumed, and it was found that the Planck function could be fit to the measured data only when values in the range of $0.5 \mu\text{m}$ were used. The spectral emissivity of aluminum oxide is shown in Figure 8 for an assumed d_{32} of $0.5 \mu\text{m}$.

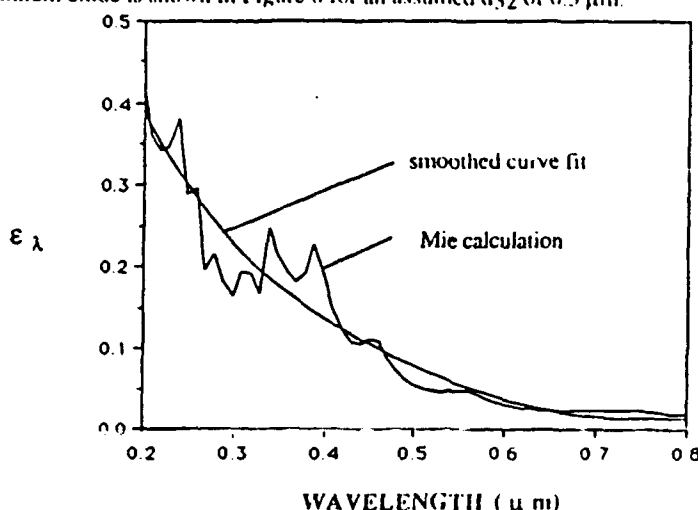


Figure 8. Spectral emissivity for Al_2O_3

The curve fit shown in Figure 8 was used in the calculation of the emitted spectral intensity, $I_{\lambda e}$, rather than the spectral emissivity calculated directly from Mie theory in order to smooth resultant $I_{\lambda e}$ curve. This treatment is valid since a polydisperse size analysis would result in a similar smoothing of the emissivity. The emitted spectral intensity, $I_{\lambda e}$, was then calculated for various values of the geometric constant C and temperatures. Good correlation between the measured data and the $I_{\lambda e}$ curves calculated from equation (21) was found for temperatures between 3600 and 3850 K and values of C between 4.1 and 2.4. The line drawn through the data shown in Figure 7 was calculated from equation (21) with a temperature of 3600 K and C equal to 4.1 and is representative of the fit obtained. The radiative heat flux emitted by the wire is estimated to be 150 W/cm^2 . This estimate was obtained by integrating the product of π times spectral intensity over all wavelengths. Depending on the value used for the heat of vaporization, the power required to evaporate the aluminum was calculated to be between 990 and 1440 W/cm^2 , so the radiative heat loss from the burning aluminum is at least 10 to 15 percent of the energy needed to maintain vapor phase combustion in a laboratory environment. Since the solid angle was overestimated, this estimate of the radiative heat loss is a lower limit. However, the radiative effects in a rocket motor or explosive environment where the effective emissivity of the Al_2O_3 approaches one will be much more significant since the effective black body temperature is between 3600 and 3850 K.

CONCLUSIONS

Results of the diffusion flame model indicate that the adjustable parameter R_k in Hermansen's model which accounts for radiative and convective environment effects plays a strong role in determining the burning rate and yet a rational basis for predicting the value of R_k under various radiative and convective environments has not been established. The velocity lag appears to be of minor importance in determining the burning rate whereas the radiative environment plays a very strong role. Radiation effects should be included in the analysis. Experimentally determined spectral intensities clearly indicate the presence of gaseous Al and AlO . These measurements also show a continuous spectrum, but the source of the continuum remains unclear. Based on the assumption that the continuum is emitted by condensed, sub-micron Al_2O_3 particles the radiative heat transfer contributes at least 10 to 15 percent of the energy needed to maintain vapor phase combustion of aluminum in a liquid water environment. The data shows that the effective blackbody temperature of aluminum burning in water at atmospheric pressure is between 3600 and 3850 K. The results of this experiment also indicate that the mean optical size, d_{32} , for Al_2O_3 is approximately $0.5 \mu\text{m}$.

NOMENCLATURE

A	surface area
A_k	constant in Hermansen's burning rate model defined by Eq. (18)
BFO	transfer number defined by Eq. (6)
BOT	transfer number defined by Eq. (7)
C	geometric constant which accounts for multiple scattering and particle concentration
C_p	constant pressure specific heat
d_s	diameter of fuel droplet
D	mass diffusivity

D_{wire} diameter of the aluminum wire

h heat transfer coefficient or molar basis enthalpy

Nu_d Nusselt number defined by Eq.(12)

H enthalpy of reaction per unit mass of fuel

i stoichiometric fuel-oxidizer ratio

k constant in HermSEN's burning rate model defined by Eq. (17) or absorption index

L wire length

Le Lewis number

m_{evap} mass burning rate of fuel

MW molecular weight

n refractive index

P pressure

Pr Prandtl number

r spatial coordinate away from the center of the fuel droplet

Re Reynolds number defined by Eq. (13)

R_k empirical constant in HermSEN's burning rate model

S signal measured by the spectrometer

s optical path length

t time coordinate

T temperature

u velocity

V_{rel} relative velocity between the gases and droplet

x mole fraction

Y mass fraction

α thermal diffusivity

$\Delta\Omega$ solid angle subtended by the burning wire

ϵ_λ spectral emissivity

ϵ_r' real part of the dielectric constant

ϵ_r'' imaginary part of the dielectric constant

K thermal conductivity

v kinematic viscosity

ρ density

ω mass generation rate

Δh_v latent heat of evaporation for fuel

Subscripts

e emitted

f fuel

g gas

go mixture of gaseous species and equilibrated aluminum oxide particles

i chemical species

o oxidizer or original state

p particle or products

s droplet surface

x mixture

∞ infinite stagnant atmosphere boundary

λ spectral

REFERENCES

1. Glassman, I., "Combustion of Metals - Physical Considerations," *Progress in Astronautics and Rocketry : Solid propellant Rocket Research*, edited by M. Summerfield, Academic Press, New York, 1960, Vol. I, pp.253-257.

2. Gordon, D. A., "Combustion Characteristics of Metal Particles," *Progress in Astronautics and Rocketry : Solid propellant Rocket Research*, edited by M. Summerfield, Academic Press, New York, 1960, Vol. I, pp.271-278.

3. Micheli, Paul L. and Schmidt, Willfred G., "Behavior of Aluminum in Solid Rocket Motors," AFRPL-TR-77-29, Vol. II, 1977.

4. Brzustowski T. A. and Glassman I., "Spectroscopic Investigation of Metal Combustion," *Progress in Astronautics and Aeronautics : Heterogeneous Combustion*, edited by H. G. Wollhard et al., Academic Press, New York, 1965, Vol. 15, pp. 41-74.

5. Kuo, K. K., *Principles of Combustion*, John Wiley & Sons, Inc., New York, 1986.
6. Nickerson, G. R., Coats, D. E., Dang, A. L., Dunn, S. S., Berker, D. R., Hernisen, R. L., and Lamberty, J. T., *The Solid Propellant Rocket Motor Performance Prediction Computer Program(SPP)*, AFAL-TR-87-078, Version 6.0, 1987.
7. Kucht, D. K., "Ignition and Combustion of Aluminum and Beryllium," *AIAA J.*, Vol. 3, No. 12, pp. 2239-2247, Sept. 1965.
8. Price, E. W., "Combustion of Metalized Propellants," *Fundamentals of Solid Propellant Combustion, Progress in Astronautics and Aeronautics Series*, Vol. 90, edited by K. K. Kuo and M. Summerfield, AIAA, New York, 1984, pp. 479-513.
9. Brewster, M. Q., and Parry, D. L., "In-Situ Measurements of Alumina Particle Size and Optical Constants in Composite Solid Propellant Flames," *AIAA87-1582*, June 1987.
10. Brewster, M. Q., and Taylor, D. M., "Radiative Properties of Burning Aluminum Droplets," *Combustion and Flame*, Vol. 72, pp. 287-299, 1988.
11. Williams, F. A., *Combustion Theory*, The Benjamin/Cummings Publishing Company, Inc., Menlo Park, California, 1985.
12. Kanury, A. M., *Introduction to Combustion Phenomena*, Gordon and Breach Science Publishers, New York, 1975. ,
13. Glassman, I., *Combustion*, Academic Press, Inc., New York, 1987.
14. Ogle, R. A., Ph.D. Thesis, The University of Iowa, 1986.
15. Pearse, R.W.B. and A.G. Gaydon, *The Identification of Molecular Spectra*, Chapman and Hall, London, 1975.
16. Brockman, F.G., "The Nature of the Light Emitter in Photo-Flash Lamps," *Journal of the Optical Society of North America*, Vol. 37, No. 8, pp. 652-659, 1947.
17. Parry, D.L., Ph.D. Thesis, The University of Illinois at Urbana-Champaign, 1989.

COMBUSTION OF ALUMINUM AND WATER

PROGRESS REPORT

M.Q. Brewster and K.C. Tang

**DEPARTMENT OF MECHANICAL AND INDUSTRIAL
ENGINEERING**

UNIVERSITY OF ILLINOIS AT URBANA-CHAMPAIGN

CONTENTS

	page
ABSTRACT	ii
NOMENCLATURE	iii
LIST OF TABLES	vi
LIST OF FIGURES	vii
1. INTRODUCTION	1
2. BURNING CHARACTERISTICS OF ALUMINUM	3
3. ANALYSIS OF THE BURNING OF A FUEL PARTICLE IN A QUIESCENT ATMOSPHERE	7
3.1 Evaporation of a single fuel droplet (no chemical reaction)	9
3.1.1 Governing equations	9
3.1.2 Boundary conditions	10
3.1.3 Derivation of mass evaporation rate of the fuel	12
3.1.4 Algorithm for the calculation of mass evaporation rate of the fuel	16
3.2 Heat and mass transfer with chemical reaction	16
3.2.1 Governing equations	16
3.2.2 Derivation of mass burning rate of the fuel	17
3.2.3 Algorithm for the calculation of mass burning rate of the fuel	21
3.3 Droplet burning in a convective atmosphere	21
4. RESULTS OF THE BURNING OF ALUMINUM (Al) AND WATER(H ₂ O)	23
4.1 Burning rate calculation of the combustion of Al and H ₂ O	23
4.2 Results	31
4.3 Discussion	34
4.3.1 Effect of R _k in Herrnsen's model	34
4.3.2 Effect of velocity lag	34
4.3.3 Effect of ambient temperature	35
4.3.4 Effect of mass fraction of ambient oxidizer	35
4.3.5 Effect of pressure	36
4.3.6 Temperature of the burning aluminum droplet	36
5. CONCLUSIONS	43
REFERENCES	44

ABSTRACT

The combustion of aluminum and water is investigated by using a simplified diffusion-limited vapor phase burning model without considering the effect of radiative heat loss. The change in droplet diameter as a function of time is calculated and compared with the corresponding result from Hermsen's model. The effects of the adjustable parameter R_k in Hermsen's model, velocity lag, ambient temperature, mass fraction of ambient oxidizer, and pressure are discussed. Results indicate that dissociation and radiative environmental effects play a very strong role in determining the burning rate, while the convective environmental effect (i.e. velocity lag) appears to be negligible. The results also show that the temperature of the Al droplet may be lower than the melting point of Al_2O_3 at low pressures which indicates that combustion may not be possible at low pressures in water atmosphere. The influence of ambient temperature on burning rate is generally not significant, except for the cases with very low oxidizer concentrations. It is recommended that dissociation and radiative transfer effects be incorporated in a more detailed model in order to adequately describe observed trends and to be able to extrapolate laboratory results to rocket and explosives environments.

NOMENCLATURE

$a_1 \sim 6$	polynomial coefficients for C_p and h
A	surface area
A_k	constant in Hermsen's burning rate model defined by Eq. (98)
b_f	constant defined by Eq. (22) or any one of b_{FO} , b_{FT} , b_{OT}
b_{FO}	constant defined by Eq. (57)
b_{FT}	constant defined by Eq. (60)
b_{OT}	constant defined by Eq. (63)
B_M	transfer number defined by Eq. (36)
B_T	transfer number defined by Eq. (47)
B_{FO}	transfer number defined by Eq. (81)
B_{FT}	transfer number defined by Eq. (83)
B_{OT}	transfer number defined by Eq. (82)
C_p	constant pressure specific heat
C_s	heat capacity
d_s	diameter of fuel droplet
D	mass diffusivity
\mathbf{f}	body force vector
h	mass basis enthalpy
\bar{h}	heat transfer coefficient or molar basis enthalpy
$\frac{*}{Nu_d_s}$	Nusselt number defined by Eq.(86)
H	enthalpy of reaction per unit mass of fuel
i	stoichiometric fuel-oxidizer ratio
k	constant in Hermsen's burning rate model defined by Eq. (97)
Le	Lewis number
L_f	heat of fusion
L_v	heat of evaporation
m	mass
\dot{m}	mass flux vector
\dot{m}_{evap}	mass burning rate of fuel
MW	molecular weight
P	pressure
Pr	Prandtl number
\mathbf{q}	heat flux vector

x	mixture
∞	infinite stagnant atmosphere boundary

Superscripts

BP	boiling point
MP	melting point

Mathematical symbol

$\frac{\partial(\)}{\partial t}$	partial derivative
$\frac{d(\)}{dt}$	total derivative
$\frac{D(\)}{Dt}$	substantial derivative
\ln	natural logarithm
Σ	summation
$\nabla \cdot$	divergence operator

\dot{Q}	heat source
r	spatial coordinate away from the center of the fuel droplet
R	universal gas constant
Re_d	Reynolds number defined by Eq. (87)
R_k	empirical constant in Hermsen's burning rate model
t	time coordinate
T	temperature
u	velocity
U	velocity
v	velocity vector
x	mole fraction
Y	mass fraction
α	thermal diffusivity
α^*	coefficient of thermal expansion
λ	thermal conductivity
ν	kinematic viscosity
ρ	density
$\dot{\omega}$	mass generation rate
Φ	viscous dissipation energy
Δh_v	latent heat of evaporation for fuel
ΔH_f	heat of formation

Subscripts

Al	aluminum
f	fuel
g	gas
go	mixture of gaseous species and equilibrated aluminum oxide particles
i	chemical species
k	coordinates index
l	liquid
o	oxidizer or original state
p	particle or products
r	reference state or reactants
s	droplet surface

LIST OF TABLES

Table		Page
1.	Properties of Aluminum And Aluminum Oxide.	4
2.	Least square coefficient for the thermodynamic functions of specific heat and enthalpy of Al, Al ₂ O ₃ , H ₂ O, and H ₂ .	27
3.	Mass diffusivity of gases at 1 atm.	29
4.	Parameters used in the calculation of droplet diameter history.	32
5.	Input data used in the calculation of droplet diameter history.	32

LIST OF FIGURES

Figure		Page
1.	Vapor phase burning processes	7
2.	Parameter variation in single droplet burning.	8
3.	Flow chart for the calculation of droplet burning rate.	24
4.	Flow chart for subroutine BEQUI	25
5.	Droplet diameter history (effect of relative velocity at $Y_{\infty} = 1.0$).	38
6.	Droplet diameter history (effect of relative velocity at $Y_{\infty} = 0.5$).	38
7.	Droplet diameter history (effect of relative velocity at $Y_{\infty} = .15$).	39
8.	Droplet diameter history (effect of ambient temperature at $Y_{\infty} = 1.0$).	39
9.	Droplet diameter history (effect of ambient temperature at $Y_{\infty} = 0.5$).	40
10.	Droplet diameter history (effect of ambient temperature at $Y_{\infty} = .15$).	40
11.	Droplet diameter history (effect of Y_{∞} at $T_{\infty} = 2400K$, $P = 100kpa$).	41
12.	Droplet diameter history (effect of pressure at $Y_{\infty} = 1.0$).	41
13.	Droplet diameter history (effect of pressure at $Y_{\infty} = 0.5$).	42
14.	Droplet diameter history (effect of pressure at $Y_{\infty} = .15$).	42

1. INTRODUCTION

The burning of metal fuel can take place on the surface of the droplet (surface oxidation process) or in a diffusion limited detached envelope flame around the droplet (vapor-phase burning). Glassman⁽¹⁾ states that the vapor phase burning occurs when the boiling point of the metal oxide is higher than that of the metal. According to this criterion, Al, Mg, Li, Na, K, Ca, and Be can burn in the vapor phase, and B, Si, Ti, and Zr can burn on the surface⁽²⁾. However, some experiments⁽²⁾ reveal that many metals can not burn in the vapor phase even if these metals satisfy Glassman's criterion. This phenomenon is due to the fact that the formation of a protective oxide layer and/or the radiation losses from the high temperature flame can inhibit the vapor phase burning⁽³⁾. The relative volatility of the fuel and its oxide and the size of the particle also play an important role on the combustion mechanism of the particle^(3,4). Therefore, the criterion suggested by Glassman may be considered as a necessary but not sufficient condition for the occurrence of vapor phase burning. Although the metal and oxide boiling points change with pressure, for most metals the vapor pressure curves do not cross and therefore a metal which burns in the vapor phase will generally do so at all pressures⁽¹⁾.

Another general observation about vapor phase combustion of metals with non-volatile oxides is that the flame temperature is limited by the boiling or dissociation point of the metal oxide. The reason is⁽¹⁾ that the heat release from the chemical reaction is not enough to supply the heat required to vaporize or dissociate the oxide for most metals. It should be noted that the flame temperature can be less than the dissociation point of the metal oxide (in which case all the oxide recombines) depending on the heat loss from flame zone. However, within the context of a set of classical assumptions (including neglect of radiative heat transfer), it can be shown that it is not necessary to determine the flame temperature in order to obtain the droplet burning rate in a diffusion limited detached envelope flame⁽⁵⁾.

Although the burning mechanisms of metals have been extensively studied, the results can not be used to predict the combustion behavior in many practical applications such as explosives and rocket motors directly⁽³⁾. This difficulty is due to the differences in burning environments between laboratory studies and rocket motors or explosives. As a result, empirical correlations based on experiments are generally relied on for predictions. Hermsen provided an empirical equation to calculate the burning rate of aluminum with an empirical factor (R_k) introduced to account for the difference in burning rates between laboratory and motor conditions⁽⁶⁾. The difference in burning rates is believed to be due to the large difference in the radiation environments and the direct effect of velocity lags. Currently, this empirical factor, R_k , is determined by comparing the predicted value of burning rate with data obtained from motor firings. In order to extend this predictive capability to account for different convective and radiative environments, it is necessary to analyze the difference in burning rates between laboratory and other conditions theoretically.

This report presents the results of a simplified, initial investigation of the vapor phase burning of aluminum (Al) and water (H₂O). A vapor phase diffusion limited model of burning of a single droplet in a quiescent atmosphere (without considering radiation heat losses) is used to calculate the burning rate of a fuel particle in an oxidizing atmosphere. The numerical results are compared with the burning rates which are calculated from Hermsen's model. It is shown that it is necessary to consider the radiation heat losses from the condensed products in the flame at high temperature in order to examine the difference in burning rates between single particle laboratory conditions and multiple droplet conditions encountered in rocket motors and explosives.

2. BURNING CHARACTERISTICS OF ALUMINUM

Aluminum must be considered⁽³⁾ as a non-volatile metal at most pressures. In addition, a thin protective oxide layer will normally form on the surface of aluminum which inhibits the vapor phase combustion reaction path. Further, aluminum oxide is insoluble in aluminum; therefore, the aluminum will expand and produce stresses in the oxide layer. Whether the oxide layer is still protective upon heating depends on the magnitude of the stresses. Hence, whether or not the aluminum will burn in the vapor phase depends on the physicochemical properties of aluminum and aluminum oxide. These properties are listed in Table 1.

The fact that the dissociation point of aluminum oxide is higher than the boiling point of aluminum indicates that the burning of aluminum can be in the vapor phase⁽⁷⁾. When an aluminum particle is heated such that the temperature of the particle is higher than the melting point of the aluminum oxide, the molten aluminum oxide retracts and the molten aluminum evaporates and diffuses outward. This outward diffusing aluminum vapor reacts with inward diffusing oxidizer in a flame zone which is detached from the droplet surface and which is often modelled as a sheet. Although the reaction occurring in this zone is often referred to as vapor phase combustion, the actual mechanism is probably still heterogeneous, involving sub-micron molten Al₂O₃ particles.

The aluminum droplets in rocket motors are usually the product of agglomeration at the burning propellant surface. Metal particles in the range of 5 μm to 200 μm are used in the propellants⁽⁸⁾ with the most common sizes being between 10 μm and 40 μm . After agglomeration, however, the size of the droplets is found to be of the order of 100 μm to 400 μm ⁽⁹⁾. The diameter of the flame surrounding the particle grows to about 1.5 to 3.5 times the initial particle, depending on the combustion system⁽³⁾.

Table 1. Properties of Aluminum and Aluminum Oxide(3)

<u>Property</u>	<u>Symbol</u>	<u>Unit</u>	<u>Aluminum</u>	<u>Al₂O₃</u>
Molecular weight	MW		27	102
Density	ρ	gm/cm ³	2.35(1000°C)	3.96(α)
				3.42(β)
Melting point	T ^{MP}	K	873	2280-2320
Boiling point	T ^{BP}	K(1 atm)	2320 ⁽¹⁾ 2767 ⁽²⁾	3250 ⁽¹⁾ 4050 ⁽²⁾
Heat of fusion	L _f	cal/gm	95	58.5
Heat of evaporation	L _v	cal/gm	2100-3050 ⁽¹⁾ 2350-2575 ⁽²⁾	1130 - (1) 1340-1360 ⁽²⁾
Heat capacity	C _s	cal/gmK	0.22-0.26 .237+5.83*10 ⁻⁵ T	0.43(3000°C)
Heat of formation	ΔH_f	kcal/mole	0	399.1-400.3
Thermal conductivity	λ	cal/cm.secK	0.5	0.025
Coefficient of thermal expansion	α^*	10 ⁻⁶ K ⁻¹	23.8	9.0

Note: (1) Pokhil
 (2) Jannaf/ASPC

The chemistry of the reaction in the detached flame zone is usually considered to be stoichiometric reaction between Al and whatever oxidizing species are present (O_2 , H_2O , CO_2 , etc.)(3). The main product in this region is sub-micron condensed Al_2O_3 (8,10). A fraction of the Al_2O_3 dissociates but most of it condenses because the energy release from chemical reaction is not enough to dissociate all of the Al_2O_3 . The kinetics of product dissociation and recombination may be important but are not well known. The condensed aluminum oxide particles have the tendency to concentrate in the flame envelope due to the fact that there is little or no net convection of gas out of the flame(8). It should be noted that the droplet temperature can become lower than the melting point of the oxide if the burning occurs under adverse combustion conditions such as low concentration of oxidizer, low pressure, and/or low temperature(8). In this case, the vapor phase model is unacceptable because the evaporation of metal is blocked by the oxide on the surface.

The oxide particle-laden flame zone surrounding the aluminum droplets is highly luminous. Intensity measurements show that⁽¹¹⁾ the effective blackbody emission temperature of the burning droplet is well above the temperature of the local ambient gas and often higher than the adiabatic flame temperature. This high intensity of radiation is due to continuous emission from condensed Al_2O_3 in the flame zone and emission from the Al droplet. The optical depth of the Al_2O_3 flame envelope surrounding the aluminum droplet has been estimated to be of the order of 0.01⁽¹¹⁾. Since the flame temperature is very high (sometimes estimated to be as high as 4500-5500K depending on the combustion environment), the radiation heat losses can be significant but a correct model of radiant transport has not been incorporated into any of the metal droplet burning models and the influence of radiant transport is still ambiguous. Initial studies of the radiant transport in burning Al droplets have concluded that scattering and absorption by the flame envelope are negligible while emission by the flame envelope is significant⁽¹¹⁾.

Some oxide is observed on the surface of the burning aluminum particle but the mechanism of its formation is not clear. Some of this oxide may be a residual of the

original protective oxide skin but experiments show that additional oxide can form or collect continuously on the burning aluminum droplet⁽⁸⁾. The continuous accumulation of oxide on the surface of the burning aluminum droplet may be due to the heterogeneous recombination of dissociated vapor products on the surface or the accumulation of condensed sub-micron Al₂O₃ smoke particles which are thermophoretically driven to the relatively cold droplet surface. The question of which mechanism dominates is important to the surface energy balance due to the substantial source of heat associated with the heterogeneous recombination mechanism. The phenomenon of surface oxide accumulation can also play an important role in the droplet fragmentation characteristics in some combustion environments.

Because diffusion is generally believed to be the limiting mechanism in aluminum droplet vapor phase combustion, a d²-law is often used to model the burning rate. The exponent of the "d²-law" is generally between 1.5 and 2.0 based on experimental data which indicates that there is a significant pressure dependence in burning rate (about P^{0.3}). The pressure dependence may be due to radiant transfer effects (through the oxide product dissociation temperature) , heterogeneous product recombination kinetics, or physicochemical properties of the combustion system.

3. ANALYSIS OF THE BURNING OF A FUEL PARTICLE IN A QUIESCENT ATMOSPHERE

In diffusion-limited vapor phase burning, fuel vapor, which evaporates from the liquid surface, diffuses outward and reacts with inward diffusing oxidizer vapor. A flame sheet is developed at a stand-off distance from the fuel droplet surface. At the flame stand-off point, the fuel vapor flux and oxidizer vapor flux are in stoichiometric proportion if the reaction kinetics are assumed to be infinitely fast. In general, the shape of the flame is non-spherical as shown in Figure 1. Non-spherical flames are generally caused by relative motion between the surrounding gases and droplet, convection effects, and buoyance effects. When the droplet is very small, the diffusion flame surrounding the droplet becomes nearly spherical due to the small relative velocity between the gases and the droplet.

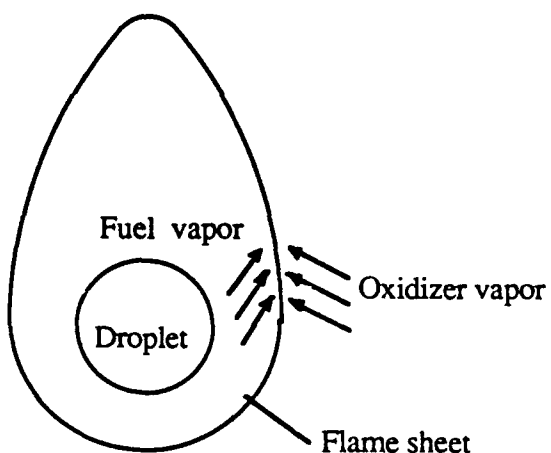


Figure 1. Vapor phase burning processes

Although the combustion of a fuel droplet will be influenced by the shape of the flame sheet, salient features other than the flame shape are found to be predicted with good accuracy by analyses which postulate that the flame sheet is spherically symmetric(12). Most experimenters have found that there is good agreement with respect to burning rate, but poorer agreement in flame temperature and position(12).

The reaction rate is assumed to be so fast that the flame is infinitely thin and the combustion system is solely controlled by the transport properties of the fuel and the oxidizer. The oxidizer and fuel are assumed to be completely consumed at the flame. That is, there is assumed to be no oxidizer present inside the flame sheet and no fuel present outside the flame sheet. The typical parameter variation in a vapor phase diffusion flame is plotted in Figure 2.

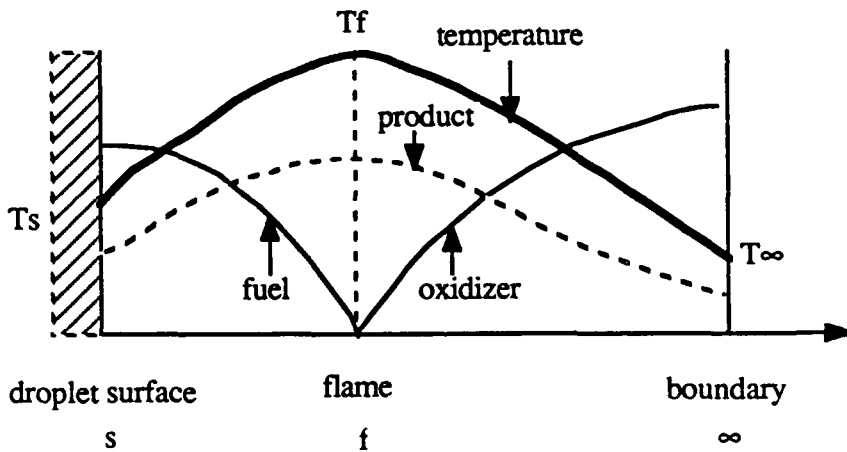


Figure 2. Parameter variation in single droplet burning

In the sections that follow the analysis of diffusion-limited evaporation and combustion of a spherical volatile fuel particle in a quiescent ambient oxidizing environment is reviewed. Similar treatments can be found in most combustion texts(5,12,13,14). The

presentation is made in two parts. First droplet evaporation without reaction is presented and the extension to include chemical reaction is made.

3.1 Evaporation of a Single Fuel Droplet (No Chemical Reaction)

3.1.1 Governing Equations

The conservation equations for a multi-component reacting system can be written as follows :

Overall mass conservation equation :

$$\frac{\partial \rho}{\partial t} + \nabla \cdot (\rho \mathbf{v}) = 0 \quad (1)$$

Energy equation :

$$\rho \frac{Dh}{Dt} - \frac{DP}{Dt} = -\nabla \cdot \mathbf{q} + \Phi + \dot{Q} + \rho \sum Y_k f_k \cdot \mathbf{v}_k \quad (2)$$

Fuel species conservation equation :

$$\frac{\partial \rho_f}{\partial t} + \nabla \cdot \dot{m}_f = \dot{\omega}_f \quad (3)$$

Oxidizer species conservation equation :

$$\frac{\partial \rho_o}{\partial t} + \nabla \cdot \dot{m}_o = \dot{\omega}_o \quad (4)$$

These equations can be solved to determine the evaporation rate of a single fuel droplet in a quiescent oxidizing atmosphere of a given temperature and pressure without combustion. The following assumptions are usually invoked:

- (1) single spherically symmetrical droplet evaporation (i.e. the problem can be described by one-dimensional spherical coordinates system),
- (2) quasi-steady evaporation (i.e. the size of the droplet is fixed),
- (3) uniform droplet temperature (i.e. droplet has sufficiently high conductivity),
- (4) no free or forced convection around the fuel droplet,

- (5) Lewis number $Le=1$ (i.e. $\alpha=D$),
- (6) the mass diffusivities of oxidizer, fuel, and mixture are all equal (i.e. $D_O=D_f=D$),
- (7) local thermodynamic equilibrium at the droplet surface,
- (8) uniform pressure field,
- (9) constant mass fraction of oxidizers in the quiescent oxidizing atmosphere (i.e. infinite oxidizing atmosphere),
- (10) dissipation energies and body-force work are negligible,
- (11) constant properties,
- (12) radiation heat transfer is negligible.

The governing equations under these assumptions can be written as

Overall continuity equation :

$$\frac{d}{dr}(\rho u r^2) = 0 \quad (5)$$

Energy equation :

$$\rho C_p u \frac{dT}{dr} = \lambda \frac{1}{r^2} \frac{d}{dr} \left(r^2 \frac{dT}{dr} \right) \quad (6)$$

Fuel species equation :

$$\rho u r^2 \frac{dY_f}{dr} = \rho D \frac{d}{dr} \left(r^2 \frac{dY_f}{dr} \right) \quad (7)$$

Oxidizer species equation :

$$\rho u r^2 \frac{dY_o}{dr} = \rho D \frac{d}{dr} \left(r^2 \frac{dY_o}{dr} \right) \quad (8)$$

3.1.2 Boundary Conditions

(a) Boundary Conditions at Fuel Droplet Surface

The boundary conditions at the droplet surface (i.e. $r=r_s$) can be obtained by considering the mass and energy conservation at the droplet surface. The consideration of fuel species conservation at the droplet surface yields

$$\dot{m}_{\text{evap}} Y_{f,1} = \dot{m}_{\text{evap}} Y_{f,s} - \rho D 4\pi r_s^2 \frac{dY_f}{dr} \Big|_{r=r_s}$$

where $Y_{f,1}=1$ for 100% purity fuel in the fuel droplet. Then,

$$\dot{m}_{\text{evap}} = \rho D 4\pi r_s^2 \frac{1}{Y_{f,s}-1} \frac{dY_f}{dr} \Big|_{r=r_s} \quad (9)$$

The consideration of conservation of energy at the droplet surface yields

$$\frac{\dot{m}_{\text{evap}}}{4\pi r_s^2} \Delta h_v = \rho u_s \Delta h_v = \lambda \frac{dT}{dr} \Big|_{r=r_s} \quad (10)$$

Other boundary conditions at the droplet surface are :

$$T(r=r_s) = T_s \quad (11)$$

$$Y_f(r=r_s) = Y_{f,s} \quad (12)$$

$$Y_O(r=r_s) = Y_{O,s} = 0 \quad (13)$$

According to assumption (7), the mass fraction of the fuel vapor at the droplet surface can be obtained from the vapor-pressure curve of the fuel. Then

$$Y_{f,s} = \frac{P_{f,s}}{P} \frac{MW_f}{MW_{x,s}} \quad (14)$$

(b) Boundary Conditions at Infinite Oxidizing Atmosphere

The boundary conditions at the infinite oxidizing atmosphere are :

$$T(r \rightarrow \infty) = T_\infty \quad (15)$$

$$Y_O(r \rightarrow \infty) = Y_{O,\infty} \quad (16)$$

$$Y_f(r \rightarrow \infty) = Y_{f,\infty} = 0 \quad (17)$$

3.1.3 Derivation of Mass Evaporation Rate of the Fuel

Integration of Eq. (5) with respect to r yields

$$\rho u r^2 = \text{Constant} \quad (18)$$

Evaluating Eq. (18) at the droplet surface gives

$$C_1 = \rho u_s r_s^2 \quad (19)$$

The mass burning rate can be written as

$$\dot{m}_{\text{evap}} = \rho u_s 4\pi r_s^2 \quad (20)$$

The constant C_1 can then be evaluated from Eqs. (19) and (20) as

$$C_1 = \rho u_s r_s^2 = \frac{\dot{m}_{\text{evap}}}{4\pi} = \rho u r^2 = \text{Constant} \quad (21)$$

(a) Fuel Species Equation

The mass fraction of fuel can be nondimensionalized by defining

$$b_f \equiv \frac{Y_f - Y_{f,\infty}}{Y_{f,s} - Y_{f,1}} = \frac{Y_f - Y_{f,\infty}}{Y_{f,s} - 1} \quad (22)$$

Therefore

$$dY_f = (Y_{f,s} - 1)db_f \quad (23)$$

Substituting Eq. (23) into Eq. (7), we have

$$\rho u r^2 \frac{db_f}{dr} - \rho D \frac{d}{dr} (r^2 \frac{db_f}{dr}) = 0 \quad (24)$$

Substituting Eq. (21) into Eq. (24) gives

$$\frac{\dot{m}_{\text{evap}}}{4\pi} \frac{db_f}{dr} - \rho D \frac{d}{dr} (r^2 \frac{db_f}{dr}) = 0 \quad (25)$$

Integration of Eq. (25) with respect to r gives

$$\frac{\dot{m}_{\text{evap}}}{4\pi} b_f - \rho D r^2 \frac{db_f}{dr} = C_2 \quad (26)$$

Upon substituting Eq. (23) into boundary condition (9), the mass evaporation rate becomes

$$\dot{m}_{\text{evap}} = \rho D 4\pi r_s^2 \frac{db_f}{dr} \Big|_{r=r_s}$$

which can be rearranged to give

$$\frac{\dot{m}_{\text{evap}}}{\rho D 4\pi r_s^2} = \frac{db_f}{dr} \Big|_{r=r_s} \quad (27)$$

Evaluating Eq. (26) at the droplet surface, we have

$$\frac{\dot{m}_{\text{evap}}}{4\pi r_s^2} b_{f,s} - \rho D r_s^2 \frac{db_f}{dr} \Big|_{r=r_s} = C_2 \quad (28)$$

Substituting Eq. (27) into Eq. (28) gives

$$C_2 = \frac{\dot{m}_{\text{evap}}}{4\pi} (b_{f,s} - 1) \quad (29a)$$

which can be substituted into Eq. (26) to give

$$\frac{\dot{m}_{\text{evap}}}{4\pi} b_f - \rho D r^2 \frac{db_f}{dr} = \frac{\dot{m}_{\text{evap}}}{4\pi} (b_{f,s} - 1) \quad (29b)$$

Separating the variables in Eq. (29b) gives

$$\frac{db_f}{(b_f - b_{f,s} + 1)} = \frac{\dot{m}_{\text{evap}}}{4\pi \rho D} \frac{1}{r} dr \quad (30)$$

Integrating Eq. (30) with respect to r , we have

$$\ln(b_f - b_{f,s} + 1) = \frac{\dot{m}_{\text{evap}}}{4\pi \rho D} \left(-\frac{1}{r} \right) + C_3 \quad (31)$$

Evaluating Eq. (31) at $r \rightarrow \infty$, where

$$b_f \Big|_{r \rightarrow \infty} = b_{f,\infty} = \frac{Y_{f,\infty} - Y_{f,s}}{Y_{f,s} - 1} = 0 \quad (32)$$

Gives

$$C_3 = \ln(b_f - b_{f,s} + 1) \quad (33)$$

Substituting Eq. (33) into Eq. (31), we have

$$\ln \frac{-b_{f,s} + 1}{b_f - b_{f,s} + 1} = \frac{\dot{m}_{\text{evap}}}{4\pi} \frac{1}{\rho D} \frac{1}{r} \quad (34)$$

Solving for \dot{m}_{evap} by evaluating Eq. (34) at $r = r_s$ gives

$$\dot{m}_{\text{evap}} = 4\pi\rho D r_s \ln(1 - b_{f,s})$$

which can also be written as

$$\dot{m}_{\text{evap}} = 4\pi\rho D r_s \ln(1 + B_M) \quad (35)$$

where

$$B_M = -b_{f,s} = \frac{Y_{f,s} - Y_{f,\infty}}{1 - Y_{f,s}} \quad (36)$$

(b) Energy Equation

The energy equation (6) can be rearranged and written as

$$\rho u r^2 \frac{dT}{dr} = \rho \alpha \frac{d}{dr} \left(r^2 \frac{dT}{dr} \right) \quad (37)$$

Substituting Eq. (21) into Eq. (37), we have

$$\frac{\dot{m}_{\text{evap}}}{4\pi} \frac{dT}{dr} = \rho \alpha \frac{d}{dr} \left(r^2 \frac{dT}{dr} \right) \quad (38)$$

Integration of Eq. (38) with respect to r yields

$$\frac{\dot{m}_{\text{evap}}}{4\pi} T = \rho \alpha r^2 \frac{dT}{dr} + C_4 \quad (39)$$

Evaluating Eq. (39) at $r=r_s$ then gives

$$\frac{\dot{m}_{\text{evap}}}{4\pi} T_s = \rho \alpha r_s^2 \frac{dT}{dr} \Big|_{r=r_s} + C_4 \quad (40)$$

Substituting Eq. (10) into Eq. (40) and solving for C_4 gives

$$C_4 = \frac{\dot{m}_{\text{evap}}}{4\pi} \left(T_s - \frac{\rho \alpha}{\lambda} \Delta h_v \right) \quad (41)$$

Substituting Eq. (41) into Eq. (39), we have

$$\frac{\dot{m}_{\text{evap}}}{4\pi} \left(T - T_s + \frac{\rho \alpha}{\lambda} \Delta h_v \right) = \rho \alpha r^2 \frac{dT}{dr} \quad (42)$$

Upon integrating Eq. (42) with respect to r , we get

$$\ln \left(T - T_s + \frac{\rho \alpha}{\lambda} \Delta h_v \right) = - \frac{\dot{m}_{\text{evap}}}{4\pi \rho \alpha} \frac{1}{r} + C_5 \quad (43)$$

Evaluating Eq. (43) at $r \rightarrow \infty$, $T = T_\infty$, then gives

$$C_5 = \ln (T_\infty - T_s + \frac{\rho \alpha}{\lambda} \Delta h_v) \quad (44)$$

Substituting Eq. (44) into Eq. (43) gives

$$\ln \frac{\left(T - T_s + \frac{1}{C_p} \Delta h_v \right)}{\left(T_\infty - T_s + \frac{1}{C_p} \Delta h_v \right)} = - \frac{\dot{m}_{\text{evap}}}{4\pi \rho \alpha} \frac{1}{r} \quad (45)$$

Evaluating Eq.(45) at $r=r_s$ gives

$$\dot{m}_{\text{evap}} = 4\pi \rho \alpha r_s \ln(1 + B_T) \quad (46)$$

where

$$B_T = \frac{C_p(T_\infty - T_s)}{\Delta h_v} \quad (47)$$

(c) Mass Evaporation Rate of the Fuel Droplet

From Eqs. (35) and (46), the mass evaporation rate of the fuel droplet can be written as :

$$\dot{m}_{\text{evap}} = 4\pi \rho D \ln(1 + B_M) = 4\pi \rho \alpha r_s \ln(1 + B_T) \quad (48)$$

For $Le=1$ (i.e. $\alpha=D$),

$$B_M = B_T \quad (49)$$

or

$$\frac{Y_{f,s} - Y_{f,\infty}}{1 - Y_{f,s}} = \frac{C_p(T_\infty - T_s)}{\Delta h_v} \quad (50)$$

This equation can be used to solve for the droplet temperature T_s as described below.

3.1.4 Algorithm for Calculating the Mass Evaporation Rate of the Fuel

The algorithm for calculating the mass evaporation rate of the fuel droplet can be described as follows :

- (1) guess the temperature of the fuel droplet T_s ,
- (2) calculate fuel vapor pressure for a given T_s ,
- (3) calculate $Y_{f,s}$ from Eq. (14),
- (4) calculate B_M from Eq. (36),
- (5) calculate B_T from Eq. (47),
- (6) if $B_M \neq B_T$, repeat (1)-(5),
if $B_M=B_T$, calculate the mass evaporation rate of the fuel from Eq. (48).

3.2 Heat and Mass Transfer with Chemical Reaction

3.2.1 Governing Equations

The governing equations of the combustion of a fuel droplet under the same assumptions as those listed in sec. 3.1.1 can be written as

Overall mass conservation equation :

$$\frac{d}{dr}(\rho ur^2) = 0 \quad (51)$$

Energy equation :

$$\rho C_p u \frac{dT}{dr} = \lambda \frac{1}{r^2} \frac{d}{dr} \left(r^2 \frac{dT}{dr} \right) - H \dot{\omega}_f \quad (52)$$

Fuel species conservation equation :

$$\rho u \frac{dY_f}{dr} + \frac{1}{r^2} \frac{d}{dr} \left[r^2 \rho Y_f \left(-\frac{D}{Y_f} \frac{dY_f}{dr} \right) \right] = \dot{\omega}_f \quad (53)$$

Oxidizer species conservation equation :

$$\rho u \frac{dY_0}{dr} + \frac{1}{r^2} \frac{d}{dr} \left[r^2 \rho Y_0 \left(- \frac{D}{Y_0} \frac{dY_0}{dr} \right) \right] = \dot{\omega}_0 \quad (54)$$

The new terms appearing are H , the enthalpy of reaction per unit mass of fuel, and $\dot{w}_{f,o}$, the volumetric fuel and oxidizer production rates.

3.2.2 Derivation of Mass Burning Rate of the Fuel

(a) Combination of Fuel and Oxidizer Species Equations (with $D_0 = D_f = D$)

A single-step stoichiometric reaction equation (no dissociation) is assumed which can be written as :

The definition of i , the stoichiometric fuel-oxidizer mass flux ratio, can be written as :

$$i \equiv \frac{\omega_f}{\dot{\omega}_o}$$

Multiplying Eq. (54) by i and subtracting from Eq. (53) yields

$$\rho u r^2 \frac{d}{dr} (Y_f - i Y_o) = \rho D \frac{d}{dr} \left[r^2 \frac{d}{dr} (Y_f - i Y_o) \right] \quad (55)$$

Dividing Eq. (55) by $Y_{f,s} - 1 + Y_{o,s}$ gives

$$\rho u r^2 \frac{db_{FO}}{dr} = \rho D \frac{d}{dr} \left(r^2 \frac{db_{FO}}{dr} \right) \quad (56)$$

where

$$b_{FO} \equiv \frac{Y_f - i Y_o}{Y_{f,s} - 1 + i Y_{o,s}} \quad (57)$$

(b) Combination of Fuel Species Equation and Energy Equation (with $\alpha=D$)

Multiplying Eq. (53) by H and adding Eq. (52) yields

$$\rho u r^2 \frac{d}{dr} (Y_f H + C_p T) = \rho \alpha \frac{d}{dr} \left[r^2 \frac{d}{dr} (Y_f H + C_p T) \right] \quad (58)$$

Dividing Eq. (58) by $\Delta h_v + H(Y_{f,s} - 1)$ gives

$$\rho u r^2 \frac{d}{dr} \frac{b_{FT}}{r} = \rho D \frac{d}{dr} \left(r^2 \frac{d}{dr} b_{FT} \right) \quad (59)$$

where

$$b_{FT} \equiv \frac{Y_f H + C_p T}{\Delta h_v + H(Y_{f,s} - 1)} \quad (60)$$

(c) Combination of Oxidizer Species Equation and Energy Equation (with $\alpha=D$)

Multiplying Eq. (54) by iH and adding Eq. (52) yields

$$\rho u r^2 \frac{d}{dr} (i Y_o H + C_p T) = \rho \alpha \frac{d}{dr} \left[r^2 \frac{d}{dr} (i Y_o H + C_p T) \right] \quad (61)$$

Dividing Eq. (61) by $\Delta h_v + i H Y_{o,s}$ gives

$$\rho u r^2 \frac{d}{dr} \frac{b_{OT}}{r} = \rho D \frac{d}{dr} \left(r^2 \frac{d}{dr} b_{OT} \right) \quad (62)$$

where

$$b_{OT} \equiv \frac{i Y_o H + C_p T}{\Delta h_v + i Y_{o,s} H} \quad (63)$$

(d) Derivation of Burning Rate

From Eqs. (56), (59), and (62), the governing equations can be written as

$$\rho u r^2 \frac{db}{dr} = \rho D \frac{d}{dr} \left(r^2 \frac{db}{dr} \right) \quad (64)$$

Where b can be either b_{FO} , b_{FT} , or b_{OT} which is defined by Eqs. (57), (60), or (63) respectively.

The boundary conditions are the same as the boundary conditions which are described in section 3.1.2. The mass conservation equation at the droplet surface can be written as

$$\dot{m}_{evap} = 4\pi r_s^2 \rho u_s = \rho D 4\pi r_s^2 \frac{1}{Y_{f,s}-1} \frac{dY_f}{dr} \Big|_{r=r_s} \quad (65)$$

Since $Y_{O,s} = 0$, Eq. (65) gives

$$\rho u_s = \rho D \frac{d}{dr} \left(\frac{Y_f}{Y_{f,s}-1} \right) \Big|_{r=r_s} = \rho D \frac{d b_{FO}}{dr} \Big|_{r=r_s} \quad (66)$$

Likewise, the energy conservation equation at the droplet surface, Eq. (10), can be rewritten as

$$\rho u_s = \rho \alpha \frac{d}{dr} \left(\frac{C_p T}{\Delta h_v} \right) \Big|_{r=r_s} = \rho D \frac{d b_{OT}}{dr} \Big|_{r=r_s} \quad (67)$$

From Eqs. (66) and (67), we have

$$\rho u_s = \rho D \frac{d b_{FO}}{dr} \Big|_{r=r_s} = \rho D \frac{d b_{OT}}{dr} \Big|_{r=r_s} \quad (68)$$

In addition, the fuel-energy combination can also be used to write

$$\rho u_s = \rho D \frac{d b_{FT}}{dr} \Big|_{r=r_s} \quad (69)$$

Based on Eqs. (66), (67), and (69), the boundary conditions at the droplet surface can be written in the general form

$$\rho u_s = \rho D \frac{db}{dr} \Big|_{r=r_s} \quad (70)$$

where b can be either b_{FO} , b_{FT} , or b_{OT} .

The boundary conditions at $r \rightarrow \infty$ are

$$b = b_\infty \quad (71)$$

Integrating Eq. (64) with respect to r , we have

$$\rho u r^2 b = \rho D r^2 \frac{db}{dr} + C_6 \quad (72)$$

Evaluating Eq.(72) at $r=r_s$ gives

$$\rho u_s r_s^2 b_s = \rho D \frac{db}{dr} \Big|_{r=r_s} + C_6 \quad (73)$$

Substituting Eq. (70) into Eq. (73) gives

$$C_6 = \rho u_s r_s^2 (b_s - 1) \quad (74)$$

Substituting Eq. (74) into Eq. (72) gives

$$\rho u_s r_s^2 (b - b_s + 1) = \rho D r^2 \frac{db}{dr} \quad (75)$$

Upon separating variables and integrating we get

$$\ln(b - b_s + 1) = -\frac{\rho u_s r_s^2}{\rho D} \frac{1}{r} + C_7 \quad (76)$$

Evaluating Eq. (76) at $r \rightarrow \infty$ gives

$$C_7 = \ln(b_\infty - b_s + 1) \quad (77)$$

Substituting Eq. (77) into Eq. (76) then gives

$$\frac{\rho u_s r_s^2}{\rho D} \frac{1}{r} = \ln \frac{b_\infty - b_s + 1}{b - b_s + 1} \quad (78)$$

The mass burning rate can be obtained by evaluating Eq. (78) at $r=r_s$ as

$$\dot{m}_{evap} = 4\pi r_s^2 \rho u_s = 4\pi \rho D r_s \ln(1 + B) \quad (79)$$

where

$$B = b_{\infty} - b_s \quad (80)$$

The value of B can be either B_{FO} , B_{FT} , or B_{OT} which are defined as

$$B_{FO} \equiv b_{FO,\infty} - b_{FO,s} = \frac{iY_{0,\infty} + Y_{f,s}}{1 - Y_{f,s}} \quad (81)$$

$$B_{OT} \equiv b_{OT,\infty} - b_{OT,s} = \frac{C_p(T_{\infty} - T_s) + iY_{0,\infty}H}{\Delta h_v} \quad (82)$$

$$B_{FT} \equiv b_{FT,\infty} - b_{FT,s} = \frac{C_p(T_{\infty} - T_s) + iY_{f,s}H}{\Delta h_v + H(Y_{f,s} - 1)} \quad (83)$$

3.2.3 Algorithm for the Calculation of Mass Burning Rate of the Fuel

The algorithm for calculating the burning rate is the same as the algorithm for calculating the mass evaporation rate of the fuel droplet (as described in sec. 3.1.4). However, the convergence criterion in section 3.1.4 (i.e. $B_M=B_T$) should change to any one of $B_{OF}=B_{FT}$, $B_{FT}=B_{OT}$, or $B_{OF}=B_{OT}$ for the calculation of the burning rate. The assumption $Le=1$ ($\alpha = D$) is still made. Once the transfer number B is known, the mass burning rate \dot{m}_{evap} can be determined from Eq. (79).

3.3 Droplet Burning in a Convective Atmosphere

When the velocity of the ambient gases relative to the velocity of the droplet is not zero, the convective heat transfer effect must be considered. The general mass transfer equation for any arbitrary fuel surface geometry and flow conditions can be described as(13)

$$\dot{m}_{evap} = A_s \frac{\bar{h}}{C_p} \ln(B + 1) \quad (84)$$

In the case of a spherical fuel droplet burning, Eq. (84) can be rewritten as(13)

$$\dot{m}_{evap} = \pi d_s \rho \alpha \overline{N u}_{d_s}^* \ln(B + 1) \quad (85)$$

where

$$\overline{\text{Nu}}_{ds}^* = 2.0 + 0.6 \text{Re}_{ds}^{1/2} \text{Pr}^{1/3} \quad (86)$$

$$\text{Re}_{ds} = \frac{|U_g - U_p|d_s}{v_g} \quad (87)$$

$$\text{Pr} = \frac{v_g}{\alpha_g} \quad (88)$$

The effect of the convective flow is represented by the $\overline{\text{Nu}}_{ds}^*$ term which reduces to the value of 2 in the limit of no flow.

4. RESULTS OF THE BURNING OF ALUMINUM (Al) AND WATER (H₂O)

4.1 Burning Rate Calculation of the Combustion of Al and H₂O

A computer code, based on the algorithm for the calculation of the burning rate (i.e. sec. 3.2.3), is used to examine the burning of aluminum (Al) in water (H₂O) atmosphere. The flow charts for implementing the numerical calculation of burning rate are shown as Figs. 3 and 4. Fig. 3 is the flow chart for the calculation of droplet burning rate. The flow chart for the subroutine BEQUI, which is used in the calculation of burning rate, is shown in Fig. 4. In this computer code, BFO and BFT are chosen to be equal in order to calculate the droplet surface temperature T_S and the mass fraction of the gas phase fuel at the droplet surface Y_{f,S} from the vapor pressure data of the fuel. When the correct value of T_S and Y_{f,S} are found, then BFO and BFT are determined for the given T_∞ and P. With the transfer number B determined, the mass burning rate can be obtained from Eq. (79), and the diameter change of the fuel droplet can be calculated accordingly.

Pressure dependence is introduced into this model only by the pressure dependence of the thermophysical properties of the fuel, oxidizer, and mixture. The pressure dependence relative to the dissociation effect is ignored by the assumption that there is no dissociation in the chemical reaction processes.

In order to implement the calculation of the burning rate, the following parameters must be determined :

(a) Chemical Reaction Mechanism

The reaction mechanism of Aluminum burning is not well understood yet. Some experimental studies indicate that Al, AlO, Al₂O, and Al₂O₂ are present in the gas phase as intermediates in the combustion processes(15). Ogle(15) postulated a reaction mechanism for the burning of aluminum droplet in oxygen atmosphere which consisted of

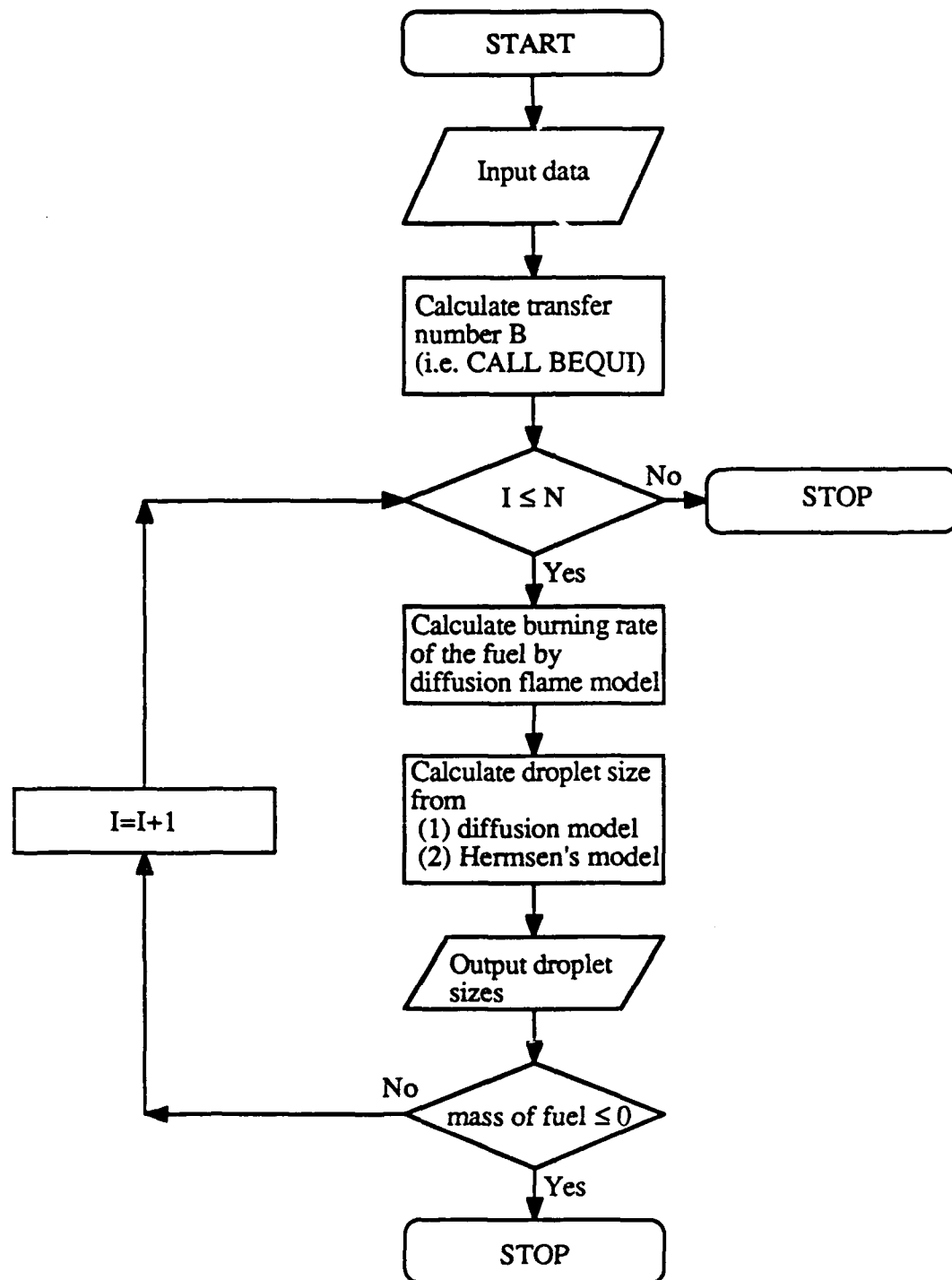


Figure 3. Flow chart for the calculation of droplet burning rate

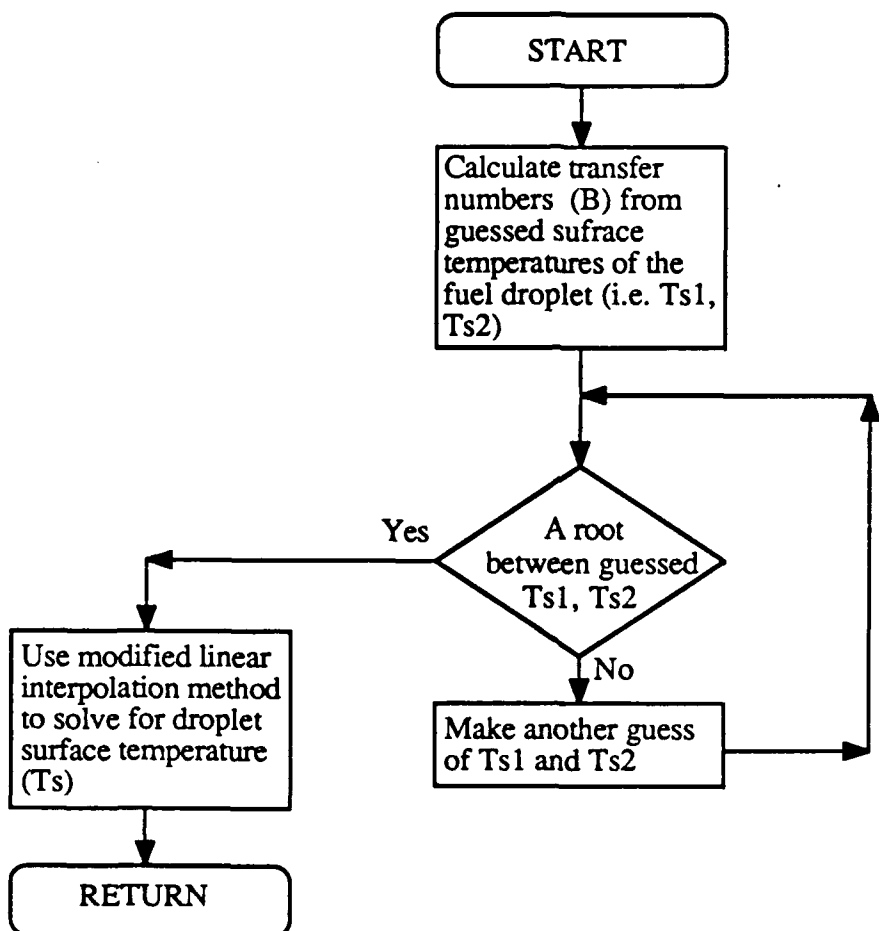


Figure 4. Flow chart for subroutine BEQUI

four gas phase reactions, one heterogeneous reaction at the aluminum droplet surface, and one heterogeneous reaction at the surface of the sub-micron aluminum oxide particles in the luminous, detached flame zone. However, in this initial study, a simple, single-step reaction without dissociation has been assumed :



Therefore the fuel-oxidizer mass flux ratio i can be calculated as

$$i = \frac{2(27)}{3(18)} = 1.0$$

The enthalpy of reaction per unit mass of fuel H can be determined by applying the first law to this process.

$$H = \sum_P m_p h_p - \sum_R m_r h_r \quad (90)$$

(b) Thermodynamic Data

The thermodynamic data for each species are taken from JANNAF⁽⁶⁾ tables. Data for the reaction species are reduced to functional form⁽¹⁶⁾. For each species, the thermodynamic functions specific heat and enthalpy are given in the form of least squares coefficients as follows⁽¹⁷⁾ :

$$\frac{C_p}{R} = a_1 + a_2 T + a_3 T^2 + a_4 T^3 + a_5 T^4 \quad (91)$$

$$\frac{\bar{h}}{RT} = a_1 + \frac{a_2}{2}T + \frac{a_3}{3}T^2 + \frac{a_4}{4}T^3 + \frac{a_5}{5}T^4 + \frac{a_6}{T} \quad (92)$$

For each species, two sets of coefficients are included for two adjacent temperature intervals, 300 to 900 K and 900 to 5000 K in general. The data have been constrained to be equal at 900 K.

The thermodynamic data of Al, Al₂O₃, H₂, and H₂O are required in this report and are listed in Table 2.

(c) Properties of the Mixture

The properties of the mixture which need to be determined include the molecular weight of the mixture at the droplet surface MW_{x,s}, density ρ, mass diffusion coefficient D, and specific heat C_p.

Table 2. Least square coefficients for the thermodynamic functions of specific heat and enthalpy of Al, Al₂O₃, H₂O, and H₂.

<u>Item</u>	<u>Al</u>	<u>Al</u>	<u>Al₂O₃</u>
Phase	liquid	gas	liquid
Year of the data	1979	1979	1979
Upper temperature range	933.5K ~ 5000K	900K ~ 5000K	2327K ~ 6000K
Lower temperature range	-	300K ~ 900K	-
a ₁ (upper range)	0.38189566E 01	0.25561389E 01	0.23148241E 02
a ₂ (upper range)	0.00000000E 00	-0.10072150E-03	0.00000000E 00
a ₃ (upper range)	0.00000000E 00	0.68901481E-07	0.00000000E 00
a ₄ (upper range)	0.00000000E 00	-0.20503307E-10	0.00000000E 00
a ₅ (upper range)	0.00000000E 00	0.22331058E-14	0.00000000E 00
a ₆ (upper range)	-0.94345795E 02	0.38899208E 05	-0.21140520E 06
a ₁ (lower range)	-	0.28588767E 01	-
a ₂ (lower range)	-	-0.16963453E-02	-
a ₃ (lower range)	-	0.32120695E-05	-
a ₄ (lower range)	-	-0.27578166E-08	-
a ₅ (lower range)	-	0.88926440E-12	-
a ₆ (lower range)	-	0.38853482E 05	-

Table 2. Least square coefficients for the thermodynamic functions of specific heat and enthalpy of Al, Al₂O₃, H₂O, and H₂ (continued).

<u>Item</u>	<u>Al₂O₃</u>	<u>H₂O</u>	<u>H₂</u>
Phase	solid	gas	gas
Year of the data	1979	1961	1977
Upper temperature range	900K ~ 2327K	900K ~ 5000K	900K ~ 5000K
Lower temperature range	300K ~ 900K	300K ~ 900K	300K ~ 900K
a ₁ (upper range)	0.11833666E 02	0.27167633E 01	0.30558123E 01
a ₂ (upper range)	0.37708878E-02	0.29451374E-02	0.59740400E-03
a ₃ (upper range)	-0.17863191E-06	-0.80224374E-06	-0.16747471E-08
a ₄ (upper range)	-0.56008807E-09	0.10226682E-09	-0.21247544E-10
a ₅ (upper range)	0.14076825E-12	-0.48472145E-14	0.25195487E-14
a ₆ (upper range)	-0.20571131E 06	-0.29905826E 05	-0.86168476E 03
a ₁ (lower range)	-0.49138309E 01	0.40701275E 01	0.29432327E 01
a ₂ (lower range)	0.79398443E-01	-0.11084499E-02	0.34815509E-02
a ₃ (lower range)	-0.13237918E-03	0.41521180E-05	-0.77713819E-05
a ₄ (lower range)	0.10446750E-06	-0.29637404E-08	0.74997496E-08
a ₅ (lower range)	-0.31566330E-10	0.80702102E-12	-0.25203379E-11
a ₆ (lower range)	-0.20262622E 06	-0.30279722E 05	-0.97695413E 03

The species at the surface of the fuel droplet can consist of inerts, intermediates, and products of the chemical process. Since the reaction mechanism of the burning of Al and H₂O is not clear and the behavior of the continuous accumulation of Al₂O₃ on the Al droplet surface is not well understood either, it is very difficult to calculate the molecular weight of the mixture theoretically. Furthermore, the present model cannot be used to examine the species that exist at the surface of the fuel droplet either. Therefore, the mixture molecular weight at the droplet surface is assumed to be the molecular weight of the fuel in the calculation of burning rate. Under this assumption, the mass fraction of the fuel at the droplet surface, Eq. (14), can be reduced to

$$Y_{f,s} = \frac{P_{f,s}}{P} \quad (93)$$

Since the value of ρD is generally independent of temperature and pressure⁽¹⁷⁾, the value of ρD is estimated at T = 2400 K and P = 100kpa. The values of D for different species are listed in Table 3⁽³⁾.

Table 3. Mass diffusivity of gases at 1 atm⁽³⁾.

<u>Species</u>	<u>D (cm²/sec)</u>		
	<u>2000K</u>	<u>3000K</u>	<u>4000K</u>
Al	3.77	8.53	14.98
AlO	3.88	7.78	12.66
CO	4.84	9.66	15.53
CO ₂	3.04	5.98	9.64
H ₂ O	7.42	15.15	24.98
HCL	3.61	7.16	11.56
Cl ₂	1.91	3.79	6.16
O ₂	5.16	10.08	16.30
H ₂	23.96	46.90	80.75
N ₂	3.45	6.31	10.88

The value of ρD is calculated from the product of ρ of H₂O at 100kpa, 2400K and D of H₂O at 100kpa, 2400K. The value of ρ of H₂O at 100kpa, 2400K is 9.025×10^{-5}

gm/cm³ which is calculated from the ideal gas equation of state. The value of D of H₂O at 100kpa, 2400K is 10.512 cm²/sec which is obtained from Table 3 by linear interpolation.

The value of the specific heat of the mixture C_p depends on the temperature which varies along the r coordinate. Since this model assumes that the properties are constant in the combustion system, it is necessary to evaluate the properties at a suitable reference temperature. Some studies have considered the effects of the variation of concentration and temperature. These results were compared with constant property models using reference conditions. Best results⁽¹⁸⁾ were achieved by using the 1/3 rule of Sparrow and Gregg, which evaluated the averaged properties at the following reference temperature T_r

$$T_r = T_s + \frac{1}{3}(T_\infty - T_s) \quad (94)$$

The value of specific heat of the mixture C_p is evaluated at this reference temperature by using the JANNAF tables.

(d) Vapor Pressure Data of Al

The vapor pressure curve can be obtained from a curve-fit of experimental data. For Al, the vapor pressure curve can be described as⁽¹⁹⁾

$$T_{Al} = TBP(K) = 393.3 \ln[P(pa)] - 2273 \quad (95)$$

(e) Comparison with Hermsen's Model

The history of the diameter of the droplet from the diffusion flame model are compared with that from the Hermsen's burning rate model. The Hermsen's burning rate model can be described as

$$\frac{d}{d_0} = (1 - kt/d_0^{1.8})^{1/1.8} \quad (96)$$

where

$$k = 8.3144 \times 10^{-5} R_k A_k^{0.9} P(\text{psi})^{0.7} (\text{cm}^{1.8}/\text{sec}) \quad (97)$$

$$A_k = 100 \sum x_i / x_{go}; \quad i = \text{H}_2\text{O}, \text{CO}_2, \text{OH}, \text{O}, \text{O}_2 \quad (98)$$

4.2 Results

In this report, the droplet burning rate is characterized by calculating the change in droplet diameter as a function of time. These calculations are presented for different environmental conditions. The parameters which were varied are listed in Table 4. The input data for the calculation of the history of the diameter of the Al droplets are listed in Table 5.

The numerical results for the history of the droplet diameter are presented in Figs. 5 - 14. In these figures, the symbol "D(E)" stands for the droplet diameter history which is calculated from vapor phase diffusion limited burning model (E stands for evaporation) and the symbol "D(H)" represents the droplet diameter history which is calculated from Hermsen's model .

Figures 5 - 7 show the effect of relative velocity on Al droplet diameter history at $Y_{O\infty} = 1.0, 0.5, .15$ respectively. In each figure, the effect of velocity lag in the diffusion model is studied, and the effect of R_k in Hermsen's model is examined also. From these three figures, the results from the diffusion mode! show that the effect of velocity lag is not significant, but the results from Hermsen's model show that the influence of R_k is quite significant.

The effect of ambient temperature on the burning of Al in H_2O atmosphere at $Y_{O\infty} = 1.0, 0.5, .15$ is shown in Figs. 8 - 10 respectively. From Fig. 8, the burning rates of the Al droplet are independent of the ambient temperature when the mass fraction of oxidizer in oxidizing atmosphere is high (i,e, $Y_{O\infty} = 1.0$). However, Figs. 9 and 10 show that the importance of ambient temperature increases when the mass fraction of

Table 4. Parameters used in the calculation of Al droplet diameter history.

<u>Parameter</u>	<u>Symbol</u>	<u>Variable</u>	<u>Unit</u>	<u>Values</u>
Ambient temperature	T_{∞}	TG	K	300, 2400, 3500
Ambient pressure	P	PTOT	kpa	100, 3440, 6870
Mass fraction of oxidizer at ∞	$Y_{O,\infty}$	YO8		0.15, 0.5 1.0
Empirical constant in Hermsen's model	R _k	RK		1.0, 2.7
Relative velocity	$U_g - U_p$	VREL	cm/sec	0.0, 100.0

Table 5. Input data for the calculation of Al droplet diameter history.

<u>Parameter</u>	<u>Symbol</u>	<u>Variable</u>	<u>Unit</u>	<u>Values</u>
Thermal diffusivity (= mass diffusivity) at 100kpa, 2400K	α (= D)	ALPHA	cm ² /sec	10.512
Specific heat of the mixture	C _p	CP	cal/gmK	JANNAF tables
Initial diameter of fuel droplet	d ₀	DS	cm	0.01
Stoichiometric fuel-oxidizer mass flux ratio	i	FI		1.0
Latent heat of evaporation of the fuel	Δh_v	HL	cal/gm	JANNAF tables
Enthalpy of reaction	H	HR	cal/gm	JANNAF tables
Prandtl number	Pr	PR		0.8
Pressure	P	PTOT	kpa	100, 3440, 6870
Empirical constant in Hermsen's model	R _k	RK		10., 2.7
Density of the fuel droplet	ρ_f	ROUF	gm/cm ³	2.35
Density of the mixture at 100kpa, 2400K	ρ	ROUM	gm/cm ³	9.025×10^{-5}
Ambient temperature	T_{∞}	TG	K	300, 2400, 3500
Initial guess of droplet surface temperature	T _s	TS	K	1900
Relative velocity	$U_g - U_p$	VREL	cm/sec	0.0, 100.0
Molecular Weight of the fuel	MW _f	WFUE	gm/mole	27.0
Molecular Weight of the mixture at the droplet surface	MW _{x,s}	WMIX	gm/mole	27.0
Mass fraction of oxidizer at ∞	$Y_{O,\infty}$	YO8		0.15, 0.5, 1.0

ambient oxidizer ($Y_{O\infty}$) decreases. Furthermore, it can be found that the difference in burning rates between $T_\infty = 2400K$ and $T_\infty = 3500K$ is small for different $Y_{O\infty}$ from Figs. 8 - 10. The temperature of burning Al droplet (T_S) increases as T_∞ increases except for the case of $Y_{O\infty} = 1.0$. The importance of the influence of T_∞ on T_S increases with decreasing $Y_{O\infty}$.

Figure 11 shows the effect of $Y_{O\infty}$ on Al droplet diameter history under the conditions of $T_\infty = 2400K$ and $P = 100$ kpa. In this figure, it is clear that the burning rate and the temperature of the Al droplet increase as $Y_{O\infty}$ increases. It can also be observed that the differences between the burning rates calculated from the diffusion model and the burning rates calculated from Hermsen's model with $R_k = 1$ increase when the mass fraction of oxidizer $Y_{O\infty}$ decreases.

The influence of pressure on the burning of Al and H₂O at $Y_{O\infty} = 1.0, 0.5, .15$ is shown in Figs. 12 - 14, respectively. It can be shown that the burning rates which are calculated from Hermsen's model increase with increasing pressure. On the other hand, the burning rates which are calculated from the diffusion model decrease with increasing pressure.

In general, results from Figs. 5 - 14 show that the temperature of burning the Al droplet (T_S) increases with increasing pressure, increasing $Y_{O\infty}$, and increasing T_∞ . However, the temperature of the Al droplet at $T_\infty = 300K$ is greater than that at $T_\infty = 2400K$ for $Y_{O\infty} = 1.0$ and $P = 100$ kpa, as shown in Fig. 8. The level of the effect of T_∞ on T_S increases with decreasing $Y_{O\infty}$ which can be found in Figs. 8 - 10. For $P = 100$ kpa, the temperature of the Al droplet T_S is always lower than the melting point of Al₂O₃ (2320K). However, T_S is always higher than the melting point of Al₂O₃ at $P = 3440$ kpa and $P = 6870$ kpa.

4.3 Discussion

4.3.1 Effect of R_k in HermSEN's Model

The empirical constant R_k in HermSEN's burning model is used to account for the change in burning rate due to the differences between laboratory and rocket motor environments. For laboratory environment, a value of $R_k = 1$ is used to calculate the burning rate of the Al droplet corresponding to non-convective, low temperature blackbody environment. For a motor environment, a value of $R_k = 2.7$ has been recommend⁽⁶⁾ for use, corresponding to a convective environment of unspecified magnitude (relative velocity probably on the order of 1 to 4 m/s) and a radiative environment of unspecified effective temperature. From Figs. 5 - 14, it can be seen that the differences in burning rates, which are calculated from the HermSEN's model, between laboratory and rocket motor are quite significant, that is the influence of R_k is quite significant. However, the relative importance of convective and radiative environmental effects is not yet clear. In the following section, the results of calculations aimed at differentiating between the relative importance of these two effects are discussed.

4.3.2 Effect of Velocity Lag

The effect of velocity lag was estimated by using the convective correlation discussed in section 3.3. Figures 5 - 7 show that the effect of velocity lag is not significant. This is because of the small Red_s in Eq. (86) which is the result of the small diameter of the fuel droplet and the high kinematic viscosity of the surrounding gases. Thus, the majority of the influence of the R_k factor in HermSEN's model can be attributed to the difference in radiative environments and not the convective environments. Therefore, these results indicate that the thermal radiation effect should be included in the analysis, while the convective effect could probably be neglected. For a single droplet burning in a laboratory environment, the surroundings can be treated as black body at 0K because the

surroundings is relatively cold. On the other hand, the surroundings in a rocket motor for example may be an adiabatic surface at high temperature due to the effect of multiple droplets.

4.3.3 Effect of Ambient Temperature

Based on the results from Figs. 8 - 10, it can be shown that the importance of the ambient temperature T_{∞} on burning rate decreases as $Y_{O\infty}$ increases. From Fig. 8, the burning rates of Al droplet are independent of the ambient temperature when the mass fraction of oxidizer in oxidizing atmosphere is high (i.e. $Y_{O\infty} = 1.0$). This phenomenon may be due to the fact that the heat feedback to evaporate the Al droplet is mainly provided by the enthalpy of reaction when the mass fraction of ambient oxidizer is high. As $Y_{O\infty}$ decreases, the importance of the heat transfer between the surroundings and the burning Al droplet becomes significant.

In general, the temperature of burning Al droplet (T_S) increases with increasing T_{∞} . The importance of the effect of T_{∞} on T_S increases when $Y_{O\infty}$ decreases. Again, this is due to the fact that the importance of the heat transfer between the surroundings and the burning Al droplet plays a more important role in the total heat feedback to the burning Al droplet as $Y_{O\infty}$ decreases.

4.3.4 Effect of Mass Fraction of Ambient Oxidizer

The differences between the burning rates calculated from the diffusion flame model and the burning rates calculated from Hermsen's model with $R_k = 1$ increase when the mass fraction of ambient oxidizer $Y_{O\infty}$ decreases. When $Y_{O\infty}$ decreases, the importance of the heat transfer between the surroundings and the burning Al droplet increases.

Consequently, the importance of T_{∞} increases as Y_{∞} decreases. However, the influence of velocity lag on burning rate is small for various values of Y_{∞} .

4.3.5 Effect of Pressure

The burning rates which are calculated from the HermSEN's model increase with increasing pressure. On the other hand, the burning rates which are calculated from the diffusion flame model decrease with increasing pressure. These different tendencies are due to the fact that the diffusion flame model has neglected dissociation of Al_2O_3 product. The correct pressure dependence cannot be incorporated into the diffusion flame model through the variation of thermophysical properties only. The dissociation effect must be included in the diffusion flame model.

4.3.6 Temperature of the Burning Aluminum Droplet

In general, the temperature of the Al droplet (T_s) increases with increasing pressure, increasing Y_{∞} , and increasing T_{∞} (except for the case of $Y_{\infty} = 1.0$). For $P = 100\text{kpa}$, the temperature of the Al droplet T_s is always lower than the melting point of Al_2O_3 (2320K). This result is potentially significant because when the temperature of the Al droplet is lower than the melting point of Al_2O_3 , the continuous accumulation of solid Al_2O_3 on the Al droplet surface will form a protective layer and tend to block the evaporation of Al vapor from the droplet; therefore, extinction may occur. From Eq. (14) it can be seen that the temperature of the Al droplet is also highly dependent on the assumed value for molecular weight of the mixture at the droplet surface ($MW_{x,s}$). If $MW_{x,s}$ is greater than the molecular weight of the fuel (MW_f), T_s may approach the boiling point of Al (2767K at 1 atm) which, for most pressures, is higher than the melting point of Al_2O_3 .

(2320K). Since this model assumes that $MW_{x,s} = MW_f$, T_s may be under-estimated if $MW_{x,s}$ is actually higher than MW_f .

$Y_{O\infty}=1.0$, $T_{\infty}=2400K$, $P=100kpa$, $i=1.0$

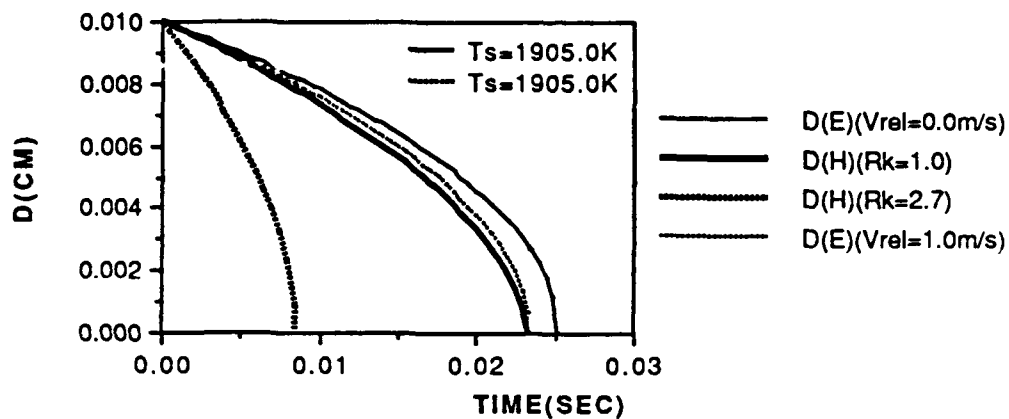


Figure 5. Droplet diameter history (effect of relative velocity at $Y_{O\infty}=1.0$).

$Y_{O\infty}=0.5$, $T_{\infty}=2400K$, $P=100kpa$, $i=1.0$

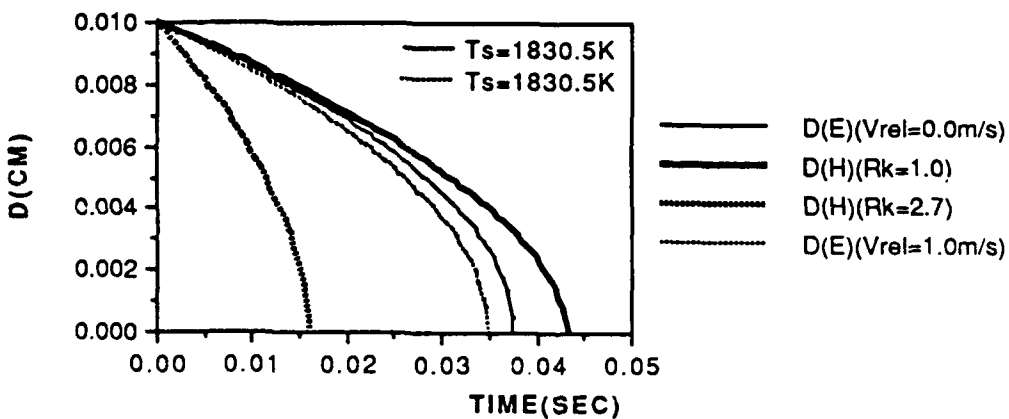


Figure 6. Droplet diameter history (effect of relative velocity at $Y_{O\infty}=0.5$).

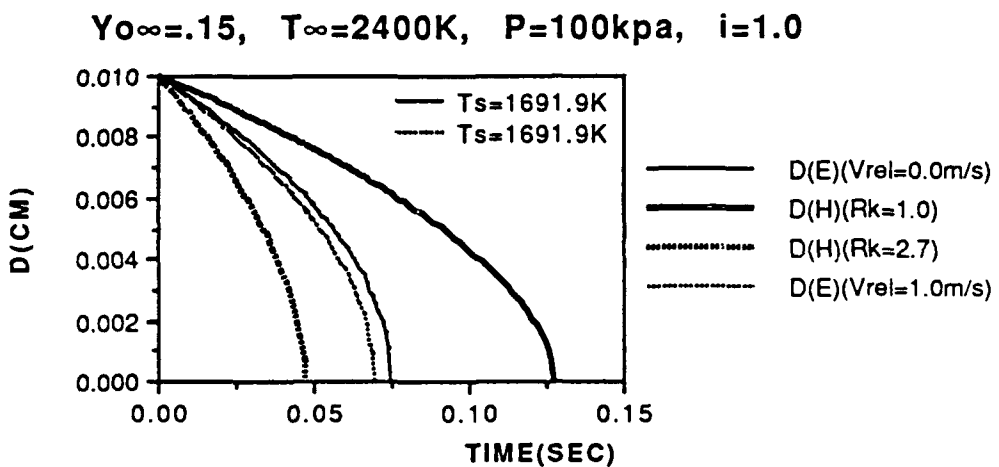


Figure 7. Droplet diameter history (effect of relative velocity at $\gamma_{\infty}=.15$).

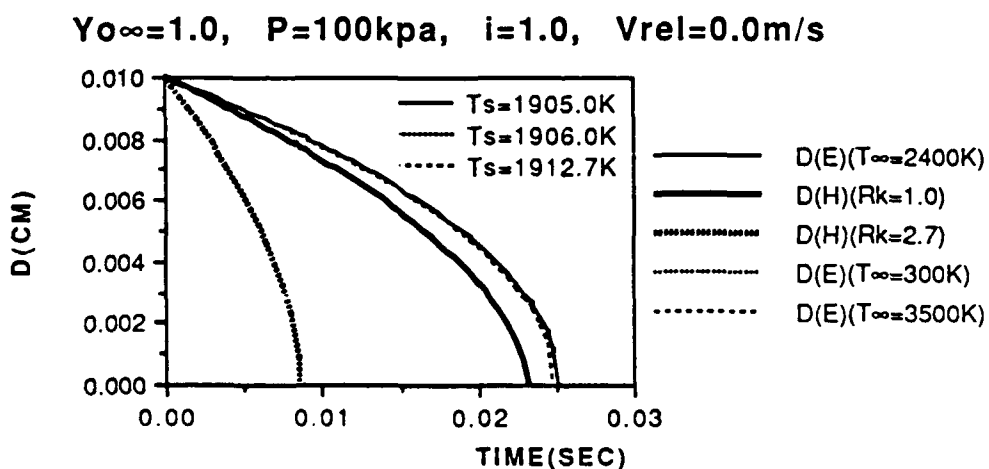


Figure 8. Droplet diameter history (effect of ambient temperature at $\gamma_{\infty}=1.0$).

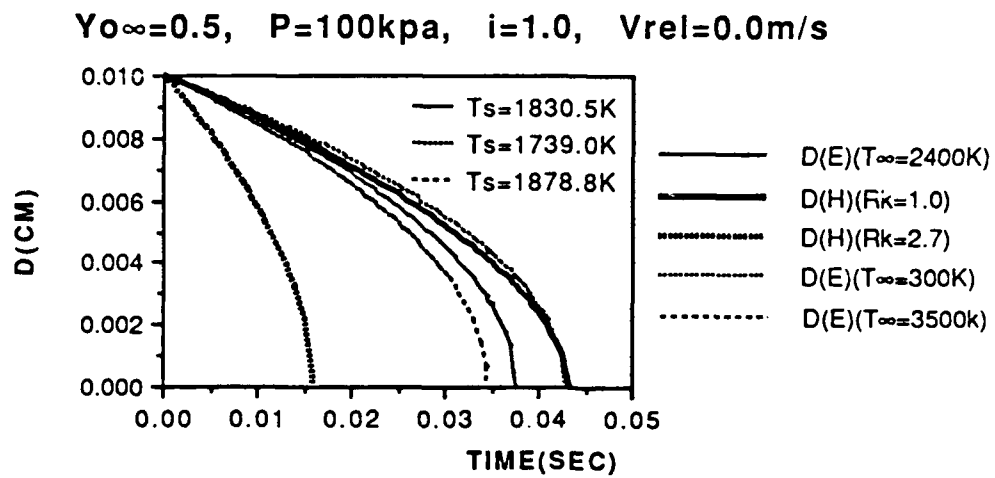


Figure 9. Droplet diameter history (effect of ambient temperature at $Y_{\infty}=0.5$).

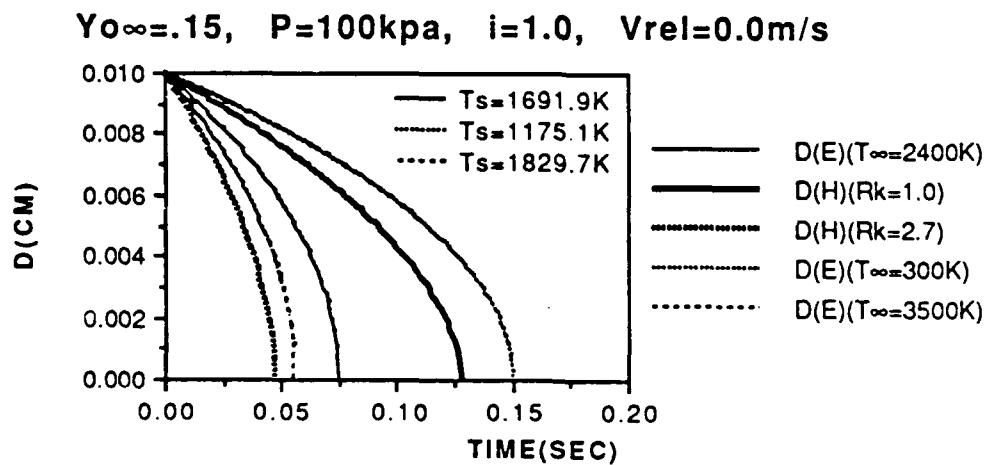


Figure 10. Droplet diameter history (effect of ambient temperature at $Y_{\infty}=.15$).

$T_{\infty}=2400K$, $P=100kpa$, $i=1.0$, $V_{rel}=0.0m/s$, $Rk=1.0$

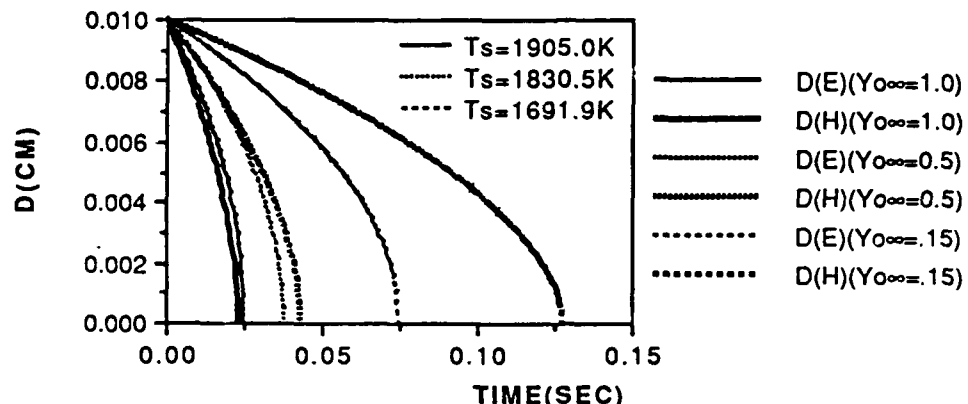


Fig. 11. Droplet diameter history (effect of Y_{∞} at $T_{\infty}=2400K$, $P=100kpa$).

$Y_{\infty}=1.0$, $T_{\infty}=2400K$, $i=1.0$, $V_{rel}=0.0m/s$, $Rk=1.0$

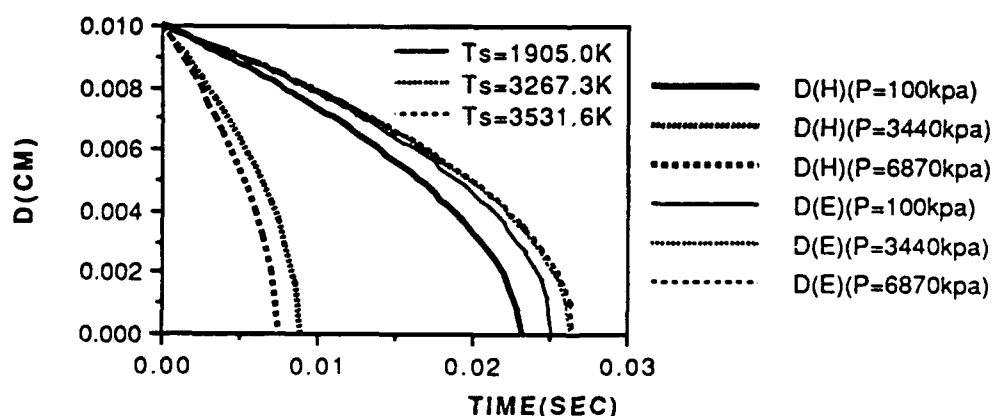


Figure 12. Droplet diameter history (effect of pressure at $Y_{\infty}=1.0$).

$\gamma_{\infty}=0.5$, $T_{\infty}=2400K$, $i=1.0$, $V_{rel}=0.0m/s$, $R_k=1.0$

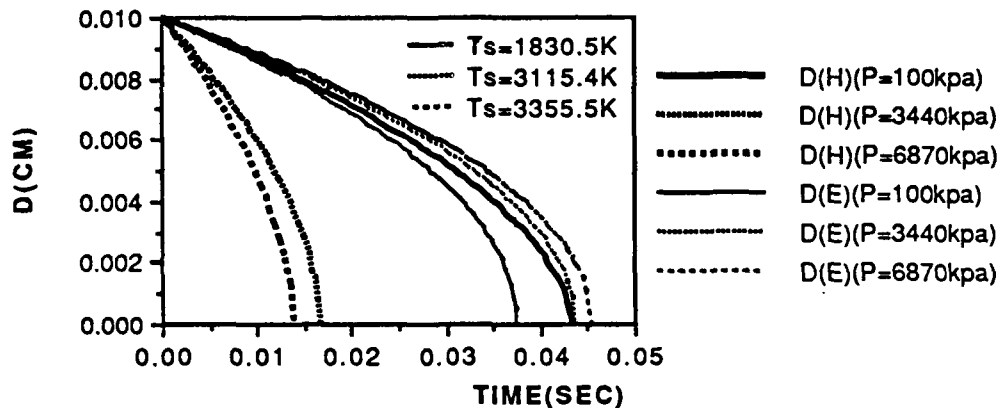


Figure 13. Droplet diameter history (effect of pressure at $\gamma_{\infty}=0.5$).

$\gamma_{\infty}=0.15$, $T_{\infty}=2400K$, $i=1.0$, $V_{rel}=0.0m/s$, $R_k=1.0$

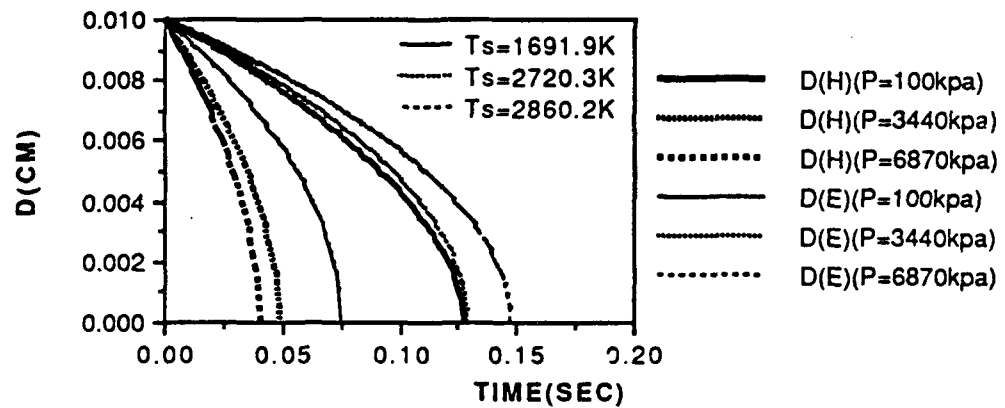


Figure 14. Droplet diameter history (effect of pressure at $\gamma_{\infty}=0.15$).

5. CONCLUSIONS

Based on the results of this preliminary comparison of a simple model for diffusion-limited burning and Hermsen's correlation for burning of aluminum and water, the following conclusions are drawn :

1. The adjustable parameter R_k in Hermsen's model which accounts for radiative and convective environment effects plays a strong role in determining the burning rate and yet a rational basis for predicting the value of R_k under various radiative and convective environments has not been established.
2. The convective environment (i.e. velocity lag) appears to be of minor importance in determining the burning rate whereas the radiative environment plays a very strong role. The radiation effect should be included in the analysis.
3. The effect of dissociation appears to play a very important role and should be included in the analysis. The observed pressure dependence of droplet burning rate is greater than what could be accounted for by thermophysical property variation and must be related to dissociation effects which were neglected in this simple analysis.
4. The burning rate is generally not very sensitive to the ambient temperature, except for very low oxidizer concentrations.
5. The temperature of Al droplets at $P = 100\text{kpa}$ is always lower than the melting point of Al_2O_3 under the assumption that the molecular weight of the mixture at the droplet surface is equal to that of the fuel ($\text{MW}_{x,s} = \text{MW}_f$), indicating that aluminum would have difficulty burning at low pressures in water atmospheres.
6. The temperature of burning Al droplets is generally somewhat below the boiling point of Al.

REFERENCES

1. Glassman, I., "Combustion of Metals - Physical Considerations," *Progress in Astronautics and Rocketry : Solid propellant Rocket Research*, edited by M. Summerfield, Academic Press, New York, 1960, Vol. I, pp.253-257.
2. Gordon, D. A., "Combustion Characteristics of Metal Particles," *Progress in Astronautics and Rocketry : Solid propellant Rocket Research*, edited by M. Summerfield, Academic Press, New York, 1960, Vol. I, pp.271-278.
3. Micheli, Paul L. and Schmidt, Willfred G., "Behavior of Aluminum in Solid Rocket Motors," AFRPL-TR-77-29, Vol. II, 1977.
4. Brzustowski T. A. and Glassman I., "Spectroscopic Investigation of Metal Combustion," *Progress in Astronautics and Aeronautics : Heterogeneous Combustion*, edited by H. G. Wolfhard et al., Academic Press, New York, 1965, Vol. 15, pp. 41-74.
5. Kuo, K. K., *Principles of Combustion*, John Wiley & Sons, Inc., New York, 1986.
6. Nickerson, G. R., Coats, D. E., Dang, A. L., Dunn, S. S., Berker, D. R., Hermsen, R. L., and Lamberty, J. T., *The Solid Propellant Rocket Motor Performance Predication Computer Program(SPP)*, AFAL-TR-87-078, Version 6.0, 1987.
7. Kuehl, D. K., "Ignition and Combustion of Aluminum and Beryllium," *AIAA J.*, Vol. 3, No. 12, pp. 2239-2247, Sept. 1965.
8. Price, E. W., "Combustion of Metalized Propellants," *Fundamentals of Solid Propellant Combustion*, *Progress in Astronautics and Aeronautics Series*, Vol. 90, edited by K. K. Kuo and M. Summerfield, AIAA, New York, 1984, pp. 479-513.
9. Nir, E. C., *Thirteenth Symposium (International) on Combustion*, The Combustion Institute, Pittsburgh, pp. 1019-1024, 1971.
10. Brewster, M. Q., and Parry, D. L., "In-Situ Measurements of Alumina Particle Size and Optical Constants in Composite Solid Propellant Flames," *AIAA87-1582*, June 1987.

11. Brewster, M. Q., and Taylor, D. M., "Radiative Properties of Burning Aluminum Droplets," *Combustion and Flame*, Vol. 72, pp. 287-299, 1988.
12. Williams, F. A., *Combustion Theory*, The Benjamin/Cummings Publishing Company, Inc., Menlo Park, California, 1985.
13. Kanury, A. M., *Introduction to Combustion Phenomena*, Gordon and Breach Science Publishers, New York, 1975.
14. Glassman, I., *Combustion*, Academic Press, Inc., New York, 1987.
15. Ogle, R. A., Ph.D. Thesis, The University of Iowa, 1986.
16. McBride, B. J. and Gordon, S., "FORTRAN IV Program for Calculation of Thermodynamic Data," NASA TN D-4097, 1967.
17. Gordon, S. and McBride, B. J., "Computer Program for Calculation of Complex Chemical Equilibrium Compositions, Rocket Performance, Incident and Reflected Shocks, and Chapman-Jouguet Detonations," NASA SP-273, 1971.
18. Faeth, G. M., "Current Status of Droplet and Liquid Combustion," *Prog. Energy Combust. Sci.*, Vol. 3, pp. 191-224, 1977.
19. Brewster, M. Q. and Parry, D. L., "Radiative Heat Feedback in Aluminized Solid Propellant Combustion," *J. Thermophysics*, Vol. 2, No. 2, pp. 123-130, 1988.

27th JANNAF Combustion Meeting
November, 1990, Cheyenne, WY

THE EFFECT OF RADIATIVE HEAT FEEDBACK ON BURNING RATE OF METALIZED PROPELLANTS*

A. Ishihara, M. Q. Brewster, T. A. Sheridan, and H. Krier
Department of Mechanical and Industrial Engineering
University of Illinois at Urbana - Champaign
Urbana, Illinois

ABSTRACT

Metalized solid propellants have higher final flame temperatures and higher flame radiant intensities than non-metalized propellants. However, the importance of radiative heat feedback in metalized propellant combustion is still unknown. In this study, radiative effects in metalized composite AP propellants containing aluminum, boron, and magnesium were examined by embedding optical fibers and micro-thermocouples in propellants to measure radiative and conductive feedback. Extinguishment by rapid depressurization was used to determine the condition and location of the thermocouple and optical fiber at the burning surface. Hemispherical reflectivity measurements were also made to determine propellant absorptivity. The reflectivity measurements showed that even a small amount of a metal powder in a propellant increases the absorptivity significantly. Incident radiative fluxes of non-metalized and metalized propellants is dependent on pressure in the pressure range less than 2 MPa. In non-metalized propellant, the effect of radiative feedback on burning rate was negligible, because of low incident flux from flame and low absorptivity of the propellant. In the metalized propellants, radiative heat feedback is a significant fraction of the total feedback and is strongly dependent on pressure and metal loading. A sensitivity analysis was performed to determine the sensitivity of burning rate on radiative feedback, condensed phase heat release and other processes. The aluminized propellant was found to be rather sensitive to radiative feedback while boron and magnesium propellants were more sensitive to condensed phase heat release.

INTRODUCTION

Metals such as aluminum, magnesium, zirconium, boron, titanium, iron, etc. are included in solid propellants to improve performance. Particularly high metal content propellants are used as pyrotechnic propellants and in ram rockets. In these propellants, metals increase flame temperature and radiant intensity significantly. This suggests that radiative feedback may play an important role in determining the burning rate of metalized solid propellants. In non-metalized propellants, the effect of radiative heat feedback on a burning rate has been shown to be negligible^{1,2}. In aluminized propellant, Zennin, et al.^{3,4,5} and Felton and Hitchcock⁶ measured incident radiative flux by a similar method. Their reported values^{3,4,5} for incident radiative flux were on the order of 1000 kW/m² at 2.5 to 4.5 MPa in aluminum-AP(ammonium perchlorate)-PF(polyformaldehyde) propellants. They concluded that the radiative heat feedback was less significant than the conductive feedback from burning aluminum droplets and that both of these contributions combined were less than the heat release in the condensed phase. The measured incident flux⁶ in aluminized composite modified double base propellants was 1100 kW/m² at 3.5 MPa and 170 kW/m² at 1.0 MPa. However, it should be pointed out that the diameter of the sensor cavity in their experiment was relatively large compared with the thickness of the combustion zone above the burning surface of propellant which raises questions as to whether the radiant flux measured was representative of the flux that would exist without the presence of the sensor. In addition there are questions as to whether the measured signal might have been reduced by smoke, ash and aluminum particles falling into the cavity.

In a theoretical study, Brewster and Parry⁷ predicted the radiative flux incident at the surface of an aluminized propellants using the two flux model. They estimated incident fluxes on the order of 3000 to 4000 kW/m² at 3.5 to 6.8 MPa while noting that these estimates were sensitive to the highly uncertain emissive properties of burning aluminum droplets⁸.

On the other hand, Kubota and Serizawa^{9,10} examined the mechanism of burning rate augmentation in Mg-Tf (tetrafluoroethylene) pellets. Kuwahara and Kubota¹¹ examined the burning rate mechanism in boron-AP-CTPB. They found that boron increases both the heat of reaction in the solid phase and the conductive heat feedback from the gas phase to the surface. However, these studies did not consider radiative heat feedback effects. Kuo and coworkers¹² also examined the heat feedback in Mg-Tf propellants. They neglected radiative feedback by reasoning that the reflectivity of the burning surface of metalized propellants is large because the intrinsic, bulk reflectivity of metals is large. They also studied the burning mechanisms of boron-based high energy propellant^{12,13}.

A new technique has been developed which uses fiber optics imbedded in propellant strands to measure the incident radiative flux¹⁴. The absorptivity of the propellant surface is measured with an integrating sphere. The conductive heat feedback is measured with micro-thermocouples. This technique has been applied to aluminized propellants¹⁴ and it was found that radiative heat feedback was 10 to 30% of the total heat feedback for typical aluminum loadings 10 to 20% and typical pressures (1 to 3 MPa). In this paper the extension of this technique to boron and magnesium propellants is described and the results compared with those of aluminized propellant. In addition, results of a burning rate sensitivity analysis are reported for all three types of propellants.

* This work was performed with partial support from ONR(N00014-87-K-0547), Thiokol(OPM 012), NSF(CBT 86-96162)

PROPELLANTS AND BURNING RATE CHARACTERISTICS

Aluminum, magnesium, and boron have been selected as metal additives in this study because these propellant have very high energy density, and are widely used in rocket propellants and pyrotechnics propellants. AP (ammonium perchlorate)-HTPB (hydroxyl terminated polybutadiene) composite propellant was used as a non-metalized baseline propellant in this study. An effort was made to use practical propellant formulations while making systematic changes in composition.

The burning rates of these propellants were measured by a fuse wire method in a chimney type strand combustion chamber pressurized by nitrogen gas. The size of a strand sample was 7x7x40 mm. A strand sample was ignited by a nichrome wire. Three fuse wires of 0.25 mm diameter were used. The distance between each wires was 10 mm. Pressure was measured by a strain type pressure transducer and recorded.

Table 1 Compositions of Propellants.

Propellant	Metal	AP _f	AP _c	HTPB
A-0		0	41	41
A-5	Al	5	41	41
A-10	Al	10	41	41
A-20	Al	20	41	41
B-5	B	5	41	41
M-5	Mg	5	41	41
M-10	Mg	10	41	41

Metal : 5 μm AP_f : 25 μm AP_c : 200 μm

Note : Indicated amounts are relative mass basis.

HEAT FEEDBACK MEASUREMENTS

The radiative heat feedback q_r to the propellant can be expressed as the absorbed flux minus the emitted flux

$$q_r = \alpha q_f - \varepsilon \sigma T_s^4 \quad (1)$$

where α is the absorptivity of the propellant, q_f is the incident radiative flux on the burning surface, ε is the emissivity of the propellant, σ is the Stefan-Boltzmann constant and T_s is the surface temperature of the propellant. The emitted flux is considered to be negligible compared with the absorbed flux. Therefore, in this study, the incident radiative flux on the burning surface and the absorptivity of the propellants were measured to estimate the radiative heat feedback. To measure radiant flux from the flame to the burning surface, a fiber optic with the outer sheath stripped away was imbedded in the propellants. Both the core and cladding of the fibers were fused silica. Two different size fibers were used. The core and cladding diameters were 100 μm and 140 μm (large fiber) and 50 μm and 125 μm (small fiber). Two types of photodiodes were used as detectors. One of the diodes was InGaAs with a 3GHz cut off frequency (reverse voltage 5V), and the other was Si with 25MHz cut off frequency (reverse voltage 12V). The condition of an imbedded fiber optic was examined by extinction of the propellant. It was confirmed that the end of the fiber remained clean and that the signal was not reduced by metal particle obscuration or smoke deposition.

Conductive heat feedback from the gas phase to the burning surface was obtained from Fourier's law

$$q_c = \lambda_g \left(\frac{1}{r} \right) \left(\frac{dT}{dt} \right)_{s+} \quad (2)$$

where λ_g is the thermal conductivity of the gas phase, r is the burning rate, and $(\frac{dT}{dt})_{s+}$ is the change in temperature with respect to time at the burning surface, which was measured using Pt-Pt 10% Rh micro-thermocouples made of 5 μm diameter wire. The errors associated with the thermocouple measurements are described in Ref. 15. Measured temperature error was estimated to be no more than 30% in the worst case and in most cases less than 10%.

The thermal conductivity λ_g of the gas phase was obtained by volume averaging the thermal conductivities of the gas and metal particles as follows.

$$\lambda_g = \lambda_{g0} + \left(\frac{PY_m}{v\rho_{gm}RT_g} \right) (\lambda_{gm} - \lambda_{g0}) \quad (3)$$

Y_m is the metal mass fraction in the propellant, R is the gas constant of combustion products, v is the ratio of the metal particle velocity to that of the combustion gases at the propellant surface. T_g is the characteristic gas temperature above the burning surface. In this calculation, T_g was set equal to the burning surface temperature. Property values used for evaluating λ_g are shown in Table 2.

Table 2 Thermal Properties for the calculation of Eq. (3)

Property	T_g	M	ρ	λ
Unit	K	kg/kmol	kg/m ³	W/mK
Non-Metal	853	26	-	0.1
Al	853	-	2483	95.4
B	853	-	2080	10
Mg	853	-	1834	81

BURNING RATE CHARACTERISTICS

Burning rates of the six propellants in Table 1 have been measured as shown in Figs. 1-2. In the case of propellant A-20, a propellant containing 16.67% aluminum, the burning rate increased by 19% at 1.0 MPa over that of the non-metalized propellant as shown in Fig. 1. The increase in burning rate for aluminized propellant is relatively small compared with that of the other metalized propellants. In the case of propellant M-10, a propellant containing 9.06% magnesium, the burning rate increased by 25% as shown in Fig. 2, and in B-5, a propellant containing 4.76 % boron, the burning rate increased by 50% as shown in Fig. 2.

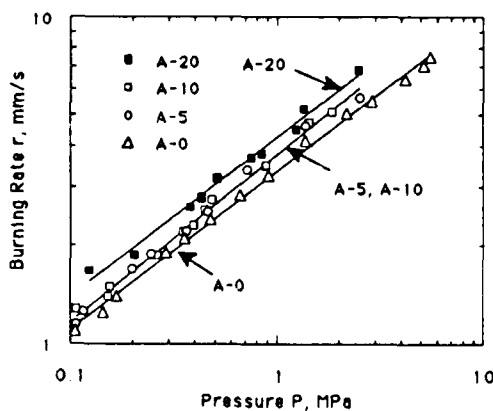


Fig. 1 Burning rate of aluminum propellants.

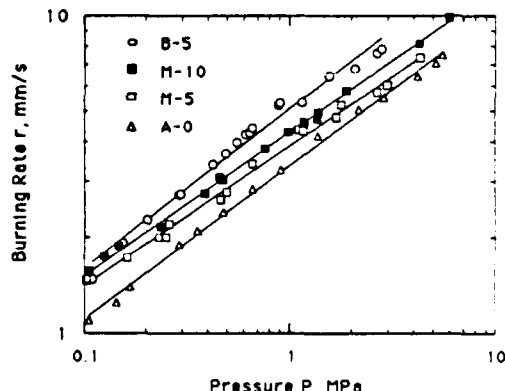


Fig. 2 Burning rate of boron and magnesium propellants.

RADIATIVE HEAT FEEDBACK

The results for the incident flux are shown in Fig. 3 for the non-metalized propellant as a function of pressure and in Fig. 4 for the metalized propellants as a function of metal loading. The incident flux increases significantly as metal loading increases (Fig. 4). For aluminum the biggest increase occurs between 10 and 20% metal. The pressure dependence for the metalized propellants is similar to that for the non-metalized propellant in Fig. 3.

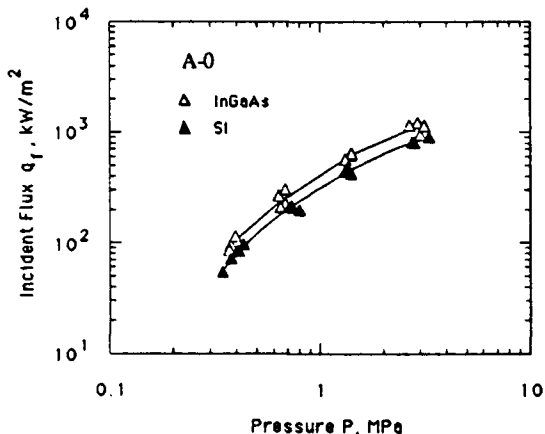


Fig. 3 Incident radiative flux in non-metalized propellant.

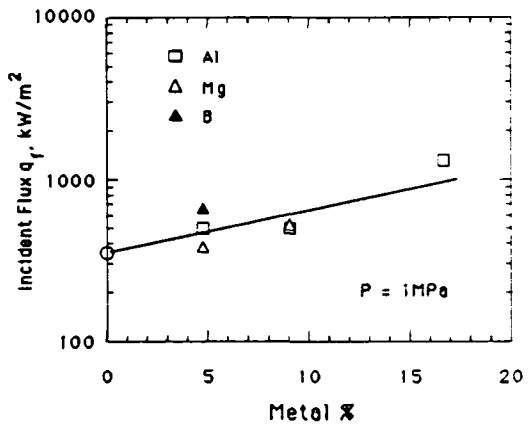


Fig. 4 Incident radiative flux in metalized propellants.

The measured reflectivities of the propellant surfaces are shown in Fig. 5. Two wavelengths were used, $0.6328 \mu\text{m}$ and $1.06 \mu\text{m}$. The difference between the results at the two wavelength was negligible. It was thus assumed that the total reflectivity was the same as the spectral reflectivity in Fig. 5. In addition, it was found that an unburned propellant surface and an extinguished propellant of the same composition had the same reflectivity. The aluminum and magnesium propellants had low reflectivities ($\rho < 0.2$) in spite of the high intrinsic, bulk reflectivity of the metals ($\rho = 0.8$). This effect is due to multiple scattering by the metal particles. Boron propellant had a slightly lower reflectivity ($\rho < 0.16$) due to the higher intrinsic absorptivity of boron particles ($\alpha > 0.7$). On the other hand, the non-metalized propellant had a higher reflectivity ($\rho = 0.6$) than that of the metalized propellants. Thus it was seen that a small amount of fine metal powder increases the absorptivity of a propellant significantly, as noted previously by Zennin et al. and Brewster and Hardt¹⁵. No measurements were made during burning due to the difficulty of this measurement. But radiative transfer considerations dictate that the reflectivity would not change much. This is because the optical properties of the propellant are dominated by the metal particles and typically the absorptivity of metals does not change significantly until their temperature approaches the boiling point.

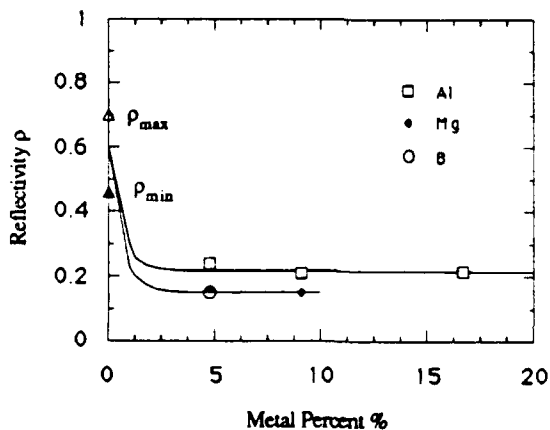


Fig. 5 Reflectivity of propellant surface

The absorptivities from Fig. 5 and the incident fluxes from Fig. 4 were combined to give the radiative heat feedback to propellant using Eq. (1). The emitted flux in Eq. (1) was so low that the assumed propellant emissivity was inconsequential. The results for q_r at 1 MPa are shown in Fig. 6. It can be seen that the radiative heat feedback in non-metallized propellant is much smaller than that in metallized propellants. Metal additives increase the radiative heat feedback significantly.

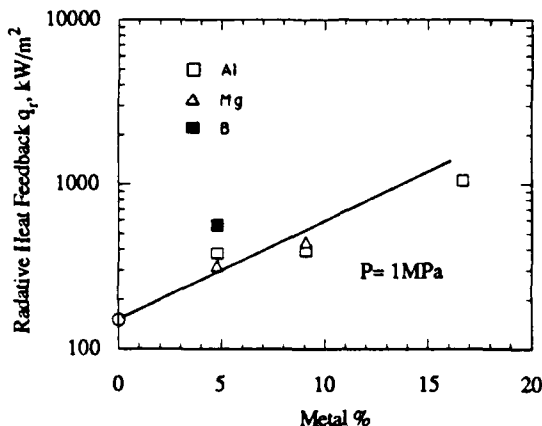


Fig. 6 Radiative heat feedback ($P = 1 \text{ MPa}$)

CONDUCTIVE HEAT FEEDBACK

The temporal temperature derivative (DT/DT) at the burning surface was measured with micro-thermocouples. The burning propellant was extinguished to determine the position of the bead and the effect of the micro-thermocouple on the burning surface. In the aluminum and magnesium propellants it was verified that the thermocouples were not being covered by metal, char, ash or binder. However, in the boron propellant many filigrees were found on the extinguished burning surface. These may have been formed by the rapid depressurization or they may have been present during normal combustion. In many of the boron propellant samples it was difficult to find the thermocouple. The thermocouples were easily covered by the boron and binder decomposition products and easily hidden by the roughness and color of the surface. Instead of relying solely on visual inspection of the extinguished surface for confirmation of the surface condition (as was done with Al and Mg propellants) an additional set of experiments were run using $2.5\mu\text{m}$ thermocouple wire in the boron propellant. These results showed no difference when compared with the $5\mu\text{m}$ wire results. Thus it is assumed that surface heterogeneity did not strongly affect the surface temperature gradient measurement even in the boron propellant. However, further testing needs to be done in the case of the boron propellant to investigate this effect in more detail.

Conductive heat feedback was obtained by using Eqs. (2) and (3). Conductive heat feedback from the gas phase is shown in Fig. 7 for non-metallized propellant as a function of pressure and in Fig. 8 for metallized propellants as a function of metal loading. In these measurements, the velocity ratio v between particles and gas is assumed to be 1. Among the three metallized propellants, the difference in conductive feedback is not significant. It is seen that metal additives do not have a strong effect on q_c . On the other hand, the metals increased the radiative heat feedback substantially as can be seen in Fig. 6.

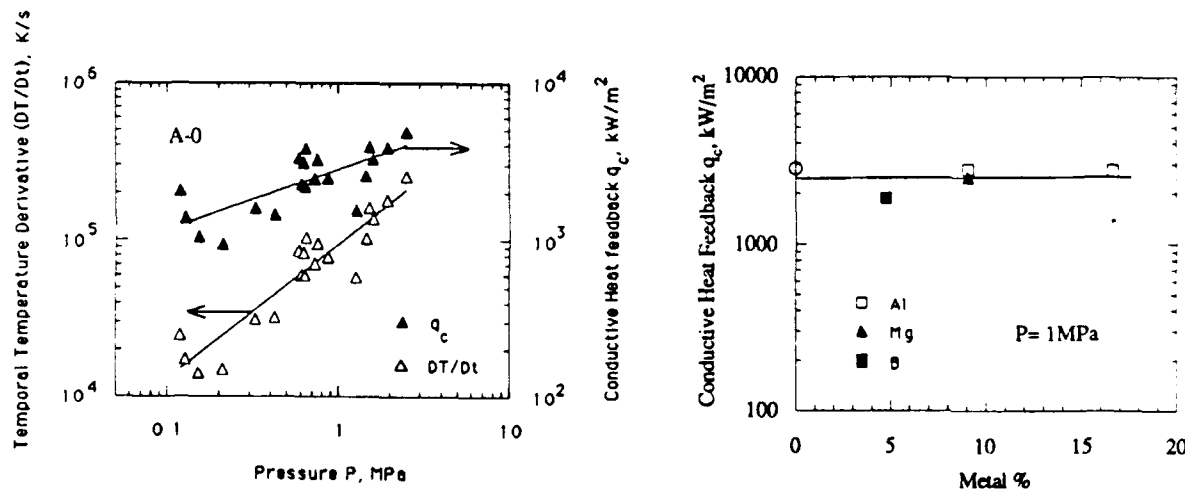


Fig. 7 Conductive heat feedback for non-metallized propellant

Fig. 8 Conductive heat feedback for metallized propellants

DISCUSSION

IMPORTANT OF RADIATIVE HEAT FEEDBACK

The burning rate can be obtained from an energy balance on the burning surface as follows¹⁷,

$$r = \frac{q_c + q_r}{\rho_s (\bar{C}_s (T_s - T_0) - Q_{sh})} \quad (4)$$

In Eq. (4), ρ_s is the average density of the propellant, \bar{C}_s is the average specific heat of the solid phase defined by the following equations,

$$\bar{C}_s = \frac{\int_{T^*}^{T_s} C_s dT}{(T_s - T^*)} \quad (5)$$

$$C_s = \sum_{i=1}^n Y_i C_{si} \quad (6)$$

where C_{si} is the specific heat of a species, Y_i is the mass fraction, and T^* is the reference temperature.

In Eq. (4), T_s is the average surface temperature and T_0 is the initial temperature. Q_{sh} is the heat of reaction (positive exothermic) in the condensed phase based on the reference temperature T^* which includes the heat of reaction between oxidizer, binder, and metal in the condensed phase and latent heat. The value of Q_s depends on the choice of the reference temperature T^* which in this case was taken to be the burning surface temperature T_s . Equation (4) shows that the heat feedback from the gas phase to the burning surface consists of two parts, conductive heat feedback q_c and radiative heat feedback q_r . These components have equivalent weight in Eq. (4). Therefore, in considering the effect of radiative heat feedback on the burning rate as determined by Eq. (4), radiative heat feedback and conductive heat feedback should be compared to each other for any given propellant.

To compare radiative and conductive feedback, the non-dimensional radiative heat feedback $\Theta = q_r/(q_c + q_r)$ is plotted as a function of pressure in Figs. 9 and 10 and as a function of metal loading in Fig. 11. For the conductive heat feedback of M-5 and A-5 propellants, the values of M-10 and A-10 were used. In the non-metalized propellant, Θ is less than 4% at 1 MPa pressure. This result is consistent with similar results of Ref. 1 and 2 and the conclusion that radiative feedback is negligible in non-metalized propellants. However, the results of Figs. 9-10 indicate that in all of the metalized propellants there is a significant increase in the relative importance of radiation as pressure increases. At 1 MPa, Θ for A-20 aluminized propellant is approximately 30%. Therefore it is concluded that the contribution of radiative feedback is not negligible in metalized propellants and that as metal loading and pressure increase so does the relative importance of radiative feedback as a fraction of the total heat feedback. This does not necessarily mean that the burning rate is strongly influenced by radiative feedback. To address the issue of burn rate sensitivity requires a sensitivity analysis.

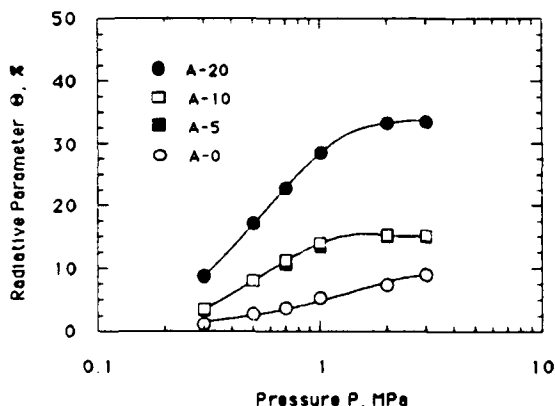


Fig. 9 Ratio of radiative to total heat feedback (A1 Prop.)

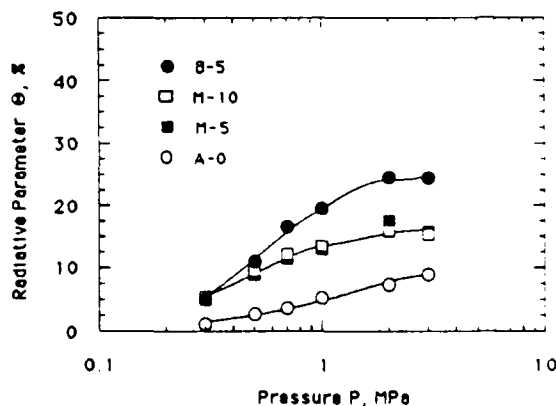


Fig. 10 Ratio of radiative to total heat feedback (B, Mg Prop.)

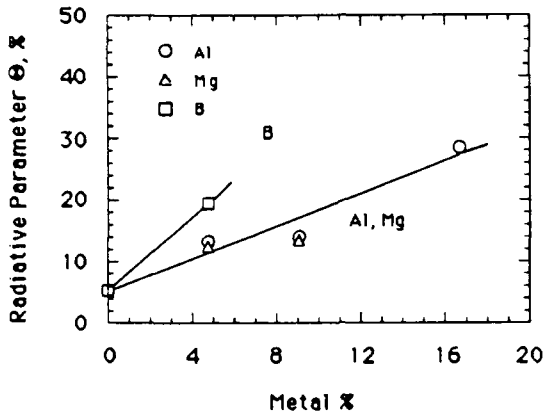


Fig. 11 Ratio of radiative to total heat feedback as a function of metal loading

SENSITIVITY ANALYSIS

To investigate the influence of radiative feedback on burn rate, a sensitivity analysis was performed. This analysis included the effects of radiative heat feedback, gas phase physical properties, gas phase processes (mixing and reaction), and solid phase properties on the burning rate. The relative change in the burning rate is given in terms of the following sensitivity parameters.

$$\frac{\Delta r}{r} = \Delta R_r + \Delta R_k + \Delta R_\tau + \Delta R_s \quad (7a)$$

$$1 = \sum_i R_i, \quad R_i = \frac{\Delta R_i}{\left(\frac{\Delta r}{r}\right)}, \quad i = r, k, \tau, s \quad (7b)$$

In Eq. (7a), ΔR_r is the radiative sensitivity parameter for burning rate augmentation, ΔR_k is the property parameter which is related to the physical properties of the gas, ΔR_τ is the sensitivity parameter for changes in gas phase processes, and ΔR_s is the sensitivity parameter for changes in solid phase processes. The R_i factors represent the normalized sensitivity parameters. These parameters show the contribution of each of the sensitivity parameters to the change in burning rate and allow the relative importance of radiation to be compared between the different propellants.

In order to evaluate ΔR_τ , the characteristic time for the gas phase processes τ_g is defined. The characteristic time τ_g includes the time for diffusion and reaction in the gas phase. τ_g can be approximately obtained by the following equation

$$\tau_g = \frac{\Delta L}{U_g} \quad (8)$$

where ΔL is the flame standoff distance near the burning surface, and U_g is the average gas velocity near the burning surface. U_g can be approximated by assuming a perfect gas and using the continuity equation

$$U_g = \frac{\rho_s r R T_g}{P} \quad (9)$$

where T_g is the characteristic temperature on the gas phase. ΔL is estimated by assuming a linear profile to the flame

$$\Delta L = \frac{T_f - T_s}{\left(\frac{dT}{dx}\right)_{s+}} \quad (10)$$

By combining Eqs. (8)-(10), τ_g is obtained as

$$\tau_g = \frac{P(T_f - T_s)}{\rho_s r R T_g \left(\frac{dT}{dx} \right)_{s+}} \quad (11)$$

The gas phase physical property parameter k_p is defined as

$$k_p = \frac{\lambda_g P (T_f - T_s)}{R T_g} \quad (12)$$

τ_g and k_p are obtained from the experimental data and physical properties of the propellant using Eqs. (11) and (12). q_c can be expressed in terms of these parameters as

$$q_c = \frac{k_p}{\rho_s r \tau_g} \quad (13)$$

By differentiating (logarithmically) Eqs. (4), (12) and (13), the various sensitivity parameters can be obtained as follows.

$$\Delta R_r = \frac{\Delta q_r}{2q_c + q_r} \quad \Delta R_k = \frac{q_c \left(\frac{\Delta k_p}{k_p} \right)}{2q_c + q_r} \quad (14)$$

$$\Delta R_\tau = - \frac{q_c \left(\frac{\Delta \tau_g}{\tau_g} \right)}{2q_c + q_r} \quad \Delta R_s = - \frac{(q_c + q_r) \left(\frac{\Delta \psi}{\psi} \right) + q_c \left(\frac{\Delta \rho_s}{\rho_s} \right)}{2q_c + q_r} \quad (15)$$

In the above equations, the solid phase parameter ψ is defined as

$$\psi = \rho_s (\bar{C}_s (T_s - T_0) - Q_{sh}) \quad (16)$$

Using the measurements of conductive feedback, radiative feedback, surface temperature, burn rate, etc. as previously described, it is possible to determine various normalized sensitivity parameters as defined in Eq. (7b).

In Figs. 12-14 each of the normalized sensitivity parameters are plotted. These figures show that each parameter has some effect on the burning rate augmentation at typical rocket motor pressures (> 1 MPa). In addition, it can be seen that in the aluminum and magnesium propellant, the radiative heat feedback and gas phase thermal properties are especially important in the burning rate augmentation above 1 MPa. On the other hand, in the boron propellant, the solid phase processes are the most important of the four considered. It is thought that the significance of this is the heat release associated with heterogeneous boron combustion on the propellant surface.

Figures 15 and 16 show the normalized radiative sensitivity parameter. These results show that the effect of radiation on the burning rate augmentation is not negligible in metalized propellants. The effect appears to be relatively important in aluminized AP propellants and less important in boron and magnesium AP propellants at normal rocket motor pressures. In aluminum propellant the addition of aluminum does not change the burning rate greatly. However, the change that does take place appears to be strongly related to the increase in radiative feedback. In boron propellant the addition of boron does increase the burning rate significantly. As noted above this increase appears to be strongly related to the heterogeneous combustion of boron on the propellant surface.

The significance of these results is still under investigation. These results suggest that one important area to investigate would be the effect of metal loading in boron and magnesium propellants, given the indicated importance of condensed phase heat release in these propellants. Another area which needs further investigation is the effect of propellant heterogeneity on measured temperatures, especially in boron propellant.

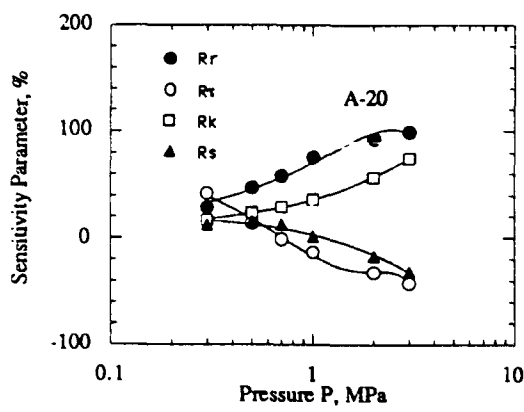


Fig. 12 Sensitivity Parameter (A-20).

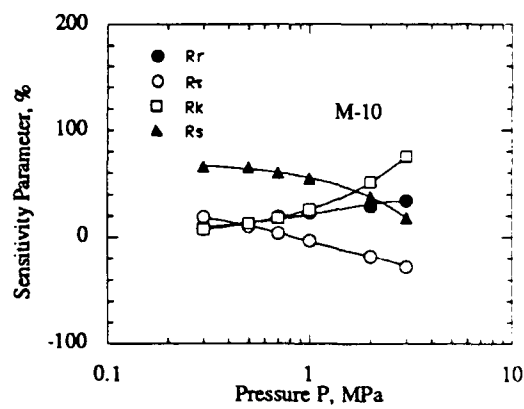


Fig. 13 Sensitivity Parameter (M-10).

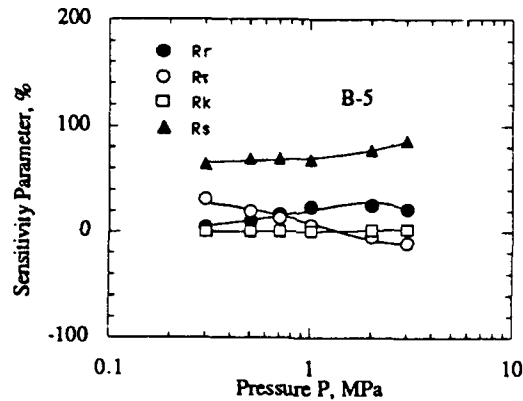


Fig. 14 Sensitivity Parameter (B-5).

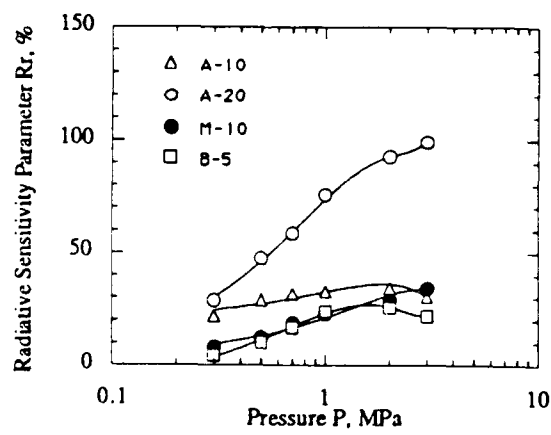


Fig. 15 Normalized sensitivity parameter for radiative feedback.

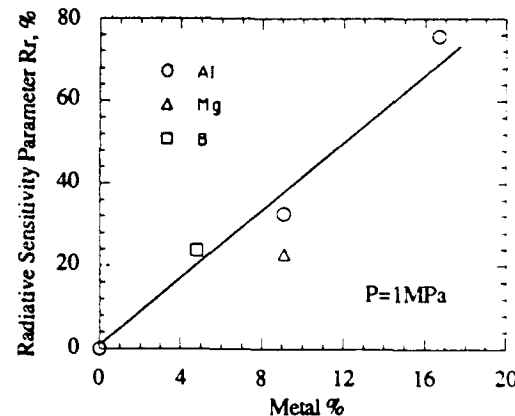


Fig. 16 Normalized sensitivity parameter for radiative feedback.

SUMMARY

Fiber optics and micro-thermocouples were used to examine radiative feedback effects in metalized and non-metalized propellant combustion. In non-metalized propellant, the effect of radiative feedback on burning rate was negligible because of low incident flux and low propellant absorptivity. A burning rate sensitivity analysis suggested that in metalized propellants radiative feedback was significant at pressures above 1 MPa. In highly loaded aluminum (20% Al) propellant radiative feedback appeared to be primarily responsible for a modest increase in burning rate. In magnesium and boron propellants radiative feedback was less important than that in the highly aluminized propellant. In the boron propellant, condensed phase heat release was responsible for a significant increase in burning rate.

ACKNOWLEDGEMENTS

The assistance of Capt. Joe Cor and personnel at the Astronautics Lab (Air Force Systems Command) is gratefully acknowledged in the preparation of the solid propellants. Partial support for this project from the National Science Foundation (CBT 86-96162), the Office of Naval Research (N00014-87-K-0547), and Thiokol Corporation is also acknowledged.

NOMENCLATURE

A	area of a fiber optic core, m^2
C	specific heat, J/kgK
k_p	gas phase physical property parameter
P	pressure, Pa
Q_{sh}	heat of reaction in a solid or condensed phase, J/kg
q	heat feedback from gas phase, kW/m^2
R	gas constant of combustion products, J/kgK or relativity sensitivity parameter
r	burning rate, mm/s
T	temperature, K or $^{\circ}C$
t	time, s
Y	mass fraction
α	absorptivity of propellant
ΔL	flame standoff distance, m
ΔR	sensitivity parameter
ϵ	emissivity of propellant
Θ	non-dimensional radiative heat feedback $\Theta=q_r/(q_c+q_r)$
λ	thermal conductivity, kW/mK or wavelength, μm
ρ	density, kg/m^3 or reflectivity
σ	Stefan-Boltzmann constant, W/m^2K^4
τ_g	characteristic time, s
v	ratio of aluminum particle to that of combustion gases at propellant surface
ψ	solid phase parameter

Subscripts

0	non-metalized propellant, normal angle, or initial condition
c	conduction
f	flame
g	gas phase
m	metal
r	radiation
s	solid or condensed phase

REFERENCES

1. Blair, D. W., Bastress, E. K., Hermance, C. E., Hall, K. P., and Summerfield, M., "Some Research Problems in the Steady-State Burning of Composite Solid Propellants," *Solid Propellant Rocket Research, Progress in Astronautics and Rocketry Series* (M. Summerfield, Ed.), Academic Press, Vol. 1, 1960, pp. 183-206.
2. Horton, M. D. and Youngberg, L. Z., "Effect of Radiation Energy on the Burning Rate of a Composite Solid Propellant," *AIAA J.*, Vol. 8, 1970, pp. 1738-1741.
3. Zennin, A. A., Glaskova, A. P., Leipunskyi, O. L., and Bobolev, V. K., "Effects of Metallic additives on the deflagration of condensed systems," *Tenth Symposium (International) on Combustion*, The Combustion Institute, 1964, pp.27-35.
4. Zennin, A. A., Glaskova, A. P., Leipunskyi, O. L., and Bobolev V. K., "Effect of Aluminum of The Burning of Ammonium Perchlorate-Polyformaldehyde Mixtures," *Combustion, Explosion, and Shock Waves*, 1968, pp. 165-168.
5. Zennin A. A., Glaskova, A. P., Leipunskyi, O. L., and Bobolev, V. K., "Microcalorimeter Measurements of Flame Emission," *Combustion, Explosion, and Shock Waves*, 1968, pp. 113-116.
6. Felton, R. F. and Hichcock, J. E. "An Optical Technique to Measurement Energy Incident on a Burning Solid Propellant Surface," *AIAA Paper No. 71-469*, 1971, AIAA.
7. Brewster, M. Q., and Parry, D. L., "Radiative Heat feedback in Aluminized Solid Propellant Combustion," *J. Thermophysics*, Vol. 2, 1988, pp 123-130.
8. Brewster, M. Q., and Taylor D. M., "Radiative Properties of burning Aluminum Droplets," *Combust. Flame*, Vol. 72, 1988, pp. 287-299.
9. Kubota, N., and Serizawa, C., "Combustion of Magnesium/Polytetrafluoroethylene, *J. Propulsion and Power*," *J. Propulsion and Power*, Vol. 3, 1987, pp. 303-307.
10. Kubota, N., and Serizawa, C., "Combustion Process of Mg/TF Pyrotechnics," *Propellants, Explosives, and Pyrotechnics*, Vol. 12, 1987, pp. 145-148.
11. Kuwahara, T., and Kubota, N., "Role of Boron in Burning Rate Augmentation of AP Composite Propellants," *Propellants, Explosives, Pyrotechnics*, Vol. 14, 1989, pp. 43-46.
12. Chen, D. M., Hsieh, W. H., Snyder, T. S., Yang, V., and Kuo, K. K., "Study of the Thermophysical Properties and Combustion Behavior of Metal-Based Solid Solid Fuels", *AIAA Paper 88-3041*, 1988, AIAA.
13. Hsieh, W. H., Cheng, J. J., and Kuo, K. K., "Strand-Burning Characteristics of advanced Boron-Based BAMO/NMMO Fuel-Rich Solid Propellants", Eastern Section of the Combustion Institute, 1988.
14. Ishihara, A., Brewster M. Q., Sheridan, T. A., and Krier, H., "The Influence of Radiative Heat Feedback on Burning Rate in Metalized Propellants", *Combust. Flame*, to be published
15. Brewster, M. Q., and Hardt, B. E. Selective Radiation Absorption in Aluminized Composite Propellant Combustion, 24th JANNAF Combustion Mtg., 1987, CPIA Publ.478, p. 157.
16. Ishihara A., Ph.D. Thesis, The University of Illinois at Urbana-Champaign, 1990.

27th JANNAF Combustion Meeting
November, 1990, Cheyenne, WY

MEASUREMENT OF PROPELLANT COMBUSTION RESPONSE TO
SINUSOIDAL RADIANT HEAT FLUX

J. C. Finlinson and D. Hanson-Parr
Naval Weapons Center,
China Lake, CA

S. F. Son and M. Q. Brewster
University of Illinois at Urbana-Champaign

ABSTRACT

Experimental and theoretical work to determine the combustion response function of solid propellants using a sinusoidal heat flux and a microforce transducer is reported. Response data for N5, A13, and NWR11 propellants are presented. The experimental work improves upon Mihlfeith's experiment (1971) by using a CO₂ laser as the source of radiant energy and a digital data acquisition system. The waveform of a laser is more easily controlled than an arc lamp. The phase relation of the imposed heat flux and the propellant thrust signal were determined using a digital cross correlation. The heat flux response, R_q, was measured for three propellants and is compared with theoretical predictions. In agreement with theory, the measured response exhibits a phase lead at non-zero frequencies below the response peak and a phase lag at frequencies above the response peak. The pressure response, R_p, is also calculated. For the models considered the transfer function, R_p/R_q, reduces to the ratio of their zero frequency values, n_p/n_q = R_p(0)/R_q(0), but only if the mean radiant flux is small and the surface absorption is very large, i.e. the ratio of the thermal length scale to radiant length scale, β, goes to infinity. The effect of in depth absorption on the transfer function is also presented.

INTRODUCTION

The pressure response function, R_p, is a necessary component in the linearized stability analysis of solid rocket motors. The most widely used and accepted experimental method of measuring R_p is the T-burner. The real component of R_p can be determined in a relatively direct manner using the T-burner. However, along with significant uncertainties in data interpretation, the T-burner requires considerable preparation time and typically costs about \$15,000 to generate response function data for a single propellant at one pressure. Clearly, a faster and less expensive method is desirable in order to compare many different propellants and attain a more fundamental understanding of the physical processes involved.

For these reasons, experimentalists have endeavored to develop alternate techniques for over two decades.²⁻¹³ Various experimental techniques used to measure the instantaneous burn rate include a microwave device,² a magnetic flux meter,³ and a microforce transducer.⁵⁻¹³ To measure R_p directly a nonsteady pressure field must be imposed and accurately measured. To accomplish this a rotating valve has been used with some success.⁴ Because of its relative simplicity, the microforce transducer method using an imposed heat flux seems to offer the possibility of obtaining the propellant response less expensively than other methods. Further, it is much easier to generate the desired waveshape of heat flux using a laser compared to available pressure modulating techniques. However, a transfer function between the heat flux response, R_q, and the more useful pressure response, R_p, must be developed before this technique will be generally accepted. Theoretical work toward this goal has been attempted by several researchers.¹⁴⁻¹⁹

Previous experimental work to determine the heat flux response, R_q, was reported by Mihlfeith,⁵⁻⁷ Strand *et al.*,¹⁸ and Soviet researchers such as Zarko *et al.*⁸⁻¹⁰ Mihlfeith reported a phase lag even at frequencies below the resonance peak probably because of the inaccurate phase measurement techniques available at the time. In a more recent work, Zarko *et al.* reported a phase lead of 10-15° at frequencies below the resonant peak and a phase lag of about 90° at high frequencies, in qualitative agreement with theory.⁸ Although the microforce transducer/heat-flux technique has shown significant promise, it has not been widely applied to experimental studies in the U.S. since Mihlfeith's work in 1971.

In this work, the complex valued pressure response function is defined in the usual manner as:

$$R_p = \frac{m'/\bar{m}}{p'/\bar{p}} = \frac{r'/\bar{r}}{p'/\bar{p}} \quad (1)$$

In a similar manner, the complex valued heat flux response, R_q, is defined as:

$$R_q = \frac{m'/\bar{m}}{q'_{r2}/\bar{q}_{r2}} = \frac{r'/\bar{r}}{q'_{r2}/\bar{q}_{r2}} \quad (2)$$

where q'_{r2} is the external heat flux directed on the burning propellant surface.

Approved for public release; distribution is unlimited.

Culick showed that all models of the pressure response can be written in a common form:²⁰

$$R_p = \frac{n_p AB}{\lambda + A/\lambda - (1+A) + AB} \quad (3)$$

Where A is a constant associated with the thermal wave in the solid and the surface reaction and B depends primarily on the flame description that is employed. It has been assumed that, (1) the problem is 1-dimensional and linear, (2) the solid phase is homogeneous and nonreacting with constant properties, (3) the surface reaction is independent of pressure, and (4) the gas phase responds quasi-statically to pressure changes.

In this study, the use of a CO₂ laser as the heat flux source and a digital data acquisition offer improved experimental accuracy over some previous studies. The waveform of a laser is easily controlled by a function generator. The objectives of this work are to improve upon the earlier work by using a sensitive microforce transducer and a CO₂ laser for direct measurement of R_q and to develop simple theoretical relationships required to transform the R_q measurements to R_p.

EXPERIMENTAL

Setup

A schematic of the NWC radiant heat flux equipment is shown in Fig. 1. Both vertically and horizontally oriented apparatus were tested previously.²¹ It was determined that the vertically oriented apparatus exhibited less mechanical resonance in the frequency band of interest, consequently this orientation was used in this study. Since the oscillations are less than 10⁻³ N, a very sensitive transducer is required. A Kistler 9207 high-sensitivity quartz force transducer, with natural frequency greater than 10 KHz, is used to measure thrust oscillations. The transducer is mounted inside an aluminum block for thermal isolation. Rubber mounts are used to minimize extraneous vibrations.

The CO₂ laser (10.6 μm, 150W) was modulated sinusoidally by a function generator which controlled the frequency, 3 to 1000 Hz, and amplitude, 10 to 60 W, of the heat flux oscillations. The laser output is not precisely linear with current input; however, over the range of oscillation, the error of assuming linearity on the waveshape is not likely to be a major error. Initially, the beam was used as it came out of the laser with a 0.64 cm diameter and a nearly gaussian energy distribution. Recently, a SPAWR beam integrator has been used to flatten the energy distribution profile of the laser beam. The lens and mirrors required to use the beam integrator are shown in Fig. 1. The beam is expanded using a plano concave lens onto the integrator which refocuses the beam into a square area approximately 1.6 cm². The larger beam allows the use of 1.27 cm diameter samples, which produce larger thrust oscillations than the 0.64 cm diameter samples. The mean heat flux, however, is reduced with the larger diameter samples. The flatter energy profile and the larger diameter samples seem to reduce experimental scatter.

After the initial laser calibration the testing time is short. Preparation for each test involves adjusting the frequency on the sine wave generator and the lowpass frequency on the antialiasing filters, and placing a fresh sample on the pedestal. The sample pedestal is removed from the force transducer and a sample is fastened to the surface using silicon grease. The samples are prepared using propellant cutters. Since there is no pressure vessel to pressurize, the testing only takes a few minutes per sample.

A data analysis display from the Silicon Graphics workstation is shown in Fig. 2. This test was performed using the 0.64 cm diameter laser beam without integration for NS propellant at 30 Hz and 220 W/cm² = 49 cal/cm²/s. The laser current monitor signal and the force transducer signal are plotted in Fig. 2a. The larger more sinusoidal trace in Fig. 2a is the output of the laser current monitor, which is controlled by a function generator. Both signals are filtered with identical filter settings. It is apparent that the thrust trace is slightly leading the laser monitor signal. NS is a mesa burning double base propellant. In the measured thrust traces, the thrust peaks were sometimes flat on top which may be due to the mesa inducing lead additives in NS. For initial theoretical comparisons it would be preferable to use a double base propellant with a linear pressure dependence, but such a propellant was not readily available at NWC.

Data Reduction

Root mean square (rms) values are used for the signal amplitudes. Figure 2b shows the f rms for each period of oscillation. The amplitude of f was found to vary as a function of frequency, as expected by response function theory. Performing the discrete-time cross correlation of the two signals, the phase lag can also be determined. This method assumes a sinusoidal input signal. The resulting phase lag vs time is plotted in Fig. 2c. As expected for this data set, the negative phase lag indicates a phase lead. To maintain a reasonably constant phase resolution, the sampling rate is increased with the input frequency of the laser. Many cycles are analyzed at each frequency and averaged to reduce data scatter. The standard deviation of the values within one test are indicated by error bars on the plots. By performing similar tests at various frequencies, the magnitude and phase of the propellant response as a function of frequency was measured.

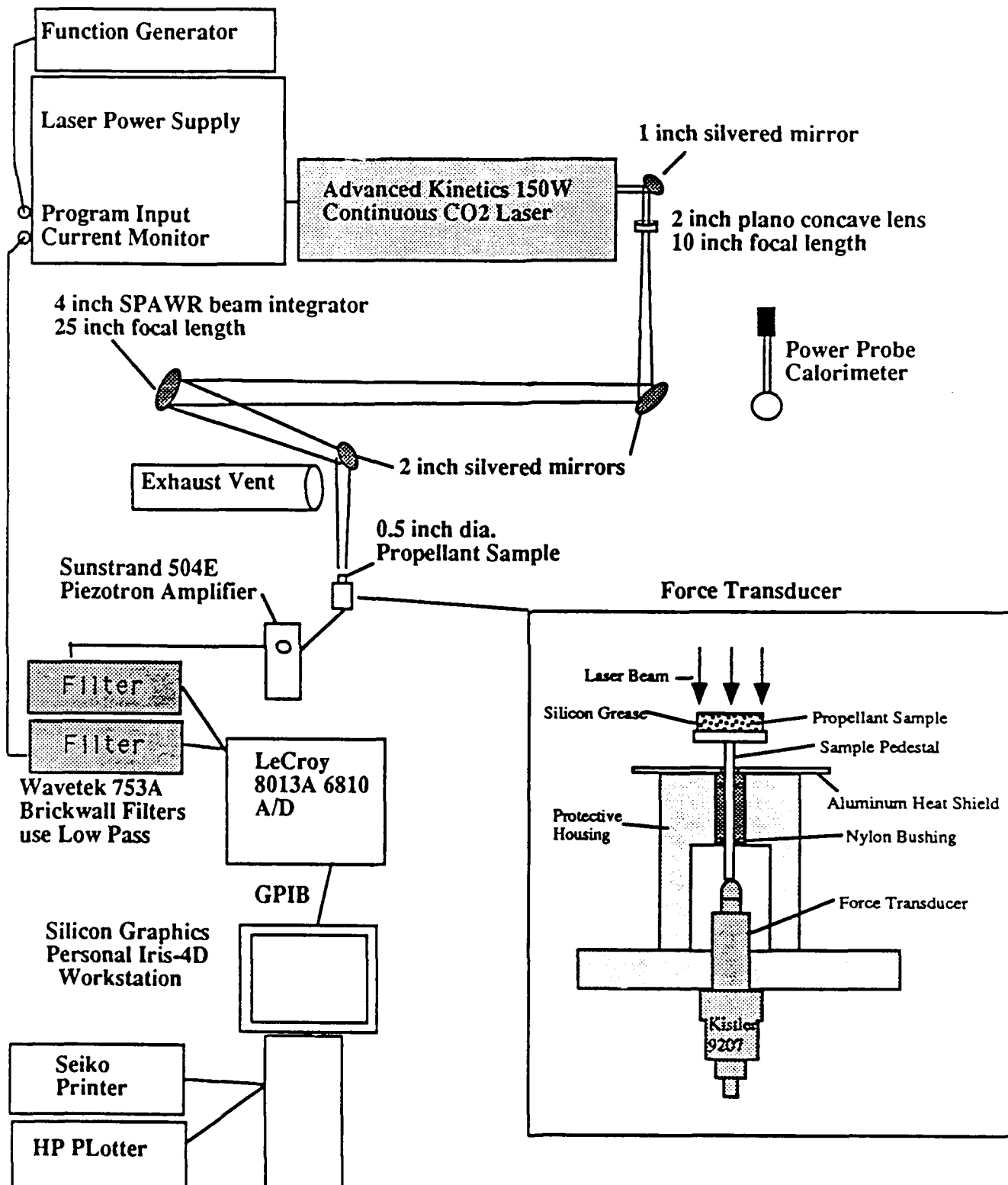


Figure 1. Schematic of the NWC Radiant Heat Flux Equipment. Showing an enlargement of the force transducer installation and sample mounting on a pedestal.

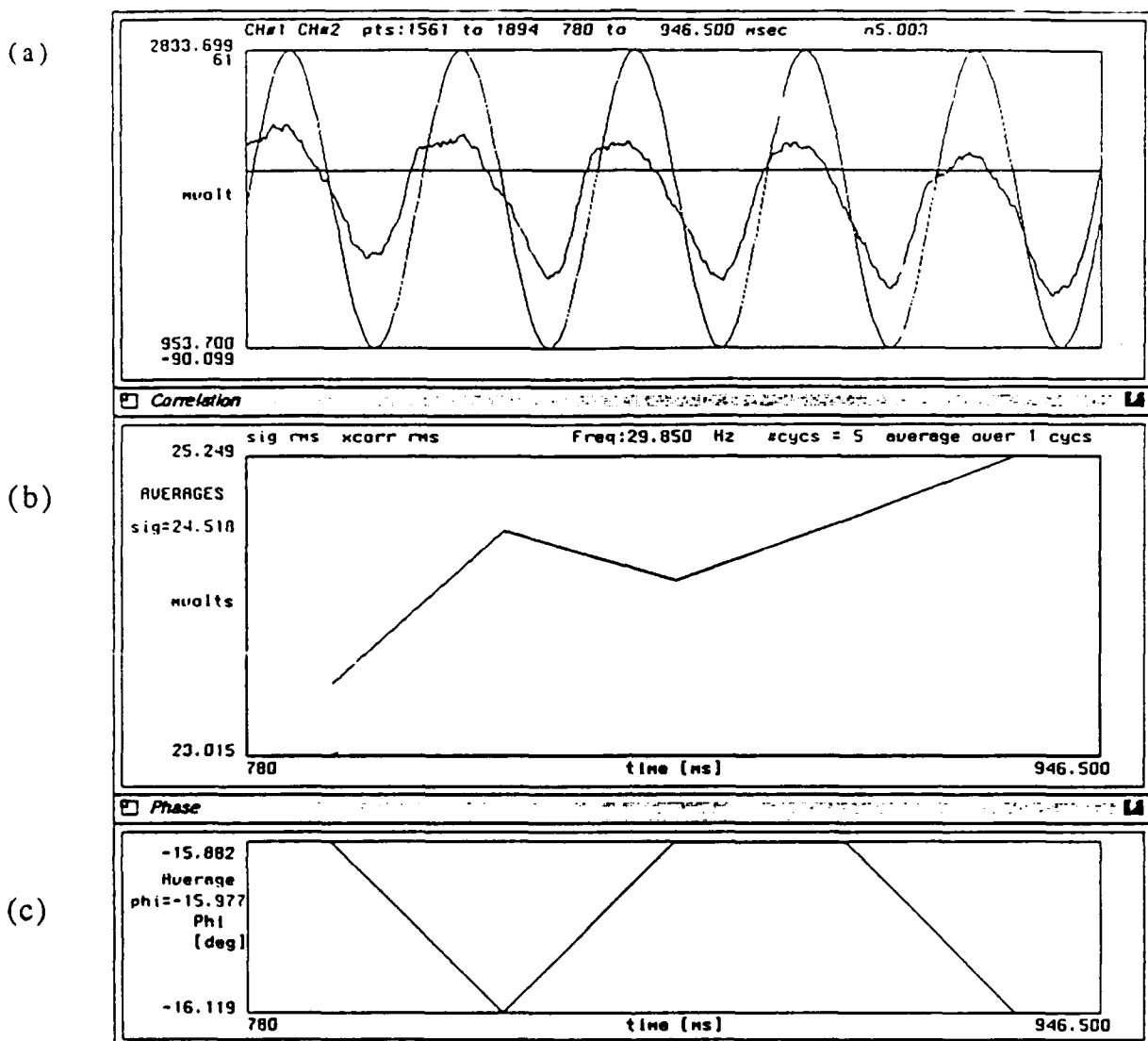


Figure 2. Data Analysis Display From the Silicon Graphics Workstation. a) Laser current monitor signal and the force transducer signal in (millivolts) vs time (milliseconds). b) f rms vs time, and c) Phase lag versus time. Test performed using the 0.64 cm diameter laser beam without integration for N5 propellant at 30 Hz and $220 \text{ W/cm}^2 = 49 \text{ cal/cm}^2/\text{s}$.

To make quantitative comparisons of the force data with the models of R_q or R_p , requires calculation of m'/\bar{m} or r/\bar{r} , as in Eqn. 1. Applying simple steady state continuity and momentum relations and neglecting the effect of nonsteady changes in the mass of the propellant sample, the thrust measurements, F , can be transformed to mass flux by:⁴⁻⁶

$$m = \sqrt{\frac{M P F}{R T_f A}} \quad (4)$$

The oscillating force data, f , was converted to mass flux, m' , using Eqn. 5, which is a perturbation of Eqn. 4. The derivation considers only small fluctuations and neglects the small changes in force due to the unsteady decrease in the sample mass in the vertical orientation.⁵⁻⁷

$$m' = \frac{M P f'}{2\bar{m} R T_f A} \quad (5)$$

Nine propellants of type double base, smokeless composite, and metallized composite have been tested at atmospheric pressure surrounded by room temperature air. Unfortunately, the laser energy is scattered by burning metal particles and smoke in the plume of highly metallized propellants. Special techniques for deflecting the plume or increasing the laser power will be necessary to measure the response of metallized propellants. However, fair agreement

with theory was obtained using double base and nonmetallized composite propellants. Zarko *et al.* report similarly that this technique works best for double base and composites containing ultra fine AP, both of which have high magnitude response functions.⁸ In the following, the latest experimental results and corresponding analyses are presented for three of the propellants tested. The three propellants are: N5 (double base), A13 (PBAN, AP), and NWR11 (HTPB, AP, minimum smoke). Over 300 samples have been tested at surface heat fluxes ranging from 4 to 49 cal/s/cm². The ingredients and physical properties of the 3 propellants are listed in Table 1.

Table 1. Propellant Ingredients and Related Physical Properties

	NS	A13	NWR11
Nitrocellulose	50%	90u AP 76%	trimodal AP 83%
Nitroglycerin	34.9%	PBAN 20.4%	HTPB 11.9%
Diethyl phthalate	10.5%	Epon 828 3.6%	burnrate suppressant 5%
2-Nitrodiphenylamine	2.0%		carbon black 0.1%
Lead Octoate	1.2%		
Lead Salicylate	1.2%		
Candelilla Wax	0.2%		
burnrate vs pressure	mesa	linear	linear
burnrate @ 13.6psi (cm/s)	0.075	0.085	0.069
n @ 25°C	approx 1.0 <600psi	.432	0.491
density g/cm ³	1.553	1.58	1.7026
<u>@ 1 atm Equilibrium Calculations</u>			
Flame Temp (degK)	2417	2082	2653
gas density (g/liter)	0.120	0.124	0.115
Molecular Weight	23.799	21.139	24.939
Cp (cal/g/K)	0.5395	0.4479	0.4363
<u>Values used in m' conversion</u>			
MW	23.8	21.139	25.5
Flame Temp K	2200	1950	2700

ANALYSIS

Three different models are considered: (1) condensed phase controlled distributed flame,^{20,22} (2) gas phase controlled sharp flame model,^{5-7,23} and (3) gas phase controlled, high activation energy asymptotics flame description.^{24,25} The expressions for R_p are developed assuming that the problem is 1-dimensional and linear, the condensed phase below the surface is homogeneous and nonreacting with constant properties, the surface reaction is independent of pressure, and the gas phase responds quasi-statically to pressure changes. Further, for the R_q expressions it is assumed that scattering is negligible, the absorption coefficient in the condensed phase (K_{q2}) is spatially constant, the thermal emission by the condensed phase is negligible, the incident flux is collimated, and that the fraction of radiant energy absorbed in the reaction layer can be collapsed to an infinitely thin surface layer (with the reaction layer).

Solid Phase

The solid phase is assumed to be nonreacting. The unsteady energy equation in the solid phase, with in-depth absorption is:

$$\rho C \frac{\partial T}{\partial t} + mC \frac{\partial T}{\partial x} = k_s \frac{\partial^2 T}{\partial x^2} + f_1 q_{r1} K_{q1} \exp(K_{q1}x) + f_2 q_{r2} K_{q2} \exp(K_{q2}x) \quad (6)$$

For simplicity, the density, thermal conductivity, and heat capacity of the solid are considered constant and the natural radiant feedback to the solid, q_{r1} , is neglected. It has been assumed that scattering is negligible, the absorption coefficient K_{q2} is spatially constant, thermal emission by the condensed phase is negligible, and the incident flux is collimated. It should be noted that the fraction of radiant flux that is absorbed below the reaction layer, f_2 , must be specified. From scaling arguments,¹⁹ the behavior is modelled using $f_2 = \exp(-L_p X_R / X_A) = \exp(-L_p \beta R T_s / E_s)$. L_p is a correction factor which has been assumed to be equal to 1.0 in these calculations. L_p could be justifiably used if the absorption coefficient in the reaction layer differs from the unreacted solid phase. The absorption coefficient could be different due to phase changes (i.e. a melt layer or phase change of the crystalline structure).

Applying a linear perturbation of m , T , and q_{r1} , the steady-state form of the solid phase energy equation and the time-dependent energy equation can be obtained and solved using the appropriate boundary conditions.¹⁹ The origin of the coordinate system used remains fixed to the surface which produces identical results as a coordinate system that moves with the mean burn rate (inertial coordinate system) and later applies a Taylor's series to relate the variables to the actual surface values. Using the solution of (6), the transient conductive heat flux (on the solid phase side of the surface) is found to be:

$$k_s \dot{\phi}_{s+} = \bar{m} C \lambda T_s + \frac{\dot{m}}{\bar{m}} \left[\frac{\bar{m} C(T_s - T_i)}{\lambda} \right] - \frac{\dot{m}}{\bar{m}} \left[f_2 \bar{q}_{r2} \frac{1-\lambda}{\lambda(1-\lambda-\beta_2)} \right] + \frac{\dot{q}_2}{\bar{q}_2} \left[\frac{f_2 \bar{q}_{r2} \beta_2}{1-\lambda-\beta_2} \right] \quad (7)$$

The first two terms on the right hand side are the familiar terms that have appeared in previous studies where radiant heat flux was not considered.²⁰ Previous theoretical studies including radiant heat flux used the extreme f_2 values of zero or one (translucent or opaque surface) and have neglected the third term, apparently without justification.^{5-7,14}

Surface Connection Relations

The surface reaction layer is collapsed to the surface; that is, it is assumed to be infinitely thin at the surface. To be consistent, the amount of radiant energy that is absorbed in the actual reaction layer, which has finite thickness, is also collapsed with the reaction layer to the surface. The perturbed energy balance at the surface is therefore:

$$k_s \dot{\phi}_{s+} = k_s \dot{\phi}_{s-} - \dot{m} Q_s + \bar{m} (C_p - C) T_s' - q_{r2}' (1-f_2) \quad (8)$$

A perturbed Arrhenius-type relationship can be assumed for the pyrolysis and perturbed to obtain:^{5-7,14,20}

$$\frac{T_s'}{T_s} = \frac{\dot{m}}{\bar{m}} \frac{1}{E} \quad (9)$$

where $E = (\alpha_e + E_e/RT_e)$ and the pressure dependence is neglected ($n_e = 0$). Alternatively, the solid phase burning rate expression formula developed by Ibiricu and Williams can be used,²⁵ as shown in Son *et al.*¹⁹, to obtain:

$$\frac{T_s'}{T_s} = \frac{\dot{m}}{\bar{m}} P_3 - \frac{\dot{q}_2}{\bar{q}_2} \left[\frac{f_2 \bar{q}_{r2}}{\bar{m} C T_s P_1 P_2} \right] \quad (10a)$$

where:

$$P_3 = \frac{1}{P_2} + \frac{f_2 \bar{q}_{r2}}{\bar{m} C T_s P_1 P_2} \quad (10b)$$

$$P_2 = 2 + \frac{E_b}{R T_s} - \frac{1}{P_1} \quad (10c)$$

$$P_1 = (1 - T_s/T_i) - \frac{f_2 \bar{q}_{r2}}{\bar{m} C T_s} - \frac{H_R}{2 C T_s} \quad (10d)$$

This description was derived using high activation energy asymptotics and explicitly includes the effect of the external heat flux. It should be noted that this expression is only applicable to gas phase controlled burning.²⁵

Gas Phase

The models considered here differ the most in the description of the gas phase. For the distributed reaction model, Culick shows that:²⁴

$$k_s \dot{\phi}_{s+} = \bar{m} C(T_s - T_i) W \frac{P'}{P} - C_p T_s \Lambda^2 \frac{\dot{m}}{\bar{m}} \quad (11)$$

which describes the fluctuating conductive heat flux to the surface. For the thin flame models:

$$k_s \dot{\phi}_{s+} = \bar{m} [Q_f' - C_p(T_f' - T_s')] + \bar{m}' [Q_f - C_p(T_f - T_s)] \quad (12)$$

can be obtained from the perturbation of a simple energy balance. If $Q_f = cP^\gamma$ is assumed then:

$$\frac{Q_f'}{Q_f} = \gamma \frac{P'}{P}. \quad (13)$$

This is in contrast to Mihlfeith's analysis, where both Q_f and Q_g were assumed constant.⁵⁻⁷

For the thin flame, gas phase controlled model the perturbed burn rate expression is:^{5-7,23}

$$F \frac{T_f'}{T_f} = \frac{\bar{m}'}{\bar{m}} - \left(v_1 + \frac{\gamma C_p(T_f - T_s)}{2[Q_f - C_p(T_f - T_s)]} \right) \frac{P'}{P} + G \frac{T_s'}{T_s}. \quad (14)$$

For the gas phase controlled, high activation energy asymptotics the perturbed expression is:¹⁹

$$\frac{\bar{m}'}{\bar{m}} = \left(v_1 + \gamma \right) \frac{P'}{P} + \left(2 + \frac{E_f}{2RT_f} \right) \frac{T_f'}{T_f}. \quad (15)$$

Response Functions

Combining Eqns. 7-9 and 11, the distributed reaction model response can be obtained. Further, using the definitions $R_p(0) = n_p$ and $R_q(0) = n_q$ to decrease the number of variables it is found that:

$$R_q = \frac{n_q AB \left[\frac{(1-f_2)(1-\lambda)-\beta_2}{1-\lambda-\beta_2} \right]}{\lambda + \frac{A}{\lambda} - (1+A) + AB - f_2 Q_R \left[\frac{1-\lambda}{\lambda(1-\lambda-\beta_2)} \right]} \quad (16)$$

for $P' = 0$. For $\bar{q}_2 = \bar{q}_{22} = 0$, R_p takes the standard form (Eqn. 3). For the distributed reaction model, $A = E(1 - T_f/T_s)$, $B = 2(1 - H) + \frac{C_p}{C} \frac{1}{A} - \frac{Q_R}{A}$, and $Q_R = \bar{q}_{22} E / \bar{m} C T_s$. If \bar{q}_{22} is zero, then A and B take on the form as derived by Culick and R_p can be calculated in the usual manner.²⁰ To calculate R_q , the Q_R term must be included in the calculation of B . It is tempting to neglect this term in the definition of B . For surface absorption only ($f_2 \rightarrow 0$), the transfer function (R_p/R_q) would simply be n_p/n_q . Indeed, this is what DeLuca claimed, but it is not sufficient.¹⁴ It is also necessary that the mean heat flux term, \bar{q}_{22} , be negligibly small. DeLuca, implicitly assumed that the term, $\frac{C_p}{C} EA^2$ (a term in the denominator of Eqns. 3 and 15 if the zero frequency limit is not used), was the same for both R_q and R_p expressions. It is easily shown that this term is related to a steady state energy balance,²⁰ hence the additional heat flux term appears in the expression for B . If, however, the Q_R term in the B expression is negligible compared to the other terms and the absorption is confined to the surface, then n_p/n_q is the correct transfer function.

Likewise, combining Eqns. 7-9 and 12-14, and applying the zero frequency limit, the same form of equations are obtained except that:

$$B = 1 - H + \frac{C_p}{C} \frac{1}{A} \left[\frac{T_f E G}{F} - \frac{E}{2G} \right]. \quad (16a)$$

It should be noted that the overall energy balance must be satisfied. Therefore, even though Q_R does not appear explicitly in this definition of B , Q_R will affect the value of B through other parameters such as T_f . Again, if the effect of Q_R

on the value of B is small compared to the other terms and the absorption is confined to the surface, then n_p/n_q is the correct transfer function.

Using the Ibiricu and Williams description; that is, combining Eqns. 7,8,10,12,13 and 15, the same form of R_p expression is obtained (Eqn. 3) but the expression for R_q is slightly different in form:

$$R_q = \frac{n_q AB \left[f_2 \frac{1-\lambda}{P_1 P_2} + \frac{(1-f_2)(1-\lambda)-\beta_2}{1-\lambda-\beta_2} \right]}{\lambda + \frac{A}{\lambda} - (1+A) + AB - f_2 Q_R \left[\frac{1-\lambda}{\lambda(1-\lambda-\beta_2)} \right]} \quad (17)$$

where $A = (1 - T_s/T_i)/P_3$, $B = C_p T_s / [C(T_s - T_i)(2 + E_f/2RT_f)] + Q_R/A$, and $Q_R = \bar{q}_{r2}/mCT_s P_3$. The change in form is due to the differences in the assumed pyrolysis expressions (Eqns. 9 and 10). If the effect of Q_R on the value of A and B is small compared to the other terms and the absorption is confined to the surface, then n_p/n_q is the correct transfer function. These results indicate that this limiting condition may be valid regardless of the flame description or controlling layer assumed.

Figure 3a and 3b are plots of the magnitude and phase of R_p and R_q versus normalized frequency for these models. - The following parameters were used: $E_s = 20$ kcal/mole, $E_f = 40$ kcal/mole, $m = 0.13$ cm/s, $Q_s = 95$ cal/g, $T_s = 950$ K, $T_f = 2082$ K, $\bar{q}_{r2} = 5$ cal/cm²s, $L_f = 1$, and $K_{s2} = 2000$ cm⁻¹. Q_R is determined from the overall energy balance. The peak of the $|R_p|$ is higher than $|R_q|$ for the condensed phase controlled distributed flame description, but shows the opposite trend for the sharp and Ibiricu and Williams (asymptotic) description. This is caused by the high sensitivity of the condensed phase controlled distributed flame to the condensed phase heat release. It should be recalled that in the expression for B in the distributed reaction model, increasing Q_R has a similar effect to increasing the nondimensional heat release parameter, H . The two gas phase controlled models do not show this sensitivity to H . However, they are much more sensitive to E_f . For the conditions considered, the sharp flame model must have E_f of approximately 60 kcal/mole to produce a more realistic response. In contrast, a lower E_f will decrease the response of the Ibiricu and Williams (asymptotic) description to more commonly observed values.

Near the zero frequency value, there is no phase difference between the heat flux and the burn rate. As the frequency is increased, the burn rate leads the heat flux signal (note that this result applies to the long time response after initial transients have disappeared). This is related to the fact that the transient burn rate is a function of the derivative of the forcing function (pressure or heat flux). Some have questioned whether a lead could really exist, implying that the propellant would be responding to the stimulus before it arrived, as in feedforward control. The low frequency phase lead can be explained as follows. At low burn rates the thermal layer extends deeper into the solid than at high burn rates. Thus, as the magnitude of the driving force (radiant flux or pressure) during a transient is increased, the new thermal layer thickness is shorter than the currently existing thermal layer. A thick thermal layer is roughly equivalent to storing energy in the propellant by conditioning at a higher initial temperature. Energy stored in the propellant produces a burn rate and thrust increase larger than the driving force increase alone would predict. Likewise, in the case of a decreasing driving force, extra energy goes into building up the thicker thermal layer (similar to lowering the conditioning temperature in the steady state) which decreases the burn rate below the steady state value. This effect thus can produce a phase lead. Further, it is interesting to recall from dynamic systems analysis that the derivative exhibits a phase lead in its frequency response. Thus, the measured and mathematically predicted phase lead is physically reasonable. As the characteristic time of the driving force is decreased relative to the characteristic time of the solid, this "leading" effect becomes less important and the thermal lag of the solid produces an intuitively comfortable phase lag. Figure 3c shows the calculated transfer function for the three models considered using the same parameters as above.

Figures 3c and 3d show the transfer function using the Ibiricu and Williams description for the same parameters used above. It can be seen that even for pure surface absorption ($\beta_2 \rightarrow \infty$, $f_2 \rightarrow \infty$) the transfer function does not approach n_p/n_q . As \bar{q}_{r2} approaches zero the expected limit is evidenced.

Radiative Properties

The important radiative properties involved were measured or estimated to better quantify how much thermal radiation energy reaches the propellant surface, how much is reflected, and where it is deposited in the propellant. Some of the radiant heat-flux will be absorbed and scattered by the combustion gases and particles above the burning propellant surface. In order to measure the transmission through the gas phase, a Nd-YAG laser was used as the radiant source. A fiber optic was placed in the center of a A13 propellant strand and a photodiode sensitive to the 1.06 μm wavelength was used to measure the incident radiation (see Ishihara *et al.*²⁶ for a description of the fiber optic technique used). The incident radiation from the laser was measured, both during combustion and without a flame present. From these measurements, the transmissivity was measured to be 0.55 ± 0.05 at the 1.06 μm (Nd-YAG) wavelength. This value can be related to the value at 10.6 μm using a narrow-band radiation model that includes both the soot and gas contributions. The value of the transmissivity at 10.6 μm was estimated to be 90%, applying the radiation model with equilibrium calculations for gas properties, the visual

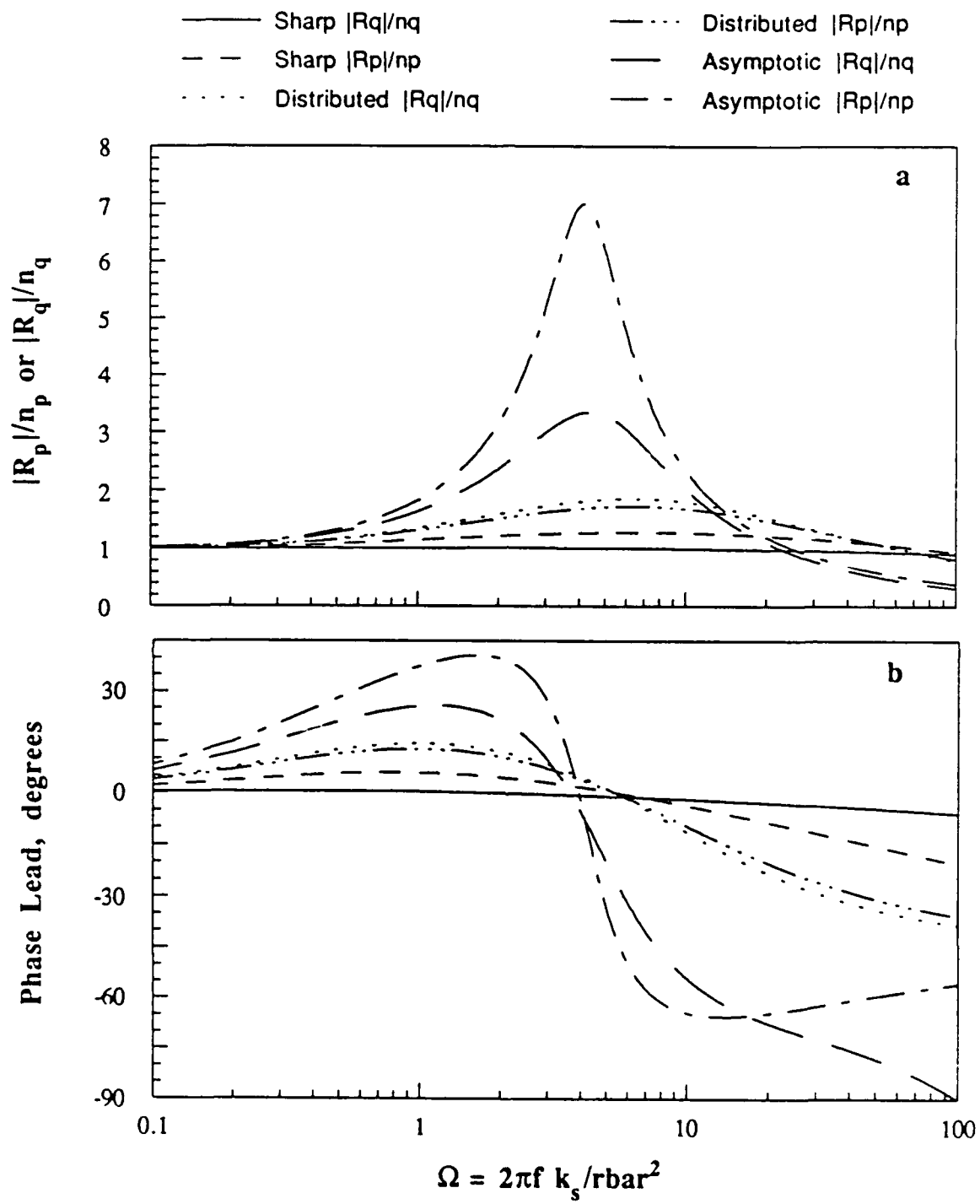


Figure 3a,b. Theoretical Calculations of the Response Function Using the Three Models.
a) $|R_q|$ and $|R_p|$, b) Phase lead of R_p and R_q vs Ω .

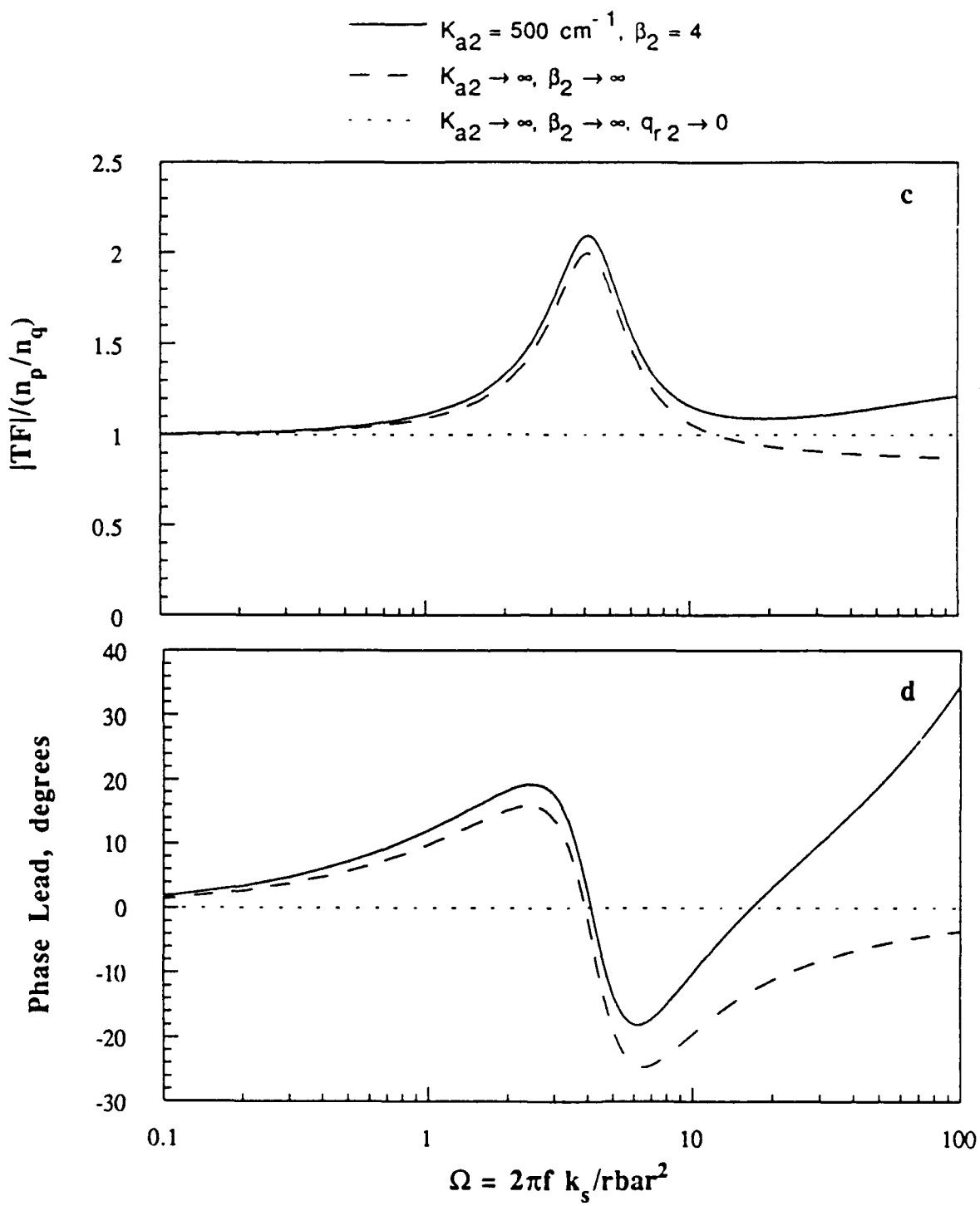


Figure 3c,d. Theoretical Calculations of the Transfer Function Using the Ibiricu and Williams Flame and Burn Rate Description. a) $|TF|$ vs Ω , b) Phase lead of (TF) vs Ω .

observations of the flame height, and the Nd-YAG measurement. Using the narrow-band model (RADCAL), the transmissivity was seen to be affected primarily by the soot volume fraction.^{27,28} It was relatively insensitive to the gas concentrations at either wavelength, but is more sensitive at the 1.06 μm wavelength. A13 appears to be the most optically thick flame so this value is likely a worst case value for the propellants considered in this study. Transmissivity values of 92% and 94% were used for the calculations involving NWR11 and N5. Mihlfeith measured transmissivity of 75 to 85% for the nonmetallized AP propellants in his study; however, his measurements were for an arc lamp which has a broad spectral content.⁵⁻⁷ To better quantify these values, direct measurements should be made using the CO₂ laser.

A certain amount of the incident laser energy will also be reflected from the propellant surface to the surroundings. Fortunately, this is a relatively simple property to measure. Samples of A13 and NWR11 were prepared by slicing with a knife blade and N5 sheet stock was used. A 2 mW CO₂ laser was pulsed normal to the surface and the reflectivity was measured. Unburnt samples of N5, A13, and NWR11 were found to have reflectivity values of 3.2 ± 0.4 , 3.6 ± 0.1 , and 4.0 ± 0.2 percent, respectively, at 10.6 μm . Extinguished samples will be tested to see if they vary significantly from the unburnt samples. Past experience with other propellants has shown that the reflectivity of unburnt surfaces and extinguished surfaces are similar.

As discussed above, the absorption coefficient, K_{a2}, (inverse length-scale of the in-depth absorption) is an important parameter of in determining where the radiant energy is deposited in the solid. Even for very high values of K_{a2} (or β_2), in depth absorption can have a significant effect on the response. Strand *et al.* used carbon black as an opacifier in the binder and reported that there was little effect on R_q.¹⁸ They concluded that the CO₂ laser energy was essentially surface absorption. However, considering that there was significant data scatter and that the opacifier is distributed in only the binder and not in the AP crystals, there is still uncertainty. Preliminary measurements were made of the absorption coefficient to determine the order of magnitude. Thin slices of propellant were prepared and the transmission measured with an FTIR. Thin uniform slices were difficult to prepare using the cutters available, decreasing our confidence in the results. HTPB binder 10 to 50 μm thick was cured on the surface of KBr crystals and the transmission was measured. Values for K_{a2} were calculated using the equation $K_{a2} = -\ln(\tau)/l$, where τ is the transmission fraction and l is the sample thickness in cm. Table 2 lists the preliminary measurements and the estimated uncertainties of these measurements. The 10.6 μm band was overlapped by adjacent absorbing peaks in the FTIR. Repeating the measurements with a CO₂ laser would increase the accuracy.

Table 2. Absorption Coefficient Measurements

Material	Thickness (cm)	Transmission fraction	K _{a2} at 10.6 μm (cm ⁻¹)
N5	0.02 \pm .01	0.11	110
A13	0.039 \pm .02	0.084	64
HTPB	.0013 \pm 0.0003	0.4	705
HTPB	.0050 \pm 0.0005	0.3	240
HTPB with 0.4 carbon black	.0045 \pm 0.0005	0.25	308

If the measured value of the absorption coefficient is used, the gas phase controlled models showed very little response. The absorption coefficients used in the calculations were 150, 3000, and 4000 cm⁻¹ for N5, A13, and NWR11, respectively. These values for A13 and NWR11 are much greater than the preliminary measured values by about an order of magnitude. A much higher value of absorption coefficient (about 2000 cm⁻¹) can be estimated from measured optical properties of pure AP, but this seems to contradict the low measured values. However, if the binder is relatively translucent, these two values may be reconciled by considering scattering. Further, it is possible that a melt layer on the surface or a crystalline phase change occurring during combustion, could result in a surface with very different optical properties. Further experimental work will be done measuring the optical properties more accurately.

Steady state results

To understand the unsteady combustion, the steady-state conditions must first be well characterized. To measure the mean mass flux as a function of radiant energy, samples of approximately 2 cm in length were irradiated with a steady heat flux. The mass loss is superimposed on the force signal and was converted to mass flux using Eqn. 18. For cylindrical samples:

$$r = \frac{-4}{\rho_s g \pi D^2} \frac{df}{dt} \quad (18)$$

The resulting steady-state profiles for the mean burn rate as a function of incident radiant flux are shown in Fig. 4. N5, the double-base propellant shows a much higher sensitivity to the radiant heat flux, especially below 2 cal/cm²/s. Of course, n_q (by definition the value of R_q at zero frequency) could be calculated from the mean burn rate data, using Eqn. 19.

$$n_q = \frac{dm}{dq_{r2}} \frac{\bar{q}_{r2}}{\bar{m}} \quad (19)$$

Unfortunately, uncertainties in the steady state burn rate data from Fig. 4 make this calculation of questionable value. Additional steady-state burn rate data will be obtained in future testing.

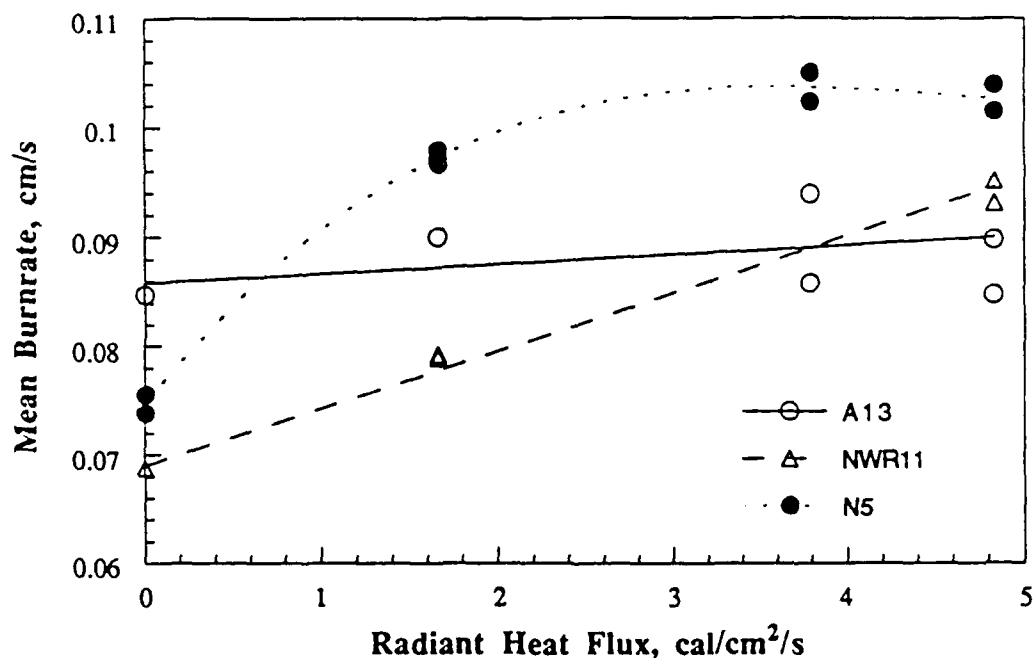


Figure 4 Mean Burn Rate as a Function of Incident Radiant Flux.

Nonsteady Results

In this section the measured response functions of N5, A13, and NWR11 are presented and compared with analytical results. Even though A13 and NWR11 are composite propellants it is reasonable to apply a homogeneous model at low pressures. At low pressures the flame standoff distance and the molecular diffusivities are large enough for nearly complete mixing to occur. At higher pressures, it is likely that flame descriptions will require a more complex structure to be included.

Experimental data for the N5 propellant is shown in Fig. 5. The oscillating thrust is shown in Fig. 5a as a function of f versus frequency for heat fluxes of 45.2 ± 8.9 , 22.5 ± 8.9 , and 4.7 ± 2.4 cal/cm²/s. The 0.64 cm diameter N5 resonated at 60 to 90 Hz ($\bar{f} = 0.22$ cm/s), while the 1.27 cm diameter integrated beam samples ($\bar{f} = 0.12$ cm/s) had a resonant peak at 20 to 30 Hz. The frequency can be converted to nondimensional frequency, $\Omega = 2\pi f k_s/\bar{r}^2$, where $k_s = 0.00041$ cm/s, the condensed phase thermal conductivity. When plotted versus non-dimensional frequency in Fig. 5b, the resonance peaks are at 7 to 10 as expected from T-burner experience and theory. The response function of N5 has a peak value at resonance that is 3 to 4 times larger than the value at high frequencies and 1.5 times larger than the zero frequency value. The force data was converted to mass flux using equation 5 and the data in Table 1. The mass flux oscillation data is plotted in Fig. 5c and 5d vs frequency and Ω . The phase lead versus frequency data is shown in 5e. A distinct phase lead is evident below the resonant frequency. At the resonant peak, the phase crosses from lead to lag, and then approaches a lag of 80 degrees at higher frequencies. Notice that the phase crosses from lead to lag at the same frequency as the resonant peak in the f plot. When plotted versus dimensionless frequency in 5f the data set converges to one resonant frequency as expected from theory.

At low pressure the solid phase would likely be the controlling reaction layer. Calculations of the response function magnitudes, R_p , R_q , and phase lead were made using the distributed flame model (solid phase controlled). The magnitudes were normalized by an estimated n_q and are compared with the data in Fig. 6. The input values used in the calculations are shown in Table 3. Some of the model inputs are quite uncertain (eg. E_s , E_f , and Q_f) such that these parameters could be adjusted until an optimal agreement was reached; however, that was not done in this study. The model shows that an increase in mean radiant flux tends to decrease the resonant peak. This trend is also shown by the data. Of the two data sets with heat flux oscillations of $8.9 \text{ cal/cm}^2/\text{s}$, the one with a smaller mean heat flux, $22.5 \text{ cal/cm}^2/\text{s}$, has higher amplitude resonant peak. The absorption coefficient of N5 (approximately 150 cm^{-1}) is low enough that much of the radiant energy is absorbed below the reaction layer, such that even for a fairly low mean heat flux the normalized R_p is slightly higher in magnitude than the calculated R_q , as shown in Fig. 6a. The calculated phase difference shown in Fig. 6b, also compares fairly well with the data.

Table 3. Inputs for Model Calculations. A, B, P's, β_2 , H & E are calculated values.
 q denotes value with external radiant flux.

	N5	N5	N5	NWR11 cold	warm	A13	A13	A13
$\alpha_c [\text{cm}^2/\text{s}]$:	0.001	0.001	0.001	0.001	0.001	0.001	0.001	0.001
qr_2 :	4.74	22.5	45.2	4.3	4.3	4.1	4.7	42.5
$\bar{r} [\text{cm/s}]$:	0.09	0.09	0.09	0.07	0.07	0.09	0.09	0.09
$\bar{r}_q [\text{cm/s}]$:	0.12	0.20	0.22	0.095	0.095	0.1	0.1	0.1
f_2 :	0.9619	0.9724	0.9691	0.1638	0.1638	0.1030	0.1030	0.09510
β_2 :	1.25	0.75	0.682	31.6	31.6	40.	40.	40.
L_F :	1.0	1.0	1.0	1.0	1.0	1.0	1.0	1.0
$K_{a2} [\text{cm}^{-1}]$:	150.	150.	150.	3000.	3000.	4000.	4000.	4000.
$T_s [\text{K}]$:	600.	600.	600.	850.	850.	850.	850.	850.
$T_{sq} [\text{K}]$:	625.	750.	925.	865.	865.	858.	858.	888.
$T_f [\text{K}]$:	1450.	1450.	1450.	2653.	2653.	2082.	2082.	2082.
$T_{f,q} [\text{K}]$:	1511.	1613.	1741.	2730.	2730.	2148.	2157.	2761.
$T_i [\text{K}]$:	300.	300.	300.	203.	300.	300.	300.	300.
$Q_{bars} [\text{cal/g}]$:	60.	60.	60.	160.	160.	95.	95.	95.
$Q_f [\text{cal/g}]$:	383.8	377.0	368.8	684.6	652.6	579.3	579.3	579.3
$E_s [\text{cal/gmole}]$:	40000.	40000.	40000.	30000.	30000.	30000.	30000.	30000.
$E_f [\text{cal/gmole}]$:				40000.	40000.	30000.	30000.	30000.
$C [\text{cal/gmole}]$:	0.35	0.35	0.35	0.33	0.33	0.33	0.33	0.33
$C_p [\text{cal/gmole}]$:	0.40	0.40	0.40	0.35	0.35	0.40	0.40	0.40
$\rho_c [\text{g/cm}^3]$:	1.55	1.55	1.55	1.70	1.70	1.58	1.58	1.58
α_{fs} :	0.0	0.0	0.0	0.0	0.0	0.0	0.0	0.0
A :	16.77	16.77	16.77	8.438	6.967	7.156	7.156	7.074
A_q :	16.75	16.10	14.70	8.614	7.122	7.257	7.267	7.832
B :	0.9253	0.9253	0.9253	0.7506	0.8830	0.8156	0.8156	0.8156
B_q :	0.7893	0.8482	0.9232	0.8725	1.026	0.9566	0.9772	2.201
H :	0.5714	0.5714	0.5714					
H_q :	0.5275	0.3810	0.2743					
E :	33.55	33.55	33.55					
E_q :	32.21	26.84	21.76					
P_1 :				-0.3680	-0.4801	-0.3965	-0.3965	-0.3493
P_{1q} :				-0.3833	-0.4953	-0.4059	-0.4073	-0.4366
P_2 :				22.17	21.54	22.12	22.12	21.86
P_{2q} :				22.06	21.47	22.06	22.05	21.29
P_3 :				0.09021	0.09287	0.0904	0.09043	0.09148
P_{3q} :				0.08885	0.09171	0.08961	0.08950	0.08454
HR:				647.0	647.0	592.8	592.8	592.8

Experimental data for the A13 propellant is shown in Fig. 7. The oscillating thrust is shown in Fig. 7a as a function of f versus frequency for heat fluxes of 43 ± 21 , 4.7 ± 1.7 , and $4.0 \pm 2.0 \text{ cal/cm}^2/\text{s}$. Notice that the f magnitude did not decrease at the low frequencies as expected. Therefore using the f plot alone it is difficult to determine the frequency of the resonant peak. The mass flux oscillation data is plotted in Fig. 7c and 7d vs frequency and Ω . The phase lead versus frequency data is shown in 5e. The phase crosses from lead to lag at a frequency of 10 to 20 Hz and then approaches a lag of 60 degrees at higher frequencies. When plotted versus dimensionless frequency in 7f the data set converge to one resonant frequency as expected from theory. Both the 0.64 cm diameter A13 ($\bar{r} = 0.15 \text{ cm/s}$) and the 1.27 cm diameter integrated beam samples ($\bar{r} = 0.10 \text{ cm/s}$) have a resonant peak near 10 to 20 Hz. When plotted versus non-dimensional frequency in Fig. 7b, the resonance peaks are at 3 to 7, a little lower than the nominal 10 as expected from T-burner experience and theory.

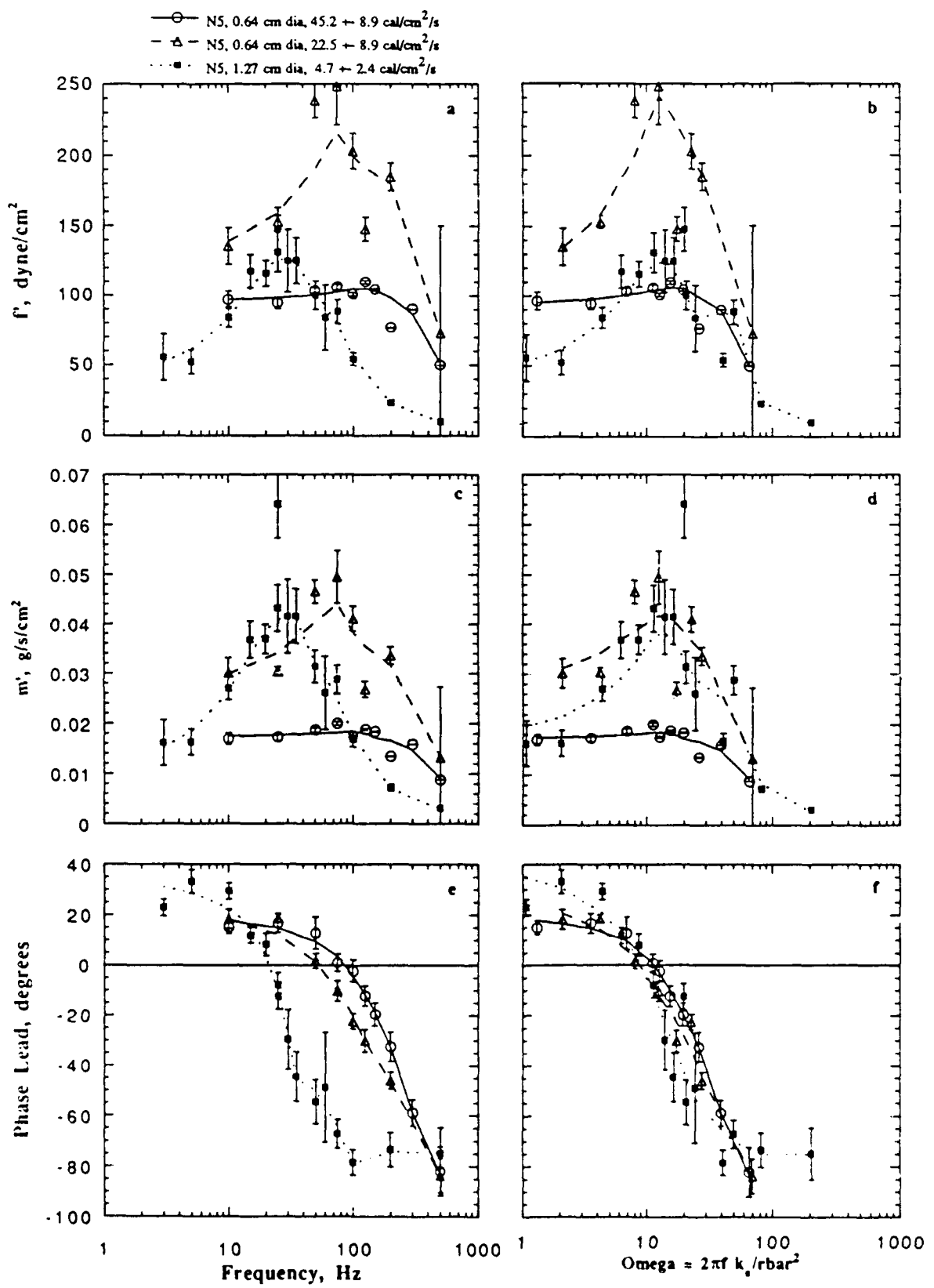


Figure 5. Experimental data for N5 propellant with heat fluxes of 45.2 ± 8.9 , 22.5 ± 8.9 , and $4.7 \pm 2.4 \text{ cal/cm}^2/\text{s}$. a) f' vs f , b) f' vs Ω , c) m' vs f , d) m' vs Ω , e) Phase lead vs f , f) Phase lag vs Ω .

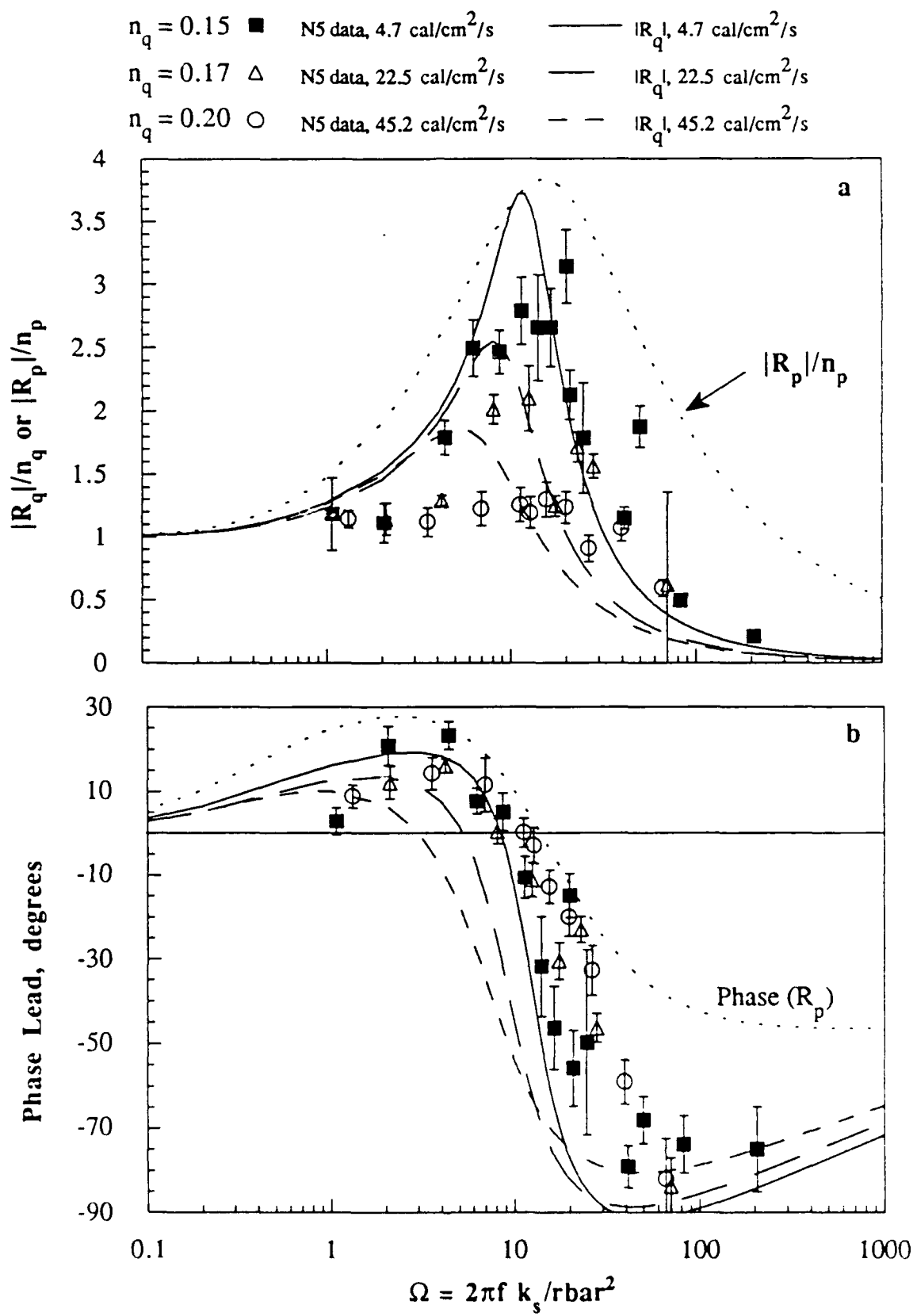


Figure 6. Comparison of N5 Combustion Response Data with Distributed Flame Model Calculations. a) $|R_q|/n_q$ vs Ω , b) Phase Lead (R_q) vs Ω .

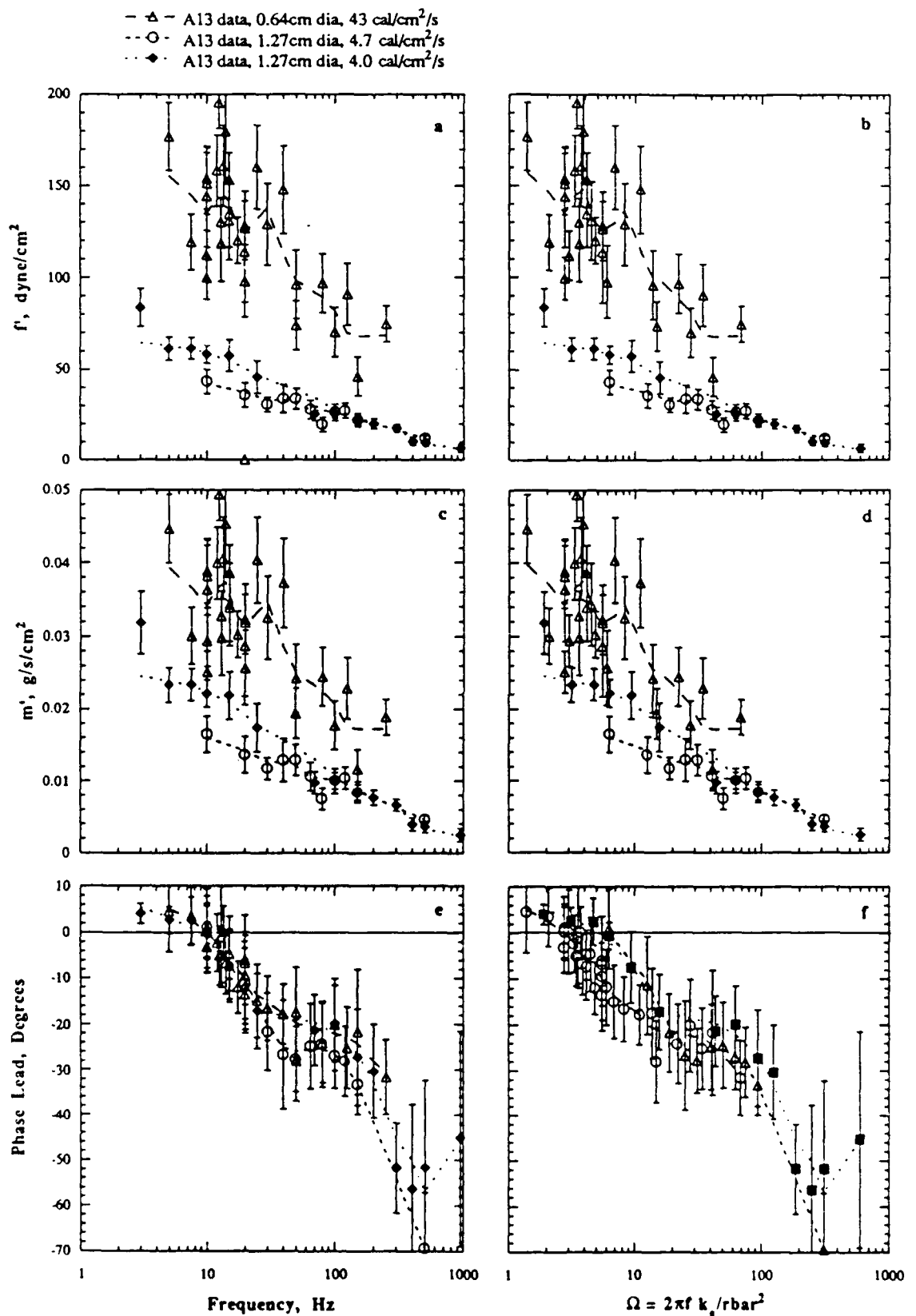


Figure 7. Experimental Data for A13 Propellant with Heat Fluxes of 4.0 ± 2.0 , 4.7 ± 1.7 , and 43 ± 21 cal/cm²/s. a) f' vs f , b) f' vs Ω , c) m' vs f , d) m' vs Ω , e) Phase lead vs f , f) Phase lag vs Ω .

Calculations of the response function magnitudes, R_p , R_q , and phase lead were made using the Ibiricu and Williams (asymptotic) flame description model. The magnitudes were normalized by an estimated n_q and are compared with the A13 data in Fig. 8. The input values used in the calculations are shown in Table 3. This model also shows that an increase in mean radiant flux tends to decrease the resonant peak, which agrees with the data. The model agrees well with the magnitude of the 4.7 and 43 cal/cm²/s data. Again the normalized R_p is slightly higher in magnitude than the calculated R_q , as shown in Fig. 8a. The two data sets with heat fluxes of 4.0 and 4.7 cal/cm²/s should have more similar magnitudes as seen from the Fig. 7a. The A13 phase lead data is compared with the Ibiricu and Williams (asymptotic) flame description model in Fig. 8b. The model predicts a larger phase lead below the resonant peak, but has a similar phase lag at high frequencies. Again the agreement is encouraging considering the unknowns in several model input parameters.

It was decided to study the effect of propellant conditioning temperature using NWR11 samples. One set of samples were placed in a styrofoam cup with dry ice in the freezer overnight, the other set was conditioned at room temperature. Both samples were tested on the same day with heat fluxes of 4.3 ± 2.1 cal/cm²/s. Experimental data for the NWR11 propellant is shown in Fig. 9. The oscillating thrust is shown in Fig. 9a as a function of f versus frequency. The magnitude of the NWR11 f oscillations is significantly smaller than for N5 and A13. There does not appear to be a significant difference in f between the two different conditioning temperatures. It could be that the samples warmed up in the few minutes that they were being prepared for combustion. Again the f magnitude did not decrease significantly at the low frequencies as expected and using the f plot alone it is difficult to determine the frequency of the resonant peak. The mass flux oscillation data is plotted in Fig. 9c and 9d vs frequency and Ω . The phase lead versus frequency data is shown in 9e. The phase crosses from lead to lag at a frequency of 20 Hz and then approaches a lag of 110 degrees at higher frequencies. When plotted versus Ω in 9f the resonant frequency is at a value of 10 as expected from T-burner experience.

Calculations of the response function magnitudes, R_p , R_q , and phase lead were made using the Ibiricu and Williams (asymptotic) flame description model. The magnitudes were normalized by an estimated $n_q = 0.012$ and are compared with the NWR11 data in Fig. 10. The value of n_q is much smaller than that used to normalize the N5 and A13 data. Qualitative agreement with the data is achieved. This model predicts that a decrease in propellant initial temperature increases the magnitude of the resonant peak. Again the normalized R_p is slightly higher in magnitude than the calculated R_q , as shown in Fig. 10a. The NWR11 phase lead data is compared with the Ibiricu and Williams (asymptotic) flame description model in Fig. 10b. This time the data has a larger phase lead at low frequencies than the model. A more sensitive propellant should be selected to measure the effect of initial temperature, i.e. fine oxidizer AP composite or double base.

CONCLUSIONS

Propellant samples are mounted on a Kistler 9207 force transducer which measures the thrust oscillations. The 150W CO₂ laser is easily modulated by a signal generator to provide a sine wave radiant heat flux. Beam integration plus increased sample size have reduced the data scatter from earlier attempts. The Silicon Graphics workstation allows for speedy data acquisition and analysis. Nine propellants of type double base, smokeless composite, and metallized composite have been tested at atmospheric pressure surrounded by room temperature air. Unfortunately, the laser energy is scattered by burning metal particles and smoke in the plume of highly metallized propellants. Special techniques for deflecting the plume or increasing the laser power will be necessary to measure the response of metallized propellants. The latest experimental results and corresponding analyses were presented for three of the propellants tested: N5 (double base), A13 (PBAN, AP), and NWR11 (HTPB, AP, minimum smoke). The samples were tested at surface heat fluxes ranging from 4 to 49 cal/s/cm². When plotted versus nondimensional frequency the resonant peaks were near $\Omega = 10$ as expected. The phase difference between the laser and the thrust was calculated using a cross correlation. Many cycles were analyzed from each test and averaged to reduce data scatter. By performing the tests at many frequencies the radiant heat flux response function was determined.

Three different models were considered: (1) condensed phase controlled distributed flame,^{20,22} (2) gas phase controlled sharp flame model,^{5-7,23} and (3) gas phase controlled, high activation energy asymptotics flame description.^{24,25} It was shown that for the distributed flame model with high surface absorption ($f_2 \rightarrow 0$) and small mean radiant flux ($\bar{q}_{r2} \rightarrow 0$), the transfer function (R_p/R_q) would reduce to n_p/n_q . Similar results were shown for the Ibiricu and Williams asymptotic flame model. The N5 was compared to the distributed flame model while A13 and NWR11 were compared to the asymptotic flame description model.

The initial objectives of this work were to improve upon the work of Mihlfeith and Zarko, *et al.* using a microforce transducer for direct measurement of propellant response function to radiant energy. At atmospheric pressure the microforce transducer method seems to allow the propellant response to be obtained faster and therefore less expensively than other methods. However, a correlation between the heat flux response and the more theoretically useful pressure response remains to be validated. The technique appears to show promise as a tool for characterizing propellant combustion stability as well as providing further understanding about combustion instability fundamentals. To become more directly useful, however, higher pressure capability will be added. Additional measurements also need to be made of the propellant optical and physical properties.

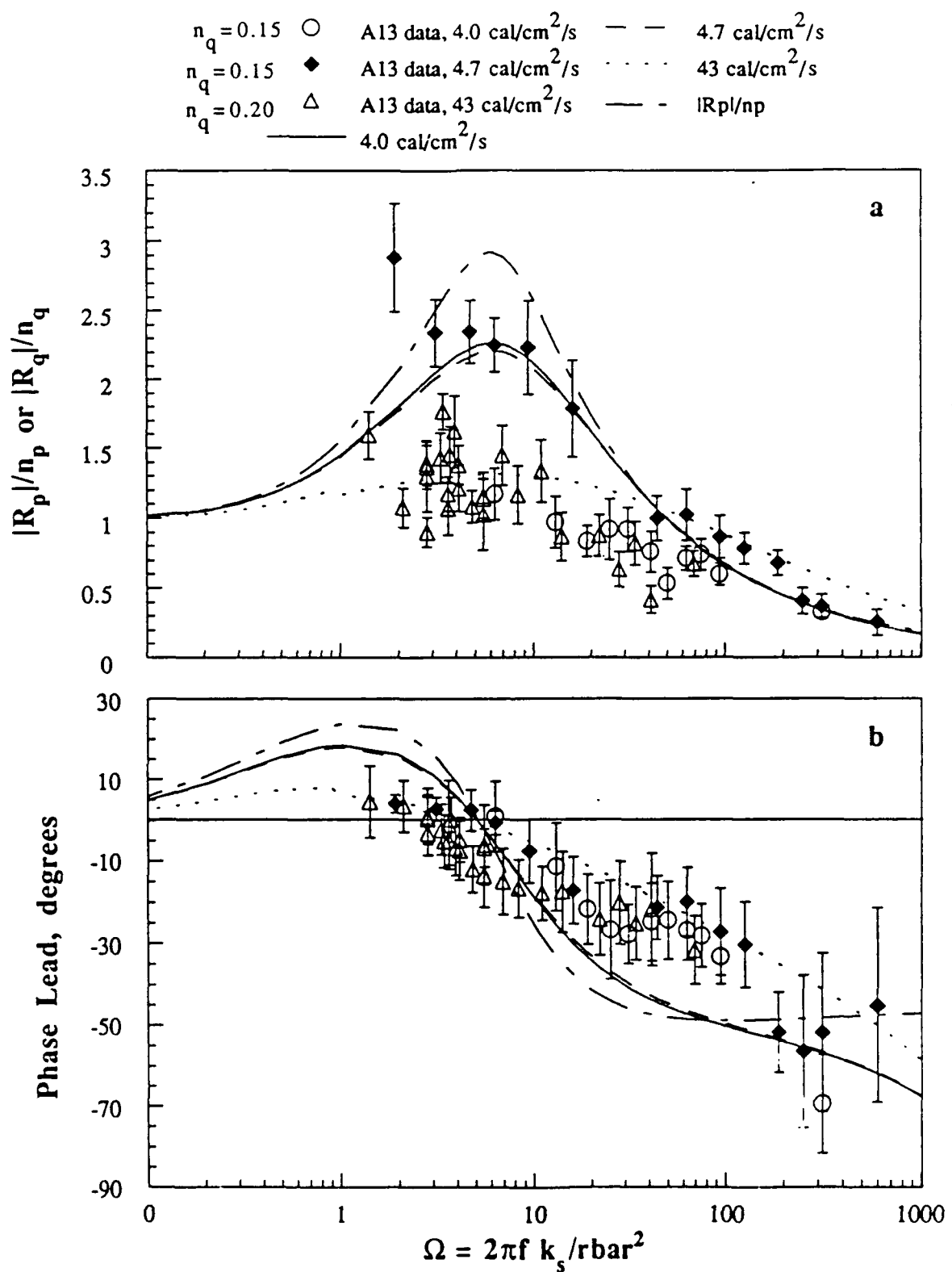


Figure 8. Comparison of A13 Combustion Response Data with Ibiricu and Williams (Asymptotic) Flame Description Model Calculations. a) $|R_q|/n_q$ vs Ω , b) Phase Lead (R_q) vs Ω .

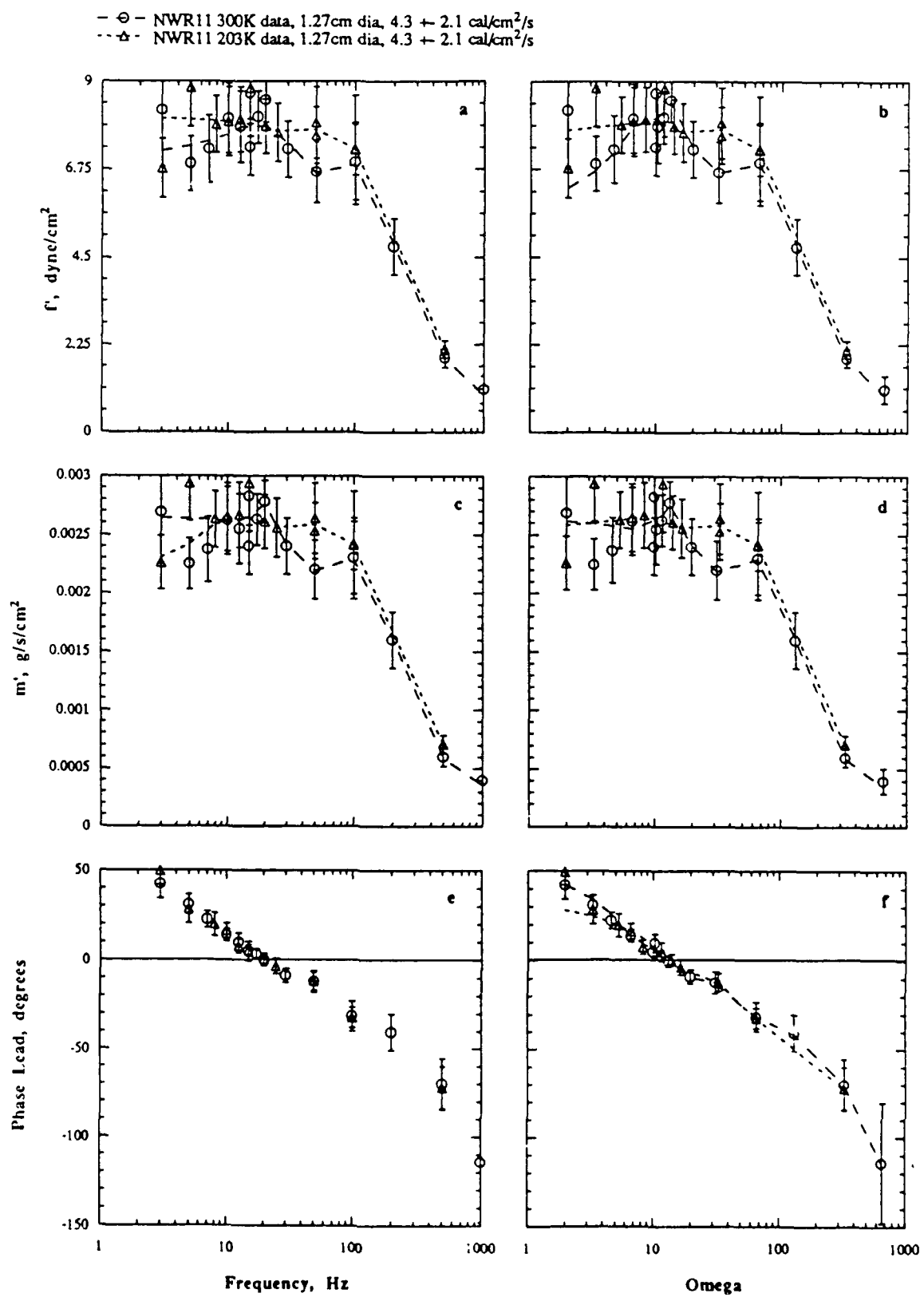


Figure 9. Experimental Data for NWR11 Propellant with Heat Flux of $4.3 \pm 2.1 \text{ cal/cm}^2/\text{s}$. a) f' vs f , b) f' vs Ω , c) m' vs f , d) m' vs Ω , e) Phase lead vs f , f) Phase lag vs Ω .

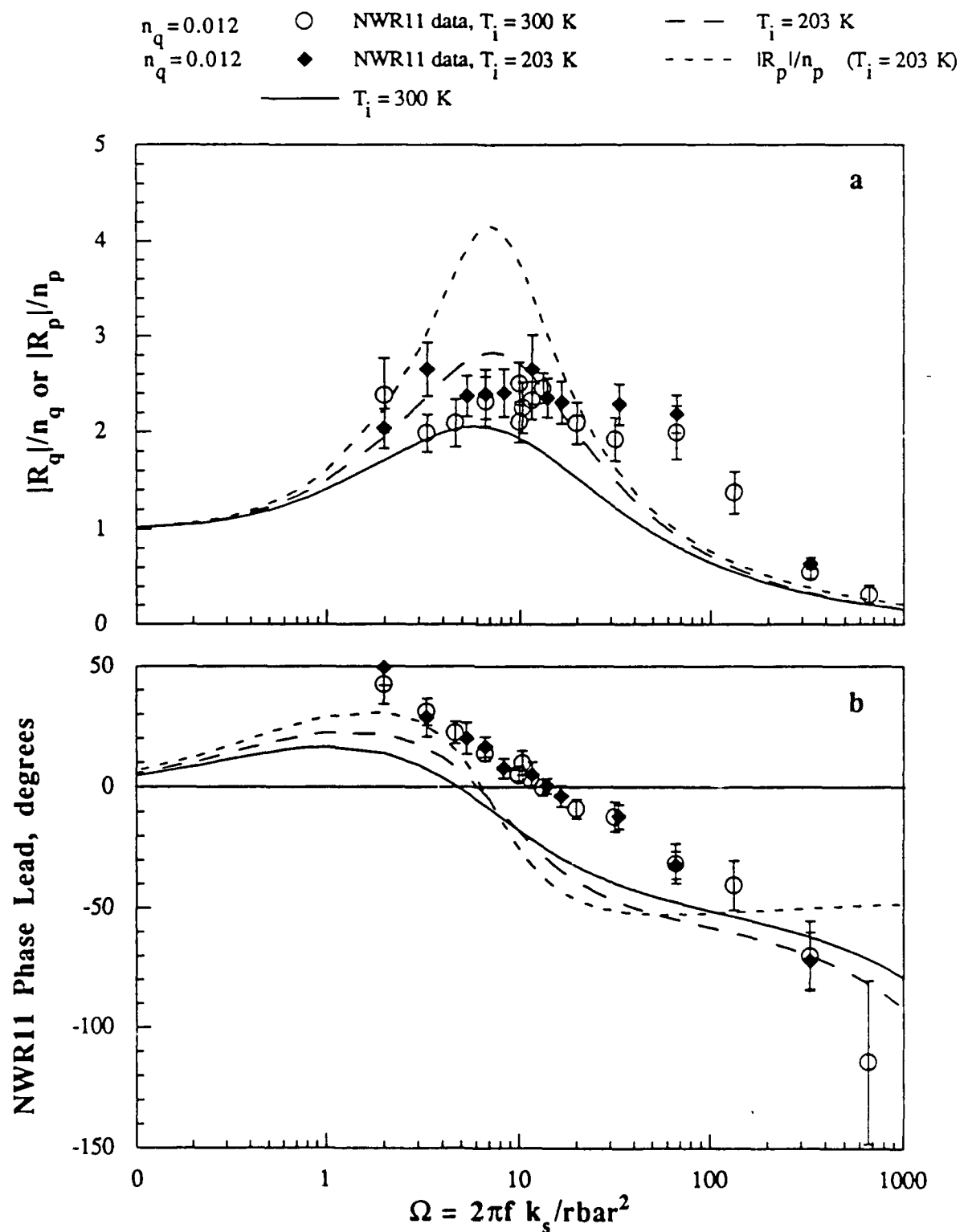


Figure 10. Comparison of NWR11 Combustion Response Data with Ibiricu and Williams Flame (Asymptotic) Description Model Calculations. a) $|R_q|/n_q$ vs Ω , b) Phase Lead (R_q) vs Ω .

ACKNOWLEDGMENTS

Thanks to Richard Stelnaker for machining work on the apparatus, Phil Archibald for performing the reflectivity measurements, and Mel Nadler for the FTIR absorption coefficient measurements. This work was supported in part by the Naval Weapons Center, the Office of Naval Research (N00014-87-k-0547) Dr. R. S. Miller (contract monitor), and the National Science Foundation (CBT86-96162).

NOMENCLATURE

(⁻) denotes steady state values and ([']) denotes perturbed values
 q denotes properties related to radiant heat flux

A_c	cross sectional area of propellant sample
A	constant in R_p and R_q expressions
B	constant in R_p and R_q expressions
C_p	specific heat of gas phase
C	specific heat of condensed phase
E_f, E_s	gas and condensed phase reaction activation energy
E	$E_s/R T_s + \alpha_s$, nondimensional activation energy
f	frequency, Hz
F	force oscillations, dynes/cm ²
f_2	fraction of radiant energy absorbed below reaction layer
F	$E_f/2RT_f - C_p T_f/2[Q_f - C_p(T_f - T_s)]$
G	$C_p T_s/2[Q_f - C_p(T_f - T_s)]$
H	$Q/C(T_s - T_i)$, surface heat release
H_R	heat released in surface reactions - does not include latent heat
K_s	absorption coefficient in Beer's Law
k_s	thermal conductivity of gas phase
k_s	thermal conductivity of condensed phase, = 0.00041 cm/s
L_f	correction factor in f_2 expression = 1.0
m	mass burning rate, g/s/cm ²
n_p	zero frequency value of the pressure response function
n_q	zero frequency value of the heat flux response function
P	pressure
Q_f	heat release from the gas-phase reactions (greater than 0 is exothermic)
q_{11}	natural feedback radiant heat flux (e.g., metallized propellants)
q_{12}	induced external radiant heat flux (e.g., laser)
Q_s	combined latent heat and heat released in surface reactions (greater than 0 is exothermic)
Q_R	nondimensional heat flux
P_1, P_2, P_3	nondimensional constants
R_p, R_q	pressure and heat flux response function
R	universal gas constant
T_f	flame temperature, K
T_i	temperature deep within the solid (conditioning temperature), K
T_s	temperature at solid surface, K
TF	complex valued transfer function, R_p/R_q
X_s	absorption length scale (1/ K_s)
X_d	thermal length scale (k_s/mC)
X_R	solid phase reaction length scale ($X_d RT_s/E_s$)
α_c	condensed phase thermal diffusivity, cm ² /s
α_s	temperature exponent in Arrhenius expression
β	ratio of thermal length scale to radiant length scale ($K_s k_s/mC$)
γ	flame heat release pressure sensitivity exponent
λ	characteristic of solid phase temperature solution ($1/2 + \sqrt{1/4 + i\Omega}$)
Λ	eigenvalue, see ref. 20
ν_1	pressure exponent in gas phase mass burning rate equation
ρ, ρ_g	condensed phase density, gas phase density
ϕ	temperature gradient
ω	frequency, radians/s
Ω	dimensionless frequency ($\rho k_s \omega / C m^2$) = $2\pi f k_s / r^2$

REFERENCES

1. Culick, F. E. C., Combustion Instability in Solid Rocket Motors, Volume II: A Guide for Motor Designers, CPIA Publ. No. 290, January 1981.
2. Strand, L. D., Schwartz, K., and Burns, S. P., "Propellant Combustion Response to Oscillatory Heat Flux". 24th JANNAF Combustion Meeting, CPIA Publ. No. 476, Vol. 1, Oct. 1987, pp. 41-50.
3. Wilson, J. R., and Micci, M. M., "Direct Measurement of High Frequency Solid Propellant Response Functions", 20th JANNAF Combustion Meeting, Vol. I, CPIA Publ. No. 383, Oct. 1983, pp. 193-202
4. Brown, R.S., Torikai, T., Babcock, W. R., "Combustion Response Function Measurements by the Rotating Valve Method," *AIAA Journal*, Vol. 12, Nov. 1974, pp. 1502-1510.
5. Mihlfeith, C. M., Baer, A. D., and Ryan, N. W., "Propellant Combustion Instability as Measured by Combustion Recoil," *AIAA Journal*, Vol. 10, No. 10, Oct. 1972, pp. 1280-1285.
6. Mihlfeith, C. M., "Some Experiments on the Effect of Thermal Radiation on Composite Rocket Propellants," Ph.D. Thesis, University of Utah, Salt Lake City, Utah, 1971.
7. Mihlfeith, C. M., Baer, A. D., and Ryan, N. W., "The Direct Measurement of the Radiant Heat Flux Response Function of Solid Propellants", 8th JANNAF Combustion Meeting, CPIA Publ. 220, Vol. 1, Nov. 1971, pp. 259-275.
8. V. E. Zarko, V. N. Simonenko, and A. B. Kiskin, "Nonstationary Combustion of Condensed Substances Subjected to Radiation," *Fiz. Gorenija Vzryva*, Vol. 23, No. 5, (Oct. 1987)
9. V. N. Simonenko, V. E. Zarko, and K. P. Kutsenogii, "Experimental Study of the Conditions for Auto- and Forced Fluctuations of the Rate of Combustion of a Powder", *Fiz. Gorenija Vzryva*, Vol. 16, No. 3, pp. 60-68 (June 1980)
10. V. E. Zarko, V. N. Simonenko, and K. P. Kutsenogii, "Effects of Light Intensity on the Nonstationary Combustion Rate in a Transient Process", *Fiz. Gorenija Vzryva*, Vol. 11, No. 4, pp. 541-548, (Aug. 1975)
11. T. J. Ohlemiller, L. H. Caveny, L. DeLuca, and M. Summerfield, "Dynamic Effects on Ignitability Limits of Solid Propellants Subjected to Radiative Heating", 14th Symposium (International) on Combustion, pp. 1297-1307, (Aug 1972)
12. V. F. Mikheev and S. M. Borin, "Measurement of the Mass Combustion Rate of Solid Explosives", *Fiz. Gorenija Vzryva*, Vol. 9, No. 2, pp. 327-329, (April 1973)
13. A. V. Khudyakov, G. V. Gorvard, E. V. Konev, and V. F. Mikheev, "Measuring the Mass Burning Rate of Solid Explosives", Brief Communication *Fiz. Gorenija Vzryva*, Vol. 3, No. 3, pp. 462-464, (1967)
14. DeLuca, L., "Frequency Response Function of Burning Solid Propellants", *Meccanica: Journal of the Italian Association of Theoretical and Applied Mechanics*, Dec 1980 p. 195-205
15. V. E. Zarko and A. B. Kiskin, "Numerical Modeling of Nonsteady Powder Combustion Under the Action of a Light Flux", *Fiz. Gorenija Vzryva*, Vol. 16, No. 6, pp. 54-59 (Dec 1980)
16. Prevish, T. D., and Brewster, M. Q., "Combustion Response of a Homogeneous Solid Propellant to an Oscillatory Radiant Heat Flux", Western States Section/The Combustion Institute, March 1989.
17. Prevish, T. D., and Brewster, M. Q., "Combustion Response of a Homogeneous Solid Propellant to Oscillatory Radiant Heat Flux", 26th JANNAF Combustion Meeting, CPIA, Oct. 1989.
18. Strand, L., Weil, M., and N. Cohen, "Solid Propellant Combustion Response to Oscillatory Radiant Heat Flux," AIAA 89-2667, AIAA/ASME/SAE/ASEE 25th Joint Propulsion Conference, 1989.
19. Son, S. F., Prevish, T. D., Brewster, M. Q., Finlinson, J. C., and D. Hanson-Parr, "Radiant Heat Flux Response of Solid Propellants", to be submitted to the *Journal of Propulsion and Power*, 1990.
20. Culick, F. E. C., Some Problems in the Unsteady Burning of Solid Propellants, NWC TP 4668, China Lake, CA: U. S. Naval Weapons Center, 1968.

21. Finlinson, J. C., Hanson-Parr, D., Parr, T., and Mathes, H. B., "Measurement of Propellant Combustion Response to Oscillatory Radiant Heat Flux", 26th JANNAF Combustion Meeting, CPIA, Oct 1989.
22. Krier, H., Tien, J. S., Sirignano, W. A., and M. Summerfield, "Nonsteady Burning Phenomena of Solid Propellants: Theory and Experiment," *AIAA J.*, Vol. 6, No. 2, pp. 278-85, 1968.
23. Culick, F. E. C. "A Review of Calculations of the Admittance Function for a Burning Surface. Appendix A." NWC TP 4244, China Lake, CA: U. S. Naval Weapons Center, 1967.
24. Williams, F. A., "Quasi-Steady Gas-Phase Flame Theory in Unsteady Burning of a Homogeneous Solid Propellant," *AIAA J.*, Vol. 11, No. 9, pp. 1328-30, 1973.
25. Ibiricu, M. M., and F. A. Williams, "Influence of Externally Applied Thermal Radiation on the Burning Rates of Homogeneous Solid Propellants," *Comb. and Flame*, Vol. 24, pp. 185-98, 1975.
26. Ishihara, A., Brewster, M. Q., Sheridan, T. A., and H. Krier, "The Influence of Radiative Heat Feedback on the Burning rate in Metallized Propellants," *Comb. and Flame*, accepted for publication, 1990.
27. Ludwig, C. B., Malkmus, W., Reardon, J. E., and Thomson, J. A. L., Handbook of Infrared Radiation from Combustion Gases, NASA SP-3080, Ed. R. Goulard and J. A. L. Thomson, available from NTIS, Publ. No. N7327807, 1973. -
28. Grosshandler, W. L., "Radiative Heat Transfer in Non-Homogeneous Gases: A Simplified Approach," *Int. J. Heat and Mass Trans.*, Vol. 23, pp. 1447-59, 1980.



AIAA-91-0204

Measurement of Propellant Combustion Response to Sinusoidal Radiant Heat Flux

**J. C. Finlinson and D. Hanson-Parr;
Research Department, Naval Weapons Center,
China Lake, CA 93555-6001**

**S. F. Son and M. Q. Brewster;
Department of Mechanical and Industrial Engineering,
University of Illinois at Urbana-Champaign,
Urbana, Illinois**

29th Aerospace Sciences Meeting

January 7-10, 1991/Reno, Nevada

MEASUREMENT OF PROPELLANT COMBUSTION RESPONSE TO SINUSOIDAL RADIANT HEAT FLUX

J. C. Finlinson* and D. Hanson-Parr**
Naval Weapons Center,
China Lake, CA

S. F. Sont† and M. Q. Brewster††
Department of Mechanical and Industrial Engineering
University of Illinois at Urbana-Champaign,
Urbana, Illinois

ABSTRACT

Experimental and theoretical work to determine the combustion response function of solid propellants using a sinusoidal heat flux and a microforce transducer is reported. Response data for N5, A13, and NWR11 propellants are presented. The experimental work improves upon Mihlfeith's experiment (1971) by using an integrated CO₂ laser beam as the source of radiant energy and a digital data acquisition system. The waveform of a laser is more easily controlled than an arc lamp. The phase relation of the imposed heat flux and the propellant thrust signal were determined using a digital cross correlation. The heat flux response, R_q , was measured for three propellants and is compared with theoretical predictions. In agreement with theory, the measured response exhibits a phase lead at non-zero frequencies below the response peak and a phase lag at frequencies above the response peak. The pressure response, R_p , is also calculated. For three models considered the transfer function, R_p/R_q , reduces to the ratio of their zero frequency values, $n_p/n_q = R_p(0)/R_q(0)$, but only if the mean radiant flux is small and the radiation is absorbed at the surface, i.e. the ratio of the thermal length scale to radiant length scale, β , goes to infinity. The effect of in depth absorption on the transfer function is also presented.

INTRODUCTION

The pressure response function, R_p , is a necessary component in the linearized stability analysis of solid rocket motors. The most widely used and accepted experimental method of measuring R_p is the T-burner. The real component of R_p can be determined in a relatively direct manner using the T-burner. However, along with significant uncertainties in data interpretation, the T-burner requires considerable preparation time and typically costs about \$15,000 to generate response function data for a single propellant at one pressure. Clearly, a faster and less expensive method is desirable in order to compare many different propellants and attain a more fundamental understanding of the physical processes involved.

* Chemical Engineer
**Physical Chemist

† Graduate Research Assistant, Student Member AIAA
††Associate Professor of Mechanical Engineering,
Member AIAA

Approved for Public Release; distribution is unlimited.
This paper is declared a work of the U.S. Government and is
not subject to copyright protection in the United States.

For these reasons, experimentalists have endeavored to develop alternate techniques for over two decades.²⁻¹³ Various experimental techniques used to measure the instantaneous burn rate include a microwave device,² a magnetic flux meter,³ and a microforce transducer.⁵⁻¹³ To measure R_p directly a nonsteady pressure field must be imposed and accurately measured. To accomplish this a rotating valve has been used with some success.⁴ Because of its relative simplicity, the microforce transducer method using an imposed heat flux seems to offer the possibility of obtaining the propellant response less expensively than other methods. Further, it is much easier to generate the desired waveshape of heat flux using a laser compared to available pressure modulating techniques. However, a transfer function between the heat flux response, R_q , and the more useful pressure response, R_p , must be developed before this technique will be generally accepted. Theoretical work toward this goal has been attempted by several researchers.¹⁴⁻¹⁹

Previous experimental work to determine the heat flux response, R_q , was reported by Mihlfeith⁵⁻⁷ Strand *et al.*,¹⁸ and Soviet researchers such as Zarko *et al.*⁸⁻¹⁰ Although the microforce transducer/heat-flux technique has shown significant promise, it has not been widely applied to experimental studies in the U.S. since Mihlfeith's work in 1971. Soviet researchers have continued to publish experimental work in this area. Mihlfeith reported a phase lag even at frequencies below the resonance peak probably because of the inaccurate phase measurement techniques available at the time. In a more recent work, Zarko *et al.* reported a phase lead of 10-15° at frequencies below the resonant peak and a phase lag of about 90° at high frequencies, in qualitative agreement with theory.⁸

In this work, the complex valued pressure response function is defined in the usual manner as:

$$R_p = \frac{m'/\bar{m}}{p'/\bar{p}} = \frac{r'/\bar{r}}{p'/\bar{p}} \quad (1)$$

In a similar manner, the complex valued heat flux response, R_q , is defined as:

$$R_q = \frac{m'/\bar{m}}{q'_{r2}/\bar{q}_{r2}} = \frac{r'/\bar{r}}{q'_{r2}/\bar{q}_{r2}} \quad (2)$$

where q'_{r2} is the external heat flux directed on the burning propellant surface.

Culick showed that all models of the pressure response can be written in a common form:²⁰

$$R_p = \frac{n_p AB}{\lambda + A/\lambda - (1+A) + AB} \quad (3)$$

Where A is a constant associated with the thermal wave in the solid and the surface reaction and B depends primarily on the flame description that is employed. It has been assumed that, (1) the problem is 1-dimensional and linear, (2) the solid phase is homogeneous and nonreacting with constant properties, (3) the surface reaction is independent of pressure, and (4) the gas phase responds quasi-statically to pressure changes.

In this study, the use of an integrated CO₂ laser beam as the heat flux source and a digital data acquisition offer improved experimental accuracy over previous studies. The waveform of a laser is easily controlled by a function generator. The objectives of this work are to improve upon the earlier work by using a sensitive microforce transducer and a CO₂ laser for direct measurement of R_q and to develop simple theoretical relationships required to transform the R_q measurements to R_p.

EXPERIMENTAL

Setup

A schematic of the NWC radiant heat flux equipment is shown in Fig. 1. Both vertically and horizontally oriented apparatus were tested previously.²¹ It was determined that the vertically oriented apparatus exhibited less mechanical resonance in the frequency band of interest, consequently this orientation is used in this study. Since the oscillations are less than 10⁻³ N, a very sensitive transducer is required. A Kistler 9207 high-sensitivity quartz force transducer, with natural frequency greater than 10 KHz, is used to measure thrust oscillations. The transducer is mounted inside an aluminum block for thermal isolation. Rubber mounts are used to minimize extraneous vibrations.

The CO₂ laser (10.6 μm, 150W) was modulated sinusoidally by a function generator which controlled the frequency, 3 to 1000 Hz, and amplitude, 10 to 60 W, of the heat flux oscillations. The laser output is not precisely linear with current input; however, over the range of oscillation, the error of assuming linearity on the waveshape is not likely to be a major error. Initially, the beam was used as it came out of the laser with a 0.64 cm diameter and a nearly gaussian energy distribution. Recently, a SPAWR beam integrator has been used to flatten the energy distribution profile of the laser beam. The lens and mirrors required to use the beam integrator are shown in Fig. 1. The beam is expanded using a plano concave lens onto the integrator which refocuses the beam into a square area approximately 1.6 cm². The larger beam allows the use of 1.27 cm diameter samples, which produce larger thrust oscillations than the 0.64 cm diameter samples. The mean heat flux, however, is reduced with the larger diameter beam. The flatter energy profile and the larger diameter samples seem to reduce experimental scatter.

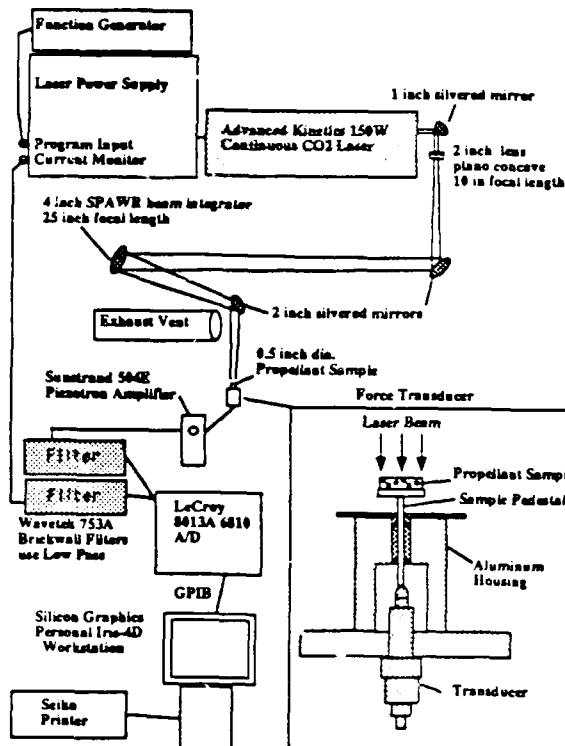


Fig. 1. Schematic of the NWC Radiant Heat Flux Equipment. Showing an enlargement of the sample mounted on a pedestal and the force transducer.

After initial laser calibration the testing time is short. Preparation for each test involves adjusting the frequency on the sine wave generator and the lowpass frequency on the antialiasing filters, and placing a fresh sample on the pedestal. The sample pedestal is removed from the force transducer and a sample is fastened to the surface using silicon grease. Samples are prepared using propellant cutters. For these open atmosphere tests a sample can be tested in less than 5 minutes.

Data Reduction

A data analysis display from the Silicon Graphics workstation is shown in Fig. 2. This test was performed using the 0.64 cm diameter laser beam without integration for NS propellant at 30 Hz and 220 W/cm² = 49 cal/cm²/s. The laser current monitor signal and the force transducer signal are plotted in Fig. 2a. The larger more sinusoidal trace in Fig. 2a is the output of the laser current monitor, which is normalized to 1 in the data reduction. Both signals are filtered with identical filter settings. It is apparent that the thrust trace is slightly leading the laser monitor signal. NS is a mesa burning double base propellant. In the measured thrust traces, the thrust peaks were sometimes flat on top which may be due to the mesa inducing lead additives in NS. For initial theoretical comparisons it would be preferable to use an uncatalyzed double base propellant with a linear pressure dependence, but such a propellant was not readily available at NWC.

Root mean square (rms) values are used for signal amplitudes. Figure 2b shows the force oscillation rms for each cycle. The phase lead was determined by performing a discrete-time cross correlation of the two signals in Fig 2a. The calculated phase lag vs time is plotted in Fig. 2c. The negative phase lag indicates an average phase lead of 16 degrees. To maintain a reasonably constant phase resolution, the sampling rate is increased with the input frequency of the laser. Many cycles are analyzed at each frequency and averaged to reduce data scatter. The standard deviation of the values within one test are indicated by error bars on the plots. By performing similar tests at various frequencies, the magnitude and phase as a function of frequency was measured. This is the response function.

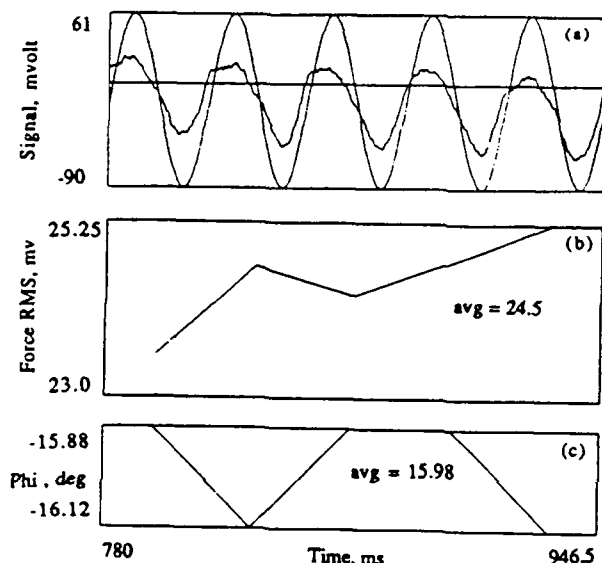


Fig. 2. Data Analysis Display From Silicon Graphics Workstation. a) Laser current monitor signal and the force transducer signal in (mv) vs time (ms). b) Force' rms vs Time, and c) Phase lag versus Time. Test performed using the 0.64 cm diameter laser beam without integration for NS propellant at 30 Hz and $220 \text{ W/cm}^2 = 49 \text{ cal/cm}^2/\text{s}$.

To make quantitative comparisons of the force data with models of R_q or R_p , requires calculation of m'/\bar{m} or r'/\bar{r} , as in Eqn. 1. Applying simple steady state continuity and momentum relations and neglecting the effect of nonsteady changes in the mass of the propellant sample, the thrust measurements, F , can be transformed to mass flux by:⁴⁻⁶

$$m = \sqrt{\frac{M P F}{R T_f A}} \quad (4)$$

The oscillating force data, f' , was converted to mass flux, m' , using Eqn. 5, which is a perturbation of Eqn. 4. The derivation considers only small fluctuations and neglects the small changes in force due to the unsteady decrease in the sample mass in the vertical orientation.⁵⁻⁷

$$m' = \frac{M P f'}{2 \bar{m} R T_f A} \quad (5)$$

Nine propellants of type double base, smokeless composite, and metallized composite have been tested at atmospheric pressure surrounded by room temperature air. Unfortunately, the laser energy is scattered by burning metal particles and smoke in the plume of highly metallized propellants. Special techniques for deflecting the plume or increasing the laser power will be necessary to measure the response of metallized propellants. However, fair agreement with theory was obtained for double base and nonmetallized composite propellants. Zarko *et al.* report similarly that this technique works best for double base and composites containing ultra fine AP, both of which have high magnitude response functions.⁸ In the following, the latest experimental results and corresponding analyses are presented for three of the propellants tested. The three propellants are: NS (double base), A13 (PBAN, AP), and NWR11 (HTPB, AP, minimum smoke). Over 300 samples were tested at surface heat fluxes ranging from 4 to 49 cal/s/cm². The ingredients and physical properties of the three propellants are listed in Table 1.

ANALYSIS

The goal of modeling is to convert heat flux response, R_q , into the pressure coupled response, R_p , required by motor stability programs such as SSP. The complex valued transfer function of interest, R_p/R_q , is labeled TF. It is shown that under certain conditions $TF = n_p/n_q$ the ratio of zero frequency pressure response to heat flux response. However, when those conditions are not valid, then a model is required to calculate the transfer function, TF. In this initial effort we were uncertain which model would be most appropriate. Three different propellant flame models developed by prior researchers were put into the standard R_p form developed by Culick²⁰ and the corresponding R_q form. The models considered are: (1) condensed phase controlled distributed flame (KTSS),^{20,22} (2) gas phase controlled sharp flame model (Mihlfeith),^{5-7,23} and (3) gas phase controlled, high activation energy asymptotics flame description (Ibiricu and Williams).^{24,25} The models were modified in the same manner to include radiant heat flux. The expressions for R_p are developed assuming that the problem is 1-dimensional and linear, the condensed phase below the surface is homogeneous and nonreacting with constant properties, the surface reaction is independent of pressure, and the gas phase responds quasi-statically to pressure changes. Further, for the R_q expressions it is assumed that scattering is negligible, the absorption coefficient in the condensed phase (K_{a2}) is spatially constant, the thermal emission by the condensed phase is negligible, the incident flux is collimated, and that the fraction of radiant energy absorbed in the reaction layer can be collapsed to an infinitely thin surface layer (with the reaction layer).

Solid Phase

The solid phase is assumed to be nonreacting. The unsteady energy equation in the solid phase, with in-depth absorption is:

$$\rho C \frac{\partial T}{\partial t} + m C \frac{\partial T}{\partial x} = k_s \frac{\partial^2 T}{\partial x^2} + f_1 q_{r1} K_{a1} \exp(K_{a1} x) + f_2 q_{r2} K_{a2} \exp(K_{a2} x) \quad (6)$$

Table 1. Propellant Ingredients and Related Physical Properties

	N5	A13	NWR11			
ingredients	Nitrocellulose Nitroglycerin Diethyl phthalate 2-Nitrodiphenylamine Lead Octoate Lead Salicylate Candelilla Wax	50.0% 34.9% 10.5% 2.0% 1.2% 1.2% 0.2%	90u AP PBAN Epon 828	76.0% 20.4% 3.6%	trimodal AP HTPB burnrate suppressant carbon black	83.0% 11.9% 5.0% 0.1%
burnrate vs pressure	mesa	linear	linear			
burnrate @ 13.6psi (cm/s)	0.075	0.085	0.069			
n @ 25°C	approx 1.0 <600psi	0.432	0.491			
density g/cm^3	1.553	1.58	1.7026			
<u>@ 1 atm Equilibrium Calculations</u>						
Flame Temp (degK)	2417	2082	2653			
gas density (g/liter)	0.120	0.124	0.115			
Molecular Weight	23.799	21.139	24.939			
Cp (cal/g/K)	0.5395	0.4479	0.4363			
<u>Values used in m' conversion</u>						
MW	23.8	21.139	25.5			
Flame Temp K	2200	1950	2700			

For simplicity, the density, thermal conductivity, and heat capacity of the solid are considered constant and the natural radiant feedback to the solid, q_{r1} , is neglected. It has been assumed that scattering is negligible, the absorption coefficient K_{a2} is spatially constant, thermal emission by the condensed phase is negligible, and the incident flux is collimated. It should be noted that the fraction of radiant flux that is absorbed below the reaction layer, f_2 , must be specified. From scaling arguments,¹⁹ the behavior is modelled using $f_2 = \exp(-L_f X_R/X_A) = \exp(-L_f \beta R T_s/E_s)$. L_f is a correction factor which has been assumed to be equal to 1.0 in these calculations. L_f could be justifiably used if the absorption coefficient in the reaction layer differs from the unreacted solid phase. The absorption coefficient could be different due to phase changes (i.e. a melt layer or phase change of the crystalline structure).

Applying a linear perturbation of m , T , and q_{r1} , the steady-state form of the solid phase energy equation and the time-dependent energy equation can be obtained and solved using the appropriate boundary conditions.¹⁹ The origin of the coordinate system used remains fixed to the surface which produces identical results as a coordinate system that moves with the mean burn rate (inertial coordinate system) and later applies a Taylor's series to relate the variables to the actual surface values. Using the solution of (6), the transient conductive heat flux (on the solid phase side of the surface) is found to be:

$$k_s \dot{\phi}_{s+} = \bar{m} C \lambda T_s + \frac{\bar{m}}{\bar{m}} \left[\frac{\bar{m} C(T_s - T_i)}{\lambda} \right] - \frac{\bar{m}}{\bar{m}} \left[f_2 \bar{q}_{r2} \frac{1-\lambda}{\lambda(1-\lambda-\beta_2)} \right] + \frac{\bar{q}_{r2}}{\bar{q}_{r2}} \left[\frac{f_2 \bar{q}_{r2} \beta_2}{1-\lambda-\beta_2} \right] \quad (7)$$

The first two terms on the right hand side are the familiar terms that have appeared in previous studies where radiant heat flux was not considered.²⁰ Previous theoretical studies including radiant heat flux used the extreme f_2 values of zero or one (translucent or opaque surface) and have neglected the third term, apparently without justification.^{5-7,14}

Surface Connection Relations

The surface reaction layer is collapsed to the surface; that is, it is assumed to be infinitely thin at the surface. To be consistent, the amount of radiant energy that is absorbed in the actual reaction layer, which has finite thickness, is also collapsed with the reaction layer to the surface. The perturbed energy balance at the surface is therefore:

$$k_s \dot{\phi}_{s+} = k_s \dot{\phi}_{s-} - \bar{m} Q_s + \bar{m} (C_p - C) T_s - q_{r2} (1-f_2) \quad (8)$$

A perturbed Arrhenius-type relationship can be assumed for the pyrolysis and perturbed to obtain:^{5-7,14,20}

$$\frac{T_s'}{T_s} = \frac{\bar{m}'}{\bar{m}} \frac{1}{E} \quad (9)$$

where $E = (\alpha_s + E_s/RT_s)$ and the pressure dependence is neglected ($n_s = 0$). Alternatively, the solid phase burning rate expression formula developed by Ibiricu and Williams can be used,²⁵ as shown in Son *et al.*¹⁹, to obtain:

$$\frac{T_s'}{T_s} = \frac{\bar{m}'}{\bar{m}} P_3 - \frac{\bar{q}_{r2}}{\bar{q}_{r2}} \left[\frac{f_2 \bar{q}_{r2}}{\bar{m} C T_s P_1 P_2} \right] \quad (10a)$$

where:

$$R_q = \frac{n_q AB \left[f_2 \frac{1-\lambda}{P_1 P_2} + \frac{(1-f_2)(1-\lambda)-\beta_2}{1-\lambda-\beta_2} \right]}{\lambda + \frac{A}{\lambda} \cdot (1+A) + AB - f_2 Q_R \left[\frac{1-\lambda}{\lambda(1-\lambda-\beta_2)} \right]} \quad (17)$$

where $A = (1 - T_f/T_s)/P_3$, $B = Cp T_s/[C(T_s - T_i)(2 + Ef/2RT_f)] + Q_R/A$, and $Q_R = \bar{q}_{r2}/mCT_s P_3$. The change in form is due to the differences in the assumed pyrolysis expressions (Eqns. 9 and 10). If the effect of Q_R on the value of A and B is small compared to the other terms and the absorption is confined to the surface, then n_p/n_q is the correct transfer function. These results indicate that this limiting condition may be valid regardless of the flame description or controlling layer assumed.

Figure 3a and 3b are plots of the magnitude and phase of R_p and R_q versus normalized frequency for these models. The following parameters were used: $E_s = 20$ kcal/mole, $E_f = 40$ kcal/mole, $\bar{m} = 0.13$ cm/s, $Q_s = 95$ cal/g, $T_s = 950$ K, $T_f = 2082$ K, $\bar{q}_{r2} = 5$ cal/cm²s, $L_f = 1$, and $K_{a2} = 2000$ cm⁻¹. Q_f is determined from the overall energy balance. For these conditions the asymptotic flame description gives the highest response and the sharp flame description gives the lowest response. The peak of the $|R_p|$ is higher than $|R_q|$ for the condensed phase controlled distributed flame description, but shows the opposite trend for the sharp and Ibiricu and Williams (asymptotic) description. This is caused by the high sensitivity of the condensed phase controlled distributed flame to the condensed phase heat release. It should be recalled that in the expression for B in the distributed reaction model, increasing Q_R has a similar effect to increasing the nondimensional heat release parameter, H. The two gas phase controlled models do not show this sensitivity to H. However, they are much more sensitive to E_f . For the conditions considered, the sharp flame model must have E_f of approximately 60 kcal/mole to produce a more realistic response. In contrast, a lower E_f will decrease the response of the Ibiricu and Williams (asymptotic) description to more commonly observed values.

Near the zero frequency value, there is no phase difference between the heat flux and the burn rate. As the frequency is increased, the burn rate leads the heat flux signal (note that this result applies to the long time response after initial transients have disappeared). This is related to the fact that the transient burn rate is a function of the derivative of the forcing function (pressure or heat flux). Some have questioned whether a lead could really exist, implying that the propellant would be responding to the stimulus before it arrived, as in feedforward control. The low frequency phase lead can be explained as follows. At low burn rates the thermal layer extends deeper into the solid than at high burn rates. Thus, as the magnitude of the driving force (radiant flux or pressure) during a transient is increased, the new thermal layer thickness is shorter than the currently existing thermal layer. A thick thermal layer is roughly equivalent to storing energy in the propellant by conditioning at a higher initial temperature. Energy stored in the propellant produces a burn rate and thrust increase larger than the driving force increase alone would predict. Likewise, in the case of a decreasing driving force,

extra energy goes into building up the thicker thermal layer (similar to lowering the conditioning temperature in the steady state) which decreases the burn rate below the steady state value. This effect thus can produce a phase lead. Further, it is interesting to recall from dynamic systems analysis that the derivative exhibits a phase lead in its frequency response. Thus, the measured and mathematically predicted phase lead is physically reasonable. As the characteristic time of the driving force is decreased relative to the characteristic time of the solid, this "leading" effect becomes less important and the thermal lag of the solid produces an intuitively comfortable phase lag. Figure 3c shows the calculated transfer function for the three models considered using the same parameters as above.

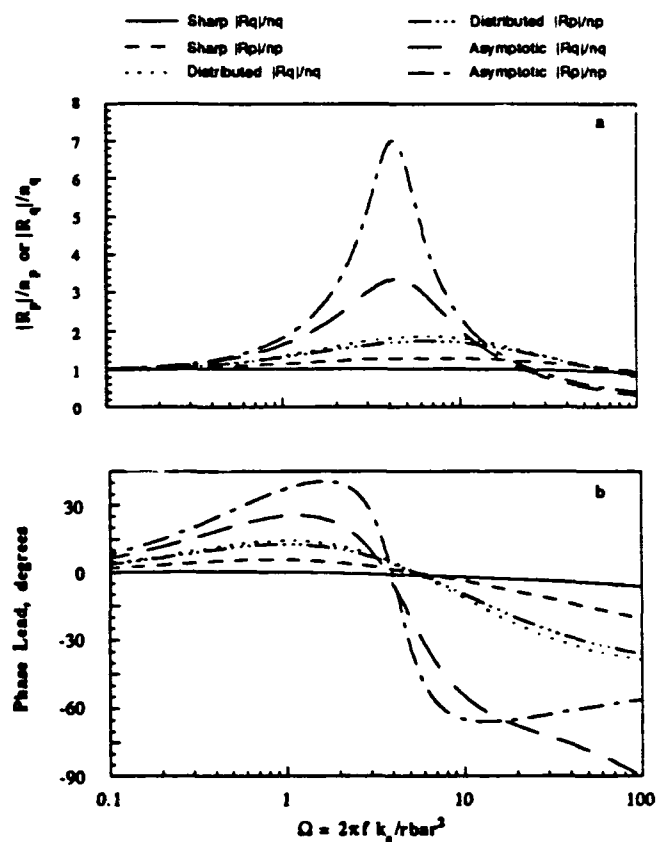


Figure 3a, b. Theoretical Calculations of the Response Function Using the Three Models. a) $|R_p|$ and $|R_q|$, b) Phase lead of R_p and R_q vs Ω .

Figures 3c and 3d show the transfer function, R_p/R_q , using the Ibiricu and Williams description for the same parameters used above. In Fig. 3c the TF = n_p/n_q at low frequencies. It can be seen that even for pure surface absorption ($\beta_2 \rightarrow \infty$, $K_{a2} \rightarrow \infty$) the transfer function does not approach n_p/n_q at the response peak. As \bar{q}_{r2} approaches zero the expected limit is evidenced.

$$P_3 = \frac{1}{P_2} + \frac{f_2 \bar{q}_{r2}}{\bar{m}CT_s P_1 P_2} \quad (10b)$$

$$P_2 = 2 + \frac{E_s}{RT_s} - \frac{1}{P_1} \quad (10c)$$

$$P_1 = (1 - T_f/T_s) - \frac{f_2 \bar{q}_{r2}}{\bar{m}CT_s} - \frac{H_R}{2CT_s} \quad (10d)$$

This description was derived using high activation energy asymptotics and explicitly includes the effect of the external heat flux. It should be noted that this expression is only applicable to gas phase controlled burning.²⁵

Gas Phase

The models considered here differ the most in the description of the gas phase. For the distributed reaction model, Culick shows that:²⁰

$$k_s \dot{\phi}_{s+} = \bar{m}C(T_s - T_f)W \frac{P'}{P} - C_p T_s \Lambda^2 \frac{\dot{m}}{\bar{m}} \quad (11)$$

which describes the fluctuating conductive heat flux to the surface. For the thin flame models:

$$k_s \dot{\phi}_{s+} = \bar{m}[Q_f - C_p(T_f - T_s)] + \dot{m}[Q_f - C_p(T_f - T_s)] \quad (12)$$

can be obtained from the perturbation of a simple energy balance. If $Q_f = cP'$ is assumed then:

$$\frac{Q_f}{Q_r} = \gamma \frac{P'}{P} \quad (13)$$

This is in contrast to Mihlfeith's analysis, where both Q_f and Q_s were assumed constant.⁵⁻⁷

For the sharp flame gas phase controlled model the perturbed burn rate expression is:^{5-7,23}

$$F \frac{T_f'}{T_f} = \frac{\dot{m}}{\bar{m}} \cdot \left(v_1 + \frac{\gamma C_p(T_f - T_s)}{2(Q_f - C_p(T_f - T_s))} \right) \frac{P'}{P} + G \frac{T_s'}{T_s} \quad (14)$$

For the gas phase controlled, high activation energy asymptotics the perturbed expression is:¹⁹

$$\frac{\dot{m}}{\bar{m}} = (v_1 - \gamma) \frac{P'}{P} + \left(2 + \frac{E_f}{2RT_f} \right) \frac{T_f'}{T_f} \quad (15)$$

Response Functions

Combining Eqns. 7-9 and 11, the distributed reaction model response can be obtained. Further, using the definitions $R_p(0) = n_p$ and $R_q(0) = n_q$ to decrease the number of variables it is found that:

$$R_q = \frac{n_q AB \left[\frac{(1-f_2)(1-\lambda)-\beta_2}{1-\lambda-\beta_2} \right]}{\lambda + \frac{A}{\lambda} - (1+A) + AB - f_2 Q_R \left[\frac{1-\lambda}{\lambda(1-\lambda-\beta_2)} \right]} \quad (16)$$

for $P' = 0$. For $\bar{q}_{r2} = \bar{q}_{r2} = 0$, R_p takes the standard form (Eqn. 3). For the distributed reaction model, $A = E(1 - T_f/T_s)$, $B = 2(1-H) + \frac{C_p}{C} \frac{1}{A} - \frac{Q_R}{A}$, and $Q_R = \bar{q}_{r2} E / \bar{m}CT_s$. If \bar{q}_{r2} is zero, then A and B take on the form as derived by Culick and R_p can be calculated in the usual manner.²⁰ To calculate R_q , the Q_R term must be included in the calculation of B. It is tempting to neglect this term in the definition of B. For surface absorption only ($f_2 \rightarrow 0$), the transfer function (R_p/R_q) would simply be n_p/n_q . Indeed, this is what DeLuca claimed, but it is not sufficient.¹⁴ It is also necessary that the mean heat flux term, \bar{q}_{r2} , be negligibly small. DeLuca implicitly assumed that the term, $\frac{C_p}{C} E \Lambda^2$ (a term in the denominator of Eqns. 3 and 15 if the zero frequency limit is not used), was the same for both R_q and R_p expressions. It is easily shown that this term is related to a steady state energy balance,²⁰ hence the additional heat flux term appears in the expression for B. If, however, the Q_R term in the B expression is negligible compared to the other terms and the absorption is confined to the surface, then n_p/n_q is the correct transfer function.

For the sharp flame gas phase controlled model, combining Eqns. 7-9 and 12-14, and applying the zero frequency limit, the same form of equations are obtained except that:

$$B = 1 - H + \frac{C_p}{C} \frac{1}{A} \left[\frac{T_f E G}{T_s F} - \frac{E}{2G} \right]. \quad (16a)$$

It should be noted that the overall energy balance must be satisfied. Therefore, even though Q_R does not appear explicitly in this definition of B, Q_R will affect the value of B through other parameters such as T_f . Again, if the effect of Q_R on the value of B is small compared to the other terms and the absorption is confined to the surface, then n_p/n_q is the correct transfer function.

Using the Ibiricu and Williams description; that is, combining Eqns. 7, 8, 10, 12, 13 and 15, the same form of R_p expression is obtained (Eqn. 3) but the expression for R_q is slightly different in form:

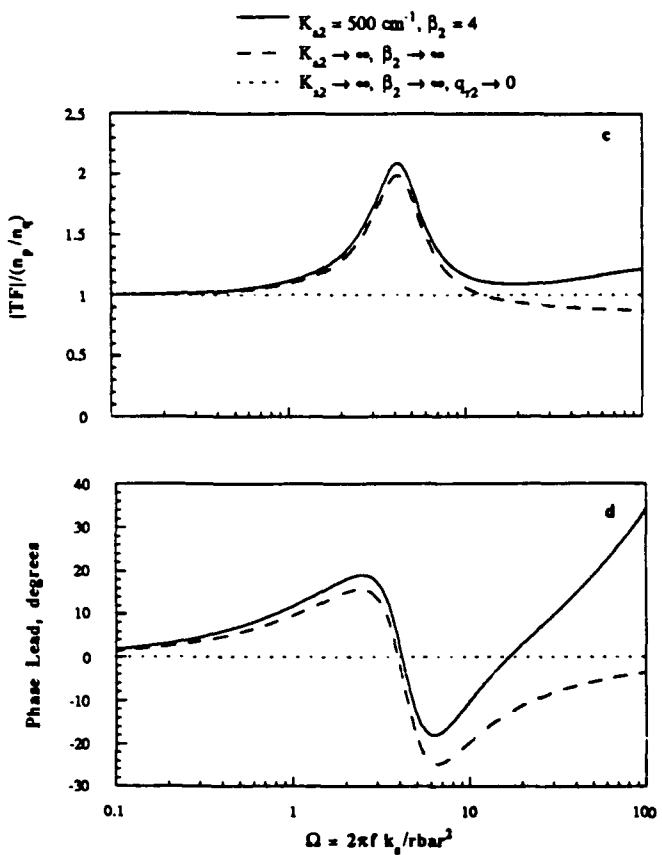


Figure 3c, d. Theoretical Calculations of the Transfer Function R_p/R_q Using the Ibiricu and Williams Model. a) $|TF|$ vs Ω ($|R_p|$), b) Phase lead of TF vs Ω .

Radiative Properties

The important radiative properties involved were measured or estimated to better quantify how much thermal radiation energy reaches the propellant surface, how much is reflected, and where it is deposited in the propellant. Some of the radiant heat-flux will be absorbed and scattered by the combustion gases and particles above the burning propellant surface. In order to measure the transmission through the gas phase, a Nd-YAG laser was used as the radiant source. A fiber optic was placed in the center of a A13 propellant strand and a photodiode sensitive to the $1.06 \mu\text{m}$ wavelength was used to measure the incident radiation (see Ishihara *et al.*²⁶ for a description of the fiber optic technique used). The incident radiation from the laser was measured, both during combustion and without a flame present. From these measurements, the transmissivity was measured to be 0.55 ± 0.05 at the $1.06 \mu\text{m}$ (Nd-YAG) wavelength. This value can be related to the value at $10.6 \mu\text{m}$ using a narrow-band radiation model that includes both the soot and gas contributions. The value of the transmissivity at $10.6 \mu\text{m}$ was estimated to be 90%, applying the radiation model with equilibrium calculations for gas properties, the visual observations of the flame height, and the Nd-YAG measurement. Using the narrow-

band model (RADCAL), the transmissivity was seen to be affected primarily by the soot volume fraction.^{27,28} It was relatively insensitive to the gas concentrations at either wavelength, but is more sensitive at the $1.06 \mu\text{m}$ wavelength. A13 appears to be the most optically thick flame so this value is likely a worst case value for the propellants considered in this study. Transmissivity values of 92% and 94% were used for the calculations involving NWR11 and N5. Mihlfeith measured transmissivity of 75 to 85% for the nonmetallized AP propellants in his study; however, his measurements were for an arc lamp which has a broad spectral content.⁵⁻⁷ To better quantify these values, direct measurements should be made using the CO_2 laser.

A certain amount of the incident laser energy will also be reflected from the propellant surface to the surroundings. Fortunately, this is a relatively simple property to measure. Samples of A13 and NWR11 were prepared by slicing with a knife blade and N5 sheet stock was used. A 2 mW CO_2 laser was pulsed normal to the surface and the reflectivity was measured. Unburnt samples of N5, A13, and NWR11 were found to have reflectivity values of 3.2 ± 0.4 , 3.6 ± 0.1 , and 4.0 ± 0.2 percent, respectively, at $10.6 \mu\text{m}$. Extinguished samples will be tested to see if they vary significantly from the unburnt samples. Past experience with other propellants has shown that the reflectivity of unburnt surfaces and extinguished surfaces are similar.

As discussed above, the absorption coefficient, K_{a2} (inverse length-scale of the in-depth absorption) is an important parameter of in determining where the radiant energy is deposited in the solid. Even for very high values of K_{a2} (or β_2), in depth absorption can have a significant effect on the response. Strand *et al.* used carbon black as an opacifier in the binder and reported that there was little effect on R_q .¹⁸ They concluded that the CO_2 laser energy was essentially surface absorption. However, considering that there was significant data scatter and that the opacifier is distributed in only the binder and not in the AP crystals, there is still uncertainty. Preliminary measurements were made of the absorption coefficient to determine the order of magnitude. Thin slices of propellant were prepared and the transmission measured with an FTIR. Thin uniform slices were difficult to prepare using the cutters available, decreasing our confidence in the results. HTPB binder 10 to $50 \mu\text{m}$ thick was cured on the surface of KBr crystals and the transmission was measured. Values for K_{a2} were calculated using the equation $K_{a2} = -\ln(t)/l$, where t is the transmission fraction and l is the sample thickness in cm. Table 2 lists the preliminary measurements and the estimated uncertainties of these measurements. The $10.6 \mu\text{m}$ band was overlapped by adjacent absorbing peaks in the FTIR. Repeating the measurements with a CO_2 laser would increase the accuracy.

If the measured value of the absorption coefficient is used, the gas phase controlled models showed very little response. The absorption coefficients used in the calculations were 150, 3000, and 4000 cm^{-1} for N5, A13, and NWR11, respectively. These values for A13 and NWR11 are much greater than the preliminary measured values by about an order of magnitude.

Table 2. Absorption Coefficient Measurements

Material	Thickness (cm)	Transmission fraction	$K_{\alpha 2}$ at 10.6 μm (cm^{-1})
N5	0.02 \pm .01	0.11	110
A13	0.039 \pm .02	0.084	64
HTPB	.0013 \pm 0.0003	0.4	705
HTPB	.0050 \pm 0.0005	0.3	240
HTPB with 0.4 carbon black	.0045 \pm 0.0005	0.25	308

A much higher value of absorption coefficient (about 2000 cm^{-1}) can be estimated from measured optical properties of pure AP, but this seems to contradict the low measured values. However, if the binder is relatively translucent, these two values may be reconciled by considering scattering. Further, it is possible that a melt layer on the surface or a crystalline phase change occurring during combustion, could result in a surface with very different optical properties. Further experimental work is being done to measure the optical properties more accurately.

Steady state results

To understand the unsteady combustion, the steady-state conditions must first be well characterized. To measure the mean mass flux as a function of radiant energy, samples of approximately 2 cm in length were irradiated with a steady heat flux. The mass loss is superimposed on the force signal and was converted to mass flux using Eqn. 18. For cylindrical samples:

$$r = \frac{-4}{\rho_s g D^2} \frac{df}{dt} \quad (18)$$

The resulting steady-state profiles for the mean burnrate as a function of incident radiant flux are shown in Fig. 4.

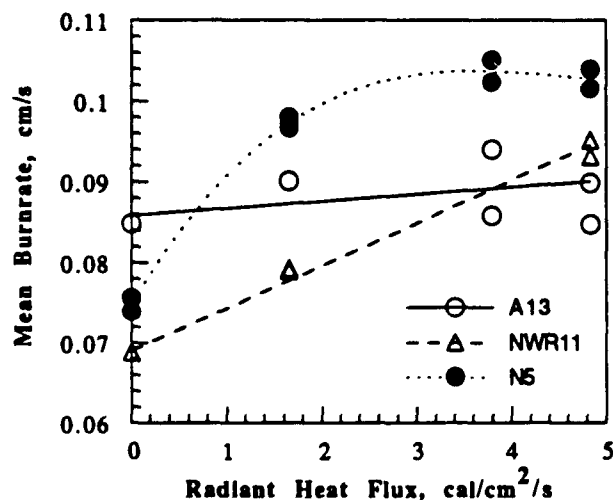


Fig 4. Mean Burn Rate as a Function of Incident Radiant Flux.

N5, the double-base propellant shows a much higher sensitivity to the radiant heat flux, especially below 2 $\text{cal/cm}^2/\text{s}$. Of course, n_q (by definition the value of R_q at zero frequency) could be calculated from the mean burn rate data, using Eqn. 19.

$$n_q = \frac{dm}{dq_{r2}} \frac{\bar{q}_{r2}}{\bar{m}} \quad (19)$$

Unfortunately, uncertainties in the steady state burn rate data from Fig. 4 make this calculation of questionable value. Additional steady-state burn rate data will be obtained in future testing.

Nonsteady Results

In this section the measured response functions of N5, A13, and NWR11 are presented and compared with analytical results. Even though A13 and NWR11 are composite propellants it is reasonable to apply a homogeneous model at low pressures. At low pressures the flame standoff distance and the molecular diffusivities are large enough for nearly complete mixing to occur. At higher pressures, it is likely that flame descriptions will require a more complex structure to be included. The input values used in the calculations are shown in Table 3. Some of the model inputs are quite uncertain (eg. E_s , E_p , and Q_s) such that these parameters could be adjusted until an optimal agreement was reached; however, that was not done in this study.

Experimental data for the N5 propellant is shown in Fig. 5. The oscillating thrust is shown in Fig. 5a as a function of f versus frequency for heat fluxes of 45.2 ± 8.9 , 22.5 ± 8.9 , and $4.7 \pm 2.4 \text{ cal/cm}^2/\text{s}$. The 0.64 cm diameter N5 resonated at 60 to 90 Hz ($\bar{f} = 0.22 \text{ cm/s}$), while the 1.27 cm diameter integrated beam samples ($\bar{f} = 0.12 \text{ cm/s}$) had a resonant peak at 20 to 30 Hz. The frequency can be converted to nondimensional frequency, $\Omega = 2\pi f k_s / \bar{f}^2$, where $k_s = 0.00041 \text{ cm/s}$, the condensed phase thermal conductivity. When plotted versus non-dimensional frequency in Fig. 5b, the resonance peaks are at 7 to 10 as expected from T-burner experience and theory. The response function of N5 has a peak value at resonance that is 3 to 4 times larger than the value at high frequencies and 1.5 times larger than the zero frequency value. The force data was converted to mass flux using equation 5 and the data in Table 1. The mass flux oscillation data is plotted in Fig. 5c and 5d vs frequency and Ω . The phase lead versus

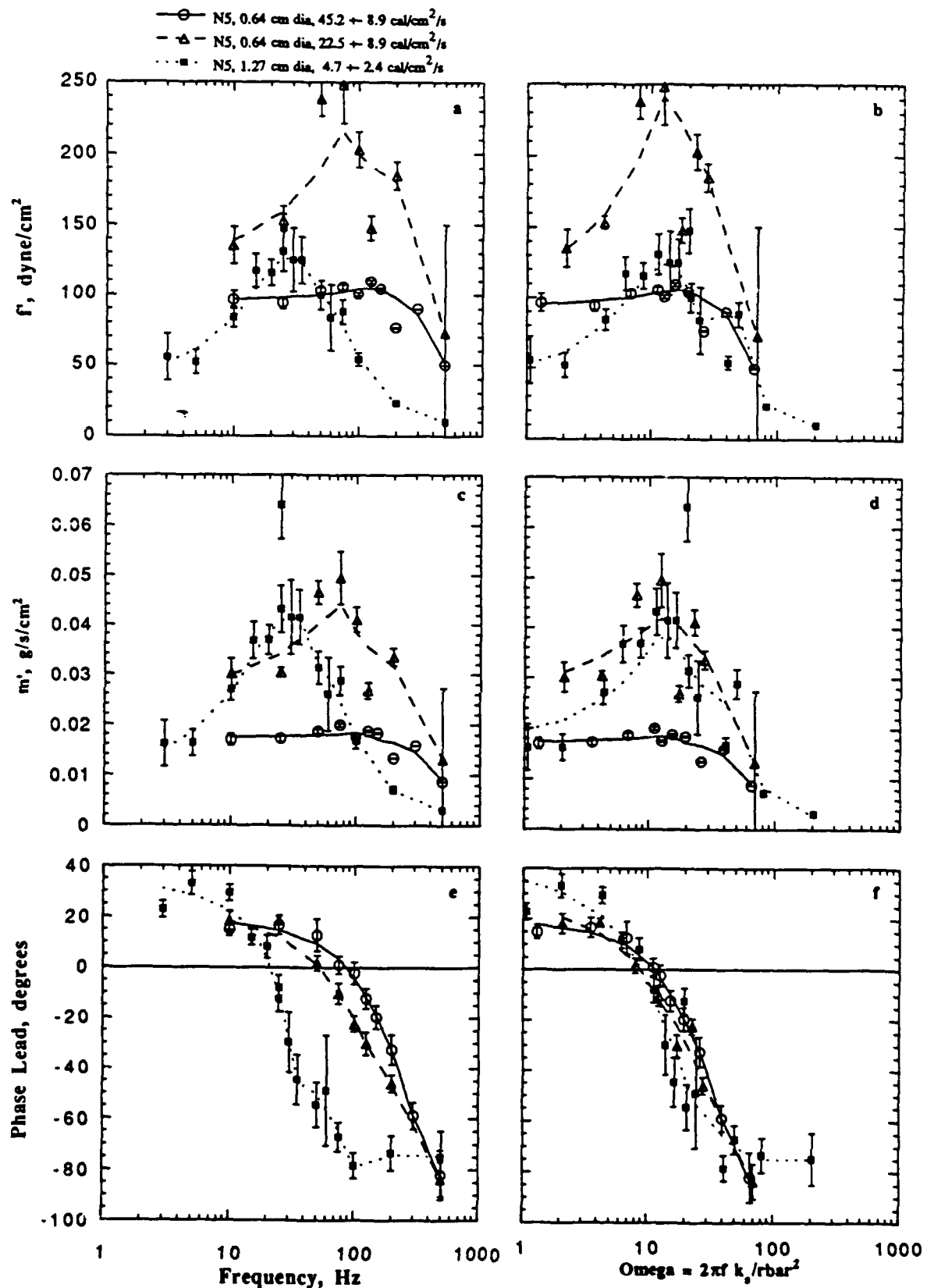


Figure 5. Experimental data for N5 propellant with heat fluxes of 45.2 ± 8.9 , 22.5 ± 8.9 , and $4.7 \pm 2.4 \text{ cal/cm}^2/\text{s}$. a) f vs f , b) f vs Ω , c) m' vs f , d) m' vs Ω , e) Phase lead vs f , f) Phase lag vs Ω .

Table 3. Inputs for Model Calculations. A, B, P's, β_2 , H & E are calculated values.
 q denotes value with external radiant flux.

	NS	NS	NS	NWR11 cold	warm	A13	A13	A13
α_c [cm ² s]:	0.001	0.001	0.001	0.001	0.001	0.001	0.001	0.001
q_{P2} :	4.74	22.5	45.2	4.3	4.3	4.1	4.7	42.5
\bar{v} [cm/s]:	0.09	0.09	0.09	0.07	0.07	0.09	0.09	0.09
\bar{v}_q [cm/s]:	0.12	0.20	0.22	0.095	0.095	0.1	0.1	0.1
f_2 :	0.9619	0.9724	0.9691	0.1638	0.1638	0.1030	0.1030	0.09510
β_2 :	1.25	0.75	0.682	31.6	31.6	40.	40.	40.
L_f :	1.0	1.0	1.0	1.0	1.0	1.0	1.0	1.0
K_{a2} [cm ⁻¹]:	150.	150.	150.	3000.	3000.	4000.	4000.	4000.
T_s [K]:	600.	600.	600.	850.	850.	850.	850.	850.
T_{sq} [K]:	625.	750.	925.	865.	865.	858.	858.	888.
T_f [K]:	1450.	1450.	1450.	2653.	2653.	2082.	2082.	2082.
$T_{f,q}$ [K]:	1511.	1613.	1741.	2730.	2730.	2148.	2157.	2761.
T_i [K]:	300.	300.	300.	203.	300.	300.	300.	300.
$Qbar_s$ [cal/g]:	60.	60.	60.	160.	160.	95.	95.	95.
Q_f [cal/g]:	383.8	377.0	368.8	684.6	652.6	579.3	579.3	579.3
E_s [cal/gmole]:	40000.	40000.	40000.	30000.	30000.	30000.	30000.	30000.
E_i [cal/gmole]:				40000.	40000.	30000.	30000.	30000.
C [cal/gmole]:	0.35	0.35	0.35	0.33	0.33	0.33	0.33	0.33
C_p [cal/gmole]:	0.40	0.40	0.40	0.35	0.35	0.40	0.40	0.40
ρ_c [g/cm ³]:	1.55	1.55	1.55	1.70	1.70	1.58	1.58	1.58
alfas:	0.0	0.0	0.0	0.0	0.0	0.0	0.0	0.0
A:	16.77	16.77	16.77	8.438	6.967	7.156	7.156	7.074
A _q :	16.75	16.10	14.70	8.614	7.122	7.257	7.267	7.832
B:	0.9253	0.9253	0.9253	0.7506	0.8830	0.8156	0.8156	0.8156
B _q :	0.7893	0.8482	0.9232	0.8725	1.026	0.9566	0.9772	2.201
H:	0.5714	0.5714	0.5714					
H _q :	0.5275	0.3810	0.2743					
E:	33.55	33.55	33.55					
E _q :	32.21	26.84	21.76					
P ₁ :				-0.3680	-0.4801	-0.3965	-0.3965	-0.3493
P _{1q} :				-0.3833	-0.4953	-0.4059	-0.4073	-0.4366
P ₂ :				22.17	21.54	22.12	22.12	21.86
P _{2q} :				22.06	21.47	22.06	22.05	21.29
P ₃ :				0.09021	0.09287	0.0904	0.09043	0.09148
P _{3q} :				0.08885	0.09171	0.08961	0.08950	0.08454
HR:				647.0	647.0	592.8	592.8	592.8

frequency data is shown in Se. A distinct phase lead is evident below the resonant frequency. At the resonant peak, the phase crosses from lead to lag, and then approaches a lag of 80 degrees at higher frequencies. Notice that the phase crosses from lead to lag at the same frequency as the resonant peak in the f plot. When plotted versus dimensionless frequency in 7f the data set converges to one resonant frequency as expected from theory.

At low pressure the solid phase would likely be the controlling reaction layer. Calculations of the response function magnitudes, R_p , R_q , and phase lead were made using the distributed flame model (solid phase controlled). The magnitudes were normalized by an estimated n_q and are compared with the data in Fig. 6. The model shows that an increase in mean radiant flux tends to decrease the resonant peak. This trend is also shown by the data. Of the two data sets with heat flux oscillations of 8.9 cal/cm²/s, the one with a smaller mean heat flux, 22.5 cal/cm²/s, has higher amplitude resonant peak. The absorption coefficient of NS (approximately 150 cm⁻¹) is low enough that much of the radiant energy is absorbed below the reaction layer, such that even for a fairly low mean heat flux the normalized R_p is slightly higher in magnitude than the calculated R_q , as

shown in Fig. 6a. The calculated phase difference shown in Fig. 6b, also compares fairly well with the data.

Experimental data for the A13 propellant is shown in Fig. 7. The oscillating thrust is shown in Fig. 7a as a function of f versus frequency for heat fluxes of 43 ± 21 , 4.7 ± 1.7 , and 4.0 ± 2.0 cal/cm²/s. Notice that the f magnitude did not decrease at the low frequencies as expected. Therefore using the f plot alone it is difficult to determine the frequency of the resonant peak. The mass flux oscillation data is plotted in Fig. 7c and 7d vs frequency and Ω . The phase lead versus frequency data is shown in Se. The phase crosses from lead to lag at a frequency of 10 to 20 Hz and then approaches a lag of 60 degrees at higher frequencies. When plotted versus dimensionless frequency in 7f the data set converge to one resonant frequency as expected from theory. Both the 0.64 cm diameter A13 ($\bar{v} = 0.15$ cm/s) and the 1.27 cm diameter integrated beam samples ($\bar{v} = 0.10$ cm/s) have a resonant peak near 10 to 20 Hz. When plotted versus non-dimensional frequency in Fig. 7b, the resonance peaks are at 3 to 7, a little lower than the nominal 10 as expected from T-burner experience and theory.

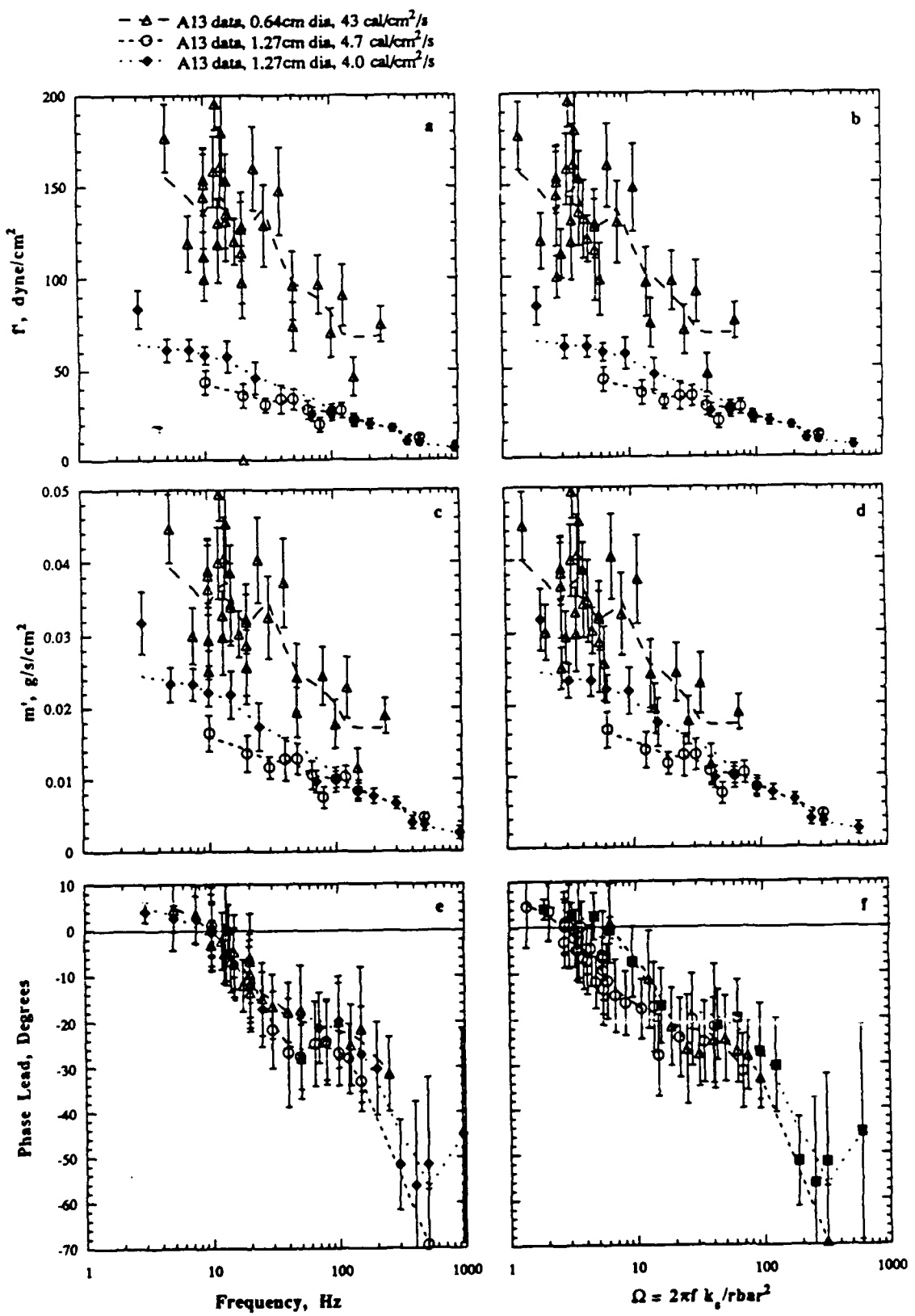


Figure 7. Experimental Data for A13 Propellant with Heat Fluxes of 45.2 ± 8.9 , 22.5 ± 8.9 , and 4.7 ± 2.4 cal/cm²/s. a) f' vs f , b) f' vs Ω , c) m' vs f , d) m' vs Ω , e) Phase lead vs f , f) Phase lag vs Ω .

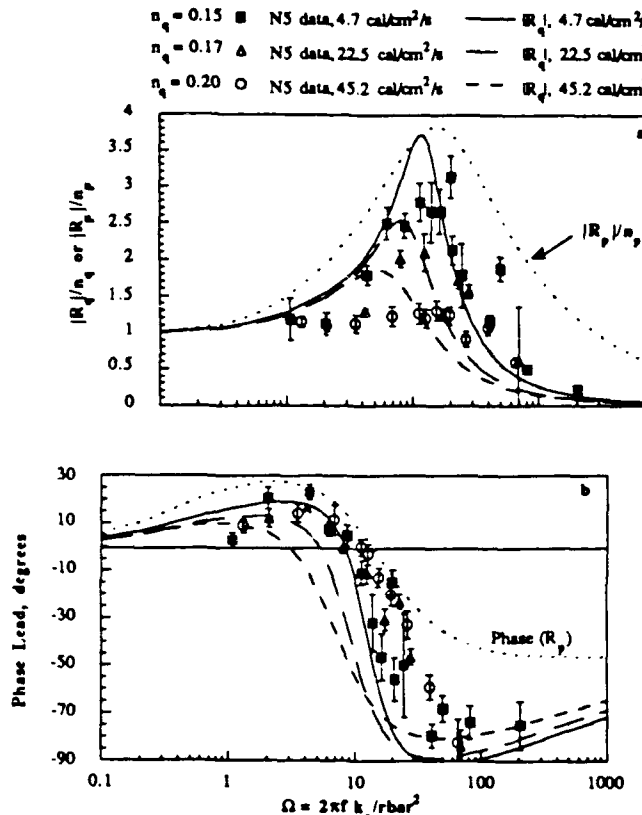


Figure 6. Comparison of NS Combustion Response Data with Distributed Flame Model Calculations. a) $|R_q|/n_q$ vs Ω , b) Phase Lead (R_q) vs Ω .

Calculations of the response function magnitudes, R_p , R_q , and phase lead were made using the Ibiricu and Williams (asymptotic) flame description model. The magnitudes were normalized by an estimated n_q and are compared with the A13 data in Fig. 8. The input values used in the calculations are shown in Table 3. This model also shows that an increase in mean radiant flux tends to decrease the resonant peak, which agrees with the data. The model agrees well with the magnitude of the 4.7 and 43 cal/cm²/s data. Again the normalized R_p is slightly higher in magnitude than the calculated R_q , as shown in Fig. 8a. The two data sets with heat fluxes of 4.0 and 4.7 cal/cm²/s should have more similar magnitudes as seen from the Fig. 7a. The A13 phase lead data is compared with the Ibiricu and Williams (asymptotic) flame description model in Fig. 8b. The model predicts a larger phase lead below the resonant peak, but has a similar phase lag at high frequencies. Again the agreement is encouraging considering the unknowns in several model input parameters.

It was decided to study the effect of propellant conditioning temperature using NWR11 samples. One set of samples were placed in a styrofoam cup with dry ice in the freezer overnight, the other set was conditioned at room temperature. Both samples were tested on the same day with heat fluxes of 4.3 ± 2.1 cal/cm²/s. Experimental data

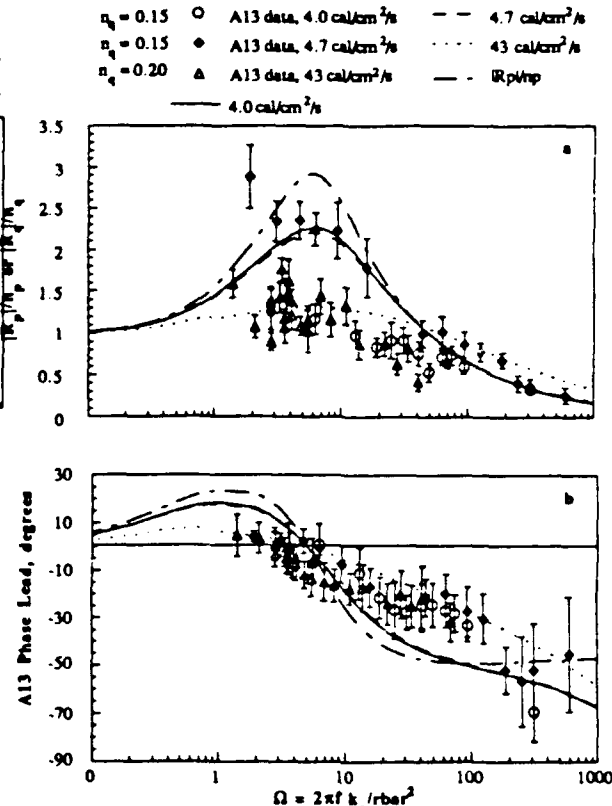


Figure 8. Comparison of A13 Combustion Response Data with Ibiricu and Williams Flame Model Calculations. a) $|R_q|/n_q$ vs Ω , b) Phase Lead (R_q) vs Ω .

for the NWR11 propellant is shown in Fig. 9. The oscillating thrust is shown in Fig. 9a as a function of f versus frequency. The magnitude of the NWR11 f oscillations is significantly smaller than for N5 and A13. There does not appear to be a significant difference in f between the two different conditioning temperatures. It could be that the samples warmed up in the few minutes that they were being prepared for combustion. Again the f magnitude did not decrease significantly at the low frequencies as expected and using the f plot alone it is difficult to determine the frequency of the resonant peak. The mass flux oscillation data is plotted in Fig. 9c and 9d vs frequency and Ω . The phase lead versus frequency data is shown in 9e. The phase crosses from lead to lag at a frequency of 20 Hz and then approaches a lag of 110 degrees at higher frequencies. When plotted versus Ω in 9f the resonant frequency is at a value of 10 as expected from T-burner experience.

Calculations of the response function magnitudes, R_p , R_q , and phase lead were made using the Ibiricu and Williams (asymptotic) flame description model. The magnitudes were normalized by an estimated $n_q = 0.012$ and are compared with the NWR11 data in Fig. 10. The value of n_q is much smaller than that used to normalize the N5 and A13 data. Qualitative agreement with the data is achieved. This model predicts that a decrease in propellant initial temperature increases the magnitude of the resonant peak.

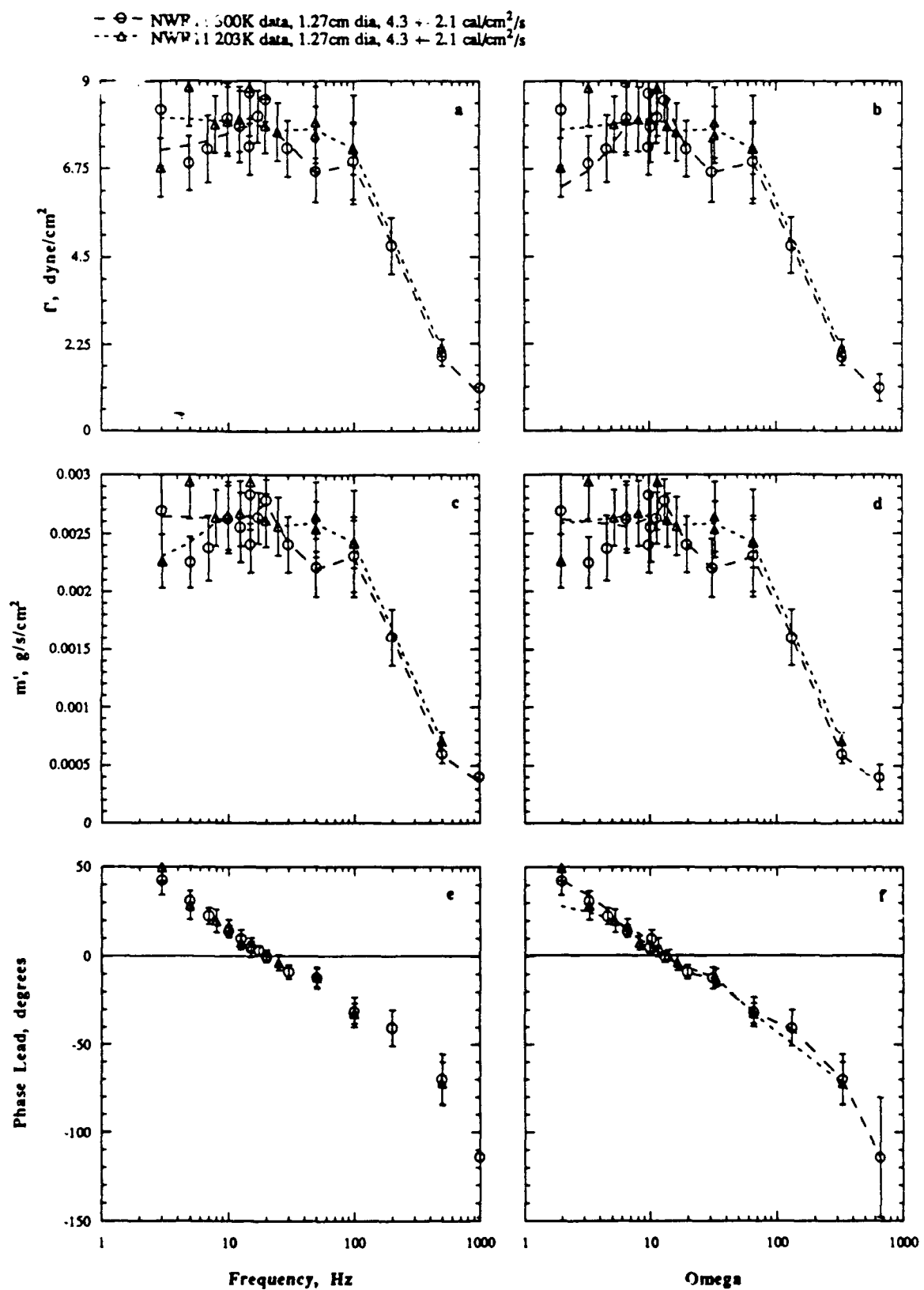


Figure 9. Experimental Data for NWR 11 Propellant with Heat Fluxes of 45.2 ± 8.9 , 22.5 ± 8.9 , and $4.7 \pm 2.4 \text{ cal/cm}^2/\text{s}$. a) f' vs f , b) f' vs Ω , c) m' vs f , d) m' vs Ω , e) Phase lead vs f , f) Phase lag vs Ω .

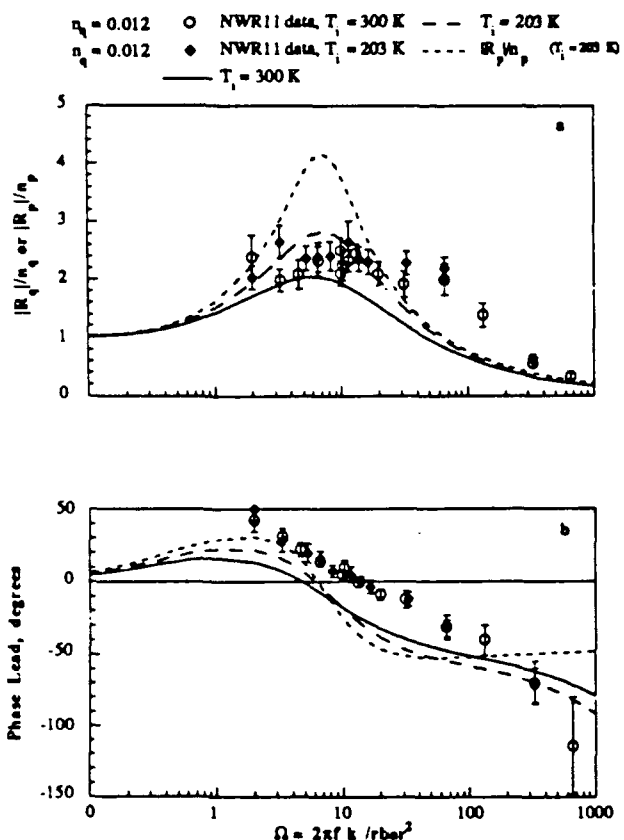


Figure 10. Comparison of NWR11 Combustion Response Data with Ibiricu and Williams Flame Model Calculations. a) $|R_q|/n_q$ vs Ω , b) Phase Lead (R_q) vs Ω .

Again the normalized R_p is slightly higher in magnitude than the calculated R_q , as shown in Fig. 10a. The NWR11 phase lead data is compared with the Ibiricu and Williams (asymptotic) flame description model in Fig. 10b. This time the data has a larger phase lead at low frequencies than the model. A more sensitive propellant should be selected to measure the effect of initial temperature, i.e. fine oxidizer AP composite or double base.

CONCLUSIONS

Propellant samples are mounted on a Kistler 9207 force transducer which measures the thrust oscillations. The 150W CO_2 laser is easily modulated by a signal generator to provide a sine wave radiant heat flux. Beam integration plus increased sample size have reduced the data scatter from earlier attempts. The Silicon Graphics workstation allows for speedy data acquisition and analysis. Nine propellants of type double base, smokeless composite, and metallized composite have been tested at atmospheric pressure surrounded by room temperature air. Unfortunately, the laser energy is scattered by burning metal particles and smoke in the plume of highly metallized propellants. Special techniques for deflecting the plume or increasing the laser power will be necessary to measure the response of metallized propellants. The latest

experimental results and corresponding analyses were presented for three of the propellants tested: N5 (double base), A13 (PBAN, AP), and NWR11 (HTPB, AP, minimum smoke). Samples were tested at surface heat fluxes ranging from 4 to 49 cal/s/cm². When plotted versus nondimensional frequency the resonant peaks were near $\Omega = 10$ as expected. The phase difference between the laser and the thrust was calculated using a cross correlation. Many cycles were analyzed from each test and averaged to reduce data scatter. By performing the tests at many frequencies the radiant heat flux response function was determined.

Three different models were considered: (1) condensed phase controlled distributed flame (KTSS),^{20,22} (2) gas phase controlled sharp flame model (Mihlfeith),^{5-7,23} and (3) gas phase controlled, high activation energy asymptotics flame description (Ibiricu and Williams).^{24,25} It was shown that for all three models with high surface absorption ($f_2 \rightarrow 0$) and small mean radiant flux ($\bar{q}_{r2} \rightarrow 0$), the transfer function (R_p/R_q) reduces to n_p/n_q . The N5 was compared to the distributed flame model while A13 and NWR11 were compared to the asymptotic flame description model. Additional modelling and experimental work remain to be done. The steady state burnrate response to radiant heat flux must be accurately determined. More accurate measurements of the absorbance of energy in the propellant surface are being done. Additional measurements also need to be made of other propellant optical and physical properties.

The initial objectives of this work were to improve upon the work of Mihlfeith and Zarko, *et al.* using a microforce transducer for direct measurement of propellant response function to radiant energy. At atmospheric pressure the microforce transducer method seems to allow the propellant response to be obtained faster and therefore less expensively than other methods. However, a correlation between the heat flux response and the more theoretically useful pressure response remains to be validated. The technique appears to show promise as a tool for characterizing propellant combustion stability as well as providing further understanding combustion instability fundamentals. To become more directly useful, however, higher pressure capability will be added.

ACKNOWLEDGMENTS

Thanks to Richard Stalnaker for machining work on the apparatus, Phil Archibald for performing the reflectivity measurements, and Mel Nadler for the FTIR absorption coefficient measurements. This work was supported in part by the Naval Weapons Center, the Office of Naval Research (N00014-87-k-0547) Dr. R. S. Miller (contract monitor), and the National Science Foundation (CBT86-96162).

NOMENCLATURE

- ($-$) denotes steady state values and
- ($'$) denotes perturbed values
- q denotes properties related to radiant heat flux

A _c	cross sectional area of propellant sample
A	constant in R_p and R_q expressions
B	constant in R_p and R_q expressions
C _p	specific heat of gas phase
C	specific heat of condensed phase
E _f , E _a	gas and condensed phase reaction activation energy
E	$E_a/R T_s + \alpha_s$, nondimensional activation energy
f	frequency, Hz
f	force oscillations, dynes/cm ²
f ₂	fraction of radiant energy absorbed below reaction layer
F	$E_f/2RT_f - C_p T_f/2[Q_f - C_p(T_f - T_s)]$
G	$C_p T_s/2[Q_f - C_p(T_f - T_s)]$
H	$Q_f/C(T_s - T_f)$, surface heat release
H _R	heat released in surface reactions - does not include latent heat
K _a	absorption coefficient in Beer's Law
k _g	thermal conductivity of gas phase
k _s	thermal conductivity of condensed phase, = 0.00041 cm/s
L _f	correction factor in f ₂ expression = 1.0
m	mass burning rate, g/s/cm ²
n _p	zero frequency value of the pressure response function
n _q	zero frequency value of the heat flux response function
P	pressure
Q _r	heat release from the gas-phase reactions (greater than 0 is exothermic)
q _{r1}	natural feedback radiant heat flux (e.g., metallized propellants)
q _{r2}	induced external radiant heat flux (e.g., laser)
Q	combined latent heat and heat released in surface reactions (greater than 0 is exothermic)
Q _R	nondimensional heat flux
P ₁ , P ₂ , P ₃	nondimensional constants
R _p , R _q	pressure and heat flux response function
R	universal gas constant
T _f	flame temperature, K
T _i	temperature deep within the solid (conditioning temperature), K
T _s	temperature at solid surface, K
T _F	complex valued transfer function, R_p/R_q
X _a	absorption length scale (1/K _a)
X _d	thermal length scale (k _s /mC)
X _R	solid phase reaction length scale ($X_d RT_s/E_a$)
α_c	condensed phase thermal diffusivity, cm ² /s
α_s	temperature exponent in Arrhenius expression
β	ratio of thermal length scale to radiant length scale (K _a k _s /mC)
γ	flame heat release pressure sensitivity exponent
λ	characteristic of solid phase temperature solution $(1/2 + \sqrt{1/4 + i\Omega})$
Λ	eigenvalue, see ref. 20
v ₁	pressure exponent in gas phase mass burning rate equation
ρ , ρ_g	condensed phase density, gas phase density
ϕ	temperature gradient
ω	frequency, radians/s
Ω	dimensionless frequency ($\rho k_s \omega / C m^2$) = $2\pi f k_s / r^2$

REFERENCES

1. F. E. C. Culick, Combustion Instability in Solid Rocket Motors, Volume II: A Guide for Motor Designers, CPIA Publ. No. 290, January 1981.
2. L. D. Strand, K. Schwartz, and S. P. Burns, "Propellant Combustion Response to Oscillatory Heat Flux", 24th JANNAF Combustion Meeting, CPIA Publ. No. 476, Vol. 1, Oct. 1987, pp. 41-50.
3. J. R. Wilson, and M. M. Micci, "Direct Measurement of High Frequency Solid Propellant Response Functions", 20th JANNAF Combustion Meeting, Vol. I, CPIA Publ. No. 383, Oct. 1983, pp. 193-202
4. R. S. Brown, T. Torikai, W. R. Babcock, "Combustion Response Function Measurements by the Rotating Valve Method," *AIAA Journal*, Vol. 12, Nov. 1974, pp. 1502-1510.
5. C. M. Mihlfeith, A. D. Baer, and N. W. Ryan, "Propellant Combustion Instability as Measured by Combustion Recoil," *AIAA Journal*, Vol. 10, No. 10, Oct. 1972, pp. 1280-1285.
6. C. M. Mihlfeith, "Some Experiments on the Effect of Thermal Radiation on Composite Rocket Propellants," Ph.D. Thesis, University of Utah, Salt Lake City, Utah, 1971.
7. C. M. Mihlfeith, A. D. Baer, and N. W. Ryan, "The Direct Measurement of the Radiant Heat Flux Response Function of Solid Propellants", 8th JANNAF Combustion Meeting, CPIA Publ. 220, Vol. 1, Nov. 1971, pp. 259-275.
8. V. E. Zarko, V. N. Simonenko, and A. B. Kiskin, "Nonstationary Combustion of Condensed Substances Subjected to Radiation," *Fiz. Gorenija Vzryva*, Vol. 23, No. 5, (Oct. 1987)
9. V. N. Simonenko, V. E. Zarko, and K. P. Kutsenogii, "Experimental Study of the Conditions for Auto- and Forced Fluctuations of the Rate of Combustion of a Powder", *Fiz. Gorenija Vzryva*, Vol. 16, No. 3, pp. 60-68 (June 1980)
10. V. E. Zarko, V. N. Simonenko, and K. P. Kutsenogii, "Effects of Light Intensity on the Nonstationary Combustion Rate in a Transient Process", *Fiz. Gorenija Vzryva*, Vol. 11, No. 4, pp. 541-548, (Aug. 1975)
11. T. J. Ohlemiller, L. H. Caveny, L. DeLuca, and M. Summerfield, "Dynamic Effects on Ignitability Limits of Solid Propellants Subjected to Radiative Heating", 14th Symposium (International) on Combustion, pp. 1297-1307, (Aug 1972)
12. V. F. Mikheev and S. M. Borin, "Measurement of the Mass Combustion Rate of Solid Explosives", *Fiz.*

- Goreniya Vzryva*, Vol. 9, No. 2, pp. 327-329, (April 1973)
13. A. V. Khudyakov, G. V. Gorvard, E. V. Konev, and V. F. Mikheev, "Measuring the Mass Burning Rate of Solid Explosives", *Brief Communication Fiz. Goreniya Vzryva*, Vol. 3, No. 3, pp. 462-464, (1967)
 14. L. DeLuca, "Frequency Response Function of Burning Solid Propellants", *Meccanica: Journal of the Italian Association of Theoretical and Applied Mechanics*, Dec 1980 p. 195-205
 15. V. E. Zarko and A. B. Kiskin, "Numerical Modeling of Nonsteady Powder Combustion Under the Action of a Light Flux", *Fiz. Goreniya Vzryva*, Vol. 16, No. 6, pp. 54-59 (Dec 1980)
 16. T. D. Prevish, and M. Q. Brewster, "Combustion Response of a Homogeneous Solid Propellant to an Oscillatory Radiant Heat Flux", Western States Section/The Combustion Institute, March 1989.
 17. T. D. Prevish, and M. Q. Brewster, "Combustion Response of a Homogeneous Solid Propellant to Oscillatory Radiant Heat Flux", 26th JANNAF Combustion Meeting, CPIA, Oct. 1989.
 18. L. Strand, M. Weil, and N. Cohen, "Solid Propellant Combustion Response to Oscillatory Radiant Heat Flux," AIAA 89-2667, AIAA/ASME/SAE/ASEE 25th Joint Propulsion Conference, 1989.
 19. S. F. Son, T. D. Prevish, M. Q. Brewster, J. C. Finlinson, and D. Hanson-Parr, "Radiant Heat Flux Response of Solid Propellants", to be submitted to the *Journal of Propulsion and Power*, 1990.
 20. F. E. C. Culick, Some Problems in the Unsteady Burning of Solid Propellants. NWC TP 4668, China Lake, CA: U. S. Naval Weapons Center, 1968.
 21. J. C. Finlinson, D. Hanson-Parr, T. Parr, and H. B. Mathes, "Measurement of Propellant Combustion Response to Oscillatory Radiant Heat Flux", 26th JANNAF Combustion Meeting, CPIA, Oct 1989.
 22. H. Krier, J. S. Tien, W. A. Sirignano, and M. Summerfield, "Nonsteady Burning Phenomena of Solid Propellants: Theory and Experiment," *AIAA J.*, Vol. 6, No. 2, pp. 278-85, 1968.
 23. F. E. C. Culick, "A Review of Calculations of the Admittance Function for a Burning Surface. Appendix A." NWC TP 4244, China Lake, CA: U. S. Naval Weapons Center, 1967.
 24. F. A. Williams, "Quasi-Steady Gas-Phase Flame Theory in Unsteady Burning of a Homogeneous Solid Propellant," *AIAA J.*, Vol. 11, No. 9, pp. 1328-30, 1973.
 25. M. M. Ibiricu, and F. A. Williams, "Influence of Externally Applied Thermal Radiation on the Burning Rates of Homogeneous Solid Propellants," *Comb. and Flame*, Vol. 24, pp. 185-98, 1975.
 26. A. Ishihara, M. Q. Brewster, T. A. Sheridan, and H. Krier, "The Influence of Radiative Heat Feedback on the Burning rate in Metalized Propellants," *Comb. and Flame*, accepted for publication, 1990.
 27. C. B. Ludwig, W. Malkmus, J. E. Reardon, and J. A. L. Thomson, Handbook of Infrared Radiation from Combustion Gases, NASA SP-3080, Ed. R. Goulard and J. A. L. Thomson, available from NTIS, Publ. No. N7327807, 1973.
 28. W. L. Grosshandler, "Radiative Heat Transfer in Non-Homogeneous Gases: A Simplified Approach," *Int. J. Heat and Mass Trans.*, Vol. 23, pp. 1447-59, 1980.

NONSTEADY BURNING OF SOLID PROPELLANTS WITH AN EXTERNAL RADIANT HEAT FLUX: A COMPARISON OF MODELS WITH EXPERIMENT

(Extended Abstract)

S. F. Son*, R. F. Burr*, and M.Q. Brewster**
Department of Mechanical and Industrial Engineering
University of Illinois at Urbana-Champaign
Urbana, IL 61801

J. C. Finlinson and D. Hanson-Parr
Naval Weapons Center
China Lake, CA

Submitted to
AIAA/SAE/ASME/ASEE 27th Joint Propulsion Conference
Sacramento, CA
June 24-27, 1991

Abstract

Data of instantaneous burn rates of solid propellants during a rapid pressure change for comparison with available transient models is scarce because of the experimental difficulties involved. In this study, various models are modified to include an external radiant heat flux, and are compared with new experimental data. It is shown that the unsteady radiant heat flux is directly related to a rapid pressure change for surface absorption (high extinction coefficient) for the models considered. The models are further modified to include the effect of in depth absorption of the radiant heat flux on the transient burning so that comparison with propellants that have lower absorption coefficients can be considered. A non-uniform grid using an explicit scheme with high-order compact differencing is used with a Runge-Kutta technique to integrate the equations. Experimental measurements of the instantaneous burn rate during a rapid irradiation transient were made using a microforce transducer and a CO₂ laser as the radiant heat source. The experimental technique was found to be relatively simple and repeatable. Several double base and composite propellants are tested and the models are found to predict many of the trends seen in the experimental data.

* Graduate Research Assistant. Student Member AIAA.

** Associate Professor. Member AIAA.

Nomenclature

A	cross sectional area of propellant sample, also used as a constant in LC model
a	constant in steady-state burning rate law, also used in Eqn. 4
b	constant in pyrolysis/burning rate law, also used in Eqn. 4
C _p	specific heat of gas phase
C	specific heat of condensed phase
c	used in Eqn. 4
D	mass diffusivity
d	used in Eqn. 4
C ₁	$\frac{\rho A_c g}{\omega}$
C ₂	$\frac{2\bar{m}\rho A_c}{\rho_g}$
E _f , E _s	gas and condensed phase reaction activation energy
E	$E_s / R \bar{T}_s + \alpha_s$
F	Force
f ₂	fraction of radiant energy absorbed below reaction layer
H	$Q_s/C(\bar{T}_s - T_i)$
K _a	absorption coefficient in Beer's Law
L _f	correction factor in f ₂ expression
M	molecular weight
m	mass burning rate, also used as the exponent in the power burn rate expression
n	pressure exponent
n _q	zero frequency value of the heat flux response function
p	pressure
P	dimensionless pressure
Q _f	heat release from the gas-phase reactions (>0 exothermic)
q _{r1}	natural feedback radiant heat flux (e.g., metalized propellants)
q _{r2}	induced external radiant heat flux (e.g., laser)
Q _s	combined latent heat and heat released in surface reactions (>0 exothermic)
Q _R	nondimensional heat flux
R _q	heat flux response function
r	burn rate
R	dimensionless burn rate
T	temperature
T _f	flame temperature

T_∞	temperature deep within the solid (conditioning temperature)
T_s	temperature at solid surface
X	dimensionless distance into the solid propellant
X_a	absorption length scale ($1/K_a$)
X_d	thermal length scale (k_s/mC)
X_R	solid phase reaction length scale ($X_d RT_s/E_s$)
α	thermal diffusivity
α_s	temperature exponent in Arrhenius expression
β	ratio of thermal length scale to radiant length scale ($K_a k_s/mC$) or a parameter in the coordinate transformation
λ_g	thermal conductivity
Θ	dimensionless temperature
ρ	density
τ	dimensionless time or characteristic time

Subscripts and Superscripts

c	condensed phase (solid propellant)
g	gas phase
s	surface
f	flame
o	reference value
∞	far upstream in the solid propellant
-	steady state value

Introduction and Background Information

The ability to predict the dynamic burn rate of a solid propellant is of prime importance in the design and safe use of high performance propulsion systems. Inaccurately characterizing important transient burning phenomena may cause significant errors in predictions of system performance; especially during ignition, extinction, and resonant burning. Various transient burn rate models exist. It is, however, difficult to determine their relative worth because little instantaneous burn rate data during a rapid pressure change are currently available primarily because of the experimental difficulties involved. The most significant of which are the control and measurement of the rapid pressure transient, and the simultaneous measurement of the instantaneous burn rate. The experimental techniques used to measure the instantaneous burn rate include a microwave device¹, a magnetic flux meter², and a microforce transducer⁴⁻⁹. To generate a transient pressure field a rotating valve³, and burst diaphragms¹⁰⁻¹¹ have been used with some success. Using a microforce transducer to measure the burn rate during a rapid change in irradiation appears to be an attractive alternative because it offers the possibility of obtaining data more dependably and less expensively than other methods. Further, it is much easier to generate the desired waveshape of radiant heat flux using a laser than with available pressure modulating techniques.

The heat flux/microforce transducer experimental technique has previously been used by Mihlfeith⁴⁻⁶ and Soviet researchers such as Zarko *et al.*⁷⁻⁹ to determine the heat flux combustion response. Although this technique has shown significant promise and has received substantial attention in the USSR, it has not been widely applied to combustion response studies in the U.S. since Mihlfeith's work in 1971. The use of fast irradiation and de-irradiation (or deradiation) has also been used successfully applied to the study of extinction and ignition phenomena in solid propellants. A thorough discussion of the use of deradiation in the study of extinction phenomena is found in a review by De Luca¹². However, in these studies, the instantaneous burn rate was generally not measured.

Transient models that can be generalized to include a rapid irradiation transient are in two general categories: (1) quasi-steady gas phase models and (2) completely unsteady models. In the completely unsteady models, an unsteady description of the gas, surface and solid regions given is used. The completely unsteady approach is analytically/computationally complex and, therefore, most modeling has used the quasi-steady assumption. In the quasi-steady approach, the solid phase is assumed to have a characteristic time constant which is much larger than that of either the gas phase or surface zones. Therefore, the surface zone and gas phase are in continual equilibrium with the solid surface boundary. Typical magnitudes of these times for typical solid propellants are $\tau_c = 0.01$ s, $\tau_s = 0.001$ s and $\tau_g = 0.0001$ s - which indicates that the gas phase responds approximately 10 times faster than the surface zone and the gas phase 100 times faster than the solid phase¹³. Therefore, for many situations the quasi-steady assumption can be justifiably applied.

The so-called dp/dt approach is the simplest type of model that can be applied within the framework of the quasi-steady assumption. Approximations are made in the analysis in order to obtain an approximate, but explicit, solution for the transient burn rate. These models, however, oversimplify the situation by failing to consider the transient coupling between heat feedback from the flame zone and the propellant surface conditions. Further, many of these burning rate expressions were derived from small perturbation analysis of the transient heat conduction equation, and thus their use is restricted to cases which deviate slightly from steady state¹³.

Another type of quasi-steady transient burning model is the flame description approach. This approach is similar to the dp/dt approach in that the unsteady term is retained only in the solid phase energy equation. The gas and surface models are quasi-steady in that they have no unsteady term, but they do vary with time due to the changing pressure or radiant heat flux, and boundary conditions at the solid interface. The KTSS¹⁴ model is among the earliest of this type of model and is the basis for several similar models developed later. Derivatives of the KTSS model include those of Levine and Culick (LC)¹⁵, Kooker and Zinn (KZ)¹⁶, and Merkle *et al.* (MTS)¹⁷.

An alternative to dp/dt and flame description models is the Zel'dovich approach. The major advantage of the Zel'dovich is that it requires no detailed knowledge of the spatial distribution of heat release in the gas phase that is needed in the flame description models. However, extensive steady-state experimental data are needed which are often difficult to obtain. In cases where extensive experimental data are unavailable, the definition of the temperature sensitivity may be used to obtain an approximation of the relationship between burn rate and initial temperature^{18,19}. In this study, the KTSS, LC, and Zeld'ovich models are modified to include radiant heat flux and are compared with new experimental data obtained using CO₂ laser as a radiant source and a microforce transducer to measure the response in the thrust of the propellant sample.

Experimental Setup

A schematic of the NWC radiant heat flux equipment is shown in Figure 1. Both vertically and horizontally oriented apparatus were tested and it was determined that the vertically oriented apparatus exhibited less mechanical resonance in the frequency band of interest, consequently this orientation was used in this study. Since the oscillations are often less than 10⁻³ N, a very sensitive transducer is required. A Kistler 9207 high sensitivity quartz force transducer, with natural frequency greater than 10 KHz, was used to measure the thrust oscillations. The transducer was mounted inside an aluminum block for thermal isolation and rubber mounts were used to minimize extraneous vibrations.

The CO₂ laser (10.6 μm, 150W) was modulated by a function generator. A SPAWR beam integrator has been used to flatten the energy distribution profile of the laser beam. The beam is expanded using a plano concave lens onto an integrator which refocuses the beam into an area approximately 1.6 cm².

Data Reduction

In order to make quantitative comparisons with the models, either the thrust data should be transformed into instantaneous burn rates or the numerical predictions of burn rate transformed to force fluctuations. Applying simple steady state continuity and momentum relations and neglecting the effect of nonsteady changes in the mass of the propellant sample, the thrust measurements can be transformed to mass flux by⁴⁻⁶

$$m = \sqrt{\frac{MpF}{RT_f A}} \quad (1)$$

The force measurements could also be converted to mass flux by considering only small fluctuations and again neglecting the effect of the unsteady changes in the mass of the propellant (vertical orientation)⁵⁻⁷. Perturbing Eqn. (1), the following is obtained

$$m' = \frac{Mp}{2\bar{m}RT_f A} F. \quad (2)$$

The effect of changes in the mass of the propellant can also be included to obtain,

$$a = \frac{C_2}{C_2^2 - C_1^2} c - \frac{C_1}{C_2^2 - C_1^2} d \quad (3)$$

$$b = \frac{C_1 C_2}{C_2(C_2^2 - C_1^2)} c + \frac{C_2^3 - 2C_2 C_1^2}{C_2^2(C_2^2 - C_1^2)} d \quad (4)$$

where c and d are the real and complex parts of the force data, respectively; and a and b are the real and complex parts of the burn rate, respectively. C_1 and C_2 are constants used for convenience. To apply Eqn. (3), the data is first transformed to discrete frequencies using a discrete Fourier transform. In the frequency domain the individual frequency components can be transformed and then an inverse transform can be performed to bring the transformed data back to the time domain.

Governing Equations and Gas Phase Modeling

In this analysis the coordinate origin is attached to and moves with the solid propellant surface. In this frame of reference, the solid is treated as a slug flow toward the reaction surface at $x=0$. Governing equations for the solid phase, the gaseous phase and the surface zone separating the two phases will be presented in the following.

Solid Phase Unsteady Energy Equation

The solid phase is assumed to be nonreacting. The unsteady energy equation, including in-depth absorption, in the solid phase (solid phase extending into the positive x -direction) is

$$\frac{\partial T}{\partial t} = \tau \frac{\partial T}{\partial x} + \alpha_c \frac{\partial^2 T}{\partial x^2} + f_1 \frac{q_{r1}}{\rho C} K_{a1} \exp(-K_{a1}x) + f_2 \frac{q_{r2}}{\rho C} K_{a2} \exp(-K_{a2}x) \quad (5)$$

or, in dimensionless form

$$\frac{\partial \Theta}{\partial \tau} = R \frac{\partial \Theta}{\partial X} + \frac{\partial^2 \Theta}{\partial X^2} + f_1 Q_R \beta_1 \exp(-\beta_1 X) + f_2 Q_R \beta_2 \exp(-\beta_2 X) \quad (6)$$

In this study, the density, thermal conductivity, and heat capacity of the solid are considered constant and the natural radiant feedback to the solid, q_{r1} , is neglected. It has been assumed that scattering is negligible, the absorption coefficient K_{a2} is spatially constant, thermal emission by the condensed phase is negligible, and the incident flux is collimated. It should be noted that the fraction of radiant flux that is absorbed below the reaction layer, f_2 , must be specified. From scaling arguments and Beer's law, the behavior is modelled using $f_2 = \exp(-L_f \bar{X}_R / X_A) = \exp(-L_f \beta R T_s / E_s)$. L_f is a correction factor which may be included to account for the uncertainties of the thickness of the reaction layer and if the absorption coefficient of a possible melt layer on the propellant surface is different from the absorption coefficient in the nonreacting solid. The numerical solution of this equation is discussed in a latter section. The steady state solution is found to be

$$\Theta(X) = \left[1 - \frac{f_2 Q_R}{(1-\beta_2)} \right] \exp(-X) + \frac{f_2 Q_R}{(1-\beta_2)} \exp(-\beta_2 X) \quad (7)$$

which is useful as an initial condition for the numerical solutions.

Surface Zone

For the KTSS description, the solid propellant pyrolysis rate is assumed to be described in terms of a power rate law¹⁴

$$R = \Theta_S^m. \quad (8)$$

Similarly as shown by Levine and Culick¹⁵ an unsteady equivalent Arrhenius expression may be used having the form

$$R = P^{n_s} \exp \left[\frac{A(\Theta_s - 1)}{1 + \frac{A}{E}(\Theta_s - 1)} \right] \quad (9)$$

where pressure dependence, n_s , is often neglected.

Gas Phase Energy Equation

The following assumptions are made in formulating the flame description quasi-steady burning models: (1) the gas phase density is spatially uniform, (2) all gas phase specific heats are equal, (3) Fick's law of diffusion is valid and all diffusivities are equal ($D_i = D$), (4) gas phase reactions are represented by a single-step forward reaction. Applying these assumptions, the quasi-steady form of the gas phase energy equation for a single-step reaction and equal solid and gas phase specific heats becomes¹⁴:

$$\lambda_g \frac{d^2T}{dx^2} + (\rho_c r) c_g \frac{dT}{dx} + \rho_g Q_f \dot{\epsilon} = 0 \quad (10)$$

Integrating between $x \rightarrow -\infty$ (far downstream in the gas phase) and $x=0$ (the propellant surface), assuming that the reaction rate term is a step function (uniform between the surface and the flame and zero elsewhere), and using an average gas phase velocity and average gas phase density, it can be shown that

$$q(0) = \frac{\lambda_g Q_f \bar{\rho}_g}{c_g \tau_c \rho_c r} \left(1 - \exp \left(- \frac{\rho_c^2 c_g r^2 \tau_c}{\lambda_g \bar{\rho}_g} \right) \right) \quad (11)$$

For most propellants, the exponential in (11) is quite large and the term may be neglected, so

$$q(0) = \frac{\lambda_g Q_f \bar{\rho}_g}{c \tau_c \rho_p r} \quad (12)$$

This approximation is valid whenever the heat transferred back to the solid surface is small compared to the heat released in the gas phase¹⁴. Next, since the reaction rate is only weakly dependent on temperature, it is assumed that τ_c is a function of pressure only. Therefore, equation (12) indicates that at constant pressure there is an inverse relationship between the burning rate and the heat feedback

$$q_g = \frac{\Phi(p)}{r} \quad (13)$$

where this equation is the definition of the pressure dependence, $\Phi(p)$. In order to determine the functional relation of $\Phi(p)$ the steady state condition is considered. We may write

$$\Phi(p) = \bar{q}_g \bar{r} \quad (14)$$

and \bar{r} is related to the pressure and surface temperature by

$$\bar{r} = ap^n \quad (15a)$$

and

$$\bar{r} = b(\bar{T}_s - T_\infty)^m \quad (15b)$$

The steady state energy balance without a radiant heat flux,

$$\bar{q}_g = -\lambda_g \left(\frac{dT}{dx} \right)_s = \rho \bar{r} (C(\bar{T}_s - T_\infty) - Q_s) \quad (16)$$

can then be used with the above relations to obtain the form of $\Phi(p)$. By substituting equation (15) for \bar{r} and $(T_s - T_\infty)$ into Eqn. (16) to determine an expression for q_g in terms of p , and then substituting this expression for \bar{q}_g into Eqn. (14), with \bar{r} again replaced by Eqn. (15), an expression for $\Phi(p)$ is obtained:

$$\Phi(p) = \rho (ap^n)^2 \left(C \left(\frac{a}{b} p^n \right)^{1/m} - Q_s \right) \quad (17)$$

An energy balance at the propellant surface results in

$$-\lambda_c \left(\frac{\partial T}{\partial x} \right)_s = q_g + \rho_c r Q_s + (1-f_2) q_{r2}. \quad (18)$$

Substituting the heat feedback expression (13) with $\Phi(p)$ in the form of Eqn. (17) into this surface boundary condition, the solid phase boundary condition

$$-\lambda_c \left(\frac{\partial T}{\partial x} \right)_s = \rho (ap^n)^2 \frac{(C(a/bp^n)^{1/m} - Q_s)}{r} + \rho r Q_s + (1-f_2) q_{r2} \quad (19)$$

is obtained, or in dimensionless variables, the gradient boundary condition becomes

$$\left(\frac{\partial \Theta}{\partial X} \right)_s = - \frac{(P^{2n} (P^{n/m} - H))}{R} - HR - (1-f_2) Q_R \quad (20)$$

For cases where $q_{r2} = 0$, Eqn. (20) becomes the boundary condition derived by Krier *et al.*¹⁴. For in depth absorption only ($f_2 = 1$), the radiant heat flux affects the solution only through the source term in Eqn. (6). Likewise as f_2 approaches zero, the radiant energy is absorbed completely at the surface and the only influence of Q_R is on the boundary condition. It is worthwhile to observe that for any given $P(\tau)$ (and the corresponding $R(\tau)$), a $Q_R(\tau)$ can be specified which results in the same boundary conditions. From Eqn. (20), it can be shown that for this condition to be met

$$Q_R = \frac{P_c^{2n+n/m} - P^{2n-n/m} - H(P_c^{2n} - P^{2n})}{R} \quad (21)$$

where P_c is the nondimensional pressure (typically constant) during irradiation. Thus, in the limit of surface absorption (and the other model assumptions), data obtained during a rapid pressurization can be transformed to data for a rapid irradiation, and vice versa.

Other flame description models can easily be substituted for Eqn. (20). For example the gradient boundary condition for the Levine-Culick (LC) model is

$$\left(\frac{\partial \Theta}{\partial X}\right)_s = \frac{P^{2n}}{R} \left\{ \frac{C_p E}{C A} \left[\frac{1}{1 + \frac{n_s - n}{E} \ln P} - 1 \right] + 1 - H \right\} + R \left[H + (1 - \frac{C_p}{C})(\Theta_s - 1) \right] - (1-f_2) Q_R \quad (22)$$

where again n_s is often neglected. The most significant differences between the LC model and the KTSS model is that the assumption of equal specific heats has been relaxed and an Arrhenius-type relationship has been used instead of the power law assumed by Krier *et al.*¹⁴ In the limit of surface absorption, the pressure and radiant flux are again directly related.

To obtain the appropriate temperature gradient boundary condition using the Zel'dovich approach, we begin with the energy balance over the nonreacting solid,

$$\lambda_c b \left(\frac{dT}{dx} \right)_s = \rho \bar{r} C (\bar{T}_s - T_\infty) \quad (23)$$

where the radiant flux does not appear because we have chosen to account for it as a source term in Eqn. (6) and in the value of T_∞ . For the Zel'dovich approach, T_∞ can be thought of as an equivalent initial temperature and not the actual initial temperature. If extensive steady state experimental data are available for $\bar{r}(T_s)$ and $\bar{r}(\bar{p}, \bar{q}_{r2}, T_\infty)$ these experimentally obtained expressions could be substituted into Eqn. (23) to eliminate T_s and T_∞ which leads to a boundary condition that is a function of the instantaneous burn rate and the driving function (either \bar{q}_{r2} or \bar{p}). The Zeld'ovich approach is valid as long as the quasi-steady assumption holds¹⁸; however, a sufficiently extensive data set is often not available. For example, for very fast deradiation or depressurization instantaneous burn rates corresponding to very low equivalent initial temperatures may occur. Often an Arrhenius type relationship can be successfully assumed and fit to available $\bar{r}(T_s)$ data and used to provide a relationship between T_s and \bar{r} . Unfortunately, $\bar{r}(\bar{p}, \bar{q}_{r2}, T_\infty)$ data is not as plentiful over the desired ranges. One alternative is to use available data as much as possible and then use the temperature sensitivity coefficient to provide a way to extrapolate to regions beyond the bounds of the experimental data¹⁸. The temperature sensitivity is defined as

$$\sigma_p = \left(\frac{\partial \ln \bar{r}}{\partial T_\infty} \right) \quad (24)$$

Integrating this expression, assuming σ_p remains constant, from the nearest known experimental values of r_o and $T_{\infty,0}$ to the desired \bar{r} and T_∞ values,

$$T_\infty = T_{\infty,0} - \frac{1}{\sigma_p} \ln \left(\frac{\bar{r}_o(\bar{p}, \bar{q}_{r2})}{\bar{r}} \right) \quad (25)$$

Substituting this into Eqn. (23) and invoking the quasi-steady assumption

$$\lambda_c \left(\frac{dT}{dx} \right)_s = \rho \bar{r} C \left((T_s - T_{\infty,0}) + \frac{1}{\sigma_p} \ln \left(\frac{T_o(p, q_{r2})}{\bar{r}} \right) \right) \quad (26)$$

or, in dimensionless form

$$\left(\frac{d\Theta}{dX}\right)_s = R \left(\Theta_s + \frac{1}{(\bar{T}_s - T_{\infty,0}) \sigma_p} \ln \left(\frac{R_o(Q_R, P)}{R} \right) \right) \quad (27)$$

for the gradient boundary condition. It should be noted that the steady state burn rate as either a function of radiant heat flux and pressure must be specified at $T_{\infty,0}$. Again, given the empirical functions $R_o(Q_R, P_c)$ and $R_o(0, P)$, a direct transformation between Q_R and P can be obtained assuming surface absorption.

Numerical Methodology

The above models result in a single partial differential equation and appropriate boundary conditions for the determination of the time-dependent dimensionless temperature distribution within the solid propellant, in response to a pressure or radiant heat flux forcing function. Because of the non-linear surface boundary condition, these equations must be solved numerically. The numerical solution of this equation, including the implementation of the boundary conditions, is discussed below.

Coordinate Transformation

A compact finite-difference algorithm used to discretize the governing equation (Eqn. (6)), will be discussed below. It is generally preferable to space the finite-difference nodes more closely near the propellant surface for maximum accuracy and to increase the grid spacing away from the surface to ensure that the upstream nodes reach the undisturbed portions of the propellant. This is most efficiently achieved by way of an algebraic coordinate transformation between the dimensionless physical coordinate system (X) and an uniformly spaced computational coordinate system (ξ):

$$\xi = \xi(x); \Delta\xi = 1 \quad (28a,b)$$

where $\Delta\xi$ is the node spacing in the computational domain. The particular form used in this study, and the associated metrics, is show below:

$$X = X(\xi) = \frac{(\beta+1)-(\beta-1)((\beta+1)/(\beta-1))^{1-\xi}}{((b+1)/(b-1))^{1-\xi}+1} \quad (29a)$$

$$\xi = 1 - \frac{\ln\{(\beta+1-X/X_{\max})/(\beta-1+X/X_{\max})\}}{\ln\{(\beta+1)/(\beta-1)\}} \quad (29b)$$

$$\xi_x = \frac{2\beta}{X_{\max}(\beta^2-(1-X/X_{\max})^2)\ln\{(\beta+1)/(\beta-1)\}} \quad (29c)$$

$$\xi_{xx} = -\frac{2}{X_{\max}} \frac{2\beta}{X_{\max}\ln\{(\beta+1)/(\beta-1)\}(\beta^2-(1-X/X_{\max})^2)^2} \quad (29d)$$

The constant β is selected to vary the grid compaction near the propellant surface ($1 < \beta < \infty$: compaction near the surface increases as $\beta \rightarrow 1$). The governing equation (Eqn. (6)), when transformed to the computational domain (ξ) becomes

$$\frac{\partial\Theta}{\partial\tau} = (\xi_x R + \xi_{xx}) \frac{\partial\Theta}{\partial\xi} + (\xi_x)^2 \frac{\partial^2\Theta}{\partial\xi^2} + f_1 Q_R \beta_1 \exp(-\beta_1 X(\xi)) + f_2 Q_R \beta_2 \exp(-\beta_2 X(\xi)). \quad (30)$$

where the metrics are given by Eqns. (29).

Numerical Algorithm

Numerical solution of the above time-dependent one-dimensional transformed governing partial equation (Eqn. (30)) is accomplished by the method of lines. An explicit compact finite-difference numerical scheme is used to spatially discretized the governing equations, resulting in a set of coupled ordinary differential equations (in time) for each of the dimensionless nodal temperatures (Θ_i). The ODEs are solved using a Runge-Kutta integration procedure.

First- ($f = \partial\Theta/\partial\xi$) and second-order ($s = \partial^2\Theta/\partial\xi^2$) spatial derivatives are evaluated using fourth-order compact finite-difference formulas (Hirsh²⁰):

$$\frac{f_{i+1} + 4 f_i + f_{i-1}}{6} = \frac{\Theta_{i+1} - \Theta_{i-1}}{2} \quad (31a)$$

$$\frac{s_{i+1} + 10 s_i + s_{i-1}}{12} = \Theta_{i+1} - 2 \Theta_i + \Theta_{i-1} \quad (31b)$$

Note that the fact that $\Delta\xi=1$ has been incorporated in the above formulae. Truncation errors for the above formulae have been shown to be

$$f_i - \left(\frac{\partial\Theta}{\partial\xi} \right)_i = -\frac{1}{180} \Delta\xi^4 \left(\frac{\partial^5\Theta}{\partial\xi^5} \right)_i; \quad s_i - \left(\frac{\partial^2\Theta}{\partial\xi^2} \right)_i = -\frac{1}{240} \Delta\xi^4 \left(\frac{\partial^6\Theta}{\partial\xi^6} \right)_i \quad (32a,b)$$

The above are of the same order as a standard five-point central difference formula, but with smaller leading coefficients (Hirsh²⁰). Substituting the above expressions into the governing equation (Eqn. (30)) results in coupled ODEs for the dimensionless nodal temperatures (Θ_i):

$$\frac{\partial\Theta_i}{\partial\tau} = (\xi_x R + \xi_{xx}) f_i + (\xi_x)^2 s_i + f_1 Q_R \beta_1 \exp(-\beta_1 X(\xi)) + f_2 Q_R \beta_2 \exp(-\beta_2 X(\xi)) \quad (33)$$

The ODEs are integrated in time using a second-order Runge-Kutta integration routine. Because this is an explicit scheme, stability limits on time-step size exist. Hirsh²⁰ has shown that the stability limits for the above compact finite-difference scheme combined with Euler forward time differencing applied to Burger's equation results in the following time-step limitations:

$$\Delta\tau \leq \frac{1}{3}; \quad R\Delta\tau \leq \left(\frac{1}{6} \right)^{1/2} \quad (34a,b)$$

These limitations were used to guide the time-step selection for the current Runge-Kutta/compact finite-difference scheme. These more restrictive step size limitations (e.g., compared to standard second explicit schemes) are counteracted by the larger axial nodal spacing allowed due to the fourth-order accuracy. In addition, because of the highly non-linear nature of the surface boundary condition, small time-steps are required to maintain stability and temporal accuracy. This similarly, favors the current explicit scheme over a more complex implicit approach. Scalar diagonal matrix inversions required by the explicit compact finite-difference derivative evaluations are accomplished with the Thomas algorithm.

Initial Conditions, Input (Forcing) Functions, and Boundary Conditions

The solid phase dimensionless temperatures profile is initialized with the steady-state solution (Eqn. (7)). Validation tests indicate that this steady-state solution is accurately calculated when no

input forcing function is applied. The transient solutions of interest results from the application of an input forcing function, either pressure (P) or an external radiant heat flux (Q_R).

In this study, only the radiant heat flux input results are presented. Various input functions have been considered. These include periodic step, exponential, and a ramped input functions. The radiant heat flux input function effects the solid phase response directly through the surface boundary conditions (surface absorption) and in-depth radiant heat flux absorption (when considered). The numerical treatment of the in-depth absorption is straight forward and is included as source terms in Eqn. (30).

Implementation of the boundary conditions (surface) is a critical part of the numerical solution, since it provides the principle coupling between the gas-phase, surface, and solid-phase portions of the propellant combustion processes. The upstream boundary condition is straight forward and involves the specification of the undisturbed propellant temperature:

$$\Theta_n = 0 \quad (35)$$

In the compact finite-difference evaluation of the spatial derivatives at the furthest upstream node, f_n and s_n are determined from standard (non-compact) one-sided finite-difference approximations. The location of node "n" is chosen to be well within the undisturbed portion of the propellant (typ., $X=15$) and these boundary conditions have little effect on the solution.

The boundary condition at the surface is specified in terms of the heat flux at the surface, due to both gas phase combustion feedback and the external radiant heat flux. This is accomplished using a second-order upwind finite-difference approximation to the surface temperature derivative. After rearrangement, these approximations provide an expression for the surface temperature:

$$\left(\frac{\partial \Theta}{\partial \xi} \right)_s = -(\xi_x)^{-1} \left(\frac{(P^{2n} (P^{n/m} - H))}{R} - HR - (1-f_2)Q_R \right) \quad (36)$$

$$\Theta_s = -\frac{3}{2} \Theta_1 + \frac{1}{2} \Theta_2 + 3 (\xi_x)^{-1} \left(\frac{(P^{2n} (P^{n/m} - H))}{R} - HR - (1-f_2)Q_R \right) \quad (37)$$

Because the above expression is non-linear (through the dependence $R=\Theta_s^m$), the boundary condition must be implemented iteratively. With the explicit compact finite-difference scheme used in this investigation, no convergence difficulties have been encountered.

In the compact finite-difference evaluations of the derivatives, Eqn. (36) is also used to specify the surface value of the first derivative (f_s):

$$f_s = \frac{\partial \Theta}{\partial \xi} s_s = - \frac{\left(P^{2n} (P^{n/m} - H) - \frac{Q_R}{P^n} \right)}{R} - HR - (1-f_2)Q_R \quad (38)$$

The surface value for the second derivative (s_s) is specified using a second-order upwind formula:

$$s_s = \frac{\partial^2 \Theta}{\partial \xi^2 s} = -\Theta_3 + 4\Theta_2 - 5\Theta_1 + 2\Theta_0 \quad (39)$$

With the above initial conditions, input forcing function(s), and boundary conditions, the governing equations (Eqn. (30)), can be integrated in time as desired.

Code Validation

The code was validated by several means. First, the compact finite-difference discretization was checked by integrating to and comparing with the steady-state solution (Eqn. (7)). The agreement was found to be excellent, with 200 nodes and a grid compaction factor (β) of 1.2. In addition, standard explicit second-order central finite-difference formulae were also used for comparison. The compact and standard schemes were then checked against each other, and with previous exponentially rising pressure input solutions in the literature. Again, the results were in good agreement on the final grid.

Results

In this section, the latest experimental results are presented for three different propellants tested at atmospheric pressure surrounded by room temperature air. The propellants tested were: N5 (double base), A13 (PBAN, AP), and NWR11 (HTPB, AP, minimum smoke). N5 is a mesa burning propellant; however, near atmospheric pressure it has linear burnrate characteristics. Experiments using other propellant compositions will shortly be performed and the results will be included in the full paper. Specifically, AP composites with fine oxidizer sizes and a double base propellant with a more linear burn rate will be tested and quantitatively compared various models; as well, experiments at elevated pressure will be performed.

Figures 1 and 2 show the response of N5 to a pulsed heat flux. The response is characterized by a sharp jump followed by an smooth decay, overshoot and damped oscillation. The overall slope of the force measurement in the figure is due to the consumption of the propellant sample as it is burned. The modified KTSS model was run for a similar case as the experiments, assuming surface absorption and typical parameters for this propellant (Fig. 3). The initial condition of the propellant was the steady state profile with no radiant heat flux, which explains the higher first burn rate peak. This initial transient soon dies out and the calculations show qualitative features similar to the experimental data. The full paper will contain a quantitative comparison between the data and the modified KTSS, LC, and Zeld'ovich models.

Since a sharp pulse was used, a wide bandwith of the frequencies are excited. Thus, for small amplitude pulses it may be possible that the combustion response, R_q , may be obtained from this data. The combustion response, R_q , is defined as

$$R_q = \frac{m'/\bar{m}}{q'r_2/\bar{q}_r} = \frac{r'/\bar{r}}{q'r_2/\bar{q}_r} \quad (40)$$

where q_r is the external heat flux directed on the burning propellant surface. This complex valued response function was obtained from the data by a spectral analysis and is shown in Figures 4 and 5. The magnitude of R_q is normalized by n_q which is the value of R_q at the zero frequency. Also shown is a comparison with results of a linearized model that was derived applying similar assumptions as the KTSS model and includes in depth absorption (Son, et al.²¹). Typical parameters were used in the linearized model and no optimization of the input parameters has been made; even though there is substantial uncertainty in the activation energy and surface heat release values. The response shows the expected phase lead at frequencies below the response peak and phase lag at higher frequencies. These results also compare well with recent data using a sinusoidal input (single frequency) (Finlinson, et al.²²). Considering the difficulties and expense in obtaining combustion response function using conventional methods (ie. T-burner), this approach may prove to be a very convenient and useful technique.

Figure 6 and 7 show the response of A13 and NWR11 to a wider pulse. The wide pulse was used to increase the response of the propellant. For narrower pulse widths, the response was below the transducers sensitivity. Experiments will shortly be performed using a higher radiant heat flux (a 10 kW CO₂ is available at UIUC) and another AP propellant will also be studied using a very fine oxidizer size which is expected to increase the combustion response. The present results do show that there is very significant difference in the response of the double base compared with the AP composites studied.

The pressure transient gradient is known to be an important parameter in the response of a propellant to a rapid pressure transient. To investigate the effect of the gradient of an irradiation transient, a simple ramp function was used in the KTSS model. Figure 8 shows that for the same change in the radiant heat flux, a very different burn rate response may result. In general, as the gradient is steepened, the burn rate response shows more of an overshoot and is more oscillatory. New experiments using a ramp irradiation transient will also be performed to provide a comparison with the model predictions and will be presented in the full paper.

References

1. Strand, L. D., Schwartz, K., and Burns, S. P., "Propellant Combustion Response to Oscillatory Heat Flux". 24th JANNAF Combustion Meeting, CPIA Publ. No. 476, Vol. 1, Oct. 1987, pp. 41-50.
2. Wilson, J. R., and Micci, M. M., "Direct Measurement of High Frequency Solid Propellant Response Functions", 20th JANNAF Combustion Meeting, Vol. I, CPIA Publ. No. 383, Oct. 1983, pp. 193-202.
3. Brown, R.S., Torikai, T., Babcock, W. R., "Combustion Response Function Measurements by the Rotating Valve Method," *AIAA Journal*, Vol. 12, Nov. 1974, pp. 1502-1510.
4. Mihlfeith, C. M., Baer, A. D., and Ryan, N. W., "Propellant Combustion Instability as Measured by Combustion Recoil," *AIAA Journal*, Vol. 10, No. 10, Oct. 1972, pp. 1280-1285.
5. Mihlfeith, C. M., "Some Experiments on the Effect of Thermal Radiation on Composite Rocket Propellants," Ph.D. Thesis, University of Utah, Salt Lake City, Utah, 1971.
6. Mihlfeith, C. M., Baer, A. D., and Ryan, N. W., "The Direct Measurement of the Radiant Heat Flux Response Function of Solid Propellants", 8th JANNAF Combustion Meeting, CPIA Publ. 220, Vol. 1, Nov. 1971, pp. 259-275.
7. V. E. Zarko, V. N. Simonenko, and A. B. Kiskin, "Nonstationary Combustion of Condensed Substances Subjected to Radiation," *Fiz. Gorenija Vzryva*, Vol. 23, No. 5, (Oct. 1987).
8. V. N. Simonenko, V. E. Zarko, and K. P. Kutsenogii, "Experimental Study of the Conditions for Auto- and Forced Fluctuations of the Rate of Combustion of a Powder", *Fiz. Gorenija Vzryva*, Vol. 16, No. 3, pp. 60-68 (June 1980).
9. V. E. Zarko, V. N. Simonenko, and K. P. Kutsenogii, "Effects of Light Intensity on the Nonstationary Combustion Rate in a Transient Process", *Fiz. Gorenija Vzryva*, Vol. 11, No. 4, pp. 541-548, (Aug. 1975).

10. Turk, S. L., Battista, R. A., Kuo, K. K., Caveny, L. H., and M. Summerfield, "Dynamic Responses of Solid Rockets During Rapid Pressure Change," *Journal of Spacecraft and Rockets*, Vol. 10, No. 2, 1973, pp. 137-42.
11. Brulard, J., Kuentzmann, P., and R. Kling, "Reponse D'un Propergol Solide a un Echelon de Pession" *LaRecherche Aerospatiale*, Vol. 5, 1975, pp. 279-87.
12. De Luca, L., "Extinction Theories and Experiments", Chapter 12 of *Fundamentals of Solid-Propellant Combustion*, K.K. Kuo and M. Summerfield Eds., Progress in Astronautics and Aeronautics (AIAA), Vol. 90, 1984.
13. Kuo, K.K., J.P. Gore and M. Summerfield, "Transient Burning of Solid Propellants", Chapter 11 of *Fundamentals of Solid-Propellant Combustion*, K.K. Kuo and M. Summerfield Eds., Progress in Astronautics and Aeronautics (AIAA), Vol. 90, 1984.
14. Krier, H., J.S. T'ien, W.A. Sirignano and M. Summerfield, "Nonsteady Burning Phenomena of solid Propellants: Theory and Experiments," *AIAA Journal*, Vol. 6, No. 2, 1968, pp. 278-285.
15. Levine, J. N., and Culick, F. E. C., "Nonlinear Analysis of Solid Rocket Combustion Instability," *AFRPL-TR-74-45*, 1974.
16. Kooker, D. and B. Zinn, "Triggering Axial Instabilities in Solid Propellant Transient Combustion," *ASME J. Heat Transfer*, Vol. 101, 1979, pp. 359-64.
17. Merkle, C., Turk, S., and M. Summerfield, "Extinguishment of Solid Propellants by Depressurization: Effects of Propellant Parameters," *AIAA Paper 69-176*, 1969.
18. Kuo, K. K., and M. Kumar, "Dynamic Burning Effects in the Combustion of Solid Propellants with Cracks, and the use of Granular Bed Combustion Models," NWC TP 6193, Naval Weapons Center, China Lake, CA, 1980.
19. Nelson, C. W., "Transient Combustion: Models vs. ONERA data," ARBRL-TR-02499, Ballistic Research Laboratory, Aberdeen Proving Ground, MD.
20. Hirsh, R.S., "Higher Order Accurate Difference Solutions of Fluid Mechanics Problems by a Compact Differencing Technique", *Journal of Computational Physics*, Vol. 19, pp. 90-109, 1975.
21. Son, S. F., Prevish, T. D., Brewster, M. Q., Finlinson, J. C., and D. Hanson-Part, "Radiant Heat Flux Response of Solid Propellants", to be submitted to the *Journal of Propulsion and Power*, 1990.
22. J. C. Finlinson, D. Hanson-Part, S. F. Son, and M. Q. Brewster, "Measurement of Propellant Combustion Response to Sinusoidal Radiant Heat Flux," to be presented at the 27th JANNAF Combustion Conference, Nov., 1990.

Heat Flux Experimental Setup

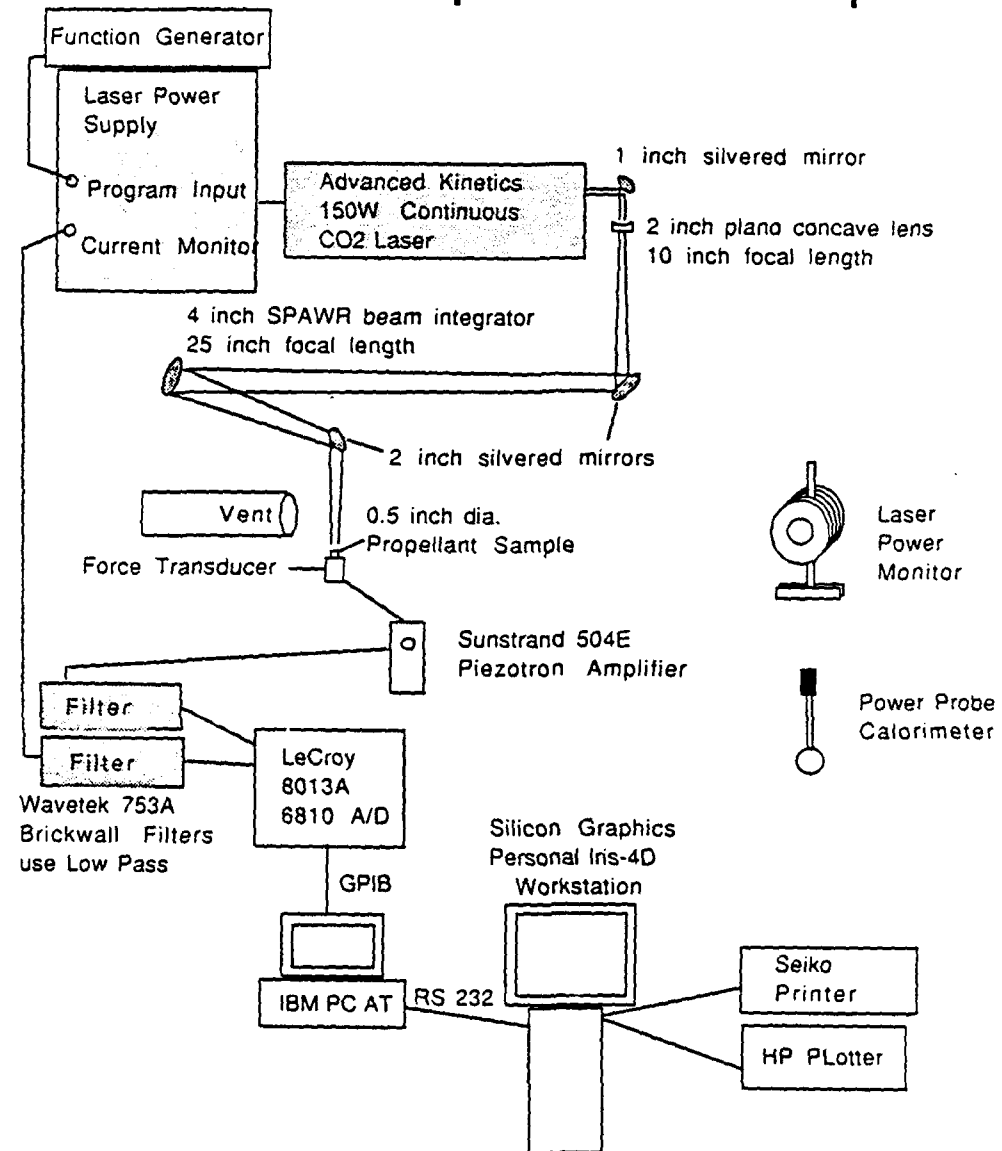


Figure 1a. Schematic of the NWC Radiant Heat Flux Equipment.

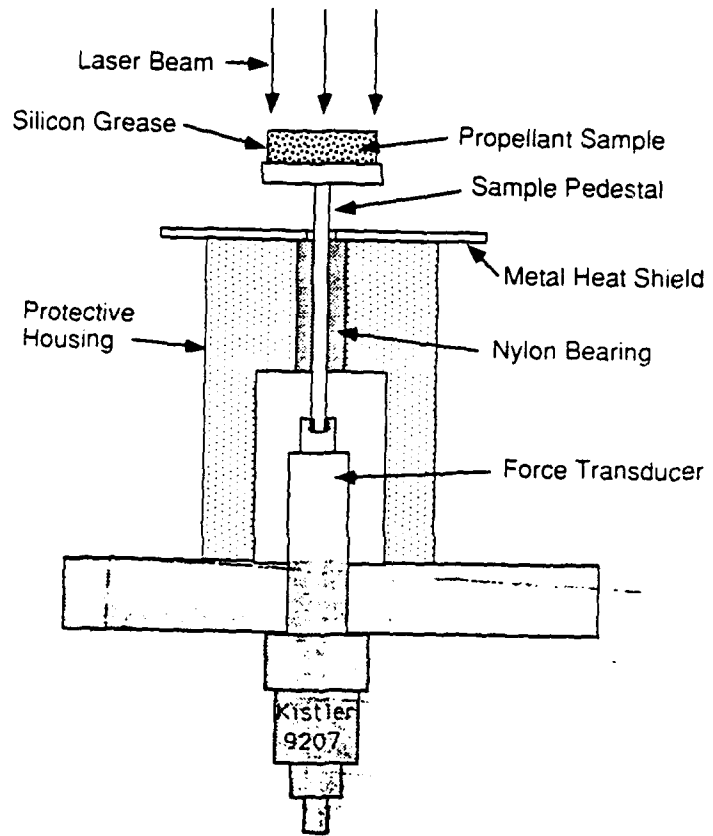


Figure 1b. Schematic of the NWC Propellant Pedestal and Microforce Transducer.

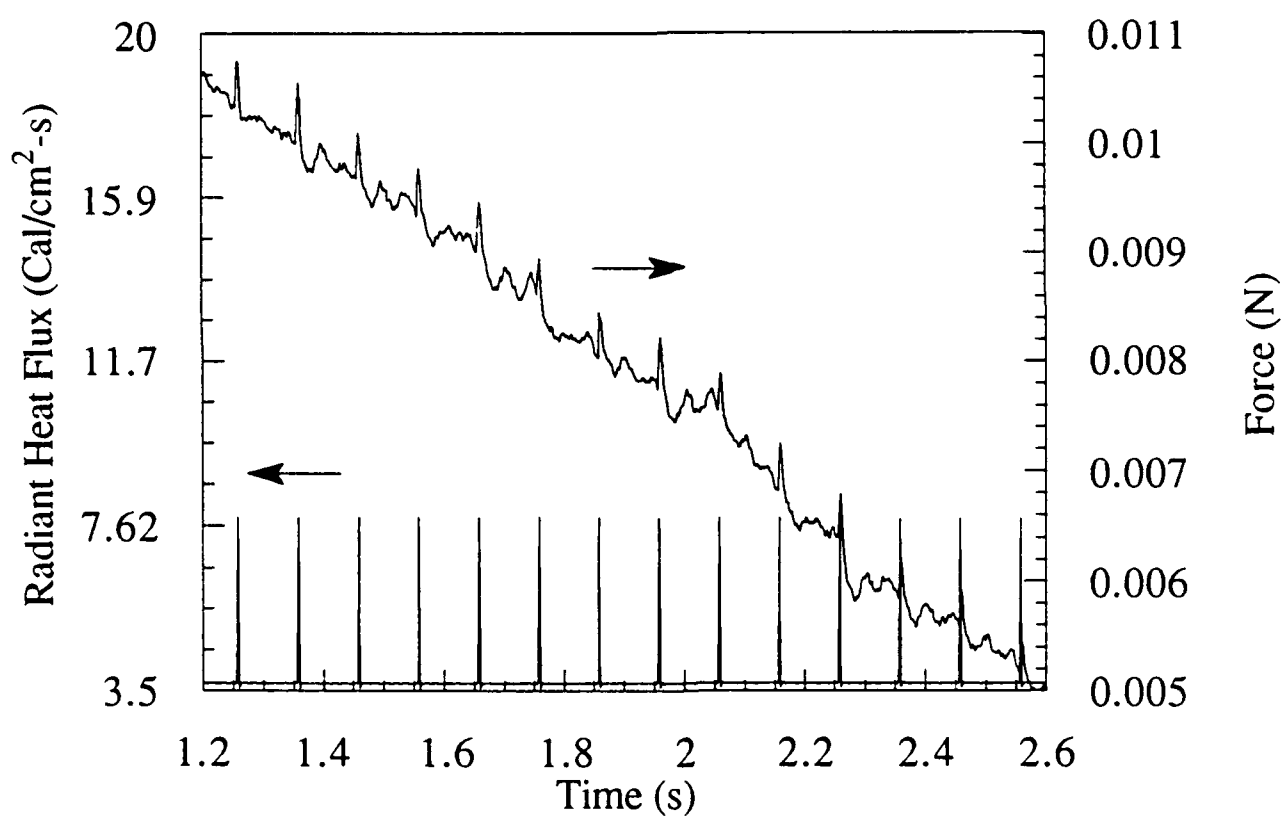


Figure 2a. Experimental Response Data to Radiant Heat Flux Pulse: N5 Propellant.

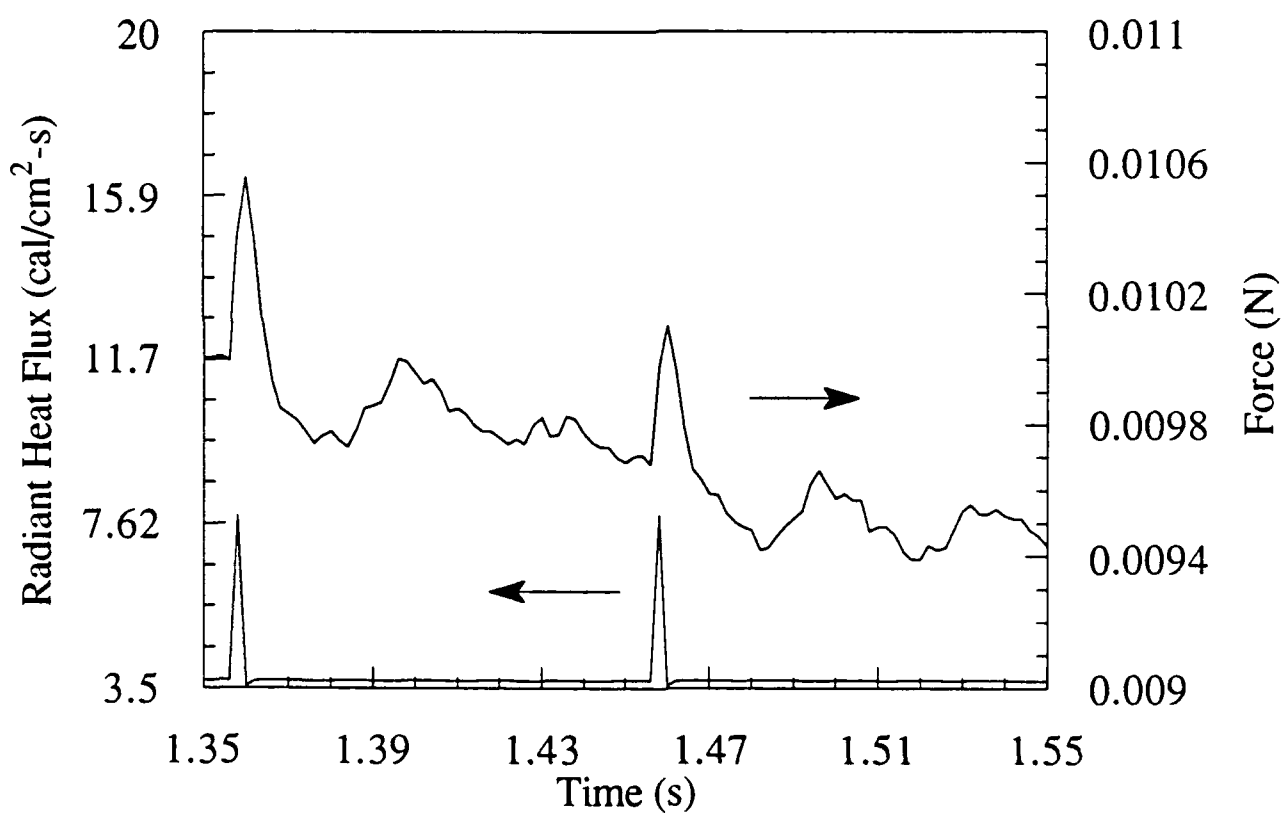


Figure 2b. Experimental Response Data to Radian Heat Flux Pulse: N5 Propellant.

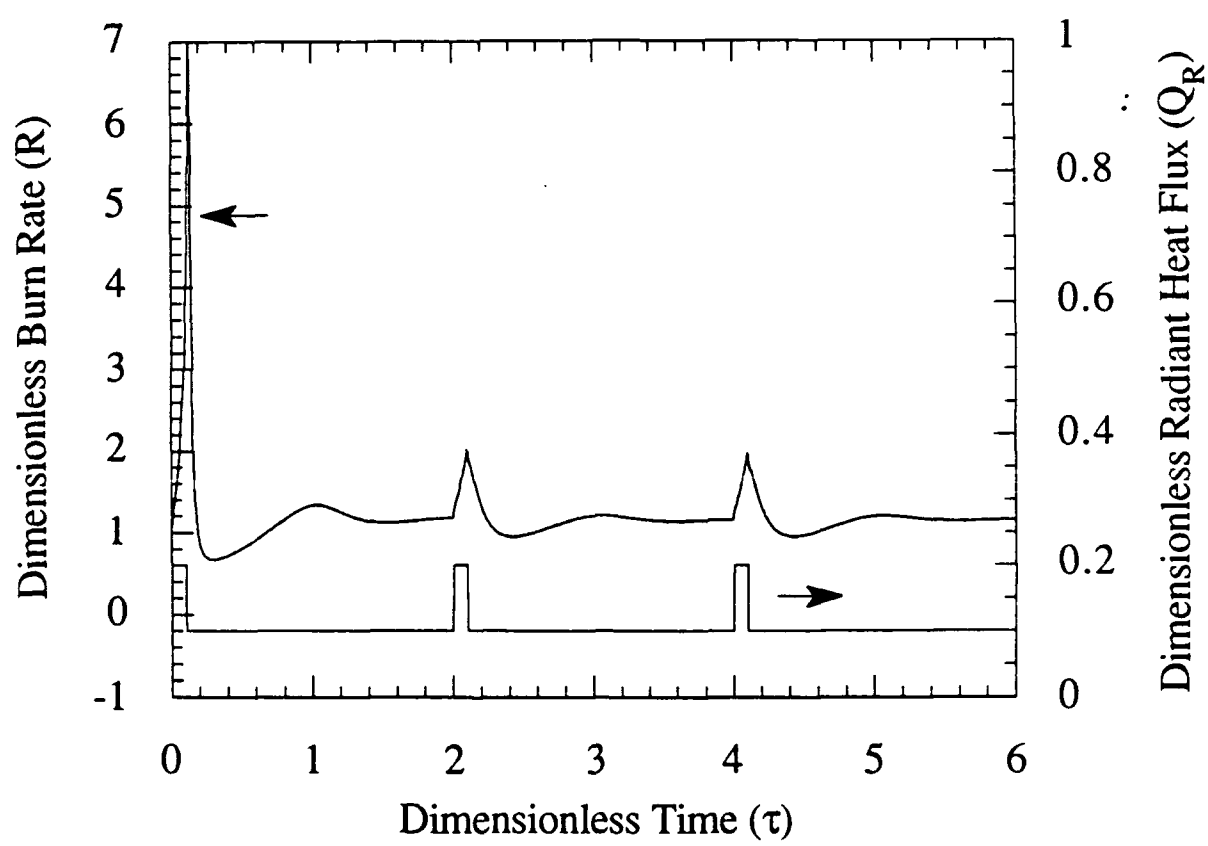


Figure 3. Calculated Response Data to Radiant Heat Flux Pulse.

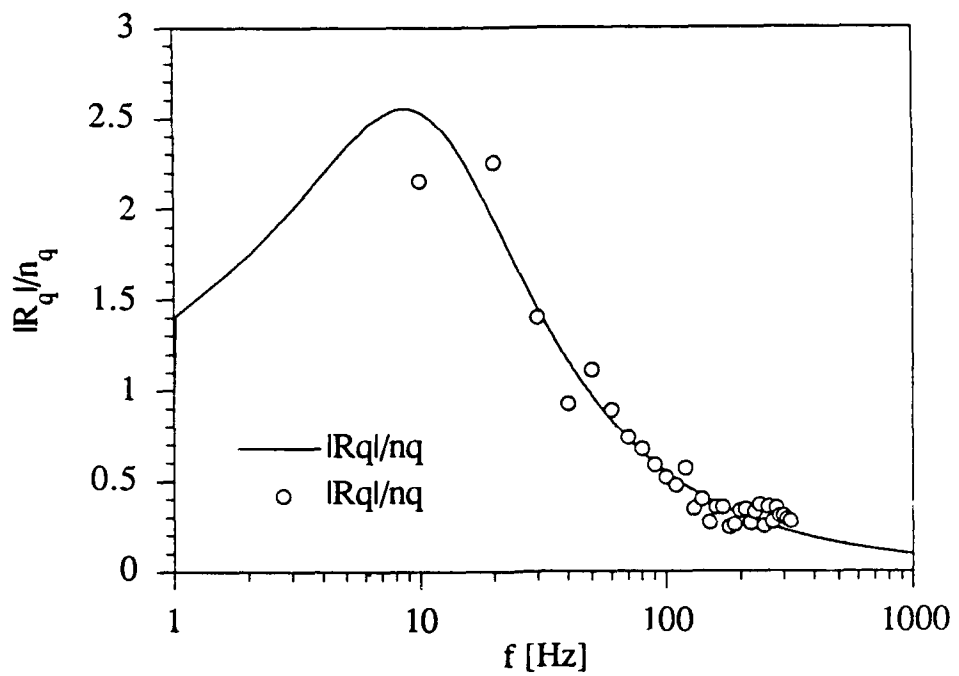


Figure 4. Magnitude of the Radiant Heat Flux Combustion Response (Experimental and Linearized Model): N5 Propellant.

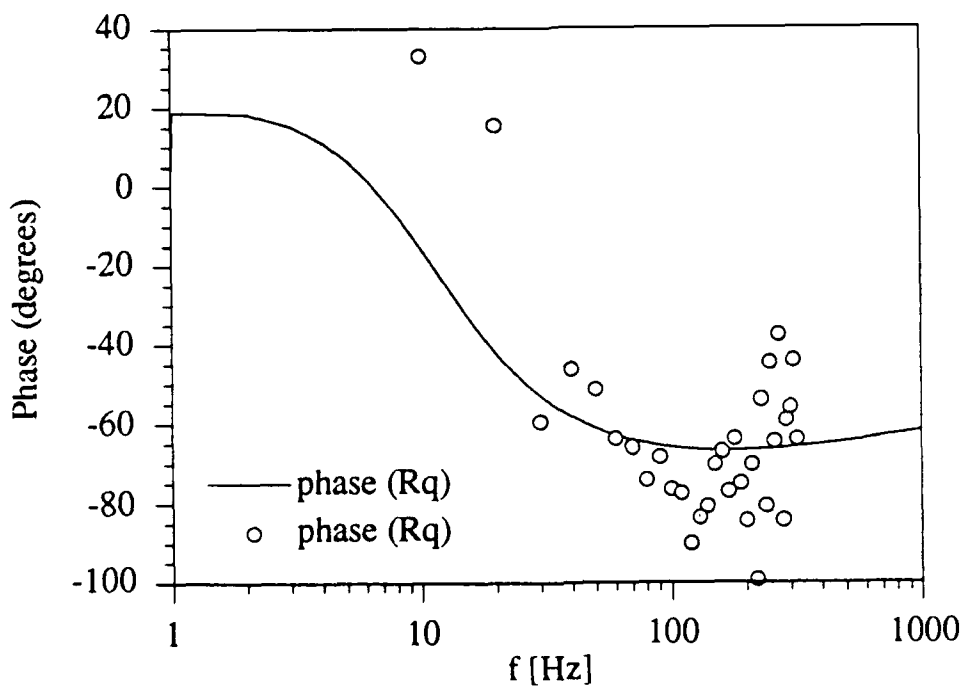


Figure 5. Phase of Radiant Heat Flux Combustion Response (Experimental and Linearized Model): N5 Propellant.

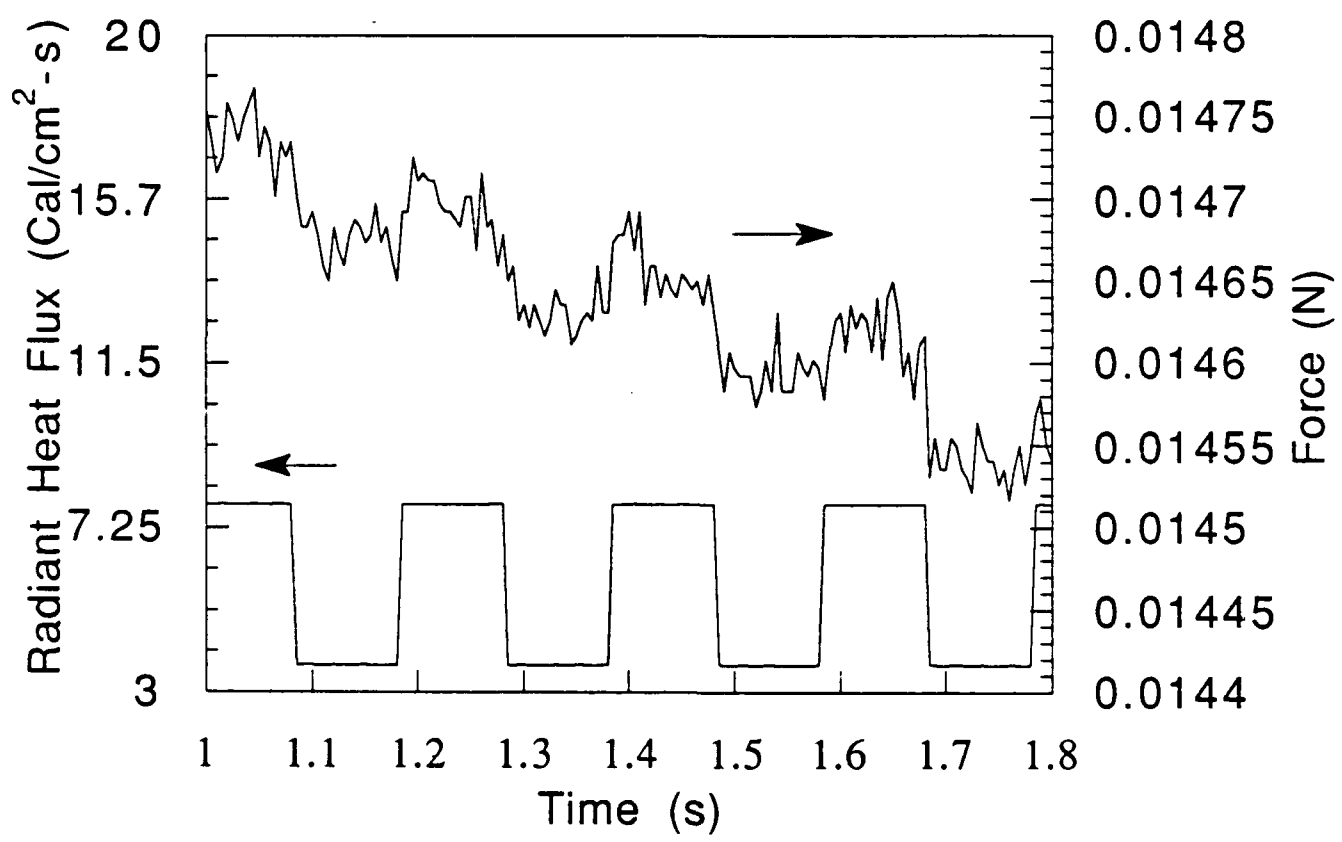


Figure 7. Experimental Response Data to Radiant Heat Flux Pulse: A13 Propellant.

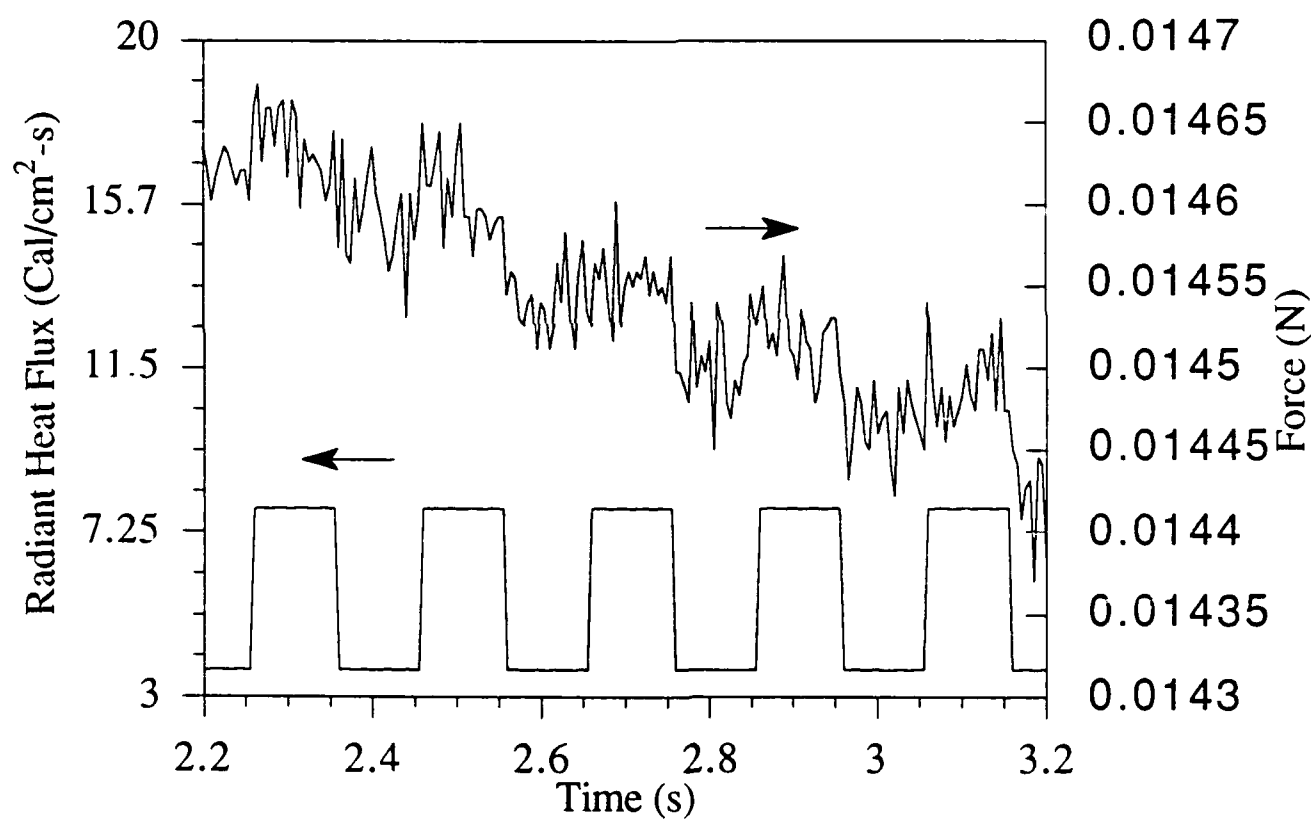


Figure 6. Experimental Response Data to Radiant Heat Flux Pulse: NWR11 Propellant.

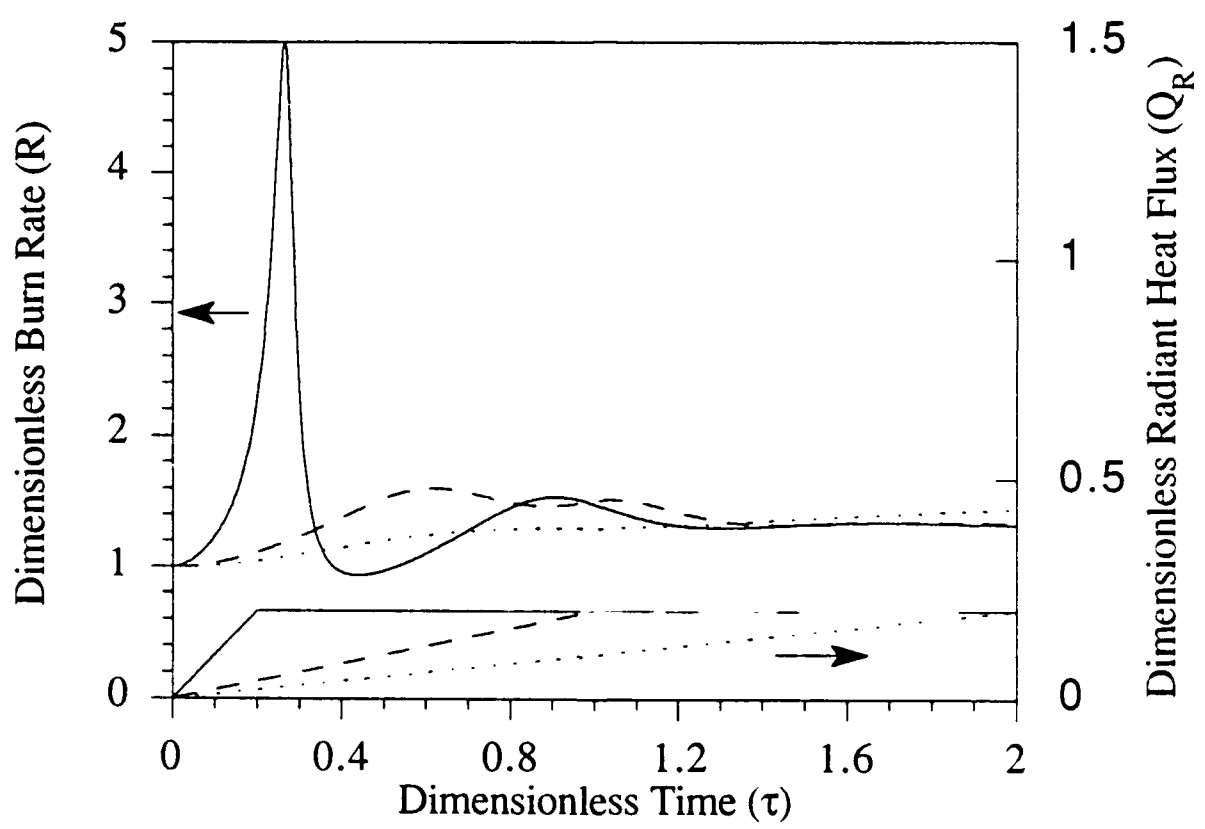


Figure 8. Model Response to Ramp Irradiation Transient.

To Appear in Journal of Propulsion and Power

INFLUENCE OF METAL AGGLOMERATION AND HEAT FEEDBACK ON COMPOSITE PROPELLANT BURNING RATE

M. Quinn Brewster¹ and Brian E. Hardt²
Department of Mechanical and Industrial Engineering
University of Illinois at Urbana-Champaign
Urbana, Illinois

INTRODUCTION

The combustion behavior of metals, particularly aluminum, in solid propellants has been studied extensively [1]. Most studies have aimed at understanding the agglomeration and ignition mechanisms with the hope of being able to reduce the extent of agglomeration at the propellant surface and thereby improve combustion efficiency [2]. Another aspect of metal combustion in solid propellants which has not received as much attention is the influence of the metal behavior on the burning rate of the propellant. While some progress has been made in this area the role of metal combustion on propellant burning rate is still not clearly defined.

Metal addition affects several propellant properties which can influence the burning rate. Metal staples and wires embedded in propellants have the effect of increasing the propellant thermal conductivity in the direction normal to the regressing surface which increases burning rate. Metal addition can also change the propellant stoichiometry, and thus burning rate, depending on what ingredients the metal replaces in the formulation. Another factor associated with metal addition which may alter the burning rate is oxidation of the metal. Either slow or fast oxidation of the metal agglomerates as they reside on or near the surface of the propellant will tend to increase the propellant burning rate by transferring heat to the propellant [1,3]. Another way metals can affect burning rate is through the inert heating (or heat sink) effect. Until they ignite and move out of range of the hot AP/binder flames near the propellant surface, metal agglomerates can act as a heat sink, siphoning off energy from the primary AP/binder flames which otherwise would have gone to increase the burning rate of the propellant [3,4]. Radiative feedback from burning metal droplets can also enhance the burning rate. Recently, Ishihara et al. [5] used fiber optics to measure radiative feedback and microthermocouples (5 μm wire) to measure conductive heat feedback in AP/HTPB/Al propellants. Their results showed that with 20% Al loading at 1 MPa, radiation accounted for 26% of the total heat feedback.

PROCEDURE

In this study, propellants were formulated varying only the metal content and type of metal. The AP-binder mass ratio was fixed (4.385:1). The ratio of coarse to fine AP was kept constant at 7 to 3. The AP was provided by Kerr-McGee. The coarse AP was 400 μm Rotary Round and the fine AP was 90 μm . The AP was coated with tricalcium phosphate (TCP). Hydroxyl-terminated polybutadiene R-45 was used as the resin and isophorone diisocyanate, IPDI, was used as the curative to produce the HTPB binder. The metal loading was varied from 0 to 30% in increments of 10%. Two types of metal were used; Alcoa 123 Aluminum and A.D. Mackey Mg-Al alloy. The alloy was 10% Mg and 90% Al. The alloy was sieved to match the size of the aluminum. Both the aluminum and the alloy size distributions were found using a Coulter Counter. The median diameter of the Alcoa 123 Aluminum was 13 μm , and of the alloy was 19 μm . The distributions were similar.

¹Associate Professor of Mechanical Engineering and Member AIAA

²Graduate Research Assistant

Propellant samples with dimensions 10 x 10 x 3 mm were mounted to a stainless steel plate and suspended inside a quartz tube. The propellant was attached to the plate by using three pins protruding from the plate. To eliminate foreign particle contamination of the quench bath, a Nd-YAG pulsed laser was used as the ignition source. The quartz tube was used to direct the flow of products downward into the bath. Buffered ethanol was used as the quench bath fluid. The buffer (ammonium acetate) was used to neutralize the HCl present in the products. Prior to the collection, particulate contaminants above 2 μm were removed from the quench bath fluid by filtering. Collected samples were analyzed within four hours for particle size distribution using a Coulter Counter. To check the effect of aging, a sample was analyzed after 3 days and no significant changes in the distribution were noted.

Burning rate was measured using a standard strand burner in conjunction with a video cassette recorder. The strands were 6 x 2 x 15 mm. It should be noted that with this small width, radiative and convective losses result in a lower measured burning rate than the actual burning rate. However, the same physical trends should be seen. The strands were coated with a thin film of petroleum jelly to inhibit the ignition of the sides of the propellant.

RESULTS

The results of the particle size analysis are given in Table 1. There was a tendency for the propellants to produce a bi-modal size distribution of metal particles leaving the propellant surface. A first peak in the distribution occurred at approximately the size of the ingredient metal, 20 μm , and a second peak occurred at much larger values, 100 - 200 μm . The first peak was thought to correspond to unagglomerated particles and the larger peak to agglomerates. As the metal content increased from 10 to 30% and as the pressure increased from 1.83 MPa (250 psi) to 5.27 MPa (750 psi) the number mean agglomerate size increased while the volume mean agglomerate size stayed relatively constant. These trends reflect an increase in the number of 130-180 μm agglomerated particles and a decrease in the number of 20 μm ingredient particles as pressure and metal loading increase. For either pressure tested (1.83 or 5.27 MPa), for any metal loading (10, 20, or 30%), and for either metal (Al or Mg-Al), the volume mean agglomerate size was relatively constant at $180 \pm 20 \mu\text{m}$ with the notable exception that for 10% Al at 5.27 MPa the volume mean agglomerate size dropped to 100 μm (Table 1). This anomaly for 10% Al at 5.27 MPa is discussed further in connection with the burning rate results.

Table 1 Volume- and Number-weighted Median Particle Sizes (μm) and Burning Rate, r

Propellant	P(MPa)	Volume	Number	r (cm/s)
0% metal	1.83	-	-	0.332
10% Al	1.83	181	29.3	0.365
20% Al	1.83	196	72.9	0.364
30% Al	1.83	169	137	0.330
10% Mg/Al	1.83	187	18.5	0.404
20% Mg/Al	1.83	155	16.3	0.411
30% Mg/Al	1.83	191	121	0.395
0% metal	3.55	-	-	0.469
10% Al	3.55	-	-	0.480
20% Al	3.55	-	-	0.422
30% Al	3.55	-	-	0.405
0% metal	5.27	-	-	0.601
10% Al	5.27	103	14.2	0.603

20% Al	5.27	201	184	0.520
30% Al	5.27	186	138	0.464
10% Mg/Al	5.27	205	152	0.619
20% Mg/Al	5.27	205	176	0.632
30% Mg/Al	5.27	179	125	0.595

The variation of burning rate with metal loading is shown in Table 1 and Fig. 1. In general, the first addition of metal increased the burning rate. Further additions decreased the burning rate. The addition of any amount of metal (either Al or Mg-Al) decreased the pressure exponent. At 1.83 MPa the influence of adding pure aluminum on burning rate was minimal, with only a slight increase in burning rate at the 10 and 20% Al loadings. With Mg-Al alloy the burning rate at 1.83 MPa increased significantly at all metal loadings. At 5.27 MPa the burning rate was relatively constant with Mg-Al loading while the burning rate for the aluminized propellants dropped sharply between 10 and 30 percent Al.

The increase in burning rate at 1.83 MPa for the Mg-Al propellants over that of the non-metallized propellant is thought to be associated with enhanced heat transfer from the oxidizing/combusting Mg-Al alloy particles at the surface of the propellant. The Mg-Al propellants showed a greater burning rate enhancement than the Al propellants due to a lower ignition temperature for the Mg-Al agglomerates which ignite and depart the propellant surface at a lower temperature than pure Al agglomerates [6]. Thus the Mg-Al agglomerates represent less of a heat sink siphoning energy from the AP/binder flames and possibly also provide more heat feedback than the Al agglomerates.

Table 2 Correlation between increase in burning rate and change in volume agglomerate size going from 1.83 to 5.27 MPa (250 to 750 psi)

Propellant	Percent increase in burning rate	Percent decrease in agglomerate size
0% metal	82	-
10% Al	65	76
20% Al	43	2
30% Al	44	9
10% Mg/Al	53	-9
20% Mg/Al	54	-24
30% Mg/Al	51	7

As the pressure increased from 1.83 to 5.27 MPa the burning rate of the non-metallized propellant increased 82% from 0.33 to 0.60 cm/s. This increase is due to an increase in conductive heat feedback from the AP and AP/binder flames. The burning rate of the Mg-Al propellants, however, increased by only 53%, indicating that the increase in Mg-Al metal heat feedback was not proportional to the increase in feedback from the AP/binder and AP monopropellant flames. The increase in burning rate of 53% for the Mg-Al propellants was constant for all three metal loadings and the volume mean agglomerate size was also relatively constant at $180 \pm 20 \mu\text{m}$. Table 2 shows that the change in volume mean agglomerate size for the Mg-Al propellants was at most 24%. This indicates that if any difference in metal heat feedback (and thus burning rate) were anticipated on the basis of a difference in agglomerate size it would not be observable in the Mg-Al propellants.

For the Al propellants, however, the increase in burning rate in going from 1.83 to 5.27 MPa did vary depending on metal content. At 20 and 30% metal loading, the Al propellant burning rate increased by about 44% in going from 1.83 to 5.27 MPa while the volume average agglomerate size was constant at about $180 \pm 20 \mu\text{m}$. This increase of 44% for the Al propellants is less than the increase of 53% for the Mg-Al propellants which is consistent with the hypothesis that the Al

agglomerates either had a higher ignition temperature than the Mg-Al agglomerates or were otherwise less effective at transferring heat to the propellant for a fixed agglomerate size. At 10% metal loading the burning rate of the Al propellants increased by 65% in going from 1.83 to 5.27 MPa which is even greater than the 53% increase exhibited by the Mg-Al propellant. However, the volume mean agglomerate size for 10% Al at 5.27 MPa dropped by 76% to 100 μm (Tables 1 and 2). This would suggest that either the ignition temperature of the agglomerates decreased with decreasing agglomerate size or that the heat feedback from the agglomerates increased with decreasing agglomerate size. This correlation between burning rate and agglomerate size is illustrated in Table 2. There is no obvious reason why the particular case of 10% Al at 5.27 MPa should be so different from the other runs in terms of agglomerate size and burning rate and one might be inclined to suspect the data except for the fact that anomalous values were obtained for both burning rate and agglomerate size, which represent independent measurements.

It should also be pointed out that these results also give some insight into the relative importance of the change in overall propellant stoichiometry and propellant thermal conductivity associated with metal addition which have been mentioned as possible factors for influencing burning rate. The differences between the burn rates of the Al propellants and the Mg-Al propellants at 5.27 MPa for 20% and 30% metal show that the change in burning rate with addition of metal is probably not a result of a change in propellant overall stoichiometry or thermal conductivity since the stoichiometry and conductivity of two metalized propellants (one containing 10% Mg-Al and the other containing pure Al) with the same metal loading are about the same but the difference in burning rate is quite substantial. This is an indication that the difference in burning rate must be more related to a difference in agglomerate ignition temperature (which may be a function of agglomerate size as well as metal type) and/or a difference in heat transfer from the agglomerates to the propellant.

SUMMARY AND CONCLUSIONS

The influence of aluminum and Mg-Al agglomeration on propellant burn rate was studied by measuring agglomerate size and burn rate in a series of AP/HTPB composite propellants. The AP/HTPB ratio was held constant so that the AP/binder flame structure would be similar for the various propellants. A correlation between burn rate and the agglomerate size was observed which indicated that smaller agglomerates are more conducive to enhanced burn rate. This effect was attributed to more efficient heat transfer from smaller agglomerates to the propellant and a smaller heat sink effect imposed on the AP/binder flames due to lower ignition temperatures for smaller agglomerates. Lower ignition temperatures for Mg-Al alloy compared with pure Al were also found to be more conducive to higher burning burn rates.

The conclusion drawn from this study is that metal heat feedback and heat sink effects are important and need to be better understood in order to make sense out of metalized composite propellant burning rate data. The temperature of the metal at the surface, the extent of agglomeration (i.e. percent metal participating in agglomeration) and the size of the agglomerates may be important parameters in the surface energy balance and burning rate determination. Furthermore, because the implications of these results are so significant, especially for understanding oscillatory pressure-coupled response behavior, it is recommended that further studies be conducted with more extensive variation of pressure and oxidizer size distribution.

ACKNOWLEDGMENTS

Support for this work from the Office of Naval Research (N00014-87-K-0547) and the National Science Foundation (CBT 86-96162) is gratefully acknowledged.

REFERENCES

1. Price, E. W., "Combustion of Metalized Propellants," Progress in Astronautics Series (K. K. Kuo, and M. Summerfield) AIAA, Vol. 90, 1988, pp.479-513.

2. Sambamurthi, J. K., Price, E. W., and Sigman, R. K., "Aluminum Agglomeration in Solid-Propellant Combustion," Georgia Institute of Technology, Atlanta, *AIAA Journal*, Vol. 22, August 1984, pp. 1132-1138.
3. Zennin, A. A., Glaskova, A. P., Leipunskyi, O.I., and Bobolev, V. K., "Effects of Metallic Additives on the Deflagration of Condensed Systems," 12th Symposium (International) on Combustion, The Combustion Institute, Holt, Winston and Rhinehart, 1968, pp. 27-35.
4. Hardt, B.E. and Brewster, M.Q., "Investigation of Al and Mg/Al Alloy Behavior in Composite Solid Propellant Combustion," 25th JANNAF Combustion Mtg, CPIA Publication No. 498, October 1988, pp. 199-206.
5. Ishihara, A., Brewster, M. Q., Sheridan, T. A., and Krier, H., "The Effect of Radiative Heat Feedback on Burning Rate of Metalized Propellants," to appear in *Combustion and Flame*.
6. Pai Verneker, V. R., Deevi, S. and Deevi, S. C., "Role of Alloys in the Thermal Decomposition and Combustion of Ammonium Perchlorate," *Combustion and Flame*, Vol. 67, 1987, pp. 163-173.

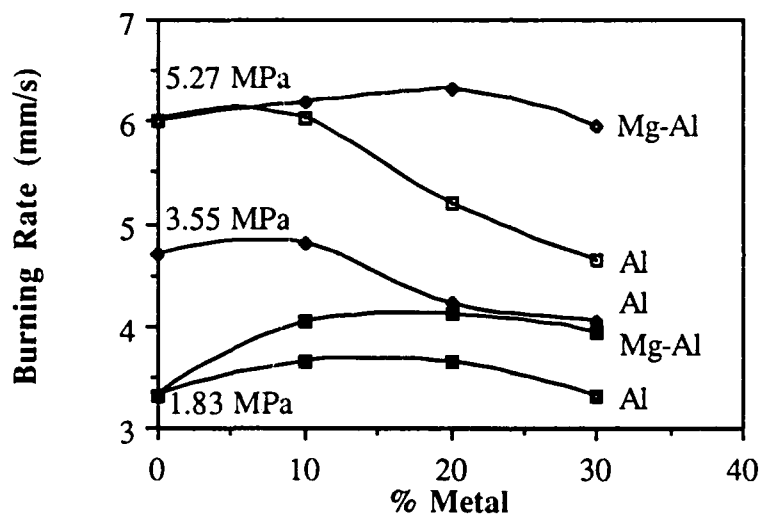


Fig. 1 Burning rate vs. Percent Loading

To Appear in Combustion and Flame

The Influence of Radiative Heat Feedback on Burning Rate in Metalized Propellants

A. Ishihara, M. Q. Brewster, T. A. Sheridan, and H. Krier
Mechanical and Industrial Engineering
University of Illinois at Urbana-Champaign
1206 W. Green St., Urbana, Illinois 61801, U. S. A.

Abstract

Metalized solid propellants have higher final flame temperatures and higher flame radiant intensities than non-metalized propellants. However, the importance of radiative heat feedback in metalized propellant combustion is still unknown. In this study, radiative effects in aluminized propellants were examined by embedding optical fibers and micro-thermocouples in propellants to measure radiative and conductive feedback. Extinguishment by rapid depressurization was used to determine the condition and location of the thermocouple and optical fiber at the burning surface. Hemispherical reflectivity measurements were also made to determine propellant absorptivity. The reflectivity measurements showed that even a small amount of aluminum powder in a propellant increases the absorptivity significantly through multiple scattering in spite of the intrinsically high bulk reflectivity of aluminum. The results of this study confirm previous findings that the effect of radiation on burning rate in non-metalized propellants is negligible due to low incident flux from the flame and low absorptivity of the propellant. On the other hand, in aluminized propellants, radiative heat feedback is a significant fraction of the total feedback and is strongly dependent on pressure and metal loading. At 1 MPa with 20% Al radiative feedback is 26% of the total heat feedback. It is concluded that while radiative feedback does not dominate the burning rate its effect is not negligible in aluminized propellants, at least in the pressure range 0.5 to 10 MPa. These results suggest that radiative feedback should also be considered in propellants containing other metals.

Introduction

In solid propellants, heat feedback from the gas phase to the burning surface consists of two parts, conductive heat feedback and radiative heat feedback. In non-metalized propellants, the effect of radiative heat feedback on a burning rate has been shown to be negligible^{1,2}. On the other hand, metals, such as aluminum, magnesium, zirconium, boron, etc, which are included in solid propellants to improve performance, also increase flame temperature and radiant intensity significantly. This suggests that radiative feedback may play an important role in determining the burning rate of metalized solid propellants.

A few studies have addressed the issue of radiative heat feedback in metalized propellants. Zennin, et al.^{3,4,5} examined experimentally the contribution of radiative heat feedback in aluminum-AP(ammonium perchlorate)-PF(polyformaldehyde) propellants. In their experiments, a microcalorimeter was placed at the bottom of a 3 mm diameter cavity in the propellant to measure radiative flux. Their reported values for incident radiative flux were on the order of 1000 kW/m² at 2.5 to 4.5 MPa. They concluded that the radiative heat feedback was less significant than the conductive feedoack from burning aluminum droplets and that both of these contributions combined were less than the heat release in the condensed phase. It should be pointed out that the diameter of the cavity in their experiment was relatively large compared with the thickness of the combustion zone above the burning surface of propellant which raises questions as to whether the radiant flux measured was representative of the flux that would exist without the presence of the sensor. In addition, there are questions as to whether smoke, ash and aluminum particles from

combustion may have fallen into the hole and reduced the measured signal, since no effort was made to extinguish the propellant and examine the condition of the burning surface.

In a similar study, Felton and Hitchcock⁶ measured radiative flux incident at the surface of aluminized composite modified double base propellants by using a light pipe and a silicon detector. The measured incident flux was 1100 kW/m^2 at 3.5 MPa and 170 kW/m^2 at 1.0 MPa. However, the authors also indicated that some difficulty was encountered in ensuring that the cavity separating the light pipe from the flame zone was unobscured by particles. Temperature profiles were not measured in Ref. 6 and neither was propellant absorptivity, hence no comparison was made between conductive and radiative heat feedback.

Blair and Lake⁷ also examined the effect of radiative transfer in a solid motor. They indicate that radiative heat feedback is significant portion of the total heat flux at the burning surface of the solid propellant. However in their analysis, no heat of reaction or latent heat is assumed in the solid phase.

In a theoretical study, Brewster and Parry⁸ predicted the radiative flux incident at the surface of an aluminized propellants using the two flux model. They estimated incident fluxes on the order of 3000 to 4000 kW/m^2 at 3.5 to 6.8 MPa while noting that these estimates were sensitive to the highly uncertain emissive properties of burning aluminum droplets⁹. No attempt was made in that work to compare radiative heat feedback and conductive heat feedback.

Many studies have also been conducted to investigate the correlation of heat feedback with burning rate in metalized propellants containing metals other than aluminum. Kubota and Serizawa^{10,11} examined the mechanism of burning rate augmentation in Mg-Tf (tetrafluoroethylene) pellets. They conclude that conductive heat feedback from the gas phase to the burning surface dominates the burning rate. Kuwahara and Kubota¹² examined the burning rate mechanism in boron-AP-CTPB composite propellants. They found that boron increases both the heat of reaction in the solid phase and the conductive heat feedback from the gas phase to the surface. However, these studies did not consider radiative heat feedback effects. Kuo and coworkers¹³ also examined the heat feedback in Mg-Tf propellants. They neglected radiative feedback by reasoning that the reflectivity of the burning surface of metalized propellants is large because the intrinsic, bulk reflectivity of metals is large. They also studied the burning mechanisms of boron-based high energy propellant^{13,14}.

The most comprehensive study of radiative feedback in metalized propellants done to date is that of Zennin et al. which used Al/AP/PF propellants. Since PF is not a common binder there is some question as to how applicable those results are to propellants with more common binders. More importantly, there are significant questions, for reasons stated earlier, as to the accuracy of the radiative measurements, especially at higher metal loadings. Hence a study was conducted using fiber optics to measure radiative feedback and thermocouples to measure conductive feedback in Al/AP/HTPB propellants. Through the use of optical fibers and propellant extinguishment it was hoped that some of the shortcomings of previous studies could be overcome.

Experimental Approach

Propellents and Burning Rate Characteristics

Composite Al/AP/HTPB propellants were used in this study. An effort was made to use practical propellant formulations. The compositions of the propellants are shown in Table I. The compositions in Table I are given on a relative basis to emphasize that the AP/binder ratio was held constant as the aluminum loading was increased. This was done to try to insure that the primary AP/binder flame temperature would be constant.

The burning rates of these propellants were measured by a fuse wire method in a chimney type strand combustion chamber pressurized by nitrogen gas. The size of a strand sample was 7x7x38 mm. A strand sample was ignited by a nichrome wire. Three fuse wires of 0.25 mm diameter were used. The distance between each wires was 10 mm. Pressure was measured by a

strain type pressure transducer and recorded. An isolator and a glycerin-filled tube were used to protect the pressure transducer from combustion products. The burning rate characteristics are shown in Fig. 1. The burning rates of the metalized propellants (A-5, A-10, and A-20) are a little larger than that of the non-metalized propellant (A-0), although the difference is not large.

Radiative Flux Measurements

To measure radiant flux from the flame to the burning surface, a fiber optic with the outer sheath stripped away was imbedded in the propellants. The core and cladding of the fibers were fused silica with diameters of 100 μm and 140 μm , respectively. Two types of photodiodes were used as detectors. One of the diodes was InGaAs with a 3GHz cut off frequency (reverse voltage 5V), and the other was Si with 25MHz cut off frequency (reverse voltage 12V). The InGaAs diode had a broad spectral sensitivity with response the wavelength range 1.0-1.6 μm . On the other hand, the Si diode had a more narrow spectral sensitivity in with a range of 0.7-1.1 μm .

A schematic diagram of the radiation measurement system is shown in Fig. 2. The size of the propellant samples used with fiber embedding was 7x7x15mm. The fiber was positioned so that the end was approximately 7 mm below the initial propellant surface. The propellant was sandwiched between plexiglas mounting plates. No binder was used in the propellant cut. The effects of the plexiglas mounting plates, the cut surface of the propellant and the embedded fiber optics on burning rate and burning surface were investigated by comparison of burning rates with Fig. 1 and by examination of the extinguished burning surface by microscope. It was confirmed that there were no effects on the burning rate or burning surface due to presence of the fiber, the cut surface or the plexiglas plates. The incident radiant flux is measured when the fiber end reached the propellant surface as shown in Fig. 2.

The hemispherical incident radiative flux q_f was obtained by using the equation

$$q_f = \int_0^{\infty} \int_0^{2\pi} \int_0^{\pi/2} I_{\lambda}(\theta, \phi) \cos(\theta) \sin(\theta) d\theta d\phi d\lambda \quad (1)$$

where I_{λ} is the spectral intensity from the flame zone. The spectral intensity was assumed to be independent of azimuthal angle ϕ . The relationship between spectral intensity I_{λ} and the voltage output E from the amplifier can be obtained from Eq. (1) as

$$E = \int_0^{\infty} \int_0^{\pi/2} \frac{\pi I_{\lambda}(\theta) \sin(2\theta)}{f_{\lambda}(\theta)} d\theta d\lambda \quad (2)$$

where f_{λ} is a spectral system response factor which relates I_{λ} to the amplifier output. The factor f_{λ} includes the effects of detector sensitivity, reflectance losses and transmission losses and is assumed to be independent of ϕ . Furthermore, Eq. (2) can be modified to produce the following equation.

$$E = \pi \int_0^{\pi/2} \left(\frac{f_{\lambda 0} \sin(2\theta)}{f_{\lambda}(\theta)} \right) d\theta \int_0^{\infty} \left(\frac{I_{\lambda}}{f_{\lambda 0}} \right) d\lambda \quad (3)$$

where $f_{\lambda 0}$ is f_{λ} evaluated at $\theta = 0$. In Eq. (3), the spectral intensity has been assumed to be independent of θ over the numerical aperture of the fiber ($NA < 0.3$) which seems reasonable, given the dimensions of the flame zone. Also, the ratio $(f_{\lambda 0}/f_{\lambda})$ is assumed to be independent of wavelength. An angular attenuation factor F and a total system response factor f_0 are defined as follows;

$$F = f_{\lambda 0} \int_0^{\pi/2} \frac{\sin(2\theta)}{f_{\lambda}(\theta)} d\theta \quad (4)$$

$$\frac{1}{f_0} = \frac{1}{I_0} \int_0^{\infty} \frac{I_{\lambda}}{f_{\lambda 0}} d\lambda \quad (5)$$

where I_0 is the total radiative intensity. The total, normal system response factor f_0 includes detector sensitivity and normal reflectance and transmission losses in the optical fiber. Eqs. (1)-(5) can be combined to give the following equation for the hemispherical incident flux, assuming the flux is diffuse.

$$q_f = \pi I_0 = \frac{f_0 E}{F} \quad (6)$$

The angular attenuation factor F and the total, normal system response factor f_0 are obtained by calibrations as described in next section.

Calibration Method

The angular attenuation factor F in Eq. (4) is obtained by an angular response calibration, using an FEL standard irradiance lamp, as shown in Fig. 3. In this calibration, the distance between the lamp and a fiber optic is held constant at $L=0.4m$, and the polar angle is changed to obtain the non-dimensional output G from an amplifier, which is defined by the ratio of $E(\theta)$ to $E(0)$. Furthermore, the relationship between the spectral system response factor and G is obtained by Eq. (7).

$$G = \frac{E(\theta)}{E(0)} = \frac{f_0 \cos\theta}{f(\theta)} \quad (7)$$

Therefore, the angular attenuation factor F is obtained by the following equation.

$$F = \int_0^{\pi/2} \frac{G \sin(2\theta)}{\cos\theta} d\theta \quad (8)$$

The typical result of this calibration is shown in Fig. 4. This value of F is constant over all fiber optics.

The total normal system response factor f_0 in Eq. (5) is obtained by radiometric calibration, using an FEL standard irradiance lamp as shown in Fig. 3. In this calibration, the polar angle is held constant at $\theta=0$, and the distance L is changed. From Eqs (1), (2) and (6), the following equation is obtained.

$$q_{cal} = f_0 E_{cal} \quad (9)$$

In Eq. (8), q_{cal} and I_{cal} are incident flux and radiative intensity from calibrated lamp on the fiber optics, and E_{cal} is output from the amplifier. The typical result of this calibration is shown in Fig. 5. This value of f_0 is also constant over all fiber optics. It should be noted, however, that in this procedure, the spectral flame intensity I_λ is assumed to be proportional to blackbody radiation at the temperature of calibration source (3065 K). This assumption, which seemed to be a reasonable initial estimate for the aluminized propellants based on Ref. 8 and Ref. 15, was confirmed to be valid by the results of this study as discussed subsequently.

The intensity of the calibrated lamp is lower than the radiative intensity of metalized propellants. Therefore, in this method, the calibrated line is extrapolated to 15 times the highest measured value. The linearity of the radiative measurement system is confirmed by a linearity calibration to insure the validity of the extrapolation. The calibration is shown in Fig. 6. In the calibration, convex lenses are used to increase the intensity of the lamp, and neutral density filters and an iris are used to adjust the intensity incident on the fiber optic. By fixing the diameter of the iris and changing intensity by neutral density filters, the geometry of the incident light cone is held constant.

Propellant Absorptivity Measurements

Total, hemispherical propellant absorptivity α was determined by measuring the spectral, hemispherical reflectivity ρ_λ with an integrating sphere. Kodak Reflectance Coating (6080) was used as a reference surface. Eq. (10) was used to determine total absorptivity.

$$\alpha = \frac{\int_0^\infty (1 - \rho_\lambda) q_{\lambda f} d\lambda}{\int_0^\infty q_{\lambda f} d\lambda} \quad (10)$$

The size of propellant samples used for reflectance measurements was 7x7x3 mm. The propellant reflectivity was measured at two wavelengths in the region of interest (0.6328 μm and 1.064 μm) and found to be independent of wavelength for both aluminized and non-aluminized propellants. Both non-burned surfaces and extinguished surfaces were examined.

Since the aluminized propellants of thickness 3 mm were opaque, Eq. (10) could be used directly to determine α without concern over transmission losses. However, the non-metalized propellant had a relatively high transmittance. To evaluate the absorptivity of the non-metalized propellant two measurements were made, using bottom surface coatings of black paint ($\rho_\lambda < 0.05$) and white reflectance coating ($\rho_\lambda = 0.97$). Since the true absorptivity is bounded by these two values,

$$(1 - \rho_{\lambda, \text{max}}) < \alpha < (1 - \rho_{\lambda, \text{min}}) \quad (11)$$

the value of α was determined by simple averaging. The net radiative flux to the propellant was determined by

$$q_r = \alpha q_f - \epsilon \sigma T_s^4 \quad (12)$$

In the calculation of q_r for non-metalized propellant, the average values of $q_{f,InGaAs}$ and $q_{f,Si}$ were used.

Measurements of Conductive Feedback

Conductive heat feedback from the gas phase to the burning surface was obtained by the following equation.

$$q_c = \lambda_g \left(\frac{1}{r} \right) \left(\frac{dT}{dt} \right)_{S+} \quad (13)$$

where λ_g is the thermal conductivity of the gas phase, and $(\frac{dT}{dt})_{S+}$ is the change in temperature with respect to time at the burning surface, which was measured using Pt-Pt 10% Rh micro-thermocouples made of 5 μm diameter wire. The method for sandwiching the thermocouples in the cut propellant was similar to that used for the fiber optics. The conditions of the burning surface and the position of the thermocouple relative to the surface were determined by examination of extinguished propellants.

The thermal conductivity λ_g of the gas phase was obtained by the volume averaging the thermal conductivities of the gas and aluminum particles as follows.

$$\lambda_g = \lambda_{g0} + \left(\frac{PY_{al}}{v\rho_{al}RT_g} \right) (\lambda_{al} - \lambda_{g0}) \quad (14)$$

Y_{al} is the aluminum mass fraction in the propellant, R is the gas constant of combustion products, v is the ratio of the aluminum particle velocity to that of the combustion gases at the propellant surface. T_g is the characteristic gas temperature above the burning surface. Property values used for evaluating λ_g are shown in Table II.

Experimental Results

Incident Radiative Heat Flux

A typical profile of the signal obtained from the fiber optics is shown in Fig. 7. The position of the burning surface was determined by examination of the location of the end of the fiber after extinguishment as shown in Fig. 7. The fiber optics were re-calibrated after extinction and compared with the signals of unused fibers as shown in Fig. 5. It was thus confirmed that the end of the fiber remained clean and that the signal was not reduced by aluminum particle obscuration or smoke deposition. The condition of the extinguished surface can be seen in an end-on view photograph, Fig 8, and in a side view photograph taken after separating the propellant halves, Fig. 9. In Fig. 8, the core of the fiber optic is black, because the reflectivity of the surface is low and the surface is clean. Also, Fig. 8 shows that the fiber optic and cut surface do not affect the burning surface condition because the burning surface is flat. However, it should be confirmed that the burning surface is effectively frozen by depressurizing to support the correlation between the location of the fiber and the measured signal as shown in Fig. 7. The distance the propellant regresses during depressurizing will be evaluated in the next section.

The results for the incident flux are shown in Fig. 10. In the aluminized propellants, the results from the two diodes with different spectral response regions were coincident. This result suggests that the characteristic radiative temperature of the gas phase was close to the assumed value of the calibration lamp temperature. However, in the non-metalized propellant, these data were different. Two reasons are considered for this difference. One is that the characteristic radiative temperature of the gas phase is lower than the calibration lamp temperature. The other is

that the gas emissivity is probably quite dependent on wavelength due to emission by H₂O which has bands at 1.38 and 1.87 μm wavelength. These bands coincide with InGaAs diode response region and therefore probably affect the InGaAs signal.

Confirmation of Frozen Burning Surface by Depressurization.

The distance the propellant regresses during depressurizing L_p was determined by using the temperature data at the surface and the following equation.

$$L_p = \int_{T_p}^{T_0} \frac{r}{\left(\frac{\partial T_s}{\partial t} \right)} dT_s \quad (15)$$

where T_s is the propellant surface temperature, r is the burning rate, T_p is the surface temperature when the depressurization occurs, and T₀ is the initial propellant temperature. ($\frac{\partial T_s}{\partial t}$) is the change of propellant surface temperature during depressurization, which was measured by an embedded micro-thermocouple which had approached the burning surface. After extinguishment, the location of the micro-thermocouple was examined. Also, for surface pyrolysis, an Arrhenius type regression was assumed as follows;

$$r = Z \exp \left(- \frac{E_s}{RT_s} \right) \quad (16)$$

where Z is the pre-exponential factor, R is the universal gas constant, and E_s is the activation energy of the reaction on the propellant surface. The pre-exponential factor Z was obtained by measuring burning rate and surface temperature.

A typical temperature trace from the micro-thermocouple experiments is shown in Fig. 11. After depressurizing, the temperature decreases rapidly from the peak temperature of 610 °C. This temperature corresponds to the burning surface temperature. This result is in agreement with that of other researchers 16-24 who have concluded that the surface temperature of AP composite propellants is generally between 400 and 700°C. Confirmation that the burning surface was being effectively frozen by depressurization was obtained by examining the location of the micro-thermocouple as shown in Fig. 12. Figure 12 shows that the burning propellant was extinguished when the micro-thermocouple was at the burning surface. By using Eqs. (15) and (16), the regression distance during depressurization is obtained as shown in Fig.13. The peak temperature is T_p. A value of 100 MJ/kmol was used for the activation energy. Therefore, based on these results, the regression distance during the depressurization is considered to be less than 4 μm. Thus it was confirmed that the burning surface was effectively frozen by depressurization. In the fiber optic method, this regression distance can be neglected.

Propellant Absorptivity

The measured reflectivities of the propellant surfaces are shown in Fig.14. The difference between the two wavelength was very small. It was thus assumed that the total reflectivity of propellants was the same as the spectral reflectivity in Fig. 14. In addition, it was found that an unburned propellant surface and an extinguished propellant of the same composition had the same reflectivity. Aluminized propellants had low reflectivities (ρ=0.2) in spite of the high intrinsic, bulk reflectivity of aluminum (ρ=0.8). This effect is due to multiple scattering by the aluminum particles. The non-metalized propellant had a higher reflectivity (ρ=0.6) than that of the aluminized

propellants. Thus it was seen that a small amount of fine metal powder increases the absorptivity of a propellant significantly, as noted previously by Zennin et al. and Brewster and Hardt²⁵.

Conductive Heat Feedback

Figure 15 shows a photograph of a micro-thermocouple which was obtained after extinguishment of the propellant. In this manner it was verified that the thermocouples were not being covered by aluminum, char, ash or binder. Figure 15 also shows that the burning surface was flat near the lead wires of the micro-thermocouple. It was assumed that the effect of lead wires on the measurement was negligible.

Conductive heat feedback is obtained as the product of the temperature gradient ($\frac{dT}{dx}$)_s + measured by the micro-thermocouple on the burning surface and the thermal conductivity λ_g of the gas phase as shown in Eq. (14). The effect of velocity lag (see Eq. (14)) on thermal conductivity was estimated using Stokes flow and found to be less than 20% at 1 MPa. Since the actual velocity ratio is difficult to estimate and its effect is small, a velocity ratio of one was assumed.

Conductive heat feedback from the gas phase is shown in Fig. 16. Among the three propellants, the difference in conductive feedback is not remarkable. From these results, the following curve fit was obtained to predict the conductive heat feedback.

$$q_c (\text{kW/m}^2) = 3600 P(\text{MPa})^{0.34} \quad (17)$$

Discussion

The absorptivities from Fig. 14 and the incident fluxes from Fig. 10 were combined to give the radiative heat feedback to propellant using Eq. (12). The emitted flux in Eq. (12) was so low that the assumed propellant emissivity was inconsequential. The results for q_r are shown in Fig. 17. It can be seen that the radiative heat feedback in non-metalized propellant is much smaller than that in metalized propellants. Metal additives increase the radiative heat feedback remarkably. On the other hand, the aluminum does not seem to increase the conductive heat feedback drastically as can be seen in Fig. 16.

The burning rate can be obtained from an energy balance on the burning surface.

$$r = \frac{q_c + q_r}{\rho_s (C_g T_s - C_s T_0 - Q_s)} \quad (18)$$

In Eq. (18) q_c is the conductive heat feedback from gas phase to solid phase, q_r is the radiative heat feedback, ρ_s is the average density of the propellant, C_g and C_s are the average specific heats of the gas phase and solid phase, Q_s is the heat of reaction (positive exothermic) in the condensed phase which includes heat of reaction between oxidizer, binder, and metal in the condensed phase, latent heat, and heat of fusion, T_s is the average surface temperature, and T_0 is the initial temperature.

Since T_s , r , q_c and q_r were all measured in this study, the condensed phase heat release Q_s could be calculated from Eq. (18). Using values for ρ_s , C_g , and C_s as shown in Table II in Eq. (18) gave values for Q_s at 1 MPa of 312 kJ/kg for A-0 propellant, 308 kJ/kg for A-10 and 215 kJ/kg for A-20. These results indicate that the heat of condensed phase reaction per unit mass of propellant decreases with increasing aluminum loading at this pressure.

Equation (18) shows that the heat feedback from the gas phase to the burning surface consists of two parts, conductive heat feedback q_c and radiative heat feedback q_r . To the extent that T_s remains constant, these two components have equivalent weight in the determination of burning rate. Therefore, in considering the effect of radiative heat feedback on the burning rate,

radiative heat feedback and conductive heat feedback should be compared to each other for any given propellant. To compare radiative and conductive feedback, non-dimensional radiative heat feedback $\Theta = q_r/(q_c + q_r)$ is plotted as a function of pressure in Fig. 18. In non-metalized propellant, Θ is less than 4% at 1 MPa pressure. This result is consistent with similar results of Ref. 1 and 3 and the conclusion that radiative feedback is negligible in non-metalized propellants. However, the results of Fig. 18 indicate that in aluminized propellants there is a remarkable increase in the importance of radiation as pressure increases. At 1 MPa pressure, Θ for A-20 propellant is 26%. Therefore, it is concluded that radiative feedback cannot be neglected in aluminized propellants. This result suggests that radiative feedback should also be considered in metalized propellants containing metals other than aluminum.

Comparing the present results with those of Zennin et al. it is seen that the measured radiative feedback is comparable at 20% aluminum loading. However with 20% aluminum the value of q_f measured in this study at 3.5 MPa (3500 kW/m^2) is more than double that of Zennin et al. at 4.5 MPa (1600 kW/m^2). One explanation for this difference is that in their experiment aluminum particles may have been obscuring the detector with 20% Al loading. This explanation is supported by their own argument that between 20 and 30% aluminum, a drop in measured q_f was observed due to obscuration by aluminum. It is reasonable to question whether some obscuration was also taking place in their experiment at 20% aluminum loading, since no effort to extinguish the propellant and examine the condition of the burning surface was reported.

Conclusions

Fiber optics and micro-thermocouples were used to examine radiative feedback effects in aluminized and non-aluminized propellant combustion. In non-aluminized propellant, the effect of radiative feedback on burning rate was negligible, because of low incident flux from flame and low absorptivity of the propellant. In aluminized propellants radiative feedback was found to be significant but not dominant in terms of determining the burning rate. These results suggest that radiative feedback should be considered in burn rate models of propellants which contain aluminum as well as other metals.

Acknowledgements

The assistance of Capt. Joe Cor and personnel at the Astronautics Lab (Air Force Systems Command) is gratefully acknowledged in the preparation of the solid propellants. Partial support for this project from the National Science Foundation (CBT 86-96162), the Office of Naval Research (N00014-87-K-0547), and Thiokol Corporation is also acknowledged.

Nomenclature

A	area of a fiber optic core, m^2
C	specific heat, J/kgK
E	output from a detector or amplifier, V
F	fiber optic angular attenuation factor
f	radiation measurement system response factor
G	non-dimensional output
I	intensity, $\text{W/m}^2\text{Sr}$
P	pressure, Pa
Q _s	heat of reaction in a solid or condensed phase, J/kg
q	heat feedback from gas phase, kW/m^2
R	gas constant of combustion products, J/kgK

r	burning rate, mm/s
T	temperature, K or C
t	time, s
Y	mass fraction
α	absorptivity of propellant
ε	emissivity of propellant
Θ	non-dimensional radiative heat feedback $\Theta=q_r/(q_c+q_r)$
θ	polar angle
λ	thermal conductivity, kW/mK or wavelength, μm
ρ	density, kg/m ³ or reflectivity
σ	Stefan-Boltzmann constant, W/m ² K ⁴
v	ratio of aluminum particle to that of combustion gases at propellant surface
ϕ	azimuthal angle

subscripts

0	non-metallized propellant, normal angle, or initial condition
al	aluminum
c	conduction
f	flame
g	gas phase
r	radiation
s	solid or condensed phase
λ	wavelcngth

References

1. Blair, D. W., Bastress, E. K., Hermance, C. E., Hall, K. P., and Summerfield, M. in *Solid Propellant Rocket Research, Progress in Astronautics and Rocketry Series* (M. Summerfield, Ed.), Academic Press, 1960, Vol. 1, p. 183.
2. Horton, M. D. and Youngberg, L. Z. AIAA J. 8: 1738-1741 (1970).
3. Zennin, A. A., Glaskova, A. P., Leipunskyi, O. L., and Bobolev, V. K. *Twelfth Symposium (International) on Combustion*, The Combustion Institute, 1964, p. 27.
4. Zennin, A. A., Glaskova, A. P., Leipunskyi, O. L., and Bobolev V. K. *Combustion, Explosion, and Shock Waves*: 165-168 (1968).
5. Zennin A. A., Glaskova, A. P., Leipunskyi, O. L., and Bobolev, V. K. *Combustion, Explosion, and Shock Waves*: 113-116 (1968).
6. Felton, R. F. and Hitchcock, J. E. *An Optical Technique to Measurement Energy Incident on a Burning Solid Propellant Surface*, AIAA Paper No. 71-469, 1971.
7. Blair, D. W., and Lake, W. AIAA J. 7: 1808-1810 (1969).
8. Brewster, M. Q., and Parry, D. L. J. Thermophysics 2: 123-130 (1988).
9. Brewster, M. Q., and Taylor D. M. Combust. Flame 72: 287-299 (1988).
10. Kubota, N., and Serizawa, C. J. Propulsion and Power 3: 303-307 (1987).
11. Kubota, N., and Serizawa, C. Propellants, Explosives, and Pyrotechnics 12: 145-148 (1987).
12. Kuwahara, T., and Kubota, N. Propellants, Explosives, Pyrotechnics 14: 43-46 (1989).
13. Chen, D. M., Hsieh, W. H., Snyder, T. S., Yang, V., and Kuo, K. K. *Study of the Thermophysical Properties and Combustion Behavior of Metal-Based Solid Fuels*, AIAA Paper 88-3041, 1988.

14. Hsieh, W. H., Cheng, J. J., Hsieh, W. H., and Kuo, K. K. *Strand-Burning Characteristics of advanced Boron-Based BAMO/NMMO Fuel-Rich Solid Propellants*, Eastern Section of the Combustion Institute, 1988.
15. Price, E. W.: *Fundamentals of Solid Propellant Combustion , Progress in Astronautics and Rocketry Series* (K. K. Kuo and M. Summerfield, Eds.), Vol. 90, p. 479, AIAA, 1984.
16. Powling J., and Smith A. W. *Combust. Flame* 6: 173-181 (1962).
17. Powling J., and Smith A. W. *Combust. Flame* 7: 269-275 (1962).
18. Powling J., and Smith A. W. *Tenth Symposium (International) on Combustion*, The Combustion Institute, 1965, p. 1373.
19. Sabadell, A. J., Wenograd, J., and Summerfield, M. *AIAA J.* 3: 1580-1584 (1965).
20. Beckstead, M. W., and Hightower, J. D. *AIAA J.* 5: 1785-1790 (1967).
21. Seleznev, V. A., Pokhil, P. F., Maltsev, V. M., and Bavykin, I. B.J. *Combust. Flame* 13: 139-142 (1969).
22. Kubota, N., Kuwahara, T., Miyazaki, S., Uchiyama, K., and Hirata, N. *J. Propulsion* 2: 296-300 (1986).
23. Kuwahara, T., and Kubota, N. *Combust. Sci. and Tech.* 47: 81-91 (1986).
24. Mitani, T., and Niioka, T. Double Flame Structure in AP Combustion, *Twenty-first Symposium (International) on Combustion*, The Combustion Institute, 1984, p. 2043.
25. Brewster, M. Q., and Hardt, B. E. *Selective Radiation Absorption in Aluminized Composite Propellant Combustion*, 24th JANNAF Combustion Mtg., 1987, CPIA Publ.478, p. 157.
26. Brandes, E. A. et al :Smithells Metal Reference Book (Brandes, E. A. Ed.), Butterworthes, 1983.

Table I Propellant Compositions.

Propellant	Al	AP _f	AP _c	Binder
A-0	0	41	41	18
A-5	5	41	41	18
A-10	10	41	41	18
A-20	20	41	41	18

Al : 5µm

AP_f : 25 µm ammonium perchlorateAP_c : 200 µm ammonium perchlorate

Binder : HTPB (hydroxy-terminated polybutadiene)

Table II Propellant Thermal Properties

Property	Unit	Value	Property	Unit	Value
$\lambda_{g,0}$	W/mK	0.1	$\lambda_{g,al}$	W/mK	95*
$C_{s,0}$	J/kgK	1600	$C_{s,al}$	J/kgK	800*
$C_{g,0}$	J/kgK	1600	$C_{g,al}$	J/kgK	1081*
$\rho_{s,0}$	kg/m ³	1800	$\rho_{s,al}$	kg/m ³	2500*
M	kg/kmol	24	$\rho_{g,al}$	kg/m ³	2366*
T _s	K	853	T _g	K	1000
T ₀	K	293			

* : Ref 26

List of Figure Captions

- Fig. 1 Burning rate of aluminized propellants.
Fig. 2 Schematic diagram of radiation measurement system.
Fig. 3 Schematic diagram for total system response factor and angular attenuation factor.
Fig. 4 Typical result from the calibration of angular attenuation factor.
Fig. 5 Typical result from the calibration of total system response factor.
Fig. 6 Schematic diagram for system linearity
Fig. 7 Typical output signal of fiber optic.
Fig. 8 End view of fiber optic on quenched burning surface (propellant A-20, P=0.7 MPa).
Fig. 9 Side view of fiber optic at quenched burning surface (propellant A-20, P=0.7 MPa).
Fig. 10 Incident radiative flux as measured by fiber optic.
Fig. 11 Typical output signal of micro-thermocouple.
Fig. 12 Side view of micro-thermocouple (propellant A-0).
Fig. 13 Regression distance during the depressurization.
Fig. 14 Reflectivity of propellant surface.
Fig. 15 Side view of micro-thermocouple at quenched burning surface (propellant A-20, P=0.7 MPa).
Fig. 16 Conductive heat feedback from gas phase.
Fig. 17 Radiative heat feedback from gas phase.
Fig. 18 Ratio of radiative to total heat feedback.

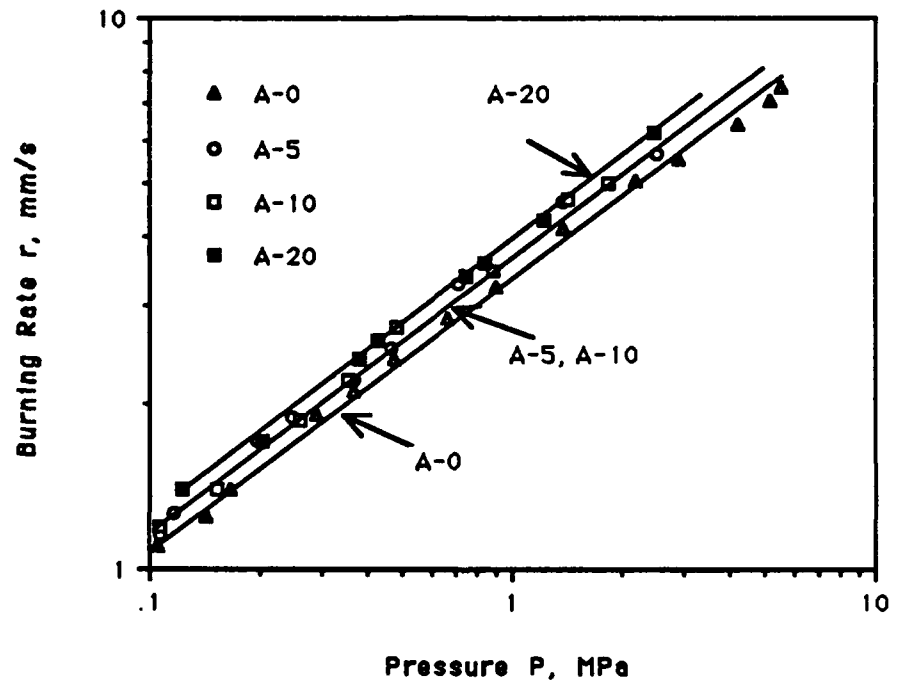


Fig. 1

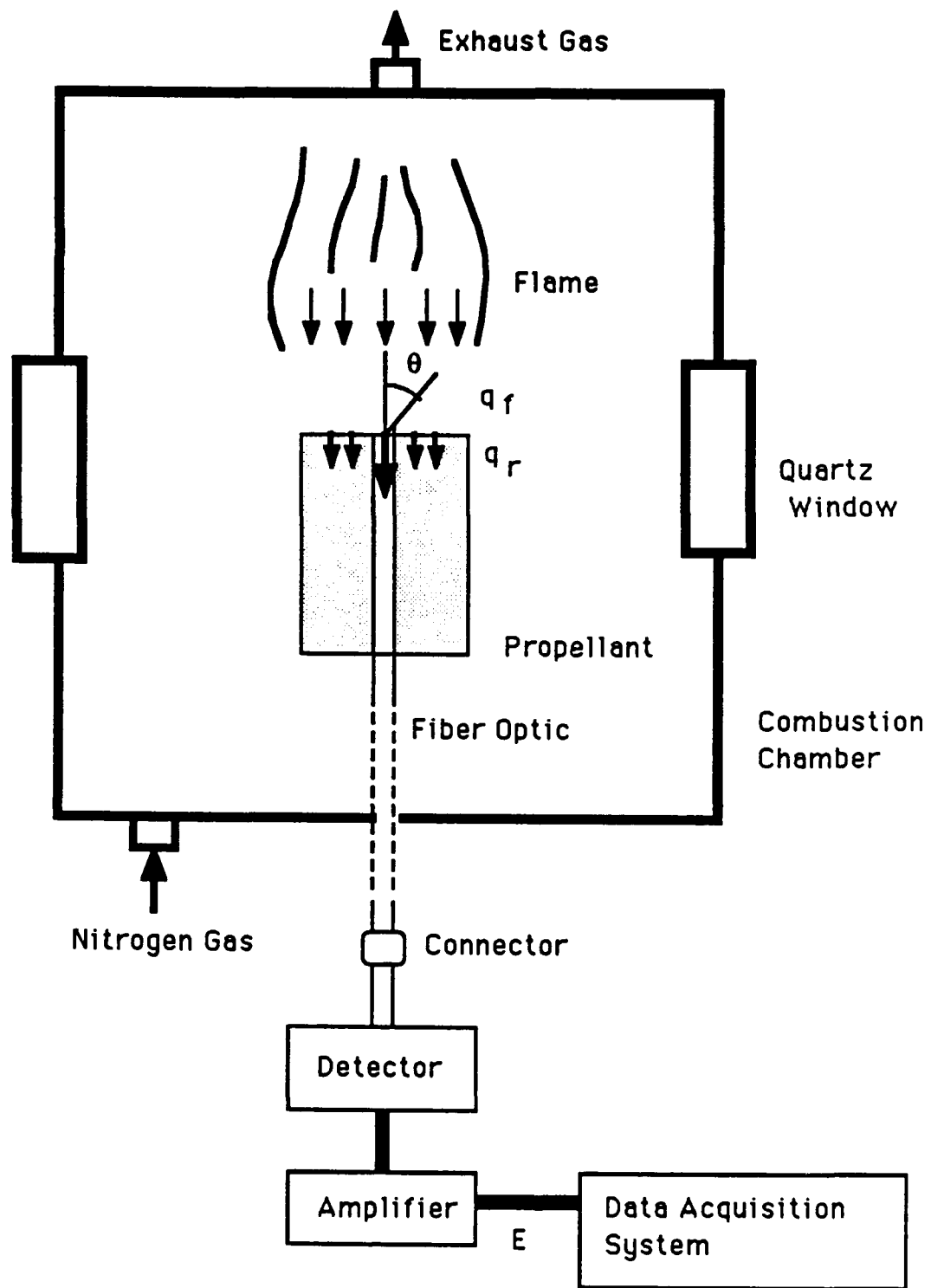


Fig. 2

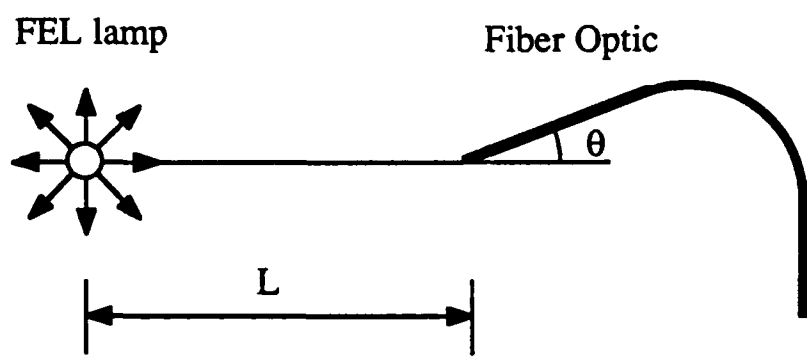


Fig. 3

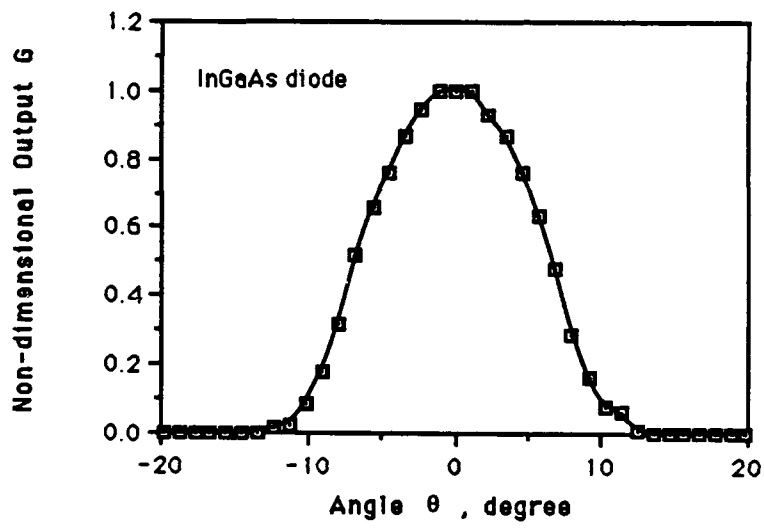


Fig. 4

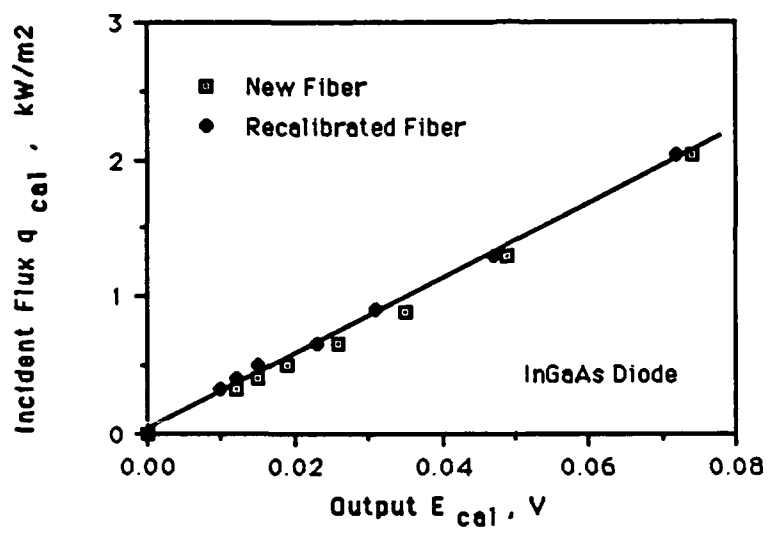


Fig. 5

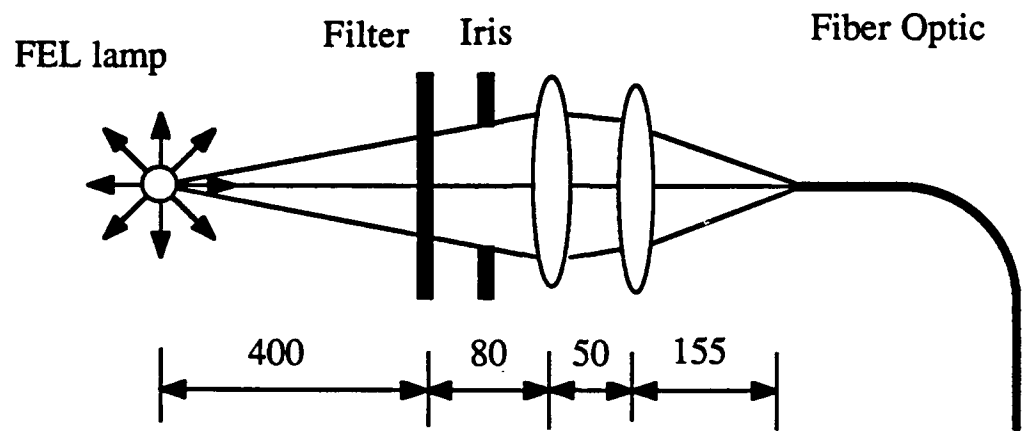


Fig. 6

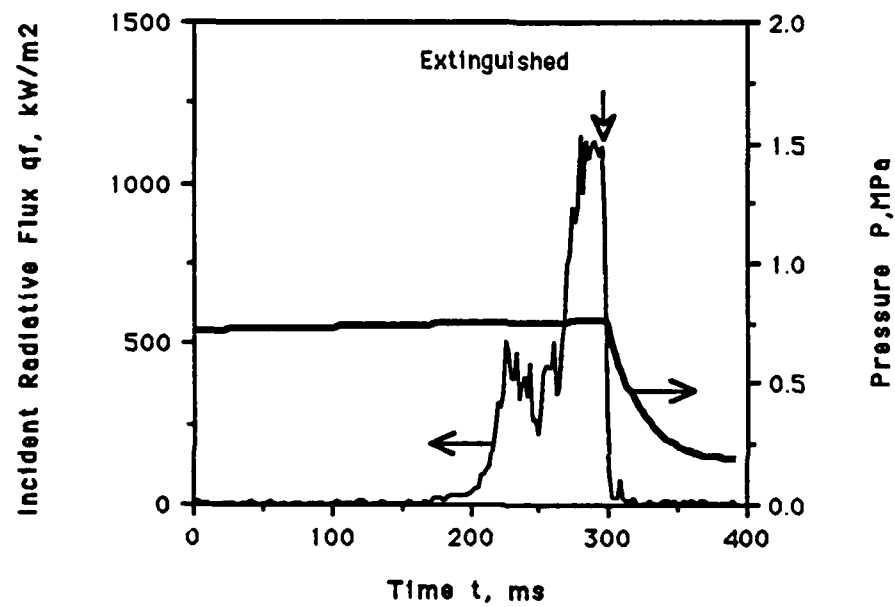
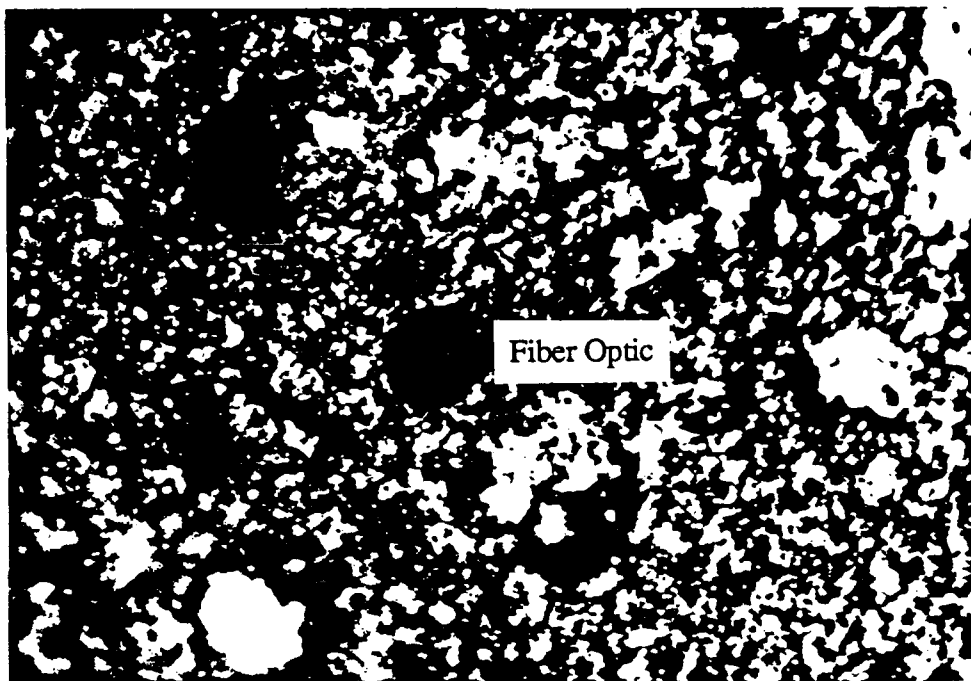


Fig. 7



F.g. 8

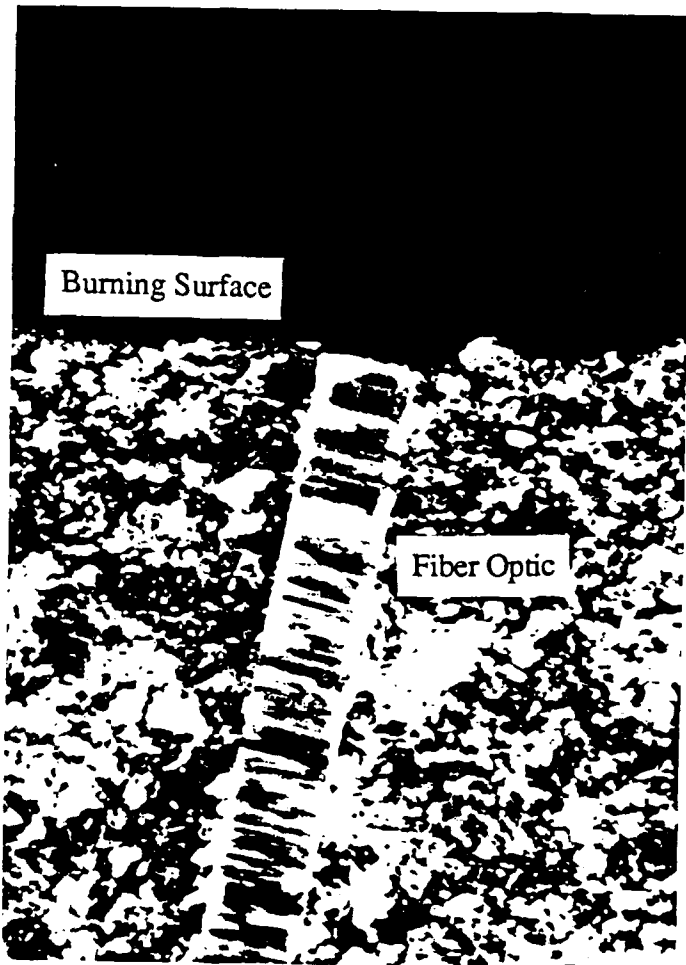


Fig. 9

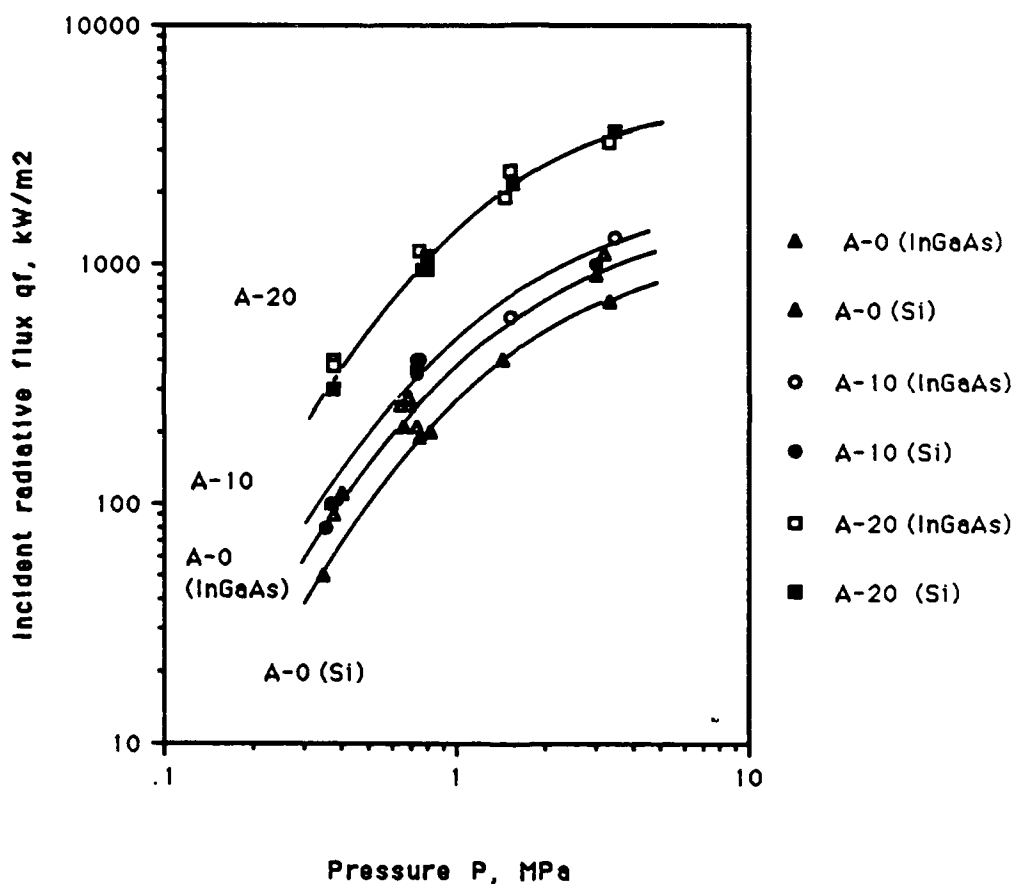


Fig. 10

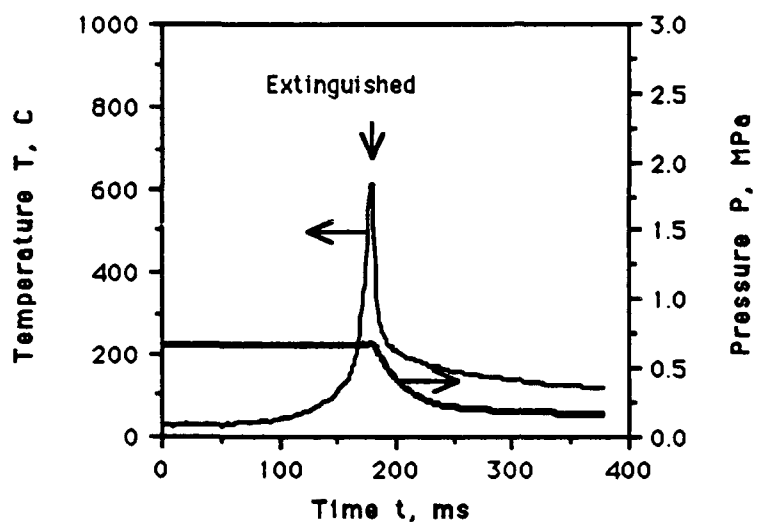


Fig. 11

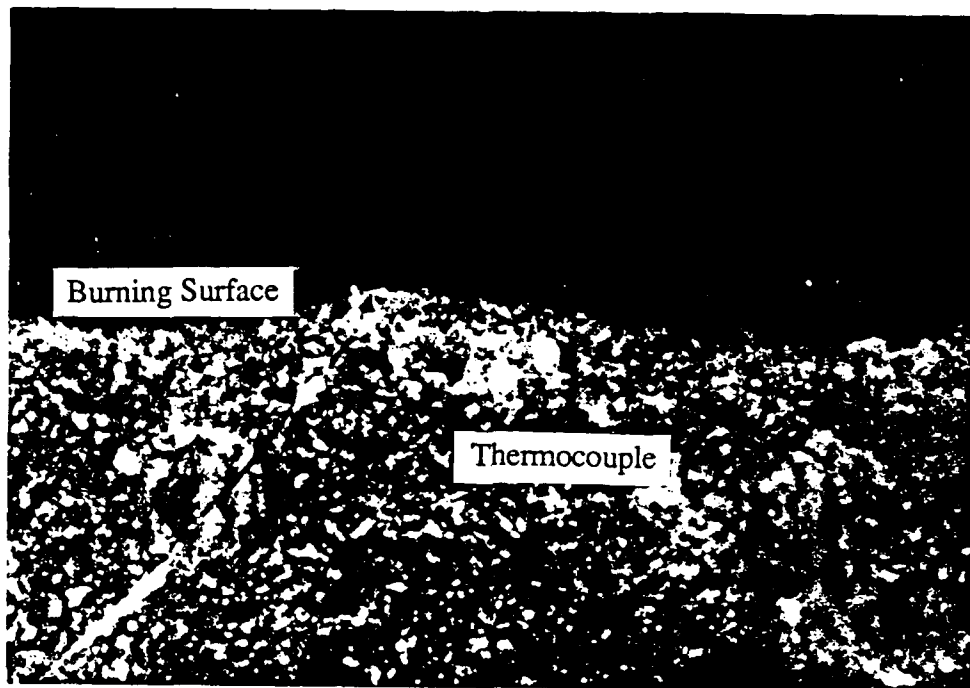


Fig. 12

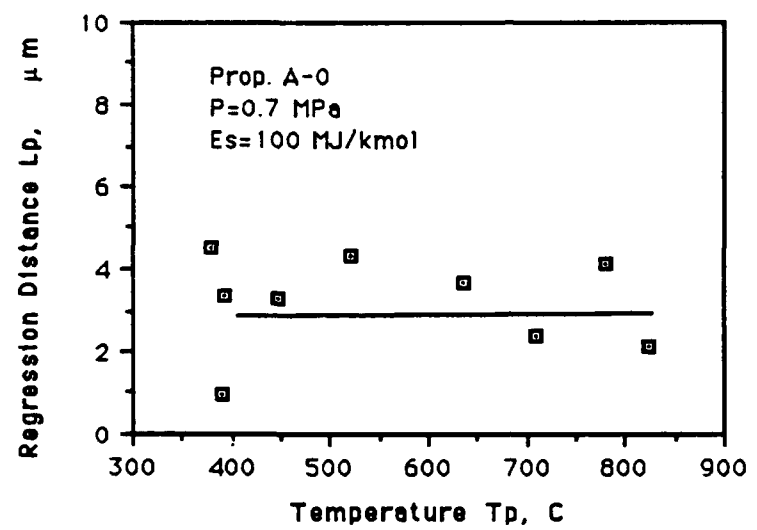


Fig. 13

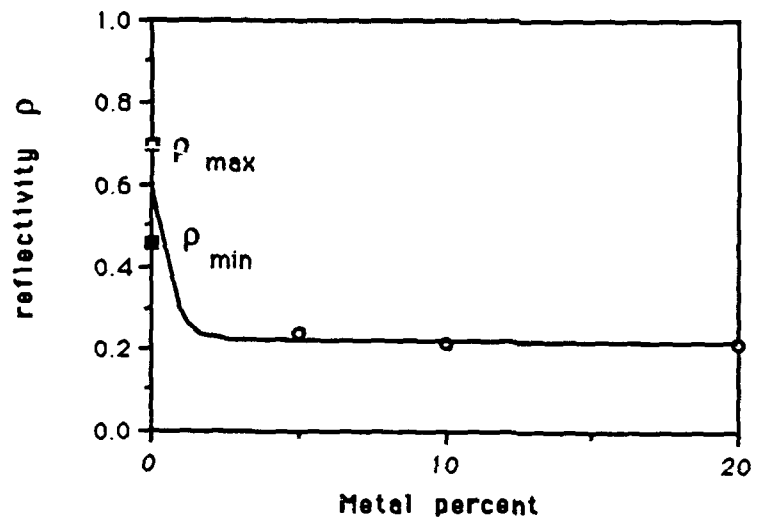


Fig. 14

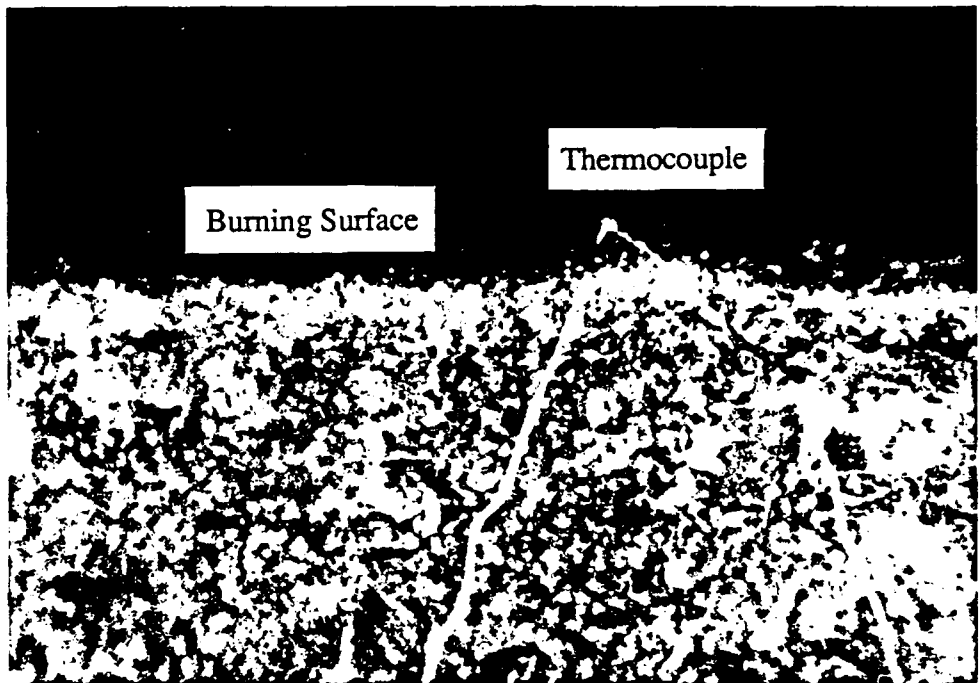


Fig. 15

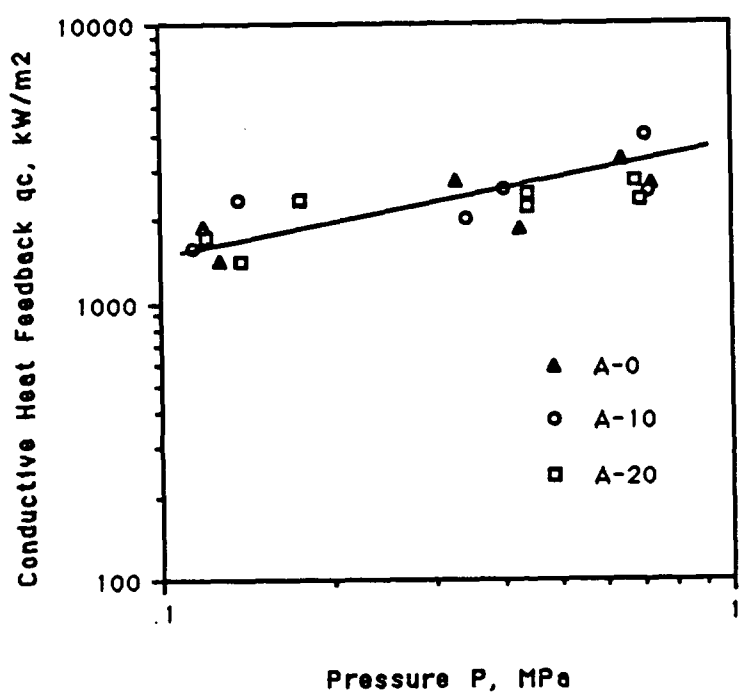


Fig. 16

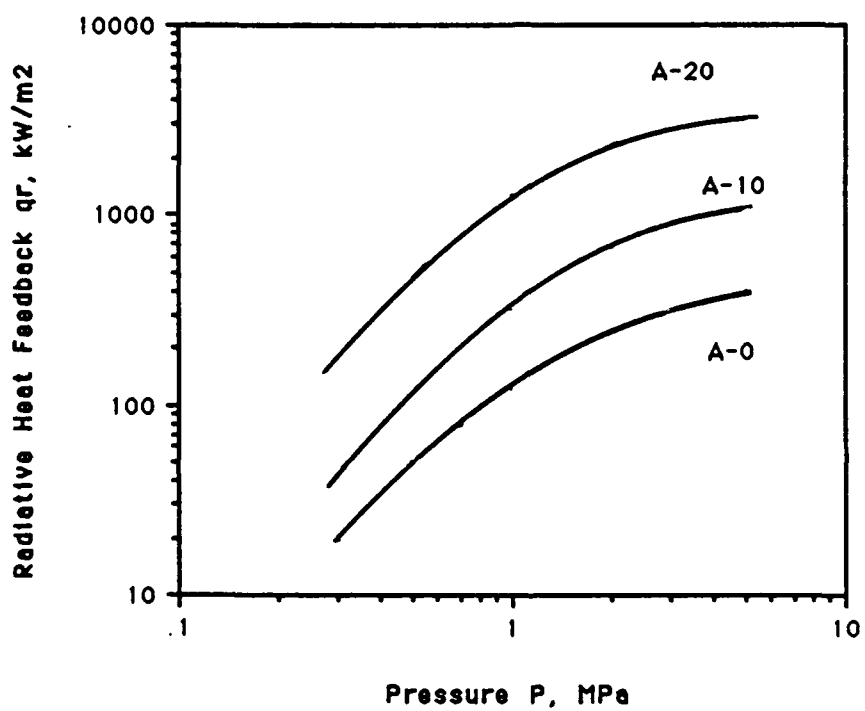


Fig. 17

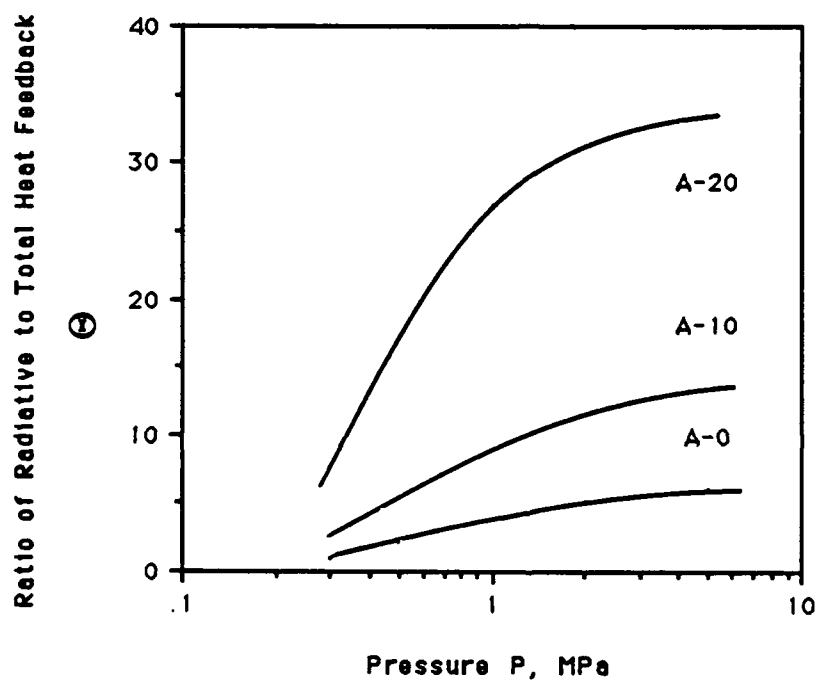


Fig. 18

Optical Constants of Al_2O_3 Smoke
in Propellant Flames

by

David L. Parry* and M. Quinn Brewster**

Department of Mechanical and Industrial Engineering
University of Illinois at Urbana-Champaign, Urbana, Illinois

to appear in

Journal of Thermophysics and Heat Transfer

Vol. 5, No. 1, January, 1991

Abstract

An in situ light scattering and extinction technique was developed to determine the optical constants ($n - ik$) and mean optical size (d_{32}) of molten Al_2O_3 smoke particles in propellant flames. Direct transmittance and bi-directional transmittance and reflectance measurements were made using scattered laser light on aluminized solid propellant flames at visible and near infrared wavelengths ($\lambda_1 = 0.6328 \mu\text{m}$ and $\lambda_2 = 1.064 \mu\text{m}$). The optical properties of the molten Al_2O_3 smoke combustion product were obtained from the light scattering and extinction measurements by inverse solution of the radiative transfer equation. A mean optical size of $d_{32} = 0.97 \mu\text{m}$ was obtained, which agrees well with other reported values. The values of n obtained for molten Al_2O_3 at 2680 K ($n_{m,\lambda_1} = 1.65$ and $n_{m,\lambda_2} = 1.64$) were significantly less than the values which have been reported for solid Al_2O_3 at temperatures just below the melting point of 2320 K ($n_{s,\lambda_1} = 1.82$ and $n_{s,\lambda_2} = 1.81$), indicating that a substantial decrease in n occurs upon melting. This decrease in n can be attributed to the expansion which takes place upon melting and is in good qualitative agreement with the predictions of the Lorentz-Lorenz equation. The value of k obtained for molten Al_2O_3 at 2680 K was 0.006 ± 0.004 (at both wavelengths) which is in reasonable agreement with other reported values. A dispersion analysis was also performed to fit this and other data over the spectral region from 0.5 to 5.0 μm and for temperatures from 2320 K to 3000 K.

Nomenclature

d	particle diameter
f_v	particle volume fraction
H	effective wavenumber
I	intensity
k	absorption index
n	refractive index
N	particle number density distribution
N_d	total particle number density
p	scattering phase function

* Graduate Research Assistant, AIAA student member

** Associate Professor of Mechanical Engineering, AIAA member

$\langle p \rangle$	scattering asymmetry factor
Q	efficiency
r	particle radius
t	optical thickness
T	temperature or direct transmittance
x	particle size parameter, $\frac{\pi d}{\lambda}$

Greek

α	particle size distribution parameter
β	particle size distribution parameter
ϵ	dielectric constant
γ	dispersion oscillator relaxtion parameter
η	wavenumber
λ	wavelength
μ	$\cos \theta$
θ	slab polar scattering angle
Θ	single scattering polar angle
ρ	density or reflectivity
ρ''	bi-directional reflectivity
σ	normalized standard deviation
τ''	bi-directional transmissivity
ω_0	single scattering albedo

Superscripts

-	average over particle size
'	real part
''	imaginary part
*	non-dimensional

Subscripts

a	absorption
b	backward
e	extinction
f	forward
L	cell or flame thickness
m	molten
mp	most probable
o	center wavenumber
p	plasma
ref	reference cell
s	solid or scattering

Introduction

The optical constants ($n - ik$) and particle size of molten Al₂O₃ are important in several areas of solid rocket motor analysis. In heat transfer analysis, these properties are necessary for predicting radiative heat transfer to the nozzle¹, internal insulator surfaces², external equipment³, and to the burning propellant surface itself⁴. In performance analysis, the size distribution of

particles entering the nozzle is of interest because of the strong influence of nozzle two-phase flow losses on performance⁵. Although the optical properties of Al₂O₃ have been studied extensively in the past there is still considerable uncertainty about what values to use in any given situation. Much of this uncertainty is a result of the fact that most previous measurements of these properties have been made either using samples other than actual particles produced by propellant combustion or under conditions different from the actual propellant product gas environment, such that the particle composition (i.e. purity and stoichiometry) is probably quite different than that which exists in the actual propellant product gas environment. In this paper, new measurements are reported for the optical constants of molten Al₂O₃ smoke particles produced by propellant combustion as well as their mean optical size (d₃₂). These measurements are based on a multi-wavelength, in-situ, inverse light scattering and extinction technique carried out in the actual propellant flame environment.

Solid Phase Optical Constants

The optical constants of Al₂O₃ in the pure solid state have been relatively well established by many previous investigations⁶⁻²¹. Figures 1 and 2 show that at room temperature, pure Al₂O₃ is essentially non-absorbing between 0.5 μm and 5 μm. Below 0.2 μm and above 6 μm electronic transitions and lattice vibrations, respectively, result in photon absorption. The refractive index, n_s, varies between 1.8 and 1.6⁶, and the absorption index, k_s, varies between 10⁻⁷ and 10⁻⁵, depending on wavelength⁷. Measurements at higher temperatures⁸ indicate that n_s increases as temperature increases with a nearly constant coefficient (2.9 × 10⁻⁵ K⁻¹)⁹ as shown in Fig. 1. The absorption index also increases with increasing temperature^{8,10,18} as shown in Fig. 2. However, the data of Konopka, et.al¹⁰, which were taken from measurements using actual rocket particles heated in a shock tube, as compared with Gryvnak's data for pure Al₂O₃, indicate that composition is an important factor in determining the absorption index as well as temperature. Other studies^{23,24} also indicate that stoichiometry can significantly influence the value of k. Sub-stoichiometric aluminum oxide (Al₂O_{3-x}) can appear grey or black even at room temperature in contrast to the normal white color of stoichiometric Al₂O₃.

Liquid Phase Optical Constants

The optical constants of Al₂O₃ in the molten state (T_m=2320 K) have not been as well characterized as those for the solid state. Most studies indicate that k increases substantially upon melting, with a bigger increase occurring in relatively pure and stoichiometric samples^{8,10,12,14,15}. Figure 3 shows that most of the reported values for k_m between 0.5 and 5 μm are in the range of 10⁻³ to 10⁻². Recently, Reed¹⁶ suggested a relation for estimating k_m between 1.7 and 4.5 μm, based on extinction and emission measurements using particles that were collected from a rocket plume and heated in a shock tube.

$$k_m = 3.7 \times 10^{-4} \cdot T(K)^{1.5} \cdot \lambda(\mu m) \cdot 10^{-13500/T(K)} \quad (1)$$

Predictions for k_m based on Eq. (1) are in reasonable agreement with other data plotted in Fig. 3, however, Eq. (1) does not extend to short enough wavelengths to predict the upswing in k_m due to electronic transitions in the long-wavelength tail of the fundamental electronic absorption edge.

Conspicuously absent from the literature are data for direct measurements of the refractive index of molten Al₂O₃. The data of Gal and Kirch¹¹ plotted in Fig. 1 at 3000 K are apparently a simple extrapolation based on solid phase data and not actual measurements. While this type of extrapolation has been widely used to estimate n_m^{10, 11, 14, 15, 19, 22} it ignores the change in density which occurs upon melting and the accompanying change in refractive index which takes place. While this approximation is reasonable for predicting emission and absorption properties it is not reasonable for predicting scattering properties.

Particle Size Distribution

It is generally recognized that the particle size distribution of Al₂O₃ produced by combustion of aluminum is bimodal due to two competing oxidation mechanisms²⁵⁻²⁷. One mechanism is detached "vapor-phase" oxidation that produces sub-micron smoke and the other is surface oxidation/condensation that produces large residual caps (10 - 100 μm). Due to their small size and large specific surface area, it is the smoke particles which dominate the optical properties of aluminized propellant flames and which are of primary interest in this study.

Both in-situ optical techniques and particle collection techniques have been used to measure the size of combustion-generated particles such as Al₂O₃²⁵⁻²⁹. While direct particle collection is generally considered to be more reliable, it is always accompanied by questions of possible biasing of the size distribution through the collection process itself. Optical techniques, on the other hand, can be carried out non-intrusively, but are usually subject to limitations in the measurable size

range ($\frac{\pi d}{\lambda} > 5$), the restriction of single scattering, and the need to know n and/or k independently.

Objective

Due to the uncertainty which still exists in the optical properties of Al₂O₃ in propellant flames, a light scattering and extinction technique was developed to determine simultaneously the optical constants and particle size of molten Al₂O₃ particles produced by aluminum combustion in solid propellant flames. An effort was made to overcome or at least mitigate several of the limiting aspects of previous studies of these properties. In that regard, measurements were made in-situ, using typical aluminized solid propellant formulations. Absolute scattering measurements were made and multiple scattering was included in the data reduction by incorporating an inverse solution of the radiative transfer equation.

Light Scattering and Extinction Technique

Light scattering and extinction measurements were made using the experimental apparatus shown in Fig. 4. Two lasers, a 5 mW He-Ne laser ($\lambda_1 = 0.6328 \mu\text{m}$) and a 50 mW Nd-YAG laser ($\lambda_2 = 1.064 \mu\text{m}$) were used to obtain data at visible and near infrared wavelengths, respectively. A beam splitter cube was used to separate each laser beam into two paths. One path was used for bi-directional transmittance (forward scattering) measurements and the other for bi-directional reflectance (backward scattering) measurements. Only one path and one laser beam were allowed to be incident on the flame zone at a time. Azimuthal angle dependence of the scattered light was eliminated by aligning the incident laser beam perpendicular to the flame zone. Light scattered in the forward direction was measured at approximately 11 degrees from the normal to the flame ($\theta_f = 11$ degrees) and light scattered in the backward direction at approximately 17 degrees from the normal ($\theta_b = 17$ degrees).

The optical system was set up and aligned to direct the scattered laser light to the entrance slit of the spectrograph. The vertical spectrograph entrance slit was imaged as a horizontal slit at the center of the flame zone by lenses 1 and 2 and a beam inverter. An optical multi-channel analyzer with a linear diode array detector was used to measure the intensity of the scattered light, I, over a spectral region of interest (ROI) from 628 to 639 nm for the He-Ne signal and from 1059 to 1069 nm for the Nd-YAG signal. Background thermal emission from the flame was subtracted from the total signal giving a signal which was proportional to only the scattered light intensity.

A photomultiplier tube (PMT) and a silicon diode detector (SDD) were used to detect the directly transmitted He-Ne and Nd-YAG laser light, respectively. Output voltages from the PMT and SDD corresponded to the direct, unscattered transmission, T, through the flame. The directly transmitted beams were also passed through narrow band pass filters to prevent a significant

amount of flame emission from reaching the PMT or SDD. The output signals of the PMT and SDD were processed by a microcomputer through an analog/digital converter. The computer was also used to trigger the ignition of the propellant with a nichrome wire and to trigger the scanning of the optical multi-channel analyzer.

The combustion chamber was equipped with a nitrogen gas purge to exhaust the combustion products, keep the windows clean, and maintain the pressure in the combustion chamber at 1.8 MPa (250 psig). A video camera with a 1000 power neutral density filter was used to estimate the linear propellant burning rate (5 mm/s) and record the combustion process to allow rejection of abnormal propellant burns. Measurements were collected from a spatial region 4 to 7 mm above the burning propellant surface to ensure that sufficient aluminum combustion had occurred so that oxide smoke dominated the optical properties of the flame. The 1 x 6 x 15 mm propellant strands consisted of 68 percent ammonium perchlorate (AP), 12 percent polymer binder (HTPB), and 20 percent aluminum (Al), by mass.

In order to make absolute scattering measurements (i.e. to obtain absolute intensity and not just intensity relative to some unknown reference intensity such as incident intensity or intensity at some other scattering angle), a reference measurement using a known reference intensity was required. A reference cell geometrically similar to the flame zone was used to obtain reference measurements for scattered intensity (I_{ref}) and direct transmission (T_{ref}) as shown in Fig 5. The reference cell consisted of two glass slides (slab thickness $L = 1$ mm) filled with an aqueous suspension of polystyrene latex spheres (two percent by mass). Latex spheres with a diameter of 107 ± 3 nm and 220 ± 6 nm were used for reference measurements at $\lambda_1=632.8$ nm and $\lambda_2=1.06$ nm, respectively. The refractive index of the latex particles was essentially the same (1.59) at both wavelengths³⁰.

Scattering and Extinction Results

The results of the scattering and extinction measurements (optical thickness, bi-directional transmittance and bi-directional reflectance) are listed in Table 1 for both wavelengths.

The optical depth, t_L , was obtained for both the flame and reference cell from the direct transmittance measurements using Beer's law.

$$T = \exp(-t_L) \quad (2)$$

Bi-directional transmittance and reflectance for the reference cell, τ''_{ref} and ρ''_{ref} , were obtained from a discrete ordinate solution of the one-dimensional radiative transfer equation using as input parameters the measured optical thickness $t_{L_{ref}}$, an albedo of $\omega_0=1$, and a single scattering phase function calculated from Mie theory (essentially Rayleigh scattering). Since the aqueous solution used for the reference measurements was contained between glass slides, the effects of multiple reflection inside, outside, and between the glass slides as well as refraction and total internal reflection were included in both the determination of T_{ref} and in the transfer equation solution for τ''_{ref} and ρ''_{ref} . Once the reference and experimental intensity values were measured (e.g. I_{ref} and I , respectively), τ'' and ρ'' were determined on a relative basis using Eqs. (3) and (4).

$$\text{Forward: } \frac{\tau''}{\tau''_{ref}} = \left(\frac{I}{I_{ref}} \right)_{\text{trans}} \quad (3)$$

$$\text{Backward: } \frac{\rho''}{\rho''_{ref}} = \left(\frac{I}{I_{ref}} \right)_{\text{refl}} \quad (4)$$

Table 1 shows that the flame bi-directional transmittance values were an order of magnitude larger than the reflectance values, which, given the value of optical depth (1.2), is an indication of strong forward scattering.

Inverse Solution for Optical Properties

An implicit method involving Mie scattering theory coupled with the radiative transfer equation was used to determine the effective optical constants (n and k) and the size distribution parameters of the Al_2O_3 smoke particles formed in the propellant flames. This method required that the particle size distribution and optical constants be assumed to obtain the Mie scattering parameters. These parameters were then used in a solution of the transfer equation to determine bi-directional transmittance and reflectance values. These calculated transmittance and reflectance values were then compared to the corresponding experimental values (Table 1). A solution (not necessarily unique) for the optical properties was obtained when the calculated values of τ'' and ρ'' were found to be equal to the corresponding measured values to within the experimental uncertainties at both wavelengths. By requiring the optical properties to also satisfy the two spectral extinction measurements and a simple dispersion relationship it was possible to find only one solution region of the system of equations. While this does not constitute a mathematical proof of uniqueness, the fact that the solution was in good agreement other reported values gives confidence that the solution found was the correct solution.

Particle Size Distribution

A monomodal gamma function size distribution was assumed to represent the Al_2O_3 particle sizes,

$$N(r) = \frac{N_d \beta^{\alpha+1}}{\Gamma(\alpha+1)} r^\alpha \exp(-\beta r) \quad (5)$$

where α and β are parameters describing the distribution and $N(r)$ is the number density of specified particle radius, r . A monomodal representation is adequate if one mode dominates the optical properties. In the present investigation the Al_2O_3 smoke particles were assumed to dominate the optical scattering and extinction characteristics of the flame. (This assumption was verified by taking high speed photographs of the region 4 to 7 mm above the surface of the burning propellant where measurements were made.) This distribution can also be characterized by the optical mean size, d_{32}

$$d_{32} = \frac{2(3+\alpha)}{\beta} = 2 \frac{\int_0^\infty r^3 N(r) dr}{\int_0^\infty r^2 N(r) dr} \quad (6)$$

and most probable size, d_{mp} (size where $dN/dr = 0$)

$$d_{mp} = \frac{2\alpha}{\beta} \quad (7)$$

The parameter d_{32} is a mean optical size which can be regarded as the location parameter of the distribution and d_{mp}/d_{32} can be regarded as the width parameter with an upper limit of 1 for a

monodispersion and a lower limit of 0 for an infinitely wide polydispersion. The significance of using d_{32} is that for relatively large particles and realistic size distributions which are wide enough to integrate out the interference oscillations in the monodisperse Mie parameters, the size-averaged

Mie parameters ($\bar{Q}_{a,s,e}$, $\bar{\omega}_0$, and $\bar{p}(\Theta)$) are independent of the width parameter d_{mp}/d_{32} . Assuming the smoke particles in this study satisfy these requirements ($x_{32} = \pi d_{32}/\lambda > 1$ and $d_{mp}/d_{32} < 0.3$) the present characterization of the size distribution in terms of d_{32} simplifies the inverse solution problem significantly by eliminating the dependence of the measured quantities on the width of the size distribution.

Mie Scattering Parameters

The equations used for calculating the Mie scattering parameters for the polydispersion (indicated by an overbar) are summarized below. The absorption (a), scattering (s), and extinction (e) efficiencies are given by

$$\bar{Q}_{a,s,e} = \frac{\int_0^\infty Q_{a,s,e} r^2 N(r) dr}{\int_0^\infty r^2 N(r) dr} \quad (8)$$

the albedo, $\bar{\omega}_0$, is given by

$$\bar{\omega}_0 = \frac{\bar{Q}_s}{\bar{Q}_a + \bar{Q}_s} = \frac{\bar{Q}_s}{\bar{Q}_e} \quad (9)$$

and the phase function, $\bar{p}(\Theta)$, is given by

$$\bar{p}(\Theta) = \frac{\int_0^\infty p(\Theta) Q_s r^2 N(r) dr}{\int_0^\infty Q_s r^2 N(r) dr} \quad (10)$$

The scattering asymmetry is often expressed in terms of the asymmetry factor, $\langle \bar{p} \rangle$, which is a measure of the relative forward-to-backward scattering ratio. The value of $\langle \bar{p} \rangle$ ranges from negative one for maximum backward scattering to positive one for maximum forward scattering.

$$\langle \bar{p} \rangle = \frac{1}{2} \int_{-1}^1 \bar{p}(\Theta) \cos \Theta d(\cos \Theta) \quad (11)$$

The functional dependence of the Mie scattering parameters can be expressed as shown in Eqs. (12) through (14).

$$\bar{Q}_{a,s,e} = \bar{Q}_{a,s,e}(n, k, x_{32}, x_{mp}/x_{32}) \quad (12)$$

$$\bar{\omega}_0 = \bar{\omega}_0(n, k, x_{32}, x_{mp}/x_{32}) \quad (13)$$

$$\bar{p}(\Theta) = \bar{p}(\Theta, n, k, x_{32}, x_{mp}/x_{32}) \quad (14)$$

where the effective size parameters based on the optical mean and most probable diameters are given by

$$x_{32,mp} = \frac{\pi d_{32,mp}}{\lambda} \quad (15)$$

Equations (12) through (14) express the Mie scattering parameters as functions of the optical constants and the particle size parameters. The Mie parameters were used to determine the bi-directional transmittance and reflectance τ'' and ρ'' from the solution of the radiative transfer equation, as discussed in the following section.

The Radiative Transfer Equation

The radiative transfer equation for a non-emitting, one dimensional, plane parallel slab is,

$$\mu \frac{dI}{dt} = -I + (\bar{\omega}_0/2) \int_{-1}^1 I \bar{p}(\mu, \mu') d\mu' \quad (16)$$

where I is the spectral scattered intensity, μ is the cosine of the slab polar angle, θ ($0 < \theta_f < \pi/2$ and $\pi/2 < \theta_b < \pi$), and t is the optical depth. Equation (16), was solved by the discrete ordinate method with 20 discrete ordinates. The solution of Eq. (16) can be expressed functionally by Eqs. (17) and (18).

$$\tau'' = \tau''(\theta_f, t_L, \bar{\omega}_0, \bar{p}(\Theta)) \quad (17)$$

$$\rho'' = \rho''(\theta_b, t_L, \bar{\omega}_0, \bar{p}(\Theta)) \quad (18)$$

where

$$t_L = \frac{1.5 f_v L \bar{Q}_e}{d_{32}} \quad (19)$$

and f_v is the particle volume fraction.

The functional relations used to solve for the particle optical properties can be obtained by substituting Eqs. (12)-(14) into (17)-(19) giving

$$\tau''\lambda_1 = \tau''\lambda_1(n\lambda_1, k\lambda_1, d_{32}, d_{mp}/d_{32}) \quad (20)$$

$$\tau''\lambda_2 = \tau''\lambda_2(n\lambda_2, k\lambda_2, d_{32}, d_{mp}/d_{32}) \quad (21)$$

$$\rho''\lambda_1 = \rho''\lambda_1(n\lambda_1, k\lambda_1, d_{32}, d_{mp}/d_{32}) \quad (22)$$

$$\rho''\lambda_2 = \rho''\lambda_2(n_{\lambda_2}, k_{\lambda_2}, d_{32}, d_{mp}/d_{32}) \quad (23)$$

for specified scattering directions θ_f and θ_b . Since the volume fraction of the ensemble of particles is unknown f_v is eliminated by taking the ratio of optical thicknesses at the two wavelengths giving

$$\frac{t_{L\lambda_1}}{t_{L\lambda_2}} = \frac{Q_{e\lambda_1}(n_{\lambda_1}, k_{\lambda_1}, d_{32}, d_{mp}/d_{32})}{Q_{e\lambda_2}(n_{\lambda_2}, k_{\lambda_2}, d_{32}, d_{mp}/d_{32})} \quad (24)$$

To obtain closure, the slope of n vs. λ for molten Al_2O_3 was assumed to be constant and equal to that for solid Al_2O_3 in the interval $0.6328 \leq \lambda \leq 1.064 \mu\text{m}$.

$$n_{\lambda_1} - n_{\lambda_2} = -0.025 (\lambda_1 - \lambda_2) \quad (25)$$

This assumption appears to be reasonable because the value of n in the visible and near infrared region is primarily determined by electronic transitions in the ultraviolet region. Although the number density of atoms undergoing electronic transitions would significantly decrease upon melting (thus causing a decrease in the magnitude of n), the spectral location and strength of the transitions which would presumably be unchanged, and thus the slope of n vs. λ would be expected to be nearly the same in both phases over this narrow spectral region.

Results

Equations (20) through (25) represent six equations with six unknowns (n_{λ_1} , n_{λ_2} , k_{λ_1} , k_{λ_2} , d_{mp} , and d_{mp}/d_{32}). Solutions to these six equations were obtained by a direct search method. The ranges considered for each variable are listed in Table 2.

The results of the direct search procedure are presented in Table 3. A range of possible sizes from $d_{32} = 0.86$ to $1.08 \mu\text{m}$ satisfied the six equations within the experimental uncertainty. For each size there was a range of possible values for n and for each n there was a range of possible values for k . Rather than present the full array of solutions, only the values which gave the best match (i.e. near the center of the uncertainty intervals) are listed in Table 3 (the full array of solutions is presented in Ref. 31). It should be noted that within the experimental uncertainty it was not possible to distinguish between values of k at the two wavelengths. Thus k_{λ_1} and k_{λ_2} are treated as a single value k . It was also found that for realistic (i.e. relatively wide) particle size distributions ($0.05 \leq d_{mp}/d_{32} \leq 0.3$) the results were insensitive to the value of d_{mp}/d_{32} . (A value of 0.15 was used just to carry out the particle size integrations). With the loss of d_{mp}/d_{32} as an unknown it would appear that the system of equations would become over-constrained. However, it should also be noted that the uncertainty interval on the measured value of $\rho''\lambda_2$ was so wide (see Table 1) as to make Eq. (23) a relatively non-constraining equation in the system.

One of the important results to point out is that the values of n_m obtained in this study are significantly less than the solid phase values at temperatures near the melting point. This result is in agreement with the reported density increase which occurs upon melting and is to be expected. It should be noted, however, that, in the absence of any measurements, it has been common practice^{10, 11, 14, 15, 19, 22} to estimate the values of n_m by extrapolating the values of n_s near the melting point, using only the temperature variation observed in the solid phase. While this procedure is probably valid within a single phase, it does not include the density change effect at the melting point and thus over-estimates the values of $n_{t,1}$.

The value of k in Table 3 is consistent with comparable values (i.e. same wavelength, temperature, and flame environment) reported in other studies. The effective temperature of the

particles was determined to be 2680 ± 50 K. This temperature was determined by two-color emission measurements.

The Mie scattering parameters which were determined as part of the solution procedure are listed in Table 4. The particle size parameter at both wavelengths is greater than one, which accounts for the insensitivity of the solution to the size distribution width parameter d_{mp}/d_{32} . The relatively large values of the asymmetry factor indicate that single scattering was predominantly in the forward direction, as evidenced by the measured bi-directional transmittance reflectance values (see Table 1).

Dispersion Analysis

Using the present results together with selected data from other investigations, a dispersion analysis was carried out to obtain temperature dependent dispersion parameters for molten Al_2O_3 . According to classical dispersion theory³² the real (ϵ') and imaginary (ϵ'') parts of the complex dielectric function are given by

$$\epsilon' = 1 + \sum_{i=1}^{N_{\text{oscillators}}} \frac{\eta_{pi}^2 (H_{oi}^2 - \eta^2)}{(H_{oi}^2 - \eta^2)^2 + \gamma_i^2 \eta^2} \quad (26)$$

$$\epsilon'' = \sum_{i=1}^{N_{\text{oscillators}}} \frac{\eta_{pi}^2 \gamma_i \eta}{(H_{oi}^2 - \eta^2)^2 + \gamma_i^2 \eta^2} \quad (27)$$

where

$$\epsilon' = n^2 - k^2 \quad \epsilon'' = 2nk \quad (28)$$

$$n = \frac{\sqrt{\epsilon'^2 + \epsilon''^2 + \epsilon'}}{2} \quad k = \frac{\sqrt{\epsilon'^2 + \epsilon''^2 - \epsilon'}}{2} = \frac{\epsilon''}{2n} \quad (29)$$

In these equations each of the oscillators is described by its plasma wavenumber, η_{pi} , its damping coefficient, γ_i , and its effective wavenumber, H_{oi} . The effective wavenumber takes the induced field effect into account while retaining the classical form of the dispersion equations. The effective wavenumber is determined from the characteristic wavenumber, η_{oi} , and the plasma wavenumber according to Ref. 33 as

$$H_{oi}^2 = \eta_{oi}^2 - \frac{\eta_{pi}^2}{3} \quad (30)$$

In the region of interest (0.5 to 5 μm) the optical constants can be satisfactorily fit by using just two oscillators, one in the ultraviolet (H_{o1}) accounting for electronic transitions and one in the infrared (H_{o2}) accounting for molecular vibrations. Since both oscillators are located outside the region of interest the approximations $H_{o1} \gg \eta \gg H_{o2}$ and $k \ll n$ can be applied to Eq. (26), giving

$$\frac{n^2 - 1}{n^2 + 2} = \frac{\eta_{pl}^2}{3\eta_{ol}^2} \quad (31)$$

By definition, the plasma wavenumber squared is proportional to the number density of oscillators, and therefore to the material density. Thus, Eq. (31) can also be expressed as

$$\frac{n_m^2 - 1}{(n_m^2 + 2)\rho_m} = \frac{n_s^2 - 1}{(n_s^2 + 2)\rho_s} \quad (32)$$

which is the Lorentz-Lorenz relation. This relation can be used to estimate the change in refractive index which occurs upon melting, if the density change is known.

A combination of data for n and k from this and other studies was used to fit the dispersion parameters. Data was used for three temperatures, 2320 K, 2680 K, and 3000 K, covering the spectral region from 0.5 μm to 5 μm . The data used for the dispersion analysis are listed in Table 5. The values of n_m at 2320 K were estimated using Eq. (32) and Plass' predictions for n_s at 2300 K as shown in Table 6. The density of solid Al_2O_3 at 2300 K was taken as $\rho_s = 3.73 \text{ g/cm}^3$ and the density of molten Al_2O_3 at 2320 K was taken as $\rho_m = 3.02 \text{ g/cm}^3$. The latter value is based on the results of Kirshenbaum and Cahill^{3,4} who give the following relation for the density of molten Al_2O_3 as a function of temperature, $T(\text{K})$.

$$\rho_m = 5.632 - 1.127 \times 10^{-3} T(\text{K}), \text{ g/cm}^3 \quad (33)$$

The values of n_m at 2680 K (at wavelengths other than 0.6328 and 1.06 μm) and at 3000 K were extrapolated from the values of n_m at 2320 K using a temperature coefficient

$$dn_m/dT = 5.87 \times 10^{-5} \text{ per K} \quad (34)$$

which was based on a linear curve fit between the experimental values of n_m at 2680 K (0.6328 and 1.06 μm) and the values predicted by the Lorentz-Lorenz relation at 2320 K.

The dispersion parameters were determined by minimizing the function F which is a measure of the error or difference between the theoretical and experimental values.

$$F = \sqrt{\sum_{j=1}^N \left(\frac{n_{ej} - n_{dj}}{n_{ej}} \right)^2} + \frac{\sigma_n}{\sigma_k} \sqrt{\sum_{j=1}^K \left(\frac{k_{ej} - k_{dj}}{k_{ej}} \right)^2} \quad (35)$$

The experimental values of n and k (from Table 5) are denoted by a subscript "e" and the theoretical values predicted by the dispersion analysis are denoted by a "d". The difference in the experimental uncertainty between n and k was accounted for by including the ratio of the normalized standard deviation of n , σ_n , to the standard deviation of k , σ_k . The normalized standard deviations used throughout this analysis were based on the experimental uncertainty reported in Table 3 for n and k . The greater uncertainty for k was reflected in σ_n and σ_k , where $\sigma_n = 1.8\%$ and $\sigma_k = 67\%$ were used. The results of fitting the data of Table 5 to Eqs. (26) and (27) by minimizing Eq. (35) are presented in Table 7.

The characteristic wavelengths of the two oscillators were assumed to be $\lambda_{o1} = 0.1107 \mu\text{m}$ in the ultraviolet region and $\lambda_{o2} = 17.57 \mu\text{m}$ in the infrared region, based on previous dispersion analyses of solid Al₂O₃^{6,7,20,21}. The characteristic wavelength in the ultraviolet region corresponds to electronic transitions and would be expected to be similar in both solid and liquid phases. The characteristic wavelength in the infrared region accounts for molecular and intermolecular vibrations (e.g. lattice vibrations for the solid phase) and therefore would be expected to change in passing from solid to liquid. Since the intermolecular restoring forces of the liquid are expected to be less than those in the solid, the characteristic wavelength in the liquid might be expected to be greater than 17.57 μm . However, it is difficult to estimate a more appropriate value for λ_{o2} , due to the lack of radiative property measurements at longer wavelengths. Thus, for simplicity the value of 17.57 was used. This assumption is of little importance in the spectral region of interest since the curve fit in this region is largely unaffected by the exact choice of the infrared oscillator wavelength outside the region of interest.

The temperature dependence of the dispersion parameters was incorporated using a standard least square curve fitting technique. The three values of each parameter were fit to a polynomial of sufficient degree to adequately represent the variation with temperature. The temperature was non-dimensionalized according to

$$T^* = \frac{T - 2320 \text{ K}}{3000 \text{ K} - 2320 \text{ K}} \quad (36)$$

The polynomial equation used for a general dispersion parameter, ψ , was

$$\psi = a_0 + a_1 T^* + a_2 T^{*2} + a_3 T^{*3} + a_4 T^{*4} \quad (37)$$

with T in Kelvin. The coefficients that best fit the dispersion parameters are listed in Table 8. The values of n_m and k_m can be calculated for wavelengths between 0.5 and 5 μm and temperatures between 2320 K and 3000 K by using the coefficients from Table 8 and Eqs. (26) through (37). Table 9 gives a list of n_m and k_m values that were determined using the results of the dispersion analysis.

The results for n_m and k_m from the dispersion analysis are plotted in Figs. 6 and 7 (labelled "theory") along with some of the values from Figs. 1, 2 and 3 for comparison. The values of n_m are lower than the values for n_s at corresponding wavelengths, but both phases exhibit a positive temperature coefficient. The values of k_m also increase with temperature as expected.

Summary

The optical properties of molten Al₂O₃ smoke particles in a typical aluminized solid propellant flame were determined by a light scattering and extinction technique. At 2680 K and 0.633 to 1.06 μm the results obtained were $n=1.65$ to 1.64, $k=0.006$ and $d_{32}=0.97 \mu\text{m}$. The value of n showed a significant decrease upon melting attributable to the density change of Al₂O₃. The value of k was in reasonable agreement with other reported values, considering how sensitive k is to impurity and stoichiometry effects and the high level of uncertainty associated with these effects. The results obtained were combined with data from other investigators to determine temperature dependent dispersion parameters for molten Al₂O₃. More effort is still needed, however, to characterize the important effects of composition (i.e. stoichiometry and impurity) on the value of the absorption index.

Acknowledgments

Support for this work from Hercules/AFAL (Contract F04611-86-C-0016), the National Science Foundation (Grant CBT 86-96162), and the Office of Naval Research (Contract N00014-87-K-0547) is gratefully acknowledged.

References

¹Pearce, B. E., "Radiative Heat Transfer within a Solid-Propellant Rocket Motor," J. Spacecraft and Rockets, Vol. 15, No. 6, 1979.

²Brewster M. Q., "Radiation-Stagnation Flow Model of Aluminized Solid Rocket Motor Internal Insulator Heat Transfer," AIAA J. Thermophysics and Heat Transfer, Vol. 3, No. 2, April 1989, pp. 132-139.

³Edwards, D. K., and Bobco, R. P., "Effect of Particle Size Distribution on the Radiosity of Solid Propellant Rocket Motor Plumes," AIAA-81-1032, 16th Thermophysics Conference, Palo Alto, CA, June 1981.

⁴Hardt, B. E., and Brewster, M. Q., "Influence of Metal Heat Feedback on Composite Solid Propellant Burning Rate," submitted to AIAA J. of Propulsion and Power.

⁵Hermsen, R. W., "Aluminum Oxide Particle Size for Solid Rocket Motor Performance Prediction," J. Spacecraft and Rockets, Vol. 18, Nov.-Dec. 1981, pp. 483-490.

⁶Malitson, I. H., "Refraction and Dispersion of Synthetic Sapphire," J. Opt. Soc. Am., Vol. 52, No. 12, 1962, pp. 1377-1379.

⁷Toon, O. B., and Pollack, J. B., "The Optical Constants of Several Atmospheric Aerosol Species: Ammonium Sulfate, Aluminum Oxide, and Sodium Chloride," J. of Geophysical Research, Vol. 81, No. 33, Nov. 1976, pp. 5733-5748.

⁸Gryvnak, D. A., and Burch, D. E., "Optical and Infrared Properties of Al_2O_3 at Elevated Temperatures," J. Opt. Soc. Am., Vol. 55, No. 6, 1965, pp. 625-629.

⁹Plass, G. N., "Temperature Dependence of the Mie Scattering and Absorption Cross Sections for Aluminum Oxide," Applied Optics, Vol. 4, No. 12, 1965, pp. 1616-1619.

¹⁰Konopka, W. L., Reed, R. A., and Calia, V. S., "Measurements of Infrared Optical Properties of Al_2O_3 Rocket Particles," Prog. In Astro. and Aero., Vol. 91, 1984, pp. 180-197.

¹¹Gal, G., and Kirch, H., "Particulate Optical Properties in Rocket Plumes," AFRPL-TR-73-99, 1973, pp. 28-29.

¹²Carlson, D. J., "Emittance of Condensed Oxides in Solid Propellant Combustion Products," Tenth (International) Symposium on Combustion, The Combustion Institute, 1965, pp. 1413-1424.

¹³Bauer, E., and Carlson, D. J., "Mie Scattering Calculations for Micron Size Alumina and Magnesia Spheres," J. Quant. Spectro. Rad. Transfer, Vol. 4, 1964, pp. 363-374.

¹⁴Adams, J. M., "A Determination of the Emissive Properties of a Cloud of Molten Alumina Particles," J. Quant. Spectro. Rad. Transfer, Vol. 7, 1967, pp. 273-277.

¹⁵Mularz, E. J., and Yuen, M. C., "An Experimental Investigation of Radiative Properties of Aluminum Oxide Particles," J. Quant. Spectro. Rad. Transfer, Vol. 12, 1972, pp. 1553-1568.

¹⁶Reed, B., "Optical Properties for Liquid Al₂O₃," Private Communication, Arnold AFB, 29 Feb 1988.

¹⁷Lee, D. W., and Kingery, W. D., "Radiation Energy Transfer and Thermal Conductivity of Ceramic Oxides," J. Am. Ceramic Soc., Vol. 43, No. 11, 1960, pp. 595-607.

¹⁸Myers, V. H., Oro, A., and DeWitt, D. P., "A Method for Measuring Optical Properties of Semi-Transparent Materials at High Temperatures," AIAA J., Vol. 24, No. 2, 1986, pp. 321-326.

¹⁹Lingart, et al., "Optical Properties of Leucosapphire at High Temperatures," Teplofizika Vysokikh Temperatur, Vol. 20, No. 5, 1982, pp. 872-880.

²⁰Barker Jr., A. S., "Infrared Lattice Vibrations and Dielectric Dispersion in Corundum," Physical Review, Vol. 132, No. 4, 1963, pp. 1474-1481.

²¹Goodwin, D. G. and Mitchner, M., "Infrared Optical Constants of Coal slags: Dependence on Chemical Composition," J. Thermophysics, Vol. 3, No. 1, pp. 53-60.

²²Pustovalov. V. K., and Bosbuchendo, D. S., "Heating, evaporation and combustion of a solid aerosol particle in a gas exposed to optical radiation," Int. J. Heat Mass Transfer, Vol. 32, No. 1, 1989, pp. 3-17.

²³Nelson, L. S., and Richardson, N. L., "Effects of Oxygen and Argon Atmospheres on Pendant Drops of Aluminum Oxide Melted with Carbon Dioxide Laser Radiation," High Temp. Sci., Vol. 5, 1973, pp. 138-154.

²⁴Kraeutle, K. J., and Bradley, H. H. Jr., "Combustion of Aluminized Propellants: The Influence of Pressure and Propellant Composition on Formation of Aluminum Combustion Residue," 14th JANNAF Combustion Mtg., CPIA Publication 292, Vol. 1, pp. 209-219.

²⁵Kraeutle, K. J., "Particle Size Analysis In Solid Propellant Combustion Research," Prog. in Astro. and Aero., Vol. 53, 1978, pp. 76-108.

²⁶Salita, M., "Quench Bomb Investigation of Al₂O₃ Formation From Solid Rocket Propellants (Part II): Analysis of Data," 25th JANNAF Combustion Meeting, CPIA Publication, Oct. 1988.

²⁷Dobbins, R. A., and Strand, L. D., "A Comparison of Two Methods of Measuring Particle Size of Al₂O₃ Produced by a Small Rocket Motor," AIAA J., Vol. 8, No. 9, pp. 1544-1550.

²⁸Orguc, S., Pruitt, T. E., Edwards, T. D., Youngborg, E. D., Powers, J. P., Netzer, D. W., "Measurements of Particulate Size in Solid Rocket Motors," Proceedings of 1987 JANNAF Combustion Meeting, CPIA Publications, Laurel, MD, 1987.

²⁹Powell, E. A., Cassanova, R. A., Bankston, C. P., and Zinn, B. T., "Combustion-Generated Smoke Diagnostics by Means of Optical Measurement Techniques," *Prog. in Astronautics and Aeronautics*, AIAA, Vol. 53, 1977, pp. 449-463.

³⁰Inagaki, T., Arakawa, E. T., Hamm, R. N., and Williams, M. W., "Optical properties of polystyrene from the near-infrared to the x-ray region and convergence of optical sum rules," Physical Review, Vol. 15, No. 6, 1977, pp. 3246-3253.

³¹Parry, D. L., "Radiative Heat Transfer from Aluminum Oxide in Solid Propellant Flames," Ph.D. dissertation in Mechanical Engineering, University of Illinois, Urbana, 1989.

³²Bohren, C. F., and Huffman, D. R., Absorption and Scattering of Light by Small Particles, John Wiley & Sons, New York, 1983, pp. 227-283.

³³Slater, J. C., and Frank, N. H., Electromagnetism, Dover Publications, Inc., New York, 1969, pp. 109-114.

³⁴Kirshenbaum, A. D., and Cahill, J. A., "The Density of Liquid Aluminum Oxide," J. Inorg. Nucl. Chem., Vol. 14, 1960, pp. 283-287.

List of Figure Captions

- Fig. 1 Survey of aluminum oxide refractive index
- Fig. 2 Survey of solid aluminum oxide absorption index
- Fig. 3 Survey of molten aluminum oxide absorption index
- Fig. 4 Optical apparatus schematic diagram
- Fig. 5 One-dimensional, planar scattering geometry for the experimental technique
- Fig. 6 Aluminum oxide refractive index (recommended)
- Fig. 7 Molten aluminum oxide absorption index (recommended)

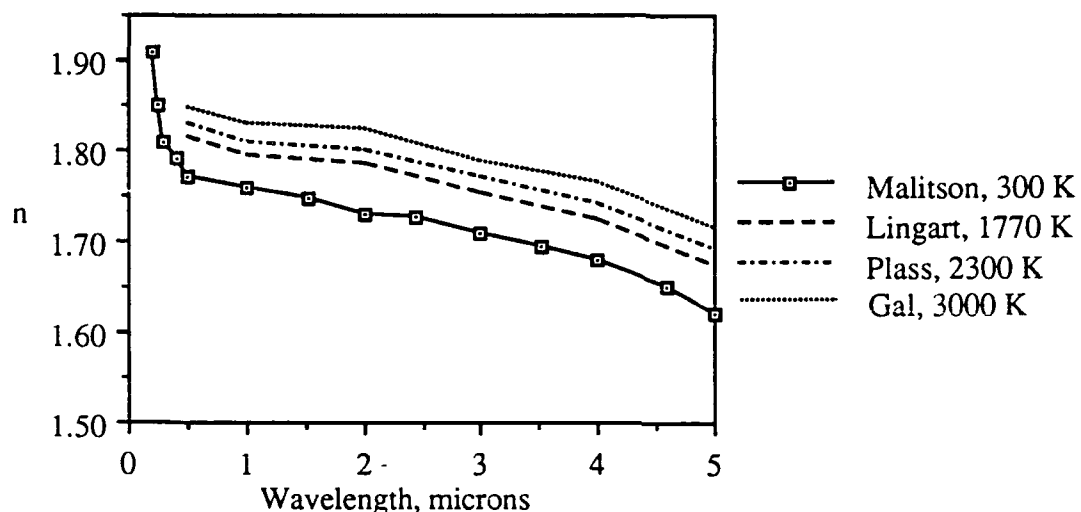


Fig. 1 Survey of aluminum oxide refractive index.

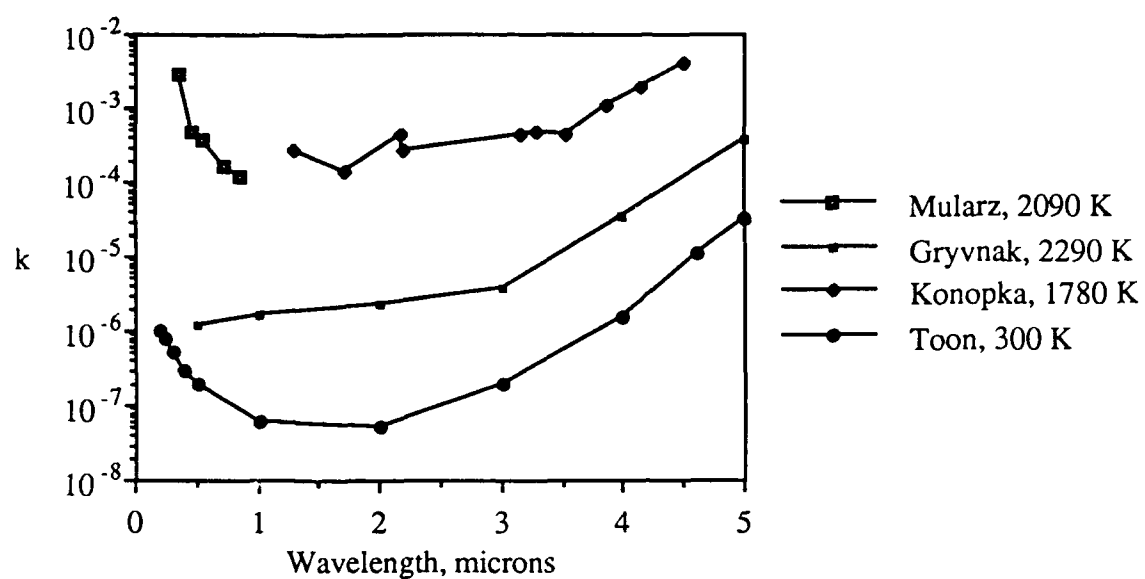


Fig. 2 Survey of solid aluminum oxide absorption index

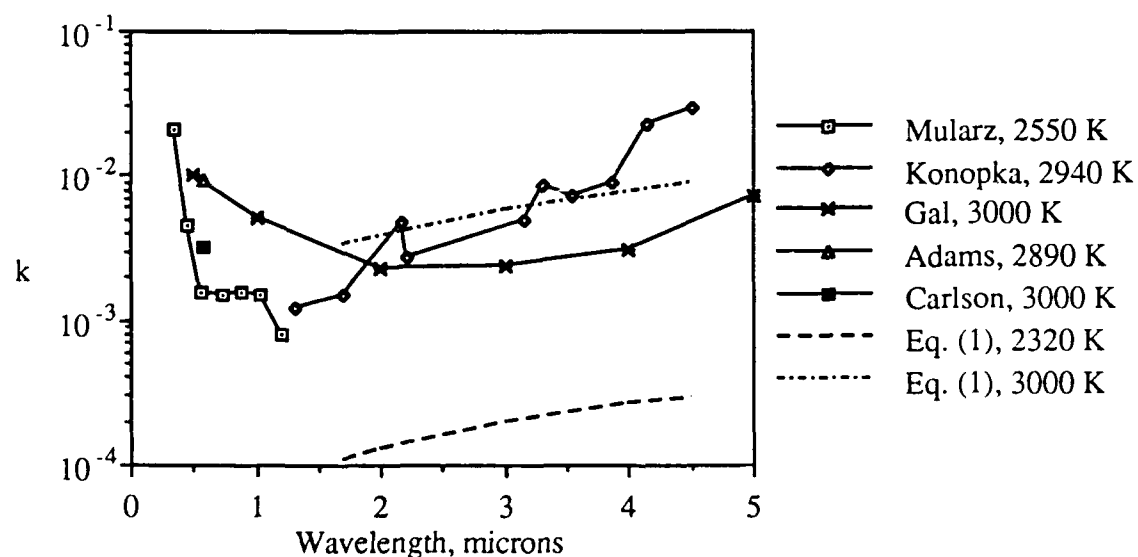


Fig. 3 Survey of molten aluminum oxide absorption index

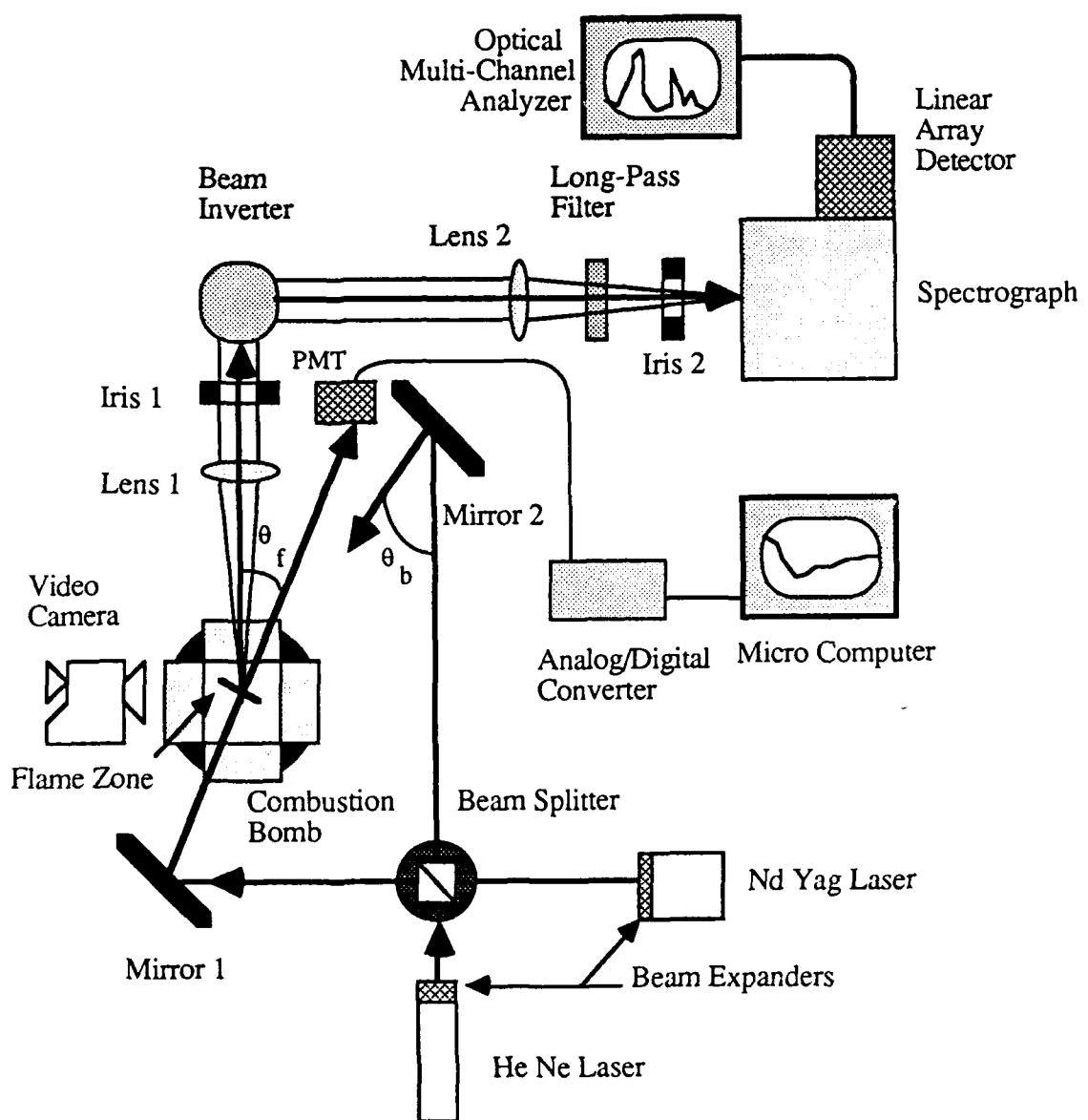


Fig. 4 Optical apparatus schematic diagram

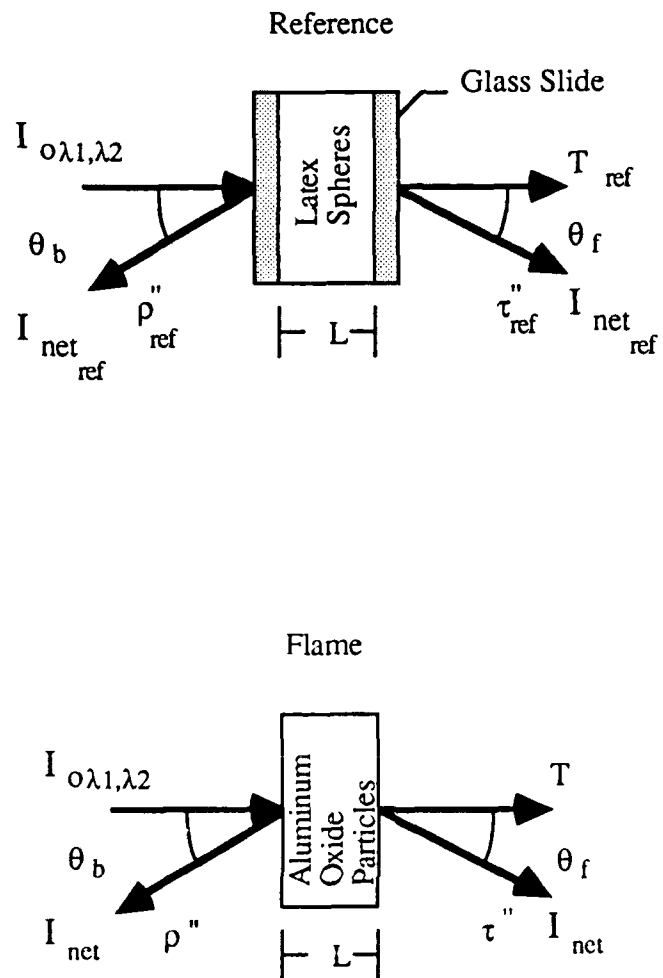


Fig. 5 One-dimensional, planar scattering geometry for experimental technique

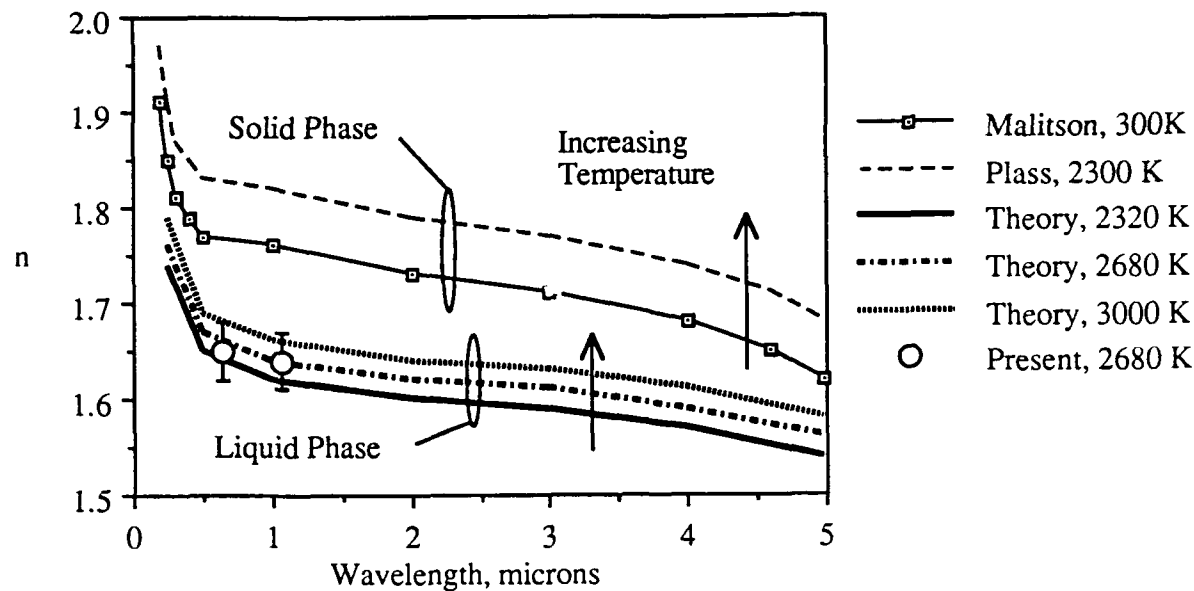


Fig. 6 Aluminum oxide refractive index (recommended)

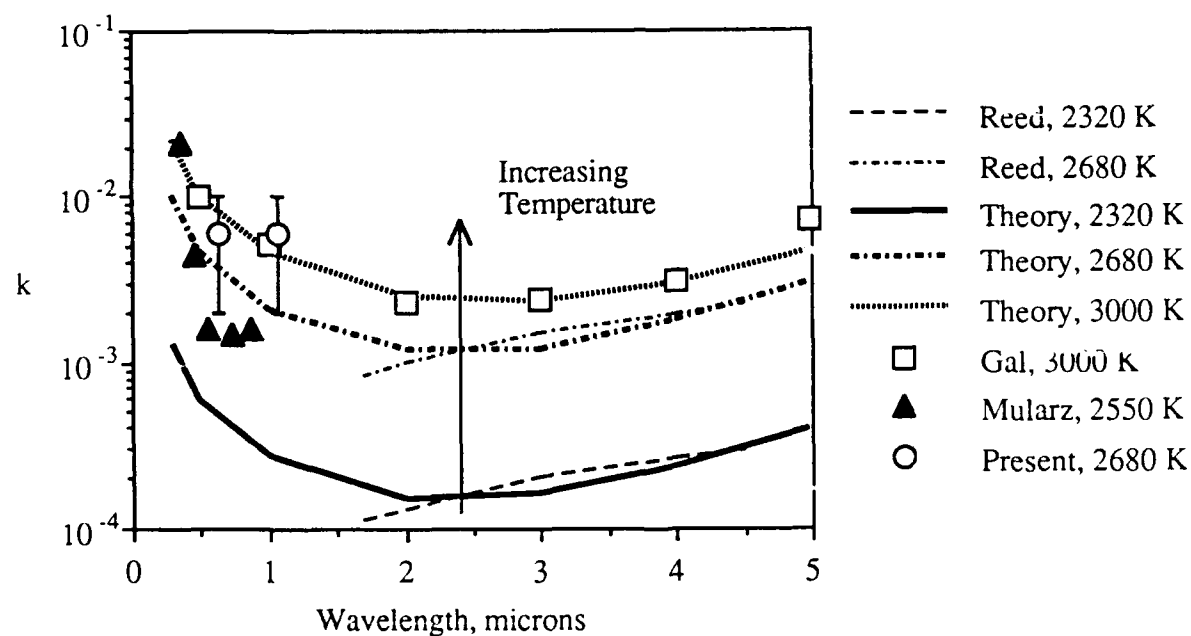


Fig. 7 Molten aluminum oxide absorption index (recommended)

Table 1 Scattering and extinction results

Type	Wavelength	t_L	τ''	ρ''
Polystyrene reference	$\lambda_1 = 0.6328 \mu\text{m}$	1.78	0.40	0.43
Polystyrene reference	$\lambda_2 = 1.064 \mu\text{m}$	1.89	0.42	0.43
Al_2O_3 in flame	$\lambda_1 = 0.6328 \mu\text{m}$	1.28 ± 0.11	1.37 ± 0.07	0.13 ± 0.03
Al_2O_3 in flame	$\lambda_2 = 1.064 \mu\text{m}$	1.21 ± 0.23	1.05 ± 0.06	0.13 ± 0.07

Table 2 Ranges considered for each unknown variable

Unknown Variable	Range Considered
n	1.40 to 1.85
k	1×10^{-5} to 2×10^{-2}
d_{32}	0.1 to 2 μm
$\frac{d_{mp}}{d_{32}} = \frac{x_{mp}}{x_{32}}$	0.05 to 1.0

Table 3 Optical properties of Al₂O₃ smoke particles (T=2680 K)

Property	Value	Standard Deviation
d ₃₂ , μm	0.97	0.11
n _{mλ1}	1.65	0.03
n _{mλ2}	1.64	0.03
k _{mλ1,λ2}	6 x 10 ⁻³	4 x 10 ⁻³
$\frac{d_{mp}}{d_{32}}$	0.15	0.10

Table 4 Mie scattering parameters for Al₂O₃ smoke particles

Parameter	λ1 = 0.6328 μm	λ2 = 1.064 μm
Particle size parameter, x ₃₂	4.82 ± 0.55	2.86 ± 0.33
Extinction efficiency, Q _e	2.65 ± 0.14	2.90 ± 0.47
Albedo, ω ₀	0.94 ± 0.04	0.97 ± 0.03
Asymmetry factor, <̄p>	0.67 ± 0.07	0.69 ± 0.07

Table 5 Data used for dispersion analysis

Temperature, K	Wavelength, μm	n_m	Source	k_m	Source
2320	0.55			1.0×10^{-3}	Ref. 15
	0.725			8.0×10^{-4}	Ref. 15
	1.0	1.62	Eq. (32)		
	1.7			1.1×10^{-4}	Eq. (1)
	2.0	1.60	Eq. (32)		
	3.0	1.59	Eq. (32)		
	3.1			2.0×10^{-4}	Eq. (1)
	4.0	1.57	Eq. (32)		
	4.5			2.9×10^{-4}	Eq. (1)
	5.0	1.54	Eq. (32)		
2680	0.6328	1.65	Table 3	6.0×10^{-3}	Table 3
	1.064	1.64	Table 3	6.0×10^{-3}	Table 3
	1.7			8.3×10^{-4}	Eq. (1)
	3.0	1.61	Eq. (34)		
	3.1			1.5×10^{-3}	Eq. (1)
	4.0	1.59	Eq. (34)		
	4.5			2.2×10^{-3}	Eq. (1)
	5.0	1.56	Eq. (34)		
3000	0.5	1.69	Eq. (34)	1.0×10^{-2}	Ref. 11
	1.0	1.66	Eq. (34)	5.2×10^{-3}	Ref. 11
	2.0	1.64	Eq. (34)	2.3×10^{-3}	Ref. 11
	3.0	1.63	Eq. (34)	2.4×10^{-3}	Ref. 11
	4.0	1.61	Eq. (34)	3.1×10^{-3}	Ref. 11
	5.0	1.58	Eq. (34)	4.5×10^{-3}	Ref. 11

Table 6 Plass' data for solid Al₂O₃ at 2300 K

$\lambda, \mu\text{m}$	0.5	1.0	2.0	3.0	4.0	5.0
n_s	1.83	1.81	1.80	1.77	1.74	1.69

Table 7 Dispersion parameters for two oscillators at three temperatures

Parameter	2320 K	2680 K	3000K
$\eta_{p1}^2 (\frac{1}{\mu\text{m}^2})$	8.513×10^1	8.723×10^1	8.934×10^1
$\eta_{p2}^2 (\frac{1}{\mu\text{m}^2})$	8.915×10^{-3}	8.806×10^{-3}	8.839×10^{-3}
$\gamma_1^2 (\frac{1}{\mu\text{m}^2})$	6.783×10^{-4}	3.423×10^{-2}	1.995×10^{-1}
$\gamma_2^2 (\frac{1}{\mu\text{m}^2})$	8.630×10^{-7}	5.344×10^{-5}	1.088×10^{-4}

	4.0	1.60	2.31×10^{-3}
	5.0	1.57	3.69×10^{-3}
3000	0.5	1.69	1.03×10^{-2}
	1.0	1.66	4.69×10^{-3}
	2.0	1.64	2.51×10^{-3}
	3.0	1.63	2.30×10^{-3}
	4.0	1.61	3.01×10^{-3}
	5.0	1.58	4.63×10^{-3}

Table 8 Temperature coefficients for dispersion parameters

ψ	a_0	a_1	a_2	a_3	a_4
η_{p1}^2	8.509×10^1	4.205	0	0	0
η_{p2}^2	8.853×10^{-3}	0	0	0	0
γ_1^2	7.450×10^{-4}	1.838×10^{-1}	-8.626×10^{-1}	1.698	-8.195×10^{-1}
γ_2^2	8.630×10^{-7}	8.961×10^{-5}	1.832×10^{-5}	0	0

Table 9 Dispersion analysis results

Temperature, K	Wavelength μm	n_m	k_m
2320	0.5	1.65	5.80×10^{-4}
	1.0	1.62	2.65×10^{-4}
	2.0	1.60	1.50×10^{-4}
	3.0	1.59	1.57×10^{-4}
	4.0	1.57	2.35×10^{-4}
	5.0	1.54	3.92×10^{-4}
2500	0.5	1.66	2.79×10^{-3}
	1.0	1.63	1.28×10^{-3}
	2.0	1.61	7.30×10^{-4}
	3.0	1.60	7.96×10^{-4}
	4.0	1.58	1.23×10^{-3}
	5.0	1.55	2.09×10^{-3}
2680	0.5	1.67	4.65×10^{-3}
	1.0	1.64	2.12×10^{-3}
	2.0	1.62	1.19×10^{-3}
	3.0	1.61	1.24×10^{-3}
	4.0	1.59	1.83×10^{-3}
	5.0	1.56	3.04×10^{-3}
2800	0.5	1.68	6.92×10^{-3}
	1.0	1.65	3.15×10^{-3}
	2.0	1.63	1.72×10^{-3}
	3.0	1.62	1.66×10^{-3}

To Appear in Journal of Quantitative Spectroscopy and Radiative Transfer

RADIANT EMISSION FROM THE ALUMINUM - WATER REACTION

M.R. Jones and M. Q. Brewster

Department of Mechanical and Industrial Engineering
University of Illinois at Urbana-Champaign
Mechanical Engineering Building
West Green Street
Urbana, IL 61801

(Received 9 November 1990)

Abstract- The exploding wire technique was used in connection with spectroscopic measurements to investigate the nature of the radiation emitted from the Al - H₂O combustion process. The absolute spectral intensity emitted from the Al - H₂O reaction throughout the 300 - 800 nm spectral region has been determined experimentally with a resolution of 4 nm at various pressures. Higher resolution (0.57 nm resolution) spectroscopic measurements were also made in several regions of interest in the 300 - 800 nm spectral region. The spectra measured in this study were dominated by line and band emission, but a low-level continuum was also present. A simplified analysis showed that the observed continuum could be plausibly attributed to emission from small (~0.01 μm) Al₂O₃(l) particles.

1. INTRODUCTION

The reaction of aluminum with water or steam is of significant practical interest in areas such as rocket propulsion, underwater explosions, and the nuclear reactor industry. A better understanding of the fundamental mechanisms involved in this reaction would greatly enhance the modeling capabilities in each of these areas. Recently, a technique in which an aluminum wire is ignited with an electrical pulse, known as the exploding wire technique, has been employed in investigations of the fundamental mechanisms of the Al - H₂O combustion process.^{1,2,3} In the present study, the exploding wire technique and spectroscopic measurements were used to examine the nature of the emitted radiation from the Al - H₂O combustion process.

Early studies of the radiation emitted from burning aluminum were conducted to determine the nature of the light emitters in photoflash lamps. In 1947, Brockman⁴ made spectroscopic measurements of the light emitted by flash lamps filled with aluminum and oxygen. The observed spectra were dominated by a continuum that extended from 320 nm to the upper measured spectral limit of 700 nm. Other prominent features included the aluminum lines at 394.4 and 396.1 nm and the AlO bands which extended from 440 to 540 nm.

Rautenberg and Johnson⁵ obtained a time-resolved spectrogram produced by the aluminum - oxygen reaction in a photoflash lamp. The AlO band appeared early in the flash but was soon obscured by a significant continuum. This blackbody emission was attributed to an incandescent gas and liquid mixture at a temperature of 3800 K.

Brzustowski and Glassman⁶ also made spectroscopic measurements of the aluminum - oxygen reaction and obtained results similar to those obtained by Rautenberg and Johnson. They attributed the continuous emission to $\text{Al}_2\text{O}_3(\text{l})$.

A spectrophotometric study of premixed trimethylaluminum - oxygen flames was conducted by Vanpee and Seamans.⁷ These flames were stabilized at reduced pressures on a flat-flame burner and showed multiple reaction zones. The primary reaction in the first zone was the oxidation of aluminum by molecular oxygen. The prominent spectral features observed in this zone were a continuum, aluminum doublets, OH bands, two CH systems, and AlO bands. Vanpee and Seamans attributed the continuum in the red and near infrared to emission by Al_2O_3 smoke particles.

Kolb et al⁸ studied the results of several laboratory experiments dealing with the gas-phase oxidation of aluminum and observations of the explosion of aluminized grenades in the upper atmosphere. They suggested that what appeared to be a continuum peaking near 500 nm was actually chemiluminescence from chemically-pumped AlO. Because the spectroscopic measurements were not capable of resolving the complex AlO band structure, the emission appeared continuous. Kolb et al discussed the various mechanisms that had been proposed as the source of the visible chemiluminescence and suggested a new mechanism involving the aluminum dimer and molecular oxygen. The results of their study showed that the chemiluminescence could be attributed to uncommon transitions involving the excited $\text{A}^2\Pi$ and/or the lowest lying $4\Sigma^+$ and 4Π states of chemically-pumped AlO. Kolb et al argued that under low resolution the broadband emission from chemically-pumped states of metal-oxide or metal-halogen diatomics could appear to be a continuum that extends over a wavelength interval of several thousand angstroms, and that the spectra observed in the aluminum - oxygen combustion reaction is continuous more by definition than by actual observation.⁸

Other investigators have suggested the continuum is due to the recombination of oxygen atoms on the surface of Al_2O_3 particles,⁹ or that it is due to the heterogeneous reaction of aluminum vapor and oxygen on the surfaces of such particles.¹⁰ One of the objectives of this study was to gain a better understanding of the source of the continuum emitted during the Al - H_2O reaction. The combustion region was modeled as an absorbing, emitting, non-scattering slab of spherical Al_2O_3 smoke particles in order to investigate the possibility that $\text{Al}_2\text{O}_3(\text{l})$ was the source of the continuous emission observed in this study. Recent measurements of the optical properties of $\text{Al}_2\text{O}_3(\text{l})$ ¹¹ were used to calculate the spectral intensity based on this model.

2. EXPERIMENTAL WORK

Using the exploding wire technique, small aluminum wires (100 μm) were ignited under water at pressures of 33.5, 101, and 446 kPa. In this technique, the wire was ignited with an electrical pulse, and the ignition process occurred in two steps. The rapid, ohmic heating melted the aluminum wire, and a vapor explosion occurred when the molten aluminum contacted the surrounding water. A vapor explosion is an interesting phenomenon of significant industrial importance, which occurs when a liquid coolant comes into contact with another liquid at a temperature above the boiling point of the coolant. Detailed discussions of vapor explosions can be found in Refs. 12 to 15. The vapor explosion fragmented the wire and created a cloud of molten aluminum drops or aluminum vapor which then reacted chemically with the surrounding H_2O .

A simple, non-imaging system was used to make low-resolution (4 nm resolution) and high-resolution (0.57 nm) spectral intensity measurements of the combustion process in the 300 - 800 nm spectral region. The intensity measurements were made using Spex Minimate 1681C 512 element diode array detector controlled by a Tracor Northern TN-6500 optical multichannel analyzer. Low-resolution, absolute spectral-intensity measurements were made of the entire spectral region from 300 - 800 nm. The 300 - 800 nm region of interest was covered by making

measurements in four overlapping regions, which extended from 300 - 500 nm, from 400 - 600 nm, from 500 - 700 nm, and from 630 - 830 nm. High resolution spectra were taken at various points of interest within these regions, but these measurements were not calibrated for absolute intensity. High resolution spectra were only measured at the highest pressure, 446 kPa.

A 100 μm diameter aluminum wire was held vertically by two micro-alligator clips. The aluminum wire was manufactured by Johnson Matthey and had a purity of 99.999%. A batch analysis of the wire was performed by the manufacturer, and the impurities detected were Si, Fe, Cu, and Ca. The alligator clips were soldered to brass electrodes that were mounted in the base of a combustion bomb fitted with four quartz windows. A rubber stopper was fit down over the bottom alligator clip and a 9.525 mm inside diameter quartz tube was pushed down onto the stopper and situated such that it surrounded the wire. The quartz tube was cleaned with alcohol before each experiment. The tube was then filled with distilled water until the wire and most of the upper alligator clip were submerged. The space between the clips was 1 mm, and this length of wire melted and exploded when a 5 V potential was applied across the gap. The electrical resistance in the entire circuit was measured prior to each experiment and was approximately 0.3 Ω . The resistance in the lead wires, in the electrodes, and in the aluminum wire was negligible compared to the contact resistance between the alligator clips and the wire, so the entire 5 V potential drop occurred at the contact points. Therefore, neglecting the heat loss to the surroundings, the power input to the wire was 83 W.

The combustion bomb was held in a sliding mount, so that the wire could be easily aligned with the entrance slit of the spectrograph. Once the wire was aligned at a fixed distance from the spectrograph, a high-speed framing camera was focused on the wire and securely mounted to the table. Long-pass filters were used to prevent higher order wavelengths from reaching the detector. Figure 1 is a schematic diagram of the apparatus.

In order to calculate absolute spectral intensities, the solid angle subtended by the combustion region $\Delta\Omega$ had to be determined. A picture of a scale was taken with the high-speed camera, and this image was used to measure the projected area A_p of the combustion zone from the photographs for each experiment.

Calibrated reference signals for each region were also needed to calculate absolute spectral intensities. The reference signals were obtained using a tungsten-filament, quartz, halogen FEL lamp with calibration traceable to NBS standards.

Synchronization of the explosion of the wire with the camera and the spectrograph was obtained in the following manner. Once the camera speed was adjusted and the spectrograph was setup, a 5 V potential was applied across the wire and the spectrograph and camera were triggered simultaneously. The spectrograph scanned continuously for about 128 ms, and the camera shutter could be kept open for 1 s. The room was darkened to prevent the film from being exposed by light other than that emitted by the reaction. Depending on the pressure, the time required to heat the wire to its melting point and initiate a vapor explosion was between 25 to 41 ms. Therefore, the event would occur while the spectrograph was scanning and the camera shutter was open and was easily captured by the spectrograph and the camera.

3. DATA REDUCTION

The optical multichannel analyzer (OMA) required 5.15 ms to scan all 512 diodes of the linear-array detector and record the signal in one subfile. Each diode was read in 10 μs , and there was a 3 μs wrap around time. Since the OMA continuously scanned the diodes, the event could occur at any point during a scan. The event generally occurred in the middle of a scan, and therefore, the radiant emission was usually recorded in two sequential subfiles. A complete record of the spectral emission was obtained by adding the two subfiles together.

Each diode was exposed for 5.15 ms when the reference signals from the FEL lamp were taken, but the reaction only lasted approximately 0.5 ms. This difference in exposure times had to be accounted for in the calibration. The length of time of the event could be determined

approximately from the number of frames exposed in the photographs of each event, but it was difficult to accurately control the speed of the camera. An estimate of the length of the event to within 10 μ s was obtained by counting the number of diodes that recorded an appreciable signal in both of the subfiles. A correction factor that accounted for the difference in exposure time between the reference signal and the actual event was calculated from the ratio of 5.15 ms to the length of time of each event. The spectral radiant heat flux was given by the product of the calibration factors, the correction factor, and the measured signal. The absolute spectral intensity was then calculated from the ratio of the spectral radiant heat flux and the solid angle subtended by the combustion region.

Three runs were made in each of the four spectral regions for each of the three different pressures. The spectral intensities presented in Sec. 4 are the average of these measurements. A complete discussion of the experimental technique and the data reduction process including program listings can be found in Ref. 16

4. LOW-RESOLUTION ABSOLUTE SPECTRAL INTENSITY MEASUREMENTS

Figure 2 shows the spectral intensity emitted by the Al - H₂O combustion process at the different pressures under low resolution (4 nm resolution). Comparison of the measurements at different pressures show that the spectra remain qualitatively the same as the pressure is varied, but the overall intensity of the signal increases with pressure. Principle features of spectroscopic measurements are two strong lines due to Al at 309 and 396 nm, band emission from AlO between 433 and 531 nm, and a continuum which extends through the 300 - 800 nm spectral region. Other species identified in these spectra are OH, AlH, and H. The lines were identified using tables compiled by Pearse and Gaydon.¹⁷

Comparison of the spectra in Fig. 2 with the spectra measured by other researchers who studied aluminum combustion^{4-7,18} showed an interesting contrast. The spectra emitted by the Al - H₂O reaction produced by the exploding wire technique were dominated by line and band emission. The spectra observed when aluminum reacted with molecular oxygen in flash lamps or when trimethylaluminum was burned in oxygen were always dominated by a continuum that began near 340 nm, peaked around 500 nm and extended into the infrared. This difference indicated that the Al - H₂O reactions produced by the exploding wire technique in this study were quenched before significant amounts of the continuum emitter were produced.

The water from several runs made at atmospheric pressure was collected and then examined and photographed using a scanning electron microscope (SEM). The only element detected in the residue was aluminum, but no information regarding its oxidation state could be obtained. This is due to the fact that the SEM that was used was not able to identify elements whose atomic numbers are less than 11. The nonspherical shape of the particles seen in the SEM photograph was similar to that seen by researchers investigating vapor explosions in which no chemical reactions took place.^{14,15} Comparison of the angular shape of the particles in the SEM photographs with the highly spherical shape of Al₂O₃ particles seen in other photographs¹⁹ also supported the conclusion that the residue was primarily unreacted aluminum and that the reaction was quenched before a significant amount of Al₂O₃ was produced.

5. HIGH-RESOLUTION SPECTROSCOPIC MEASUREMENTS

High-resolution (0.57 nm resolution) spectroscopic measurements were made at 446 kPa and are shown in Figs. 3 to 7. These figures show that the dominant spectral features are band and line emission. However, a low-level continuum is also observed throughout the 300 - 800 nm spectral region. The high-resolution measurements shown in Figs. 3 and 7 also give an indication of the strength of the continuum at short and long wavelengths. The radiant emission near 330 nm and away from the Al and OH line structure in Fig. 3 shows the continuum level is slightly less than 20 counts. The level of the continuum near 645 and 670 nm and away from the 656 nm H line shown in Fig. 7 is approximately 30 counts. It is important to note that these measurements are not calibrated for absolute intensity. However, calibration involves factors such as the solid

angle subtended by the combustion region and the correction factor for the difference in exposure times which are relatively constant from run to run. Therefore, calibration would not have much effect on the relative strengths of the continua shown in these figures. Thus, the high-resolution spectroscopic measurements indicate the level of the continuum decreases at shorter wavelengths.

The wavelength axis in the insert shown in Fig. 3 has been reduced so that the different peaks are readily distinguished. The measurement shown in Fig. 4 is centered at 395 nm, and shows more detailed structure of the strongest Al line. Figures 5 and 6 show the complex band structure in the 455 to 510 nm spectral region. The emission here was primarily that of the AlO green system, $B^2\Sigma^+ \rightarrow X^2\Sigma^+$, which Pearse and Gaydon describe as a sequence of red degraded single headed bands.¹⁷ Figure 7 shows the most prominent spectral feature at long wavelengths, the 656 nm H line.

6. TEMPERATURE DETERMINATION FROM THE INTENSITY RATIO OF TWO AL₂O BANDS

High-speed photographs of the combustion process showed a bright inner region surrounded by a darker fringe. This observation indicated that the temperature was relatively constant across the center of the cloud and decayed at the edges. Brzustowski and Glassman⁶ reported that AlO only existed at the highest temperature when Al reacted with O₂ in flashlamps. Therefore, if the system was in equilibrium, the temperature of the inner region could be determined by measuring the temperature of the AlO.

In the absence of self absorption and assuming local thermodynamic equilibrium (LTE), the temperature of an emitting source can be determined from²⁵

$$T = \frac{(\epsilon_a - \epsilon_b)}{k} \ln \left(\frac{I_b f_a \lambda_b^3}{I_a f_b \lambda_a^3} \right) \quad (1)$$

if the *f*-numbers and the intensities for two transitions between different upper energy levels and the same lower level are known. Since self absorption affects stronger lines (larger *f*-number) more than weaker lines (smaller *f*-number), the ratio of the intensity emitted by the weaker line to the intensity emitted by the stronger line will increase due to self absorption. Equation (1) shows that the temperature will increase as this ratio of intensities increases, so this two line technique for temperature measurement will overestimate the temperature when self absorption occurs.

The *f*-numbers for two AlO transitions were also needed to calculate the temperature from Eq. (1). Johnson et al used a pulsed dye laser to selectively pump three vibrational levels of the AlO $B^2\Sigma^+ \rightarrow X^2\Sigma^+$ transition, and measured the radiative lifetimes from semilog plots of the fluorescence decay. The *f*-numbers for the 2,0 , the 1,0 , and the 0,0 vibrational transitions were then calculated from the measured lifetimes and the results are shown in Table 1.²⁶

Table 1. Absorption oscillator strengths of AlO ($B^2\Sigma^+ \rightarrow X^2\Sigma^+$).

<i>v'</i> , <i>v''</i>	<i>f</i>	I (counts)
2,0	0.0208	
1,0	0.68	85
0,0	0.13	70

The intensities for two lines were the final parameters needed to calculate the temperature of the AlO in the flame. The peak values for the 1,0 and the 0,0 AlO transitions were obtained from Fig. 5 and are listed in Table 1. These peak values were assumed to be representative of the intensity of these transitions. Using Eq. (1) and the data listed in Table 1, the temperature of the system was then calculated to be 4850 K. This temperature is much higher than the expected flame temperature of approximately 3000 K.²⁷ Although it was expected that the indicated temperature

would be higher than the actual flame temperature because of self absorption, the difference in temperature could also indicate the AlO was not in LTE and was being chemically-pumped as postulated by Kolb et al.⁸ However, the mechanism suggested for obtaining chemically-pumped AlO involves Al₂ as an intermediate species. Since the measurements made in this study did not show the presence of Al₂, the AlO was probably not chemically-pumped, and the error in the temperature measurement was due to self absorption. This result shows that care must be taken when using relative intensity measurements to determine the flame temperature when a continuum emitter is present. The presence of the continuum emitter increases the optical depth at the wavelengths of interest and can lead to significant error in determining the temperature.

7. SOURCE OF THE CONTINUOUS EMISSION

Although extensive spectroscopic studies of the combustion of aluminum have been conducted, the source of the continuous emission seen in the measured spectra has not been determined conclusively. In order to investigate the possibility that Al₂O₃(l) smoke particles were the source of the continuous emission observed in this study, the emission from a non-scattering cloud of molten, spherical Al₂O₃(l) smoke particles was modeled. Scattering was neglected in the model for two reasons; the optical thickness was not large and the single scattering albedo was small. Optical pyrometry studies in coal flames²⁰ have shown that scattering can be neglected in modeling flame emission if the optical thickness is not large (0.1 to 1.0) and the particles are weakly scattering (such as coal and soot particles). In this study, the continuum optical thickness was estimated to vary between 1.0 and 0.1 over the spectral region from 0.3 to 0.8 μm.

The value of the single-scattering albedo depends strongly on particle size and optical constants. The size depends on many factors including the time available for particle growth.²¹ Particles which grow to sizes typically seen in propellant flames and rocket plumes (0.1 to 1.0 μm) have a rather large albedo in the visible region (> 0.9)²² due to the intermediate value of the size parameter $x=\pi D/\lambda \sim 0.6$ to 6.0 and the small value of the absorption index $k \sim 0.01$.^{11,22,23,24} However, given the rapid quenching and short reaction time (0.5 msec) of the exploding wire technique, it is unlikely that a significant number of particles would grow to sizes larger than about 0.01 μm. No particles in the 0.1 to 1.0 μm size range were observed in the combustion residue micrographs, so a maximum diameter of 0.01 μm was used to estimate the albedo. For a characteristic wavelength of $\lambda=0.5$ μm the particle size parameter is $x=\pi D/\lambda=0.06$ and the optical constants are $n=1.7$ and $k=0.01$.¹¹ Since $k \ll n \sim O(1)$ and $x \ll 1$, the particles can be characterized as lossy dielectric particles in the Rayleigh region, and the albedo can be shown to be given by

$$\omega_0 = \frac{1}{1 + \frac{9nk}{x^3(n^2 - 1)^2}} = 0.006 \ll 1. \quad (2)$$

Thus, based on estimates of the optical thickness of the reaction zone and the albedo of the particles, the neglect of scattering seems reasonable.

The emitted intensity from the reaction zone was given by the radiative transfer equation for a non-scattering, absorbing, emitting medium, viz.

$$I_\lambda(s) = \int_0^s I_{\lambda}(s')(1 - \exp(K_a s')) ds', \quad (3)$$

where the absorption coefficient is given by

$$K_a = 1.5 Q_a f_v / D. \quad (4)$$

The absorption efficiency $Q_{a\lambda}$ was calculated from the Rayleigh limit of Mie theory. The volume fraction of the smoke f_v was assumed to be constant and was obtained from a parametric study. As previously discussed, a value of $0.01 \mu\text{m}$ was used for the diameter D . Since the absorption efficiency is proportional to diameter in the Rayleigh limit, the absorption coefficient calculated from Eq. (4) is actually independent of diameter. Gas emission was neglected, so only the radiation emitted by $\text{Al}_2\text{O}_3(\text{l})$ was considered in this analysis. A program was written to solve Eq. (3) numerically. The optical constants for $\text{Al}_2\text{O}_3(\text{l})$ were calculated from classical dispersion theory using recently determined dispersion parameters.¹¹

The analysis also required an estimate of the flame temperature profile. As previously discussed, photographs of the combustion process indicated the temperature was constant across the center of the cloud and decayed at the edges. The inner region was approximately $800 \mu\text{m}$ wide, and the fringe regions were each about $400 \mu\text{m}$ wide. The inner region was assumed to be isothermal and an exponentially decaying temperature profile was assumed in the fringe regions. Values for the temperature in the center of the combustion region, for the temperature at the edges, and for the volume fraction of the $\text{Al}_2\text{O}_3(\text{l})$ smoke particles were the final parameters needed to complete the analysis. A parametric study was conducted to determine the effect each of these parameters and is described in detail in Ref. 16. The results of the parametric study were compared with the measurements made at atmospheric pressure, and the calculated spectral intensity fit the measured spectral intensity best with 3300 K for the temperature in the center, 300 K for the temperature at the edges, and 0.00105 for the volume fraction of $\text{Al}_2\text{O}_3(\text{l})$ smoke particles. The results of the model are compared with the spectrum measured at atmospheric pressure in Fig. 8. The calculated continuum matches the measured continuum at wavelengths above 560 nm, but the measured continuum appears to increase at shorter wavelengths while the calculated continuum decreases at shorter wavelengths. As previously mentioned, high resolution spectroscopic measurements indicated the actual continuum was lower than that shown in Fig. 8 at shorter wavelengths in agreement with the calculated results.

8. SUMMARY AND CONCLUSIONS

The absolute spectral intensity emitted from the $\text{Al} - \text{H}_2\text{O}$ reaction in the 300 - 800 nm spectral region has been experimentally determined with a resolution of 4 nm at pressures of 33.5, 101, and 446 kPa. High-resolution (0.57 nm resolution) spectroscopic measurements were also made in various regions of interest within the 300 - 800 nm spectral region at 446 kPa. Attempts to measure the flame temperature using the intensity ratio of two AlO bands were unsuccessful due to the presence of a continuum emitter. Recent measurements of the optical properties of $\text{Al}_2\text{O}_3(\text{l})$ ¹¹ were used to calculate the spectral intensity that would be emitted by an absorbing, emitting, non-scattering cloud of spherical $\text{Al}_2\text{O}_3(\text{l})$ smoke particles. Comparison of the results of this analysis with spectra measured at atmospheric pressure showed that the observed spectrum is consistent with the interpretation that the continuum was emitted by small $\text{Al}_2\text{O}_3(\text{l})$ smoke particles. Comparison of the spectra measured in the present study with the spectra measured by other researchers who studied aluminum combustion^{4-7,18} showed that the $\text{Al} - \text{H}_2\text{O}$ reactions produced by the exploding-wire technique were quenched before a significant amount of the continuum emitter was produced.

Acknowledgement - Funding for this work was provided by the Office of Naval Research under Contract N00014-87-K-0547.

REFERENCES

1. M. Friedman and M. Ury, *Rev. Sci. Instrum.* **48**, 279 (1977).

2. W.M. Lee and R.D. Ford, *J. Appl. Phys.* **64**, 3851 (1988).
3. W.M. Lee and R.D. Ford, *Metallurgical Transactions B*, **19B**, 255 (1988).
4. F.G. Brockman, *J. Opt. Soc. Am.* **37**, 652 (1947).
5. T.H. Rautenberg and P.D. Johnson, *J. Opt. Soc. Am.* **50**, 602 (1959).
6. T.A. Brzustowski and I. Glassman, *Heterogeneous Combustion, Progress in Astronautics and Aeronautics Series*, H.G. Wolfhard, I. Glassman, and L. Green eds., Academic Press, New York, **15**, 41 (1965).
7. M. Vanpee and T.F. Seamans, *Eleventh Symposium (International) on Combustion*, The Combustion Institute, pp. 931-939, Pittsburgh, PA (1966).
8. C.E. Kolb, M.E. Gersh, and D.R. Herschbach, *Combust. Flame* **25**, 31 (1975).
9. E.B. Armstrong, *Planet. Space Sci.* **11**, 751 (1963).
10. G.H. Markstein, *Eleventh Symposium (International) on Combustion*, The Combustion Institute, pp. 219-234, Pittsburgh, PA (1966).
11. D.L. Parry, Ph.D. Thesis, The University of Illinois at Urbana-Champaign, Urbana, IL 61801 (1989).
12. R.H. Bradley, and L.C. Witte, *Nucl. Sci. Engng.* **48**, 387, (1972).
13. M. Epstein, *Nucl. Sci. Engng.* **55**, 462, (1974).
14. L.C. Witte and J.E. Cox, *J. Metals* **30**, 29 (1978).
15. L.C. Witte, T.J. Vyas, and A.A. Gelabert, *J. Heat Transfer*, 521 (Nov. 1973).
16. M.R. Jones, Master's Thesis, The University of Illinois at Urbana-Champaign, Urbana, IL 61801 (1990).
17. R.W.B. Pearse and A.G. Gaydon, *The Identification of Molecular Spectra*, 4th edn., Chapman & Hall, London, (1984).
18. M. Vanpee, E.C. Hinck, and T.F. Seamans, *Combust. Flame* **9**, 393 (1965).
19. E.W. Price, *Fundamentals of Solid Propellant Combustion, Progress in Astronautics and Aeronautics Series*, K. K. Kuo and M. Summerfield eds., AIAA, New York, **90**, 479 (1984).
20. R.A. Altenkirch, D.W. Mackowski, R.E. Peck and T.W. Tong, *Combust. Sci. Technol.* **41**, 327 (1984).
21. C.M. Drew, A.S. Gordon and R.H. Knipe, *Heterogeneous Combustion, Progress in Astronautics and Aeronautics Series*, H.G. Wolfhard, I. Glassman, and L. Green eds., Academic Press, New York, **15**, 17 (1965).
22. R.B. Lyons, J. Wormhoudt, and C.E. Kolb, *Spacecraft Radiative Transfer and Temperature Control, Progress in Astronautics and Aeronautics Series*, T.E. Horton ed., AIAA, New York, **83**, 128 (1982)

23. V. Calia, A. Celentano, M. Soel, W. Konopka, R. Gutowski and R. Ryan, *18th JANNAF Exhaust Plume Technology Subcommittee Meeting*, CPIA Publication 530, 183-192, Monterey, CA (14-17 Nov. 1989)
24. T.E. Parker, R.R. Foutter, J.C. Person and W.T. Rawlins, *18th JANNAF Exhaust Plume Technology Subcommittee Meeting*, CPIA Publication 530, 193-201, Monterey, CA (14-17 Nov. 1989)
25. P.W.J.M. Boumans, *Theory of Spectrochemical Excitation*, Plenum Press, New York (1966).
26. S.E. Johnson, G. Capelle and H.P. Broida, *J. Chem. Phys.* **56**, 663 (1972).
27. J. Kol, A.E. Fuhs and M. Berger, *AIAA-85-0323, AIAA 23rd Aerospace Sciences Meeting*, Reno, NV (14-17 Jan. 1985).

List of Figures

- Fig. 1. Schematic diagram of the experimental apparatus.
- Fig. 2. Exploding-wire spectra at 33.5, 101, and 446 kPa.
- Fig. 3. High-resolution spectroscopic measurements of the 308.216 and 309.272 nm Al lines and 4 branches of the 0,0 transition of the OH $A^2\Sigma^+ \rightarrow X^2\Pi$ system.
- Fig. 4. High-resolution spectroscopic measurements of the 394.402 and 396.154 nm Al lines.
- Fig. 5. High-resolution spectroscopic measurements of the AlO green system, $B^2\Sigma^+ \rightarrow X^2\Sigma^+$ 1,0 and 0,0 transitions.
- Fig. 6. High-resolution spectroscopic measurements of the AlO $B^2\Sigma^+ \rightarrow X^2\Sigma^+$ 0,1 and 0,0 transitions and the OH $B^2\Sigma^+ \rightarrow A^2\Sigma^+$ 1,7 transition.
- Fig. 7. High-resolution spectroscopic measurements of the 656.279 nm H line.
- Fig. 8. Comparison of the calculated and measured continua.

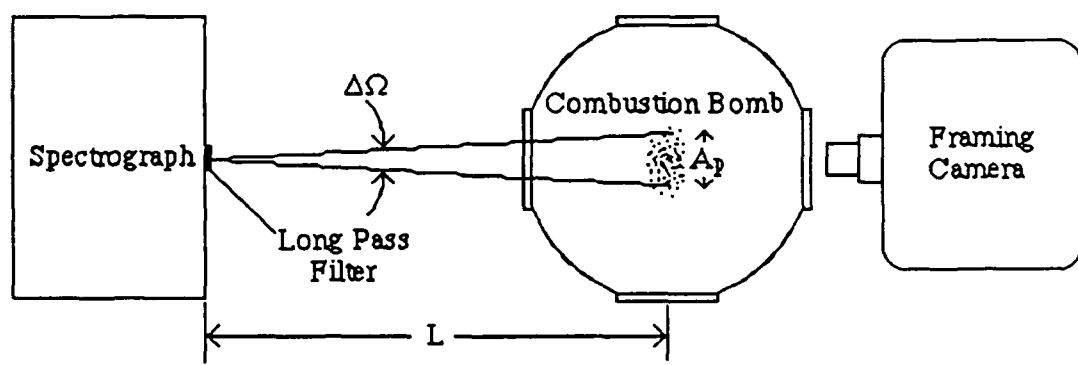


Fig. 1

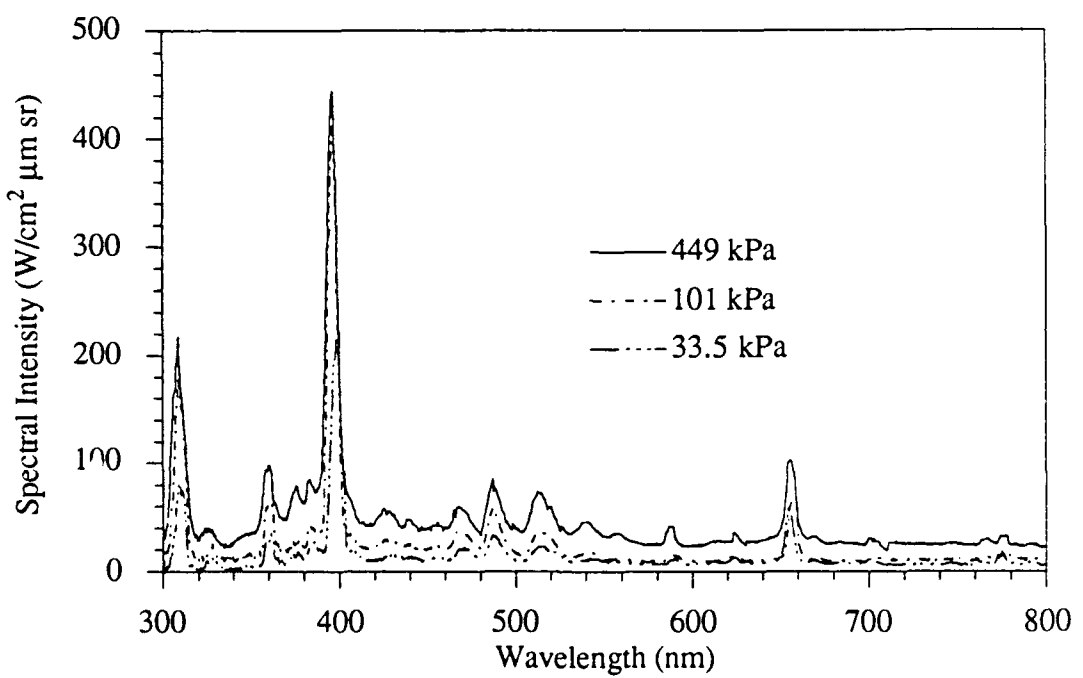


Fig. 2

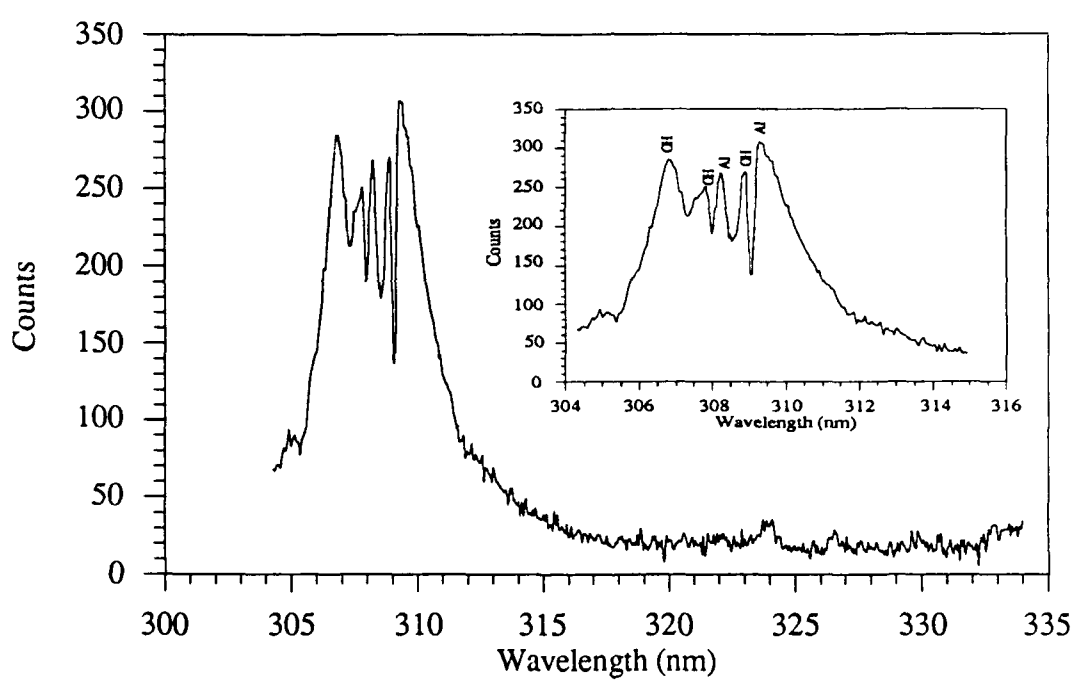


Fig. 3

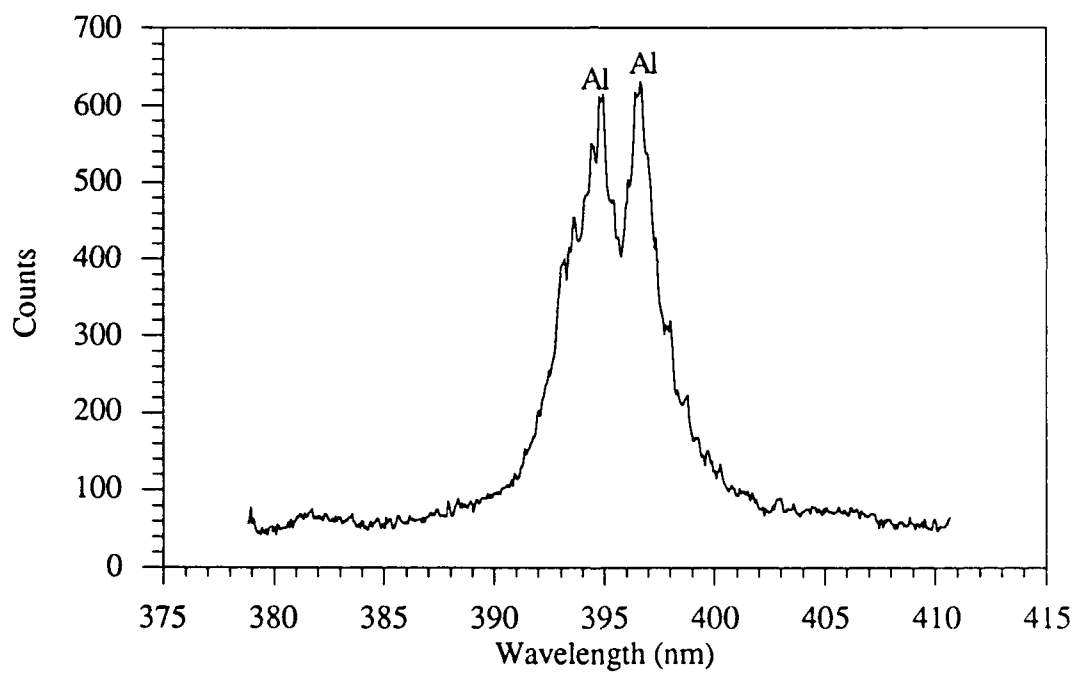


Fig. 4

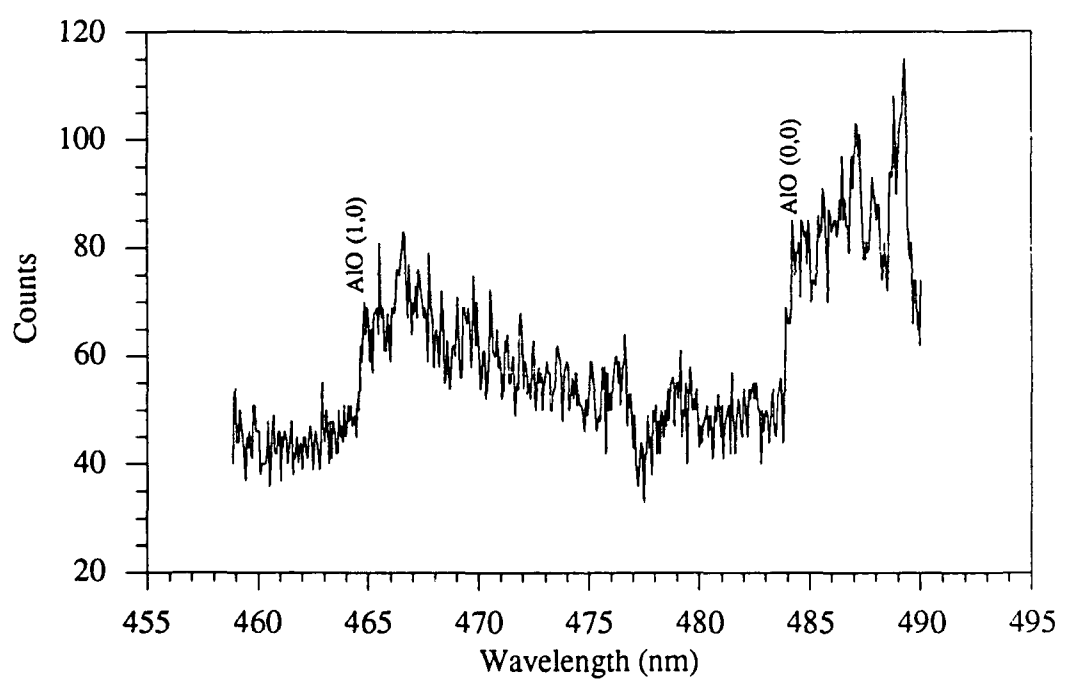


Fig. 5

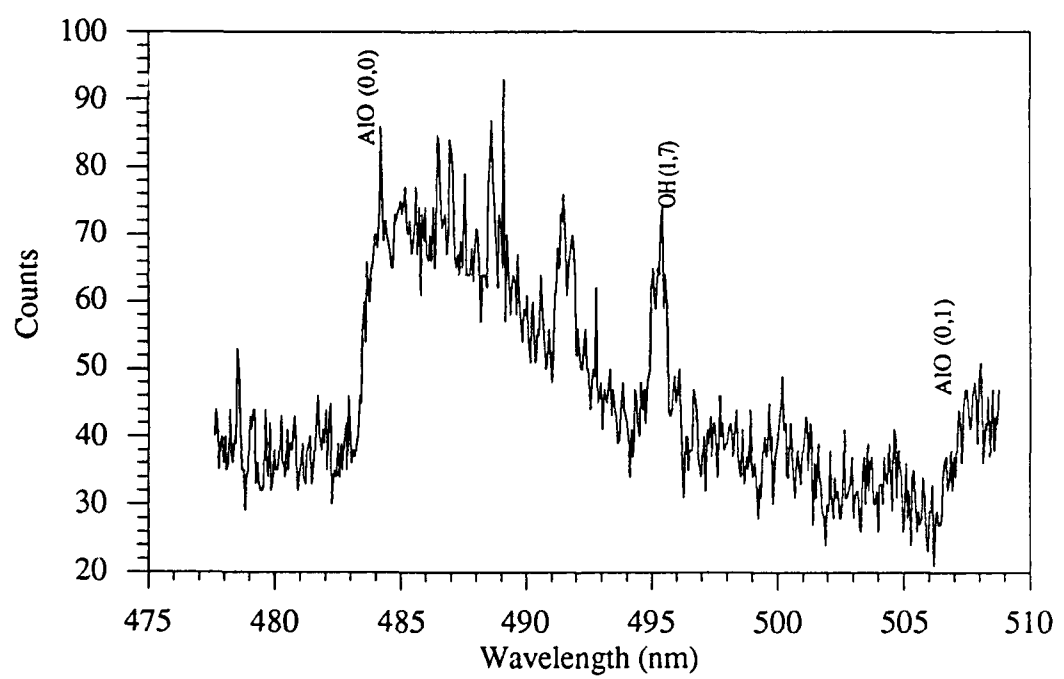


Fig. 6

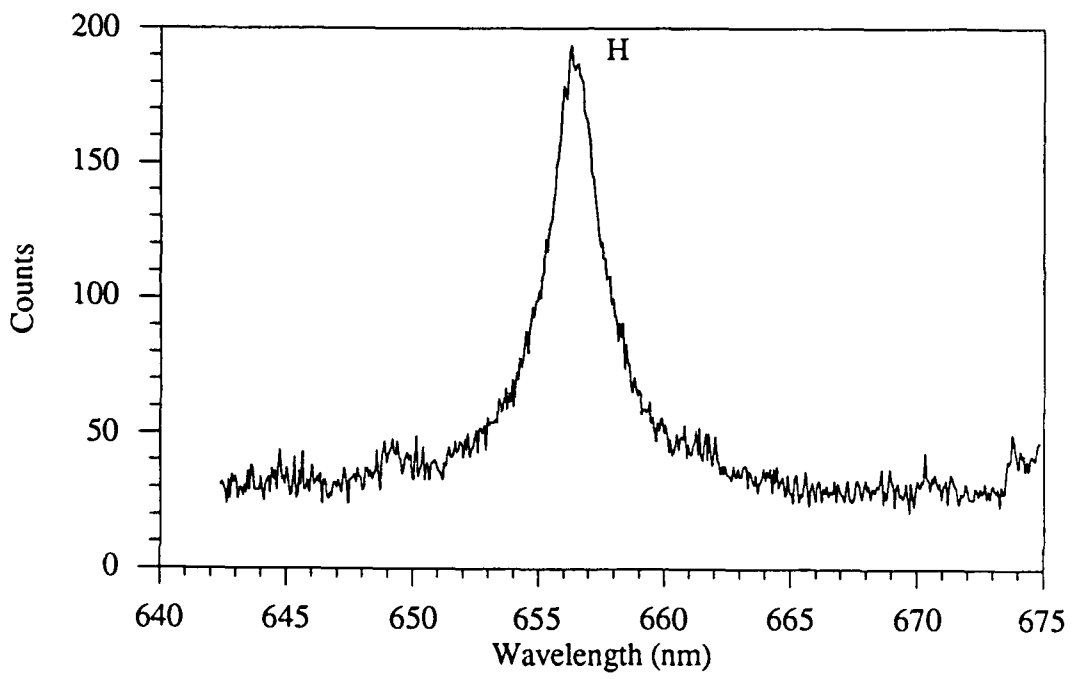


Fig. 7

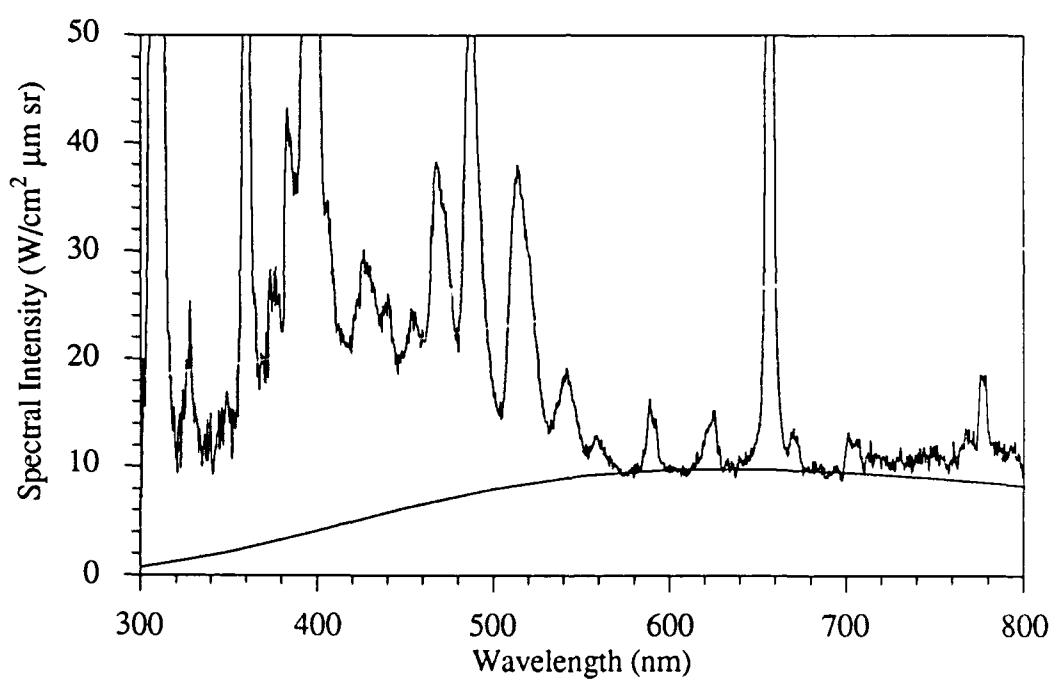


Fig. 8

Heat Transfer in Heterogeneous Propellant Combustion Systems

by

M. Quinn Brewster
Associate Professor of Mechanical Engineering

Department of Mechanical and Industrial Engineering
University of Illinois at Urbana-Champaign
1206 West Green Street
Urbana, IL 61801

to appear in

Annual Review of Heat Transfer, Volume IV

ABSTRACT

Heat transfer plays an important role in several critical areas of heterogeneous, solid propellant combustion systems. These areas include heat feedback to the propellant surface, heat transfer between burning aluminum droplets and their surroundings, heat transfer to internal insulation systems, and heat transfer to aft-end equipment. Gas conduction dominates heat feedback to the propellant surface in conventional ammonium perchlorate (AP) composite propellants, although particle radiative feedback also plays a significant role in combustion of metalized propellants. Particle radiation plays a dominant role in heat transfer to internal insulation, compared with that of convection. However, conduction by impingement of burning aluminum particles, which has not been extensively studied, may also be significant. Radiative heat loss plays an important role in determining the burning rate of molten aluminum particles due to a highly luminous, oxide particle-laden, detached flame envelope. Radiation by aluminum oxide smoke particles also plays a dominant role in heat transfer from the exhaust plume to aft-end equipment. Uncertainties in aluminum oxide particle size distribution and optical properties still make it difficult to accurately predict radiative plume heat transfer from first principles.

NOMENCLATURE

- A_k ambient oxidizer factor
- C specific heat
- d particle or droplet diameter
- G crossflow mass flux
- k thermal conductivity, rate constant, absorption index
- L motor port length
- m mass regression rate
- N particle number density distribution, conduction radiation parameter
- n refractive index
- p pressure

q heat flux
 q''' volumetric heat generation rate
 R_k ambient environment factor
 r propellant regression rate
 T temperature
 t time, optical thickness
 u velocity component
 v velocity component
 x mole fraction
 x distance from propellant surface
 Y mass fraction

Greek

δ boundary layer thickness

ϵ emissivity

κ thermal diffusivity

μ viscosity

ρ density

Subscripts

0 initial

∞ ambient

c characteristic, conductive

e envelope

f flame

g gas

L characteristic length, thickness

m melt, molten

mp most probable

O oxidizer

ox oxide

r radiative

rel relative

s solid, surface

T thermal

1. INTRODUCTION

Heat transfer plays an important role in several key areas of heterogeneous solid propellant combustion systems. These areas include internal rocket motor ballistics as well as thermal protection systems. In the area of internal ballistics, heat transfer plays a critical role in determining both the surface regression rate of the solid propellant as well as the combustion rate of liquid aluminum droplets distributed throughout the motor. In the area of thermal protection, the heat transfer rate to both internal and external thermal protection systems is of critical importance. In particular, radiation is often a strong component of heat transfer which remains relatively poorly characterized in terms fundamental properties as well as transport.

Three key areas where heat transfer plays a significant role in solid propellant rocket systems are labelled in the schematic drawing shown in Fig. 1a. First, near the inside surface of the exposed propellant grain, conductive heat feedback from the

primary flame zone to the propellant plays a crucial role in determining the regression rate of the propellant. Radiative heating from burning aluminum droplets distributed away from the propellant surface also influences the propellant regression rate. Since the regression rate of the propellant and the corresponding mass production rate of combustion gases at the propellant surface, together with nozzle discharge characteristics, determine the internal motor pressure and thrust, the rate of heat transfer to the propellant surface is an extremely important factor in internal ballistics considerations. Heat transfer considerations also play a dominant role in determining the size of aluminum agglomerates produced at the surface of the propellant. Large agglomerates are associated with a significant loss in performance. Therefore, the extent of aluminum agglomeration and size of agglomerates are also key performance parameters determined in part by heat transfer considerations.

The second key area of heat transfer concern is near the head end of the motor or in any other region where propellant does not protect the case from hot combustion products. In these regions, radiation, convection and particle impingement heat transfer combine to impose a significant heat load from which the case must be insulated. The primary source of thermal radiation is molten aluminum oxide Al_2O_3 smoke particles produced by distributed combustion of aluminum. Impingement heat transfer is the result of burning aluminum droplets which are convected by recirculating flows patterns. Since ablative insulation represents inert, dead weight and therefore lost payload, optimal insulation design is essential to competitive performance.

The third area of concern labelled in Fig. 1a is the aft end of the rocket. Thermal radiation from the highly luminous exhaust plumes of aluminized propellants constitutes a substantial heat load from which external aft end equipment must be protected. Aside from heat transfer considerations, thermal radiation in plumes is also a subject of intense interest currently because of observability considerations and remote sensing applications.

2. PROPELLANT HEAT FEEDBACK

Heat feedback to the propellant is a key consideration in solid propellant systems because it determines the regression rate of the propellant which determines the pressure and thrust of the propulsion system. Conductive, convective and radiative heat feedback mechanisms have all been recognized as having an influence on the propellant regression rate. Conduction is the principal mechanism of heat feedback to the propellant surface. Conductive heat feedback can originate either with the primary gas phase flames or, in aluminized systems, with aluminum droplets which often ignite and begin to burn as they move away from the surface of the propellant. Convective heat transfer also plays a role in certain situations. The enhancement of propellant regression rate by flow tangent to the surface of the propellant is known as erosive burning and is a serious concern in systems with high L/D ratios. Radiation also plays a role in burning rate augmentation, although its importance is generally considered to be limited to low burning rate propellants. It should be noted, however, that radiation effects are mostly likely to be significant in aluminized propellants (which emit a high intensity continuum) but that aluminum addition changes many features of the propellant combustion. Yet only a few careful, systematic studies with aluminized propellants have been done to delineate the role of radiation. Therefore conclusions about the role of radiative transfer in aluminized propellant combustion should probably be considered as tentative.

2.1. Conductive Heat Feedback in Primary Flame Zone

Conductive heat feedback from the primary gas flames represents the principal "driving force" which establishes the regression rate of most composite solid propellants. The primary flame zone is confined to a very thin region near the surface of the propellant. Figure 1b shows a magnified schematic diagram of the surface region of a conventional ammonium perchlorate (AP) oxidizer, hydrocarbon fuel binder, composite propellant. To achieve the high solids loading necessary for maximum density and optimum stoichiometry the AP is usually present in a bi-modal or tri-modal particle size distribution. Aluminum powder (5 to 60 μm) may also be present in the propellant formulation. The length scale of the heterogeneity of this surface region is approximately 100 μm which corresponds to the size of the largest AP particles. Because of the heterogeneous nature of the propellant, an intricate flame structure exists above the surface of the propellant. The heat feedback from this complex flame structure is the primary factor in determining the regression rate of the propellant.

2.1.1. One-dimensional heat transfer models

Although any realistic description of the heat transfer in the primary flame zone must address the heterogeneous, multi-dimensional nature of the problem, it is instructive to first review the simple, one-dimensional heat transfer models of the system under consideration [1]. Figure 1c shows a representation of the average temperature profile near the surface of the propellant. By average is meant an average over the plane parallel to the surface of the propellant. The propellant is assumed to be fed upward at the regression rate r so that the origin at the mean propellant surface stays fixed in space. Under steady state conditions the mass flux $m=p_s r$ is a constant.

The energy balance in the condensed phase is a standard convective-diffusive balance (assuming no chemical reaction).

$$k_s \frac{d^2T}{dx^2} - mC_s \frac{dT}{dx} = 0 \quad (1)$$

The solution of Eq. (1) gives an exponential temperature profile in the condensed phase.

$$\frac{T(x)-T_0}{T_s-T_0} = \exp\left(\frac{x}{x_c}\right) \quad (2)$$

The characteristic length scale of the thermal wave in the condensed phase is

$$x_c = \frac{k_s}{mC_s} = \frac{k_s}{r} \quad (3)$$

and its value depends on the regression rate r and the thermal diffusivity k_s . Typical values for x_c range from 100 μm at low pressures (low regression rates) to 1 μm at high pressures (high regression rates).

The energy balance in the gas phase includes a source term due to conversion of chemical enthalpy to sensible enthalpy q''' as shown in Eq. (4).

$$k_g \frac{d^2T}{dx^2} - mC_{pg} \frac{dT}{dx} + q''' = 0 \quad (4)$$

The solution of Eq. (4) depends on the spatial distribution of the heat release $q'''(x)$ which depends on reaction and mixing rates. Integrating Eq. (4) once, assuming constant properties, gives the heat flux conducted back to the propellant surface.

$$q_{s+} = \int_0^\infty q'''(x) \exp\left(-\frac{mC_{pg}x}{k_g}\right) dx \quad (5)$$

From Eq. (5) it can be seen that the distribution of the average heat release $q'''(x)$ is of prime importance in determining the heat flux to the surface and the regression rate.

Since many negative comments have been made about one-dimensional combustion models it is worthwhile to point out that a one-dimensional energy balance, as such, is still a perfectly valid concept. While it is not possible to predict $q'''(x)$ adequately without resorting to multi-dimensional arguments, nevertheless the importance of accurately representing the average spatial distribution of the heat release $q'''(x)$, as illustrated by the one-dimensional analysis, is a lesson to be remembered. In addition, the length scale of the thermal wave in the condensed phase, which can be estimated from the one-dimensional analysis, is an important parameter to keep in mind when expanding the analysis to include propellant heterogeneity.

2.1.2. Heat feedback from competing flames (BDP model)

The first published study to recognize the importance of the multi-dimensional heat feedback from multiple, competing flames which exist above the surface of composite propellants was that of Beckstead, Derr and Price [2-4]. As outlined in their original model (the BDP model), there are two principal, competing flames which are of importance in determining the heat feedback and linear regression rate of the propellant: the AP monopropellant, self-deflagration flame and the primary AP/binder flame (see Fig. 2). The AP self-deflagration flame is a relatively low temperature, premixed, oxidizer rich flame (1400 K) which, in the absence of heat from any other source, extinguishes at pressures below 2 MPa. The primary AP/binder flame is a hybrid, premixed-diffusion flame which reaches temperatures on the order of the stoichiometric adiabatic flame temperature (3000 K). The conductive heat feedback from both of these flames provides most of the energy for sustaining the pyrolysis of the condensed propellant constituents. Due to its premixed nature and close proximity to the AP surface, the AP flame conductive feedback is considered to be one-dimensional. On the other hand, the conductive feedback from the primary flames is generally recognized to be three dimensional, although the BDP model (as well as most subsequent models) assumes one-dimensional heat feedback for the primary flame with an effective flame stand-off distance.

Perhaps the most significant contribution of the BDP model is its description of the competing flames which explains how the heat feedback varies with pressure and AP

particle size. Figure 3 shows two sketches of the multiple flame structure for two different pressures. At low pressures (Fig. 3a) the colder AP flame is relatively far from the AP surface. Most of the AP decomposition products are fed into the primary flame which takes on the nature of a premixed flame over that of a diffusion flame (i.e. it is more kinetically limited than mixing limited). As a result, most of the heat feedback to the propellant comes from the primary flames. Upon examining the propellant surface after extinction of the combustion by rapid depressurization it is observed that the AP particles are peaked in the middle, which is evidence of the dominant heat feedback from the primary flames. At high pressures (Fig. 3b) the AP flame moves closer to the AP surface and most of the AP decomposition products are fed into the AP monopropellant flame. The primary flames, which are somewhat diminished in their overall importance, take on the nature of a diffusion flame over that of a premixed flame and tend toward being mixing limited. The extinguished propellant surface for combustion at high pressures shows that the AP particles are recessed in the middle, which is consistent with the increased importance attributed to the AP flame in the multiple flame model. The other important aspect of the BDP model is that it correctly predicts the general trend of increased heat feedback and burn rate with decreasing AP particle size.

While the BDP model was able to successfully describe the important first order features of composite propellant combustion behavior it soon became apparent that the model was not a complete mechanistic description of the heat transfer process. The discrepancies between predicted and measured regression rates for some propellant formulations were still too large for the model to be reliable as a predictive tool in the solid propellant industry. Particularly in propellants with wide AP size distributions, the failure of the model to include some important mechanism was noticeable [5]. Many similar models emerged attempting to improve on the original BDP model, most of which involved evolutionary refinements rather than revolutionary changes. Refinements in terms of oxidizer size distribution statistics [6] and multiple surface temperatures were included [7]. Of these various evolutionary models which followed after BDP, Cohen has written an instructive summary [8].

2.1.3. *Sandwich propellant studies and KLLEF model*

The next significant advance in understanding of surface combustion behavior and the role of heat transfer came with studies which used a simplified, propellant sandwich geometry [9-10]. Price and co-workers systematically investigated the combustion behavior of propellant sandwiches which consisted of a thin lamina of binder (25 to 175 μm) between two pressed AP slabs as shown in Figure 4. From these studies came two significant conclusions: (1) lateral heat transfer from the AP to the endothermic binder was probably altering the normal AP self-deflagration process and (2) the anomalous AP deflagration was probably affecting the site of heat release in the gas phase flames which is so important in determining propellant regression rate.

Figure 4 shows a schematic diagram of the profile of an extinguished propellant sandwich surface and the postulated flame structure according to Price. The essential features of the flame structure in Fig. 4 are similar to those of the BDP model. Heat feedback from the AP flame controls the surface regression in regions far away from the binder lamina. Near the plane of symmetry the primary AP/binder flame provides the heat feedback to the surface. In the absence of a better understanding of its structure, the primary flame is postulated to consist of a kinetically limited leading edge

flame (KLLEF) and a trailing diffusion flame. The combination of the KLLEF and trailing diffusion flame can be thought of as playing the same role as the BDP primary flame.

Most of the features of the competing flame heat feedback which were accounted for in the BDP model are also exhibited in the propellant sandwiches. For example at low pressures the heat feedback from the primary flame is greater than that from the AP flame and the regression rate in the binder/AP interface region is greater than that away from the interface. At high pressures the heat feedback from the AP flame dominates and the regression rate in the AP slabs away from the lamina is greater than that near the binder region. Thus the general correctness of the BDP concepts is verified by the sandwich experiments. In addition to this validation of the general BDP concepts, however, there are some interesting new insights into the heat transfer near the surface that resulted from the sandwich experiments.

Price noticed that in the region adjacent to the binder/AP interface the AP always protruded above the binder and had a smooth texture when burning was interrupted. This was in contrast to the AP surface away from the binder lamina which was always rough. Price postulated that this observation could be explained by lateral heat conduction from the AP into the endothermic binder, as indicated in Fig. 4. The drain of energy from the AP by the binder results in a lower AP surface temperature in that region and a lower regression rate normal to the local surface. Lateral heat flow causes a significant change in the AP deflagration mechanism. In the AP region away from the binder lamina the AP deflagrates in what might be called "augmented" self-deflagration. In this region the flame heat feedback from the gas phase AP flame combines with some feedback from the primary flame to give a local maximum heat flux and maximum AP surface temperature. (That there is some contribution of heat from the primary flame is known from the fact that the underlying AP regression rate is greater than the AP self-deflagration rate.) This type of deflagration is characterized by an exothermic decomposition reaction in the condensed phase on the surface of the AP followed by further heat release in the gas phase AP flame. The exothermic surface reaction is responsible for the rough surface which remains after extinguishment. In the protruding AP region near the binder, however, the AP probably decomposes at a lower temperature, in an endothermic, dissociative sublimation process. This hypothesis was verified both experimentally and theoretically [9]. Experimental verification was obtained by substituting thermally conductive but non-reactive gold and non-conductive, non-reactive mica for the binder lamina. It was observed that the AP near the lamina still protruded and appeared smooth with gold but with mica the AP did not protrude and appeared rough like the AP far from the lamina. Theoretical verification was also obtained by performing a two-dimensional heat conduction analysis [11] which predicted the occurrence of lateral heat transfer.

One important ramification of Price's postulated lateral heat transfer mechanism is that the site of the energy release in the gas phase is probably affected by the siphoning of heat from the AP into the binder. Support for this argument is found in the change in AP decomposition mechanism observed between the AP near the binder and that far from the binder. Knowledge of the site (i.e. distribution) of the energy release is of critical importance in determining the heat feedback to the surface as demonstrated earlier by the one-dimensional heat transfer analysis. Since the lateral heat transfer mechanism alters the AP decomposition it indirectly affects $q''(x)$ and a

realistic combustion model must address these issues of multi-dimensional, coupled heat transfer.

The propellant sandwich studies of Price appear to be very useful for elucidating the multi-dimensional nature of the heat transfer and combustion in composite propellants. It is recommended that further investigations be conducted with sandwiches, making use of microthermocouples to characterize the temperature profiles near the surface. Extensive experience has been gained using microthermocouples in standard composite propellants and the results of these studies have been very useful for characterizing the surface temperature of propellants. However, this potentially useful technique has apparently not been tested in propellant sandwiches which offer a much more well defined geometry with which to work.

2.2. Aluminum Heating, Agglomeration, Ignition and Conductive Feedback

The behavior of aluminum in solid propellents has been studied extensively. Most studies have aimed at understanding the agglomeration and ignition mechanisms with the hope of being able to reduce the extent of aluminum agglomeration at the propellant surface. Another aspect of metal combustion in solid propellants which has not received as much attention is the influence of the metal behavior on the burn rate of the propellant. Aluminum can influence the burn rate through a variety of mechanisms including conductive feedback and inert heating effects.

2.2.1. *Aluminum behavior: accumulation, agglomeration and ignition*

Much of the original work on metal behavior in propellants tried to explain the mechanisms which determine the size of metal agglomerates produced at the surface of the propellant [12-14]. Early theories proposed a correlation between the agglomerate size and the amount of aluminum available in pockets between AP particles [15]. Later work by Price [16] demonstrated that the process of agglomeration involved heat transfer considerations which were not included in the original pocket models.

Price and co-workers showed that powdered aluminum undergoes a series of complicated processes in the region near the surface of a burning solid propellant [17]. These processes include heating as the particles approach the propellant surface, accumulation or concentration of particles on the surface of the propellant, formation of extended filigrees protruding into the hotter gases above the propellant surface, agglomeration of filigrees or surface accumulates into larger molten droplets and departure of the molten agglomerates from the surface, usually accompanied by ignition. Sambamurthi et al. [18] demonstrated that the size of the agglomerates seemed to be related to their proximity to a hot AP/binder flame. For an agglomerate to become hot enough to ignite and leave the propellant surface it had to grow large enough to be in close proximity to a high temperature stoichiometric AP/binder flame. Since local flame conditions depend on the AP particle size distribution and on pressure, the size distribution of agglomerates leaving the surface also depends on these variables. Generally it has been observed that as pressure increases, agglomerate size decreases, because increasing pressure causes the hot AP/binder flames to move closer to the propellant surface. However, as observed in Ref. 18, the decrease in agglomerate size with increasing pressure is distinctly non-linear. Near a critical value of pressure the agglomerate size decreases rapidly with increasing pressure. The value of the critical pressure depends on the AP particle size

distribution. A recent model developed by Kovalev attempts to incorporate most of what is currently understood about the processes affecting aluminum agglomeration to predict agglomerate size in AP composite propellants [19]. Other details of aluminum behavior near the surface have been described by Babuk and co-workers [20].

One of the key questions which has remained unanswered is what temperature is reached by aluminum before its departure from the surface of a propellant. Particularly puzzling is the fact that window bomb studies often reveal ignited aluminum droplets leaving the surface of a propellant [19] yet the decomposition temperatures of AP and binder are thought to be below typical aluminum agglomerate ignition temperatures. Certainly a lower bound for the temperature of the aluminum at the surface of the propellant would be the binder decomposition temperature (1000-1200 K), assuming negligible surface char layer formation, and an upper bound would be the melting point of aluminum oxide (2320 K) which is the upper limit for ignition of aluminum droplets. Ignition studies have established that aluminum ignition temperature is a strong function of particle size and oxidizer concentration [21-23]. For very small particles (< 10 mm) the ignition temperature decreases with increasing particle size. At intermediate particle sizes (10-20 mm) the ignition temperature goes through a minimum on the order of 1000 K and for larger particles the ignition temperature increases, approaching the oxide melting point for particles greater than 50-100 mm. The phase of the protective solid oxide film on the surface of the aluminum may also play an important role in aluminum ignition as pointed out by Gurevich [22]. Crystalline oxide is much more resistive to diffusion of oxidizer than amorphous oxide and thus crystal formation is thought to raise the ignition temperature.

2.2.2. *Aluminum effect on regression rate*

While ignition and agglomeration have been rather extensively studied, the influence of metal behavior and heat feedback on regression rate is still not well defined. Nevertheless, some general guidelines have been proposed to suggest what influence metal addition might have on propellant regression rate [17]. One of the propellant properties which metal addition affects is thermal conductivity. Metal staples and wires embedded in propellants have the effect of increasing regression rate which is usually attributed to higher propellant thermal conductivity [24]. Metal addition can also change the propellant stoichiometry, and thus regression rate, depending on what ingredients the metal replaces in the formulation. Miller [5] systematically varied propellant composition to study the effects of metal addition on regression rate. However, it is generally recognized that in those formulations the dominant mechanism for changing regression rate was replacement of a rate-controlling oxidizer size with metal. Thus it is hard to separate the effect of metal behavior on regression rate from other effects associated with changes in the AP/binder flame structure in those results.

Another factor associated with metal addition which may alter the regression rate is oxidation of the metal. Oxidation of the metal agglomerates as they reside on or near the surface of the propellant will tend to increase the propellant regression rate by transferring heat to the propellant [17, 25]. This oxidative heating can take the form of slow oxidation or fast oxidation (i.e. combustion). Slow oxidation occurs on the surface of the molten metal particles as they accumulate and agglomerate on the surface of the propellant (see Fig. 1b). As the agglomerates reach the ignition temperature, thermal runaway occurs, the reaction shifts over into a detached flame in the vapor phase surrounding the droplet, and fast oxidation takes over [19]. As this

ignition process is happening, the droplets become detached and begin to move away from the propellant surface. The slow oxidation mechanism has an inherently lower heat transfer rate associated with it than does the fast oxidation mechanism. On the other hand, the agglomerates spend a much shorter period of time in the vicinity of the propellant surface during fast oxidation than during slow oxidation. Thus both oxidative heat transfer mechanisms are potentially significant, and both mechanisms are included in referring to the conductive heat feedback from the metal to the propellant. It should be noted that this conductive heat feedback may depend on the size of agglomerates. For the same mass fraction of agglomerates, smaller agglomerates would have a greater surface area and presumably would transfer more energy to the propellant than would larger agglomerates.

It may be conjectured that the way itself in which agglomerates are carried away from the propellant surface (as observed by high speed photography) is evidence of the occurrence of oxidative heat feedback from metal agglomerates to the rest of the propellant. It is generally agreed that at low Reynolds number the drag coefficient on a burning droplet is lower than that for a non-burning droplet, for the same Reynolds number. Therefore the acceleration of an agglomerate away from the surface must be due to an increase in the local Reynolds number (i.e. velocity) of the flow around the agglomerate. Such an increase in local velocity could only be due to an increase in the pyrolysis rate of the binder in the immediate vicinity of the agglomerate, which increase much be associated with heat feedback from the metal droplet undergoing thermal runaway and ignition.

Another way aluminum can affect regression rate is through the inert heating (or heat sink) effect. Until they ignite and move out of range of the hot AP/binder flames near the propellant surface, metal agglomerates can act as a heat sink, siphoning off energy from the primary AP/binder flames which otherwise would have gone to increase the burn rate of the propellant [25-26]. The higher the ignition temperature of an agglomerate, the more severe the heat sink effect would be. Thus the heat sink effect would depend on particle size, if ignition temperature were a function of agglomerate size.

From the previous discussion it is clear that aluminum behavior and propellant regression rate must be regarded as coupled. Each is influenced by the details of the AP/binder flame structure near the surface of the propellant. It is therefore too simplistic to speak of how the regression rate affects the agglomerate size or how the agglomerate size affects the regression rate. They are both strongly coupled to more fundamental processes such as oxidizer and binder melting, decomposition and gas phase reaction.

A recent study [26-27] sought to make some progress in shedding light on this matter by looking at the correlation between agglomerate size and regression rate in a series of metalized, ammonium perchlorate (AP), composite propellants. An attempt was made to insure that other burn rate controlling variables were fixed so that differences in regression rate could be correlated to metal behavior and, in particular, agglomerate size. In order to do this propellants were formulated so as to keep the AP/binder ratio constant, thus holding constant the primary regression rate determining influence of the AP/binder flame heat feedback. Two metals, Al and Mg-Al, with similar thermophysical and thermodynamic properties, but different oxidative kinetic properties (i.e. ignition temperature) were used to help distinguish between changes in regression rate due to propellant thermal conductivity, propellant stoichiometry, metal heat feedback and metal heat sink effects. The results showed a

significant correlation between regression rate and agglomerate size (see Table 1 and Fig. 5) which indicate that smaller agglomerates are more conducive to enhanced regression rate. This effect was attributed to more efficient heat transfer from smaller agglomerates to the propellant and a smaller heat sink effect imposed on the AP/binder flames due to lower ignition temperatures for smaller agglomerates. Lower ignition temperatures for Mg-Al alloy compared with pure Al were also found to be more conducive to higher regression rate. The main conclusion and recommendation drawn from that study is still relevant and is therefore reiterated here: metal heat feedback and heat sink effects are important and need to be better understood in order to make sense out of composite propellant regression rate data. Hopefully, future and on-going studies will shed additional light in this area.

Table 1. Correlation between increase in regression rate and change in volume agglomerate size going from 1.83 to 5.27 MPa (250 to 750 psi)

Metal (%)	Percent increase in burn rate	Percent decrease in agglomerate size
none	82	not applicable
Al (10)	65	76
Al (20)	43	2
Al (30)	44	9
Mg-Al (10)	53	-9
Mg-Al (20)	54	-24
Mg-Al (30)	51	7

2.3. Radiative Heat Feedback

Radiative heat feedback has also been considered as a mechanism for enhancing propellant regression rate. For purposes of considering radiative feedback it is convenient to discuss aluminized and non-aluminized systems separately. For several reasons, these two types of systems behave quite differently. In terms of their absorptivities they are very different. Non-aluminized propellants are generally translucent at visible and near infrared wavelengths unless an opacifier or opaque catalyst has been added to the propellant. Aluminized propellants are very opaque at all wavelengths due to the aluminum powder [28]. Thermal emission in non-aluminized systems originates with molecular gas combustion products and soot [29]. In aluminum-containing propellants, burning aluminum droplets and molten, sub-micron aluminum oxide particles emit a broad continuum of high temperature radiation.

2.3.1. Steady radiative heat feedback in non-aluminized propellants

Several investigators [30-34] have studied the effect of a constant radiant heat flux (q_r) on the steady mass regression rate (m) in non-aluminized propellants. The principal conclusion of these studies is that at low to moderate flux levels (<400 W/cm²) radiant energy absorbed in-depth, below the location of the rate-controlling chemical reactions, is equivalent to an increase of $\Delta T = \frac{q_r}{mC_s}$ in the initial temperature of the propellant T_0 (the so-called equivalence principle). This conclusion has both positive and negative consequences, as pointed out by Ibiricu and Williams and Caveny, Ohlemiller and Summerfield. On the positive side, it means that in-depth,

radiation absorption effects can be relatively easily incorporated into the theoretical analyses of both steady and unsteady combustion (assuming the absorption takes place beneath the rate-controlling reaction layers). On the negative side, the equivalence principle means that no new information about the chemical or physical reaction mechanisms can be obtained from externally supplied radiant heat flux experiments that could not be obtained from regression rate temperature sensitivity studies.

The radiant flux emitted by non-aluminized propellant combustion gases and soot has been measured by Zennin, et al. using calorimeters [25]. The magnitude of the flux is typically of the order of 20 W/cm^2 which is not enough to influence the regression rate appreciably. Other studies of propellants burning in electrically heated tubes have also shown that, except for low regression rate propellants, the radiant flux present in a non-aluminized rocket is not large enough to significantly increase the regression rate. Hence, radiative feedback is generally ignored in non-aluminized systems, except for propellants with very low regression rates or in laboratory studies where an external flux is supplied to study the combustion behavior.

2.3.2. Unsteady external radiative flux in non-aluminized propellants

Many investigators have also studied the effect of a time-varying, external radiant flux incident on non-aluminized solid propellants for the purpose of understanding the unsteady combustion response of propellants [35-44]. One of the first studies in this area was conducted by Mihlfeith, Baer and Ryan [35]. They used a piezoelectric, micro-force transducer to measure the combustion recoil induced by an oscillatory incident radiant heat flux. Recently workers at the Naval Weapons Center have revived the original Mihlfeith experiment [43] while Strand at the Jet Propulsion Laboratory [42] has developed a microwave technique for measuring the instantaneous propellant response. In all of these efforts a combustion model is needed to relate the measured heat flux coupled response function to the desired pressure coupled response function. A key assumption in the combustion model has to do with the absorption of the radiant flux. It is analytically more convenient to assume that the radiant flux is absorbed uniformly at the surface of the propellant rather than deal with in-depth absorption and selective absorption by different propellant constituents. However, it is still uncertain if the assumption of uniform absorption is valid (in light of the fact that the constituents have markedly different optical properties [28, 45]). It is also uncertain if the effect of in-depth absorption is important. Although AP is known to be absorptive at $10.6 \mu\text{m}$ [45] (the CO_2 laser is commonly used as a radiation source) a recent study [44] indicates that there would still be significant in-depth absorption in AP which covers a substantial fraction of the propellant surface area. Concerns such as these need to be investigated further before the oscillatory radiant heat flux experiment can be used as a reliable tool for propellant characterization and development.

2.3.3. Radiative feedback in aluminized propellants

It is safe to say that radiative feedback in aluminized propellants is definitely more significant than that in non-aluminized propellants, due to the broadband, high temperature radiant emission from burning aluminum droplets and aluminum oxide particles. Whether or not the radiative feedback is large enough relative to the conductive feedback to influence the regression rate, however, is still not certain. In any event, radiative feedback is still usually ignored in aluminized propellant

combustion studies. One reason for the neglect of radiation even in aluminized systems is that studies comparing regression rates of aluminized and non-aluminized propellants have been inconclusive. Sometimes aluminum enhances the regression rate and sometimes the opposite result is obtained. This behavior at first is puzzling in light of evidence that external radiation at flux levels typical of that emitted by burning aluminum droplets (at least 100 W/cm^2) increases the regression rate of non-metalized propellants significantly [32, 33].

The question of whether or not radiative heat feedback is important is complicated by the fact that, as mentioned earlier, addition of aluminum changes several properties of the propellant and flame simultaneously (in addition to increasing the radiant heat flux). The thermal conductivity of the propellant is increased by adding aluminum, which, like the radiant flux, would also tend to increase the regression rate. However, addition of aluminum also introduces a heat sink effect which tends to decrease the regression rate [27]. Thus conclusions drawn from regression rate studies about the importance of radiative feedback are subject to considerable error.

A more satisfactory method of judging the importance of radiative feedback, rather than inference from regression rate studies, is to measure the radiative flux directly. Zennin et al. [25] measured radiative heat flux and conductive heat flux using microthermocouples and calorimeters embedded in stoichiometric, AP/polyformaldehyde mixtures and concluded that radiative feedback played a minor role in determining regression rate relative to that of conductive feedback from oxidizing aluminum particles. The radiant heat flux was measured as 80 to 100 W/cm^2 . Felton and Hitchcock [46] measured radiative feedback in aluminized propellants using light pipes and obtained total radiant flux levels on the same order as those of Zennin, et al., 80 to 100 W/cm^2 at 2 to 5 MPa. In both of these studies, however, there is some question as to whether smoke and aluminum agglomerates may have reduced the measured signal.

Analytical studies have also been performed to predict the radiant flux back to the surface of an aluminized propellant [47] and its effect on aluminum agglomeration via in-depth absorption [48]. From these studies it is estimated that the radiant flux incident on the propellant surface is between 300 and 400 W/cm^2 which is a factor of four larger than reported measured values. However, it should be noted that the emissive properties of burning aluminum droplets play a strong role in such predictions and these properties are not very well characterized, though some attempts have been made [49].

Another important property which influences the radiative feedback is the propellant absorptivity. The absorptivity of metalized propellants has been estimated in some cases [50] to be negligibly small based on the fact that metals have intrinsically low bulk absorptivities. However, this view is too simplistic and overlooks the phenomenon of multiple scattering. More realistic estimates based on the solution of the radiative transport with multiple scattering in the propellant [28, 48] indicate that the propellant total absorptivity is at least 0.4. Hemispherical, spectral reflectance measurements [25, 51] give propellant spectral absorptivities of 0.8 in the visible and near infrared for aluminized propellants. Binder optical properties can also influence the absorptivity, particularly in the infrared region. Measurements of transmissivity of composite propellants by Mihlfeith [36] indicate that binder absorption coefficients are temperature dependent and that certain binders have positive temperature coefficients while others have negative temperature coefficients. Observations of the influence of external CO_2 laser radiation on propellant regression rate reported in a recent paper

by Yin [34] also seem to confirm the influence of temperature dependent (both positive and negative) binder absorption coefficients, although that interpretation was not given in the paper.

To summarize the influence of radiative feedback on propellant regression rate it must be said that it is still uncertain. Further careful measurements are needed. In undertaking such measurements it is important to effectively deal with the problem of obscuration of the radiation detector by smoke, soot and aluminum agglomerates. If the radiation signal is measured when the detector or collection optics are located at the bottom of a cavity (such as in [25] and [46]) there is the uncertainty of obscuration by particles which is very difficult to account for unless the propellant is extinguished and examined. This precaution has been taken in a current study [51] using optical fibers embedded in the propellant and initial results indicate radiant fluxes of 350 W/cm² with 20% aluminum loading at 3.5 MPa which is more than double the previously reported value of Zennin at 4.5 MPa of 160 W/cm².

2.4. Convective Heat Feedback

Convective effects also play a role in altering the heat feedback to the propellant surface. There is always a mean component of velocity tangent to the propellant surface which is usually small near the head end of the motor but can become rather large (hundreds of meter per second) near the aft end of the motor (Fig. 1a). This crossflow usually results in an increase in the heat feedback to the propellant which causes an increase in the regression rate. The enhancement of the regression rate by the mean flow tangent to the surface of the propellant is known as erosive burning and is a significant factor which must be dealt with in systems with high L/D ratios. Usually the effect of flow tangent to the propellant is to increase the heat feedback and thereby increase the propellant regression rate as shown in Fig. 6a. However, with certain propellants, negative erosive burning (a reduction in regression rate) has also been observed at low crossflow velocities, as indicated by Fig. 6b.

The mechanism of enhanced regression rate due to crossflow is associated with an increase in heat feedback due to the mean convective crossflow, much like a boundary layer flow. Various levels of sophistication have been used to describe this mechanism ranging from the simple analysis of Lenoir and Robillard which uses the Chilton-Colburn correlation with a correction for transpiration [52] to the turbulent, chemically reacting boundary layer analyses of Beddini and Razdan [53, 54]. Because of its simplicity and widespread use the Lenoir-Robillard result is repeated here. The regression rate is given by the following.

$$r = ap^n + \alpha \frac{G^{0.8}}{L^{0.2}} \exp\left(-\frac{53m}{G}\right) \quad (6)$$

$$\alpha = \frac{0.0288 C_{pg} \mu_g^{0.2} Pr^{-2/3}}{\rho_s C_s} \left(\frac{T_f - T_s}{T_s - T_o} \right) \quad (7)$$

The first term in Eq. (6) is the normal pressure dependent regression rate law and the second term accounts for the erosive burning effect. In Eq. (6) G is the mass flux of the crossflow and L is the port length of the motor. King [55] took a slightly different approach to modeling erosive burning effects. King's model focussed on the BDP model and tried to simulate the way in which a convective crossflow might distort the

AP/binder flames and push them closer to the propellant surface. The net result of pushing the primary gas flames closer to the surface is to increase the conductive heat feedback and regression rate of the propellant.

While convective heat transfer analyses, such as those just mentioned, appear to be adequate for describing positive erosive burning, the observation of negative erosive burning (Fig. 6b) indicates that the actual mechanism of erosive burning may be more complicated in some situations. In negative erosive burning, an increase in crossflow velocity is accompanied by a decrease in regression rate. One explanation which has been offered is that negative erosive burning is caused by competing mass transfer and convective heat transfer effects [56]. At low crossflow velocities, it is argued, a decrease in heat feedback associated with mass blowing causes a decrease in regression rate, while at high velocities convective heat transfer dominates. This argument sounds reasonable because of the familiar concept of reduced heat transfer that is associated with mass blowing in a convective boundary layer. However, it must be remembered that the reduction in heat transfer which occurs in boundary layer flows occurs between a boundary layer flow without blowing and a similar boundary layer flow with blowing. There is no reason to expect a decrease in heat transfer due to blowing when crossflow is added to situation where blowing already existed. Only an increase in heat transfer would be expected. A more plausible explanation for negative erosive burning is that partial coverage of AP surfaces by melted binder flowing under the effect of shear stresses is responsible for reduced regression rate. This argument would explain why some propellants (perhaps those with high melting binders) exhibit negative erosive burning and others do not. An experimental effort should be conducted using extinguishment of propellants burning under crossflow conditions to test this hypothesis. By examining the propellant surface after extinguishment it should be possible to determine if binder melting and flowing plays a role in erosive burning. Much more could be said on the topic of erosive burning but to keep the topic of convective feedback in balance with the rest of this article the reader is referred to a recent review on erosive burning by Razdan and Kuo [57].

Often there is also an unsteady, oscillatory component of velocity tangent to the propellant surface arising from longitudinal acoustic flow oscillations. The enhancement in regression rate which accompanies the oscillatory tangential flow is referred to as velocity coupling (Ed Price, the originator of the term "velocity coupling" has suggested that "convective coupling" might be a more accurate description of the phenomenon). Velocity coupling is an abnormal situation which is to be avoided. The topic of velocity coupling involves interactions between the mean and unsteady flowfield and is complicated by distinctly non-linear behavior. A recent workshop was held on the topic of velocity coupling and can be consulted for more details [58-59].

3. HEAT AND MASS TRANSFER IN ALUMINUM DROPLET COMBUSTION

Aluminum agglomerates formed at the surface of an aluminized solid propellant do not burn to completion in the vicinity of the surface of the propellant, like the rest of the propellant constituents, but burn in a distributed fashion away from the surface. Whether or not the droplets burn completely before exiting the nozzle depends on their initial size, their burning rate, and their residence time in the motor. Because of the negative performance consequences of exhausting unburned aluminum from the nozzle, the complete combustion of aluminum is of great interest. Hence the

combustion rate of aluminum particles, which is very dependent on heat and mass transfer rates, is of considerable interest in aluminized propulsion systems.

The subject of heat and mass transfer in metal combustion (particularly aluminum combustion) was studied extensively twenty to thirty years ago [60-81]. Following that very prolific period there was a period of relative inactivity (at least as far as the open literature is concerned) as metals found wide application in propulsion systems and explosives, while fundamental interest waned [82-84]. In the past few years, however, fundamental interest in metal combustion has been revitalized both for propulsion and explosives applications [85-90] as well as other applications such as materials synthesis [91-93].

3.1. General Features of Aluminum Combustion

A brief review of the essential features of aluminum combustion is given, with an emphasis on the heat and mass transfer aspects of the problem. A model of a burning aluminum droplet is shown in Fig. 7. There are two distinct reaction zones, an inner zone and an outer zone. These two zones are distinguished from each other by luminosity (continuum emission), temperature, and sub-micron Al_2O_3 particle population. The inner zone is relatively non-luminous (in continuum emission), achieves the highest temperature in the system (T_f) and is rather devoid of particles (at least particles large enough to emit significant continuum radiation). The outer zone, on the other hand, is highly luminous, somewhat cooler than the inner zone, and is populated by particles which are sufficient in size and number density to emit a strong continuum of radiation. Heat release occurs throughout the inner zone, primarily due to condensative recombination of sub-oxide vapors to form $\text{Al}_2\text{O}_3(\text{liq})$. The condensed phase $\text{Al}_2\text{O}_3(\text{liq})$ particles thus formed in the inner zone are rapidly transported both outward away from the droplet (by bulk convection and thermophoresis) forming a luminous trail, and inward toward the droplet (by thermophoresis) where they are deposited on the droplet surface and often coalesce into a large cap (see Fig. 7). In the inner flame zone the combustion-generated, sub-micron particles are too small (and possibly too few in number density) to emit a significant continuum of radiation. In the outer zone, where conditions are more favorable for particle growth and the bulk velocity component away from the droplet is much lower the Al_2O_3 smoke particles achieve sufficient size and number density to emit a substantial continuum of thermal radiation. While the above features are based on observations from many studies, it should be mentioned that there is disagreement over various aspects of this description. For example, the continuum radiation in the flame zone has also been attributed to chemiluminescence [81] and plausible reaction mechanisms have been set forth.

3.2. Radiative Heat Transfer Considerations in Aluminum Droplet Combustion

Glassman, who did much of the pioneering work in metal combustion, suggested that radiative transport plays an important role in metal combustion [60]. Brzustowski and Glassman even went so far as to suggest that Glassman's original vapor phase burning criterion for metal combustion needed to be modified to include the effect of radiative heat loss [61]. The original vapor phase combustion criterion was that if the boiling point of the metal oxide was greater than that of the metal, combustion would occur in the vapor phase. Otherwise surface combustion would occur. According to this criterion (and thermodynamic data available at that time), however, it was predicted that Ti and Zr should burn in the vapor phase, which they do not. Hence,

Brzustowski and Glassman suggested that the boiling point criterion was only a necessary but not sufficient condition, subject to radiant heat loss considerations. It should be noted that more recent, and therefore presumably more accurate, estimates of TiO_2 and ZrO_2 boiling points were found to be less than the corresponding metal boiling points [94] which re-validates the original vapor phase criterion. Nevertheless, the issue of the influence of radiative transfer in aluminum droplet combustion has never been adequately addressed.

Following Glassman's original suggestion about the importance of radiative transfer, several studies tried to include the effects of radiation in combustion models. Kuehl [64] included the term $\epsilon_{ox}\epsilon_s\sigma(T_f^4-T_s^4)$ in the droplet energy equation to represent the net radiative flux to the droplet. Micheli and Schmidt [83] used the term,

$$\frac{\sigma(T_o^4-T_s^4)}{\frac{1}{\epsilon_s} + \left(\frac{d_s}{d_f}\right)^2 \left(\frac{1}{\epsilon_{ox}} - 1\right)}$$

which correctly accounts for curvature and multiple reflection effects between the droplet and flame, but still assumes the flame is opaque. Both of these studies included the term $\epsilon_{ox}\sigma(T_f^4-T_\infty^4)$ to represent the net radiative flux from the droplet to the surroundings. Neither study mentions the values of ϵ_{ox} and ϵ_s that were assumed. A serious problem with the radiative representations of these models is that they treat the detached flame as an opaque, non-transmitting surface. There is no allowance made for emission loss from the droplet surface to the surroundings through the flame envelope. Furthermore, the contribution to the emission loss from the flame which is reflected from the droplet is not included.

A more realistic model of the radiative transfer in a burning aluminum droplet is shown in Fig. 7 [49]. Three important components of radiant emission are designated in Fig. 7. Component 1 is the direct emission from the luminous detached flame envelope to the surroundings. Component 2 is the flame emission which is reflected by the droplet and transmitted through the flame. Component 3 is the emission by the droplet surface which is transmitted through the flame envelope. Based on this more rigorous representation it can be seen that the optical thickness of the envelope t_e becomes a very important parameter in determining the radiative properties of burning aluminum droplets. While it is virtually impossible to predict the optical thickness of the flame envelope from first principles, it has been suggested that the envelope is probably optically thin [49]. This conclusion is drawn from comparisons between theoretical predictions and measurements of spectral intensity emitted by burning aluminum droplets.

3.3. Convective and Radiative Heat Transfer Effects on Droplet Burning Rate

In most metal combustion applications the most important consideration is the combustion rate or droplet burnout time. The droplet combustion rate has been widely estimated using Hermsen's correlation [95-96].

$$\frac{d_s}{d_{so}} = \left(1 - \frac{kt}{d_{so}^{1.8}}\right)^{1/1.8} \quad (8)$$

$$k = 8.3144 \times 10^{-5} R_k A_k^{0.9} p(\text{psi})^{0.27} (\text{cm}^{1.8}/\text{sec}) \quad (9)$$

$$A_k = \sum_i X_i, \quad i = \text{H}_2\text{O}, \text{CO}_2, \text{OH}, \text{O}, \text{O}_2 \quad (10)$$

$$R_k = \begin{cases} 1, & \text{laboratory} \\ 2.7, & \text{motor} \end{cases} \quad (11)$$

Eq. (8) gives the droplet diameter as a function of time in the form of a classical "d²" law where the diffusion-limited exponent of two has been modified to 1.8. The influence of ambient oxidizer concentration is included in the factor A_k.

Two important effects which can influence the burning rate of liquid droplets (metal or otherwise) are convective heat transfer and radiative transfer with the ambient environment. Burning rate data obtained from motor firings and from laboratory tests indicate that combustion rates are substantially higher in motors than in the laboratory and this difference has been attributed to the difference in convective and radiative environments. In Hermsen's correlation the influence of convective and radiative heat transfer are lumped together and represented by the adjustable constant R_k. A value of R_k=1 corresponds to burning rate data which have been obtained in a laboratory environment with a single burning droplet where there is no convective effect (other than natural convection) and the radiative environment is a blackbody at room temperature. A factor of R_k=2.7 has been recommended for motor environments.

In an effort to improve on Hermsen's correlation and to separate the effects of convective and radiative heat transfer, a comparative study was done between Hermsen's correlation and the classical theory of diffusion-limited droplet combustion including convective heat and mass transfer [90]. Stoichiometric, single-step reaction between aluminum and water vapor (the primary oxidizer in most solid propellant combustion gases) was assumed. A typical result of that comparison is shown in Fig. 8. Figure 8 shows four cases of droplet diameter as a function of time. Two cases represent the situation with no convective heat transfer (V_{rel}=0 in the diffusion model and R_k=1 in Hermsen's correlation). The other two cases represent the situation with convective heat transfer (V_{rel}=1 m/s in the diffusion model and R_k=2.7 in Hermsen's correlation). A velocity of 1 m/s is a reasonable estimate of the average relative velocity between burning aluminum droplets and the surrounding propellant gases at typical rocket pressures. As can be seen in Fig. 8, a slight increase in droplet burning rate (decrease in combustion time) due to convective heat transfer is predicted by the diffusion model. At the same time, Hermsen's correlation predicts a much larger increase in burning rate. Assuming the increase in burning rate predicted by the diffusion model corresponds to the convective heat transfer effect, then the much larger increase in burning rate predicted by Hermsen's correlation would suggest that radiation is the dominant heat transfer mechanism acting to increase the droplet combustion rate in motors.

The situation just described is the reverse of the "usual" situation encountered with hydrocarbon droplets, where convective effects are much more important than radiative effects. However, the reversal in roles of radiative and convective heat transfer is quite understandable. In hydrocarbon droplet combustion, the droplets are typically injected into the combustor at high velocities (hundreds of meters per second). Thus relative Reynolds numbers are high and convective effects are important in hydrocarbon combustion. In solid propellant metal droplet combustion

relative velocities are low, thus convective heat transfer effects are small. However the oxide smoke combustion product of metals as well as the burning droplets themselves are more luminous and hotter than their hydrocarbon counterparts. Thus radiative transfer plays a more important role than convection in typical metal combustion applications.

Based on the foregoing discussion, some suggestions can be made of ways in which future studies might contribute to the understanding of heat transfer effects in aluminum droplet combustion: (1) include a more realistic model of radiative transfer in detailed droplet combustion models, (2) develop a simple engineering combustion correlation which delineates convective and radiative effects, and (3) do experimental studies to characterize the radiative properties of burning droplets, such as envelope optical thickness and temperature.

4. INTERNAL INSULATOR HEAT TRANSFER

Near the head end of many rocket motors and in other regions there are exposed surfaces where propellant does not protect the case from hot combustion products (Fig. 1a). In these regions, radiation, convection and particle impingement heat transfer combine to impose a significant heat load from which the case must be insulated. Typically an ablative, rubber insulation is used as thermal protection. Since ablative insulation represents inert, dead weight and therefore lost payload, optimal insulation design is essential to competitive and reliable performance.

4.1. Heat Transfer Mechanisms and Relative Importance

The three principle mechanisms of heat transfer to internal insulating surfaces are gas convection, radiation and particle impingement. Gas convection is usually considered to be of importance as a heat transfer mechanism near the nozzle throat where the combination of high velocities and high temperatures results in maximum convective heat transfer. Inside the motor, gas temperatures are high (3600 K) but velocities are usually low enough (<1 m/s near head end) that convective heat transfer is not a serious problem. At the exit of the supersonic nozzle velocities reach a maximum but the gas temperature is reduced such that convective heat transfer is also reduced. Thus convective heat transfer is of primary concern in the nozzle throat region. However, it should be pointed out that the gas flowfield plays a significant role in heat transfer to forward dome internal insulation in the way that it modifies the radiative heat transfer. The gas flow has a significant effect on the aluminum particle trajectories and on the optical thickness of the thermal boundary layer and thus can strongly influence the heat transfer to the head end.

Radiative heat transfer is usually considered to be of importance inside the motor, especially in aluminized propellant systems [29]. The primary source of thermal radiation is molten aluminum oxide Al_2O_3 smoke particles produced by distributed combustion of aluminum. Pearce [97] modeled radiative heat transfer in aluminized solid rockets using an isothermal cylinder and concluded that radiation was of minimal importance at the nozzle throat (relative to convection) but of major importance at the nozzle entrance and inside the motor. Near the head end, where velocities are low, radiation is the dominant mechanism of heat transfer to forward dome internal insulation surfaces.

Particle impingement is also a potentially significant mechanism of heat transfer to insulation surfaces which has not been extensively studied. Impingement heat transfer is the result of burning aluminum droplets which are convected by recirculating flow

patterns near the head end. Because of the very efficient heat transfer between burning, molten metals and any surface they impact, particle impingement is a very important heat transfer mechanism. The effects of impinging, molten, burning metal particles are often evidenced in catastrophic ways. For example, severe damage to forward motor enclosures has been observed in high pressure, unstable combustion of highly aluminized propellants which is attributable to impingement heat transfer [98]. In another impressive demonstration of the tremendous heat transfer capacity of burning metals, Grosse and Conway [99] reported using a premixed flame of aluminum and pure oxygen to cut a three inch (7.5 cm) hole in a thirty inch (75 cm) thick concrete slab at a rate of more than one inch (2.5 cm) per minute.

4.2. Buoyancy Induced Recirculating Flow

Buoyancy induced recirculation has been suggested as a possible mechanism for enhancing heat transfer to forward dome internal insulators [100]. Buoyancy induced recirculation is driven by acceleration of the flight vehicle. In flight, the acceleration vector is aligned with the axis of the motor which imposes a body force on fluid particles in the direction of the nozzle. Acceleration in solid rockets may range from 3 g's (space shuttle solid rocket boosters) to tens and hundreds of g's (missile systems). In the presence of acceleration body forces, colder gas near the head end insulator is unstable relative to the warmer gas in the chamber interior. Thus the potential exists for a recirculating flow pattern to be established near the head end, as shown in Fig. 9. Purcell and Daines [100] have simulated the non-reacting, non-aluminized flowfield near the head end of a typical motor and concluded that buoyancy could play a significant role in determining the head end flow pattern.

The buoyancy induced recirculating flow has a primary stagnation point (or locus of points) and a secondary stagnation point as shown in Fig. 9. Since the primary stagnation point is the region of greatest heat transfer, this region is of particular interest. A study which considered the local stagnation flow in the primary stagnation region, including radiation (see Fig. 10), indicated the following interesting features of the flow: (1) for typical aluminized propellant compositions the thermal boundary layer is optically thick with aluminum oxide smoke, (2) radiation is the dominant mode of heat transfer (assuming negligible particle impingement), (3) the flow behaves like that of a low Prandtl number fluid ($\delta \ll \delta_T$ even though fluid Pr is of order one) due to the strong radiation influence, and (4) the important dimensionless parameters which determine dimensionless heat flux are wall-to-bulk fluid temperature ratio T_0/T_∞ , conduction-radiation parameter N_o , boundary layer optical thickness t_δ , wall emissivity ϵ_w , and fluid Prandtl number Pr (see Fig. 11).

4.3. Flowfield Simulation with Distributed Aluminum Combustion

As might be expected, multi-dimensional flowfield simulation which includes distributed aluminum combustion is not as advanced as non-reacting flow simulation. Studies which include distributed aluminum combustion typically do not include buoyancy effects [101-102], for example, and often utilize the assumption that complete combustion of aluminum occurs at the propellant surface [103]. The inclusion of aluminum introduces the added complexity of multi-phase flow as well as chemical reaction. In order to develop a reliable tool for predicting aluminum particle impingement, it will be necessary to include the effects of buoyancy and distributed aluminum combustion in a multi-dimensional, viscous, turbulent internal flowfield code. A fully coupled, turbulent, multi-phase, multi-dimensional flow simulation with

chemical equilibrium calculated at each grid point is computationally prohibitive and probably unwarranted. A reasonable first approximation is to assume a one-step, global reaction in which the restricted equilibrium composition consisting of AP/binder products and aluminum are converted to the final equilibrium state products [102]. Salita and Levine have given recent workshop summary reports on the status of internal flow code development [104-105].

Recommendations for future development in this area are as follows. Better models for predicting particle impingement heat transfer are needed. There is also a need for a better capability to predict aluminum oxide particle flowfields and concentrations. To accomplish these goals, a multi-dimensional, body-fitted flowfield model should be developed which includes distributed aluminum combustion, buoyancy, and radiative transfer.

5. PLUME RADIATION

The final area of heat transfer interest to be considered here is the aft end of the motor (Fig. 1a) where radiative heating of aft end equipment by the exhaust plume is of concern. During the development of the Saturn launch vehicles, which began in the late 1950's, concerns over radiative base heating became the driving force behind much of the progress made in the understanding of gas radiation heat transfer [106]. Nowadays, with more widespread use of solid rockets and aluminum fuel, plume radiation is an even bigger concern because of the intense continuum radiation emitted by condensed aluminum oxide particles [107]. Hence, this discussion will focus on radiation by aluminum oxide particles.

Initial calculations of aluminized plume radiosity used Mie theory to predict the emission by aluminum oxide laden plumes. Optical constants based on pure Al_2O_3 (sapphire) were used and particle size distribution was assumed. Most of these predictions resulted in estimates which grossly underpredicted the measured values of plume radiosity. In hindsight it can be seen that there were two reasons for the disagreement: (1) the absorption index was severely underestimated and (2) the aluminum oxide particle size distribution was not well known. Unfortunately the predicted radiosity is very sensitive to these two sets of data which, even still, are known with very little confidence. Thus much research in plume radiation is focussing on understanding the physics and chemistry of the processes which determine the optical constant and size distribution of aluminum oxide, and trying to measure these properties with better accuracy.

5.1. Aluminum Oxide Particle Size Distribution

Al_2O_3 particle size distribution in aluminized plumes and motors has been studied extensively over the years [108]. It is generally recognized that the size distribution is bi-modal due to the two competing mechanisms of aluminum oxidation: (1) detached "vapor-phase" oxidation which produces submicron smoke particles (0.1 to 2 μm) and (2) surface accumulation which produces large residual caps (10 to 100 μm). However, several mechanisms act which change the size distribution, including:

- (1) distributed combustion of aluminum
- (2) growth by collision due to velocity slip induced coalescence
- (3) break-up of large droplets due to viscous drag forces
- (4) deposition and shedding of molten Al_2O_3 in nozzle
- (5) density change due to solidification and melting
- (6) condensation of AlCl_3

Efforts to measure particle size have proceeded along two different lines of approach. One approach is to physically capture particles and then measure the size distribution. The other is to use non-intrusive optical techniques. These two techniques and their relative merits are discussed in the following sections.

5.1.1. Particle capturing techniques

Most of the early experimental studies of aluminum oxide particle size were based on capturing particles at the exit of the nozzle and measuring the size from the captured samples. A critical review of the work up to 1980 has been given by Hermsen [109]. This review forms the basis for particle size prediction used in the industry standard SPP code [96]. It is based on empirical correlation of particle size data with motor and propellant variables. The most important variables for correlating the size data are taken to be chamber pressure, chamber aluminum oxide concentration, nozzle throat diameter, and residence time. Correlations of this type are usually given in terms of d_{43} which has shown to be the appropriate moment for predicting two-phase flow loss.

$$d_{nm} = \left[\frac{\int_0^{\infty} d^n N(d) d(d)}{\int_0^{\infty} d^m N(d) d(d)} \right]^{1/(n-m)} \quad (12)$$

In Eq. (12) $N(d)$ is the number density distribution as a function of diameter d . Typically, the value of d_{43} reported in [109] ranges between 2 and 10 μm .

Experimental determination of the size distribution has been discussed in detail by Kraeutle [110]. By breaking the distribution up into sub-fractions, analyzing the sub-fractions using appropriate microscopy (i.e. optical or electron), and recombining the sub-fractions, Kraeutle demonstrated that the size distribution is bi-modal with the transition between lobes occurring between 2 and 20 μm . That study pointed out that although microscopic analysis could be done accurately, it was very tedious. For example, for a combustion product sample obtained in a T-burner, analysis showed that by number 98 percent of the particles were below 1 μm , while by mass only 15 percent were smaller than 1 μm . That is, 10^3 particles would have to be counted to count one 2.5 μm particle and 3×10^8 particles would have to be counted to count one 40 μm particle. This points out the tedious nature of measuring size distribution and why often the form of the size distribution is assumed (e.g. log-normal, Rosin-Rammler, Gamma function, etc.) and attention is focussed on determining just the appropriate averages (e.g. d_{32} , d_{43} , d_{63} , etc.). Unfortunately, when seven different commercial, automated size analyses were compared with the "exact" distribution only one came close, illustrating the caution with which such techniques should be viewed [110].

Another study of particle size using a quench collection bomb was reported by Salita [111]. Burning particles of aluminum, aluminum oxide caps and aluminum oxide smoke particles were collected in a buffered isopropyl alcohol bath. A mass balance was conducted to account for all of the original aluminum in the propellant. Lost mass was attributed to aluminum oxide smoke which is difficult to capture in a quench bath. A bimodal size distribution was obtained with the small mode attributed to aluminum oxide smoke particles and the large mode to conglomerates of aluminum

and aluminum oxide. The size and mass fraction of the large mode varied depending on the distance of the quench bath from the propellant and pressure. However, the small mode (smoke) had a mass mean diameter of 1.5 μm ($d_{32}=1 \mu\text{m}$) which was independent of pressure and collection distance. The actual particle sizing was done in that study with a Microtrac optical sizing system.

5.1.2. Optical techniques

Attention has also been given to in-situ optical techniques for measuring particle size. A review of the various optical techniques for measuring particle size in propellant combustion systems has been given recently by Koo [112]. Optical techniques have the advantage that they are generally non-intrusive. However, usually the form of the size distribution must be assumed and the optical constants must usually be known. In addition, most of the techniques reported (except multi-wavelength extinction) are limited to optically thin, single-scattering media. Many techniques are limited to measuring only a certain portion of the size distribution. For example, diffraction based techniques can usually only measure particles above 2 or 3 μm such that $\pi d/\lambda > 5$. Many different techniques have been reported, including extinction, emission and scattering measurements.

One of the first to apply optical techniques to rocket particle size measurements was Dobbins [113]. He used a two-wavelength extinction technique (0.365 and 1.01 μm) and obtained d_{32} values of 0.4 to 0.6 μm which was significantly smaller than sizes indicated by particle collection techniques. In a follow-on study to try to explain the discrepancy, Dobbins and Strand [114] compared results from particle collection and optical extinction measurements (three wavelengths), assuming various mono-modal size distributions. Again, the d_{32} sizes obtained by the optical technique were significantly smaller than the collected sizes (less than 1 μm for optical compared with 1 to 3 μm for collected samples). They also noted that the optically determined sizes were internally inconsistent in that the magnitude of d_{32} differed by a factor of two depending on which combination of wavelengths was used. They concluded that self-consistent optical results could only be obtained if a bi-modal size distribution was assumed; however, such an attempt was not reported.

Powell et al. [115] developed an optical technique for determining unknown size d_{32} , refractive index n , and volume fraction f_v , simultaneously from forward scattering and extinction measurements. Drawbacks of this technique which limit its usefulness for aluminized propellant flames and plumes are the assumption of diffraction-dominated scattering ($\pi d/\lambda > 5$), the assumption of non-absorbing particles, the assumption of single scattering and the assumption of a mono-modal size distribution.

Konopka et al. [116] used in-situ, multi-wavelength extinction, SEM photographic analysis and a Coulter counter to determine size distribution for samples from two rocket exhausts. They presented both log-normal and Gamma function correlations for size distribution. The agreement between the various methods was quite reasonable, with a d_{32} value of 1.15 μm and most probable size of $d_{mp}=0.153 \mu\text{m}$ for the Gamma function distribution (rocket 2).

Recently efforts have been reported [117] to measure particle size both inside a small motor as well as outside by using purged windows on the motor. Two techniques have been used : (1) diffraction scattering (similar to the Malvern system using a linear array detector instead of a ring array) and (2) holography. While this work represents an important step in trying to look inside the motor, both of these techniques require optically thin, single scattering conditions. This limits the

application to aluminum loadings of about two percent or less. Also, the diffraction based Malvern type of approach is again limited to larger particles ($> 3 \mu\text{m}$ in [117]) so that only a portion of the size distribution can be characterized, and the sub-micron smoke particles are missed.

A two-dimensional, digital imaging technique has also been reported [118]. This technique offers the benefit of an instantaneous and spatially resolved measurement as opposed to a time and line-of-sight averaged measurement obtained by the previously discussed optical methods. However, this method (which uses 90 degree scattered light) is also limited to single scattering and particles larger than about $10 \mu\text{m}$.

A recent design study [119] has also been reported which examines the advantages and disadvantages of various optical techniques (e.g. emission, extinction, and scattering) for determining particle size and optical constants over various ranges. The main conclusion of that study is that extinction and emission measurements (using a shock tube for heating) are the most generally suitable. They also conclude that scattering measurements are difficult and therefore unsuitable due to the highly structured angular dependence of scattered intensity for moderate to large particle size parameters ($\pi d/\lambda$). It should be pointed out that this conclusion is basically true for single scattering, monodisperse systems (although a broadband laser can be used to overcome this difficulty [118]). However, polydispersity and multiple scattering quickly smooth out this structure. Thus, the only remaining valid objections to scattering measurements from [119] are the need to have many lasers to cover the spectrum (which is not a serious fundamental problem) and the difficulty of calibrating for absolute scattered intensity.

In an effort to overcome some of the difficulties of the previous studies, an experimental investigation was conducted using two wavelength, extinction and absolute scattering measurements (forward and backward) in optically intermediate propellant flames [120]. Multiple scattering was included in the data reduction by incorporating an inverse solution of the radiative transfer equation. Optical constants were not assumed but were simultaneously measured. A monomodal Gamma function size distribution was assumed. The resulting optical mean size was $d_{32}=1 \mu\text{m}$, in agreement with the reported size of the smoke fraction from [111].

From the work on particle size analysis done to date several observations can be made.

- (1) Particle collection techniques are subject to questions as to what changes may have occurred in size during collection and separation.
- (2) Particle collection inside a motor is not feasible at present.
- (3) The physical separation and size analysis which must follow particle collection techniques are tedious but accurate.
- (4) Optical techniques are subject to questions of the assumed size distribution.
- (5) Optical measurements often indicate sizes smaller than those from collection techniques.
- (6) Optical techniques are useful for obtaining mean sizes but not the full size distribution.

5.1.3. Evolution of particle size distribution

Based on the results of these past investigations a scenario for the evolution of aluminum oxide particle size distribution is presented. Figure 12 shows the bimodal aluminum oxide particle size distribution which exists inside the motor after aluminum

combustion has reached near completion. The submicron smoke phase from the detached flame envelopes constitutes 85 to 90 percent (by mass) of the oxide product. The surface residual caps constitute the remaining 10 to 15 percent. As the flow proceeds through the motor and especially through the nozzle the smoke fraction grows due to velocity slip induced coalescence (smaller, faster particles colliding with larger, slower particles). This growth is depicted by an arrow in Fig. 12 indicating a shift of the smoke fraction to larger sizes. At the same time the small particles are coalescing with the larger particles, the large fraction is breaking up due to shear forces in the nozzle. At Weber numbers ranging from 4 to 8 [121] viscous drag forces overcome surface tension forces holding the droplet together and the droplet breaks up. This analysis indicates that particles larger than about 20 μm cannot survive passage through the nozzle. Thus there is a shift in the large mode to smaller sizes. Since coalescence and breakup mechanisms depend on residence time and velocity lag in the nozzle, the size distribution in the plume will vary considerably from motor to motor. Further systematic study is needed before particle sizes can be predicted with enough confidence for accurate plume radiation simulation.

5.2. Aluminum Oxide Optical Constants

Initial attempts to predict plume emission from first principles gave results which underestimated plume radiosity. It is now apparent that this was due to a lack of information about the particle size distribution and optical constants [122-124]. It was soon recognized that the absorption index of molten aluminum oxide must be much bigger than that of solid aluminum oxide [122] and that impurities such as carbon [125] and aluminum [125-126] might be playing a significant role. Other factors which have been mentioned as influencing the optical constants are supercooling, crystalline phase and lately the possible influence of condensation of aluminum trichloride on the outside of aluminum oxide particles has come to light as a possible mechanism for changing optical properties [127].

5.2.1. Solid phase

The optical constants of Al_2O_3 in the pure solid state have been relatively well established by many previous investigations[116,128-142]. Figures 13 and 14 show that at room temperature, pure Al_2O_3 is essentially non-absorbing between 0.5 μm and 5 μm . Below 0.2 μm and above 6 μm electronic transitions and lattice vibrations, respectively, result in photon absorption. The refractive index, n_s , varies between 1.8 and 1.6 [128], and the absorption index, k_s , varies between 10^{-7} and 10^{-5} , depending on wavelength [129]. Measurements at higher temperatures [130] indicate that n_s increases as temperature increases with a nearly constant coefficient ($2.9 \times 10^{-5} \text{ K}^{-1}$) [131] as shown in Fig. 13. The absorption index also increases with increasing temperature [116,130,139] as shown in Fig. 14. However, the data of Konopka, et.al [116], which were taken from measurements using actual rocket particles heated in a shock tube, as compared with Gryvnak's data for pure Al_2O_3 , indicate that composition is an important factor in determining the absorption index as well as temperature.

Polycrystalline structure and porosity also play a potentially significant role in determining aluminum oxide optical properties. Lee and Kingery [138] studied the transmission of both single crystal (sapphire) and sintered ceramic aluminum oxide samples. The ceramic samples were porous and polycrystalline. Their experimental results and theoretical interpretations showed that the effects of porosity (pore size and volume fraction) are much stronger than the effects of polycrystallinity (grain size).

Their results pointed out that while both pores and grain boundaries increase photon scattering, the porosity effect dominates for normal sintered ceramics which usually have at least two percent porosity with a typical pore size of 1 to 5 μm . The presence of pores does not alter the intrinsic optical constants of the material (n and k) but the multiple scattering effect does significantly increase the apparent emissivity of a given sample. The same enhancement of apparent emissivity by multiple scattering has also been noticed in MgO [143]. This multiple scattering enhancement effect could be significant for particles of the order of tens or hundreds of microns but not for micron-sized or submicron particles.

Other studies [144-145] have indicated that stoichiometry can also significantly influence the value of the absorption index. Sub-stoichiometric aluminum oxide ($\text{Al}_2\text{O}_{3-x}$) can appear grey or black even at room temperature in contrast to the normal white color of stoichiometric Al_2O_3 . In oxygen deficient aluminum oxide free aluminum atoms act as free charge carriers to increase the absorption index.

5.2.2. Liquid phase

The optical constants of Al_2O_3 in the molten state ($T_m=2320$ K) have not been as well characterized as those for the solid state. Most studies indicate that k increases substantially upon melting, with a bigger increase occurring in relatively pure and stoichiometric samples [116,130,133,135,136]. Figure 15 shows that most of the reported values for k_m between 0.5 and 5 μm are in the range of 10^{-3} to 10^{-2} . Recently, Reed [137] suggested a relation for estimating k_m between 1.7 and 4.5 μm , based on extinction and emission measurements using particles that were collected from a rocket plume and heated in a shock tube.

$$k_m = 3.7 \times 10^{-4} \cdot T(\text{K})^{1.5} \cdot \lambda(\mu\text{m}) \cdot 10^{-13500/T(\text{K})} \quad (13)$$

Predictions for k_m based on Eq. (13) are in reasonable agreement with other data plotted in Fig. 15, however, Eq. (13) does not extend to short enough wavelengths to predict the upswing in k_m due to electronic transitions in the long-wavelength tail of the fundamental electronic absorption edge. Conspicuously absent from the literature are data for direct measurements of the refractive index of molten Al_2O_3 . The data of Gal and Kirch [132] plotted in Fig. 13 at 3000 K are apparently a simple extrapolation based on solid phase data and not actual measurements. While this type of extrapolation has been widely used to estimate n_m [116,132,135,136,140] it ignores the change in density which occurs upon melting and the accompanying change in refractive index which takes place. Ignoring the change in refractive index due to melting is probably reasonable for predicting emission and absorption properties but it is not reasonable for predicting scattering properties.

Recently, Parry and Brewster [120] reported the development of an in situ light scattering and extinction technique for determining the optical constants and mean optical size (d_{32}) of molten Al_2O_3 smoke particles in propellant flames. Direct transmittance and bi-directional transmittance and reflectance measurements were made using scattered laser light on aluminized solid propellant flames at visible and near infrared wavelengths ($\lambda_1 = 0.6328 \mu\text{m}$ and $\lambda_2 = 1.064 \mu\text{m}$). The optical properties of the molten Al_2O_3 smoke combustion product were obtained from the light scattering and extinction measurements by inverse solution of the radiative transfer equation. The values of n obtained for molten Al_2O_3 at 2680 K ($n_{m,\lambda_1} = 1.65$ and $n_{m,\lambda_2} = 1.64$)

were significantly less than the values which have been reported for solid Al₂O₃ at temperatures just below the melting point of 2320 K ($n_{s,\lambda 1} = 1.82$ and $n_{s,\lambda 2} = 1.81$), indicating that a substantial decrease in n occurs upon melting. This decrease in n can be attributed to the expansion which takes place upon melting and is in good qualitative agreement with the predictions of the Lorentz-Lorenz equation. The value of k obtained for molten Al₂O₃ at 2680 K was 0.006 ± 0.004 (at both wavelengths) which is in reasonable agreement with other reported values. A dispersion analysis was also performed to fit this and other data over the spectral region from 0.5 to 5.0 μm and for temperatures from 2320 K to 3000 K.

A summary of aluminum oxide optical properties is given in Fig. 16. Molten aluminum oxide can be classified as a lossy dielectric in terms of its optical constants ($n \sim 1.65$ and $k \sim 10^{-3}$ to 10^{-2}). Because the particle size varies so widely, the scattering regime ranges from Rayleigh scattering to geometric optics scattering. In the detached flame envelopes, the particle size is submicron, the size parameter is small and Rayleigh scattering prevails. Because the refractive index is finite while the particle size is small the particle "emissivity" (one minus albedo) is of order one. However the extinction efficiency is very small. In the semi-equilibrated smoke trails the particles have grown in size to the order of a micron and Mie scattering predominates. Now the size is large enough to give extinction efficiency of order one but not large enough for the weakly absorbing particle to be semi-infinite and thus the particle "emissivity" is small. The residual caps, however are large enough to be in the geometric optics regime, with extinction efficiency and emissivity of order one. Thus a wide range of aluminum oxide particle sizes is present through a heterogeneous propellant combustion system, and a corresponding wide range of scattering regimes is also evident.

5.3. Plume Radiation Models

While it is always a desirable goal to be able to predict everything including heat transfer from first principles, reality dictates that models based on empirical coefficients are usually necessary. The Bobco engineering model [146] for calculating plume radiation to aft-end equipment has been employed in the aerospace industry for the past 23 years and represents a reasonable balance between design needs and accurate physical representation. Many improvements have also been made to the Bobco model. Edward et al. [147] included a two particle model to represent cold, small scattering particles and hot, large emitting/absorbing particles in overlapping conical clouds. The clouds have axially varying radiative properties with the hot particles imagined to lose emissive power and particle emissivity with increasing axial distance. Parametric calculation were made using a hybrid Monte Carlo, radiosity/irradiation technique to show which parameters are critical and how they may be inferred from engineering tests.

Edwards and Babikian [148] also considered the effects of non-gray gas radiation and soot radiation. They concluded that gas radiation and soot radiation are negligible compared with emission by aluminum oxide. In that study the limiting anomalous diffraction results [149] were used to predict particle scattering and extinction efficiencies. These results assume $n-1 \ll 1$ and $\pi d/\lambda > 1$ which is not necessarily satisfied for aluminum oxide particles ($n=1.6$ to 1.8 ; $\pi d/\lambda = 3$ to 5). Also the limiting results of Rayleigh Gans theory [149] were used to predict the particle scattering asymmetry factor. Rayleigh Gans theory also assumes $n-1 \ll 1$, in addition

to assuming that $(n-1)\pi d/\lambda \ll 1$. Again these conditions are not necessarily satisfied and the asymmetry factor is overpredicted by using the Rayleigh Gans results. Comparing exact Mie calculations for extinction efficiency, albedo and asymmetry factor with corresponding anomalous diffraction and Rayleigh Gans results for $n=1.62$, $k=0.001$ and $d=1\mu\text{m}$ gives significant differences, but it is not certain how much these differences would influence the conclusions of [148]. It is not likely that the conclusions of the study would change significantly, although the numbers may be altered somewhat.

6. SUMMARY

Heat transfer plays an important role in several areas of heterogeneous propellant combustion systems. Heat feedback to the propellant surface determines the regression rate of the propellant which helps determine the thrust and action time of the motor. Heat transfer to internal and external surfaces creates the need for insulation systems which must be optimally designed for maximum performance. Gas and particle conduction, gas convection, and radiation by aluminum oxide particles all play significant roles at various locations through the propulsion system.

In the past, design of heterogeneous propellant combustion systems has relied on extensive testing and empiricism. This is partly because understanding of the fundamental processes has been limited and partly because extensive research has not been viewed as being cost effective when compared with testing. This trend will change as testing becomes prohibitively expensive and confidence in numerical simulation increases. In the future, improvements in performance will come in small increments. Emphasis will be given to improving system reliability, safety and environmental compatibility. At the same time, the need for accurate fundamental property data will always be present.

ACKNOWLEDGEMENT

Support for the author's research from the National Science Foundation (CBT 86-96162), the Office of Naval Research (N00014-87-K-0547), and Thiokol Corporation is gratefully acknowledged.

REFERENCES

1. N. Kubota, Survey of Rocket Propellants and Their Combustion Characteristics, in K. K. Kuo and M. Summerfield (ed.), **Fundamentals of Solid Propellant Combustion**, chap. 1, Prog. in Astronautics and Aeronautics, Vol. 90, AIAA, New York, 1984.
2. M. W. Beckstead, R. L. Derr, and C. F. Price, A Model of Composite Solid Propellant Combustion Based on Multiple Flames, **AIAA Journal**, vol. 8, pp. 2200-2207, 1970.
3. M. W. Beckstead, Combustion Calculations for Composite Solid Propellants, **13th JANNAF Combustion Mtg.**, CPIA Publications, pp. 299-312, 1976.
4. M. W. Beckstead, A Model for Solid Propellant Combustion, **14th JANNAF Combustion Mtg.**, CPIA Publication 292, vol. 1, pp. 281-306, 1977.
5. R. R. Miller, M.T. Donohue, R.A. Yount, and J.R. Martin, Control of Solids Distribution in HTPB Propellants, AFRPL-TR-78-14, Hercules Inc., Allegheny Ballistics Laboratory, Cumberland, MD, April 1978.

6. R. L. Glick and J. A. Condon, Statistical Combustion Modeling - The Effect of Additives, **Proceedings of the 14th JANNAF Combustion Meeting**, CPIA Publication 261, Vol. 1, pp. 341-378, Dec. 1977.
7. N. S. Cohen and L. D. Strand, An Improved Model for the Combustion of AP Composite Propellants, **AIAA Journal**, vol. 20, pp. 1739-1746, 1982.
8. N. S. Cohen, Review of Composite Propellant Burn Rate Modeling, **AIAA Journal**, vol. 18, pp. 277-293, 1980.
9. E. W. Price, J. K. Sambamurthi, R. K. Sigman, and R. R. Panyam, Combustion of Ammonium Perchlorate-Polymer Sandwiches, **Combustion and Flame**, vol. 63, pp. 381-413, 1986.
10. E. W. Price, C. Markou, and R. K. Sigman, Effect of Types of Binder and Burning Rate Catalyst on Edge Burning of AP-Binder-AP Sandwiches, **Proceedings of the 26th JANNAF Combustion Meeting**, CPIA Publications, (to appear), 1989.
11. R. R. Panyam, Combustion at the Interface of an Oxidizer-Fuel Slab System, Ph.D. thesis, Georgia Institute of Technology, Atlanta, GA, 1983.
12. J. E. Crump, Aluminum Combustion in Composite Propellants, **ICRPG Combustion Conference**, CPIA Publication No. 105, vol. I, pp. 321-329, May 1966.
13. H. L. Churchill, R. W. Fleming, and N. S. Cohen, Aluminum Behavior in Solid Composite Propellant Combustion, AFRPL-TR-74-13, May 1974.
14. V. G. Grigoyerm, V. A. Arko, and K. P. Kutsenogy, Experimental Study of Aluminum Particle Agglomeration by Combustion of Condensed Systems, **Fizika Goreniya i Vzryva**, vol. 17, no. 3, pp. 3-10, May-June 1981.
15. N. S. Cohen, A Pocket Model for Aluminum Agglomeration in Composite Propellants," **AIAA Journal**, vol. 21, no. 5, pp. 720-725, May 1983.
16. E. W. Price, R. K. Sigman, J. K. Sambamurthi, and C. J. Park, Behavior of Aluminum in Solid Propellant Combustion, AFOSR-TR-77-0050, Nov. 1976.
17. E. W. Price, Combustion of Metalized Propellants, in K. K. Kuo and M. Summerfield (ed.), **Fundamentals of Solid Propellant Combustion**, chap. 9, Prog. in Astronautics and Aeronautics, Vol. 90, AIAA, New York, 1984.
18. J. K. Sambamurthi, E. W. Price and R. K. Sigman, Aluminum Agglomeration in Solid-Propellant Combustion, **AIAA Journal**, vol. 22, pp. 1132-1138, August 1984.
19. O. B. Kovalev, Physicomathematical Model of the Agglomeration of Aluminum in the Combustion of Mixed Condensed Systems, **Fizika Goreniya i Vzryva** , vol. 25, no. 1, pp. 39-48, Jan.-Feb. 1989.
20. V. A. Babuk, V. P. Belov, V. V. Khodosov and G. G. Shelukhin, Study of the Structure of Agglomerates with Combustion of Aluminized Mixed Condensed Systems, **Fizika Goreniya i Vzryva** , Vol. 24, No. 5, Sept.-Oct., 1988, pp. 52-57.
21. M. A. Gurevich, K. I. Lapkina, and E. S. Ozerov, Ignition Limits of Aluminum Particles, **Fizika Goreniya i Vzryva** , vol. 6, no. 2, pp. 172-175, Apr.-June, 1970.
22. M. A. Gurevich, G. E. Ozerova and A. M. Stepanov, Heterogeneous Ignition of an Aluminum Particle in Oxygen and Water Vapor, **Fizika Goreniya i Vzryva** , vol. 6, no. 3, pp. 326-335, July-Sept., 1970.

23. A.F. Belyaev, Y.V. Frolov, and A.I. Korotkov, Combustion and Ignition of Particles of Finely Dispersed Aluminum, **Fizika Goreniya i Vzryva**, vol. 4, no. 3, pp. 323-329, 1968.
24. M. K. King, A Model of the Effect of Wires on Solid Propellant Burning Rate, **25th JANNAF Combustion Mtg.**, CPIA Publication No. 498, pp. 95-108, 1988.
25. A. A. Zennin, A. P. Glaskova, O.I. Leipunskyi, and V. K. Bobolev, Effects of Metallic Additives on the Deflagration of Condensed Systems, **12th Symposium (International) on Combustion**, The Combustion Institute, Holt, Winston and Rhinehart, pp. 27-35, 1968.
26. B. E. Hardt and M. Q. Brewster, Investigation of Al and Mg/Al Alloy Behavior in Composite Solid Propellant Combustion, **25th JANNAF Combustion Mtg.**, CPIA Publication No. 498, pp. 199-206, 1988.
27. M. Q. Brewster and B. E. Hardt, Influence of Metal Agglomeration and Heat Feedback on Composite Solid Propellant Burn Rate, submitted to **Journal of Propulsion and Power**.
28. M. Q. Brewster and B. E. Hardt, Selective Radiation Absorption in Composite Propellant Combustion, **24th JANNAF Combustion Meeting**, vol. 1, CPIA Publication 476, pp. 157-163, 1987.
29. M. Q. Brewster and K. W. Gross, Radiation Effects on Flow Characteristics in Combustion Chambers, **Proceedings of the 26th JANNAF Combustion Meeting**, CPIA Publications, (to appear), 1989.
30. M. D. Horton and L. Z. Youngberg, Effect of Radiant Energy on the Burning Rate of a Composite Solid Propellant, **AIAA Journal**, vol. 8, pp. 1738-1741, 1970.
31. R. L. Coates and S. Kwak, Effect of External Radiation on the Burning Rates of Solid Propellants, **Journal of Spacecraft and Rockets**, pp. 742-744, 1972.
32. L. H. Caveny, T. J. Ohlemiller and M. Summerfield, Influence of Thermal Radiation on Solid Propellant Burning Rate, **AIAA Journal**, vol. 13, pp. 202-205, 1975.
33. M. M. Ibiricu and F. A. Williams, Influence of Thermal Radiation on the Burning Rates of Homogeneous Solid Propellants, **Combustion and Flame**, vol. 24, pp. 185-198, 1975.
34. J. Yin, B. Chen, Q. Luo, J. Ma and K. Wang, Effect of External Radiation on the Burning Rates of Composite Solid Propellants, **AIAA 89-2533**, 25th Joint Propulsion Conference, 1989.
35. C. M. Mihlfeith, A. D. Baer and N. W. Ryan, Propellant Combustion Instability as Measured by Combustion Recoil, **AIAA Journal**, vol. 10, pp. 1280-1285, 1972.
36. C. M. Mihlfeith, Some Experiments on the Effect of Thermal Radiation on Composite Solid Rocket Propellants, Ph.D. thesis, University of Utah, Salt Lake City, UT, 1971.
37. V. F. Mikheev, V. E. Zarko, S. M. Borin, K. P. Kutsenogii and V. N. Simonenko, Measurement of Burning Rates in Transient Combustion Processes Under the Influence of External Radiation, in T. Boggs and B. Zinn (ed.), **AIAA Prog. Astro. and Aero.**, vol. 63, pp. 173-187, 1978.
38. V. E. Zarko and A. B. Kiskin, Numerical Modeling of Nonsteady Powder Combustion Under the Action of a Light Flux, **Combustion, Explosion and Shock Wave**, vol. 16, pp. 650-654, 1980.
39. V. E. Zarko, V. N. Simonenko and K. P. Kutsenogii, Effects of Light Intensity on the Nonstationary Combustion Rate in a Transient Process, **Combustion, Explosion and Shock Wave**, vol. 11, pp. 459-464, 1975.

40. T. J. Ohlemiller, L. H. Caveny, L. DeLuca and M. Summerfield, Dynamic Effects on Ignitability Limits of Solid Propellants Subjected to Radiative Heating, **Fourteenth Symposium (International) on Combustion**, The Combustion Institute, Holt, Winston and Rhinehart, pp. 1297-1307, 1972.
41. L. DeLuca, Frequency Response Function of Burning Solid Propellants, **Meccanica**, pp. 195-205, Dec. 1980.
42. L. Strand, M. Weil and N. S. Cohen, Solid Propellant Combustion Response to Oscillatory Radiant Heat Flux, AIAA 89-2667, 25th Joint Propulsion Conference, 1989.
43. J. C. Finlinson, T. P. Parr and R. Stalnaker, Measurement of Propellant Combustion Response to Oscillatory Radiant Heat Flux, **Proceedings of the 26th JANNAF Combustion Meeting**, CPIA Publications, (to appear), 1989.
44. T. D. Prevish and M. Q. Brewster, Combustion Response of Solid Rocket Propellants to Oscillatory Radiant Heat Flux, **Proceedings of the 26th JANNAF Combustion Meeting**, CPIA Publications, (to appear), 1989.
45. R. S. Patel and M. Q. Brewster, Optical Constants of Propellant Grade Ammonium Perchlorate, **AIAA Journal**, vol. 24, pp. 1878-1880, 1986.
46. R. F. Felton and J. E. Hitchcock, An Optical Technique to Measure Energy Incident on a Burning Solid Propellant Surface, AIAA 71-469, 6th Thermophysics Conference 1971.
47. M. Q. Brewster and D. L. Parry, Radiative Heat Feedback in Aluminized Solid Propellant Combustion, **Journal of Thermophysics and Heat Transfer**, vol. 2, pp. 123-130, 1988.
48. M. Q. Brewster and R. S. Patel, Selective Radiative Preheating of Aluminum in Composite Solid Propellant Combustion, **Journal of Heat Transfer**, vol. 109, pp. 179-184, 1987.
49. M. Q. Brewster and D. M. Taylor, Radiative Properties of Burning Aluminum Droplets, **Combustion and Flame**, vol. 72, pp. 287-299, 1988.
50. D. M. Chen, W. H. Hsieh, W. H. Snyder, T. S. Yang and K. K. Kuo, Study of the Thermophysical Properties and Combustion Behavior of Metal-Based Solid Fuels, AIAA 88-3041, 1988.
51. A. Ishihara, M. Q. Brewster, T. A. Sheridan and H. Krier, The Influence of Radiative Heat Feedback on Burning Rate in Metalized Propellants, submitted to 23rd Symposium (International) on Combustion.
52. J. M. Lenoir and G. Robillard, A Mathematical Method to Predict the Effects of Erosive Burning in Solid Propellant Rocket, **Sixth Symposium (International) on Combustion**, Reinhold, New York, pp. 663-667, 1957.
53. M. K. Razdan and K. K. Kuo, Turbulent Flow Analysis of Erosive Burning of Cylindrical Composite Solid Propellants, **AIAA Journal**, vol. 20, pp. 122-128, 1982.
54. R. A. Beddini, Aerothermochemical Analysis of Erosive Burning in a Laboratory Solid Rocket Motor, **AIAA Journal**, Vol. 18, pp. 1346-1353, 1980.
55. M. K. King, A Model of Erosive Burning of Composite Propellants, **Journal of Spacecraft and Rockets**, vol. 15, pp. 139-146, 1978.
56. M. J. Zucrow, J. R. Osborn and J. M. Murphy, An Experimental Investigation of the Erosive Burning Characteristics of a Nonhomogeneous Solid Propellant, **AIAA Journal**, Vol. 3, pp. 523-525, 1965.
57. M. K. Razdan and K. K. Kuo, Erosive Burning of Solid Propellants, in K. K. Kuo and M. Summerfield (ed.), **Fundamentals of Solid Propellant**

- Combustion**, chap. 10, Prog. in Astronautics and Aeronautics, Vol. 90, AIAA, New York, 1984.
- 58. M. K. King, One Person's View of Velocity Coupled Instability, **24th JANNAF Combustion Meeting**, CPIA Publication 476, pp. 115-130.
 - 59. G. L. Vogt, Workshop Report: Velocity Coupling, **24th JANNAF Combustion Meeting**, CPIA Publication 476, pp. 131-140.
 - 60. I. Glassman, Combustion of Metals. Physical Considerations, in M. Summerfield (ed.), **Solid Propellant Rocket Research**, Progress in Astronautics and Rocketry, vol. 1, Academic Press, pp. 253-258, 1960.
 - 61. T. A. Brzustowski and I. Glassman, Spectroscopic Investigation of Metal Combustion, in H. G. Wolfhard, I. Glassman, and L. Green (ed.), **Heterogeneous Combustion**, Progress in Astronautics and Rocketry, vol. 15, Academic Press, pp. 41-74, 1964.
 - 62. A. M. Mellor and I. Glassman, Vapor Phase Diffusion Flames in the Combustion of Magnesium and Aluminum: III. Experimental Observations in Carbon Dioxide Atmospheres, in H. G. Wolfhard, I. Glassman, and L. Green (ed.), **Heterogeneous Combustion**, Progress in Astronautics and Rocketry, vol. 15, Academic Press, pp. 159-176, 1964.
 - 63. R. Friedman and A. Macek, Ignition and Combustion of Aluminum Particles in Hot Ambient Gases, **Combustion and Flame**, vol. 6, pp. 9-19, 1965.
 - 64. D. K. Kuehl, Ignition and Combustion of Aluminum and Beryllium, **AIAA Journal**, vol. 3, pp. 2239-2247, 1965.
 - 65. G. H. Markstein, Combustion of Metals, **AIAA Journal**, vol. 1, pp. 550-562, 1963.
 - 66. A. M. Mellor and I. Glassman, A Physical Criterion for Metal Ignition, **Pyrodynamics**, vol. 3, pp. 43-64, 1965.
 - 67. W. M. Fassell, C. A. Papp, D. L. Hildebrand and R. P. Sernka, The Experimental Nature of the Combustion of Metallic Powders, in M. Summerfield (ed.), **Solid Propellant Rocket Research**, Progress in Astronautics and Rocketry, vol. 1, Academic Press, pp. 259-260, 1960.
 - 68. R. W. Bartlett, J. N. Ong, W. M. Fassell and C. A. Papp, Estimating Aluminum Particle Combustion Kinetics, **Combustion and Flame**, vol. 7, pp. 227-234, 1963.
 - 69. G. H. Markstein, Heterogeneous Reaction Processes in Metal Combustion, **Eleventh Symposium (International) on Combustion**, The Combustion Institute, Holt, Winston and Rhinehart, 1967.
 - 70. A. Macek, Fundamentals of Combustion of Single Aluminum and Beryllium Particles, **Eleventh Symposium (International) on Combustion**, The Combustion Institute, Holt, Winston and Rhinehart, 1967.
 - 71. A. Macek, R. Friedman and J. M. Semple, Techniques for the Study of Combustion of Beryllium and Aluminum Particles, in H. G. Wolfhard, I. Glassman, and L. Green (ed.), **Heterogeneous Combustion**, Progress in Astronautics and Rocketry, vol. 15, Academic Press, pp. 3-16, 1964.
 - 72. A. Davis, Solid Propellants: The Combustion of Particles of Metal Ingredients, **Combustion and Flame**, vol. 7, pp. 395-367, 1963.
 - 73. L. S. Nelson, N. L. Richardson and J. L. Prentice, Apparatus for the Production and Ignition of Metal Droplets with a Pulsed Laser, **Review of Scientific Instruments**, vol. 39, pp. 744-747, 1968.

74. R. P. Wilson and F. A. Williams, Experimental Study of the Combustion of Single Aluminum Particles in O₂/Ar, **Thirteenth Symposium (International) on Combustion**, The Combustion Institute, pp. 833-845, 1971.
75. J. L. Prentice and L. S. Nelson, Differences between the Combustion of Aluminum Droplets in Air and in an Oxygen-Argon Mixture, **J. Electrochem. Soc.**, vol. 115, pp. 809-812, 1968.
76. C. M. Drew, A. S. Gordon and R. H. Knipe, Study of Quenched Aluminum Particle Combustion, in H. G. Wolfhard, I. Glassman, and L. Green (ed.), **Heterogeneous Combustion**, Progress in Astronautics and Rocketry, vol. 15, Academic Press, pp. 17-39, 1964.
77. C. K. Law, A Simplified Theoretical Model for the Vapor Phase Combustion of Metal Particles, **Combustion Science and Technology**, vol. 7, pp. 197-212, 1973.
78. W. G. Courtney, Condensation During Heterogeneous Combustion, **Eleventh Symposium (International) on Combustion**, The Combustion Institute, pp. 237-244, 1967.
79. T. H. Rautenberg and P. D. Johnson, Light Production in the Aluminum-Oxygen Reaction, **J. Opt. Soc. America**, vol. 50, pp. 602-605, 1960.
80. I. Glassman, A. M. Mellor, H. F. Sullivan and N. M. Laurendeau, A Review of Metal Ignition and Flame Models, AGARD-CP52, pp. (19)1-(19)29, 1970.
81. C. E. Kolb, M. E. Gersh and D. R. Herschbach, A Suggested Mechanism for the Visible Chemiluminescence Observed in Gas Phase Aluminum Oxidation, **Combustion and Flame**, vol. 25, pp. 31-41, 1975.
82. P. L. Micheli, Prediction of Burning Rate of Aluminum in Solid Rocket Motors, **13th JANNAF Combustion Mtg.**, CPIA Publications, pp. 487-499, 1976.
83. P. L. Micheli and W. G. Schmidt, Behavior of Aluminum in Solid Rocket Motors, AFRPL-TR-77-29, 1977.
84. W. G. Schmidt, R. L. Lovine and R. C. Poynter, Zirconium/Aluminum Combustion, AFRPL-TR-81-19, 1981.
85. A. Fontijn, Temperature Dependence of the Kinetics of Elementary Combustion Reactions of Refractory Species, **Combustion Science and Technology**, vol. 50, pp. 151-162, 1986.
86. R. A. Ogle, J. K. Beddow, L. D. Chen and P. B. Butler, An Investigation of Aluminum Dust Explosions, **Combustion Science and Technology**, vol. 61, pp. 75-99, pp. 1988.
87. S. R. Turns, S. C. Wong and E. Ryba, Combustion of Aluminum-Based Slurry Agglomerates, **Combustion Science and Technology**, vol. 54, pp. 299-318, 1987.
88. S. C. Wong and S. R. Turns, Ignition of Aluminum Slurry Droplets, **Combustion Science and Technology**, vol. 52, pp. 221-242, 1987.
89. A. G. Merzhanov, Y. M. Grivorjev and Y. A. Galchenko, Aluminum Ignition, **Combustion and Flame**, vol. 29, pp. 1-14, 1977.
90. M. R. Jones, K. C. Tang and M. Q. Brewster, An Investigation of the Combustion of Aluminum in Water, **Proceedings of the 26th JANNAF Combustion Meeting**, CPIA Publications, (to appear), 1989.
91. K. Brezinsky, K. Davis and I. Glassman, Gas Phase Combustion Synthesis of TiN, paper 89-6, Western States Section/The Combustion Institute, 1989.

92. W. Felder and H. F. Calcote, A Sodium Flame Process for Synthesis of Pure Metals, Alloys and Ceramics, paper 89-8, Western States Section/The Combustion Institute, 1989.
93. E. V. Chernenko, L. F. Afanaseva, V. A. Lebedeva and V. I. Rozenband, Inflammability of Mixtures of Metal Oxides with Aluminum, **Fizika Goreniya i Vzryva**, vol. 24, pp. 3-11, 1988.
94. I. Glassman, **Combustion**, 2nd ed., p. 388, Academic Press, 1987.
95. R. W. Hermsen, Improved Technical Elements for SPP: Combustion Efficiency Models, CPIA Publication 321, pp. 53-60.
96. G. R. Nickerson, D. E. Coats, R. W. Hermsen and J. T. Lamberty, A Computer Program for the Prediction of Solid Propellant Rocket Motor Performance (SPP), vols. 1-5, AFRPL-TR-83-036, 1984.
97. B. E. Pearce, Radiative Heat Transfer within a Solid Propellant Rocket Motor, **Journal of Spacecraft and Rockets**, vol. 15, pp. 125-128, 1978.
98. T. P. Rudy, R. S. Brown, E. J. Shanabrook, H. H. Weyland and L. S. Bain, Unstable Combustion of HTPB/AP Propellants at High Pressure, **24th JANNAF Combustion Meeting**, vol. III, CPIA Publication 476, pp. 1-14, 1987.
99. A. V. Grosse and J. B. Conway, Combustion of Metals in Oxygen, **Ind. Eng. Chem.**, vol. 50, pp. 663-672, 1958.
100. S. P. Purcell and W. L. Daines, Buoyant Flow and its Effect on Internal Insulator Performance-Numerical Approach, **Proc. of 1985 JANNAF Propulsion Meeting**, CPIA Publications, pp. 1-10, 1985.
101. R. S. Larson, Prediction of Aluminum Combustion Efficiency in Solid Propellant Rocket Motors, **AIAA Journal**, vol. 25, pp. 92-101, 1987.
102. E. G. Bradley and M. Q. Brewster, A Multi-dimensional Combustion Model for Solid Propellant Flowfields, with Burning Aluminum Droplets, **Proceedings of the 26th JANNAF Combustion Meeting**, CPIA Publications, (to appear), 1989.
103. R. Madabhushi, J. Sabnis, F. DeJong and H. Gibeling, Navier-Stokes Analysis of Aft Dome Flow Field in Solid Motors with Submerged Nozzle, AIAA 89-2781, 1989.
104. M. Salita, Solid Rocket Motor Performance: A Workshop Report, **24th JANNAF Combustion Meeting**, CPIA Publication 476, pp. 253-276, 1987.
105. J. N. Levine, Application of Internal Flow Field Modeling to Solid Rocket Motor Design: A Workshop Report, **25th JANNAF Combustion Meeting**, CPIA Publication 498, pp. 213-226, 1988.
106. C. B. Ludwig, W. Malkmus, J. E. Reardon and J. A. L. Thomson, Handbook of Infrared Radiation from Combustion Gases, NASA SP-3080, NTIS N73-27807, 1973.
107. J. Walker, W. Malkmus and C. B. Ludwig, Handbook of the Standardized Infrared Radiation Model (SIRRM), AFRPL-TR-81-61, 1981.
108. D. K. Edwards and R. P. Bobco, Effect of Particle Size Distribution on the Radiosity of Solid Propellant Rocket Motor Plumes, AIAA-81-1032, 16th Thermophysics Conference, 1981.
109. R. W. Hermsen, Aluminum Oxide Particle Size for Solid Rocket Motor Performance Prediction, **Journal of Spacecraft and Rockets**, vol. 18, pp. 483-490, 1981.
110. K. J. Kraeutle, Particle Size Analysis in Solid Propellant Combustion, **Prog. in Aeronautics and Astronautics**, AIAA, pp. 76-108, 1978.

111. M. Salita, Quench Bomb Investigation of Al_2O_3 Formation from Solid Rocket Propellants (Part II): Analysis of Data, **25th JANNAF Combustion Meeting**, CPIA Publication 498, pp. 185-198, 1988.
112. J. Koo, A Review of Particle Sizing Methods in Rocket Propulsion, **24th JANNAF Combustion Meeting**, CPIA Publication 476, pp. 141-156, 1987.
113. R. A. Dobbins, Remote Size Measurements of Particulate Products of Heterogeneous Combustion, **Eleventh Symposium (International) on Combustion**, The Combustion Institute, pp. 921-926, 1967.
114. R. A. Dobbins and L. D. Strand, A Comparison of Two Methods of Measuring Particle Size of Al_2O_3 Produced by a Small Rocket Motor, **AIAA Journal**, vol. 8, pp. 1544-1550, 1970.
115. E. A. Powell, R. A. Cassanova, C. P. Bankston and B. T. Zinn, Combustion Generated Smoke Diagnostics by Means of Optical Measurement Techniques, **Prog. in Astronautics and Aeronautics**, AIAA, vol. 53, pp. 449-463, 1977.
116. W. L. Konopka, R. A. Reed and V. S. Calia, Measurements of Infrared Optical Properties of Al_2O_3 Rocket Particles, **Prog. in Aeronautics and Astronautics**, vol. 91, pp. 180-197, 1984.
117. S. Orguc, T. E. Pruitt, T. D. Edwards, E. D. Youngborg, J. P. Powers and D. W. Netzer, Measurement of Particulate Size in Solid Propellant Rocket Motors, **24th JANNAF Combustion Meeting**, CPIA Publication 476, pp. 165-182, 1987.
118. D. L. Hofeldt, M. G. Allen and R. K. Hanson, Instantaneous Two-Dimensional Multiple Particle Sizing Diagnostic, **24th JANNAF Combustion Meeting**, CPIA Publication 476, pp. 183-192, 1987.
119. T. E. Parker, D. I. Rosen and W. T. Rawlins, Infrared Optical Property Measurement Techniques: Definition and Preliminary Design, AFRPL-TR-86-034, 1986.
120. D. L. Parry and M. Q. Brewster, Optical Constants of Al_2O_3 Smoke in Propellant Flames, to appear in **Journal of Thermophysics and Heat Transfer**.
121. M. Salita, Implementation and Validation of the One-Dimensional Gas/Particle Flow Code OD3P, **Proceedings of the 26th JANNAF Combustion Meeting**, CPIA Publications, (to appear), 1989.
122. C. D. Bartky and E. Bauer, Predicting the Emittance of a Homogeneous Plume Containing Alumina Particles, **Journal of Spacecraft and Rockets**, vol. 3, pp. 1523-1527, 1966.
123. S. J. Morizumi and H. J. Carpenter, Thermal Radiation from the Exhaust Plume of an Aluminized Composite Propellant Rocket, **Journal of Spacecraft and Rockets**, vol. 1, pp. 501-507, 1964.
124. B. W. Worster, Particulate Infrared Radiation in Aluminized Solid Fuel Rocket Plumes, **Journal of Spacecraft and Rockets**, vol. 11, pp. 260-262, 1974.
125. A. B. Pluchino and D. E. Masturzo, Emissivity of Al_2O_3 Particles in Rocket Plume, **AIAA Journal**, vol. 19, pp. 1234-1237, 1981.
126. T. J. Rieger, On the Emissivity of Alumina/Aluminum Composite Particles, **Journal of Spacecraft and Rockets**, vol. 16, pp. 438-439, 1979.
127. W. R. Cofer III, E. L. Winstead and L. E. Key, Surface Composition of Solid Rocket Exhausted Aluminum Oxide Particles, **Journal of Propulsion and Power**, vol. 5, pp. 674-677, 1989.
128. I. H. Malitson, Refraction and Dispersion of Synthetic Sapphire, **J. Opt. Soc. Am.**, vol. 52, no. 12, pp. 1377-1379, 1962.

129. O. B. Toon and J. B. Pollack, The Optical Constants of Several Atmospheric Aerosol Species: Ammonium Sulfate, Aluminum Oxide, and Sodium Chloride, *J. of Geophysical Research*, vol. 81, no. 33, pp. 5733-5748, Nov. 1976.
130. D. A. Gryvnak and D. E. Burch, Optical and Infrared Properties of Al_2O_3 at Elevated Temperatures, *J. Opt. Soc. Am.*, vol. 55, no. 6, pp. 625-629, 1965.
131. G. N. Plass, Temperature Dependence of the Mie Scattering and Absorption Cross Sections for Aluminum Oxide, *Applied Optics*, vol. 4, no. 12, pp. 1616-1619, 1965.
132. G. Gal and H. Kirch, Particulate Optical Properties in Rocket Plumes, AFRPL-TR-73-99, pp. 28-29, 1973.
133. D. J. Carlson, Emittance of Condensed Oxides in Solid Propellant Combustion Products, *Tenth (International) Symposium on Combustion*, The Combustion Institute, pp. 1413-1424, 1965.
134. E. Bauer and D. J. Carlson, Mie Scattering Calculations for Micron Size Alumina and Magnesia Spheres, *J. Quant. Spectro. Rad. Transfer*, vol. 4, pp. 363-374, 1964.
135. J. M. Adams, A Determination of the Emissive Properties of a Cloud of Molten Alumina Particles, *J. Quant. Spectro. Rad. Transfer*, vol. 7, pp. 273-277, 1967.
136. E. J. Mularz and M. C. Yuen, An Experimental Investigation of Radiative Properties of Aluminum Oxide Particles, *J. Quant. Spectro. Rad. Transfer*, vol. 12, pp. 1553-1568, 1972.
137. R. Reed, Optical Properties for Liquid Al_2O_3 , Private Communication, Arnold AFB, 29 Feb 1988.
138. D. W. Lee and W. D. Kingery, Radiation Energy Transfer and Thermal Conductivity of Ceramic Oxides, *J. Am. Ceramic Soc.*, vol. 43, no. 11, pp. 595-607, 1960.
139. V. H. Myers, A. Oro, and D. P. DeWitt, A Method for Measuring Optical Properties of Semi-Transparent Materials at High Temperatures, *AIAA Journal*, vol. 24, no. 2, pp. 321-326, 1986.
140. Y. K. Lingart, V. A. Petrov and A. A. Tikhonova, Optical Properties of Leucosapphire at High Temperatures, *Teplofizika Vysokikh Temperatur*, vol. 20, no. 5, pp. 872-880, 1982.
141. A. S. Barker Jr., Infrared Lattice Vibrations and Dielectric Dispersion in Corundum, *Physical Review*, vol. 132, no. 4, pp. 1474-1481, 1963.
142. D. G. Goodwin and M. Mitchner, Infrared Optical Constants of Coal slags: Dependence on Chemical Composition, *Journal of Thermophysics and Heat Transfer*, vol. 3, no. 1, pp. 53-60, 1989.
143. V. G. Skogarev and A. V. Florko, Effect of the Temperature on the Integrated Emissivity of Magnesium Oxide, *Fizika Gorenija i Vzryva*, vol. 23, pp. 92-94, 1987.
144. L. S. Nelson and N. L. Richardson, Effects of Oxygen and Argon Atmospheres on Pendant Drops of Aluminum Oxide Melted with Carbon Dioxide Laser Radiation, *High Temperature Science*, vol. 5, pp. 138-154, 1973.
145. K. J. Kraeutle and H. H. Bradley, Jr., Combustion of Aluminized Propellants: The Influence of Pressure and Propellant Composition on Formation of Aluminum Combustion Residue, *14th JANNAF Combustion Meeting*, CPIA Publication 292, vol. 1, pp. 209-219, 1977.

146. R. P. Bobco, Radiation from Conical Surfaces with Nonuniform Radiosity, **AIAA Journal**, vol. 4, pp. 544-546, 1966.
147. D. K. Edwards, Y. Sakurai and D. S. Babikian, A Two Particle Model for Rocket Plume Radiation, **Journal of Thermophysics and Heat Transfer**, vol. 1, pp. 13-20, 1987.
148. D. K. Edwards and D. S. Babikian, Radiation from a Nongray Scattering Emitting and Absorbing SRM Plume, AIAA-89-1721, 24th Thermophysics Conference, 1989.
149. H. C. van de Hulst, **Light Scattering by Small Particles**, Dover Publications, Inc., New York, 1981.

FIGURE CAPTIONS

1. Areas of heat transfer importance in propellant combustion systems
2. BDP model of competing flame heat feedback
3. Effect of low pressure (a) and high pressure (b) on flame heat feedback
4. Lateral sub-surface heat flux in 2-D propellant sandwiches
5. Regression rate for metalized composite propellants
6. Regression rate augmentation due to crossflow (a) positive only (b) mixed
7. Model of burning aluminum droplet showing radiative transfer contributions: (1) flame emission, (2) reflected flame emission, and (3) droplet emission
8. Comparison between Hermsen's correlation and diffusion model showing effect of convective environment ($Y_{O\infty}=0.5$, $T_\infty=2400$ K, $p = 0.1$ MPa)
9. Buoyancy induced flow pattern near head end
10. Optically thick, radiating stagnation flow
11. Non-dimensional radiative (q_r^*) and conductive (q_c^*) heat flux components in optically thick, two-dimensional planar stagnation flow ($Pr=0.5$, $\epsilon_w=1$)
12. Bimodal size distribution of aluminum oxide produced by aluminum combustion
13. Survey of refractive index of aluminum oxide
14. Survey of absorption index of solid aluminum oxide
15. Survey of absorption index of molten aluminum oxide
16. Summary of liquid aluminum oxide particle radiative properties

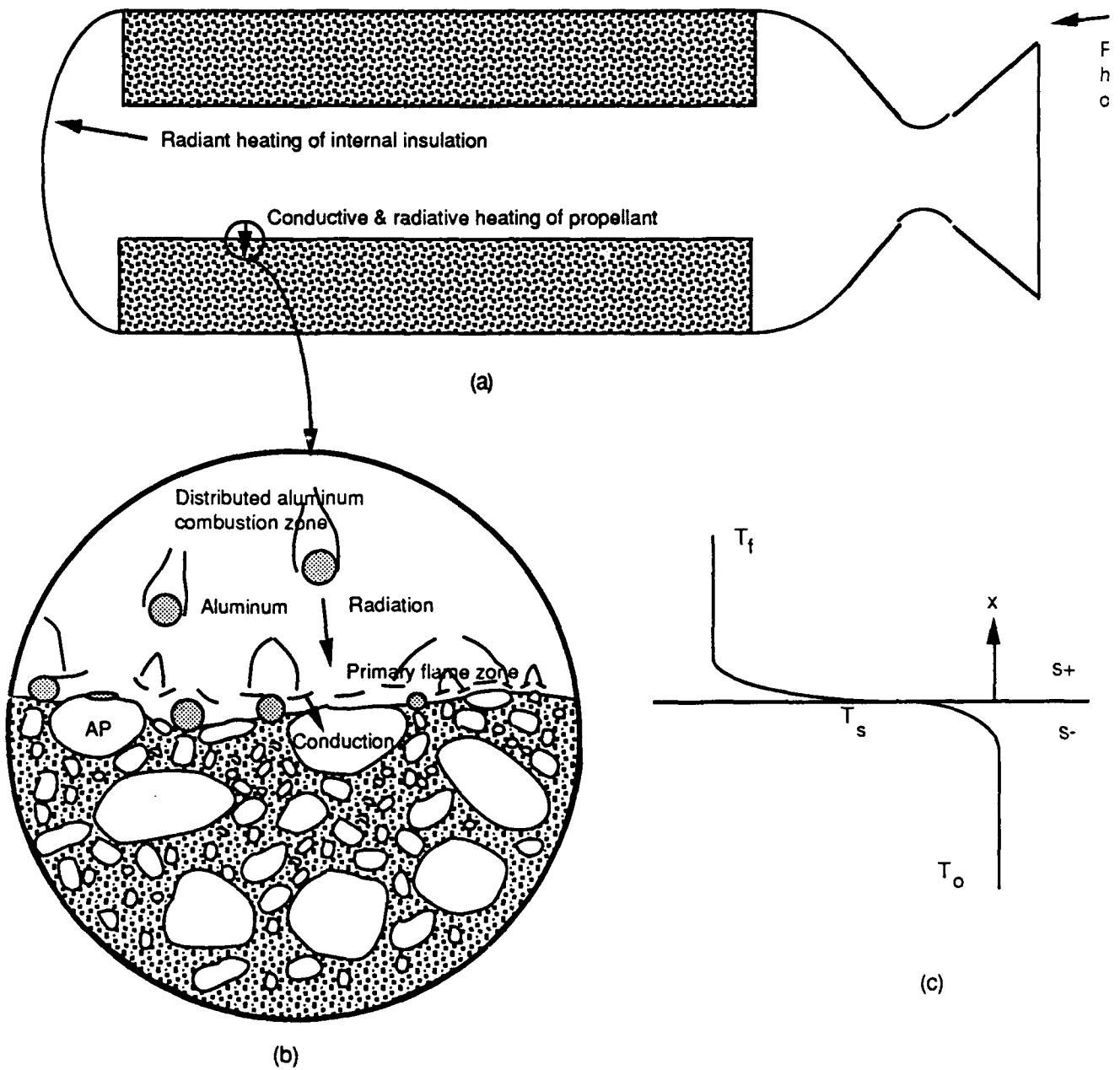


Fig. 1 Areas of heat transfer importance in propellant combustion systems

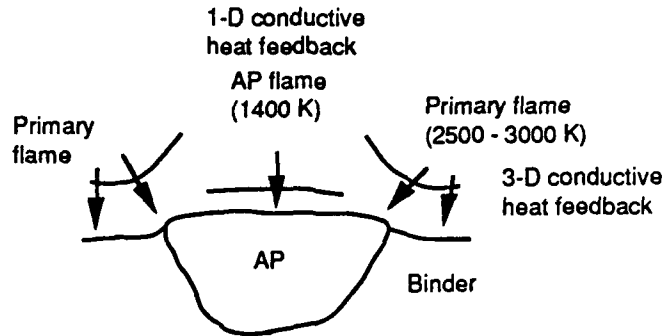


Fig. 2 BDP model of competing flame heat feedback

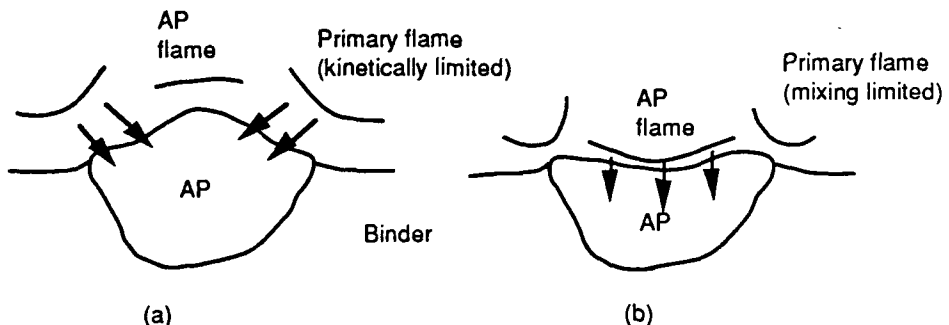


Fig. 3 Effect of low pressure (a) and high pressure (b) on flame heat feedback

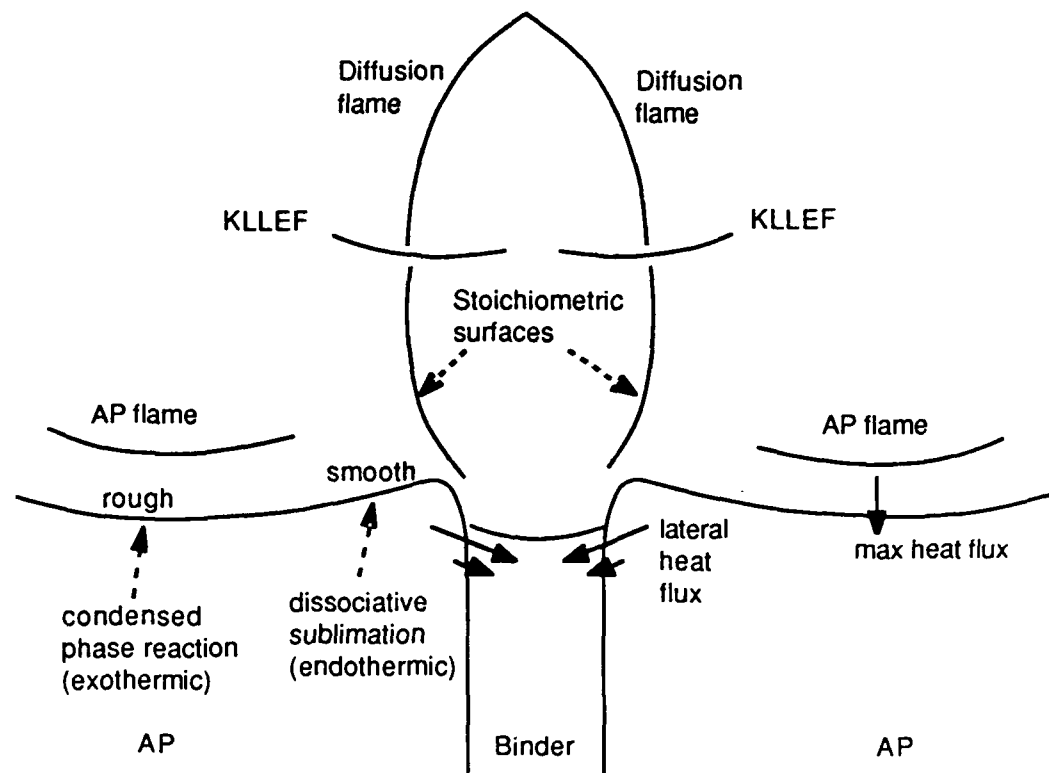


Fig. 4 Lateral sub-surface heat flux in 2-D propellant sandwiches

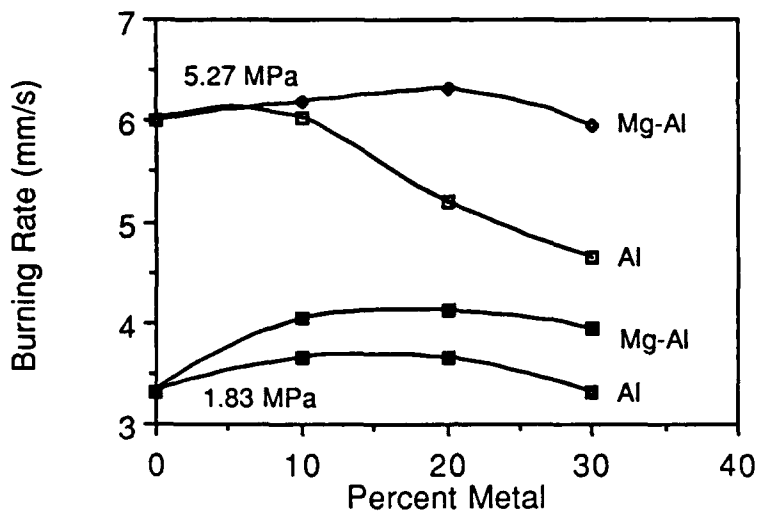


Fig. 5 Regression rate for metalized composite propellants

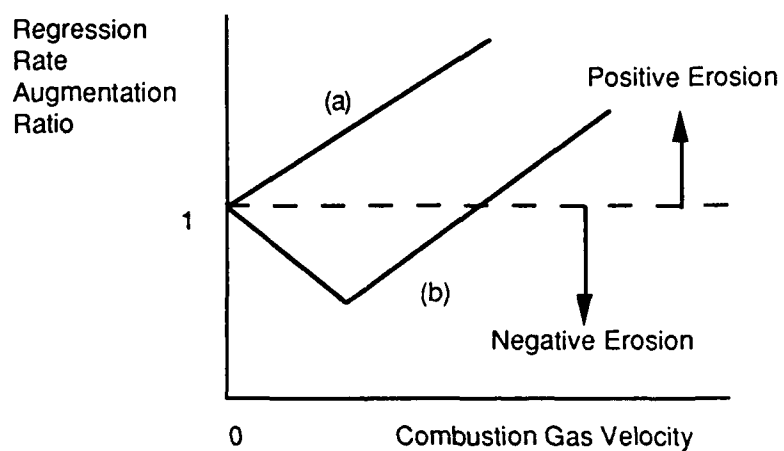


Fig. 6 Regression rate augmentation due to crossflow (a) positive only and (b) mixed

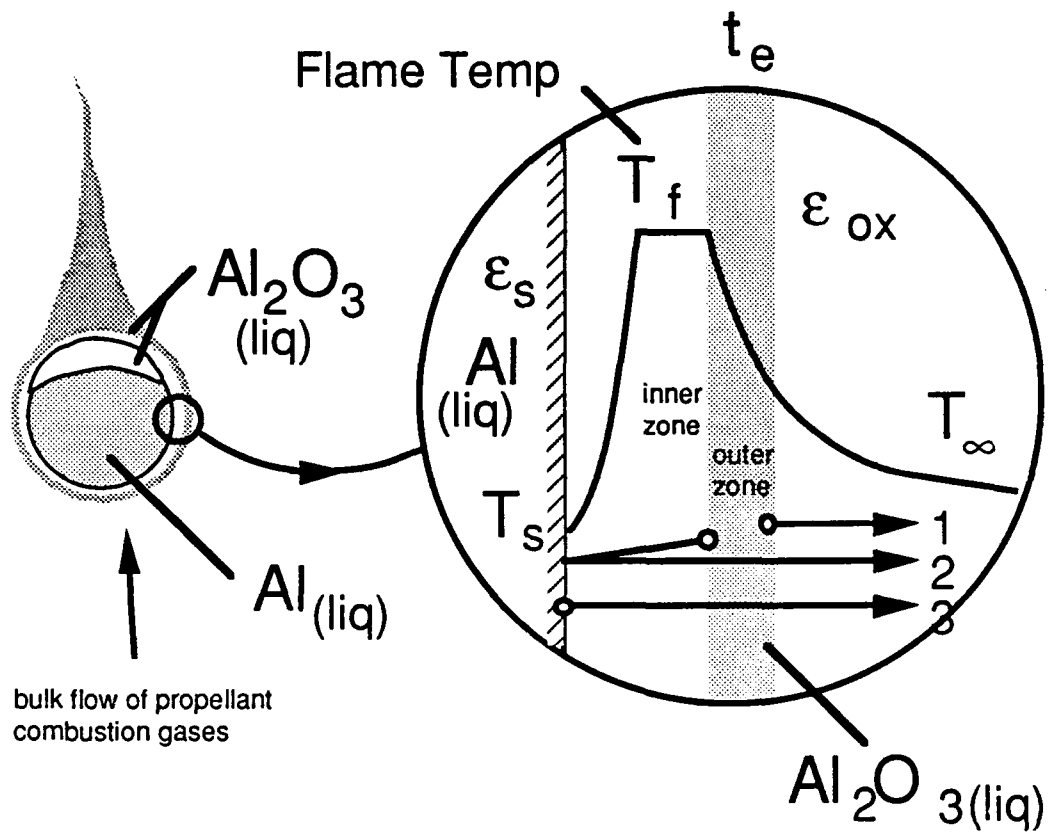


Fig. 7 Model of burning aluminum droplet showing radiative transfer contributions:(1) flame emission, (2) reflected flame emission, and (3) droplet emission

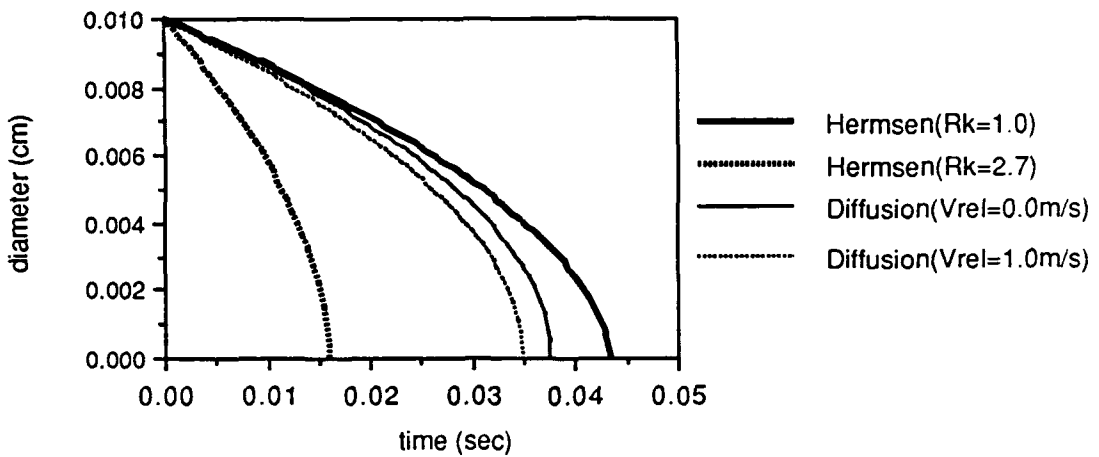


Fig. 8. Comparison between Hermsen's correlation and diffusion model showing effect of convective environment ($Y_{0\infty}=0.5$, $T_\infty=2400$ K, $p = 0.1$ MPa)

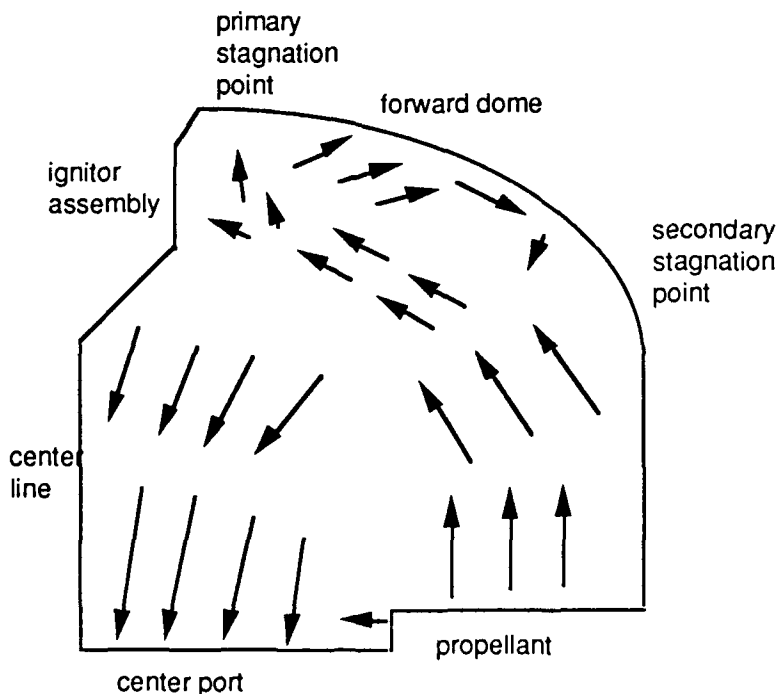


Fig. 9 Buoyancy induced flow pattern near head end

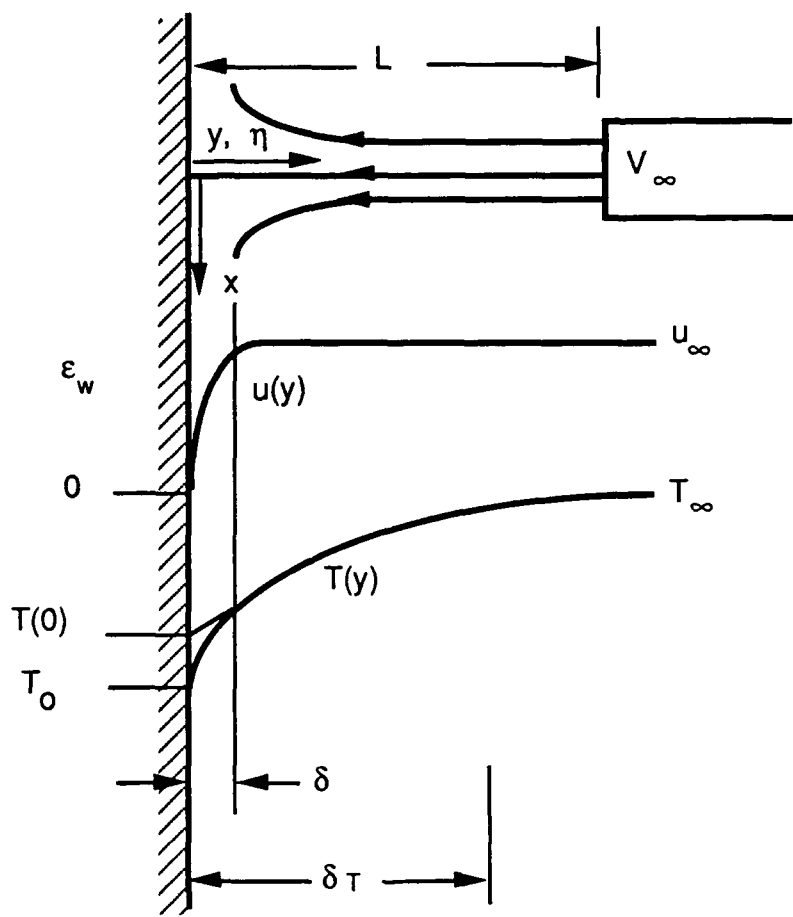


Fig. 10 Optically thick, radiating stagnation flow

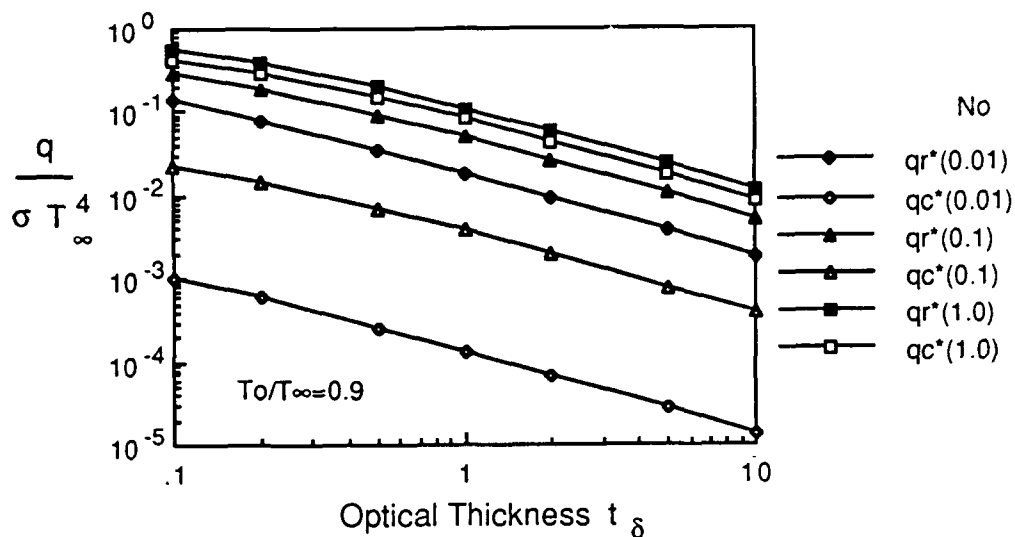


Fig. 11 Non-dimensional radiative (q_r^*) and conductive (q_c^*) heat flux components in optically thick, two-dimensional planar stagnation flow ($\text{Pr}=0.5$, $\varepsilon_w=1$)

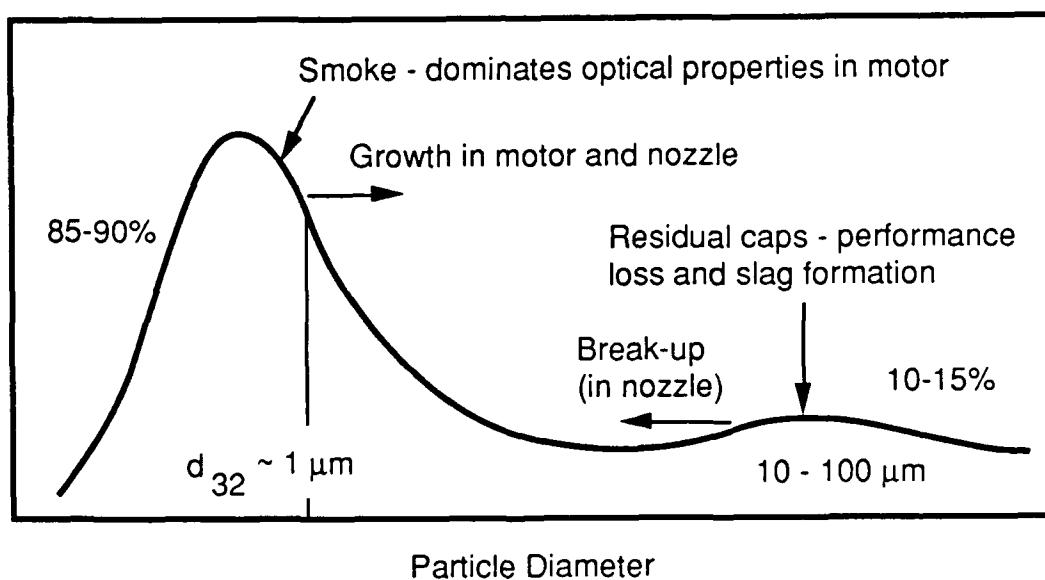


Fig. 12 Bimodal size distribution of aluminum oxide produced by aluminum combustion

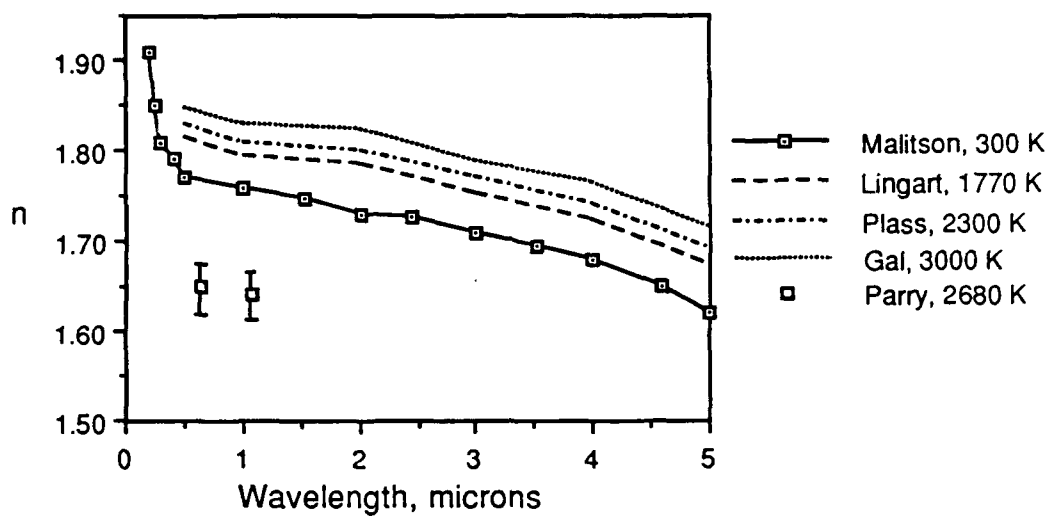


Fig. 13 Survey of refractive index of aluminum oxide

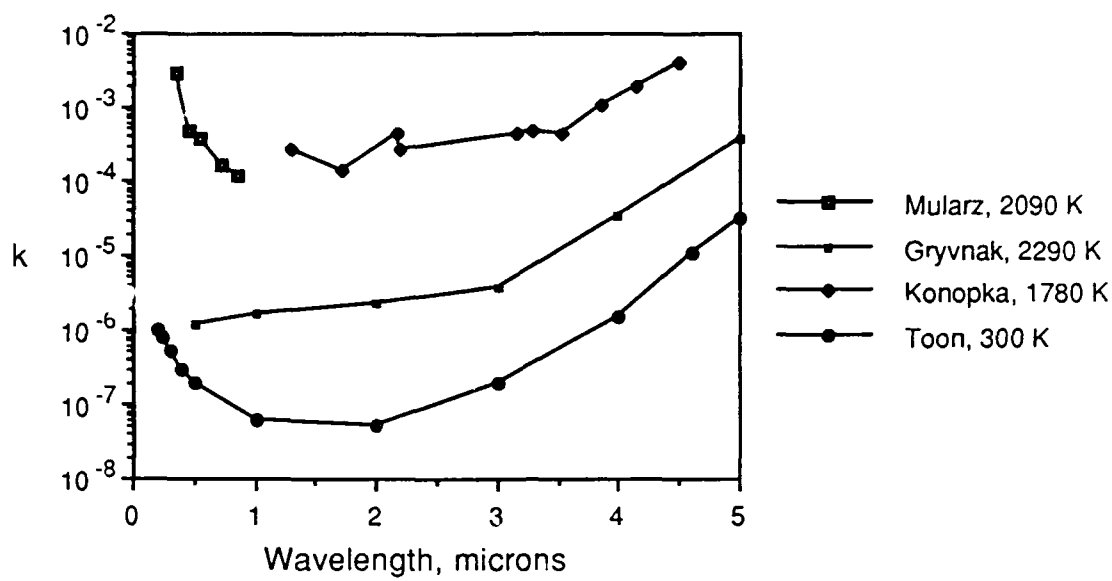


Fig. 14 Survey of absorption index of solid aluminum oxide

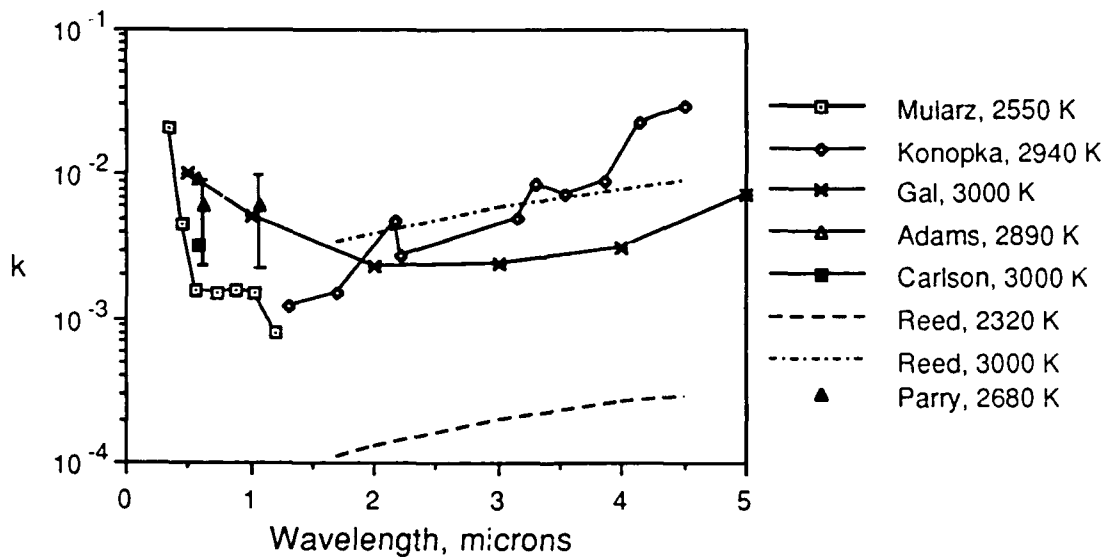


Fig. 15 Survey of absorption index of molten aluminum oxide

Size, d (μm)	10^{-2} to 10^{-1}	1	10 to 100
Source of particles	Detached flame envelope	Semi-equilibrated smoke trails	Caps from surface accumulation
Size parameter $\frac{\pi d}{\lambda}$	$<<1$	~ 1	$>>1$
Radiative scattering regime	Rayleigh	Mie	Geometric Optics
Particle emissivity	0.5 - 1	0.03 - 0.06	$\frac{4n}{(n+1)^2} \sim 0.94$
Extinction efficiency	10^{-5} - 10^{-3}	2 - 4	2 (1)

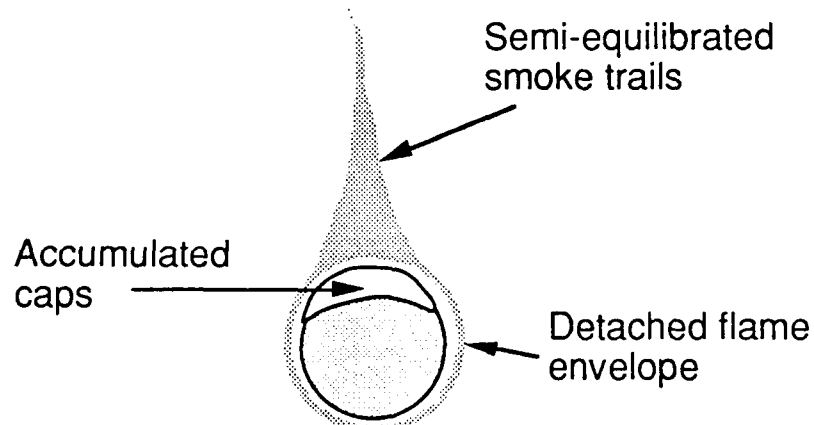


Fig. 16 Summary of liquid aluminum oxide particle radiative properties

Submitted to Journal of Heat Transfer
and

Symposium on Heat and Mass Transfer in Fires and Combustion Systems, National Heat Transfer Conference, Minneapolis, MN, July 1991

ANALYSIS OF RADIATIVE HEAT TRANSFER IN AN ALUMINUM DISTRIBUTED COMBUSTION REGION

K. C. Tang

Graduate Research Assistant.
Student Member, ASME.

M. Q. Brewster

Associate Professor.
Member, ASME.

Department of Mechanical and Industrial Engineering
University of Illinois at Urbana-Champaign
Urbana, Illinois 61801

ABSTRACT

The discrete-ordinate method was used to model the radiative heat transfer in an aluminum distributed combustion region resulting from the burning of aluminized solid propellant. The participating medium in the aluminum distributed combustion region, which consisted of gas and particle phases, had non-homogeneous, emitting, absorbing, and anisotropic scattering radiative properties. In this study, the contribution from gas radiation was neglected and a one-dimensional gray analysis was used to study the radiant heat transfer due to particles. The contributions from both the burning aluminum droplets and the condensed aluminum oxide particles were included. The coupling effect of the energy and radiative transfer equations was studied by the iteration method through the divergence of radiative heat flux vector term in the energy equation. Results showed that the coupling effect between the energy and radiative transfer equations was not significant. The decoupled equations predicted the radiative heat feedback about 5% higher than that predicted by the coupled equations. Several factors such as aluminum loading of the propellant, pressure, agglomerate size of aluminum droplets, emissive properties of burning aluminum droplets, and albedo of aluminum oxide, which affect the magnitude of the radiative heat feedback, were also examined.

NOMENCLATURE

AP	ammonium perchlorate
d_{32}	Sauter mean diameter
D_{AI}	initial aluminum agglomerate size
f_m	mass fraction
f_v	volume fraction
I	intensity
K_a	absorption coefficient
K_e	extinction coefficient
K_{em}	emission coefficient
K_{ei}	equivalent isotropic extinction coefficient for diffusion
	approximation defined by Eqn. (6)
K_s	scattering coefficient
L	characteristic length for temperature change
N	half of the order of Gaussian quadrature

p	phase function
p^*	optically thick, multiple-scattering asymmetry parameter defined by Eqn. (7)
P	pressure
PBAN	Polybutadiene-acrylonitrile-acrylic acid
q	heat flux
q''''	volumetric heat source
\tilde{q}	heat flux vector
Q	efficiency
r_B	propellant burning rate
t	time coordinate
t_e	mean optical thickness of Al_2O_3 laden flame envelope
T	temperature
T_g^*	non-dimensional gas temperature
W	weight factor of Gaussian quadrature
x	spatial coordinate
ϵ	emissivity
ϕ_s and ϕ_s'	slab azimuthal angles
μ	direction cosine of considered polar angle θ ($\mu = \cos\theta$)
μ'	direction cosine of irradiation polar angle θ' or dummy argument
ρ	reflectivity or density
θ	polar angle
θ_p	single-scattering angle
τ	transmissivity
ω	single-scattering albedo ($\omega = K_s/K_e$)
Φ	viscous dissipation energy

Subscripts

a	absorption
b	blackbody
c	conduction
d	burning aluminum droplet
e	extinction or envelope
em	emission
g	gas
i	species (Al , Al_2O_3)
j,k	dummy index
ox	aluminum oxide
oxbp	aluminum oxide boiling point
p	propellant
r	radiation
s	scattering or aluminum droplet surface
∞	infinity boundary

INTRODUCTION

Radiative heat transfer becomes significant in many engineering systems which are operated at high temperature levels. One engineering system in which radiation is important but not well understood is metalized solid propellant rockets. Metalized composite solid propellants consist of several ingredients such as fuel, oxidizer, binder, and additives (Sutton, 1986). In

most cases, powdered aluminum and crystalline Ammonium Perchlorate (AP) particles are used as fuel and oxidizer, respectively. The particle sizes of fuel and oxidizer in the range of 5-200 μm are randomly mixed with rubber-like polymeric binder (Price, 1984). The combustion of AP and binder forms a complicated flame structure about 100 μm above the propellant surface. The formation of a protective oxide skin on the surface of aluminum particles delays the ignition of the aluminum particles. These particles tend to accumulate and form large agglomerates on the burning surface. The typical size range of aluminum agglomerates is 50-200 μm (Price, 1984). Due to the low volatility of aluminum, these agglomerates can not completely burn in the vicinity of the burning surface as the AP and binder do. These burning aluminum droplets will therefore be accelerated away from the burning surface by the hot, high speed gases resulting from the combustion of AP and binder to form a two-phase, aluminum distributed combustion region above the burning surface of propellant. The products of the combustion of AP and binder serve as oxidizers in the aluminum droplet combustion. A diffusion-limited, condensed oxide particle-laden flame envelope surrounding the aluminum droplets is formed.

In the aluminum distributed combustion region above the propellant surface, a two-phase reacting flow field is generated which consists of gases and liquid particles. The gases are the products of the combustion of AP, binder, and burning aluminum droplets. The dispersed liquid phase is composed of burning aluminum droplets and aluminum oxide particles. This two-phase flow field is highly inhomogeneous due to the rapid change in temperature, species concentration, and burning aluminum droplet size (Brewster and Parry, 1988; Parry, 1989).

Both gas and particle phases may contribute to the radiative heat transfer especially at high temperatures and high pressures. Aluminum oxide particles have non-gray, emitting, absorbing, and anisotropic scattering properties and the non-scattering gases are highly non-gray. A better understanding of the radiative heat transfer mechanism in the aluminum distributed combustion region will help in understanding both the propellant combustion processes and the aluminum distributed combustion flow field. This study applies the discrete-ordinate method to predict the radiative heat transfer from the particle phase and examine the influence of several factors on the magnitude of the radiative heat feedback. The radiative contribution from the gas phase is neglected.

ANALYSIS

Aluminum Combustion Flow Model

Calculation of the radiative heat flux in the aluminum distributed two-phase reacting flow field requires as input the temperatures, volume fractions, and particle sizes of the aluminum and aluminum oxide as a function of distance above the propellant surface. The emission from these particles represents the source term in the radiative transfer equation. The volume fraction and particle size are used to calculate the absorption, scattering, and extinction coefficients (i.e. $K_{a,e,s} = 1.5f_v Q_{a,e,s}/d_{32}$). This information was obtained from a one-dimensional, two-phase aluminum combustion-flow model developed by Brewster and Parry (1988).

To simulate the aluminum distributed two-phase reacting flow field, the one-dimensional steady-state continuity, momentum, energy, and burning rate equations are solved by the finite difference method. Both the particle phase and gas phase are considered. In the flow field analysis, the particle phase consists of the burning aluminum droplets. The condensed aluminum oxide smoke is considered to be part of the gas phase in the flow analysis because the sub-micron condensed oxide particles are assumed to be at the same temperature and velocity of gaseous species (i.e. thermal and hydrodynamic equilibrium between oxide particles and gases is assumed). These coupled equations are solved as an initial value problem. The calculation ends when the aluminum droplets burnout. A detailed formulation and description of the aluminum combustion flow model can be found in the literature (Brewster and Parry, 1988; Parry, 1989).

Radiative Transfer Equation

By considering the propagation of radiation in a one-dimensional, gray, emitting, absorbing, and scattering medium, the radiative transfer equation, radiative heat flux, and divergence of radiative heat flux vector for a multi-component medium can be written as follows:

Radiative Transfer Equation :

$$\mu \frac{dI(\mu)}{dx} = - \sum_i (K_{si} + K_{ai}) I(\mu) + \sum_i K_{em,i} I_b(T_i) + \sum_i \frac{K_{si}}{2} \int_{-1}^1 I(\mu') p_i(\mu, \mu') d\mu' \quad (1)$$

Radiative Heat Flux :

$$q_r = 2\pi \int_{-1}^1 I(\mu') \mu' d\mu' \quad (2)$$

Divergence of Radiative Heat Flux Vector :

$$\nabla \cdot q_r = \sum_i [4\pi K_{em,i} I_b(T_i) - 2\pi K_{ai} \int_{-1}^1 I(\mu') \mu' d\mu'] \quad (3)$$

where I is the radiation intensity, T_i is the local temperature of species i , I_b is the intensity of blackbody emission at T_i , K_a , K_s , and K_{em} are the gray absorption, scattering, and emission coefficients of the medium, μ is the direction cosine of the polar angle measured from the x-axis, $p(\mu, \mu')$ is the phase function of the medium which is a representation of intensity scattered from the incident radiation from direction μ' into the direction under consideration μ . The subscript i represents the species considered in radiative transfer analysis which are burning aluminum droplets and aluminum oxide particles for this case. The first term on the right hand side of radiative transfer equation represents the attenuation of intensity due to absorption and scattering, the second term is the gain due to emission, and the last term is the gain due to the in-scattering into the direction μ from all other directions μ' . The sum of these three terms is equal to the left hand side which is the gradient of radiant intensity in the direction of propagation. The intensity can be obtained by solving the radiative transfer equation and the associated specific boundary conditions for different cases. Then, the radiative heat flux and divergence of radiative heat flux vector can be obtained by the integral equations (2) and (3), respectively.

Boundary Conditions

The boundary conditions at the propellant surface and at the location far away from the surface are specified as follows. The surface of burning propellant is assumed to emit and reflect diffusely with reflectivity ρ_p equal to 0.3. The value of 0.3 is based on measured results obtained by Ishihara et al. (1991). Then the radiative boundary condition for Eqn. (1) is given by

$$I(x=0, \mu > 0) = \epsilon_p I_b(T_p) + 2\rho_p \int_{-1}^0 I(x=0, \mu') \mu' d\mu'. \quad (4)$$

For typical propellant surface temperatures (600 to 1000 K), the first term on the right hand side of Eqn. (4) representing emission by the propellant surface can be neglected. In the region far away from the burning surface, the optical thickness based on the length scale of temperature change is

very large and therefore the diffusion approximation is applicable. The boundary condition at the location far away from the surface is thus written as (Tang and Brewster, 1991)

$$I(x=\infty, \mu < 0) = I_b - \frac{\mu}{K_{e_l}} \frac{dI_b}{dx} \quad (5)$$

$$K_{e_l} = K_e(1 - \omega p^*), \quad (6)$$

$$p^* = \int_0^1 \int_{-1}^1 p(\mu, \mu') \mu' d\mu' d\mu, \quad (7)$$

where ω is the albedo, K_e is the extinction coefficient, and K_{e_l} is the equivalent extinction coefficient for an optically thick anisotropic scattering medium (Tang and Brewster, 1991). Due to the fact that the aluminum oxide dominates the radiative heat transfer in this region, the contribution from the burning aluminum droplets is neglected in Eqn. (5).

Discrete-Ordinate Method

The difficulty which arises in solving the radiative transfer equation is due to the integral in the transfer equation. The discrete-ordinate method transforms the integro-differential equation to a set of differential equations by replacing the integral in the transfer equation with Gaussian quadrature as

$$\mu_j \frac{dI(\mu_j)}{dx} = - \sum_i (K_{s_i} + K_{a_i}) I(\mu_j) + \sum_i K_{e_m} I_b(T_i) + \sum_i \frac{K_{s_i}}{2} \sum_k I(\mu_k) p_i(\mu_j, \mu_k) W_k, \\ j, k = -N, \dots, N, \quad j, k \neq 0, \quad (8)$$

where $-1 \leq \mu_j, \mu_k \leq 1$ are the quadrature coordinates, and W_k are the weight factor corresponding to coordinates μ_k . This transformation constitutes a $2N^{\text{th}}$ order system of ordinary differential equations. These equations are then solved by the 4th order Runge-Kutta method (Gerald and Wheatley, 1984) associated with the double-sweeping technique. The double-sweeping technique calculates the intensity field by dividing the intensity field into two groups. One group consists of the forward intensity (i.e. $\mu_j > 0$) and the other group contains the backward intensity (i.e. $\mu_j < 0$). The forward sweeping updates the forward intensity at grid point $n + 1$ based on the information at grid point n (starting from $x = 0$ to $x = \infty$) while keeping the backward intensity unchanged. The backward sweeping updates the backward intensity at grid point $n - 1$ based on the information at grid point n (starting from $x = \infty$ to $x = 0$) while keeping the forward intensity unchanged. This technique avoids the numerical overflow phenomenon which appears in the numerical calculation of the intensity field by using the pure 4th order Runge-Kutta method.

The radiative heat feedback from the aluminum distributed combustion region to the propellant surface can be determined by

$$q_r = -2\pi \sum_k I(x = 0, \mu_k) \mu_k W_k, \quad (9)$$

where the emission from the propellant surface is neglected due to the relatively low temperature of the propellant.

Radiative Properties of Particles

The radiative heat transfer model considers only the effects of Al and Al₂O₃ particles. The Al₂O₃ particles are assumed to be spherical and polydisperse (monomodal) and to be in thermal equilibrium with the gases. The effective single-scattering albedo of aluminum oxide (ω_{ox}) is highly variable due to the fact that the optical constants are very sensitive to temperature, phase, and the level of contaminants present (Konopka et al., 1984). Reported values range from near zero for very small molten particles ($d < 0.01 \mu\text{m}$) which form in the detached flames (Glassman, 1960; Jones and Brewster, 1991) to 0.95 for larger molten particles ($d \sim 1 \mu\text{m}$) which grow from the smaller particles formed in the detached flame envelopes (Pearce, 1978; Parry and Brewster, 1991). The study by Parry and Brewster (1991) used an in-situ light scattering technique on propellant flames to measure oxide particle sizes of $1\mu\text{m}$ and an albedo of 0.95 in the vis./n.i.r. region. Since these measurements indicate that the sub-micron particles formed in the detached flames grow quickly to the one micron size range, the value of 0.95 probably best represents the albedo of the bulk smoke particles in the gas phase. Thus an albedo of 0.95 was used to represent the oxide particles in most of the calculations and the mean optical size was assumed to be $d_{32_{ox}} = 1 \mu\text{m}$. However, an albedo of 0.1 was also used to investigate the lower albedo limit.

The aluminum oxide smoke particles have highly anisotropic forward-scattering characteristics. The following phase function has a single-scattering asymmetry similar to that of the oxide smoke particles and is used as a single-scattering phase function for the smoke particles.

$$p(\theta_p) = 0.4936 \exp(2.2 \cos \theta_p) \quad (10)$$

The associated slab phase function for the Al₂O₃ particles is given by

$$p(\mu, \mu') = \frac{1}{\pi_0} \int_0^\pi p(\theta_p) d\phi_s, \quad \phi_s = 0 \quad (11)$$

where

$$\cos \theta_p = \mu \mu' + \sqrt{(1-\mu^2)(1-\mu'^2)} \cos(\phi_s - \phi_s'). \quad (12)$$

The temperature of the burning aluminum particles (T_s) is assumed to be the melting point of aluminum oxide throughout the whole region. The radiant properties of the burning aluminum droplet system are effective properties representing the complex radiative transfer which actually occurs in the luminous, oxide-laden flame envelope surrounding the droplet and between the flame envelope and the droplet itself (Brewster and Taylor, 1988). The emission from the burning droplet includes three terms : (1) the direct emission from the flame envelope with aluminum oxide at the oxide boiling or dissociation temperature, (2) the envelope emission reflected from the aluminum droplet surface, and (3) the emission from the aluminum droplet. The effective emissivity, reflectivity, and absorptivity of the burning aluminum droplet system are obtained by adding these three contributions, including multiple reflection (Brewster and Taylor, 1988) as

$$\epsilon_d = \epsilon_e \left[\frac{I_b(T_{oxbp})}{I_b(T_s)} \right] + \epsilon_e \tau_e \left[\frac{\rho_s}{1 - \rho_s \rho_e} \right] \left[\frac{I_b(T_{oxbp})}{I_b(T_s)} \right] + \epsilon_s \tau_e \left[\frac{1}{1 - \rho_s \rho_e} \right], \quad (13)$$

$$\rho_d = \rho_e + \tau_e^2 \left[\frac{\rho_s}{1 - \rho_s \rho_e} \right], \quad (14)$$

$$\alpha_d = 1 - \rho_d, \quad (15)$$

where ϵ_e , τ_e , and ρ_e represent the envelope emissivity, transmissivity, and reflectivity. The boiling (dissociation) point of aluminum oxide was taken from Glassman's data (1960) :

$$T_{\text{boiling}}(P) = 250.365 \ln(P) + 876.85. \quad (16)$$

In Eqn. (16) P is in pascals and T is in degrees K.

By assuming the particle size parameter of the aluminum oxide in the flame envelope is very small, the scattering of aluminum oxide is negligible. Assuming the envelope is isothermal, the emissivity, reflectivity, and transmissivity of the aluminum oxide-laden flame envelope are therefore :

$$\epsilon_e = 1 - \exp(-t_e), \quad (17)$$

$$\rho_e = 0, \quad (18)$$

$$\tau_e = 1 - \epsilon_e, \quad (19)$$

where t_e is the mean optical thickness of the aluminum oxide laden flame envelope. It should be noted that the emissivity of a burning aluminum droplet ϵ_d based on T_s is highly dependent on pressure and may be much greater than one due to the strong emission from the aluminum oxide at the boiling point in the flame envelope even if the optical thickness of the flame envelope is fairly small.

The size of the aluminum particles ejected from the propellant surface is very important in both the flow field and radiative heat transfer calculations. The initial aluminum agglomerate diameter (D_{AI}) in micrometers is calculated from a correlation of Nickerson et al. (1987)

$$D_{AI} = \frac{1}{(1.1508 r_B f_{m,s})^2} \quad (20)$$

where r_B is the burning rate of propellant in m/s, and $f_{m,s}$ is the total mass fraction of solids in the propellant. According to this correlation, the agglomerate size is predicted to decrease as the pressure (i.e. burning rate) and/or the metal loading increases.

Coupling of the Energy Equation and Radiative Transfer Equation

The energy equation which accounts for radiation, conduction, convection, internal energy generation, and dissipation modes of energy transport can be written in the general form (Ozisik, 1973)

$$\rho \frac{Dh}{Dt} = \frac{DP}{Dt} - \nabla \cdot (\underline{\underline{q}_c} + \underline{\underline{q}_r}) + q''' + \Phi \quad (21)$$

The energy and radiative transfer equations are coupled through the divergence of the radiative flux vector ($\nabla \cdot \underline{\underline{q}_r}$) and/or the temperature dependent properties of the medium in the flow field. The fact that the divergence depends on the local temperature at each point throughout the medium makes the problem implicit in temperature. To solve this implicit problem, the iteration method associated with successive over-relaxation technique (Anderson et al., 1984) was used.

RESULTS AND DISCUSSION

One-Dimensional Two-Phase Aluminum Combustion-Flow Field

Four different compositions of propellant were studied (Table 1). The number in Table 1 is the relative mass basis of the component in aluminized solid propellant. Propellant Al-19 is the original space shuttle propellant formulation. Figs. 1-2 show the results obtained from the one-dimensional, two-phase reacting flow model for the propellant Al-19 burning at 34 and 68 atm. The volume fraction distributions of aluminum and aluminum oxide as a function of distance from the propellant surface (x) are plotted in Fig. 1. The volume fraction of Al rapidly decreases as the volume fraction of Al_2O_3 increases. The very rapid decrease in the volume fraction of aluminum

near the propellant surface is mostly due to the acceleration of the aluminum droplets by the high speed gas away from the propellant surface. Figure 2 shows the change in aluminum diameter and the gas temperature profile. It indicates that the Al diameter decreases above the burning surface of the propellant and that burnout occurs at approximately 50 mm for pressure equal to 34 atm and 15 mm for pressure equal to 68 atm. The initial gas temperature is the adiabatic flame temperature of the AP/PBAN reactions which is approximately 2400 K. It shows that the gas temperature rises rapidly from the initial temperature near the surface and eventually reaches the AP/PBAN/Al adiabatic flame temperature of 3372 K (34 atm) and 3429 K (68 atm).

Table 1. Propellant Compositions.

Propellant	AP	PBAN	Fe ₂ O ₃	Al
Al-19	0.697	0.140	0.003	0.160
Al-15	0.722	0.145	0.003	0.130
Al-10	0.755	0.151	0.003	0.091
Al-5	0.791	0.159	0.003	0.047

The extinction coefficients of Al and Al₂O₃ are plotted in Fig. 3. The extinction coefficient of aluminum decreases rapidly as distance from the propellant increases, while the extinction coefficient of aluminum oxide increases. The extinction coefficients of Al and Al₂O₃ are of comparable magnitude only at the location very near the surface. Beyond this region, the oxide dominates the optical properties. Figure 4 shows the characteristic length for temperature change which is defined as $L = T_g^*/(dTg^*/dx)$ and $T_g^* = (T_g(x) - T_g(0)) / (\Gamma_g(\infty) - \Gamma_g(0))$. The characteristic length increases very rapidly as the distance from the propellant surface increases. The optical thicknesses of Al and Al₂O₃ based on this characteristic length are shown in Fig. 5. It is clear that near the propellant surface, burning Al droplets may play a role while far from the surface, Al₂O₃ dominates the radiative transport. As far as the pressure effect is concerned, an increase in pressure tends to increase the AP/PBAN/Al adiabatic flame temperature and push the flame closer to the propellant surface.

Coupling Effect of Energy Equation and Radiative Transfer Equation

Propellants Al-19 and Al-5 with aluminum agglomerate sizes 50 and 100 μm burning at 34 and 68 atm are examined in order to understand the coupling effect of the energy and radiative transfer equations. An aluminum oxide albedo of $\omega_{\text{ox}} = 0.95$ and a mean detached flame envelope optical thickness of $t_e = 0.2$ are used in these calculations. Table 2 lists the radiative heat feedback resulting from considering the coupling effect of the energy and radiative transfer equations. Figure 6 is a plot of gas temperature profile and local radiative heat flux distribution for the Al-19 propellant burning at 68 atm with aluminum agglomerate size of $D_{\text{Al}} = 100 \mu\text{m}$.

Table 2. Results of the coupling effect of energy and radiative transfer equations.

Propellant	Pressure (atm)	Agglomerate size (μm)	Radiative Heat Feedback (W/cm ²)	
			Coupled	Decoupled
Al-19	34	100	296	309
Al-19	34	50	314	329
Al-19	68	100	333	346
Al-19	68	50	350	364
Al-5	34	100	204	214
Al-5	34	50	205	213
Al-5	68	100	221	230
Al-5	68	50	218	225

Figure 6 shows that the gas temperature decreases slightly when the coupling effect of the transfer and energy equations is considered (except at $x \rightarrow \infty$ where the same temperature is approached). Coupling also decreases the local radiative heat flux slightly as can be seen in Fig. 6. For different propellants burning under conditions other than those of Fig. 6, the coupling effect has a similar influence on gas temperature and radiative heat flux. Table 2 shows that the predicted radiative heat feedback, for different propellants burning under different circumstances, will be about 5% lower if the coupling effect is considered. These results suggest that the coupling effect is not significant in the prediction of the radiative heat feedback. This is due to the fact that the divergence of the radiative heat flux vector is relatively small compared with the heat release from the combustion of aluminum. Although the results for the case of $\omega_{\text{ox}} = 0.1$ are not presented here, the same trends are observed and the same conclusions can be drawn. Therefore, the radiative heat feedback obtained from the decoupled energy and radiative transfer equations is used in the remaining calculations.

Effect of the Albedo of Aluminum Oxide (ω_{ox}) on Radiative Heat Feedback

The effect of aluminum oxide albedo is illustrated in Fig. 7. Radiative heat feedback to the propellant surface is plotted as a function of metal loading for a pressure of 68 atm. Two aluminum oxide smoke albedos are investigated, 0.1 and 0.95. The emissivity, absorptivity, and reflectivity of the burning aluminum droplets are assumed to be 1.0, 0.1, and 0.9 for both cases. For the case of $\omega_{\text{ox}} = 0.1$ the radiative heat feedback decreases as the metal loading of the propellant increases. This is due to the shielding effect of the very optically thick aluminum oxide smoke layer near the propellant which prevents radiative heat transfer from the high temperature core region to the propellant for the high metal loading cases. However, for the high albedo case ($\omega_{\text{ox}} = 0.95$), scattering by the smoke particles allows more efficient radiative transport of energy from the hot core region to propellant surface. Since the core temperature increases from 2994 to 3429 K (P = 68 atm) as the metal loading increases from Al-5 to Al-19, the radiative heat feedback increases with metal loading in this case. A trend similar to that of the $\omega_{\text{ox}} = 0.95$ case presented in Fig. 7 has been measured experimentally. Recently, Ishihara et al. (1991) measured the radiative heat feedback from the aluminum distributed combustion region above a burning aluminized solid propellant strand in a three-window bomb by optical fiber and showed that the radiative heat feedback increases as the metal loading increases. This suggests that $\omega_{\text{ox}} = 0.1$ may not be realistic. Therefore, $\omega_{\text{ox}} = 0.95$, which also agrees with the in-situ measurements of (Parry and Brewster, 1991), is used for further studies in this work.

Effect of Pressure on Radiative Heat Feedback

The radiative heat feedback to the propellant from burning aluminum droplets and aluminum oxide smoke particles can vary with pressure through three pressure-dependent terms : (1) the flow field¹, (2) initial aluminum agglomerate size, and (3) emissivity of burning aluminum droplets (see Eqns. (13) and (16)). Table 3 lists the results of radiative heat feedback to the propellant for the Al-19 and Al-5 propellants burning at 34, 50, and 68 atm considering the influence of flow field only while keeping the other parameters unchanged ($D_{\text{Al}} = 100 \mu\text{m}$, $\epsilon_d = 3.0$, $\alpha_d = 0.1$, $\rho_d = 0.9$). From the results in Table 3, it is clear that the pressure-dependent flow

¹ This includes primarily variations in temperature and particle volume fraction which are induced by the fact that the gas density is inversely proportional to pressure and therefore, for fixed mass flux, gas velocity is inversely proportional to pressure (see Figs. 1-5).

field has a very weak influence on the magnitude of the radiative heat feedback. This weak correlation is due to the fact that the different radiative parameters, such as volume fraction, aluminum droplet size, and gas temperature, change in a similar way with varying pressure as can be seen in Figs. 1 to 5.

Figure 8 shows results which consider the combined effect of the pressure-dependent flow field and initial aluminum agglomerate size (i.e. Eqn. (20) is used) while keeping the emissivity of burning aluminum droplets constant (i.e. $\epsilon_d = 1.0$, $\rho_d = 0.9$, $\alpha_d = 0.1$). In Figure 8, the radiative heat feedback for propellant Al-19 increased from 170 W/cm^2 to 210 W/cm^2 as the pressure increased from 10 atm to 68 atm while the agglomerate size decreased from $135 \mu\text{m}$ to $106 \mu\text{m}$. This increase in the magnitude of the radiative heat feedback is partly due to the fact that the adiabatic flame temperature increases slightly and that the high temperature core region is closer to the propellant burning surface for higher pressures. In addition, smaller aluminum agglomerates burn faster which also causes the high temperature region to move closer to the propellant burning surface. The smaller aluminum size also tends to increase the extinction coefficient of the burning aluminum droplets which results in an increase in the radiative heat flux from the distributed burning aluminum droplets to the propellant surface.

Table 3. Results of the radiative heat feedback calculation considering flow field effect only ($D_{Al} = 100 \mu\text{m}$, $\epsilon_d = 3.0$, $\alpha_d = 0.1$, $\rho_d = 0.9$).

Propellant	Pressure (atm)	Radiative Heat Feedback(W/cm^2)
Al-19	34	266
Al-19	50	271
Al-19	68	275
Al-5	34	201
Al-5	50	205
Al-5	68	208

Results considering pressure-dependent flow field and emissive properties of the burning aluminum droplets while keeping the initial agglomerate size constant at $100 \mu\text{m}$ are plotted in Fig. 9. For constant flame envelope optical thickness (i.e. $t_e = 0.2$ or 0.1), the influence of the pressure-dependent burning aluminum droplet emissivity (see Eqns. (13)-(19)) on the radiative heat feedback is not significant as can be seen in Fig. 9. The small increase which does appear in the magnitude of the radiative heat feedback as pressure increases is due to the fact that the emissivity of the burning aluminum droplets increases with increasing pressure through the oxide dissociation temperature (see Eqn. (16)).

Among the three pressure-dependent terms which may affect the magnitude of radiative heat feedback, the term (1) is probably relatively unimportant. With regard to term (2), the results from this study, based on the correlation of the initial aluminum droplet size described by Eqn. (20), show that this term is relatively weak. However, other solid propellant combustion studies have shown that the initial aluminum agglomerate size decreases with increasing pressure in a non-linear manner which is much more complicated than that described by Eqn. (20) (Sambamurthi et al., 1984). Presumably this decrease in agglomerate size occurs through the mechanism of enhanced gas-phase chemical reaction rates which compress the AP/binder flames closer to the propellant surface, resulting in smaller agglomerates. This mechanism is complicated by variable flame stoichiometry associated with heterogeneity of the propellant due to various AP particle sizes (Sambamurthi et al., 1984). Thus term (2) may be a potentially important pressure-dependent mechanism but it is not well understood at this time. A separate parametric study regarding the initial aluminum droplet size is therefore desireable and is described in the next section. As far as term (3) is concerned, the pressure-dependence of the flame envelope optical thickness has a minor

effect on the radiative heat feedback. However, the value of t_e , which itself may be pressure-dependent, is highly uncertain and further investigation of this parameter is needed.

With regard to the influence of the flame envelope optical thickness t_e on the magnitude of the radiative heat feedback, the results in Fig. 9 show that the effect of the detached flame envelope optical thickness t_e becomes more significant as the metal loading increases. Although the pressure-dependence of the emissivity of the burning aluminum droplet shows weak influence on the radiative heat feedback, the radiative heat feedback increases from 275 W/cm^2 to 346 W/cm^2 as the mean optical thickness of flame envelope increased from 0.1 to 0.2 for Al-19 propellant burning at 68 atm. This suggests that the value of the emissive properties of the burning aluminum droplets plays a more important role in determining the radiative heat feedback as the optical thickness of flame envelope increases. Further investigation of the emissive properties of the burning aluminum droplets is recommended.

Effect of Aluminum Agglomerate Size

The size of the aluminum agglomerates may have a potentially significant effect on radiative heat feedback in distributed aluminum combustion regions. However it is very difficult to predict aluminum agglomerate size at this point. Therefore a parametric study of the agglomerate size effect was conducted.

In an effort to study aluminum agglomerate size effects, Brewster and Hardt (1991) measured the aluminum agglomerate sizes of Al-AP-HTPB propellants with different metal loadings and constant AP/HTPB ratio. Their results showed that the agglomerate size increased from $100 \mu\text{m}$ to $200 \mu\text{m}$ as the metal loading increased from 10% to 20% at 52.7 atm. Further addition of metal loading to 30% did not change the agglomerate size significantly. However, the correlation of the aluminum agglomerate size described by Eqn. (20) is too crude to reveal this kind of dependence of the aluminum agglomerate size on metal loading. Furthermore, from Eqn. (20), at constant pressure, the agglomerate size is predicted to decrease as metal loading increases which is the opposite trend of that reported by Brewster and Hardt (1991). Therefore, a separate parametric study of the effect of aluminum agglomerate size on the radiative heat feedback is needed.

The results of the radiative heat feedback as a function of the aluminum agglomerate size at 68 atm are shown in Fig. 10. In this figure, the emissive properties of the burning aluminum droplets are held constant (i.e. $\epsilon_d = 3.0$, $\rho_d = 0.9$, $\alpha_d = 0.1$). Figure 10 indicates that the radiative heat feedback increases as the aluminum agglomerate size decreases. This trend becomes more significant as the metal loading of the propellant increases. At very low metal loading (Al-5) the aluminum agglomerate size shows almost no influence on the magnitude of the radiative heat feedback. For the case of $P = 34 \text{ atm}$ similar trends were found while the magnitude of the radiative heat feedback was lower by approximately 3% than the values in Fig. 10 for 68 atm.

Figure 11 is a plot of the radiative heat feedback as a function of pressure associated with different metal loadings and different agglomerate sizes. In this figure, the emissive properties of the burning aluminum droplets are still held constant at $\epsilon_d = 3.0$, $\rho_d = 0.9$, and $\alpha_d = 0.1$. Since it is not yet possible to predict agglomerate size one can only speculate on its effect. However, guided by the limited experimental results available, it is possible to make some interesting comparisons between the predictions of the present model and the limited experimental results which are available and thereby propose pertinent conditions to examine in future studies. For example, in the study of radiative heat feedback in Al-AP-HTPB propellants by Ishihara, et al. (1991), as the metal loading increased from 5 to 10% the radiative feedback remained essentially constant (although it increased from 10 to 20% Al). This observation disagrees with the present model which predicts a relatively uniform increase in radiative feedback with increasing metal loading, if agglomerate size is held constant. However, if the agglomerate size (which was not measured in the experiment (Ishihara, et al. (1991)) increased as metal loading increased from 5 to 10% the effect of increasing agglomerate size would tend to counteract that of increasing metal loading (see Fig. 10) and thus explain the observed results between 5 and 10% metal. Such a

trend of increasing agglomerate size was observed by Brewster and Hardt (1991) as noted earlier. This effect can also be observed in Fig. 11. If the change in agglomerate size with metal loading observed by Brewster and Hardt (1991) were projected to the results of Fig. 11 (i.e. if the agglomerate size increased from 100 μm to 150 μm as the metal loading changed from Al-10 to Al-15 at 68 atm), the radiative heat feedback from the Al-10 propellant with agglomerate size $D_{\text{Al}} = 100 \mu\text{m}$ (243 W/cm^2) would be very close to that of the Al-15 propellant with agglomerate size $D_{\text{Al}} = 150 \mu\text{m}$ (249 W/cm^2) as can be seen in Fig. 11. Thus there is a logical physical explanation for the observed results of Ishihara, et al. (1991) although there is admittedly a need for further experimental corroboration which could be obtained by simultaneous agglomerate size and radiative feedback measurements.

In addition to comparing predicted trends with experimental results, an effort was also made to compare the magnitudes of the radiative heat feedback. The magnitude of the radiative feedback predicted by the discrete-ordinate method ranges between 250 and 300 W/cm^2 for propellant Al-19 burning at 34 atm. This value compares favorable with the measured value of 300 W/cm^2 by Ishihara et al. (1991) under similar conditions. However, for lower metal loading, the numerically calculated value (around 230 W/cm^2 for Al-10 at 34 atm) is higher than the value (100 W/cm^2 for Al-10 at 34 atm) measured by Ishihara et al. (1991). This discrepancy at low metal loadings is probably due to the fact that the experimental conditions of Ishihara et al. (1991) did not satisfy the semi-infinite, optically thick conditions assumed in the present analysis for all runs, particularly those at low pressures and low metal loading.

SUMMARY AND CONCLUSIONS

The radiative heat transfer due to burning metal and oxide smoke particles in a two-phase, distributed aluminum combustion flow field was examined by the discrete-ordinate method. The coupling effect of the energy and radiative transfer equations was studied and found to be relatively insignificant in predicting the magnitude of the radiative heat feedback. This was attributed to the fact that the divergence of the radiative heat flux vector is relatively small compared with the heat release from the combustion of aluminum. Results showed that the magnitude of the radiative heat feedback is over-predicted by only 5% if coupling is neglected. The effect of the aluminum oxide smoke albedo was also investigated. A value of $\omega_{\text{ox}} = 0.95$ gave trends for the radiative feedback which agreed with experimental measurements for various metal loadings. The predicted radiative heat feedback was found to increase only slightly with increasing pressure, although the highly uncertain pressure-dependence of the initial aluminum agglomerate size makes this conclusion only tentative. The aluminum agglomerate size was found to have a significant effect on radiative heat feedback at high metal loading. However, the influence of agglomerate size was found to be relatively insignificant at low metal loadings. The emissive properties of the burning aluminum droplets were found to play an important role in determining the magnitude of radiative heat feedback. Since these properties are quite uncertain at this time further investigations of the emissive properties of burning aluminum droplets and the aluminum agglomerate size correlated with pressure and metal loading are recommended.

ACKNOWLEDGMENTS

Support for this work from the National Science Foundation (CBT 86-96162) and the Office of Naval Research (N00014-87-K-0547) is gratefully acknowledged. Computer time was provided by the National Center for Supercomputing Applications (NCSA) at the University of Illinois, Urbana, IL.

REFERENCES

- Anderson, D. L., Tannehill, J. C., and Pletcher, R. H., 1984, *Computational Fluid Mechanics and Heat Transfer*, McGraw-Hill Book Company, New York.

- Brewster, M. Q. and Parry, D. L., 1988,"Radiative Heat Feedback in Aluminized Solid Propellant Combustion," *Journal of Thermophysics and Heat Transfer*, Vol. 2, No. 2, pp. 123-130.
- Brewster, M. Q., and Taylor, D. M., 1988,"Radiative Properties of Burning Aluminum Droplets," *Combustion and Flame*, Vol. 72, pp. 287-299.
- Brewster, M. Q. and Hardt, B. E., 1991,"Influence of Metal Agglomeration and Heat Feedback on Composite Propellant Burning Rate," to appear in *Journal of Propulsion and Power*.
- Gerald, C. F. and Wheatley, P. O., 1984, *Applied Numerical Analysis*, Addison-Wesley Publishing Company, Inc., Reading, Massachusetts.
- Glassman, I. , 1960,"Combustion of Metals Physical Considerations," in *Solid Propellant Research, Progress in Astronautics and Rocketry*, Vol. 1, edited by M. Summerfield, Academic Press, pp. 253-258.
- Ishihara, A., Brewster, M. Q., Sheridan, T. A., and Krier, H., 1991,"The Influence of Radiative Heat Feedback on Burning Rate in Metalized Propellants," to appear in *Combustion and Flame*.
- Jones, M. R. and Brewster, M. Q., 1991,"Radiant Emission from the Aluminum-Water Reaction ," to appear in *Journal of Quantitative Spectroscopy and Radiative Transfer*.
- Konopka, W. L., Reed, R. A., and Calia, V. S., 1984," Measurements of Infrared Optical Properties of Al_2O_3 Rocket Particles," *Progress in Astronautics and Aeronautics*, Vol. 91, pp. 180-197.
- Nickerson, G. R., Coats, D. E., Dang, A. L., Dunn, S.S., Berker, D. R., Hermsen, R. L., and Lamberty, J. T., Oct. 1987,"The Solid Propellant Rocket Motor Performance Prediction Computer Program (SPP)," Version 6.0, Vols. 1-6, AFAL-TR-87-078.
- Ozisik, M. N., 1973, *Radiative Transfer and Interactions with Conduction and Convection*, John Wiley and Sons, Inc., New York.
- Parry, D. L., 1989,"Radiative Heat Transfer from Aluminum Oxide in Solid Propellant Flames," Ph.D. Thesis, University of Illinois at Urbana-Champaign.
- Parry, D. L. and Brewster, M. Q., Jan. 1991,"Optical Constants of Al_2O_3 Smoke in Propellant Flames," to appear in *Journal of Thermophysics and Heat Transfer*, Vol. 5, No. 1.
- Pearce, B. E., 1978,"Radiative Heat Transfer within a Solid Rocket Motor," *Journal of Spacecraft*, Vol. 15, No. 2, pp. 125-128.
- Price, E. W., 1984,"Combustion of Metalized Propellants," *Fundamentals of Solid Propellant Combustion, Progress in Astronautics and Aeronautics Series*, Vol. 90, edited by K. K. Kuo and M. Summerfield, AIAA, New York, pp. 479-513.
- Sambamurthi, J. K., Price, E. W., and Sigman, R. K., 1984,"Aluminum Agglomeration in Solid-Propellant Combustion," *AIAA Journal*, Vol. 22, No. 8, pp. 1132-1138.
- Sutton, G. P., 1986, *Rocket Propulsion Elements*, 5th ed., John Wiley & Sons, Inc., New York.
- Tang, K. C. and Brewster, M. Q., 1991,"Equivalent Isotropic Scattering in Optically Thick Anisotropic Scattering Media," (in preparation for submission to *International Journal of Heat and Mass Transfer*).

Captions for Figures

1. Al₂O₃ and Al Volume Fraction (Al-19).
2. Diameter of Al Droplets and Gas Temperature (Al-19).
3. Al₂O₃ and Al Extinction Coefficients (Al-19).
4. Characteristic Length for Temperature Change (Al-19).
5. Al₂O₃ and Al Optical Thicknesses Based on the Characteristic Length for Temperature Change (Al-19).
6. Coupled Gas Temperature and Radiative Heat Flux (Al-19, $\omega_{ox} = 0.95$, $t_e = 0.2$, $D_{Al} = 100 \mu\text{m}$, $P = 68 \text{ atm}$).
7. Albedo of Aluminum Oxide Effect on Radiative Heat Feedback ($P = 68 \text{ atm}$, $\epsilon_d = 1.0$, $\alpha_d = 0.1$, $\rho_d = 0.9$, D_{Al} Calculated by Eqn. (20)).
8. Pressure Effect on Radiative Heat Feedback ($\omega_{ox} = 0.95$, $\epsilon_d = 1.0$, $\alpha_d = 0.1$, $\rho_d = 0.9$, D_{Al} Calculated by Eqn. (20)).
9. Radiative Heat Feedback vs. Pressure ($\Gamma_{Al} = 100 \mu\text{m}$).
10. Radiative Heat Feedback vs. Al Agglomerate Size ($P = 68 \text{ atm}$, $\epsilon_d = 3.0$, $\alpha_d = 0.1$, $\rho_d = 0.9$).
11. Radiative Heat Feedback vs. Pressure for Different Al Agglomerate Sizes ($\epsilon_d = 3.0$, $\alpha_d = 0.1$, $\rho_d = 0.9$).

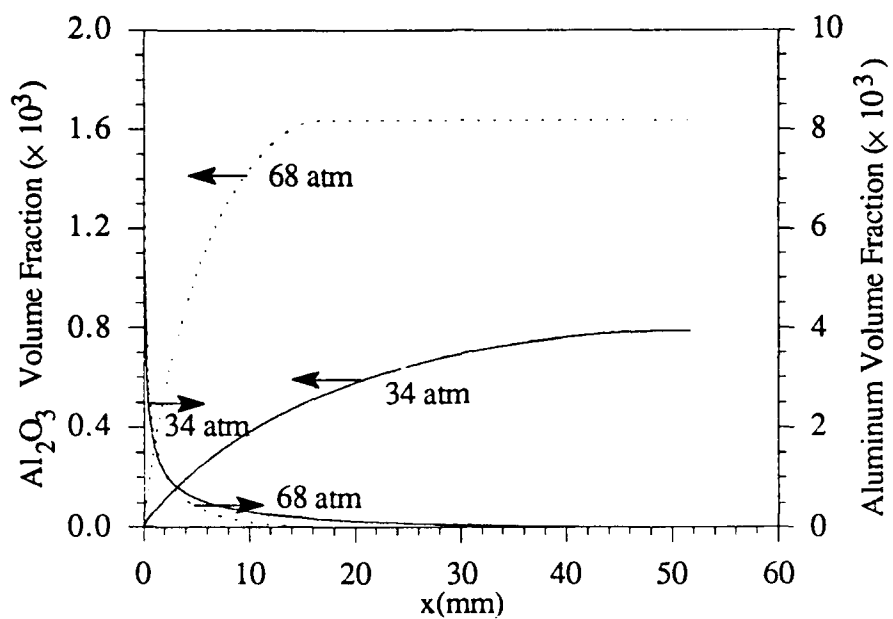


Figure 1. Al_2O_3 and Al Volume Fraction (Al-19).

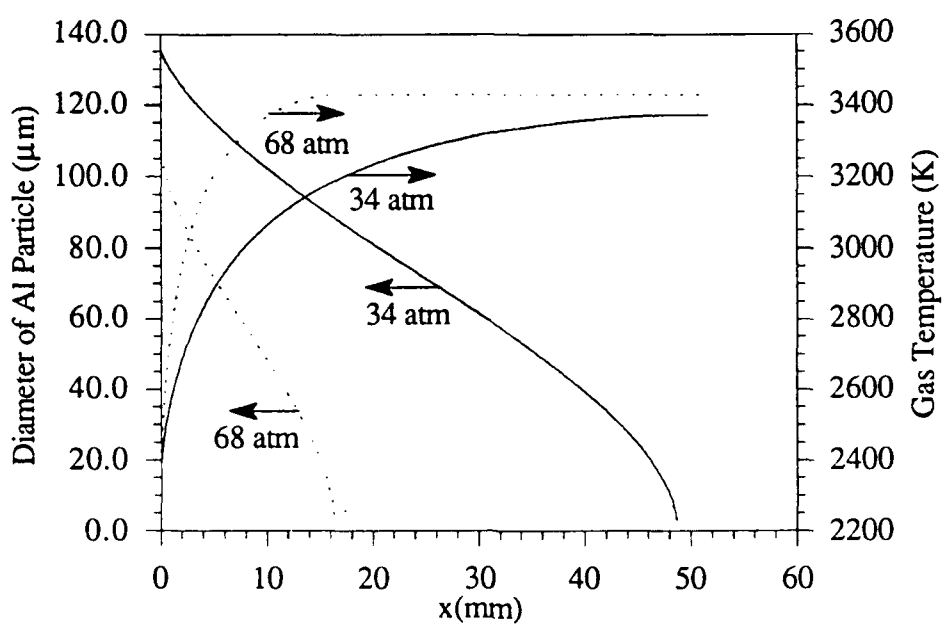


Figure 2. Diameter of Al Droplets and Gas Temperature (Al-19).

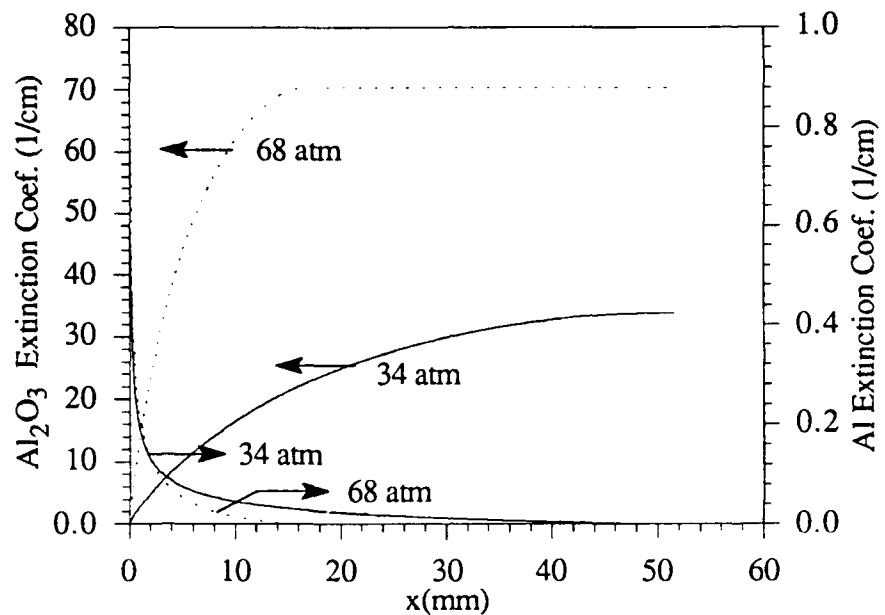


Figure 3. Al_2O_3 and Al Extinction Coefficients (Al-19).

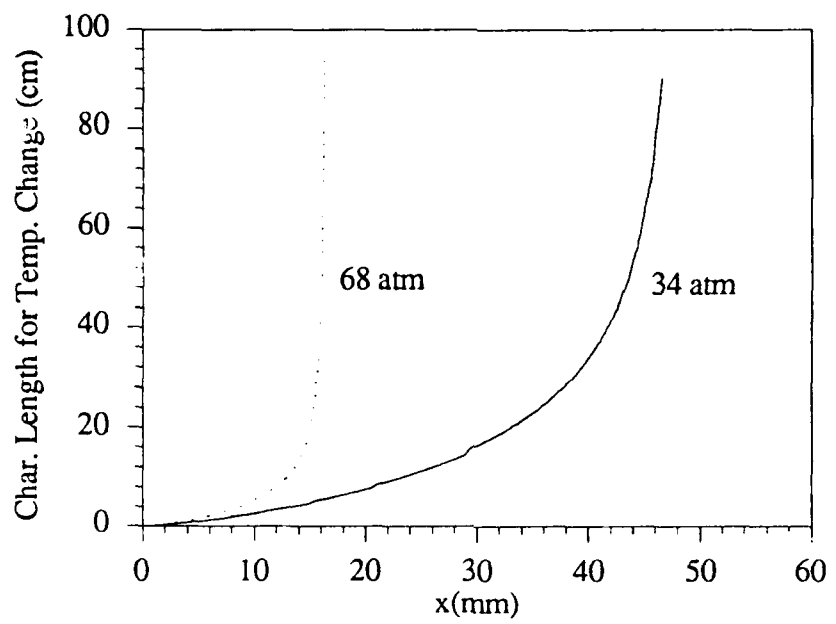


Figure 4. Characteristic Length for Temperature Change (Al-19).

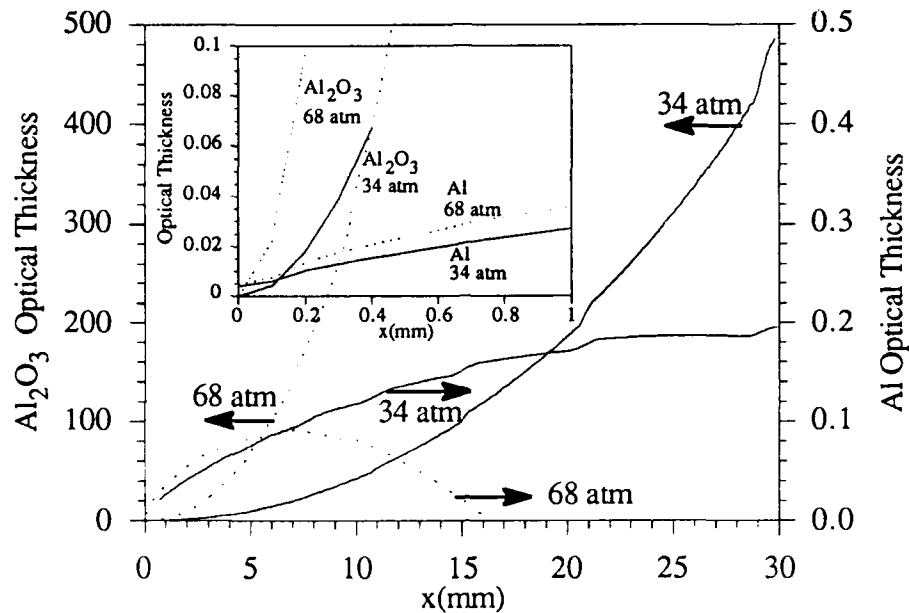


Figure 5. Al_2O_3 and Al Optical Thicknesses Based on the Characteristic Length for Temperature Change (Al-19).

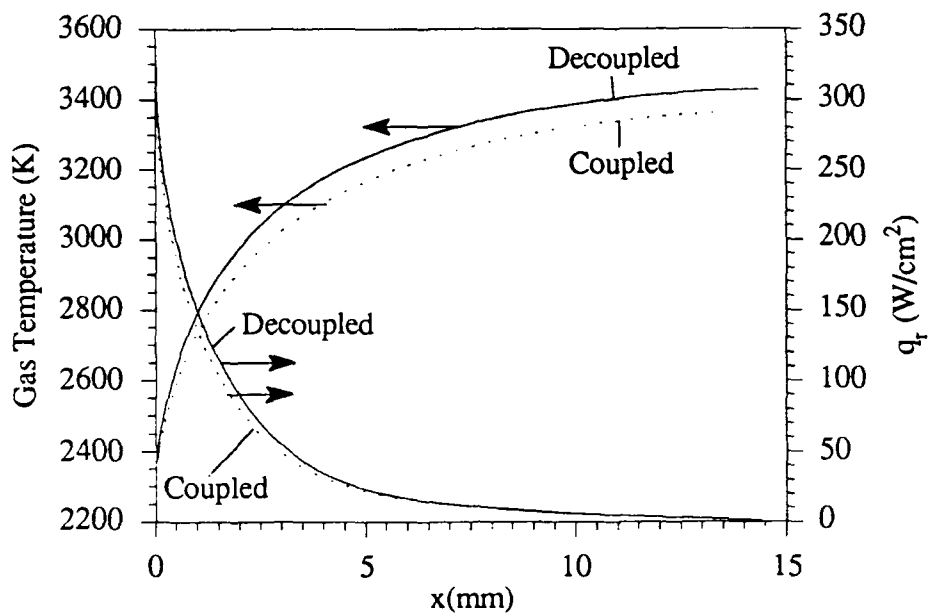


Figure 6. Coupled Gas Temperature and Radiative Heat Flux (Al-19 , $\omega_{\text{ox}} = 0.95$, $t_e = 0.2$, $D_{\text{Al}} = 100 \mu\text{m}$, $P = 68 \text{ atm}$).

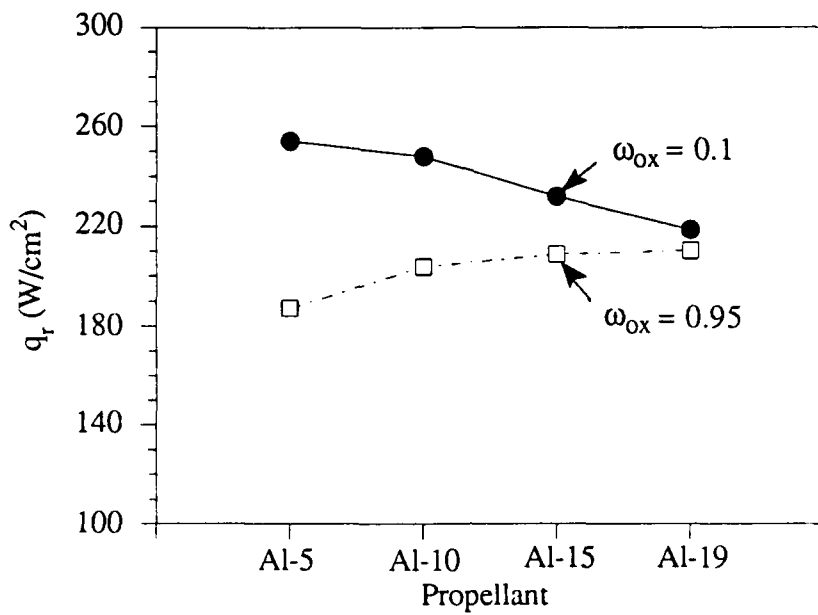


Figure 7. Albedo of Aluminum Oxide Effect on Radiative Heat Feedback ($P = 68$ atm, $\epsilon_d = 1.0$, $\alpha_d = 0.1$, $\rho_d = 0.9$, D_{Al} Calculated by Eqn. (20)).

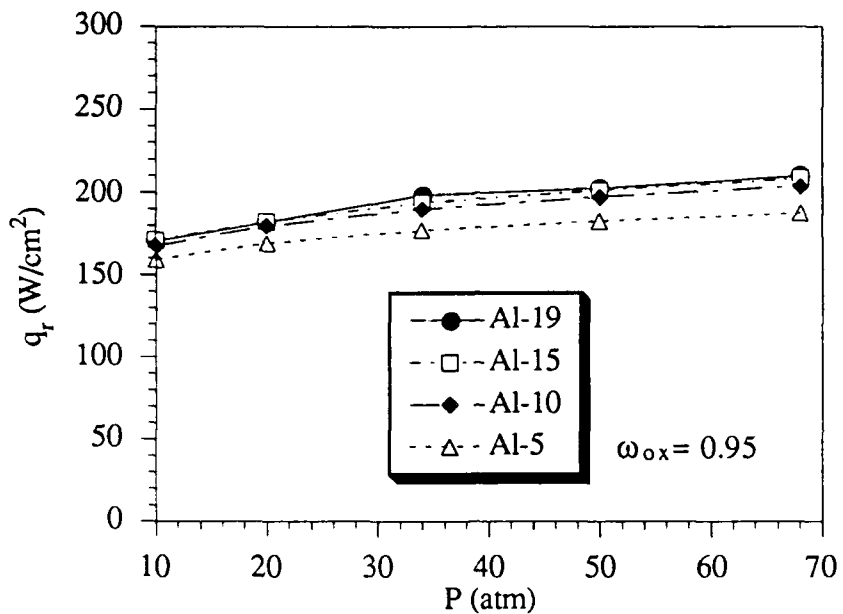


Figure 8. Pressure Effect on Radiative Heat Feedback ($\omega_{ox} = 0.95$, $\epsilon_d = 1.0$, $\alpha_d = 0.1$, $\rho_d = 0.9$, D_{AI} Calculated by Eqn. (20)).

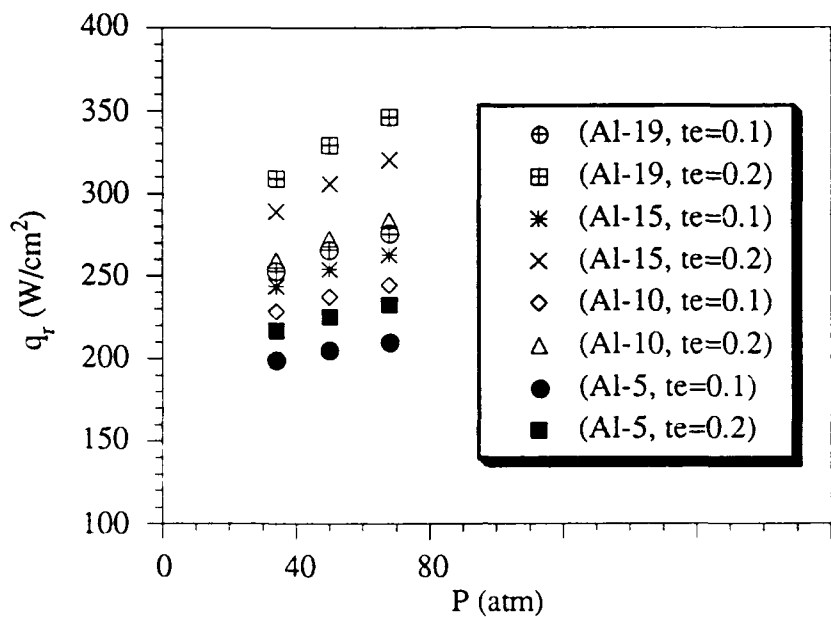


Figure 9. Radiative Heat Feedback vs. Pressure ($D_{\text{Al}} = 100 \mu\text{m}$).

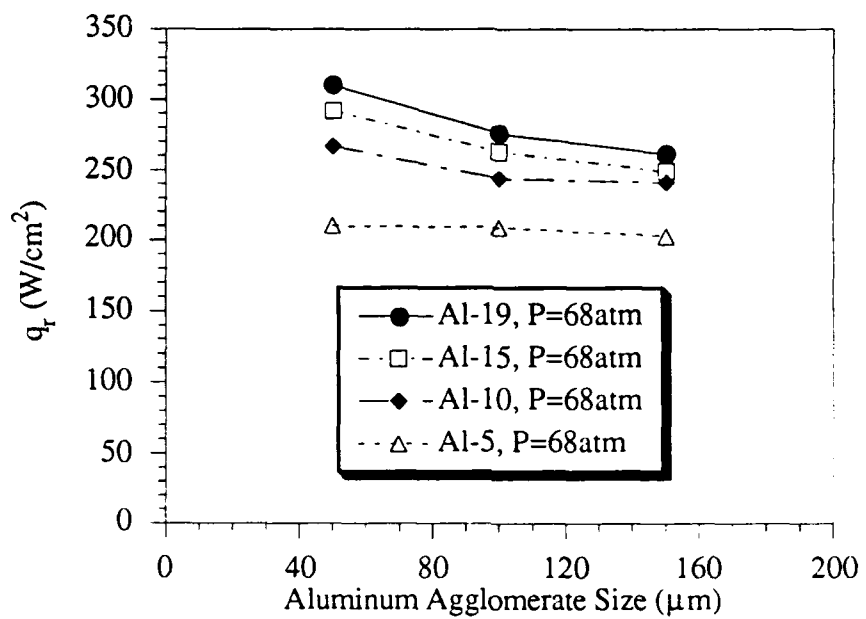


Figure 10. Radiative Heat Feedback vs. Al Aggiomerate Size ($P = 68\text{atm}$, $\varepsilon_d = 3.0$, $\alpha_d = 0.1$, $\rho_d = 0.9$).

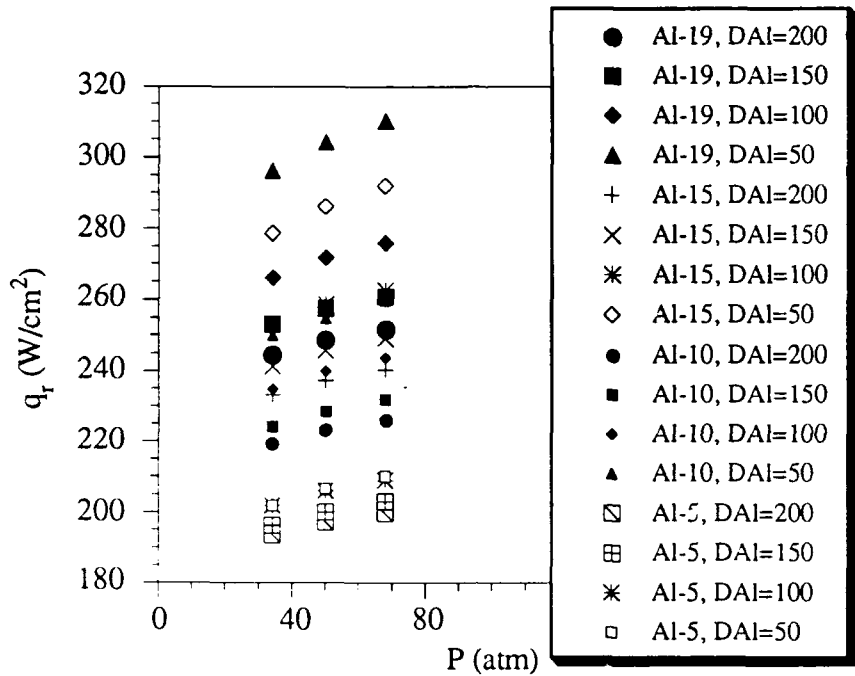


Figure 11. Radiative Heat Feedback vs. Pressure for Different Al Agglomerate Sizes
 $(\epsilon_d = 3.0, \alpha_d = 0.1, \rho_d = 0.9)$.

Radiative Heat Feedback in Aluminized Solid Propellant Combustion

M. Q. Brewster and D. L. Parry

Reprinted from



Journal of Thermophysics and Heat Transfer

Volume 2, Number 2, April 1988, Pages 123-130

AMERICAN INSTITUTE OF AERONAUTICS AND ASTRONAUTICS, INC
370 L'ENFANT PROMENADE, SW • WASHINGTON, DC 20024

Radiative Heat Feedback in Aluminized Solid Propellant Combustion

M. Quinn Brewster* and David L. Parry†
University of Illinois, Urbana, Illinois

A one-dimensional model has been developed to describe the combustion, flow, and radiant transport processes by aluminum and alumina particles near the surface of a burning aluminized composite solid propellant. The equations of mass, momentum, and energy have been solved to obtain the species concentration, velocity, and temperature profiles near the propellant surface. The decoupled radiative transfer equation has also been solved using the two-flux model to obtain the radiant flux profiles and the radiative heat feedback to the propellant surface. The results of the model indicate that the radiant heat feedback to the surface of a typical aluminized composite propellant would be 300–400 W/cm² or about 20% of the total energy flux required to heat the solid propellant to the surface temperature.

Nomenclature

<i>a</i>	= two-flux absorption coefficient
<i>a_j</i>	= polynomial coefficients for <i>C_j</i> and <i>H</i>
<i>B</i>	= two-flux back-scatter fraction
<i>C_d</i>	= aluminiun droplet drag coefficient
<i>C_p</i>	= constant pressure specific heat (mass basis)
<i>C_s</i>	= specific heat of solid propellant (mass basis)
<i>c</i>	= constant in linear regression rate law
<i>D</i>	= particle diameter
<i>fm_i</i>	= mass fraction of species or mixture <i>i</i>
<i>fv_i</i>	= volume fraction of species or mixture <i>i</i>
<i>H_i</i>	= enthalpy (molar basis) of species <i>i</i>
<i>I</i>	= total radiant intensity (forward/backward)
<i>k</i>	= two-flux emission coefficient and proportionality constant in Al burn rate equation
<i>M_i</i>	= molecular weight of species or mixture <i>i</i> or generalized chemical species symbol
<i>m''_i</i>	= mass production rate of species <i>i</i> through chemical reaction
<i>n''_i</i>	= molar production rate of species <i>i</i> through chemical reaction
<i>P</i>	= pressure
<i>Q</i>	= molar enthalpy of combustion
<i>q</i>	= total radiant heat flux (forward/backward)
<i>R</i>	= molar specific (universal) gas constant
<i>R_r</i>	= mass specific gas constant
<i>r</i>	= propellant linear regression rate
<i>s</i>	= two-flux scattering coefficient
<i>T</i>	= temperature
<i>t</i>	= time (combustion-flow model) or optical depth (radiation model)
<i>U</i>	= velocity
<i>w</i>	= single-scatter albedo
<i>x</i>	= spatial coordinate normal to and away from propellant surface
<i>y_i</i>	= mole fraction of species or mixture <i>i</i>
<i>α</i>	= absorptivity
<i>ε</i>	= emissivity or effective emission coefficient (droplet system)
<i>ν', ν''_i</i>	= stoichiometric coefficients of reactants and products
<i>ρ_i</i>	= density of species or mixture <i>i</i> or reflectivity

Received May 18, 1987; revision received Sept. 23, 1987. Copyright © American Institute of Aeronautics and Astronautics, Inc., 1988. All rights reserved.

*Assistant Professor, Department of Mechanical and Industrial Engineering. Member AIAA.

†Graduate Research Assistant, Department of Mechanical and Industrial Engineering.

Σ	= summation over <i>i</i> or <i>j</i>
μ	= dynamic viscosity

Subscripts

AP	= ammonium perchlorate
al	= aluminum droplet (including flame envelope)
B	= binder
b	= blackbody
bp	= boiling point
g	= mixture of gaseous species
go	= mixture of gaseous species and equilibrated aluminum oxide particles
<i>i</i>	= chemical species or mixture of species
<i>l</i>	= liquid
mp	= melting point
<i>o, ox</i>	= aluminum oxide or initial value
<i>s</i>	= solid propellant or surface of aluminum droplet
sp	= surface of solid propellant
<i>x</i>	= mixture quantity

Introduction

RADIATIVE heat feedback is often ignored in aluminized composite propellant combustion studies in spite of potentially significant levels of radiant flux produced by condensed Al and Al₂O₃ particles. One reason is that studies comparing the burn rates of aluminized and nonaluminized propellants have been inconclusive.¹ Sometimes aluminum enhances the burn rate and sometimes the opposite result is obtained. The percent change in the magnitude of the burn rate in either case is usually small. This behavior is puzzling in light of evidence that external radiation usually increases the burn rate of nonmetallized propellants significantly.^{2,3}

The question of whether or not radiative heat feedback is important is complicated by the fact that addition of aluminum changes several properties of the propellant and flame simultaneously (in addition to increasing the radiant heat flux). The thermal conductivity of the propellant is increased by adding aluminum, which tends to increase the burn rate. However, spectrally selective in-depth absorption of the radiant energy by opaque aluminum tends to decrease the burn rate.⁴ The overall stoichiometry is often changed by aluminum addition, which could lead to either an increase or a decrease in the burn rate. Also, the replacement of a rate controlling oxidizer particle size often occurs when aluminum is added. For example, replacing fine ammonium perchlorate (AP) with aluminum usually decreases the burn rate.

From these few considerations it can be seen that generalizations about the role of aluminum are still difficult to make. Further systematic study is needed, and one question that needs to be answered is whether the level of radiant flux is sufficient to warrant inclusion in future mechanistic studies or whether it can be neglected. This study tries to answer that question by developing a realistic yet relatively simple model of the flow and combustion of aluminum and the associated thermal radiative transport near the surface of a burning aluminized solid propellant.

Scope of the Combustion-Radiation Model

The objective of this effort is to predict the radiative heat feedback to a burning composite propellant. This is not intended to be an aluminum combustion efficiency model per se, although it includes many of the same features, such as Al droplet burn rate and two-phase flow considerations. Therefore, not included in this work are Al droplet size distribution effects and two-dimensional flow considerations, both of which are vital to combustion efficiency predictions but of minimal importance to predicting radiative feedback. A recent example of a detailed combustion efficiency model, which is similar in many aspects to this work (but neglects radiation), is that of Larson.⁵

The present model encompasses the region of space several centimeters thick adjacent to the surface of a burning AP composite propellant (Fig. 1). The origin of the x coordinate is at the surface of the burning propellant, which is stationary. The propellant is assumed to move upward at the linear regression rate r . The region above the propellant is occupied by combustion gas products of the AP/binder reaction, molten, burning aluminum droplets $\text{Al}_{(l)}$, and molten smoke oxide product $\text{Al}_2\text{O}_{3(l)}$. The AP/binder reaction is assumed to reach equilibrium at the surface of the propellant. The molten aluminum agglomerates are then dragged away from the surface by the hot, high-velocity gaseous species. As the flow proceeds in the positive x direction away from the surface, the Al droplets are accelerated by the flow and, at the same time, reaction with the oxidizing species (H_2O , CO_2 , O , OH , and O_2) in the AP/binder products occurs. This results in a decrease in the Al droplet size as the Al is consumed and an increase in the Al_2O_3 concentration as the flow moves away from the surface. Eventually the Al is totally reacted and the mixture reaches the final equilibrium composition of the AP/Al/binder flame.

Two phases are considered to be present, a gas phase and a particle phase. (The word "phase" is used broadly here to mean species that have common fluid dynamic and thermodynamic properties, in this case velocity and temperature, as opposed to strictly gas, solid, and liquid.) The gas phase is composed of all the gaseous species as well as the condensed Al_2O_3 particles, which have been swept away from the luminous flame envelope surrounding the burning aluminum droplets. These oxide particles and gas are assumed to be in thermal equilibrium at temperature T_g and to have the same

velocity U_g . The particle phase consists of the burning Al droplets (with temperature T_{al} and velocity U_{al}) and the luminous, oxide-laden flame envelope surrounding the droplets.

The entire combustion-flow-radiation model is actually composed of two separate models, a combustion-flow model and a radiation model. This separate treatment is made possible by assuming that radiation has negligible influence on energy transport in the gas phase, thus decoupling the energy and radiative transfer equations. The combustion-flow model is first solved to obtain the flowfield and thermodynamic properties. These results are then used in the radiative transfer model to solve for the intensity I^+ and I^- using the two-flux model. The quantity of primary interest is the radiant flux $q^-(x=0) = \pi I^-(x=0)$ incident on the propellant surface, assuming reflection and emission by the propellant to be negligible.

Input parameters for the model correspond to those of a typical aluminized AP composite propellant, with 70% AP, 16% Al, and 14% PBAN binder (by mass). Calculations are made at two pressures, 3.44 MPa (500 psia) and 6.87 MPa (1000 psia), covering the most important operating range experienced by most solid rocket motors.

Aluminum Combustion-Flow Model

The combustion and flow model consists of solving the coupled momentum, energy, mass, and burn rate equations (Table 1). The unknowns are the particle velocity U_{al} , gas velocity U_g , gas temperature T_g , aluminum particle diameter D_{al} , and species volume fractions f_{Vi} or mole fractions y_i .

Table 1 Aluminum combustion-flow model

Equations	Unknowns
Al particle momentum	U_{al}
Gas momentum	U_g
Energy	T_g
Al burn rate	D_{al}
Species conservation	f_{Vi} or y_i

Table 2 Governing equations (combustion-flow model)

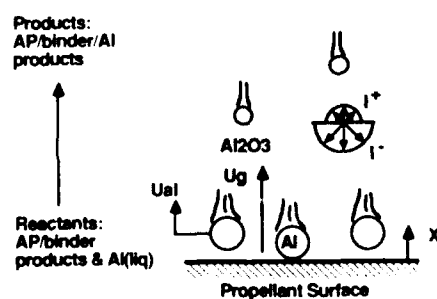


Fig. 1 1-D, 2-phase aluminum flow/combustion-radiation model.

Al particle momentum

$$\rho_{al} U_{al} dU_{al}/dx = 3\rho_g (U_g - U_{al}) (U_g - U_{al}) C_d / 4D_{al}$$

Gas momentum

$$\rho_g f_{Vi} U_g dU_g/dx = (U_g - U_{al}) m^-_{eqn} - 3\rho_g f_{Vi} U_{al} \\ \cdot (U_g - U_{al}) (U_g - U_{al}) C_d / 4D_{al}$$

Gas energy

$$\rho_g f_{Vi} C_{pr} U_g dT_g/dx = m^-_{eqn} Q(T_g, T_{eqn})$$

Al energy

$$T_{al} = T_{bp} = 393.3 \ln [P(\text{Pa})] - 2273$$

Al burn rate

$$D_{al}/D_{al} = (1 - k t / D_{al})^{1/2} \text{ (Hermsen)}$$

Species conservation

$$d(\rho_f v_i U_i)/dx = m^-_i,$$

Table 3 Supporting equations (combustion-flow model)**Drag coefficient**

$$C_d = 24/Re \quad (Re < 0.34)$$

$$C_d = 0.48 + 28 Re^{-0.8} \quad (0.34 < Re < 10^5)$$

$$Re = |U_x - U_{al}|D_{al}\rho_x/\mu_x$$

Aluminum production

$$m''_{aln} = -1.667\rho_{aln}fv_{aln}k/(D_{al})^{1/8} - kt \quad (\text{Hermsen})$$

$$k = 8.3314 \times 10^{-1} R_k A_k^{1/9} P(\text{psi})^{0.2} \quad (\text{cm}^{1/8}/\text{s})$$

$$A_k = 100 \sum y_i / y_{go} \quad i = \text{H}_2\text{O}, \text{CO}_2, \text{OH}, \text{O}, \text{O}_2$$

$$R_k = 2.70$$

$$m''_r = M_r n''_r$$

$$n''_r = (\nu'_r - \nu''_r) n''_{aln}$$

Reaction equation

$$\Sigma \nu'_r M_r + Al_{lo} \rightarrow \Sigma \nu''_r M_r$$

Enthalpy of combustion

$$Q[T_x, T_{aln}] = \Sigma (\nu''_r - \nu'_r) H_r$$

$$H_r/RT_x = a_{1r} + a_{2r}T_x/2 + a_{3r}T_x^2/3 + a_{4r}T_x^3/4 + a_{5r}T_x^4/5 + a_{6r}/T_x$$

Specific heat

$$C_{pr}/R = a_{1r} + a_{2r}T_x + a_{3r}T_x^2 + a_{4r}T_x^3 + a_{5r}T_x^4$$

Mixture relations

$$\rho_x = \Sigma f v_i \rho_i / \Sigma f v_i$$

$$f v_i = f m_i \rho_x / \rho_i = y_i \rho_x M_i / (\rho_x M_i)$$

$$M_x = \Sigma y_i M_i / \Sigma y_i$$

$$C_{px} = \Sigma f v_i \rho_i C_{pr} / \Sigma f v_i \rho_i$$

Equation of state

$$\rho_x = PM_x/RT_x$$

Al particle kinematics

$$U_{al} = dx/dt$$

Governing Equations

The governing equations for the combustion-flow model are given in Table 2. The particle momentum equation accounts for acceleration of the aluminum droplets due to the drag force of the gas phase. The gas momentum equation balances the gas acceleration (negative) with the drag force exerted by the aluminum droplets and the momentum required to accelerate the oxide and gas products from the aluminum particle velocity U_{al} to the gas velocity U_x . In both momentum equations, pressure and buoyancy forces are neglected. In the gas energy equation, the convective sensible enthalpy rise of the gas/oxide mixture is equal to the chemical energy release

due to combustion. Both conductive and radiative heat transport have been neglected. Aluminum energy is represented by the assumption that the droplets are isothermal at the metal boiling point. In the species conservation equation, the increase of mass of species i is equal to the volumetric mass production rate of that species through chemical reaction with diffusion mass transport being neglected. The aluminum burn rate is modeled with a "D₂-law" using Hermsen's data.⁸

Supporting Equations

Supporting equations for the combustion-flow model are listed in Table 3. These include the aluminum particle drag coefficient C_d , the volumetric mass (m''_r) and molar (n''_r) species production terms, the chemical reaction equation, the molar enthalpy of combustion Q (T_x , T_{aln}), the species enthalpies H_r (mass basis) and specific heats C_{pr} (molar basis), the mixture relations, the ideal gas equation of state, and the aluminum particle kinematic equation. Drag on the burning aluminum particles is modeled as drag over a sphere. The volumetric species production terms are generated from reaction stoichiometry and Hermsen's aluminum burn rate model. The thermodynamic properties H_r and C_{pr} are obtained from the widely used NASA polynomial curve-fits of McBride and Gordon.⁸⁻¹⁰ The mixture relationships express mixture density, molecular weight, and specific heat in terms of the corresponding individual constituent quantities.

In this work, any of three equivalent concentration parameters may be used to indicate chemical composition: volume fraction, mass fraction, or mole fraction. Mole fractions are used most commonly in connection with chemical equilibrium calculations. Volume fractions are the easiest to use in deriving the governing conservation equations and also appear in the particulate radiative transfer relations. And mass fractions are commonly used for specifying propellant composition. Therefore, all three descriptors are used in various places in this work and an equation is supplied in the mixture relations for converting between any two of the three. It should also be noted that the use of volume fractions implies adoption of the Amagat model of ideal gas mixtures and, therefore, all species are envisioned as having the same pressure but occupying individual volumes (i.e., partial pressure has no meaning).

Aluminum Burn Rate Modification

One term in the Hermsen burn rate law deserves special discussion. In the aluminum production terms of Table 3, the term A_k describes the influence of the ambient chemical composition on Al burn rate. This term is defined in Ref. 8 as the sum of the mole percent of oxidizing species in the ambient environment. High values of A_k corresponding to high oxidizer concentrations result in higher burning rates and vice versa. Since the empirical constants in the model are obtained from laboratory experiments where the radiation environment and velocity lag are different than the motor environment, an empirical factor R_k has also been added to compensate for these two effects.

The problem unique to this study is that if the prescribed definition of A_k is used, the predicted Al burn rates near the surface will probably be too low. This is because the empirical constants have been obtained assuming constant oxidizer mole fractions. In a rocket motor environment, the highest mole fraction of aluminum, when calculated in a "batch" sense (i.e., neglecting velocity slip of aluminum droplets), is about 16%. However, near the surface of the propellant, the velocity slip between aluminum droplets and oxidizing gases and the high density of aluminum relative to the gaseous species results in mole fractions of aluminum of approximately 97 and 59% at the propellant surface at 3.44 MPa (500 psia) and 6.87 MPa (1000 psia), respectively. If the mole fractions of oxidizing gases are based on the total mixture (with aluminum occupying 59-97% near the surface), the predicted aluminum burn rates will be too low. Therefore, the term y_{go} [moles of gas/oxidizer (gas phase) per mole of total mixture] is included

in the denominator of the A_k expression. This has the effect of putting the oxidizer mole fractions used in A_k on a basis relative to the gas phase rather than the total mixture, more in line with the experiments used to obtain the burn rate data.

Initial Conditions

The initial conditions used in solving the governing equations for the combustion-flow model are listed in Table 4. The initial aluminum volume fraction is obtained from conservation of aluminum across the propellant surface, assuming that there is no reaction between aluminum and the surrounding AP/binder and that the initial aluminum velocity at the moment the droplet ignites and begins to leave the surface is the linear regression rate of the propellant. The initial aluminum volume fraction is thus the volume fraction in the propellant modified by a slight change in density of the aluminum upon melting. This treatment does not address the mechanism of aluminum agglomeration. Thus, it does not preclude the possibility of aluminum concentration on the surface prior to agglomeration. It does not predict the agglomerate size either. The initial velocity of aluminum is so small compared with the surrounding gas velocity that it could be taken as zero.

The initial gas velocity is obtained from conservation of mass of the AP/binder matrix across the propellant/gas interface, assuming that the AP/binder reactions reach equilibrium at or very near the surface. As the AP and binder react, the density decreases by a factor of 200–300 (depending on pressure) resulting in an increase of similar magnitude in the gas velocity over the propellant burn rate.

Table 4 Initial conditions for combustion-flow model

$U_{al} = r$	$[fV_{aln} = fV_{aln1} \rho_{aln1}/\rho_{aln}]$
$U_e = fV_{APB} r \rho_{APB}/(\rho_a fV_x)$	$[fV_x = 1 - fV_{aln}]$
$T_s = 2384 \text{ K}$	
$D_{int} = 1/[1.1248 r(\text{m/s})] fM_{AP}$	
$y_j = \nu' [1 - y_{aln}]/\Sigma \nu', [\text{sum over all } j \text{ except Al}(l)]$	
$y_{aln} = fM_{aln} M_{al}/M_{al}$	
$M_{al} = M_A y_A + M_B y_B$	
$y_A = 1 - y_{aln}$	
$M_A = \Sigma \nu' M_j / \Sigma \nu', [\text{sum excludes Al}(l) \text{ and Al}_2O_3]$	
$fM_{aln} = fV_{aln} \rho_{aln}/\rho_a$	
$\rho_a = fV_{aln} \rho_{aln} + fV_x \rho_x$	
$fV_x = fV_{AP} + fV_B$	
$\rho_x = PM_x/RT_s$	
$fV_{aln} = fV_{aln1}$	
$fV_{aln1} = fM_{aln1} \rho_1/\rho_{aln1}$	
$fV_{AP} = fM_{AP}/\rho_{AP}$	
$fV_B = fM_B/\rho_B$	
$\rho_1 = 1/[fM_{aln1}/\rho_{aln1} + fM_{AP}/\rho_{AP} + fM_B/\rho_B]$	

The initial gas temperature is taken as the equilibrium adiabatic flame temperature of the AP/binder reaction at 3.44 MPa (500 psia), 2384 K. Since this is above the melting point of aluminum oxide (2320 K), solid Al_2O_3 is never encountered. Also, since energy is required to melt the solid aluminum in the propellant and raise it to its boiling point, an appropriate amount of energy 116 KJ/mole (27,767 cal/mole) is removed from the initial enthalpy of AP in this calculation to account for the energy lost from the AP/binder system. The temperature of 2384 K reflects this modification.

The initial aluminum agglomerate diameter is calculated from a correlation of Nickerson et al.⁸ The initial droplet sizes were 145 μm and 115 μm at 3.44 and 6.87 MPa (500 and 1,000 psia), respectively.

Determining the mole fractions at the surface is a little more difficult than just taking the equilibrium mole fractions from the AP/binder reaction and adding the proper stoichiometric proportion of aluminum. To do so would neglect the aluminum velocity lag at the surface and grossly underpredict the aluminum mole fraction at the surface. Instead, the starting point for the initial mole fraction determination is the statement of conservation of aluminum across the propellant surface, $fV_{aln} = fV_{aln1} \rho_{aln1}/\rho_{aln}$. The initial volume fraction fV_{aln1} can be determined from the initial mass fraction of aluminum in the propellant, fM_{aln1} . The volume fraction of liquid aluminum above the surface fV_{aln} can then be converted into the mole fraction y_{aln} , using the mixture relations of Table 3. From y_{aln} , the initial mole fractions of all the other species can be determined using the mole numbers ν_j , which are developed from the equilibrium AP/binder flame composition. It should perhaps be noted that the expression for gas molecular weight M_g in Table 4 is used only for the initial calculation, and thereafter the general mixture relation of Table 3 is used. In solving the system of governing equations, the volume fractions were actually converted into mole fractions, and the product of mole fraction times mixture density $y_j \rho_i$ was solved. This quantity could then be summed over all species to obtain the mixture density ρ_1 , which could be divided into $y_j \rho_i$ to give the mole fractions.

Numerical Solution of the Governing Equations

The governing equations were written in finite-difference form and solved numerically on a digital computer. Input data for the AP/binder and AP binder/Al/chemical equilibrium problems were obtained from the ODE module of the Air Force Rocket Propulsion Laboratory solid propellant program (SPP).⁹ A step size Δx of 10 μm was used in the combustion-flow model. The step size was increased to 100 μm for the radiation model. This increase in step size was found to be necessary to adequately model the radiative influence of the agglomerates on the surface, which were of the order of 100 μm . The aluminum volume fraction decreased so quickly away from the surface that it was necessary to force the surface value of aluminum volume fraction to extend over a step size of the order of the agglomerate size to correspond to the actual physical situation and thus accurately model the presence of the droplets near the surface.

Since diffusive mass, heat, and momentum transfer effects are neglected in the governing equations, the corresponding second-order derivative terms do not appear. The equations are forward-differenced and solved in an explicit marching scheme. That is, the known values at the first half-node are used to calculate the unknown values at the second full node, and so on.

Parameters Used in the Combustion-Flow Model

Other properties and parameters used in the aluminum combustion-flow model are listed in Table 5. The gas viscosity was taken to be constant at the value of the AP/binder flame products (3.44 MPa). Aluminum and oxide densities were also assumed to be independent of temperature.¹¹ Burn rate and propellant composition data for a typical AP composite

propellant were used in the calculations. The reactant and product stoichiometric coefficients for the 27 chemical species considered are listed in Table 6. The reactant values ν' , were calculated from the equilibrium mole fractions of the AP/binder flame based on one mole of Al₁₀ (with the input enthalpy of AP reduced to compensate for the aluminum melting and preheating, as noted earlier). The product values ν'' , were calculated from the equilibrium mole fractions of the AP/Al/binder flame based on zero moles of Al₁₀ in the products. Reactant mole numbers of aluminum compounds other than Al₁₀ are set to zero to be consistent with the assumption of no reaction between aluminum and AP below the propellant surface.

Radiation Model

Previous efforts to model radiative transfer in aluminized rocket motors have pointed out the need for including the effect of scattering by condensed Al₂O₃.¹² In this study the two-flux model of radiative transport is used. The surface of the propellant is taken to be a blackbody at zero degrees as indicated by the nonreflecting, nonemitting boundary condition. This condition can be easily modified later by including the actual scattering characteristics of the propellant and treating the problem as radiant interchange between two plane, parallel walls with the appropriate effective absorptivities, emissivities, and reflectivities.

Particulate radiation only is considered (gaseous radiation would be negligible). Participation by both oxide smoke particles in the gas phase and the burning aluminum droplets of the particle phase is considered. The alumina particles are assumed to be spherical and monodisperse (as are the aluminum droplets). The appropriate expressions for the scattering, absorption, and emission coefficients for these assumptions are given in Table 7.

The use of an emission coefficient separate from the absorption coefficient in Table 7 should be noted, since they usually are the same. This distinction is made necessary here by the fact that the burning Al/Al₂O₃ droplet systems are not in thermodynamic equilibrium. The properties of these droplets are effective properties representing the complex radiative transfer that actually occurs in the luminous, nonisothermal, oxide-laden flame envelope surrounding the droplet and between the flame envelope and the droplet itself. These effects have been considered elsewhere,¹³ and the appropriate results of that study have been incorporated here.

The key finding of Ref. 13 is that the envelope around the burning droplet, although optically thin (thus contributing

negligibly to scattering and absorption), is nevertheless a strong source of emission due to the high temperature in the envelope (approximately the oxide boiling point T_{oxbp}). The effective emissivity of a burning droplet (based on droplet temperature T_s) can be represented by the three-term expression in Table 7 for ϵ_{al} in which t_e is the optical depth of the flame envelope. The three terms correspond to direct emission (1), envelope emission reflected from the droplet surface (2), and droplet emission (3). From measurements of intensity emitted by burning aluminum droplets at the surface of aluminized AP pressed pellets, it was determined that ϵ_{al} was the order of 1.0 (Table 8). This estimate is based on the following values: $T_s = 2320$ K, $T_{oxbp} = 4820$ K (6.9 MPa), $t_e \epsilon_{ox} = 0.01$ to 0.02, $\rho_s = 0.9$, and $\epsilon_c = 0.1$. Based on a different assumed droplet temperature T_s , ϵ_{al} would be increased or decreased by the ratio $(T_s/2320)^4$ but the emitted

Table 6 Stoichiometric coefficients

M_i	ν'	ν''
Al ₂ O ₁₀	0	0.475
Al ₁₀	1	0
Al	0	0.560 $\times 10^{-1}$
AlCl	0	0.247 $\times 10^{-1}$
AlCl ₂	0	0.845 $\times 10^{-2}$
AlCl ₃	0	0.750 $\times 10^{-1}$
AlH	0	0.800 $\times 10^{-4}$
AlO	0	0.114 $\times 10^{-2}$
AlOCl	0	0.947 $\times 10^{-2}$
AlOH	0	0.225 $\times 10^{-2}$
AlO ₂	0	0.210 $\times 10^{-1}$
AlO ₂ H	0	0.378 $\times 10^{-2}$
Al ₂ O	0	0.180 $\times 10^{-1}$
CO	0.104 $\times 10^1$	0.148 $\times 10^1$
CO ₂	0.545	0.106
Cl	0.530 $\times 10^{-2}$	0.829 $\times 10^{-1}$
H	0.488 $\times 10^{-2}$	0.235
HCl	0.999	0.870
HCN	0	0.300 $\times 10^{-4}$
H ₂	0.658	0.164 $\times 10^1$
H ₂ O	0.198 $\times 10^1$	0.915
N	0	0.400 $\times 10^{-4}$
NO	0.140 $\times 10^{-3}$	0.433 $\times 10^{-2}$
N ₂	0.528	0.527
O	0.100 $\times 10^{-4}$	0.484 $\times 10^{-2}$
OH	0.262 $\times 10^{-2}$	0.566 $\times 10^{-1}$
O ₂	0.200 $\times 10^{-4}$	0.107 $\times 10^{-2}$

Table 5 Parameters used in combustion-flow model

Gas	$\mu_t = 0.744 \times 10^{-4}$ kg/ms
Aluminum (liquid)	$\rho_{al} = 2350$ kg/m ³
Aluminum oxide (liquid)	$\rho_{ox} = 3690$ kg/m ³
Burn rate	$r(\text{m/s}) = cP(\text{Pa})^n$ $c = 0.44652 \times 10^{-4}$ $n = 0.35$

Solid propellant properties

Constituent	$\rho(\text{kg/m}^3)$	AP/Al/Binder		AP/Binder	
		$H(\text{Cal/mole})$	f_m	$H(\text{Cal/mole})$	f_m
Al (s)	2700	0	0.16	0	0
AP	1950	-70,690	0.70	-98,457	0.833
Binder	950	-15,110	0.14	-15,110	0.167

Table 7 Governing equations (radiation model)

Two-flux model

$$\frac{dI^+}{dx} = -(a + s)I^+ + sI^- + k_{al}I_b(T_s) + k_{ox}I_b(T_s)$$

$$- \frac{dI^-}{dx} = -(a + s)I^- + sI^+ + k_{al}I_b(T_s) + k_{ox}I_b(T_s)$$

$$I^+(x=0) = 0$$

$$\frac{dI^+}{dx}(x=\infty) = 0$$

Two-flux coefficients

$$a = a_{al} + a_{ox}$$

$$s = s_{al} + s_{ox}$$

$$a_i = 3fv_i \alpha_i / D_i; i = al, ox$$

$$s_i = 3fv_i \rho_i Z_i / D_i$$

$$k_i = 3fv_i \epsilon_i / D_i$$

$$\epsilon_{al}(T_s) = 2t_e \epsilon_{ox} I_b(T_{oxbp}) / I_b(T_s) + 2t_e \epsilon_{al} \rho_s I_b(T_{oxbp}) / I_b(T_s) + \epsilon_c^2 \quad (1)$$

$$(2)$$

$$(3)$$

*Ref. 13.

Table 8 Parameters used in radiation model

	α	ρ	ϵ	B
Burning aluminum droplets (including flame envelope)	0.10	0.90	1.0 ^a	0.50
Aluminum oxide	0.45	0.55	0.45	0.30

^aBased on 2320 K.

intensity would be the same. Thus, the use of 2320 K for the droplet temperature in the radiation calculation is arbitrary and is not inconsistent with the use of the metal boiling point in the thermodynamic analysis. Substituting the given values into the relation for ϵ_{al} in Table 7 shows that emission by the envelope (terms 1 and 2) contributes 90% of total droplet emission, in spite of the low optical thickness of the envelope. Thus, the envelope represents a significant portion of the droplet emission.

The optical constants and size distribution of rocket Al₂O₃ have been studied by many investigators.¹⁴⁻²⁶ Although extinction efficiency, albedo, and scattering asymmetry are strong functions of particle size and wavelength for total radiant heat flux predictions, the concept of an effective gray monodispersion is valid provided the correct size, effective albedo, and scattering asymmetry are used.¹⁸ In this study an effective size of 0.3 μm , an effective albedo of 0.55 (emissivity of 0.45), and a two-flux back scatter of 0.3 were used. These values, obtained from Ref. 17, are in line with results of other investigators.^{15,16} Reference 15 reports measured size distributions for rocket exhaust particles with most probable sizes of 0.2 μm . Calculations comparing actual polydispersion properties with effective monodispersions for typical size distribution functions indicate that the effective monodisperse diameter is usually about 1.5 times the most probable diameter in this size parameter range.¹⁸ Thus, an effective diameter of 0.3 μm seems quite reasonable.

The effective albedo of molten alumina is highly uncertain at this time. Part of the reason is that it is very sensitive to the level of contaminants present (e.g., carbon, aluminum, ferric oxide, etc.),^{19,20,26} and part of the reason is that it is very sensitive to the combination of optical constants and size distribution assumed.¹⁵ Where incompatible sets of data for optical constants and size distribution are mixed, arbitrary and erroneous effective albedos are obtained. As a result, albedos for molten alumina have been reported ranging from near zero²¹ to as high as 0.925.¹² Other recent studies favor values in the 0.7–0.8 range.¹⁵ Obviously this issue needs further investigation. For the purposes of this study we have chosen to use the effective albedo of 0.55 from Ref. 17.

Results

The combustion-flow model results at 3.44 MPa (500 psia) and 6.87 MPa (1000 psia) are presented in Figs. 2–6, with radiation results in Figs. 7–9. Figure 2 shows the decrease in aluminum diameter above the propellant with burnout occurring 6 cm (3.44 MPa) and 2 cm (6.87 MPa) from the surface. The initial rapid decrease in the aluminum diameter with distance is due to the velocity slip near the surface, which can be seen in Fig. 3. Figure 4 shows that the gas temperature rises rapidly near the surface and eventually approaches the adiabatic AP/binder/Al flame temperature of 3374 K.

The mole fractions of the major fuel (Al₁₀) product (Al₂O₃) and oxidizer species (H₂O) are plotted in Fig. 5 for 6.87 MPa. The oxide mole fraction increases due to progressive aluminum combustion, and the aluminum fraction decreases as expected. The very rapid decrease in aluminum fraction in the first few millimeters is due mostly to acceleration of the aluminum droplets. The H₂O profile (which is typical of the other oxidizing species) increases initially due to aluminum

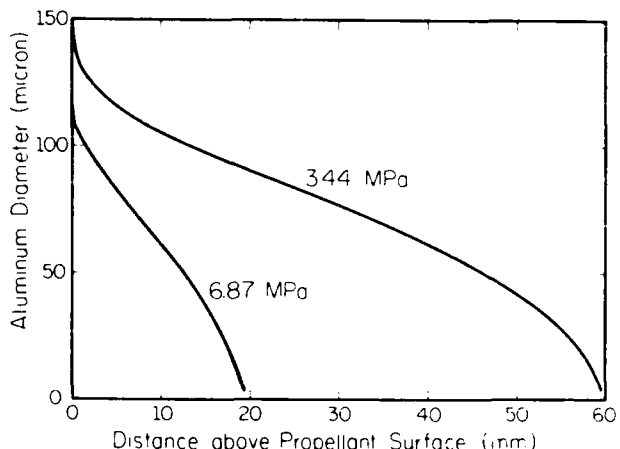


Fig. 2 Aluminum diameter.

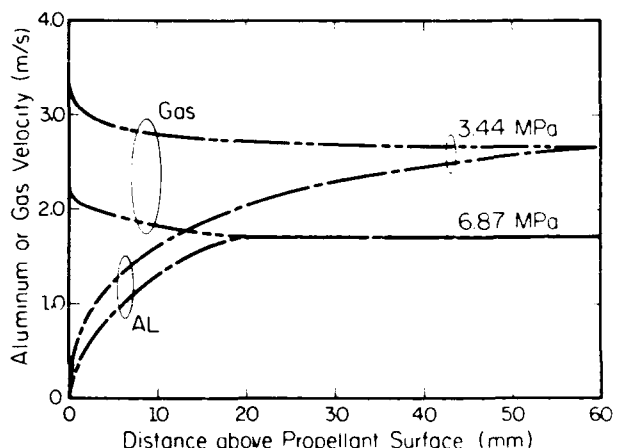


Fig. 3 Aluminum and gas velocity.

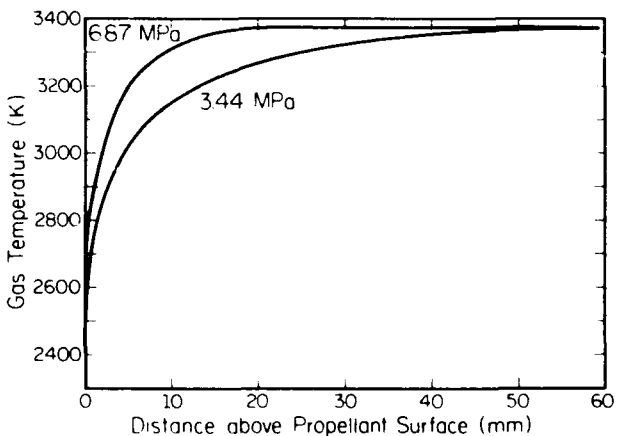


Fig. 4 Gas temperature.

acceleration and then decreases as it is consumed by combustion. Similar species profiles are obtained for the 3.44-MPa case with the variations stretched over 60 mm instead of 20 mm.

Volume fractions of alumina and aluminum are also plotted in Fig. 6 because of the important role they play in the radiative properties. The alumina volume fraction reaches 10^{-4} within 1 mm of the surface at 3.44 MPa, while the aluminum drops from 10^{-1} to 10^{-3} in the same distance.

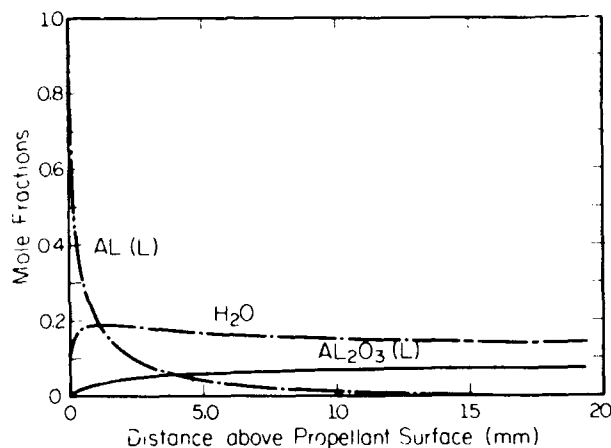
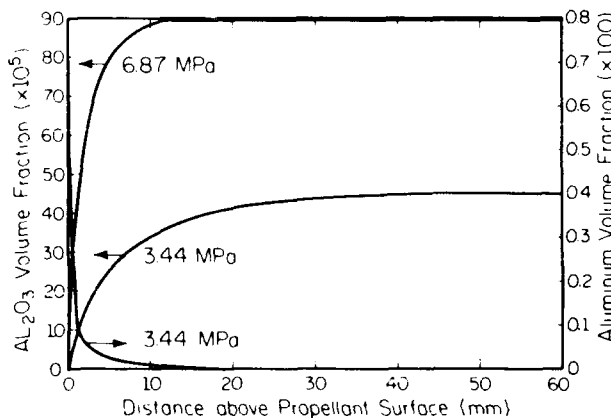
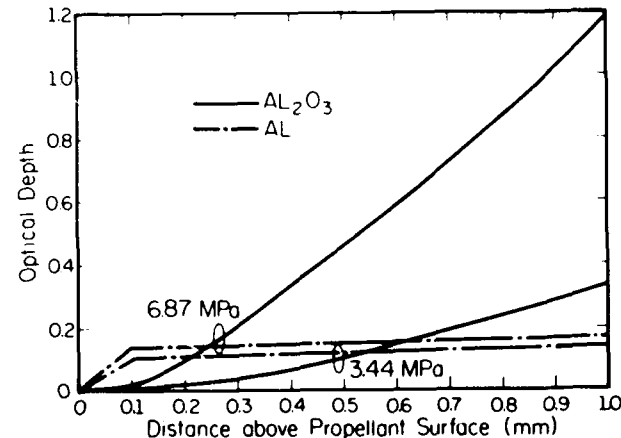


Fig. 5 Major constituent mole fractions (6.87 MPa).

Fig. 6 Al₂O₃ and Al volume fractions.Fig. 7 Optical depth of Al and Al₂O₃.

The optical depth normal to the propellant surface due to alumina and that due to aluminum are plotted in Fig. 7. Within about 300-600 μm of the surface, the two optical depths are of comparable magnitude. Beyond that point, the oxide begins to dominate, and the medium eventually becomes optically thick due to oxide.

The radiant fluxes ($q = \pi I$) are plotted in Fig. 8. Near the surface the forward flux (away from the surface) is very small due to the nonreflecting, nonemitting boundary condition. The backward flux (toward the propellant) at $x = 0$ represents the flux that would be incident on the propellant surface and for $\epsilon_{al} = 1$ has a magnitude of 290 W/cm^2 (3.44 MPa) and 330

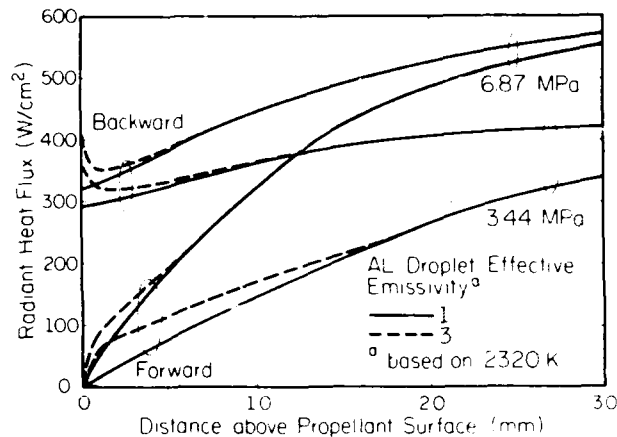
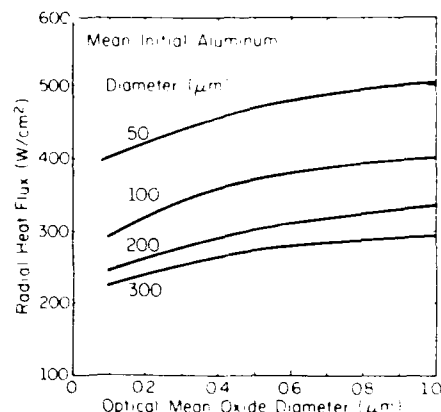


Fig. 8 Forward and backward radiant heat flux.

Fig. 9 Effect of Al and Al₂O₃ size on radiant heat feedback (6.87 MPa, $\epsilon_{al} = 1$).

W/cm^2 (6/87 MPa). Because of the uncertainty that still remains in the actual value of the effective emissivity of burning aluminum droplets, the radiant flux is also presented for an assumed value of $\epsilon_{al} = 3$ (based on 2320 K). This value is felt to be near the upper limit and is based on extrapolation from reported brightness and color temperatures of aluminum photo flash lamps.²² It may be argued that since the value of $\epsilon_{al} = 1$ was determined from measurements of burning droplets in pure AP flames, a higher value is appropriate for propellant flames due to the higher temperature of the gas surrounding the droplets (2300-2400 K compared with 1200-1400 K for AP). This difference in gas temperature could make a significant difference in the intensity emitted by the condensed Al₂O₃ in the flame envelope. The results in Fig. 8 for $\epsilon_{al} = 3$ show that the burning aluminum droplets contribute significantly to the radiant heat feedback to the propellant surface by increasing the flux to 360 W/cm^2 (3.44 MPa) and 400 W/cm^2 (6.87 MPa). Since the flame envelope is at such a high temperature and is such a significant source of emission from the droplets, the spectral distribution of the flux back to the propellant would be represented by blackbody radiation at 4000-4800 K, while the magnitude of the flux would correspond to a blackbody at 2700-2900 K.

To investigate the effect of the assumed aluminum and oxide particle sizes on the radiant flux, additional calculations were performed varying these sizes, and the results are presented in Fig. 9. It can be seen that smaller aluminum droplets, which would tend to burn out closer to the propellant surface, would result in more radiant heat feedback. Smaller oxide particles, on the other hand, would tend to decrease the radiant feedback due to an increase in optical depth in the relatively cold region near the propellant surface.

Table 9 Heat flux to propellant surface (W/cm²)

Incident radiant heat flux (% of total)

Heat flux (W/cm ²)	3.44 MPa	6.87 MPa
q^*	1240	1560
q rad ($\epsilon_{\text{rad}} = 1$)	290 (23%)	330 (21%)
q rad ($\epsilon_{\text{rad}} = 3$)	360 (29%)	400 (26%)

$$q^* = \rho_{\text{sp}} C_{\text{sp}} (T_{\text{sp}} - T_{\infty})$$

$$\rho_{\text{sp}} = 1.77 \text{ g/cm}^3; C_{\text{sp}} = 1.4 \text{ J/gK}$$

$$T_{\text{sp}} = 875 \text{ K}; T_{\infty} = 300 \text{ K}$$

*Required to heat propellant to surface temperature T_{sp} .

Comparison with Total Heat Feedback Requirement

The radiant heat feedback predicted by this model is compared in Table 9 with an estimate of the total energy flux required to raise the initial, cold solid propellant to an average surface temperature of 875 K. Although complex details of the heat transfer at the surface are ignored by taking the energy balance below the propellant surface, this comparison is probably still valid because most of the radiant energy would be transmitted past the complex surface zone and absorbed or scattered in depths below the surface. The total energy flux requirement is estimated as 1240 and 1560 W/cm² at 3.44 and 6.87 MPa, respectively. For a burning droplet emissivity of $\epsilon_{\text{rad}} = 1$, the fraction of radiant contribution to the total heat feedback is estimated as 23% at 3.44 MPa and 21% at 6.87 MPa. These percentages increase to 29% and 26%, respectively, for $\epsilon_{\text{rad}} = 3$, based on 2320 K.

It is also interesting to consider radiative effects connected with the spectral distribution of the radiation heat feedback. As noted earlier, although the flux levels correspond to blackbody radiation at 2700–2900 K, the spectral distribution is probably closer to that of a blackbody at 4000–4800 K, depending on pressure. Assuming 4000 K, half of the radiant energy would be below 1 μm wavelength, which is the approximate cutoff wavelength for absorption for many of the transition metal oxides that have demonstrated significant catalytic behavior in composite propellants (e.g., Fe₂O₃, Cr₂O₃, Cu₂O, CuO, copper chromite, etc.). This suggests the possibility of a selective absorption/emission mechanism acting instead of or in addition to the chemical catalytic mechanism.

Conclusions

Development of a model for combustion, flow, and radiation by aluminum and aluminum oxide near the surface of a burning solid propellant has led to the conclusion that the level of radiant flux back to the propellant surface is 300–400 W/cm², which represents about 20% of the total energy flux required to heat the solid propellant to the surface temperature. This radiant contribution may be partially responsible for the pressure decoupling influence aluminum addition seems to have on oscillatory solid propellant combustion. The radiation contribution should be considered more carefully in future mechanistic combustion studies.

Acknowledgments

Support for this work from the National Science Foundation (CBT86-96162), Morton Thiokol Inc./Wasatch Division, and the Office of Naval Research is gratefully acknowledged.

References

- Price, E. W., "Combustion of Metallized Propellants," *Fundamentals of Solid Propellant Combustion, Progress in Astronautics and Aeronautics Series*, Vol. 90, edited by K. K. Kuo and M. Summerfield, AIAA, New York, 1984, p. 502.
- Caveny, L. H., Ohlemiller, T. J., and Summerfield, M., "Influence of Thermal Radiation on Solid Propellant Burning Rate," *AIAA Journal*, Vol. 13, Feb. 1975, p. 202–205.
- Ibiricu, M. M. and Willimas, F. A., "Influence of Externally Applied Thermal Radiation on the Burning Rates of Homogeneous Solid Propellants," *Combustion and Flame*, Vol. 24, 1975, pp. 185–198.
- Brewster, M. Q. and Patel, R. S., "Selective Radiative Preheating of Aluminum in Composite Solid Propellant Combustion," *Journal of Heat Transfer*, Vol. 109, No. 1, 1987, pp. 179–184.
- Larson, R. S., "Prediction of Aluminum Combustion Efficiency in Solid Propellant Rocket Motors," *AIAA Journal*, Vol. 25, Jan. 1987, pp. 92–91.
- Hermans, R. W., "Improved Technical Elements for SSP: Combustion Efficiency Models," CPIA 321, 7180, pp. 53–60.
- Salita, M., "Physical Model and Numerical Correlations to Predict Combustion Inefficiency in Solid Rocket Motors," Morton-Thiokol/Wasatch Div., UT, IOM 2814-80-M154, Dec. 1980.
- Nickerson, G. R., Coats, D. E., Hermans, R. W., and Lamberty, J. T., "A Computer Program for the Prediction of Solid Propellant Rocket Motor Performance (SPP)," Vols. 1–5, AFRPL TR-83-036, Sept. 1984.
- Gordon, S. and McBride, B. J., "Computer Program for Calculation of Complex Equilibrium Compositions, Rocket Performance, Incident and Reflected Shocks, and Chapman-Jouget Detonations," NASA SP 273, 1971.
- McBride, B. J. and Gordon, S., "Fortran IV Program for Calculation of Thermodynamic Data," NASA TN-D-4097, 1967.
- Micheli, P. L. and Schmidt, W. G., "Behavior of Aluminum in Solid Rocket Motors," AFRPL TR-77-29, Vol. 1, 1977.
- Pearce, B. E., "Radiative Heat Transfer within a Solid Propellant Rocket Motor," *Journal of Spacecraft and Rockets*, Vol. 15, March–April, 1978, pp. 125–128.
- Brewster, M. Q. and Taylor, D. M., "Radiative Properties of Burning Aluminum Droplets," presented as Paper WSS-CT 87-13 at Western States Section Combustion Institute Meeting, Provo, UT, April 6–7, 1987; also *Combustion and Flame* (submitted for publication).
- Gal, G. and Kirch, H., "Particulate Optical Properties in Rocket Plumes," AFRPL TR-73-99, Nov. 1973, pp. 28–29.
- Konopka, W. L., Reed, R. A., and Calia, V. S., "Measurements of Infrared Optical Properties of Al₂O₃ Rocket Particles," *Progress in Astronautics and Aeronautics*, Vol. 91, 1984, pp. 180–197.
- Driscoll, J. E., Nicholls, J. A., Patel, V., Shahidi, B. K., and Liu, T. C., "Aluminum Combustion at 40 Atmospheres Using a Reflected Shock Wave," *AIAA Journal*, Vol. 24, May 1986, pp. 856–858.
- Brewster, M. Q. and Parry, D. L., "In-Situ Measurements of Alumina Particle Size and Optical Constants," AIAA Paper 87-1582, June 1987.
- Hansen, J. E. and Travis, L. D., "Light Scattering in Planetary Atmospheres," *Space Science Reviews*, Vol. 16, 1974, pp. 527–610.
- Pluchino, A. B. and Masturzo, D. E., "Emissivity of Al₂O₃ Particles in a Rocket Plume," *AIAA Journal*, Vol. 19, Sept. 1981, pp. 1234–1237.
- Rieger, T. J., "On the Emissivity of Alumina-Aluminum Composite Particles," *Journal of Spacecraft and Rockets*, Vol. 16, Nov.–Dec. 1979, pp. 438–439.
- Glassman, I., "Combustion of Metals Physical Considerations," *Progress in Astronautics and Rocketry*, Vol. 1, 1960, pp. 253–257.
- Rautenberg, T. H. Jr. and Johnson, P. D., "Light Production in Aluminum-Oxygen Reaction," *Journal of the Optical Society of America*, Vol. 50, No. 6, June 1960, pp. 602–606.
- Drew, C. M., Gordon, A. S., and Knipe, R. H., "Study of Quenched Aluminum Particle Combustion," *Progress in Astronautics and Aeronautics*, Vol. 15, 1964, pp. 17–39.
- Carlson, D. J., "Emittance of Condensed Oxides in Solid Propellant Combustion Products," Tenth Symposium (International) on Combustion, The Combustion Institute, 1965, pp. 1413–1424.
- Adams, J. M., "A Determination of the Emissive Properties of a Cloud of Molten Alumina Particles," *Journal of Quantitative Spectroscopy and Radiative Transfer*, Vol. 7, 1967, pp. 273–277.
- Dobbins, R. A. and Strand, L. D., "A Comparison of Two Methods of Measuring Particle Size of Al₂O₃ Produced by a Small Rocket Motor," *AIAA Journal*, Vol. 8, No. 9, Sept. 1970, pp. 1544–1550.
- Mularz, E. J. and Yuen, M. C., "An Experimental Investigation of Radiative Properties of Aluminum Oxide Properties," *Journal of Quantitative Spectroscopy and Radiative Transfer*, Vol. 12, 1972, pp. 1553–1568.
- Orguc, S., Pruitt, T. E., Edwards, T. D., Youngborg, E. D., Powers, J. P., and Netzer, D. W., "Measurement of Particulate Size in Solid Propellant Rocket Motors," *Proceedings of 1987 JANNAF Combustion Meeting* (to be published) CPIA Publications.

Radiative Properties of Burning Aluminum Droplets

M. QUINN BREWSTER

Department of Mechanical and Industrial Engineering, University of Illinois at Urbana-Champaign, Urbana, IL 61801

and

DALE M. TAYLOR

Hercules Incorporated, Aerospace Division Bacchus Works

The spectral intensity (790 nm) emitted during the combustion of pressed pellets composed of ammonium perchlorate (AP) and aluminum has been measured. Aluminum mass fraction content was varied from 0.5% to 6.0%. The combustion bomb pressure ranged from the low pressure deflagration limit (near 650 psia or 4.5 MPa) to 1100 psia or 7.6 MPa. Based on the intensity measurements, the effective blackbody emission temperature of the burning droplets was well above the local gas temperature and in excess of the adiabatic flame temperature assuming complete Al combustion. The higher intensities were attributed to continuous emission by molten Al₂O₃ in the flame envelope surrounding the molten Al droplets as well as emission by the Al droplets themselves. A two part model of the radiant transport in the burning droplet system and between droplets was developed for comparing the theoretical and measured spectral intensities to estimate the magnitude of the radiative parameters of the burning Al droplets. From this model, the optical depth of the Al₂O₃ flame envelope surrounding the droplet was estimated to be of the order of 10⁻². It was concluded that scattering and absorption by the envelope were negligible whereas emission was not. The effective radiative properties of the burning droplet system were predicted and the importance of radiative transfer in vapor phase combustion of liquid metal droplets was discussed.

1. INTRODUCTION

While it is generally recognized that radiative heat transfer plays a minor role in the burning behavior of nonmetallized solid propellants it is quite possible that radiative transfer plays a significant role in the combustion of metallized (particularly aluminum-containing) solid propellants. When aluminum is added as a fuel to modern composite solid propellants, its combustion generally takes place in the form of vapor-phase droplet combustion in the gas phase away from the propellant surface. Since the aluminum combustion usually takes place away from the main combustion surface of the solid propellant some investigators

feel that it could not influence the burn rate of the solid propellant [1]. However, some studies have shown that addition of aluminum to composite propellants can, in certain cases, significantly alter the burn rate of the propellant [2, 3]. In addition, recent studies [4] have shown that the optical properties of modern composite propellants are such that radiative heat feedback to the propellant would be selectively absorbed by the aluminum, leading to preferential preheating of the aluminum in the solid propellant. Clearly, the role of radiative heat feedback in solid propellant combustion is still uncertain and needs to be given further careful consideration.

There have been numerous studies on the

combustion of single aluminum droplets [5-8]. Most of these have indicated that the radiant flux present is sufficient to affect appreciably the combustion of a single droplet. However, no attempts appear to have been made to estimate the radiative properties of a burning aluminum droplets. In order to estimate the radiative heat feedback to the burning surface of an aluminized solid propellant, the optical properties of the burning aluminum droplets must be determined. The purpose of this study was to estimate these properties from a comparison of experimental data, obtained from the combustion of pressed pellets of ammonium perchlorate (AP) and aluminum, with an analytical model of the radiant transport process.

2. DESCRIPTION OF THE BURNING DROPLET MODEL

A depiction of the radiative transfer model applied to the burning aluminum droplets in the pellet flame can be seen in Fig. 1. The droplets are commonly the product of aluminum agglomeration at the burning surface. These droplets have been found to be of the order of 100 μm to 400 μm depending on burn rate and AP mass fraction [9, 10]. However, they can be near the size of the original aluminum particles added to the propel-

lant. The size of the condensed oxide particles remains a subject of investigation, but several studies indicate that they are predominantly submicron [1, 11, 12].

The molten aluminum droplet is surrounded by a highly luminous metal vapor flame envelope containing a large concentration of the metal oxide (Al_2O_3). The temperature profile through the thickness of the envelope is assumed to be constant at the oxide boiling point temperature T_o because the oxide is condensing in the envelope following its formation [5, 7]. One-dimensional, plane-parallel radiant exchange between the envelope and the droplet is assumed. The plane-parallel assumption is reasonable at pressures above 600 psia (4.1 MPa) where the ratio of the envelope to droplet diameters is reported to be 1.1-1.2 [13]. No pellets were successfully burned below this pressure.

The droplet temperature T_s is constrained to be at or below the metal boiling point (2500-3800K depending on pressure) and above the oxide melting point temperature (2320K) [1]. The emissivity of the droplet surface ϵ_s is not known with great accuracy, but is probably considerably larger than that of solid aluminum. Studies of molten aluminum optical properties indicate that the visible and near infrared emissivity at 1200K is around 0.1 [14, 15]. Laser target studies indicate

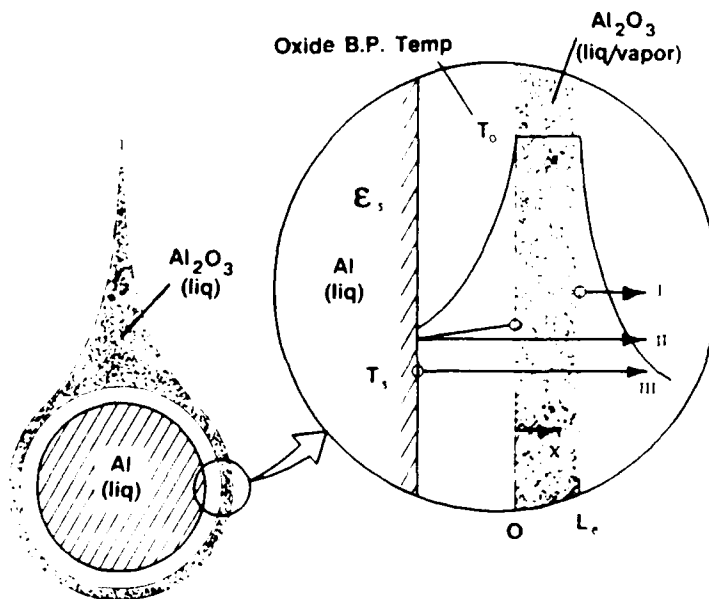


Fig. 1. Radiative model of oxide envelope/aluminum droplet.

that as the temperature of the metal approaches the boiling point the emissivity may increase substantially [16, 17]. In addition, the droplet surface emissivity may increase due to accumulation of oxide on the surface either by condensation or heterogeneous reaction.

The temperature profile near the droplet increases rapidly from the droplet temperature to the oxide boiling point temperature at the inner edge of the oxide envelope ($x = 0$). A fraction of the metal oxide perhaps dissociates [6-8] while the majority of it condenses. The oxide envelope itself is considered isothermal due to the oxide condensation process which is occurring. The temperature then rapidly decreases as the condensed oxide mixes with the relatively cold gases generated from the combustion of AP. These particles are then transported away by bulk convective motion of the surrounding gases [8]. For droplets near the pellet surface the surrounding gas would be composed of monopropellant combustion products.

The effect of a nonisothermal temperature profile through the oxide envelope has been investigated [18]. Due to the complexity and uncertainty associated with the additional parameters of a nonisothermal profile an isothermal profile is adopted here. The net effect of the isothermal assumption is to decrease slightly the effective envelope optical thickness obtained from the model. (It should be noted that the values reported for the envelope oxide thickness in [18] were actually orders of magnitude larger than those reported here. This is not due to the difference between isothermal and nonisothermal assumptions but is due to a neutral density filter calibration error in [18].)

3. DESCRIPTION OF THE RADIATIVE TRANSPORT MODEL

The radiative transport within the pellet flame is treated in two parts. The first part is the transport in the oxide envelope (denoted by the subscript e) described above and pictured in Fig. 1. The result of this first analysis is the determination of the effective properties of the droplets. The second part is the transport among the burning droplets in

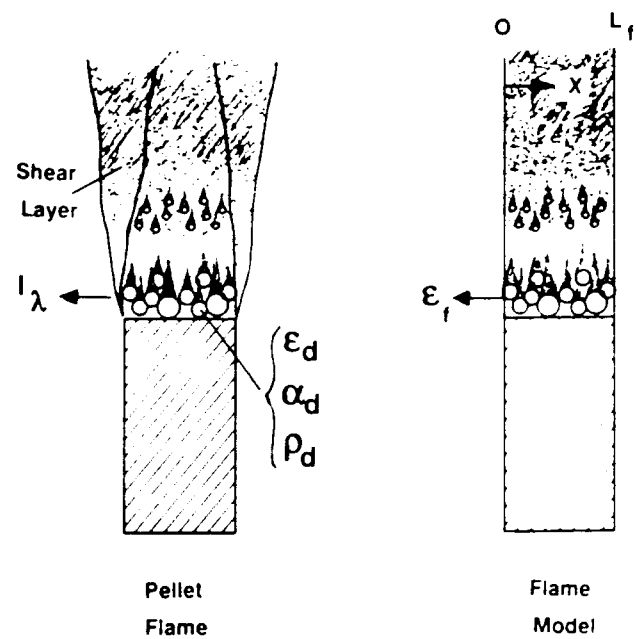


Fig. 2. Radiative model of pellet flame.

the pellet flame (denoted by the subscript f) to determine the resultant intensity emitted by the flame as shown in Fig. 2. In this part of the analysis, participation by oxide particles entrained in the gas phase (excluding the portion comprising the droplet envelope) is neglected. This is justified by the fact that in the experimental study intensities were measured at the pellet surface before significant concentrations of oxide had been produced by Al combustion.

The radiative transfer equation is solved by making the semiisotropic intensity approximation [19, 20] in both the oxide envelope (part one of the analysis) and in the droplet-to-droplet transfer in the pellet flame (part two of the analysis). The solution of the envelope problem is further reduced to two simpler problems by superposition. The first envelope subproblem is that of emission by the oxide layer with the assumed constant temperature profile discussed above. This emission is into blackbody surroundings at 0K. The oxide envelope emissivity has been denoted ϵ_e . The second envelope subproblem is that of absorption, reflection, and transmission of diffuse incident flux by a nonemitting particle envelope to determine the effective absorptivity, reflectivity, and transmissivity of the envelope. These properties are denoted by α_e , ρ_e , and τ_e . With the

determination of the envelope properties, the net intensity $I_e(x = 0)$ emitted from the oxide envelope toward the aluminum droplet is obtained from Eq. (1). The net intensity $I_e(x = L_e)$ emitted by the oxide envelope/droplet system into the surrounding is obtained from Eq. (2):

$$I_e(x=0) = \epsilon_e \left(\frac{1 - \rho_s}{1 - \rho_s \rho_e} \right) I_b(T_o) \\ - \epsilon_s \left(\frac{1 - \rho_e}{1 - \rho_s \rho_e} \right) I_b(T_s), \quad (1)$$

In Eqs. (1) and (2), the droplet surface properties are denoted by the subscript s. The three terms on the right-hand side of Eq. (2) are the three envelope/droplet intensity contributions depicted in Fig. 1. These can be described as follows: (I) the direct emission from the oxide particle envelope toward the surroundings, (II) the inward emission from the envelope toward the aluminum droplet which is subsequently reflected back and transmitted through the envelope and out into the surroundings, and (III) the emission from the aluminum droplet transmitted through the oxide envelope and out into the surroundings.

The solution of the pellet flame problem does not require any subformulation since there is not an appreciable amount of radiation incident on the flame from the surroundings. Thus, it is purely an emission problem.

Although the semiisotropic intensity model equations are well known, they are repeated here in nondimensionalized form [Eqs. (3)-(10)] as a reminder. Note the two forms of the nondimensionalized intensity given in Eqs. (5) and (6):

$$\frac{d\bar{I}^{(+)}}{d\bar{\chi}} = -\xi_1 \bar{I}^{(+)} + \xi_2 \bar{I}^{(-)} + \xi_3 \bar{I}_b(T), \quad (3)$$

$$-\frac{d\bar{I}^{(+)}}{d\bar{X}} = -\xi_1 \bar{I}^{(+)} + \xi_2 \bar{I}^{(-)} + \xi_3 \bar{I}_b(T), \quad (4)$$

$$\bar{I} = \frac{I}{I_p(T_o)} \text{ (for envelope emission problem and flame problem),} \quad (5)$$

$$\bar{I} = \frac{I}{I_0} \text{ (for envelope absorption/reflection/transmission problem)}, \quad (6)$$

$$\bar{X} = \frac{X}{L}, \quad (7)$$

$$\xi_1 = 2t(\rho B + \alpha), \quad (8)$$

$$\xi_2 = 2t(\rho B), \quad (9)$$

$$\xi_3 = 2t(\epsilon), \quad (10)$$

$$t = 1.5 f_\vee L Q_e / D. \quad (11)$$

For the two oxide envelope subproblems, the appropriate optical properties to apply to Eqs. (3)-(11) are the oxide particle properties. These are given as ϵ_{ox} ($= \alpha_{ox}$, one minus albedo), ρ_{ox} (albedo), D_{ox} , B_{ox} , L_e , and $f_{v,e}$. The parameter B is the semisotropic model back-scattering fraction. The boundary conditions for the envelope emission problem (subproblem one) are $\bar{I}^{(+)}(0) = \bar{I}^{(+)}(1) = 0$ with $T = T_o$, and the results are given by $\epsilon_e = \bar{I}^{(+)}(0) = \bar{I}^{(+)}(1)$. For the envelope absorption, reflection, and transmission problem (subproblem two), $T = 0.0K$ and the boundary conditions are $\bar{I}^{(+)}(0) = 1$ and $\bar{I}^{(+)}(1) = 0$. The results are given as $\tau_e = \bar{I}^{(+)}(1)$, $\rho_e = \bar{I}^{(+)}(0)$, and $\alpha_e = 1 - \tau_e - \rho_e$.

For the flame emission problem, the appropriate optical properties applied to Eqs. (3)-(11) are the droplet properties α_d , ϵ_d , ρ_d , D_d , B_d , L_f , and f_{ref} . The first three of these properties are given in terms of the oxide envelope properties and the aluminum droplet surface properties by Eqs. (12)-(14) which account for multiple reflections between the molten aluminum droplet and the oxide

environment surrounding it:

$$\epsilon_d = \epsilon_e + \epsilon_e \tau_e \left(\frac{\rho_s}{1 - \rho_s \rho_e} \right) \quad (I)$$

(II)

$$+ \epsilon_s \tau_e \left(\frac{1}{1 - \rho_s \rho_e} \right) \left(\frac{I_b(T_s)}{I_b(T_o)} \right), \quad (12)$$

(III)

$$\rho_d = \rho_e + \tau_e^2 \left(\frac{\rho_s}{1 - \rho_s \rho_e} \right), \quad (13)$$

$$\alpha_d = 1 - \rho_d. \quad (14)$$

Upper and lower limits for the mean aluminum droplet diameter were estimated from a correlation by Nickerson et al. [9] to be 350 μm ($r = 0.25 \text{ cm/s}$) and 100 μm (0.80 cm/s):

$$D_d = \frac{89}{r Y_{AP}}. \quad (15)$$

In Eq. (15) D_d is the droplet diameter (in μm), r is the burn rate (in cm/s), and Y_{AP} is the AP mass fraction.

The droplet volume fraction in the flame was estimated from mass and momentum balances on the aluminum and surrounding "matrix" (matrix means the AP combustion gases above the propellant surface and solid AP below the surface). The mass balances assume negligibly small Al fraction (which was satisfied in this work) resulting in Eq. (16):

$$f_{v,f} \approx \left[\frac{P Y_{Al}}{VR \eta_{Al} (\bar{R}/M_g) T_g} \right]. \quad (16)$$

Equation (16) indicates that the aluminum droplet volume fraction in the flame ($f_{v,f}$) was proportional to the pressure (P) and the aluminum mass fraction (Y_{Al}) in the samples. M_g is the molecular weight of the combustion gases for a sample containing no aluminum. \bar{R} is the universal gas constant, and η_{Al} is the density of the aluminum droplets. T_g is the adiabatic flame temperature of the nonaluminized AP combustion gases, modified

to account for the energy required to raise the aluminum to 2320K. In Eq. (16), VR is the ratio of the droplet velocity to the velocity of the combustion gases, which is estimated from a two-phase momentum balance [21] to be 0.07 at the point of measurement 0.2 mm above the surface for 350 μm agglomerates and 0.20 for 100 μm droplets.

The formulation of the flame emission problem is completed by applying the boundary conditions $\bar{I}^{(+)}(0) = \bar{I}^{(-)}(1) = 0$ and noting that $T = T_o$. The oxide boiling point temperature (T_o) is taken from Glassman's data [5, 7]:

$$T_o(P) = 250.365 \ln(P) + 876.84. \quad (17)$$

In Eq. (17) P is in pascals and T is in degrees K. The solution in terms of the flame emissivity is then $\epsilon_f = \bar{I}^{(-)}(0) = \bar{I}^{(+)}(1)$.

The respective solutions to the two primary problems are given below:

$$\tau_e = \frac{\xi}{(\xi_1 \sinh \xi + \xi \cosh \xi)}, \quad (18)$$

$$\rho_e = \frac{\xi_2 \sinh \xi}{(\xi_1 \sinh \xi + \xi \cosh \xi)}, \quad (19)$$

$$\epsilon_e = \frac{(\xi \cosh \xi + (\xi_1 - \xi_2) \sinh \xi - \xi)}{(\xi_1 \sinh \xi + \xi \cosh \xi)}, \quad (20)$$

$$\epsilon_f = \frac{\xi_3 (\xi \cosh \xi + (\xi_1 - \xi_2) \sinh \xi - \xi)}{(\xi_1 - \xi_2)(\xi_1 \sinh \xi + \xi \cosh \xi)}, \quad (21)$$

$$\xi = (\xi_1^2 - \xi_2^2)^{1/2}. \quad (22)$$

Since the layer is assumed to be isothermal and the droplet surface diffuse, Eqs. (18)-(20) demonstrate that Kirchhoff's law applies to the envelope ($\epsilon_e = \alpha_e = 1 - \tau_e - \rho_e$). In addition, Eqs. (8)-(11) indicate that the envelope properties ϵ_e , ρ_e , and τ_e are functions of the three dimensionless parameters ϵ_{ov} , B_{ov} , and $t_e = 1.5 Q_{e,ov} f_{v,e} L_e / D_{ov}$ (the envelope optical thickness) in which $f_{v,e}$ and D_{ov} are the oxide particle volume fraction and effective optical diameter, respectively.

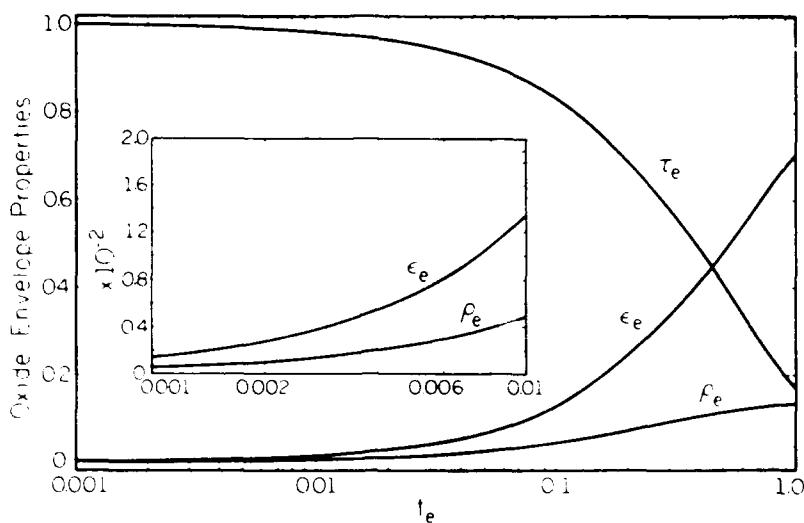


Fig. 3. Oxide particle envelope emissivity/absorptivity, reflectivity, and transmissivity.

4. RESULTS OF PARAMETRIC STUDY OF RADIATIVE TRANSFER IN A SINGLE BURNING ALUMINUM DROPLET

The predicted variations in the oxide envelope properties ϵ_e ($= \alpha_e$), ρ_e , and τ_e relative to variations in the envelope optical thickness are shown in Fig. 3. These results are for $B_{ox} = 0.3$ and $\epsilon_{ox} = 0.45$ [11]. A detail of the very thin optical depth region is also included in the same figure.

The net intensity $I_e(x = 0)$ from the oxide envelope toward the molten aluminum droplet (the net radiant heat feedback) and the net intensity emitted by the envelope/droplet system $I_e(x = L_e)$ into the surroundings are given in Figs. 4 and 5 for the following assumed parameters: $T_c = 2500\text{K}$, $T_e = 4500\text{K}$, $B_{ox} = 0.3$, and $\epsilon_{ox} = 0.45$. These

intensities are plotted as a function of the droplet surface emissivity for several values of the envelope optical thickness. The corresponding fluxes may be obtained by multiplying these terms by a factor of π . Note that for small optical thicknesses (Fig. 4), the net radiative feedback, $I_e(x = 0)$, is negative and steadily decreases as the droplet surface emissivity increases (perhaps due to oxide condensation on the droplet surface). This indicates net transfer from the aluminum droplet to the transmissive oxide envelope (Fig. 3). Thus, an optically thin envelope may result in excessive amount of radiant energy loss from the droplet which could conceivably cause the droplet to be extinguished.

Another point of interest is the reduction in the slope of the outward intensity leaving the droplet

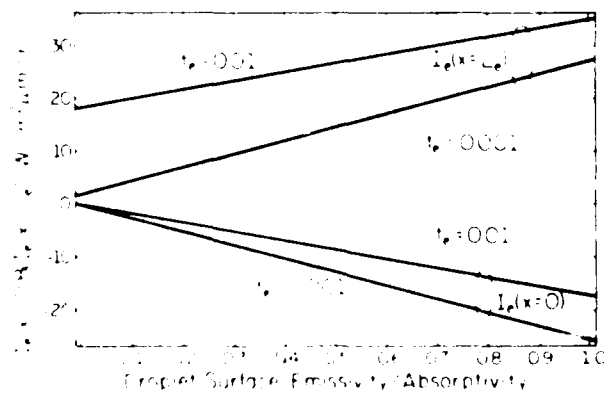


Fig. 4. Effect of droplet surface emissivity/absorptivity on droplet radiative transfer for optically thin envelope

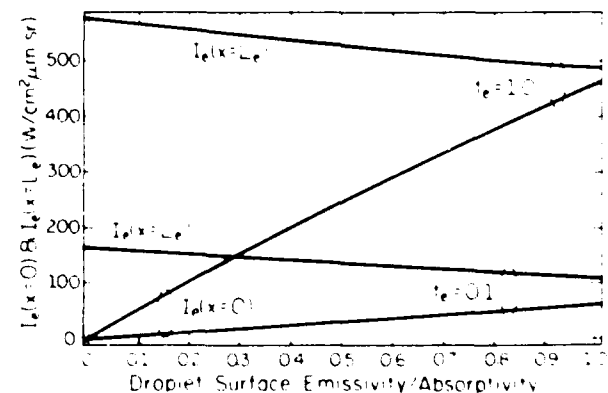


Fig. 5. Effect of droplet surface emissivity/absorptivity on droplet radiative transfer for optically intermediate envelope

TABLE 1
Percent Contribution to Total Droplet/Envelope System Emission Loss^a

ϵ_s	$t_e = 0.001$			$t_e = 0.01$			$t_e = 0.1$			$t_e = 1.0$		
	I	II	III	I	II	III	I	II	III	I	II	III
0.05	29.6	28.1	42.3	48.1	45.1	6.8	54.5	44.8	0.7	84.7	15.3	0.0
0.1	21.0	18.9	60.1	46.1	40.9	13.1	55.4	43.1	1.5	85.4	14.5	0.1
0.5	6.3	3.2	90.5	34.1	16.9	48.7	64.3	27.3	8.4	91.4	8.1	0.5
0.6	5.4	2.2	92.4	32.3	12.7	54.9	66.9	22.7	10.4	92.9	6.5	0.6
0.7	4.7	1.4	93.9	30.5	9.0	60.5	69.8	17.6	12.6	94.5	4.9	0.6
1.0	3.4	0.0	96.6	26.1	0.0	73.9	79.7	0.0	20.3	99.1	0.0	0.9

^a I = direct oxide layer emission; II = reflected oxide layer emission; III = transmitted droplet surface emission.

envelope system [$I_e(x = L_e)$] as the envelope optical thickness is increased. This change is particularly evident when the outward intensity for $t_e = 0.01$ in Fig. 4 is compared to the outward intensity for $t_e = 0.1$ in Fig. 5. Here, the slope is found to change from a positive value to a negative value. A negative slope for the outward intensity from the droplet/envelope system as a function of the droplet surface emissivity/absorptivity (Fig. 4) indicates that the droplet reflection of the inward emission from the envelope [term II in Eq. (2)] decreases more than the droplet emission [term III in Eq. (2)] increases. In other words, for values of t_e term II of Eq. (2) decreases a greater amount than term III increases when the droplet surface emissivity/absorptivity is increased. This effect can also be seen in Table 1 where a comparison of the relative contributions of terms I, II, and III to the net emission from the droplet/envelope system (Fig. 1) are given.

Table 1 helps to show the progressive dominance of the envelope's contribution to the total emission from the droplet/envelope system as t_e is increased. On the other hand, it can also be seen that the droplets dominate the net emission from the system when the envelope optical depth is near 0.001. The contributions from the envelope become significant for an optical depth of 0.01 and begin to dominate when the optical depth is only 0.1. This is a result of the magnitude of the oxide particle temperature (4500K) in the envelope relative to the aluminum droplet temperature

(2500K) and the nonlinear behavior of radiant emission with temperature. The envelope dominates emission from the system when $t_e = 1.0$. In addition, at $t_e = 1.0$, the net radiative feedback from the envelope to the droplet is quite sensitive to the droplet absorptivity and becomes very large as the droplet surface absorptivity approaches 1.0 (Fig. 5).

As the parametric results indicate, the droplet burning behavior can be significantly influenced by radiative transfer, depending on the actual magnitude of the radiative properties. To estimate the magnitude of these properties spectral intensity measurements were made as described in the next section.

5. SPECTRAL INTENSITY MEASUREMENTS

The equipment used to measure spectral intensity consisted of a combustion window bomb with nitrogen purge gas, a photomultiplier tube (PMT) detector, and a video recording system. These components and the entire system are shown in a schematic diagram in Fig. 6. The PMT signal was calibrated using a spectral irradiance ($SI = I \Delta\Omega$) standard and a flat diffuse reflective surface of known spectral reflectivity to obtain an absolute reference intensity I_{ref} in $\text{W}/\text{cm}^2 \mu\text{m sr}$. A conversion was performed to obtain the desired intensity I_{ref} from the known quantity SI .

The radiant energy per unit perpendicular area,

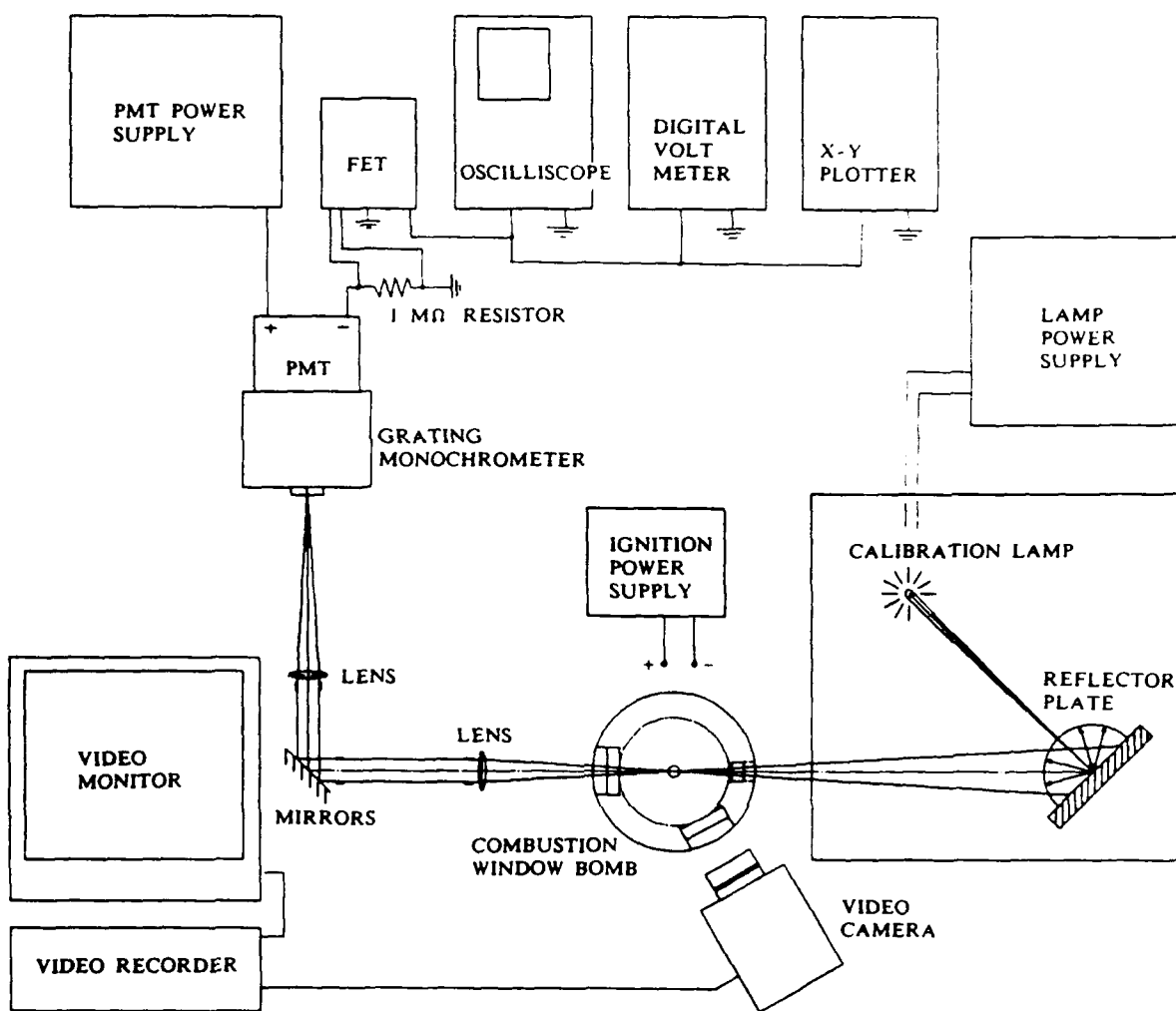


Fig. 6. Schematic diagram of experiment apparatus.

time, and wavelength incident on the reflector plate a distance of L (in cm) from the lamp is given by the expression (SI in $\text{W}/\text{cm}^2 \text{ nm}$) $(50/L)^2 = I/\Delta\Omega$ where 50 is the calibration distance (in cm) of the lamp. The flux reflected from the plate is then $\rho(SI)(50/L)^2$ where ρ is the spectral directional-hemispherical reflectivity. The reflected reference intensity is then given by

$$I_{\text{ref}} = \frac{\rho(SI)(50/L)^2}{\pi}. \quad (23)$$

As indicated in Fig. 6, the PMT signal was recorded by a storage oscilloscope as well as an $X-Y$ plotter. A digital voltmeter was also included for periodically reestablishing the reference PMT signal from the lamp intensity. Figure 6 also shows the additional optics required to image the

vertical monochromator entrance slit (0.4 mm width) as a horizontal slit (1 : 1) in the center of the sample flame. A grating monochromator was used to separate out the spectral intensity emitted at 790 nm. A bandpass filter positioned at the opening of the monochromator eliminated the additional detection of higher order wavelengths by the PMT. The 790 nm wavelength was chosen because it is in the spectral region near the emission peak for the flame temperatures involved, and because it is away from any strong gaseous emission lines of the product species. It was then assumed that the intensity emitted from the combustion flame was due to spectrally continuous emission from the particles within the flame.

A cross-sectional drawing of the widow bomb has been included in Fig. 7. The pellets were aligned with the axis of the bomb and positioned

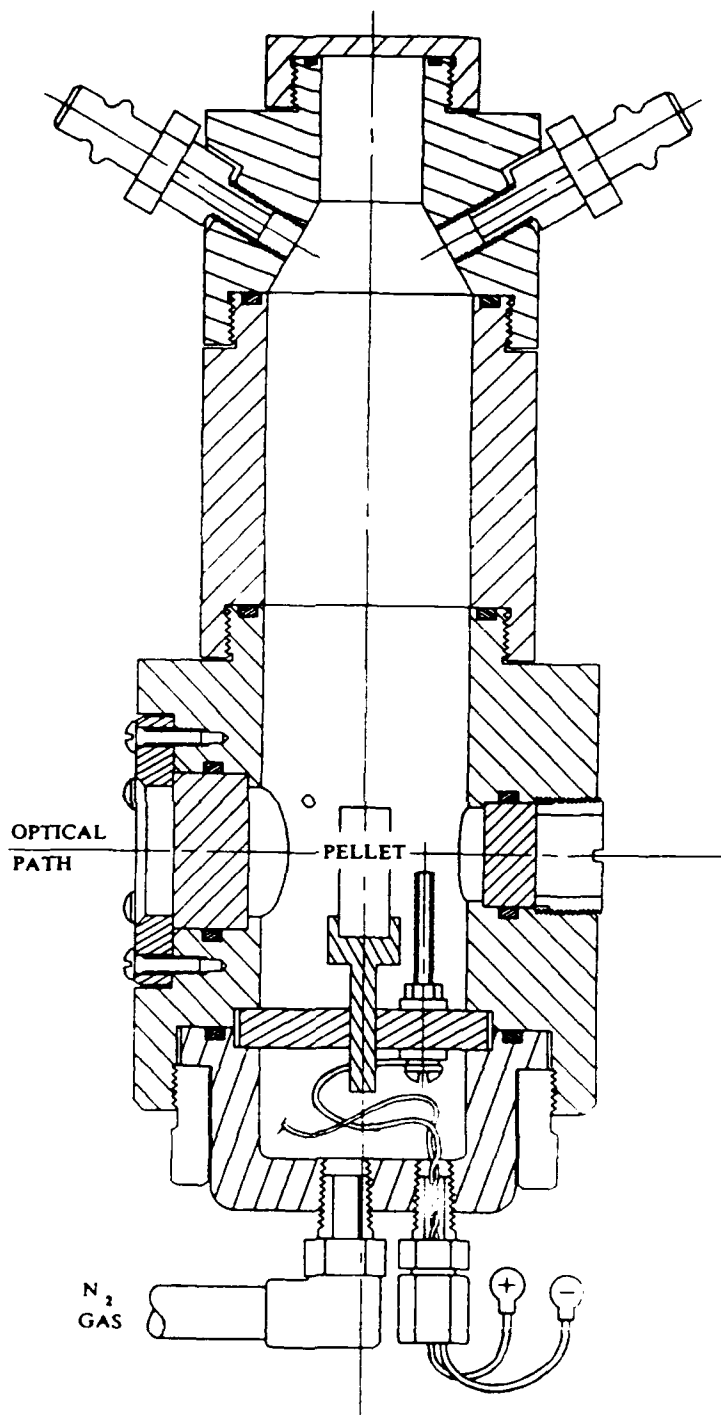


Fig. 7. Cross section of a window bomb.

with the top surface of the pellet well above the optical path of the detector. This assured that the large intensity spike which occurred during sample ignition was not confused with the emission from the actual burning of the pellet. The samples were ignited by a pyrotechnic igniter paste and a hot nichrome wire. The bomb was purged during

and after sample combustion with cold nitrogen gas. The cold gas did not affect the combustion process at the pellet surface where the peak intensity was measured. The time averaged sample burn rate was determined by recording the deflagration process on a video recorder at 30 frames per second and later measuring the pellet surface

regression distance. Typical burn rates were from 0.3 to 0.6 cm/s and pellet lengths were between 1 and 2 cm.

The pressed pellets used in this study were made using nominal 100 μm propellant grade AP and ground semispherical aluminum with a mean diameter of approximately 15 μm . The AP and aluminum were mixed together by hand using a mortar and pestle. Photomicrographs of the mixture revealed that the mean diameter of the AP was closer to 90 μm after mixing. The mixture was poured into a 1/2 in. (1.27 cm) diameter single ram pressing die and held at a compaction pressure of 2000 psi (13.7 MPa) for 2 min.

6. COMPARISON OF MODEL WITH INTENSITY MEASUREMENTS

The intensity measurements and the comparison of these results with the radiative transfer model will now be discussed. The measured intensities from the AP/Al pellet flames represent peak emission values. The point of maximum emission was found to lie very close to the burning surface of the pellets and extended over a relatively narrow region of the flame (0.2 mm to 0.4 mm, depending on pressure and aluminum content). For example, the typical band midpoint for the peak flame emission was approximately 0.2 mm above the burning pellet surface for a pressure of 1000 psia (6.87 MPa) and an aluminum mass fraction of 6.0%. A decrease in the pressure or aluminum mass fraction tended to move the point of maximum emission slightly further away from the pellet surface as well as broaden the band over which it occurred. For all pressures and aluminum fractions, however, this maximum emission zone corresponded approximately to the volume of spatial resolution of 0.4 mm determined by the monochromator entrance slit. Following the peak emission point, the intensity rapidly decreased as the aluminum droplets were consumed and the relatively cold AP combustion gases (near 1240K) began to be clouded by scattering, nonemitting solid Al_2O_3 particles. The flame intensity eventually dropped to zero as the cold nitrogen purge gas mixed with the final combustion products.

The range of the peak spectral intensities

TABLE 2

Range of Measured Intensities from Pressed AP/Al Pellets

% Al	Pressure (psi/MPa)	I_* (W cm^{-2} μm sr)	T_b (K)	AFT (K) ^a
0.5	750/5.1	1.47 (min.)	1789	1502
	1100/7.6	8.30 (max.)	2156	
1.0	820/5.6	2.37 (min.)	1877	1598
	1000/6.9	9.15 (max.)	2181	
1.5	900/6.2	8.73 (min.)	2169	1694
	950/6.5	10.20 (max.)	2246	
2.0	650/4.5	6.55 (min.)	2097	1787
	940/6.5	12.10 (max.)	2256	
4.0	800/5.5	12.60 (min.)	2269	2146
	1000/6.9	32.30 (max.)	2455	
6.0	750/5.1	2.040 (min.)	2412	2450
	930/6.4	36.30 (max.)	2612	

^a Adiabatic flame temperature at 1000 psi (6.9 MPa).

measured during the combustion of the AP/Al pellets can be seen in Table 2. As Table 2 indicates, the intensity increases with increasing aluminum mass fraction. There is also a tendency for the intensity to increase with pressure. The equivalent blackbody temperatures range from 1789K to 2612K. These temperatures are in excess of the corresponding adiabatic flame temperatures (AFT) assuming equilibrium at 6.87 MPa (also given in Table 2), and the local AP combustion gas temperature. This can be attributed to radiation emitted by the flame envelope surrounding each molten aluminum droplet and emission from the droplet surface, as discussed in the model.

In Fig. 8 model predictions are compared to the measured intensities as a function of pressure and aluminum mass fraction. The parameters used in the model predictions are given in Table 3. Each combination of parameters resulted in an equally satisfactory fit of the data. Other parameters not listed in Table 3 which were used but not varied were $T_g = 1240\text{K}$ and $B_d = 0.5$. The strategy behind the selection of model parameters was to vary the ones which are known to some degree between the possible extremes and let the radiative transfer model determine the rest. The former group (and the associated extreme values) consisted of the droplet-to-gas velocity ratio, VR

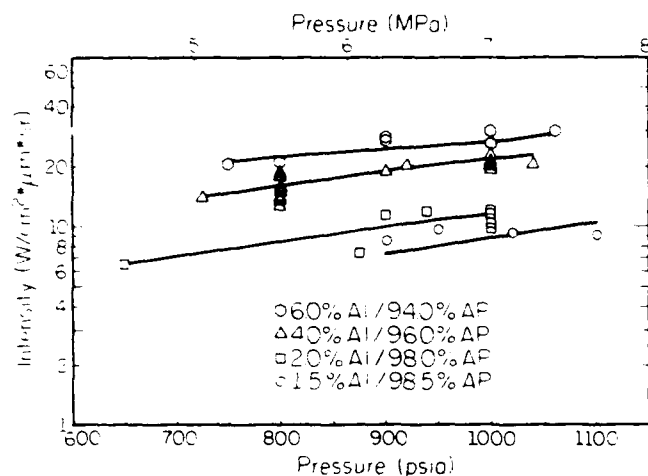


Fig. 8. Comparison of predicted and measured AP/Al pellet flame intensity.

(0.07–0.2), droplet temperature, T_s (2320–3800K), droplet surface emissivity, ϵ_s (0.1–0.6), and oxide emissivity, ϵ_{ox} (0.45–1.0). Combinations of these extreme values were used to construct a test matrix. The optical depth parameter t_e was then determined by fitting the experimental data. The droplet properties, ϵ_d , α_d , and ρ_d , which are uniquely determined by the parameters

TABLE 3

Optical Properties of Burning Aluminum Droplets

	$T_s = 2320\text{K}$	$T_s = 3800\text{K}$	
ϵ_s ^a	0.10	0.60	0.1
$t_e(\epsilon_{ox} = 0.45)$	0.025	0.033	0.0030
$t_e(\epsilon_{ox} = 1.0)$	0.011	0.015	0.0020
ρ_d	0.86	0.38	0.90
α_d	0.14	0.62	0.10
$\epsilon_d(T_s)$	2.5	2.9	0.11

$T_s = 2320\text{K}$

ϵ_s ^b	0.1	0.6
$t_e(\epsilon_{ox} = 0.45)$	0.020	0.026
$t_e(\epsilon_{ox} = 1.0)$	0.013	0.017
ρ_d	0.87	0.39
α_d	0.13	0.61
$\epsilon_d(T_s)$	2.0	2.4

^a VR = 0.07, $D_d = 350 \mu\text{m}$.

^b VR = 0.2, $D_d = 100 \mu\text{m}$.

just described according to Eqs. (12)–(14), are also listed in Table 3.

The results of Table 3 indicate that the envelope is optically thin (≤ 0.03) for all parameter combinations. This simplification leads to the following set of equations for the droplet radiative properties:

$$\epsilon_d \cong 2t_e\epsilon_{ox} + 2t_e\epsilon_{ox}\rho_s + \epsilon_s I_b(T_s)/I_b(T_o), \quad (24)$$

(I)

(II)

(III)

$$\rho_d \cong \rho_s, \quad (25)$$

$$\alpha_d \cong \alpha_s. \quad (26)$$

The factor 2 in Eq. (24) accounts for the mean obliquity of the rays along a slant path through the envelope surrounding the spherical droplets. The appearance of the product $t_e\epsilon_{ox}$ in Eq. (24) indicates that the determined value of t_e is inversely proportional to the assumed value of ϵ_{ox} . Thus, scattering and absorption by the oxide-laden flame envelope can probably be neglected.

The condition of optically thin envelope does not mean, however, that emission by the envelope is necessarily negligible (as indicated also by high-speed combustion photography results). The low droplet temperature ($T_s = 2320\text{K}$) results of Table 3 can be taken as an example of this. As ϵ_s is increased from 0.1 to 0.6 (ρ_s decreases from 0.9 to 0.4) the envelope optical thickness necessary to match the measured intensities increases by about 30%. That is, the increase in the Al emission (contribution III) is overwhelmed by the decrease in reflection (contribution II) and an increase in envelope emission (i.e., optical thickness) is required. The extremely high temperature of the envelope in this case is compensating for its low optical thickness, and envelope emission is significant.

At the higher droplet temperature ($T_s = 3800\text{K}$) the situation is reversed from the low temperature case. Aluminum surface emission at 3800K is so high that even for $\epsilon_s = 0.1$, t_e must be reduced to 0.0030 to match the data. Droplet surface emission is strong in this case and envelope emission is relatively weak. Surface emission is so strong, in fact, that the data cannot be matched for assumed ϵ_s values much above 0.1. Since high-speed

photography results indicate that the envelope is a significant source of emission, and fitting the model at $T_s = 3800\text{K}$ requires a negligible envelope emission contribution, this would indicate that the burning droplet surface temperature must actually be somewhat below the boiling point.

Table 3 also indicates that the sensitivity of the results on assumed droplet size is rather weak. For a rather large variation in D_d (350–100 μm) the variation in t_e and ϵ_d is seen to be relatively small, about 20–25 %. The reason the determined properties are so insensitive to the assumed droplet diameter can be seen from Eqs. (11) and (16). The flame optical thickness is proportional to $f_{v,f}/D_d$. The volume fraction of droplets is inversely proportional to VR which is proportional (approximately) to $D_d^{-0.83}$. This latter relation follows from the calculated VR values of 0.07 and 0.2 corresponding to $D_d = 350$ and 100 μm , respectively. Thus $f_{v,f}/D_d$ is proportional to $D_d^{-0.17}$. In other words, the increased specific surface area and optical opacity of smaller droplets is compensated for by a higher velocity and reduced volume fraction indicating that the measured flame intensity is relatively insensitive to assumed droplet diameter.

7. CONCLUSIONS

Based on comparison between spectral (790 nm) intensity measurements and a two-part radiative transfer model, the following conclusions regarding the optical properties of burning aluminum droplets are made:

1. The burning droplet temperature is somewhat below the metal boiling point.
2. The optical thickness of the $\text{Al}/\text{Al}_2\text{O}_3$ flame envelope surrounding the aluminum droplets is small (on the order of 10^{-2}). A more exact determination of this parameter would require more exact knowledge of the droplet temperature and the emissivity of the submicron molten Al_2O_3 smoke particles in the envelope.
3. Scattering and absorption of radiation by the envelope cloud may be neglected in analyzing

radiative transfer in burning aluminum droplets, but emission may not.

4. Droplet surface emission [term III Eq. (2)] and reflection (of inward envelope emission—term II) are significant and should be included in analyzing the radiative transfer.
5. The spectral emissivity (790 nm) of the droplet/envelope system based on droplet temperature is approximately 0.1 for $T_s = 3800\text{K}$ or 2.0 for $T_s = 2320\text{K}$.
6. Given accurate droplet properties (T_s and ϵ_d) the total (spectrally integrated) properties of the burning droplet system could be estimated from Eqs. (24)–(26).

It should be recognized that the quantitative conclusions drawn here are limited somewhat by the one-dimensional radiative transfer model involved. Certainly a higher order, multidimensional transfer model would lead to somewhat different values for the parameters than those reported here but the essence of the findings would be the same. The extreme complexity of such an undertaking, however, places it beyond the scope of this work.

NOMENCLATURE

AFT	adiabatic flame temperature
AP	ammonium perchlorate
Al	aluminum
B	back-scatter fraction
$D_{\text{ox or } d}$	oxide (ox) or droplet (d) particle diameter
$f_{v,e \text{ or } v,f}$	oxide particle volume fraction in envelope (e) or aluminum droplet volume fraction in flame (f)
I	intensity of radiation ($\text{W}/\text{cm}^2 \mu\text{m sr}$)
$L_{e \text{ or } f}$	thickness of oxide particle envelope or propellant flame
M_g	molecular weight of AP combustion gases = 28
P	pressure
Q_c	extinction efficiency
r	linear burn rate of pellet
t	optical thickness
VR	velocity ratio of droplets to gas
Y	mass fraction

Greek Letters

α	absorptivity (one minus albedo for particles)
ϵ	emissivity
λ	wavelength
ρ	reflectivity (albedo for particles)
τ	transmissivity
η	density
Ω	solid angle

Subscripts

a	absorption
b	blackbody
d	droplet of burning aluminum, including surrounding oxide envelope
e	envelope or extinction
f	flame comprised of burning aluminum droplets
g	gases from combustion of AP
ox	oxide particles
s	surface of molten aluminum droplet or scattering

Superscripts

$+$	forward direction
$-$	backward direction

Support for this work from the National Science Foundation (Grant CBT 83-51243), Morton Thiokol Inc./Wasatch Division, and the Office of Naval Research (Contract N00014-87-K-0547) is gratefully acknowledged.

REFERENCES

- Price, E. W., in *Fundamentals of Solid Propellant Combustion*, Progress in Astronautics and Aeronautics Series (K. K. Kuo and M. Summerfield, Eds.), AIAA, New York, Vol. 90, 1984, pp. 479-514.
- Miller, R. R., Donohue, M. T., Yount, R. A., and Martin, J. R., AFRPL-TR-78-14, April 1981.
- Schmidt, W. G., Lovine, R. L., and Poynter, R. C., AFRPL-TR-81-19, April 1981.
- Brewster, M. Q., and Patel, R., *J. of Heat Transfer* 109:179-184 (1987).
- Glassman, I., *Solid Propellant Rocket Research*, Progress in Astronautics and Rocketry Series (M. Summerfield, Ed.), Academic Press, New York, Vol. 1, 1960, pp. 253-258.
- Brzustowski, T. A., and Glassman, I., *Heterogeneous Combustion*, Progress in Astronautics Series (H. G. Wolfhard, I. Glassman, and L. Green, Jr., Eds.) AIAA, New York, Vol. 15, 1964, pp. 41-47.
- Micheli, P. L., and Schmidt, W. G., AFRPL-TR-77-29, Dec. 1977.
- Wilson, R. P., and Williams, F. A., *Thirteenth Symposium (International) on Combustion*, The Combustion Institute, Pittsburgh, 1971, pp. 833-845.
- Nickerson, G. R., Coats, D. E., Hermans, R. W., and Lamberdy, J. T., Vols. 1-5, AFRPL-TR-83-036, Sept. 1984.
- Nir, E. C., *Thirteenth Symposium (International) on Combustion*, The Combustion Institute, Pittsburgh, 1971, pp. 1091-1024.
- Parry, D. L., and Brewster, M. Q., Paper AIAA87-1582, presented at 22nd AIAA Conference, Honolulu.
- Konopka, W. L., Reed, R. A., and Calia, V. S., *Progress in Astronautics and Aeronautics* 91:180-197 (1984).
- Grigorev, V. G., Zarko, V. E., and Kutsenogii, K. P., *Combustion, Explosion, and Shock Waves* 17:245-250 (1981).
- Comins, N. R., *Philosophical Magazine* 25:817-831 (1972).
- Miller, J. C., *Philosophical Magazine* 20:1115-1132 (1969).
- Chan, P. W., Chan, Y. W., and Ng, H. S., *Physics Letters* A61:151-153 (1977).
- Walter, W. T., Solimene, N., Park, K., Kim, T. H., and Mukherjee, K., in *Lasers in Metallurgy* (Mukherjee and Mazumder, Eds.), The Metallurgical Society of AIME, 1981.
- Brewster, M. Q., *Int. Heat Transfer Conference* 2:741-746 (1986).
- Siegel, R., and Howell, J., *Thermal Radiation Heat Transfer*, McGraw-Hill, New York, 1983.
- Brewster, M. Q., *Journal of Heat Transfer* 108:710-713 (1986).
- Brewster, M. Q., and Parry, D. L., presented at WSS-The Combustion Institute, April 1987; *Journal of Thermophysics and Heat Transfer*, Jan. 1988.

Received 7 May 1987; revised 29 September 1987